DEVELOPMENT OF CONTINUUM DAMAGE MECHANICS MODELS TO PREDICT THE CREEP DEFORMATION AND FAILURE OF HIGH TEMPERATURE STRUCTURES.

by

Frank Richard Hall B.Eng.(Hons).

A thesis submitted to the
University of Sheffield for the
degree of Doctor of Philosophy.

Department of Mechanical and Process Engineering,
The University of Sheffield.

February, 1990.

'Let us now praise famous men '--

Men of little showing—

For their work continueth,

And their work continueth,

Broad and deep continueth,

Greater than their knowing!

Contents.

Acknowledgements.

Many thanks to my supervisor Prof.D.R.Hayhurst, for his enthusiasm, encouragement and for our usefull discussions; and, to John Makin (Technician) who assisted me in my laboratory investigations.

I acknowledge the financial support of the Science and Engineering Research Council.

Finally, mention is made of the Central Electricity Generating Board for providing valuable creep data and photographs from their tests on welds.

Declaration.

This thesis is based on research work carried out by the author, in the Department of Mechanical and Process Engineering at the University of Sheffield. The content is original except where specific reference is made to the work of other researchers.

No part of this work has been submitted to any other University for a degree.

F.Richard Hall,

February, 1990.

Summary.

The use of classical creep continuum damage mechanics, constitutive and damage equations is restricted, to model certain types of creep deformation and fracture mechanisms, under isothermal conditions; and, to extend their predictive capabilities for a wider range of problems they have to be modified. The constitutive and damage equations are modified to represent the bi-linear, log. stress vs. log. rupture, and the log. stress vs. minimum strain rate, characteristics of materials; so that the change in material behaviour, as a mechanism change occurs, is represented in the constitutive model, by a change in the slope of these characteristic lines.

Uni-axial creep tests of as-cast (OFHC) Copper have been performed at $150°C$, $250°C$ and $500°C$; and, an anisothermal constitutive model has been developed for the temperature range $150°C$ to $500°C$, which highlights how the constitutive equations may be modified, to model creep behaviour under varying temperature conditions. The model predictions are in good agreement with the test results.

A compact tension specimen has been studied, which has shown the importance of modelling the effects on rupture, of the high tri-axial stress-state present at the crack-tip, which accelerates void growth. Modified constitutive equations, have been used to model the mechanism of constrained cavity growth, and has enabled improved damage distribution and lifetime predictions to be obtained for the compact tension specimen, similar to those expected from experimental tests.

Non-local damage techniques are developed to model the effects of grain size characteristic dimension, on the failure of large and small cracked tension specimens. Non-local damage techniques are shown to be necessary to give accurate, physically related, finite element solutions.

Suitably modified constitutive and damage rate equations are used to model the high temperature failure of a circumferential weld, in a thick steam-pipe, operating at a constant temperature and pressure. The models developed predict, the growth of damage in certain microstructural regions of the weld, and the lifetime of the component; which are observed to be in close agreement with the reults from a full-size pressure vessel tests.

It will be shown that it is essential to use creep constitutive and damage equations in computer models, which accurately represent the underlying physics of

the predominant creep mechanisms present.

The implications of the research work on future computer modelling and on design are discussed.

Introduction.

The earliest observations of the phenomenon of creep must have been made in furnaces and steam boilers or in the processes of the blacksmith's art. Early boiler and furnace components, when they became too deformed and/or cracked to function properly, were simply replaced. As the admission temperature of steam power plant increased towards the end of the 19th century, engineers and scientists started to investigate the influence of temperature on the behaviour of structural metals. In 1910, E.N. da Costa Andrade [1] observed the true character of metallic creep. With the advent of superheated steam and the use of steam turbines operating at still higher temperatures to give improved thermal efficiency, creep deformations became a problem for safety. This caused increased research activity. Metallurgists endeavoured to understand the microstructural mechanics of creep and to develop new creep resistant alloys; whilst engineers and scientists formulated constitutive models to predict creep deformation and rupture, for use in design.

This thesis is concerned with the use and development of modern mathematical constitutive models to predict material deformation and failure in engineering structures. The development of the constitutive models must be in accordance with the observed microstructural mechanisms of creep deformation and creep failure, which are described in Chapter 1. The constitutive models are based on the notion of a damage state variable (ω), which is introduced in Chapter 2, through the theory of continuum damage mechanics. The damage state variable is in some sense a measure of the amount of internal voiding present within the material which increases monotonically with time. Damage is included in the constitutive model to provide a coupling with strain rates, as damage evolves then material softens and strain rates increase, during tertiary creep, until the material ultimately fails.

Having obained the isothermal creep strain rate constitutive and damage rate governing laws, Chapter 3 exemplifies how the creep constants in these two equations are obtained from uni-axial constant load creep tests. As-cast (OFHC)-Copper has been tested by the author for the wide temperature range of 150 to 500°C and the data is used is used to exemplify the prodcedure followed. An understanding of the controlling creep mechanisms in these tests; and, of the problems encountered when testing a variable grain sized material is then presented. The formulation of a non-

isothermal constitutive model is detailed; and, the predicted uni-axial creep curves for a range of test stresses and temperatures are given.

In Chapter 4 the creep continuum damage mechanics constitutive relationships are included within the finite element method to predict the variation of the creep strain, stress and damage fields with time, for engineering structures represented by a finite element mesh. The creep continuum damage finite element method is incorporated within a Fortran computer program called Damage-(XX), which has been developed over a period of approximately 15 years by a number of researchers including the recent contributions of the author. The use of the program has been enhanced by the author, by interfacing the program with the pre-processors FAMBUILD and FEMGEN, and the post-processors FAMRESULT and FEMVIEW. This has allowed the author to quickly generate finite element meshes using automatic mesh generation and to obtain colour contour plots as output from the program using modern post-processing facilities.

In Chapter 5 this computer program is used to model creep crack growth in a compact tension specimen. Problems have been encountered in modelling the failure of this particular specimen using finite element creep continuum damage mechanics. These problems are addressed and new procedures are used to try and ovecome them. A new constitutive model allowing for the effects of tri-axiality on rupture is developed in accordance with the physically based constitutive models and observations of Cocks and Ashby [66] and is shown to give improved predictions.

The continuum damage finite element method is modified in Chapter 6, using a non-local damage theory, where the local damage parameter is spatially averaged using the grain characteristic dimension of the material to predict grain size effects on the failure of cracked plate specimens. The non-local damage theory is important to restrict the localisation of the field variables, and to overcome the problems associated with spurious mesh refinement; with the aim of producing more physically related finite element solutions, through the characteristic material volume.

Chapter 7 discusses the metallurgy of weldments, the current codes used for the design of high temperature welded components and the recent research developments to improve design methodology. Chapters 8 is concerned with the particular application of the computer program Damage-(XX) to model the creep deformation

and failure of typical, circumferentially welded, thick-steam pipe. In the development of the computer model, various regions of the finite element mesh are assigned the creep properties of the weld metal; the heat affected zone material; and, the parent metal. The appropriate data having been collected from laboratory specimens prepared from the same material or simulated material having the same isolated microstructures. Representation of both the coarse and fine grained bainitic regions of the weld metal are included in the final weld model. Comparisons of the predicted damage distributions within the weldment of a circumferentially-welded cylindrical pressure vessel subjected to constant internal pressure under isothermal conditions, with the observed damaged regions are made and the predicted lifetime compared with the experimental lifetime.

Conclusions from the research work are made in Chapter 9; and, possible future developments of creep continuum damage mechanics finite element modelling are discussed in Chapter 10.

Chapter 1.

Creep Deformation And Failure In Metals And Alloys.

1.1 Introduction.

When a metal or alloy is subjected to a load at a constant temperature, above about 0.3 T_m, (where T_m is the absolute melting temperature of the metal or alloy), and its strain (extension) increases continuously with time, it is said to creep. To determine the creep curve of a metal, a constant load is applied to a tensile specimen at a constant temperature and the increase in strain across the gauge length of the specimen is measured with time. A typical creep curve is shown in Fig 1.1. Da Costa Andrade [1] first introduced the notion of dividing the creep curve into three regions, namely the primary, secondary and tertiary creep regions. The time independent elastic and plastic strain (ϵ_0) is obtained on initial loading the creep specimen and is usually subtracted from the creep curve to give the curve purely due to creep strain. Subsequent creep deformation during the primary creep region involves a gradual decrease of the creep strain rate (Fig 1.2). During primary creep the partial recovery or softening process competes against the increasing creep resistance of the material caused by strain hardening. The mechanism of cross-slip of dislocations, controls the partial recovery process (Section 1.2.1). Strain hardening is caused by the interaction between dislocations, forming dislocation tangles; hence the dislocations lock. Unlocked dislocation movement causes permanent deformation. For low temperatures (close to 0.3 T_m), and moderate stresses, primary creep is the predominant creep process. During the secondary creep region full recovery is obtained through the climb mechanism (Section 1.2.1). A balance now exists between strain hardening and recovery, giving a steady state creep rate (Fig 1.2). During the tertiary creep region the matérial undergoes increased strain rates (Fig 1.2) due to a reduction in the effective cross sectional area, because of the nucleation and growth of voids, forming cracks or necking or both. The creep specimen is said to fail when breakage occurs at time, t_f .

The sizes of primary, secondary or tertiary creep regions in the formation of

the creep curve are dependent on the material; and, the test temperature and the applied stress. All creep mechanisms are present at all times during the creep test, but only one deformation and one fracture mechanism predominates for a particular test temperature and stress level. The dominant mechanisms of material deformation and fracture can be observed from microsections of creep tested specimens, using electron and optical microscopes. Having identified the dominant creep mechanisms the correct, physically based, mathematical laws governing the material deformation and failure may be used in structural calculations.

What follows is a description of creep deformation mechanisms, followed by a description of creep fracture mechanisms and how the mechanisms pertaining to a particular material may be summarised in the form of Ashby deformation and fracture mechanism maps.

1.2 Mechanisms Of Creep Deformation In Metals And Alloys.

There are two main mechanisms involved with creep deformation. The first is called **Dislocation Creep**, in which the factor controlling the creep rate is the ability of dislocations to glide. The second is called **Diffusional Creep**, in which the factor controlling the creep rate is continuous annealing at high temperatures.

These two mechanisms are unavoidably interconnected, as they may both take place at the same time.

1.2.1 Dislocation Creep (giving power-law creep).

Dislocations [2,13] are caused by lattice irregularity at grain boundaries, at impurities or at larger interstitial atoms and other lattice defects. Whole planes of atoms, in crystallographic planes which are preferentially oriented relative to the shear forces, may move or slip through the propagation of a dislocation along the plane. This process requires much less energy than that required to move the whole plane of atoms at once. Dislocations may move from one slip plane to another, by the mechanism known as cross-slip, which allows dislocations a futher degree of freedom. In certain cases this may impede dislocation movement through dislocation interaction, causing dislocations to become entangled or locked. Dislocation motion

may also be arrested by obstacles such as second phase particles and inclusions. Diffusion of atoms can unlock dislocations from obstacles allowing them to climb and enabling further slip. This mechanism is termed the Climb Mechanism [3,13] and controls the dislocation creep process.

Dislocation creep may be represented by a secondary creep rate law, where the secondary creep strain rate is dependent on the applied stress raised to a power:

$$\dot{\epsilon}_s = B\sigma^n \qquad (1.1)$$

hence the term power-law creep. The power (n) is known as the creep exponent and usually has a value between 1 and 10. Equation (1.1) is also known as Norton's Law.

Harper-Dorn Creep, [4].

This mechanism is similar to that of dislocation creep, and occurs only at very low stress , where the creep strain rate becomes proportional to the applied stress (i.e. the creep exponent in (1.1) is $n = 1.0$). This is thought to occur only when the diffusional creep fields are suppressed by a large grain size, allowing climb controlled creep, with dislocation density which does not change with stress.

1.2.2 Diffusional Creep.

This involves the transport of atoms due to thermal activation within a material.

(i) Bulk Diffusion

This occurrs at high temperatures and relatively low stresses. Here the creep process is controlled by stress-directed atomic diffusion through the body or bulk of a metallic crystal (Fig 1.3). The stress changes the chemical potential of atoms at the surfaces of grains in a polycrystal. This causes vacancies to flow preferentially from grain boundaries under tensile stress to those under compressive stress. At the same time atoms flow in the opposite direction, which stack up on the tensile stress boundaries causing grain elongation. This creep mechanism is also called Nabarro-Herring creep [5,6]. As the bulk diffusion path is dependent on grain size, the creep rate is also dependent on grain size for high temperature diffusion. Usually for most materials, creep rate is found to be proportional to ($1/d^2$), where d is the grain diameter.

(ii) Grain Boundary Diffusion.

At higher temperatures bulk diffusion is short circuited by diffusion along a grain boundary or a dislocation core. The grain boundary acts as a planar channel about two atoms wide, with a high local diffusion rate, sometimes 10^6 times greater than in the bulk of the crystal. Grain boundary diffusion is also called Coble creep [7].

1.2.3 Ashby Deformation Mechanism Maps.

A practical way of illustrating the mechanistic behaviour of creeping materials is with the deformation mechanism maps of Ashby et al [8,9]. These diagrams show distinct areas in stress vs. temperature space, where a particular creep mechanism is dominant over all others. A typical Ashby mechanism map is that for pure nickel shown in Fig.1.4. The normalised tensile stress (σ/μ) or the shear stress (σ_s/μ) is used as ordinate, where μ is the shear modulus and the homologous temperature (T/T_m) is used as abscissa. The maps are constructed on the basis of empirical microstructural observations and data from uni-axial creep tests. Theoretical calculations are also used by equating constitutive equations of different mechanisms and solving these for stress as a function of temperature, to give the positions of the boundaries separating dominant mechanism map areas. Contours of constant strain rate are shown on deformation mechanism maps, which are useful in both engineering and experimental design.

Grain Boundary Sliding.

Whilst grain boundary sliding is an observed creep process, it does not contribute significantly to steady state creep, but it is important in the initiation of intergranular voids. Hence it is not represented in the Ashby deformation mechanism maps.

Power-Law Breakdown.

At larger stresses (above about $10^{-3}\mu$), the simple power law breaks down as the measured strain rates are larger than those determined by this law (Equation 1.1). The creep mechanism changes from one which is climb controlled to glide controlled flow (Fig.1.4).

1.3 Mechanisms Of Creep Fracture In Metals And Alloys.

Here the only fracture and rupture modes which matter are the tensile ones. Failure in compression is by sliding, slip or crumbling, unless buckling occurs. The latter is usually avoidable by careful design to limit deformation behaviour.

The following description of fracture mechanisms is in accordance with Ashby et al [11] and [12]. When a cylindrical specimen of a crystalline metal is pulled in tension, it may fail in several ways. At low temperature, where ($T < 0.3T_m$), the specimen may fail by neck-down until the cross section is reduced to zero, or by cleavage, brittle intergranular fracture or in a ductile manner. At high temperatures, where($T > 0.3T_m$), the specimen may fail by various creep fracture mechanisms, some transgranular and some intergranular. These failure modes are summarised in Fig. 1.5.

1.3.1 Temperature below $0.3T_m$.

(i) Cleavage.

Almost all crystalline solids may fail by cleavage (Fig. 1.5), where the metal or alloy contains small cracks, which become nucleated and grow rapidly. Such cracks are initiated from abrasion scores, corrosion growth defects, or cracks due to block slip. These cracks concentrate stress and may propagate by cleavage, before the stress equals the ideal stress. (The ideal stress is that required to overcome the interatomic forces, allowing the normal separation of two adjacent atomic planes of metal atoms).

(ii) Ductile Failure At Low Temperature.

When a metal or alloy does not fail by cleavage, it may fail in a ductile transgranular way (Fig. 1.5). Holes nucleate at inclusions or pre-existant holes and further plasticity makes them grow. When large enough they may coalesce and the material fractures. The inclusions, if small, may produce a large local stress raiser, which on reaching a critical value may fracture the inclusion or its interface with the matrix, thereby nucleating a void. The void is initially spherical, then elongates and becomes ellipsoidal. The void grows, until it connects with others and fracture results. Ductile fracture usually follows transgranular fracture, but it may follow intergranular fracture, if the void density is higher in the boundaries. Necking or shear of the test specimen, can aid the coalescence of voids which results in fracture (Fig.1.6).

1.3.2 Temperature Above $0.3T_m$.

(i) Transgranular Creep Fracture.

In metals and alloys which creep above $0.3T_m$, the flow stress depends on the strain rate, which is governed by power-law creep. One transgranular fracture mechanism is similar to the low temperature ductile failure mechanism described above, where holes nucleate and grow to coalesce and ultimately fracture, due to plastic deformation around inclusions (Fig 1.6). As the material is now creeping the stresses in the material tend to be lower than before, and relatively large strains are needed for nucleation. Diffusion is responsible for postponing the nucleation of voids, as the temperature permits the movement of atoms from regions of compression to those of tension, on the surface of inclusions. This results in local recovery and transition to rupture may occur (Fig. 1.5).

(ii) Intergranular Creep Controlled Fracture.

At lower stresses and larger times to fracture, than those where transgranular creep fracture occurs, a transition from transgranular to intergranular fracture is observed. Grain boundaries slide, allowing wedge type cracks or round type voids to nucleate and grow at grain boundaries lying normal to the axis of the tensile stress. [10]. Power-law creep is the dominant mechanism, yet diffusion contributes to both the void and crack growth. The local shear strain rate in the boundary may be many times greater than that in the grain, causing boundary inclusions to nucleate before those in the grains. When the voids are small they grow by diffusion, and their growth rate is controlled by power-law creep of the surrounding grains. Therefore the growth is controlled by coupled diffusion and power-law creep. (Fig. 1.7). The deformation of creeping material in the shaded region of Fig. 1.7, controls the rate of cavity growth. At very low stress and high temperature the power-law creep cage, as shown in Fig. 1.7, disappears and pure diffusional growth takes over, as described below. This occurs in the limiting case, where the boundaries between diffusion and power-law creep, surrounding the voids, overlap.

(iii) Pure Diffusional Fracture.

At low stress and high temperature, where the stress is so low power-law creep is negligible, holes on the grain boundaries grow by the mechanism of diffusion alone. Matter flows out of holes and is deposited in the grain boundary, causing

the surrounding grains to move apart. They do not always maintain their rounded shape, and often become flatter and penny shaped, as they grow until the mechanism changes to that of (ii) and (i), as the stress increases to fracture (Fig. 1.8).

(iv) Rupture.

If no fracture mechanism intervenes, a material pulled in tension ultimately becomes mechanically unstable. Deformation becomes localised in a neck or shear band and the cross section reduces almost to zero. The material then breaks open into two parts, when it is said to have ruptured (Fig. 1.5). Rupture involves large reductions in area. It requires that nucleation of internal voids is suppressed, or if they do nucleate, that they do not grow and coalesce. High local recovery, to relieve stresses at inclusions, may also prevent nucleation of voids and cracks. Dynamic recrystallisation can cause rapid recovery and hence stress relief, and is the cause of rupture in most face centered cubic metals. Recrystallisation is a process which is not well understood (Fig. 1.5).

1.3.3. Ashby Fracture Mechanism Maps.

Similar to the mechanism maps for deformation, fracture mechanism maps may be used to illustrate the dominant fracture mechanisms as distinct areas in stress vs. temperature space. A typical fracture mechanism map is that for pure nickel shown in Fig. 1.9. Here, the normalised tensile stress (σ/E) is the ordinate, where (E) is the elastic modulus at a particular test temperature and the homologous temperature (T/T_m) is the abcissa. The fracture mechanism maps are constructed from uni-axial creep rupture data, together with microstructural observations of the fracture surface, [11].

1.4. Conclusions.

(i) Within this chapter the study of creep deformation and fracture mechanisms has been briefly described. For a more in-depth study [13] may be referred to.

(ii) The study of creep deformation and fracture mechanisms is an important one, enabling physically based mathematical creep laws to be developed pertaining to a particular creep mechanism. From the Ashby mechanism maps the

stress/temperature region may be determined where a governing law is valid, so that the law is only applied to materials which lie in this same region of the diagram.

(iii) Mechanism maps are useful in extrapolating creep rupture data forward in time, when using constitutive equations, by verifying where mechanism changes occur.

(iv) Mechanism maps also prove useful to the design engineer enabling the optimum choice of creep resistant material for its application.

(v) Mechanism maps are also used in the design of creep tests, giving guidlines for the temperature and stress levels to be used.

(vi) A wide range of deformation maps are currently available for pure metals, ferrous and non-ferrous alloys, some co-valent elements, metal halides, transition metals, metal oxides and ice. [8,9]. A more limited range of fracture mechanism maps are available [11,12].

(vii) An understanding of creep mechanisms has allowed the design of new materials with increased creep resistance, providing improved component performance. For example, good power-law creep resistance is produced by having a large number of obstructions to dislocation movement. This has been achieved through alloying metals, to produce solid-solution precipitates within the material. To resist diffusional flow, diffusional distances should be as large as possible through the use of large grain size materials or even single crystals. This has lead to the development of the method of directional solidification, where long thin crystals are produced in the direction of the maximum tensile stress, to make gas turbine blades.

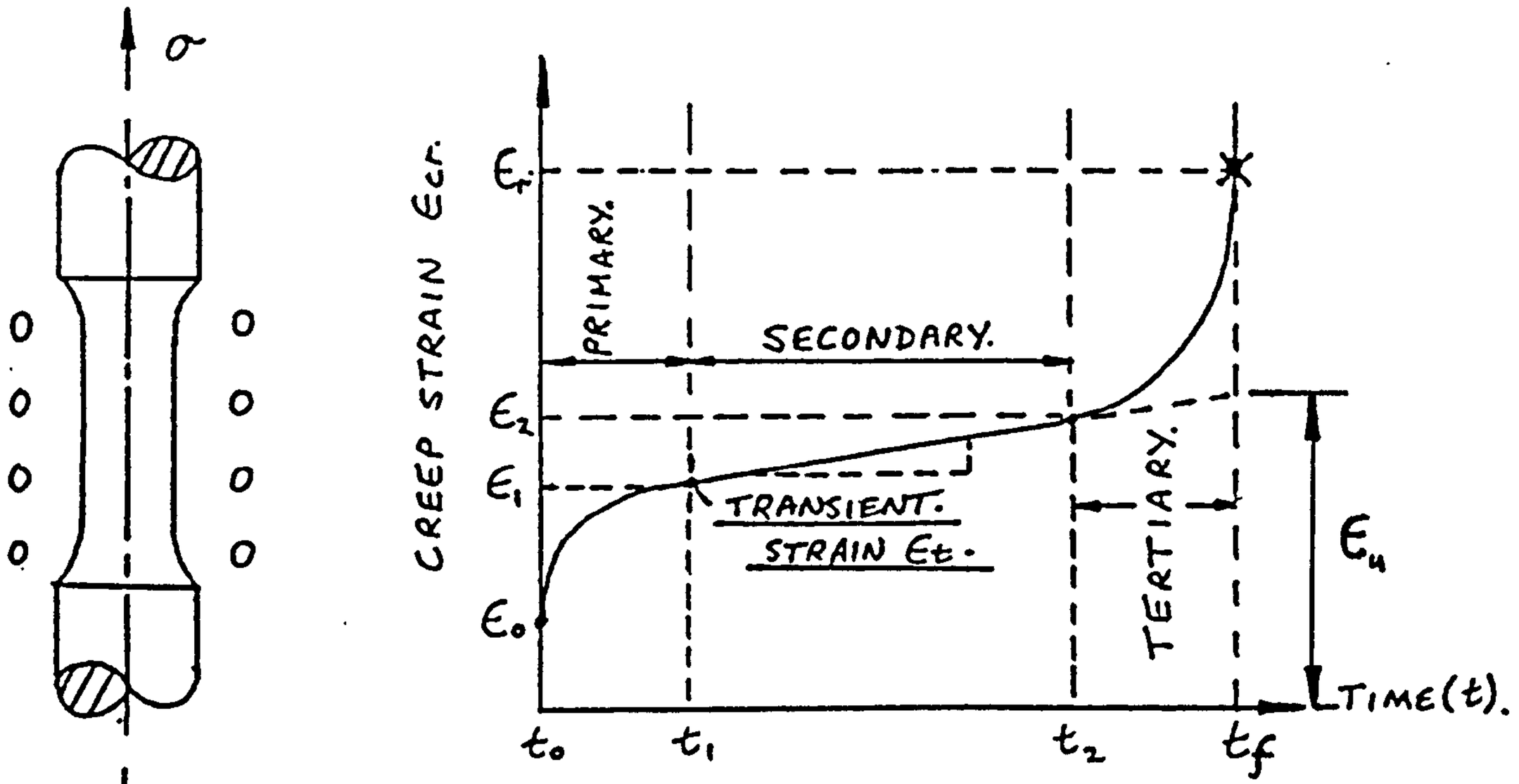

Figure 1.1: a typical uni-axial creep curve.

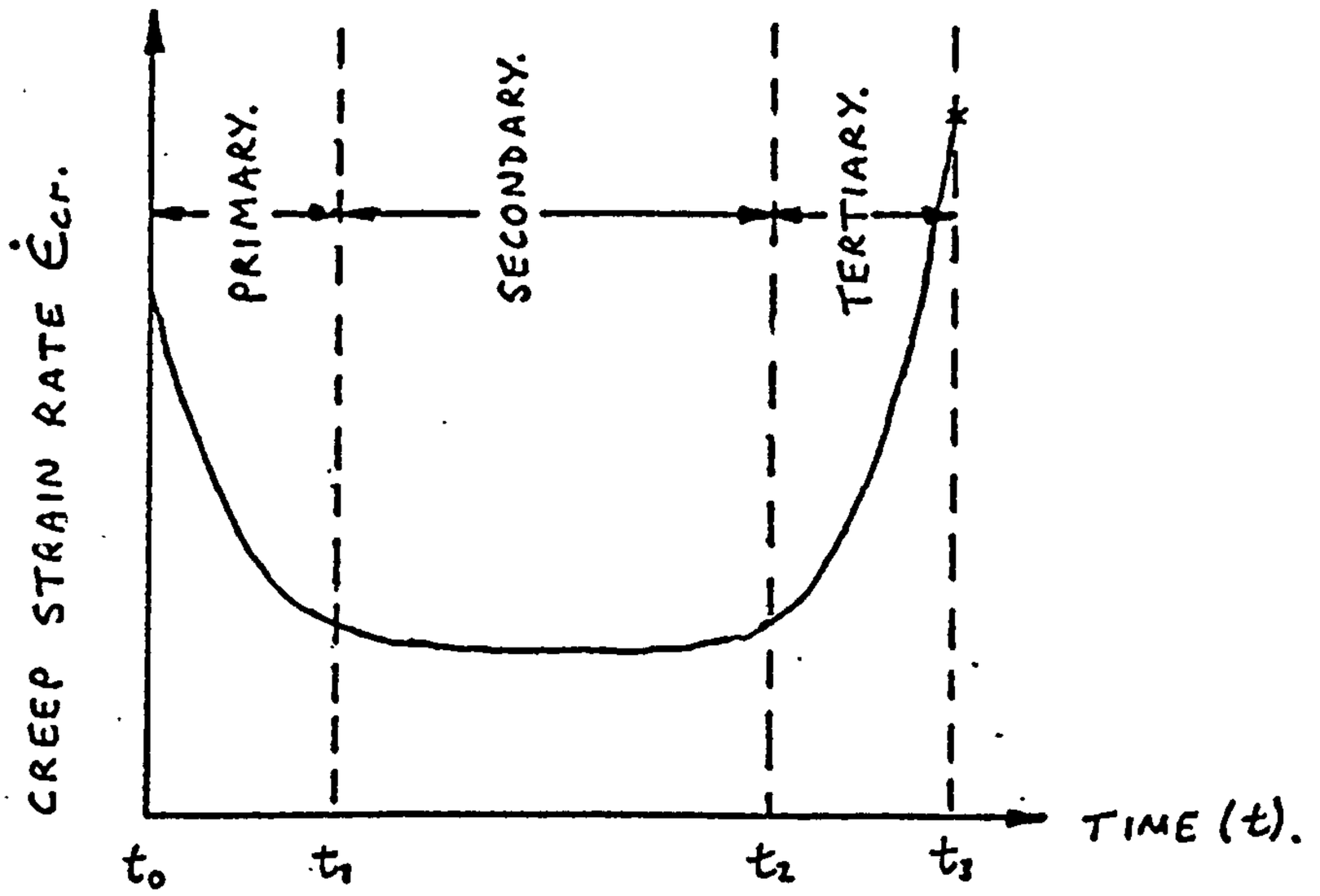

Figure 1.2: strain rate variation during the typical creep test of Fig. 1.1.

Figure 1.3:
schematic representation of a metallic crystal, showing bulk and grain-boundary diffusion paths of atoms.

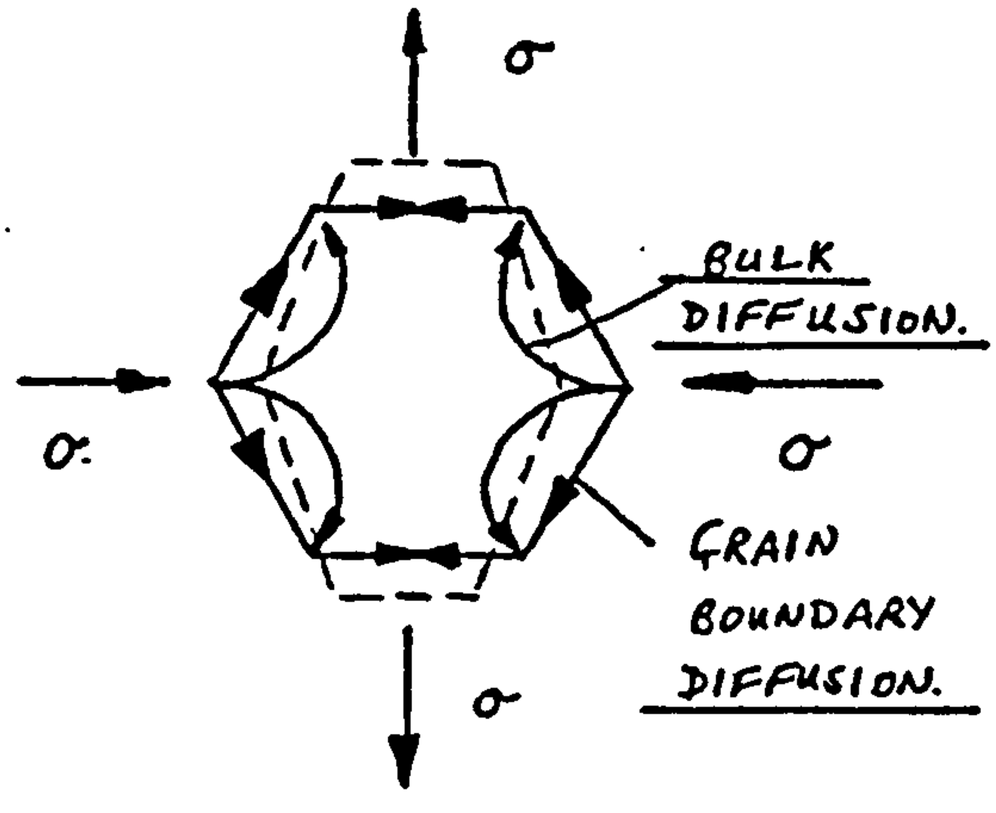

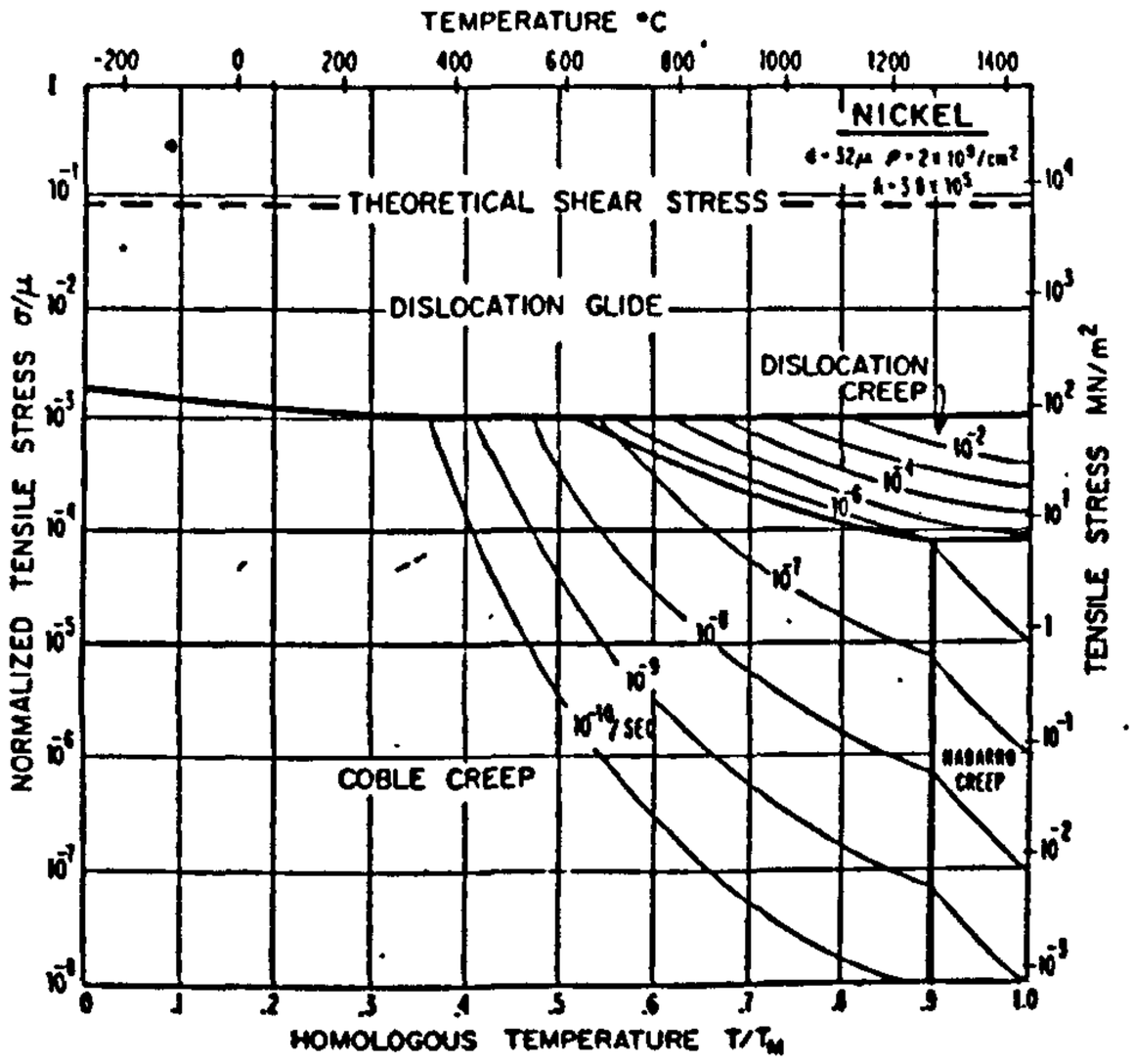

Figure 1.4: An Ashby deformation mechanism map for pure Nickel [9].

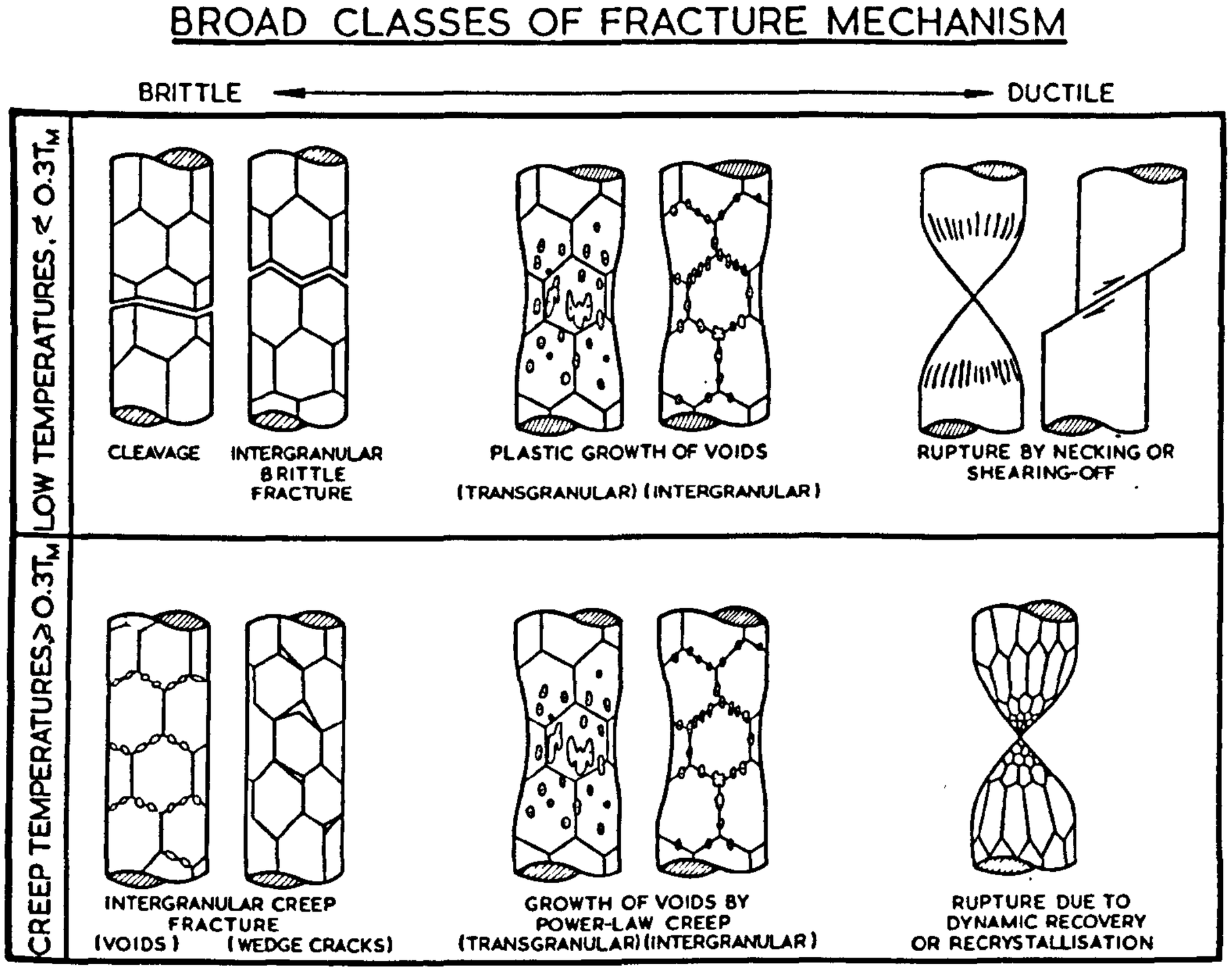

Figure 1.5: broard classes of fracture mechanisms, after Ashby et al [11],[12].

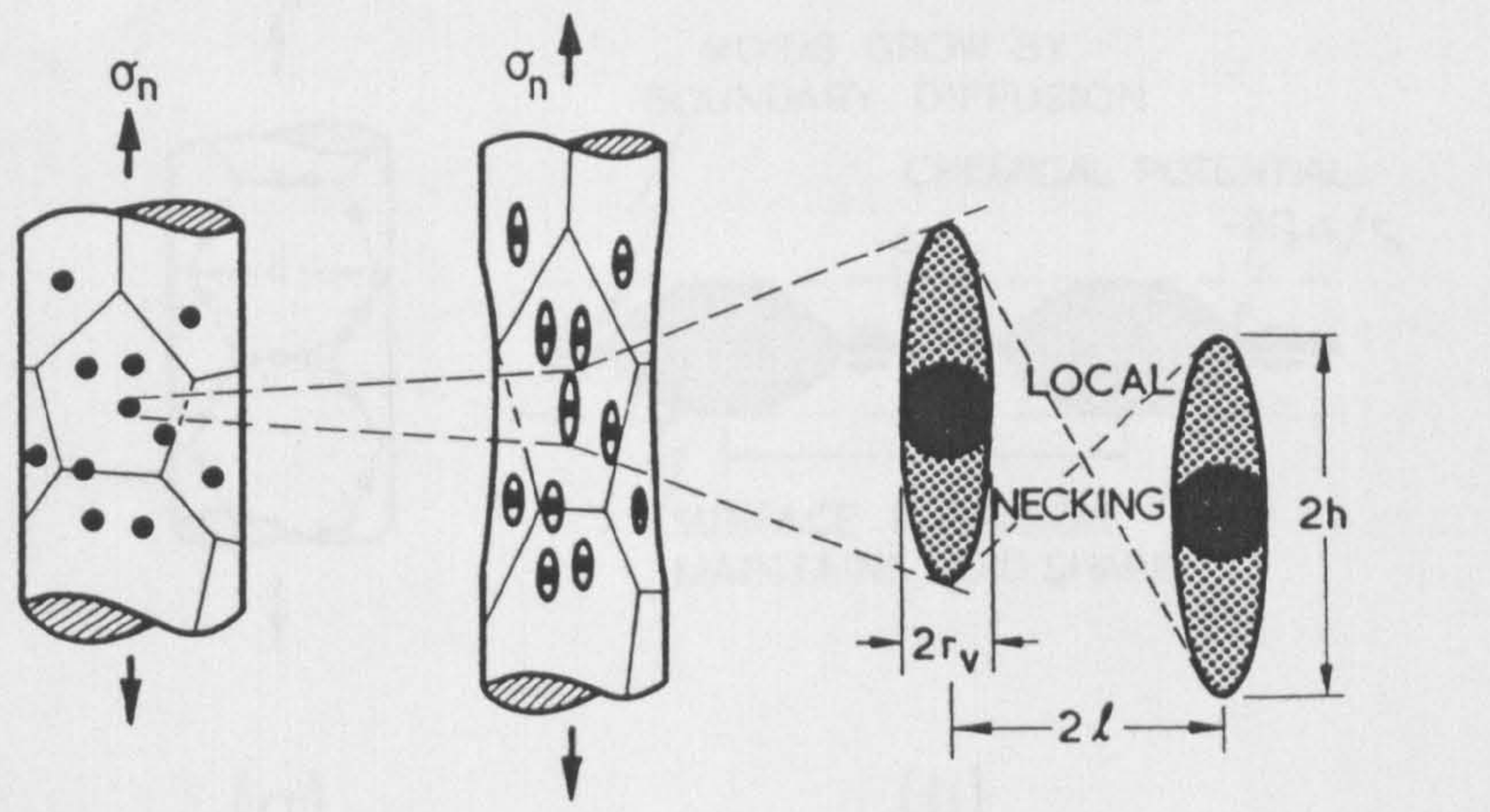

Figure 1.6: (a) ductile fracture and transgranular creep fracture requires that holes pre-exist or that they nucleate at inclusions;
(b) holes elongate as the specimen elongates;
(c) when their length is about equal to their separation, they link, causing fracture.
(Diagram due to Ashby et al [11],[12]).

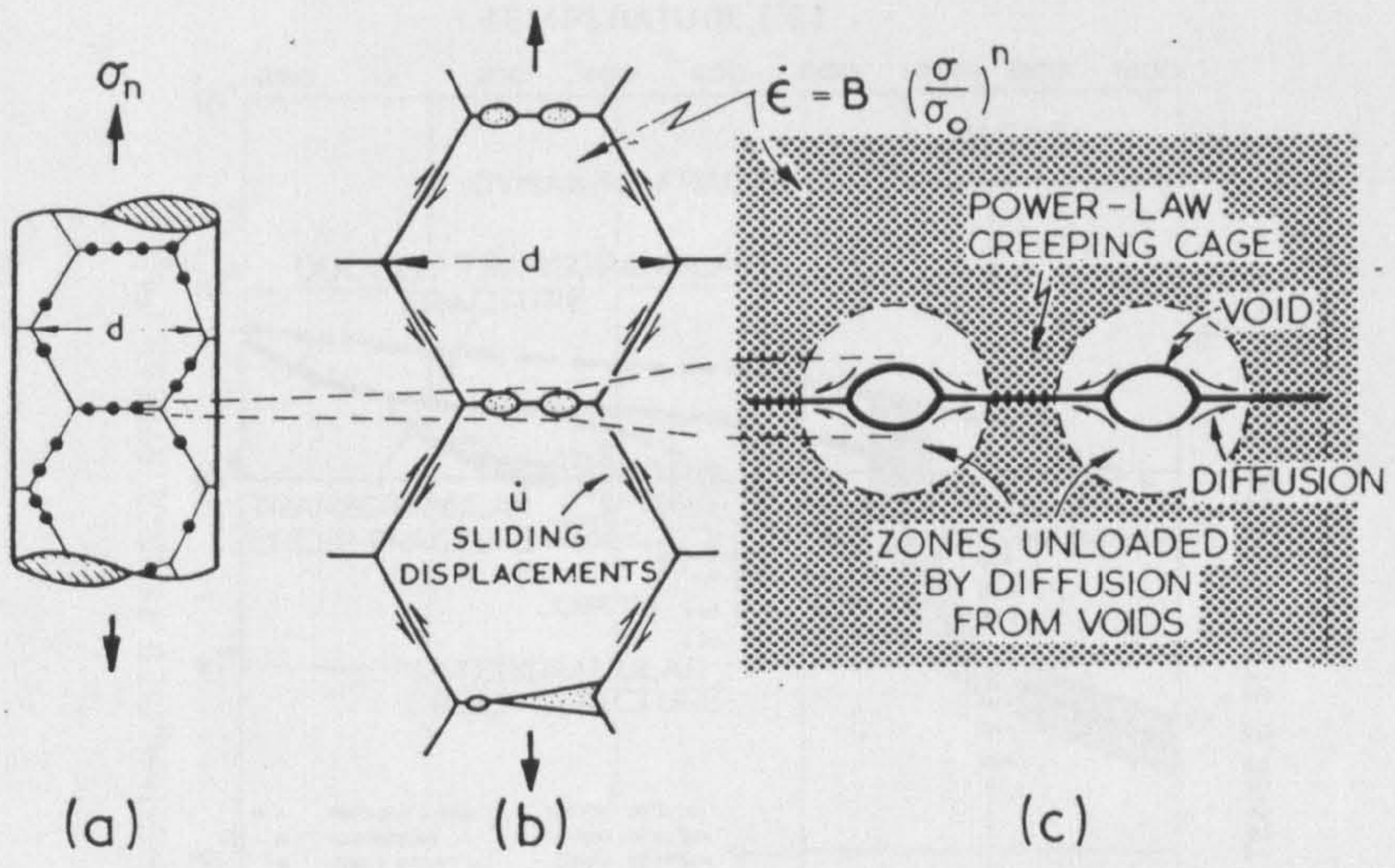

Figure 1.7: (a) and (b) grain boundary sliding initiates the nucleation of voids. In this case grain boundary voids form (c) and grow by diffusion. The diffusion fields of neighbouring voids do not overlap; each void is contained within a cage of power-law creeping material.
(Diagram due to Ashby et al [11],[12])

Figure 1.8: (a) and (b) voids which lie on boundaries carrying a tensile stress grow by diffusive transfer of mater along the grain boundary plane. The voids become crack like. Here the diffusive fields of Fig. 1.7 overlap.
(Diagram due to Ashby et al [11],[12]).

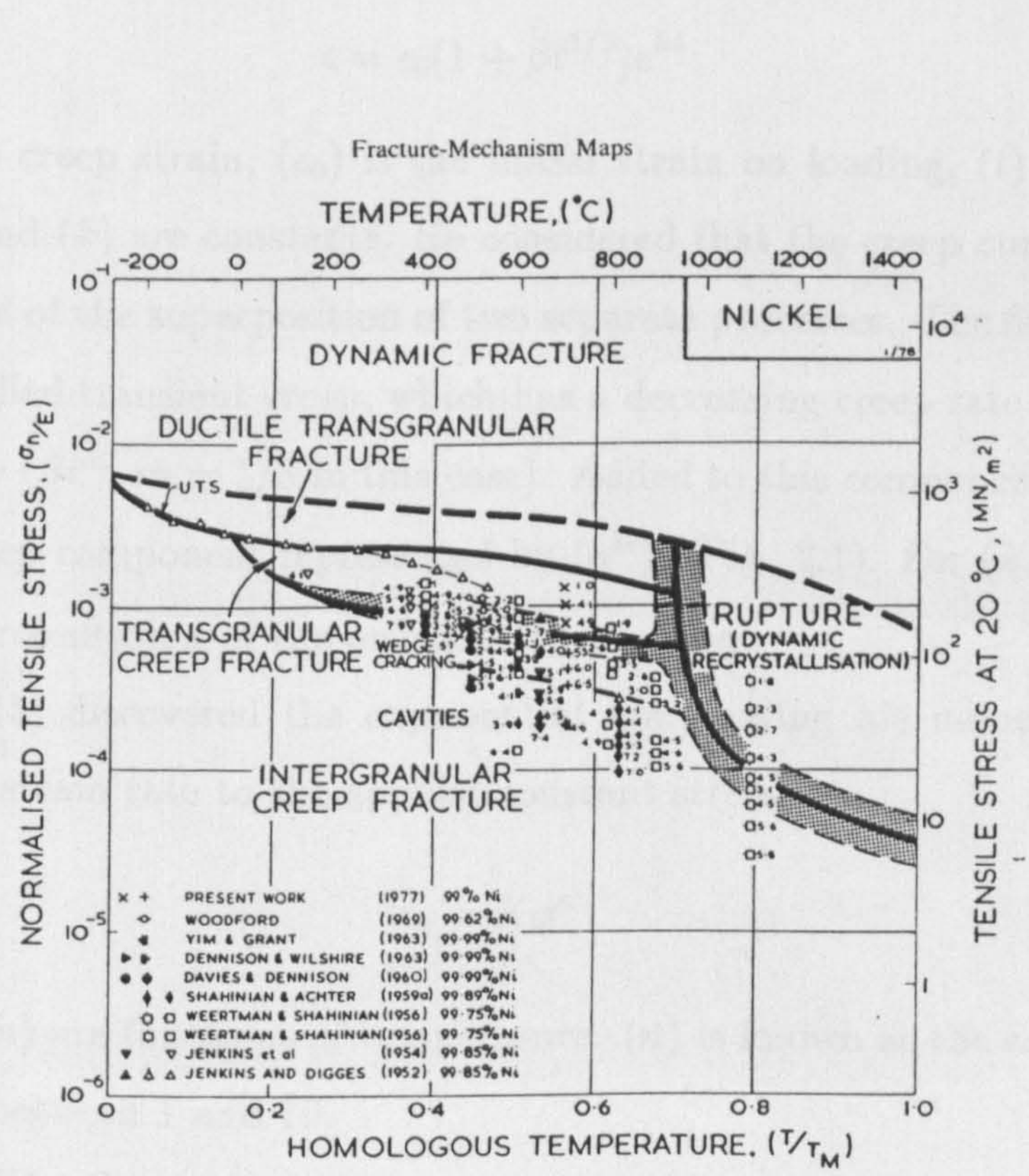

Figure 1.9: fracture mechanism map for pure Nickel, due to Ashby et al [12].

Chapter 2.

The Development Of The Creep Continuum Damage Model For The Mathematical Representation Of Creep Deformation And Failure Of Metals And Alloys.

2.1 Introduction

Early mathematical representations were concerned with the representation of the primary and secondary creep strains obtained from uni-axial creep tests. A review of these equations is given by Garofalo [10]. The most noteworthy expressions are those due to Andrade [14], Norton [15], Garofalo [16] and Arrhenius [17].

Andrade [14] found that the primary and secondary creep curve could be represented by:

$$\epsilon = \epsilon_0(1 + \beta t^{1/3})e^{kt} \tag{2.1}$$

where (ϵ) is the creep strain, (ϵ_0) is the initial strain on loading, (t) is the time in hours and (β) and (k) are constants. He considered that the creep curve after initial loading consisted of the superposition of two separate processes. The first creep curve component is called transient creep, which has a decreasing creep rate with time and is represented by (βt^m, $m = 1/3$ in this case). Added to this component is a constant rate, viscous creep component,represented by (e^{kt}), (Fig. 2.1). For ($k = 0$) equation (2.1) gives a representation of the primary creep region.

Norton [15] discovered the exponential law bearing his name, relating the secondary creep strain rate to the applied constant stress:

$$\dot{\epsilon}_s = K\sigma^n \tag{2.2}$$

where (K) and (n) are functions of temperature. (n) is known as the creep exponent and usually lies between 1 and 10.

Garofalo [10,16] proposed a primary and secondary creep constitutive law:

$$\epsilon = \epsilon_0 + \epsilon_t(1 - e^{-rt}) + \dot{\epsilon}_s t \tag{2.3}$$

where (ϵ_0) is the instantaneous strain on loading; (ϵ_t) is the limiting transient creep strain; (r) is the ratio of transient creep rate to the transient creep strain and ($\dot{\epsilon}_s$) is the steady state creep rate, which is given by equation (2.2).

By plotting the natural logarithm of the secondary creep strain rate ($ln(\epsilon_{ss})$) against the reciprocal of the absolute temperature $(1/T)$, it has been established that the slope of the resulting line is $(-Q/R)$ where (Q) is the activation energy $(Jmol^{-1})$ for the creep deformation present and (R) is the universal gas constant (8.31 $Jmol^{-1}K^{-1}$), giving the dependency of the secondary creep strain rate on temperature at constant stress:

$$\dot{\epsilon}_s = Ce^{-Q/RT} \tag{2.4}$$

This equation is termed Arrhenius's law [17].

The dependence of the creep strain rate on both stress and temperature may be obtained from equations (2.4) and (2.2) as:

$$\dot{\epsilon}_s = B\sigma^n e^{-Q/RT} \tag{2.5}$$

Therefore, reliable uni-axial constitutive equations have been developed to predict the creep strains during the primary and secondary creep regions. Though no attempt has been made in these equations to represent tertiary creep strains or to model multi-axial creep behaviour.

In this chapter a phenomenological approach describing macroscopic rather than microscopic materials behaviour will be presented for both uni-axial (section 2.2) and multi-axial creep behaviour (section 2.3). The concept of continuum damage will be developed and the single state variable (damage parameter, ω) will be used to represent the tertiary creep behaviour in section 2.4. An allowance for the multi-axial rupture behaviour of different materials is included in the damage-evolution law. Comparisons are made in section 2.5 between the phenomenological creep continuum damage model and physically based constitutive and damage laws proposed by material scientists on the basis of microstructural observations. In section 2.6 the bi-linear representation will be presented, which is used to represent the changes in the slope of the stress-rupture diagram and the minimum strain rate vs. stress diagram to model both high stress, ductile rupture and low stress, brittle creep fracture.

2.2 The Uni-Axial State Of Stress.

In this analysis the elastic deformation is omitted from the argument, assuming elastic deformation to be small in comparison with the much larger creep strains.

The stress dependence of the secondary creep strain rate is given by equation (2.2) due to Norton [15]. Odqvist [18] states that the representation of both primary and secondary creep regions may be obtained by modifying (2.2) to include ($f(t)$), which is some function of time:-

$$\dot{\epsilon} = K\sigma^n f(t) \tag{2.6}$$

where the simplest form of ($f(t)$) is (t^m) obtained in accordance with equation (2.1) due to Andrade [14]. (m) is a material constant (which is different to that of (m) in the strain/time equation (2.1)), in theory ($-1.0 < m < 0$), so that (t^m) represents the decreasing strain rate in the primary creep region, using (2.6).

2.3 The Multi-Axial State Of Stress.

Odqvist [18] has derived a generalised form of Norton's law (2.2) for a multi-axial stress system:

$$\dot{\epsilon}_{ij}^{(s)} = \frac{3}{2} K \sigma_e^{n-1} s_{ij} \tag{2.7}$$

where (s_{ij}) is the deviatoric stress tensor:

$$s_{ij} = \sigma_{ij} - \delta_{ij}\left(\frac{\sigma_{kk}}{3}\right) \tag{2.8}$$

and (δ_{ij}) is Kronecker's delta i.e.

$$\delta_{ij} = \begin{cases} 1 & \text{if } i = j \\ 0 & \text{if } i \neq j \end{cases}$$

Here the tensorial notation of [19,20] is used, where the shear strain rates (ϵ_{ij}, for $i \neq j$) are defined as the absolute shear strain rates in accordance with the shear strain tensor [20]. (c.f. equation 4.6 which uses the engineering shear strain definition)

Odqvist formulated equation (2.7) on the basis of the following assumptions:

(i) The material is incompressible i.e. no dilatation (no volume change) where:

$$\dot{\epsilon}_{11} + \dot{\epsilon}_{22} + \dot{\epsilon}_{33} = 0 \tag{2.9}$$

(ii) The creep rate is independent of superimposed hydrostatic pressure;

(iii) There exists a flow potential or co-axiality of the stress and strain rate tensors;

(iv) The material is isotropic;

(v) Norton's law (2.2) holds for the special case of uni-axial stress.

2.4 The Tertiary Creep Region And The Concept Of Continuum Damage.

2.4.1 The Concept Of Continuum Damage.

Hayhurst [21] observed that defects may begin to grow during the primary creep region at low stresses ($0.2\sigma_y < \sigma < 0.4\sigma_y$) and for homologous temperatures above ($0.3Tm$), typically found in many engineering components . The subsequent growth of such defects causes an increasing strain rate, from the constant rate observed in the secondary creep region (Fig. 1.2), giving the teriary creep region (Fig. 1.1). Creep during the tertiary creep region may last for up to 50 % of the component life. Therefore, it is important to consider tertiary creep in the design of engineering components.

The voids or cavities observed to have grown within the material (Section 1.3.2) link to form cracks, producing tertiary creep strains. Such voids and cracks within the material are termed damage. Hayhurst [21] has also observed from uni-axial tests for a range of different materials, that damage forms on grain boundaries perpendicular to the maximum principal tensile stress and that the distribution of damage is uniform throughout the uniform stress field. Hayhurst [22] also performed equal bi-axial creep tests for specimens of both Aluminium and Copper which also gave a uniform distribution of damage in the uniform stress field, but it was not possible to assign a prefered direction for the growth of damage. From creep tests of both British Standard and circular notched bars [23]. Hayhurst concluded that the British Standard notch fails by the formation of concentrated damage (in the region of the concentrated initial elastic stress field) close to the notch. This damage propagates slowly to the centre of the bar, accompanied by the peak of the axial

stress component, until breakage occurs. Whereas the circular notched bar behaves as a homogeneously stressed specimen, with failure occurring across the whole of the section at the same time, due to stress redistribution from the edge of the blunt notch towards the centre of the specimen.

Therefore, with reference to the results of Hayhurst et al [21,22,23], no single crack was found to grow in preference to others. Instead the tertiary creep damage was observed to be distributed uniformly in a uniform stress field and was observed to be concentrated in a non-uniform or a concentrated stress field. Creep damage, therefore posesses a field or continuum property analogous to that of stress; hence the term continuum damage. This leads to the definition of the damage state variable, which is given in the next section.

2.4.2 The Damage State Variable.

Tertiary creep damage is quanitified mathematically through the normalised damage parameter (ω), sometimes (D). There are many different ways of measuring material damage. The amount of damage present within a material may be quantified in terms of the volume or area of voids on a material plane. Measurements of damage may be made by optical means, giving an area measurement or by material density changes, giving a volume measurement. Some researchers [24] relate the damage state to the ratio of the damaged area to the original un-damaged area of a material element. Though the damage state variable is representative of a wide range of internial material weakening effects [25], such as unstable dislocation sub-structure, particle coarsening, internal oxidation and so on; where the actual physical quantification of the damage state variable is complicated.

The concept of the actual stress (σ_a) is introduced for the case of uni-axial tension where:

$$\sigma_a = \frac{\sigma}{(1-\omega)} \tag{2.10}$$

and (σ) is the nominal stress. Here, (σ_a) is the uni-axial stress required in an undamaged material element to give the same strain rate effect as the damaged material element experiences under the uni-axial nominal stress (σ).

Therefore the strain response of a deteriorating body is modelled using the material

damage state variable, by replacing the nominal stress with the actual stress (σ_a) in Norton's law, equation (2.2).

Kachanov [24] first proposed the form of the uni-axial creep continuum damage, creep strain rate and damage rate laws, which were subsequently modified by Rabotnov [26] and are given by:

$$\dot{\epsilon} = K' \left(\frac{\sigma}{1-\omega} \right)^n \tag{2.11}$$

$$\dot{\omega} = M' \frac{\sigma^\nu}{(1-\omega)^\phi} \tag{2.12}$$

where K', M', n, ν, and ϕ are material constants. (n) and (ν) are obtained from the gradients $(1/n)$ and $(-1/\nu)$ of the stress vs. minimum creep rate and the stress-rupture diagrams, respectively. It is noticed that (2.11) reduces to Norton's law (2.2) when the material is in the un-damaged state (i.e $\omega = 0$).

2.4.3 The Generalisation Of The Damage State Variable Description For Continuum Damage.

The generalisation of equations (2.11) and (2.12) for multi-axial stresses has been made, by considering the effect of damage on the strain rate as a scalar effect. This generalisation is achieved by using the strain rate expression of Odqvist, given by equation (2.7), substituting the actual stress (σ_a), given by equation (2.10) for the nominal stress (σ). Equation (2.11) for the multi-axial stress state may then be written as:

$$\dot{\epsilon}_{ij} = \frac{3}{2} \frac{K' \sigma_e^{n-1}}{(1-\omega)^n} s_{ij} f(t) \tag{2.13}$$

where s_{ij} is given by equation (2.8) and ($f(t)$) is included to represent the primary creep region.

For the generalisation of (2.12), a stress function of degree one ($\Delta(\sigma_{ij})$) is introduced, to allow for the effects of the multi-axial stress-state on uni-axial rupture behaviour (Section 2.4.7). ($\Delta(\sigma_{ij})$) may also be identified as the representative rupture stress. Equation (2.12) is then rewritten as:

$$\dot{\omega} = M' \frac{\Delta^\chi(\sigma_{ij})}{(1-\omega)^\phi} f(t) \tag{2.14}$$

Again ($f(t)$) is included to represent the primary creep region and is taken as $f(t) = t^m$. In equation (2.14) (χ) is now introduced, where $\chi = \nu(m+1)$ allowing

for the effect of the time scale modification on the gradient $(-1/\nu)$ of the stress-rupture diagram, by the inclusion of the (t^m) term.

2.4.4 Normalisation Of The Constitutive And Damage Laws.

The constitutive and damage laws used by Hayhurst [23] and by the author, use normalised values of stress, strain and time, to reduce numerical error when the equations are used for finite element analysis. The normalised stress and strain are defined as $\Sigma_{ij} = \sigma_{ij}/\sigma_0$, $S_{ij} = s_{ij}/\sigma_0$ and $V_{ij} = \epsilon_{ij}/e_0$, where (e_0) is the uni-axial elastic strain at a stress of (σ_0), given as $e_0 = \sigma_0/E$. Equations (2.13) and (2.14) are then rewritten, with the introduction of:

$$M = M'(1+\phi) \tag{2.15}$$

(to simplify the integration of (2.14)), as:

$$\frac{dV_{ij}}{dt} = \frac{3}{2}\frac{KE\sigma_0^{n-1}t^m\Sigma_e^{n-1}}{(1-\omega)^n}\left(\frac{s_{ij}}{\sigma_0}\right) \tag{2.16}$$

$$\frac{d\omega}{dt} = \frac{M\sigma_0^{\chi}t^m}{(1+\phi)(1-\omega)^{\phi}}\left(\frac{\Delta(\sigma_{ij})}{\sigma_0}\right)^{\chi} \tag{2.17}$$

Equations (2.16) and (2.17) are simplified by the introduction of the normalised time (τ) and the constant (V_u) where:

$$d\tau = KE\sigma_0^{n-1}t^m dt \tag{2.18}$$

and are re-written as:-

$$\frac{dV_{ij}}{d\tau} = \frac{3}{2}\frac{\Sigma_e^{n-1}}{(1-\omega)^n}Sij \tag{2.19}$$

$$\frac{d\omega}{d\tau} = \frac{\Delta^{\chi}(\Sigma_{ij})}{V_u(1+\phi)(1-\omega)^{\phi}} \tag{2.20}$$

where:

$$V_u = \frac{KE}{M}\sigma_0^{(n-\chi-1)} \tag{2.21}$$

which is derived in section 3.6 and may be identified to be the normalised uni-axial creep strain at failure, $(V_u = \epsilon_u/e_o)$,(Fig.1.1); predicted by extrapolating the secondary creep region line, corresponding to a creep test conducted at a stress of (σ_0), to the failure time, (t_f).

N.B. Equations (2.18) and (2.21) are divided by 100 for creep strains measured in percent strain.

The equations (2.19) and (2.20) are the creep constitutive and damage rate equations used by the author in finite element computer predictions of creep deformation and failure. Equation (2.20) may be integrated for constant stress between the limits $\omega = 0$, at normalised time $\tau = 0$ and ($0 < \omega < 1.0$), at ($0 < \tau < \tau_f$) to give:

$$(1 - \omega) = \left\{1 - \Delta^{\chi}(\Sigma_{ij}) \left(\frac{\tau}{V_u}\right)\right\}^{\frac{1}{\phi+1}} \tag{2.22}$$

At $\tau = \tau_f$, $\omega = 1$ which gives:

$$\tau_f = \frac{V_u}{\Delta^{\chi}(\Sigma_{ij})} \tag{2.23}$$

Equation (2.22) may be substituted into the strain rate equation (2.19) and integrated between the limits $V_{ij} = 0$, at $\tau = 0$ and ($0 < V < V_f$), at ($0 < \tau < \tau_f$), using equation (2.23) giving:

$$\dot{V}_{ij} = \frac{3}{2} \frac{V_u \Sigma_e^{n-1} S_{ij}}{\Delta^{\chi}(\Sigma_{ij})(1 - \frac{n}{\phi+1})} \left\{1 - \left(1 - \left(\frac{\tau}{\tau_f}\right)\right)^{(1 - \frac{n}{\phi+1})}\right\} \tag{2.24}$$

at $\tau = \tau_f$, $V_{ij} = V_{ij}^{(f)}$:

$$V_{ij}^{(f)} = \frac{3}{2} \frac{V_u \Sigma_e^{n-1} S_{ij}}{\Delta^{\chi}(\Sigma_{ij})(1 - \frac{n}{\phi+1})} \tag{2.25}$$

and (2.24) is re-written in terms of $V_{ij}^{(f)}$:

$$\frac{V_{ij}}{V_{ij}^{(f)}} = \left\{1 - \left(1 - \left(\frac{\tau}{\tau_f}\right)\right)^{(1 - \frac{n}{\phi+1})}\right\} \tag{2.26}$$

This equation (2.26), for $i = j = 1$ (i.e. uni-axial conditions) represents the shape of the creep curve with the normalised time scale, which linearises the primary creep region. The corresponding uni-axial strain/time equation for the real time scale is given by equation (3.9). The relationship between the real time scale and the normalised time scale is given by the integration of (2.18):-

$$t = \left\{\frac{\tau(m+1)}{K E \sigma_0^{n-1}}\right\}^{(\frac{1}{m+1})} \tag{2.27}$$

Hayhurst [34] used the creep tests of Johnson et al [27] for tension-torsion specimens and verified the multi-axial strain rate equation (2.19), in that the ratio of normalised shear strain to the normalised linear strain remained constant during the creep tests, at a similar value to the ratio predicted by the equation (2.19), for tests on both Copper and Aluminium.

2.4.5 Determination Of The Material Constants.

The material constants in equations (2.19) and (2.20) are determined using uni-axial forms of these equations, which are integrated to give the uni-axial strain time equation (3.4), which is fitted using an optimisation scheme to a set of uni-axial creep curves obtained from experimental creep tests for a range test stress levels. The full procedure for the determination of the material constants is detailed in section 3.6.

2.4.6 Creep Rupture Under Multi-Axial States Of Stress

The stress function $\Delta(\Sigma_{ij})$ in equation (2.20) is used to model the effect of the multi-axial stress-state on the uni-axial stress-rupture behaviour. Hayhurst [22] has investigated the bi-axial creep rupture behaviour of metals and alloys and he concluded that there or two extreme types of stress sensitive rupture behaviour. These are the bi-axial rupture behaviours of Copper and Aluminium, which may be closely represented by a maximum principal stress rupture criterion $\Delta(\Sigma_{ij}) = \Sigma_1$ and an effective stress rupture criterion $\Delta(\Sigma_{ij}) = \Sigma_e$ respectively. The behaviours of all other materials is said to lie between these two extremes of behaviour. Hayhurst [22] proposed a multi-axial rupture criterion of the form:

$$\Delta(\sigma_{ij}) = \{\alpha\sigma_1 + \beta_H I_1 + \gamma\sigma_{ef}\} \equiv \sigma_{Rup} \tag{2.28}$$

where $\alpha+\beta_H+\gamma = 1$, $I_1 = \sigma_1+\sigma_2+\sigma_3$ and $\sigma_{ef} = \frac{1}{\sqrt{2}}\{(\sigma_1-\sigma_2)^2 + (\sigma_2-\sigma_3)^2 + (\sigma_3-\sigma_1)^2\}^{\frac{1}{2}}$. Using equation (2.23) and (2.27) the failure time may be written as:

$$t_f = C\{\alpha\sigma_1 + \beta_H I_1 + \gamma\sigma_e\}^{\frac{-\chi}{m+1}} \tag{2.29}$$

where (C) is a constant.

By writing $\Sigma_i = \sigma_i/\sigma_0$ and $T = t_f/t_0$, where (t_0) is the time to rupture of a uni-axial test conducted at stress, (σ_0), (2.29) may be written in normalised form for the principal bi-axial stresses under plane stress conditions:

$$T = \left\{\alpha + \beta_H(\Sigma_1+\Sigma_2) + \gamma(\Sigma_1^2+\Sigma_2^2-\Sigma_1\Sigma_2)^{\frac{1}{2}}\right\}^{\frac{-\chi}{m+1}} \tag{2.30}$$

Expressing Σ_2 as the ratio ζ of the stress Σ_1, (2.30) may be re-written as:

$$T^{m+1} = \left\{\alpha + \beta_H(1+\zeta) + \gamma(1+\zeta^2-\zeta)^{\frac{1}{2}}\right\}^{-\chi}\Sigma_1^{-\chi} \tag{2.31}$$

By setting the normalised rupture time (T) to unity the equation defining the shape of the isochronous rupture surface (i.e. the shape of the locus of points having the same rupture time) in the (Σ_1, Σ_2) -plane is given as:

$$\Sigma_1 = \left\{ \alpha + \beta_H (1 + \zeta) + \gamma (1 + \zeta^2 - \zeta)^{\frac{1}{2}} \right\}^{-1} \tag{2.32}$$

which is noticed to be independent of the value of (χ). The isochronous rupture surfaces for extreme values of α , β_H and γ are shown in Fig.2.2. Similarly the equation representing the isochronous rupture surface for plain strain conditions may be obtained:

$$\Sigma_1 = \left\{ \alpha + \beta_H \left(\frac{3}{2} + \frac{3}{2}\zeta \right) + \gamma \left(\frac{3}{4} - \frac{3}{2}\zeta + \frac{3}{4}\zeta^2 \right)^{\frac{1}{2}} \right\}^{-1} \tag{2.33}$$

For most materials the multi-axial rupture criterion of (2.28) may be simplified (as β_H is small) [35] to:

$$\Delta(\sigma_{ij}) = \{ \alpha\sigma_1 + (1 - \alpha)\sigma_{ef} \} \equiv \sigma_{Rup} \tag{2.34}$$

which is equivalent to the representative rupture stress. The representative rupture stress is defined as the test stress level required in a uni-axial specimen, so that the rupture time in the uni-axial specimen is the same as that in the component or the multi-axial test piece.

In order to determine the values of (α) from the shape of the isochronous rupture surface for a material, at least three sets of rupture tests must be conducted, one set of uni-axial tests and two sets of bi-axial tests.

2.4.7 Creep Under Non-Proportional Loading And The Directional Nature Of Creep Damage.

Non-proportional loading, occurs where the stress field within a material element rotates relative to the element. Trampczynski et al [29], details single and multiple reverse torsion tests of thin walled tubes made from Copper and Aluminium, where the maximum principal stress rotates through about 34°. For Copper, damage was observed to grow on two discrete planes without interaction. Both the damage planes are perpendicular to the maximum principal tension stress. This indicates that creep damage is in fact a vector functional quantity for non-proportional loading histories

and that a more complicated two state or a three state variable theory is required. Murakami [30] details how the tensorial creep damage theory is extended to three dimensional states of material damage, in defining the damage tensor. Fortunately in many engineering components the loading history is proportional in character; and, this assumption will be made in the finite element models detailed in this thesis.

2.5 The Material Science Approach To The Formulation Of Constitutive Equations And Their Comparison With The Phenomenological Approach.

The method of the formulation of constitutive equations to represent material behaviour during the tertiary creep region, by the material scientist, differs from that of the engineering scientist. The method of the material scientist is to formulate mathematical models from a fundamental understanding of the dominant microstructural mechanisms present during the tertiary creep region. The two dominant mechanisms, which are thought to dominate during tertiary creep are nucleation of voids and their subsequent growth by vacancy diffusion or power-law creep (section 1.3.2). Dyson and McLean [31], and Greenwood [32] have formulated constitutive models for these mechanisms on the basis of their experimental observations of void growth in Nimonic 80A and Copper respectively. They both formulated nucleation, void growth and creep strain rate constitutive equations, which when used in conjunction with the double integral of Ashby and Raj [33] gave expressions for the total volume of voids at a point in time, from which an expression for the damage parameter (ω) was derived. Leckie and Hayhurst [34] have shown that the predictions for damage growth using the Dyson and McLean theories, the Greenwood theories and the single state variable theory all lie close to the experimental. This shows that the continuum damage equations (2.19), (2.20) not only fit macroscopic observations, but also describe the growth of the physical damage within the material. Hayhurst et al [28] used the Dyson and McLean theory to predict the behaviour of the reverse torsion-tube tests for Nimonic 80A at $750°C$ and were able to conclude that nucleation appears to be scalar and creep damage is vectorial in character. For a more detailed study reference [36] may be referred to.

2.6 Modelling The Creep Behaviour Of Materials With Different High And Low Stress Characteristics: The Bi-Linear Representation.

Some materials exhibit different strain-rate and stress-rupture behaviour at high and low stresses (Figs 2.3 (a) and (b)). The value of ($\hat{\sigma}$) is determined by the cross-over point of the high and low stress lines from the experimental uni-axial data. Above the stress ($\hat{\sigma}$) the material behaves in a more ductile manner, where the strain rate and rupture time are more sensitive to stress, than at stresses lower than ($\hat{\sigma}$). The changes in the slope of the stress-rupture line are caused by a mechanism change within the material.

To model such high and low stress behaviour necessitates the use of two pairs of constitutive laws, the first pair of laws having parameters to represent the high stress line (I) and the second pair to represent the low stress line (II); hence the term bi-linear representation. These two pairs of constitutive and damage laws representing the high and low stress behaviour must be compatibile at the break-stress, ($\hat{\sigma}$).

Consider first the uni-axial strain behaviour of a particular material (Fig. 2.3(a)) which may be represented by:

$$\dot{\epsilon} = Kt^m \left(\frac{\sigma}{1-\omega}\right)^n \tag{2.35}$$

from(2.19),where K , m , n are material constants and (n) is the gradient of a line in Fig. 2.3(a). Two equations must be used to represent the strain rate behaviour of the bi-linear material at high and low stress levels. For compatiblity the strain rates given by both high and low stress equations must be equal at the break stress ($\hat{\sigma}$). The condition for the compatibility of the time scales is that (t^m) is the same for both high and low stress behaviour, hence:

$$\dot{\epsilon} = K_I t^m \left(\frac{\hat{\sigma}}{1-\omega}\right)^{n_I} = K_{II} t^m \left(\frac{\hat{\sigma}}{1-\omega}\right)^{n_{II}} \tag{2.36}$$

is obtained, yielding:

$$\frac{K_I}{K_{II}} = \hat{\sigma}^{(n_{II}-n_I)} = \Phi \tag{2.37}$$

Hence, the two strain rate curves may be represented as:

$$\dot{\epsilon}_I = \Phi K_{II} t^m \left(\frac{\sigma}{1-\omega}\right)^{n_I} \tag{2.38}$$

$$\dot{\epsilon}_{II} = K_{II} t^m \left(\frac{\sigma}{1-\omega}\right)^{n_{II}} \tag{2.39}$$

Normalising these two equations, as previously detailed in section 2.4.4, gives:

$$\frac{dV^{(I)}}{d\tau} = \left(\frac{\hat{\sigma}}{\sigma_0}\right)^{(n_{II}-n_I)} \left(\frac{\Sigma}{1-\omega}\right)^{n_I} \tag{2.40}$$

$$\frac{dV^{(II)}}{d\tau} = \left(\frac{\Sigma}{1-\omega}\right)^{n_{II}} \tag{2.41}$$

The multi-axial creep strain rate constitutive equations may be obtained from the previous two equations (similarly to the generalisation of equation (2.11) in section 2.4.3):-

$$\frac{V_{ij}^{(I)}}{d\tau} = \frac{3}{2}\left(\frac{\hat{\sigma}}{\sigma_0}\right)^{n_{II}-n_I} \frac{\Sigma_e^{n_I-1}}{(1-\omega)^{n_I}} \left(\frac{s_{ij}}{\sigma_0}\right) \tag{2.42}$$

$$\frac{V_{ij}^{(II)}}{d\tau} = \frac{3}{2}\frac{\Sigma_e^{n_{II}-1}}{(1-\omega)^{n_{II}}} \left(\frac{s_{ij}}{\sigma_0}\right) \tag{2.43}$$

Consider next the uni-axial stress-rupture characteristics of a particular material (Fig. 2.3(b)). The uni-axial damage rate equation which will define such behaviour is given by:

$$\dot{\omega} = \frac{M t^m \sigma^\chi}{(1+\phi)(1-\omega)^\phi} \tag{2.44}$$

where M , m , χ , ϕ are material constants. For a uni-axial specimen under constant stress (σ_0) equation (2.44) may be integrated between the initial condition $t = 0$, at $\omega = 0$ and the final condition $t = t_f$ at $\omega = 1.0$ giving:

$$t_f = \left\{\frac{(m+1)}{M\sigma^\chi}\right\}^{\frac{1}{m+1}} \tag{2.45}$$

where t_f is the time to failure or rupture of the uni-axial specimen. At the break stress ($\hat{\sigma}$), the time to rupture is the same for both high and low stress equations. Assuming (t^m) is common for both high and low stress equations the failure time at the break-stress may be written in terms of both the high and low stress material constants:-

$$\hat{t_f} = \left\{\frac{(m+1)}{M_I \hat{\sigma}^{\chi_I}}\right\}^{\frac{1}{m+1}} = \left\{\frac{(m+1)}{M_{II} \hat{\sigma}^{\chi_{II}}}\right\}^{\frac{1}{m+1}} \tag{2.46}$$

giving:

$$\frac{M_I}{M_{II}} = \hat{\sigma}^{(\chi_{II}-\chi_I)} = \Lambda \tag{2.47}$$

Hence the two damage rate equations which describe the stress-rupture lines (Fig. 2.3(b)) are given by:

$$\frac{d\omega_I}{dt} = \Lambda \frac{M_{II} t^m \sigma^{\chi_I}}{(1+\phi_I)(1-\omega)^{\phi_I}} \tag{2.48}$$

$$\frac{d\omega_{II}}{dt} = \frac{M_{II} t^m \sigma^{\chi_{II}}}{(1+\phi_{II})(1-\omega)^{\phi_{II}}} \tag{2.49}$$

Normalising these two equations, (as previously detailed in section 2.4.4) gives:

$$\frac{d\omega_I}{d\tau} = \left(\frac{\hat{\sigma}}{\sigma_0}\right)^{(x_{II}-x_I)} \frac{\Sigma^{x_I}}{V_u(1+\phi_I)(1-\omega)^{\phi_I}} \tag{2.50}$$

$$\frac{d\omega_{II}}{d\tau} = \frac{\Sigma^{x_{II}}}{V_u(1+\phi_{II})(1-\omega)^{\phi_{II}}} \tag{2.51}$$

where:

$$V_u = \frac{K_{II}E}{M_{II}}\sigma^{(n_{II}-x_{II}-1)} \tag{2.52}$$

The multi-axial damage laws, allowing for the multi-axial rupture criterion, may be obtained as follows:

$$\frac{d\omega_I}{d\tau} = \left(\frac{\Delta(\hat{\sigma}_{ij})}{\sigma_0}\right)^{(x_{II}-x_I)} \frac{\Delta^{x_I}(\Sigma_{ij})}{V_u(1+\phi_I)(1-\omega)^{\phi_I}} \tag{2.53}$$

$$\frac{d\omega_{II}}{d\tau} = \frac{\Delta^{x_{II}}(\Sigma_{ij})}{V_u(1+\phi_{II})(1-\omega)^{\phi_{II}}} \tag{2.54}$$

where $\Delta(\sigma_{ij})$ is given by equation (2.34). Both (Φ) and (Λ) are constants and are usually determined for uni-axial plane stress conditions where:

$$\left(\frac{\hat{\sigma}_e}{\sigma_0}\right) = \left(\frac{\Delta(\hat{\sigma}_{ij})}{\sigma_0}\right) = \left(\frac{\hat{\sigma}_1}{\sigma_0}\right) \tag{2.55}$$

The multi-axial constitutive and damage laws used in the finite element creep program Damage-(XX) are given in equations (2.42), (2.43) and (2.53),(2.54) respectively. On the basis that (2.42) and (2.43) govern the creep deformation of the material and (2.53) and (2.54) the failure.

The following rules apply, showing when each equation is to be used on the basis of the prevailing stress state present:-

(a) Creep Strain Rate Equations (2.42) and (2.43):

For $\Sigma_e > (\sigma_e/\sigma_0)$ then use the high stress equation (2.42);

For $\Sigma_e \leq (\sigma_e/\sigma_0)$ then use the low stress equation (2.43);

(b) Damage Rate Equations (2.53) and (2.54):

For $\Delta(\Sigma_{ij}) > (\Delta(\hat{\sigma_{ij}})/\sigma_0)$ then use the high stress equation (2.53);

For $\Delta(\Sigma_{ij}) \leq (\Delta(\hat{\sigma_{ij}})/\sigma_0)$ then use the low stress equation (2.54);

The values of the high and low stress parameters should ideally be obtained by fitting the creep strain/time equation (3.4) to sets of high and low stress creep curves. In many cases the creep tests at high stress (i.e. $\sigma > \hat{\sigma}$) are of very short duration, due to the quick failure of the specimens and only rupture data is available from such tests. For this case a rupture time on the high stress-rupture line is chosen. Equation (2.48) may be integrated between the limits ($t = 0$) at ($\omega = 0$) and ($t = t_f$) at ($\omega = 1.0$) to give:

$$t_f = \left\{ \frac{(m+1)}{M_{II}\hat{\sigma}^{(\chi_{II}-\chi_I)}\sigma^{\chi_I}} \right\}^{\frac{1}{m+1}} \tag{2.56}$$

where M_{II} , χ_{II} , m are known from the fitting procedure for the low stress creep curve data. Thus the value of (χ_I) may be obtained and (M_I) is obtained using equation (2.47). Then the value of (n_I) is obtained from the gradient of the high stress line in Fig. 2.3(a) and the value of (K_I) is obtained from equation (2.37). Having determined all the parameters in the pair of constitutive equations and the pair of damage laws, the equations may given an incompatibility in the uni-axial failure strain across the break point ($\hat{\sigma}$), (Fig. 2.4(a)). The uni-axial failure strain must be continuous at the break point (Fig. 2.4(b)). Compatibility of failure strain at the break point is obtained by adjusting (ϕ_I) such that:

$$\left(\frac{n_I}{\phi_I + 1}\right) = \left(\frac{n_{II}}{\phi_{II} + 1}\right) \tag{2.57}$$

which is obtained from equation (3.4). The material constants can be substituted into the relevant high and low stress constitutive and damage rate laws in the finite element program Damage-(XX), where they may be tested with the uni-axially loaded plane stress finite element mesh shown in Fig. 2.5. Different loads (P) may be applied to this mesh and the resultant failure time and failure strain correlated against both theoretical predictions using the analytically integrated constitutive equations and the experimental results. At this stage modifications in the allowable integration error parameters EPSL and EPSR (section 4.3.3) may be made to give the desired numerical solution accuracy.

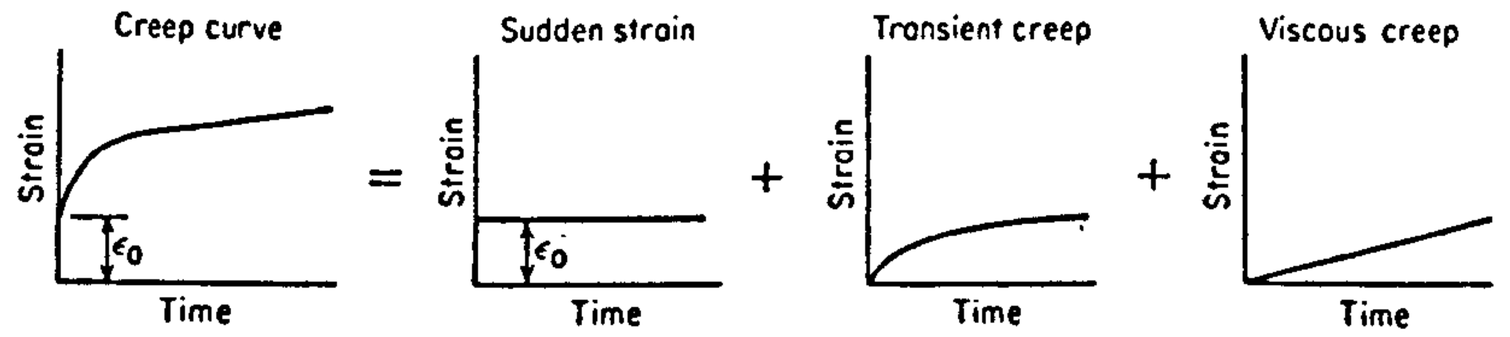

Figure 2.1: Andrade's analysis [14], showing the creep curve components he used to formulate his constitutive equation (2.1).

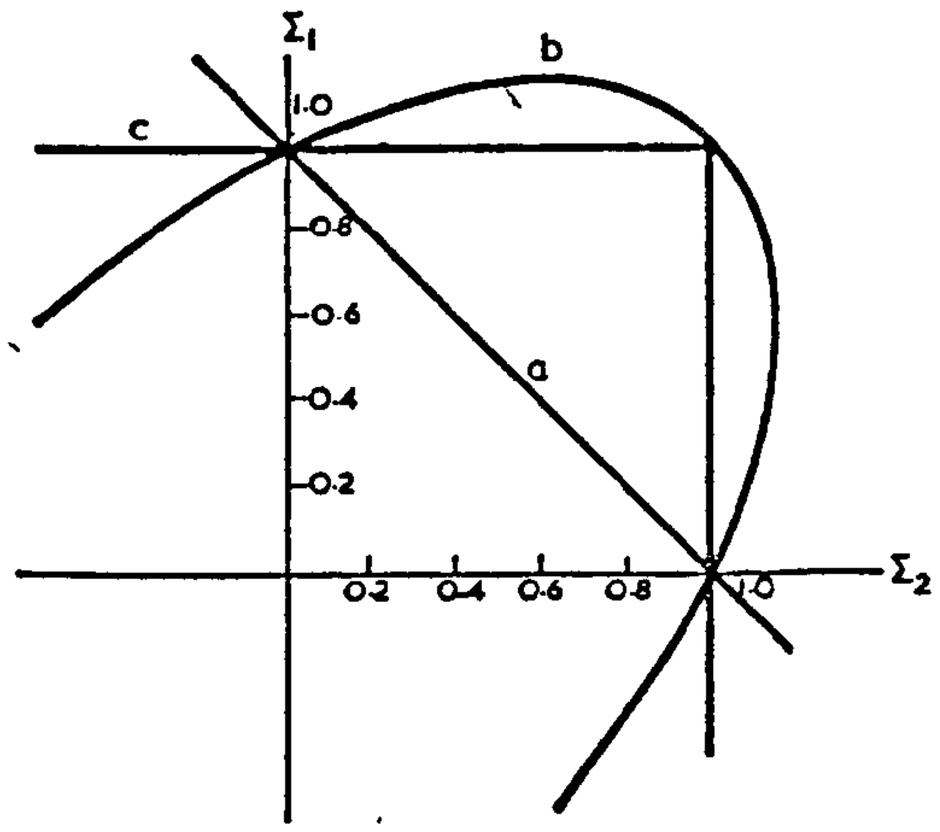

Figure 2.2: The isochronous rupture surfaces obtained from equation (2.32) for plane stress conditions and extreme values of (α, β, γ): maximum, (a) hydrostatic stress (0,1,0); (b) effective stress (0,0,1); (c) tensile stress (1,0,0); after Hayhurst [22].

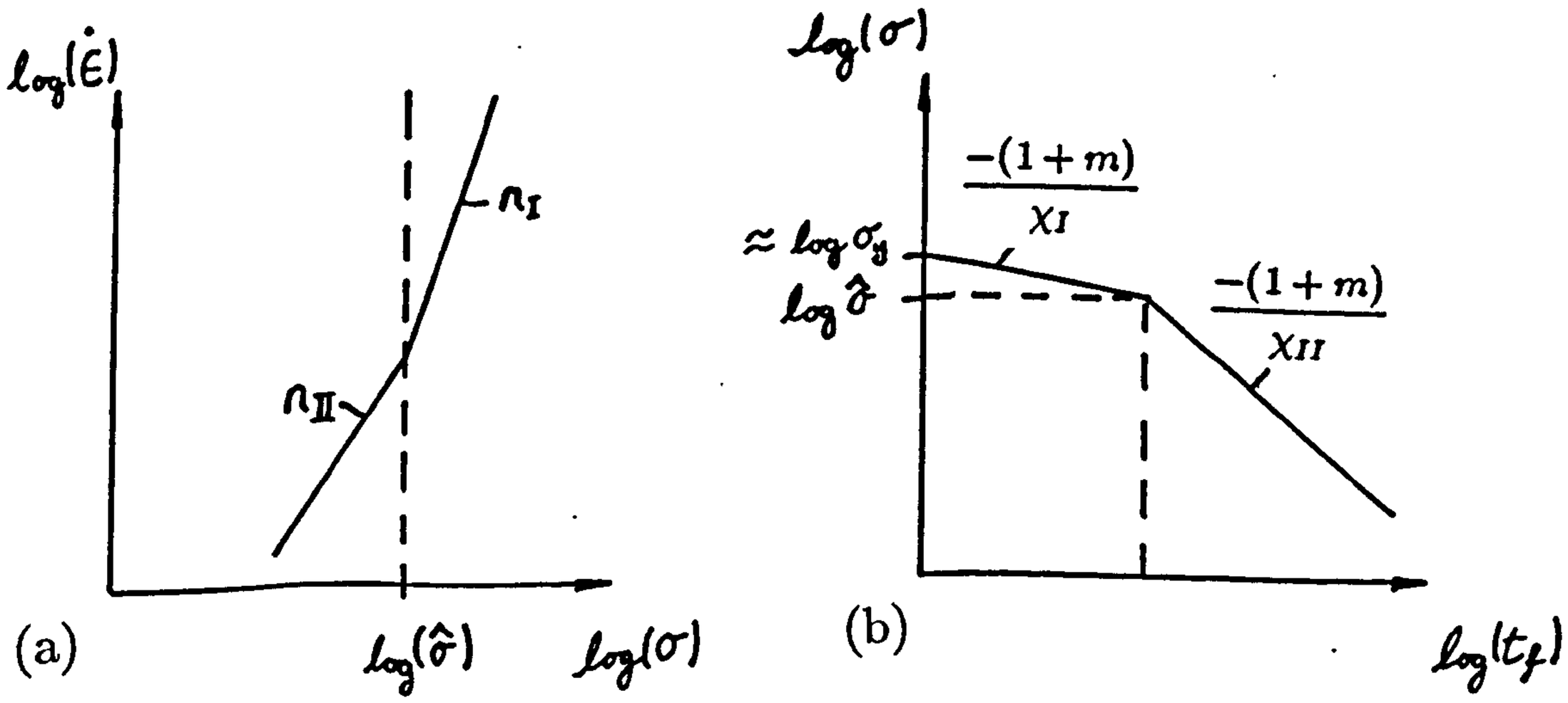

Figure 2.3: Typical uni-axial, bi-linear (a) log(min.strain-rate) vs. log(stress) diagram and (b) stress-rupture diagram.

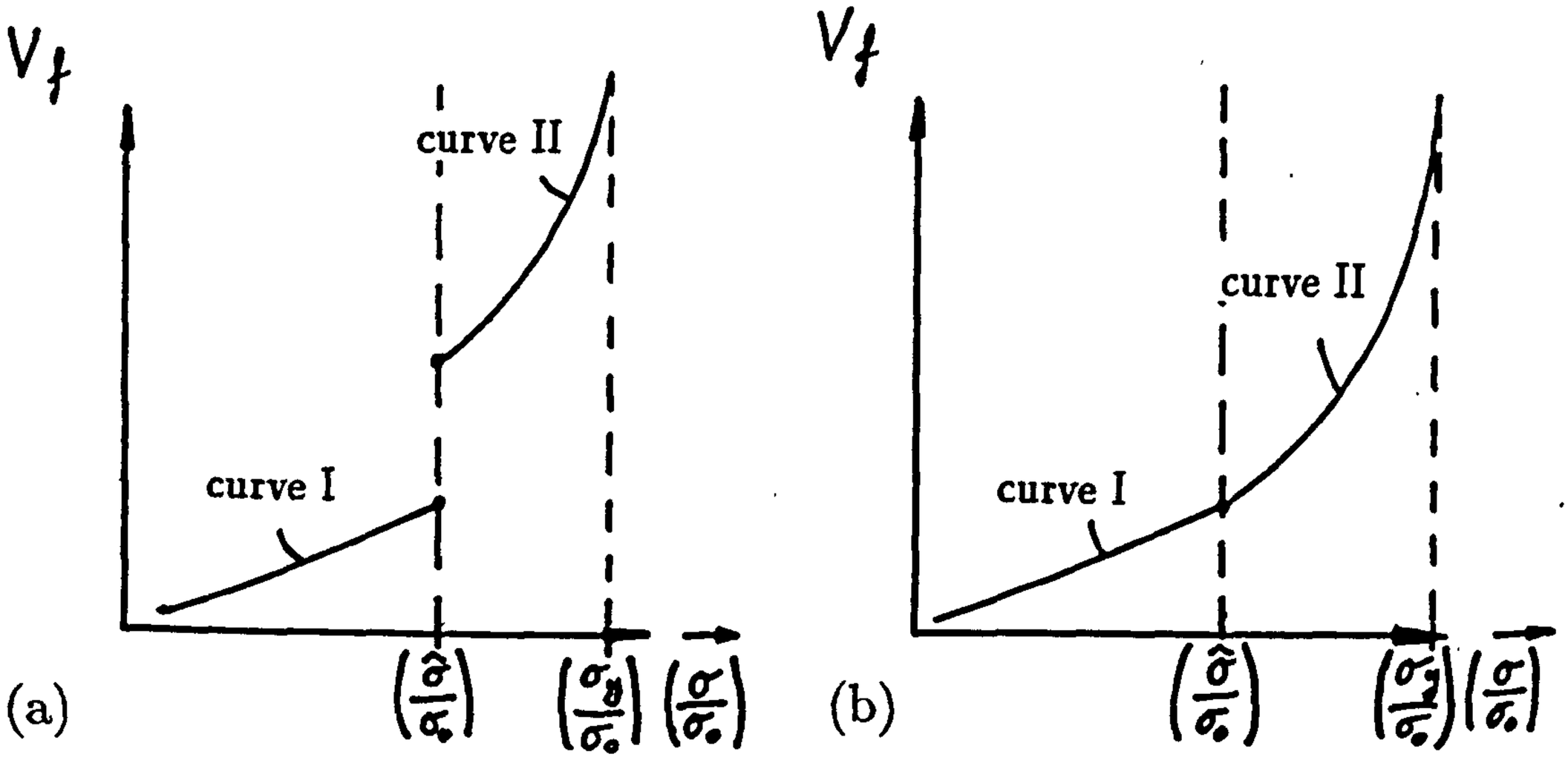

Figure 2.4: Predicted uni-axial rupture ductiliy obtained using quation (2.25) with high and low stress material constants to give curves I and II respectively. (a) shows incompatible high and low stress failure strain predictions at the break stress, which are made compatible (b) using equation (2.57) to give a new value for (ϕ_I).

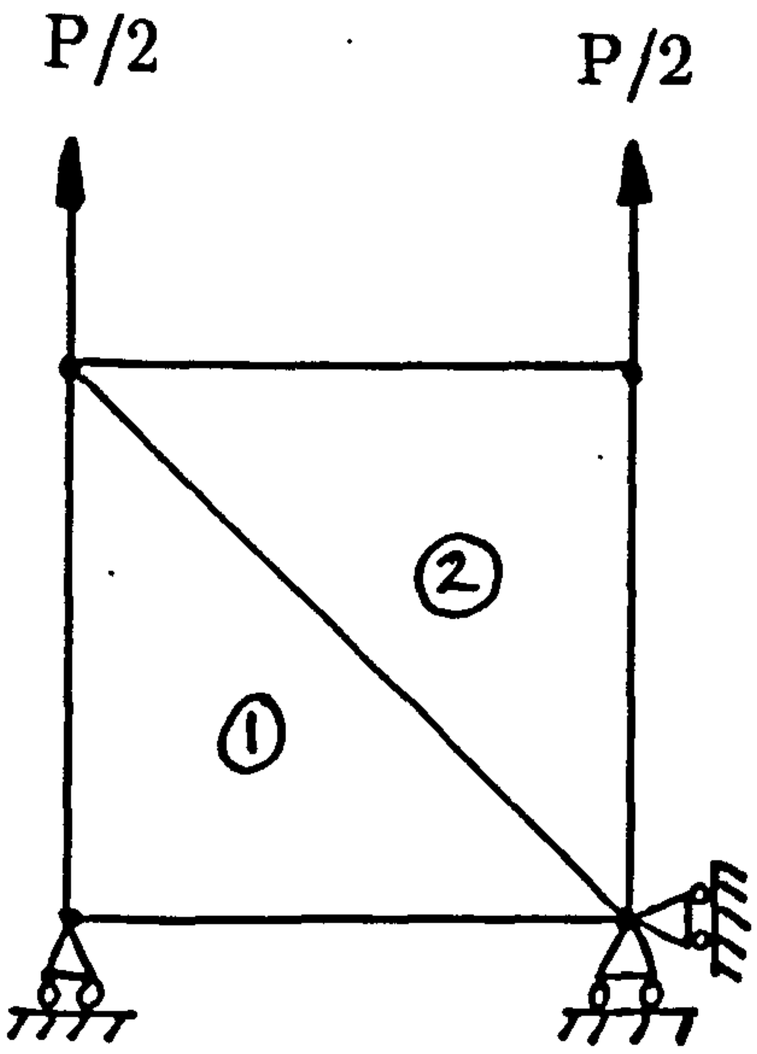

Figure 2.5: Simple uni-axial finite element mesh used to check both numerical and constitutive model accuracy.

Chapter 3.

Tensile Creep Testing.

3.1 Introduction.

All theories used for the mathematical modelling and design of high temperature structural components, are related to the macroscopic mechanical properties of the materials to be used, by the material constants. The material constants are obtained by performing tensile creep tests, using specimen samples of the material from which the final component is to be made (sometimes samples may be taken from a prototype component). In tensile creep tests, specimens are subjected to uni-axial loads at the test temperature, to provide data which may be used directly, or which may be interpolated and/or extrapolated to data relating to the in-service condtions of the component. In order to establish an effective component design with confidence and safety, more sophisticated mathematical models and design theories are sought; but such models and theories are only as good as the material data they use. Therefore, testing techniques, equipment and laboratory standards must also improve, in parallel with the theoretical advancements; to provide materials data with smaller scatter bands.

What follows is a detailed account of the tensile creep tests performed by the author for (OHFC) Copper. A description of the creep testing equipment is given in section 3.2, where special alignments are required to ensure small (ideally zero) induced specimen bending stresses and test accuracy. The manufacture and measurement of specimens is detailed in section 3.3 and the subsequent creep testing procedure, experimental design and material data acquisition is presented in section 3.4. The material test data obtained is given in the form of creep curves, stress-rupture and minimum creep rate-stress diagrams in section 3.5. This data may be used directly in design via hand calculations, or used as in section 3.6 to obtain the uni-axial constitutive and damage law creep constants under isothermal conditions. These material constants when used in the creep-damage finite element method enable the study of deformation and failure behaviour of real high temperature components made from this tested material; to provide an improved design accuracy, over standard hand calculations which give conservative designs.

In section 3.7 a uni-axial anisothermal constitutive model is developed, so that creep strain rates and damage rates may be predicted as a function of both test stress level and test temperature. Finally, predicted stress-rupture and stress-minimum creep rate lines are compared with the experimental lines and predicted creep curves in the test temperature range are shown to have the characteristic shapes observed in tests.

3.2 Tensile Creep Testing Equipment.

3.2.1 General Description.

Three identical, constant load, uni-axial tension creep rigs are used for the creep tests and are shown in Fig. 3.1. A schematic diagram of one such creep rig is shown in Fig. 3.2. A typical creep specimen is shown in the engineering drawing of Fig. 3.3. The creep specimen is held at either end by clamp blocks with a bolt and ceramic collars (Fig. 3.2 and 3.4). The collars are ceramic as steel collars creep at high temperature and may weld to the specimen. The collars grip the specimen flats and take some of the load away from the load holes, which reduces load hole deformation and eases removal of the specimen after the test. The pins, clamp blocks and pull rods are made from Nimonic superalloy for its good creep resistance at high temperatures.

Referring to Fig. 3.2, the load is transferred from the load hanger via a 1:10 lever-ratio load arm, supported on a knife edge fulcrum. The load is then transfered through a knife-edge, a universal joint and a pull rod, to the specimen top clamp block and then the creep specimen. Such an arrangement of knife edges and universal joints incorporated into the load-train restricts induced bending stresses in the creep specimen to very low levels. (Better than 5 % bending for all test loads. Refer to section 3.2.2 (a) for the definition of percentage bending).

The test load is applied at a constant rate at the start of a test by a hydraulic jack, which is manually controlled by the operator. The constant heating effect is supplied by a Donaldson 3-zone resistance heating furnace, which is linked to a proportional temperature controller. The controller has a resistance type thermocouple placed in the centre of the furnace to provide temperature feedback control. Three

separate manual potentiometers control the bias of each of the three furnace zones T, M and B to ensure there is no temperature gradient along the specimen. Extensometer rods are connected to the creep specimen protrusions or pips (Fig.3.3), which in turn are connected to a linear variable transformer (L.V.D.T.) to measure the extension of the gauge length during a test (Fig. 3.5).

As a creep test proceeds the specimen extends and the capstan needs adjusting to retain the load arm in the horizontal position to prevent change of the lever arm, beam ratio, and hence changes of the specimen stress level. The L.V.D.T. offset screw may also need periodically adjusting to keep the extensometer core within the linear range of the device ($\pm$ 6 volts about 0V or $\pm$ 2 mm core displacement).

A strain bridge type load cell is connected to the lower pull rod to measure the actual load transferred to the specimen. All sensor readings (Table 3.1) are measured digitally using a digital volt meter (D.V.M.) connected to a Solatron switch box, which is controlled remotely by an Opus personal computer using an IEEE 488 (IBM) interface board (Fig. 3.6). An expert system developed by Dunne [37] records sensor readings at specified or automatically determined intervals of time. The digital readings are stored in files on a hard disc and may be periodically examined between logging times using the expert system graph examination/display facility. Having completed a test the data file may be dumped to floppy disc and transferred to mainframe computer for evaluation and constitutive parameter fits.

An X/t or X/Y-chart recorder is also available to plot load vs. strain curves for the determination of stress/strain curves, or for monitoring fast changes in strain or load, during the initial loading period. An independent chart recorder also allowed other output signals of interest to be monitered continuously, where a descrete digital record was not satisfactory.

All the test equipment is surrounded by a controlled atmosphere monitored to be $20°C \pm 0.5°C$ by a laboratory air conditioner, Fig. 3.7. The controlled atmosphere enbles improved accuracy control of test temperature and ensures that machine and instumentation deflection changes are minimised, by counteracting the external atmospheric changes.

3.2.2 Special Experimental Arrangements.

(a) Restriction Of Bending In Tension Specimens.

Bending occurs in uni-axial creep tension specimens as a result of poor specimen alignment, where the load line does not coincide with the central axis of the specimen gauge length. The effects of bending on creep tension tests have been studied in detail, first by Penny et al [38,39] and then by Hayhurst [40]. If alignment is poor the bending stress superimposed on the mean axial stress may be high enough to cause a significant reduction in the rupture life, over a specimen which is correctly aligned. Hayhurst [40] details that a creep test, for a material having a Norton's law creep exponent of ($n = 5$, equation 2.2) and a constant eccentricity of ($\delta/d = 0.015$), (where (δ) is the displacement of the specimen centre line, from a specimen centre line corresponding to zero eccentricity and (d) is the diameter of the specimen), the rupture time may be reduced by a maximum of 60 %. Hayhurst also showed that the life reduction was also a function of the creep exponent of the material (n). The rupture life increases with higher values of (n) for specimens with the same constant eccentricity. These studies showed that much of the scatter in materials data previously attributed to material variation could be explained as a direct result of varying amounts of bending, which is qualified by a tolerance due to test temperature variations.

The percentage bending in an elastically loaded tension specimen is defined by Hayhurst [40] in terms of the elastic surface strains:-

$$PercentageBending = \left(\frac{\epsilon_1 - \epsilon_2}{\epsilon_1 + \epsilon_2}\right) \times 100 = 8\left(\frac{\delta}{d}\right) \times 100 \qquad (3.1)$$

where (ϵ_1) and (ϵ_2) are the uni-axial elastic strains measured at diametrically opposite points on the surface of the specimen. Figure 3.8 shows values of the percentage bending as a function of load for different creep testing machines [38]. It shows the ability of the universal joints and the blocks to restrict bending caused by specimen misalignment and bent pull-rods, in comparison with the large bending levels produced by commercially available machines. The commercially available machines have button head type specimens and specimens directly threaded to the pull-rods.

Even with the use of the universal joints and blocks in the load train Penny [38] suggests that the initial specimen eccentricity should be restricted to better than

(δ/d=0.005), which corresponds to a bending value of less than 5 % using (3.1). Hayhurst [40] suggests that for truly repeatable creep tests with low scatter initial eccentricity must be maintained to a value below (δ/d=0.002), which corresponds to less than 2 % bending. For the 8 mm diameter specimen used by the author, this corresponds to an eccentricity of less than approximately $0.025mm$. With the aim of ensuring this accuracy special surfaces (A) and (B), (Fig. 3.2) were scraped by hand to be planar and parallel with one-another to within an accuracy of $\pm 0.01mm$. An inexpensive yet accurate measuring instrument has been designed by the author to enable this accuracy to be achieved. The instrument comprises a 5ft vertical bar supported between two lathe centres. A dial gauge of resolution $0.0025mm$ is mounted on the bar and may be rotated in a horizontal arc about an axis passing through the lathe centres. Accurate spirit levels were used to arrange each creep rig to have its lower pull rod precisely vertical. The axis of rotation of the measuring bar is also arranged to be vertical in a similar manner. The lower surface (A) was then hand scraped until flat, judged by the deviation of the clock-gauge when the surface is scanned by moving the clock-gauge in horizontal arcs of increasing radius. An optical flat and a surface plate with marking ink was also used to highlight high spots to be scraped. The clock-gauge was then used to scan both surfaces (A) and (B) until over correspondingly similar arcs for top and bottom surfaces, the deviation of the clock gauge is within the required tolerance of $\pm 0.01mm$, by scraping the top surface (A) only. After the plates were scraped the position of the lower bearing and the upper knife-edge support (see Fig. 3.2) were located by the use of an accurate plumb-bob suspended from the end of the load arm. The load train was then fully assembled and checked with spirit levels to make sure that the pull rods and blocks were precisely vertical and in line.

The universal joints and blocks in the load train allow alignment of the creep specimen in two mutually perpendicular directions before a test proceeds. Feeler gauges are used to align the specimen axis between the clamp-block slots; straight edges ensure the clamp-blocks are in line and an engineers spirit level ensure the clamp-blocks are vertical [41].

The percentage bending results for each creep rig for a wide range of test loads was tested with a stainless steel specimen, which had four strain gauges mounted at

right angles to one another on the surface of a mid-cross-section of the specimen, (Fig. 3.9). The percentage bending is measured in accordance with equation (3.1) in two mutually perpendicular directions for increasing values of load. A typical bending graph is shown for creep rig No. 2 also in Fig. 3.9. Three bending tests were carried out for each creep rig, removing then re-positioning and aligning the specimen in the creep rig each time, to judge reproducibility of the results. All three creep rigs gave results of less than 6 % bending across the whole load range 0.7 KN to 3.5 KN, with some tests yielding less than 3 % bending even at the lowest test load. Bending results obtained for the three creep rigs set up by the author compare favourably against results for other creep rigs in Fig. 3.8.

(b) Extensometer Grip Design.

The large deformations which could occur in the Copper creep tension specimens during some creep tests meant that the initial bolt pressure clamping the extensometer clamps to the pips, could relax during a test, allowing the extensometer clamp positions to move, producing discontinuous results. The extensometer clamps were re-designed by the author to incorporate a four spring arrangement (Fig. 5.10 (a) and (b)) to allow the extensometer clamps to close as the specimen creeps, to maintain its grip position on the specimen protusions; thus giving accurate strain readings.

Nimonic springs were specified for the design using a specific spring force so as not to produce large compressive stresses in the specimen, whilst retaining enough spring force to retain the clamps fixed to the specimen at the test temperature during specimen deformation. The use of the four spring extensometer clamp also allowed a larger specimen diameter of 8 mm to be used with the same extensometer clamps previously used for 6.35 mm diameter specimens, without further modification.

(c) Calibration Of Sensors And Calibration Tests.

The load cells were calibrated for both loading and unloading of a test specimen within the elastic region at ambient temperature. The displacement transducers (L.V.D.T.'s) were calibrated using a micrometer calibration rig. Temperature calibration and temperature stability tests were performed for each test temperature for a period of two weeks duration, using a dumb specimen containing three thermocouples equispaced over the gauge length. Temperatures did not deviate from the test

temperature even at the highest test temperature of $500°C$ by more than $0.5°C$.

3.3 Manufacture Of (OFHC) Copper, Creep Tension Specimens.

The (OFHC) Copper, creep tension specimens were manufactured to the specifications given in the engineering drawing of Fig. 3.3. The creep tension specimen is classified as a non-proportional test piece by BS 3500 [42] for creep and rupture testing of materials; though the specimen dimensions do lie close to those of a proportional test piece of 8 mm diamter. A proportional test piece is defined in the standard as having a gauge length ($L_0 = 5.65\sqrt{A}$) where (A) is the initial cross-section area of the specimen.

The blanks of Copper material from which the creep specimens were machined, came from a large as-cast billet as shown in Fig. 3.11. The billets are cast using cast iron chills placed either side of the casting box to remove heat from surfaces (A) and (B). Etched sections of the cast block reveal that the chills produce a refined grain structure to a depth of about 3 mm from the surfaces (A) and (B), with long thin grains forming deeper into the material (Figs. 12(a) and (b)). These long thin grains grow inwards away from the two cooled surfaces (A) and (B) due to a directional solidification process and meet in the middle of the block forming a central rift. The creep specimen blanks are cut from the block as shown in Fig. 3.11 so that the long thin grains are transverse to the loading direction in the creep specimens.

The specimen blanks are initially machined flat leaving $1.0mm$ depth of material either side to be removed later. The blanks are then turned in a profiling lathe using a hard steel master specimen as template. Severe problems were encountered on machining the as-cast Copper blanks, due to its extreme softness and low shear strength. Even at very slow spindle speeds, taking fine cuts, at low feed rates, the cutter force is sufficient to bend the specimen and results in the specimen being thrown out of the machine as the tool digs into the material (Fig. 3.13). Unacceptably large amounts of twist along the length of the specimens also presented a problem. Good specimens were produced by the following production route:

The specimen diameter is increased from 6.35 mm to 8.0 mm, increasing the

tortional rigidity of the speicmen some 50%. The driven end of the specimen blank is supported in a collet-chuck whilst the other end is supported by a lathe rotating centre. This increases the rigidity of the specimen in bending over a specimen supported by a lathe centre at either end. The lathe spindle speed is restricted to 300 r.p.m. A high speed steel cutting tool is used with a large rake and face angle to restrict chip build up and prevent large cutter forces. The cutting tools are ground precisely in a grinding gig which produces a tool tip radius of 0.4mm to form the radii at the specimen pips. The lubricant is paraffin and oil mixture which is applied with a bush to the Copper specimen. Machine cuts are taken with extreme care and the depth of cut is reduced as the final diameters of the specimen are approached. Final cuts were of the order of two thousandths of an inch depth with a very slow feed rate to give the surface finish of 0.8 μm as required. The specimen is then held betweem flat steel plates on a magnetic table and the specimen flats are ground on either side, until the specimen is of the required thickness and the specimen flats are equispaced about the axis of the specimen gauge length. This is ensured using an accurate clock gauge. The specimen load holes are then jig bored to within 0.01mm of the centre line of specimen gauge length. This tolerance corresponds to the loading eccentricity tolerance δ/d=0.002 specified by Hayhurst [40].

The produced specimens were measured for accuracy using an S.I.P. Generthat voise machine to check all specified dimensions are explicitly satisfied. Specimens not satisfying the designed tolerances were rejected and not used in the tests..

B.S. 3500 [42] specifies that the gauge diameter shall not vary by more than 0.03 mm and a tolerance of $\pm$ 0.03 mm, on the axiality of the load hole centre lines relative to the centre line of the gauge length, shall be satisfied. The former and later measurements for the specimens measured were typically 0.015mm and $\pm$ 0.015mm respectively.

3.4 Creep Testing Procedure And Experimental Design.

3.4.1 Procedure.

Before a creep test is performed the specimen must have thermocouples fitted and must be accurately aligned in the creep test rig. The set-up procedure is detailed elsewhere [41]. With a pre-load on the load hanger the furnace is switched on and the

creep specimen left to soak for up to 24 hours [42,44] for a creep test. The pre-load ensures that the alignment of the universal joints and specimen are maintained in position. The pre-load may be reduced from 20 N to 5 N for high temperature tests where the 20 N load may cause significant creep to occur during the soak period. The soak period ensures that the steady thermal state is reached before a test is performed. For tensile tests, the soak time may be as little as 15 minutes after a stable temperature is obtained [43].

Having reached the end of the soak period and a stable test temperature ($\pm 0.5°C$) has been obtained for a period of at least one hour, the full test load may be applied to the specimen. It is important to apply the load at a constant rate, with a load-up period which is constant for each test performed. Tilly [45] studied the effect of varying loading rate upon the shape of the creep curve obtained from identical creep tests. He observed that the slower the loading rate the higher the initial strain (ϵ_0) at the end of the loading period. He notes that after this initial loading period creep rates are as much as four times slower than those following fast loading. The differences in the shapes of the creep curves for slow and fast loading tests are seen to diminish with time, both tests eventually stabilising at the same minimum creep rate showing the same tertiary creep profile and having the same failure time. It is apparent that rapid loading gives a fundamental form of creep curve which approximates to an (at^m) term in the Andrade law, (equation 2.1) but slow loading causes creep to occur at intermediate stresses causing subsequent creep at the stable test load to follow a primary curve with a decreasing exponent (m). This implies that rapid loading is preferable. Therefore, loading times are maintained at a duration of 3 seconds with the use of a manually operated hydraulic jack, which steadily lowers the weights onto the load hanger (Fig. 3.2).

Penny discusses [46] strain rate changes during the creep and tensile tests. He states that on loading, though the cross-head velocity may be constant the specimen may be subjected to vast changes in strain rate, which may be related to the stiffness of the machine and the specimen design. He states that constant strain-rate tests must be performed if the effects of machine stiffness and specimen design on the test results are to be eliminated; so that meaningful constitutive constants can be derived from test data. Constant strain rate tests upon loading may be performed by

manually controlling the loading rate or cross-head velocity. This may be done with the existing load jack by monitoring the strain time curve on the X/t-plotter, whilst controlling the hydraulic loading jack valve, to maintain a linear strain time profile on loading. This requires considerable practice and concentration and the load time has to be increased; but could be peformed accurately in future tests with the use of a suitable feedback controller and a variable speed screw-jack to load the specimen.

From experience it is important to control the loading rate which determines the initial strain value (ϵ_0), since (ϵ_0) is subtracted from the whole total strain creep curve, giving the final creep curve (Fig.3.14(a)). The error in (ϵ_0) is directly transferred to an error in the whole creep curve. Therefore, values of initial strain have been calculated in two ways within the author's tests. The first method involves using fast scan data from the data logging system. Two data points per second are obtained for load and strain during load application. The data may be plotted and the strain (ϵ_0) at time (t_0), where the full test load is first seen by the creep specimen, is taken as the initial strain (Fig.3.14(b)). The second method involves performing a uni-axial tensile test at the creep test temperature and directly reading the strain (ϵ_0) at the test load from the stress/strain curve. The loading rate should be maintained as fast as possible, ideally it should be same as that in the creep test. If slower loading rates are used then the stress/strain curve drops low and hence the initial strain reading at a particular test stress will be large, and may even exceed the primary total strain value. The values of initial strain (ϵ_0) calculated by the two different methods should be the same.

Stress/strain curves are obtained from load/strain curves, which are directly read from a creep rig by the X/Y-plotter. The use of the initial cross-sectional area of the specimen seemed reasonable to convert the load/strain curve to an engineering stress/strain curve, as initial strain values were obtained well away from the point on the curve where significant necking occurred.

3.4.2 Experimental Design.

When material creep data is required for a new material, it is not known what test loads are required to give reasonable creep failure times. Test temperatures are easily identified for a range of fractions of the homologous temperature, relating to

the service temperatures of the components to be made from the material. At each test temperature a series of at least two creep rupture tests must be performed, at different stress levels, to define constitutive equation parameters representative of material behaviour at this temperature level (Fig. 3.15). For each temperature level a tensile test is conducted to determine the tensile strength and the 0.2 % yield stress or actual yield point stress, before creep testing proceeds. This is done in accordance with BS 3688, part 1, [43] and BS 4A4, part 1, section two [44]. From the yield stress (σ_y) and the tensile strength (σ_{TS}) an initial estimate of the highest stress level for the first creep test may be calculated, as the minimum of ($\sigma_y/2$) and ($\sigma_{TS}/2$). This procedure is only appropriate for some materials but provides a starting value of stress to test at. Ashby deformation and fracture mechanism maps (section 1.2.3, 1.3.3 and 1.4) may also prove useful in determining test stress levels . It is always preferable to test at the highest stress level initially, giving the quickest failure times first, then test at lower stress levels giving long failure time tests finally. In this way the previous test values may be used to extrapolate along a straight line on a log(stress) vs. log(rupture time) plot, to define a stress level for the next test having a longer lifetime. Before each creep test is performed it is important to try to determine which dominant creep deformation and failure mechanism will be present during the test. Figures 3.16 and 3.17 show Ashby deformation and fracture mechanism maps respectively for a pure Copper material similar to that used in creep tests by the author. The homologous test temperature and uni-axial stress level will define a point on an Ashby deformation and fracture mechanism maps [8,9,11,12] for a similar test material, which will give some indication of the creep mechanisms present and if the test will be valid for use with the constitutive model; which is only representative of certain creep mechanisms. In creep tests failure times of 100 hours, 300 to 500 hours and greater than 1,000 hours are aimed for, together with a longer term test of 2,000 hours or so if time permits. Usually for creep tests, the larger the test duration the more representative the data is of the mechanisms occurring in the real structure and extrapolation will be of increased accuracy.

3.5 Results And Observations From Creep Tension Tests For As-Cast (OFHC) Copper.

Uniaxial creep tension tests were performed on two different batches of a pure Copper material in the as-cast condition, at the test temperatures of 150, 250 and $500°C$. The majority of tests used batch-(C) material, having long thin grains of 1.35mm average diameter, arranged transversely across the specimen gauge length (section 3.3). Some creep tests for the test temperatures $150°C$ and $250°C$ used batch-(M) material, which had a equi-axed grain structure of average grain diameter 0.5 mm. The batch-(M) Copper was used for comparison with batch-(C) Copper test data, to highlight the variation in material properties caused by grain size variation as a result of a different production route.

Values of the elastic modulus (E), the 0.2 % proof stress and the ultimate tensile strength (U.T.S.) were obtained from tensile tests on batch-(C) material over the temperature range $20°C$ to $500°C$. The results are summarised in Figs. 3.18 and 3.19 respectively. Using these material properties and the specimen stress levels used in the creep tests, areas (A1), (A2) and (A3) at each test temperature of 150, 250 and $500°C$ respectively, are identified on both the Ashby deformation mechanism map and the Ashby fracture mechanism map in Figs. 3.20 and 3.21 respectively, for a similar Copper material. The areas (A2) and (A3) show that both the $250°C$ and $500°C$ creep tests lie in the power-law creep regime, and fail by an intergranular creep fracture mechanism. The area (A1), corresponding to the $150°C$ tests, crosses mechanism map bondaries in both Figs. 3.20 and 3.21, with high stress tests lying in the power-law breakdown region and failing transgranularly respectively. Power-law breakdown means that Norton's power law (equation (2.2)) no longer holds true for the material deformation in this region. Hence, the creep constitutive equation and damage law (equations 2.19 and 2.20) cannot be applied to represent creep behaviour in this region. Testing at $150°C$ was still carried out, as the Ashby maps only provide a guideline and may not precisely represent the mechanistic behaviour of the test material.

Thirty-two creep tests and three stress/strain tests were carried out, with some stress/strain data provided by parallel tests on creep fatigue specimens [47]. The results from the creep tests are presented in Table 3.2 and in the stress-rupture

and stress-minimum strain rate graphs of Figs. 3.22 and 3.23 respectively. It is noticed that as the temperature of the creep tests increases, the magnitude of the gradients of both the stress-rupture and stress-minimum strain rate lines, through the experimental data, decreases.

Samples of failed specimens at each temperature level are shown in Fig. 3.24. The fracture surfaces corresponding to specimens (A),(D),(E) and (F) of Fig. 3.24 are shown in Figs. 3.25, 3.26, 3.27, 3.28 respectively. All the specimens shown except specimen (F) are made from batch-(C) material; specimen (F)is made from batch-(M) material. Referring to Figs. 3.24 specimens (A) and (B), were tested at $500°C$ which show intergranular cavitation (Fig. 3.25, Fig. 3.26) and fail on a fracture surface perpendicular to the tensile axis. Similar is true for specimens (C) and (D) which were tested at 250 °C . Observing the fracture surfaces corresponding to specimens (A) and (D), (Fig. 3.25 and Fig. 3.26) the transversely orientated columnar grain boundaries are seen as a serrated fracture surface. Bending has occurred in specimen (C), (Fig. 3.24), at rupture due to uneven damage propagation across the specimen. Specimens (E) and (F) were tested at $150°C$ and show local necking as the final rupture mode (Fig. 3.27 and 3.28 respectively), due to the high applied test stress levels, which were necessary to give reasonable rupture times, causing large deformation to occur in the specimens (Fig 3.24). The fracture surface for specimen (F), (Fig. 3.28), shows the equi-axed grain structure of the batch-(M) material. The fracture surface for specimen (E) is for batch-(C) material and shows the dominance of a ductile rupture mode, not seen in the specimens tested at higher temperatures and lower stress levels, which fail in a creep-brittle manner. Therefore the specimens tested at $150°C$ at these high stress levels do not show a true creep deformation and failure mode, but one which is controlled by plastic deformation resulting from increased net-section stresses in the vicinity of the specimen neck. It may be that the material is bi-linear in rupture behaviour (section 2.6) and will deform and fail in a creep-brittle manner without necking at lower test stress levels.

Creep specimens at each of the test temperatures were sectioned and etched [48] so that a full metallurgical examination of the mechanisms present during the prevailing test conditions could be determined. The report from the metallurgical examinations confirmed the observations made above. The report details that the

specimens tested at $150°C$ were heavily deformed showing extensive surface-slip and cracks at 45° and 90° to the tensile axis, with final failure due to high ductility creep rupture in a necked region. Some slip-banding within the grains was observed, but it was not as extensive as that observed in the specimens tested at $250°C$, which had a high etch pit density revealing a high density of dislocation networks. The final failure was through the formation of intergranular cracks with some voiding present causing a creep brittle type fracture. The $500°C$ specimens also showed the formation of intergranular cracks, again with some voiding, but no slip was observed. The specimen had a small etch-pit density, revealing reduced dislocation networks due to the dominance of the climb mechanism (section 1.2.1); which is a thermally activated mechanism. Therefore, the specimens tested at $500°C$ also fail in a creep brittle manner. Hence, a mechanism change occurs in stepping from the high stress level tests at $150°C$ to the lower stress level tests at $250°C$. It is thought that if the stress levels for the $150°C$ tests were lowered sufficiently, so that large initial loading strains and necking were not present, a creep brittle fracture could be obtained. Two specimens were tested at lower stress levels, see Test No.5 and 6 Table 3.2, both of which had to be aborted due to rupture never being obtained. Test No.6 continued to creep into the secondary creep region for some 3,500 hours without any turn-up in the creep curve, to show the presence of tertiary creep. It was therefore not possible to prove this theory in the time available.

The results of the metallurgical examinations [48] are summarised in Table 3.3. Metallurgical examination also highlighted significant variations of the grain sizes within specimens. Two out of four specimens, which were cut from the batch-(C) columnar grained cast block, when sectioned were revealed to have equi-axed or irregular grain size distributions within the specimens. This must explain some of the scatter in the test results obtained.

3.6 Obtaining The Uni-Axial Constitutive Equation And Damage Law Material Constants Under Isothermal Conditions, From the Experimental Data, For Use In Computer Finite Element Structural Analysis.

The constitutive equation and damage law to be used (equation 2.19 and 2.20) may be writen in simple uni-axial, non-normalised form:-

$$\dot{\epsilon} = Kt^m \left(\frac{\sigma}{1-\omega}\right)^n \tag{3.2}$$

$$\dot{\omega} = At^m \frac{\sigma^\chi}{(1-\omega)^\phi} \tag{3.3}$$

where K, A, m, n, χ, ϕ are the material constants to be determined. Equations (3.2) and (3.3) may be integrated analytically to give a relationship for the creep strain as a function of the applied stress level and time:

$$\epsilon = \frac{K\sigma^n t_f^{1+m}}{(1+m)\left(1-\frac{n}{\phi+1}\right)} \left\{1 - \left(1 - \left(\frac{t}{t_f}\right)^{1+m}\right)^{\left(1-\frac{n}{\phi+1}\right)}\right\} \tag{3.4}$$

where t_f is the time to failure or rupture and is given by the integration of (3.3) between $\omega = 0$, at $t = 0$ and $\omega = 1.0$ at t_f:-

$$t_f = \left\{\frac{(1+m)}{A(\phi+1)\sigma^\chi}\right\}^{\frac{1}{1+m}} \tag{3.5}$$

Equation (3.4) gives a full primary, secondary and tertiary creep curve representation and may be simplified by noticing that the creep strain (ϵ_f) at the failure time (t_f) is given by:-

$$\epsilon_f = \frac{K\sigma^n t_f^{1+m}}{(1+m)\left(1-\frac{n}{\phi+1}\right)} \tag{3.6}$$

N.B. Equation (2.6) may be integrated where $f(t) = t^m$, for a constant uni-axial stress (σ_0) and equation (3.5) may then be used to give a primary and secondary analysis failure strain prediction:

$$\epsilon = \frac{K\sigma_0^{n-\chi}}{A(\phi+1)} \tag{3.7}$$

analogous to that of equation (3.6). Equation (3.7) gives a normalised failure strain prediction of:

$$V_u = \frac{KE}{M}\sigma_0^{(n-\chi-1)} \tag{3.8}$$

where $V = \epsilon/e_0$, $e_0 = \sigma_0/E$ and $M = A(\phi + 1)$. V_u is identified to be a material constant which appears in the damage rate equation (2.20). V_u defines both the normalised time scale and the normalised strain scale.

Equation (3.4) may be written in normalised form using (3.6) as:

$$\frac{\epsilon}{\epsilon_f} = \left\{1 - \left(1 - \left(\frac{t}{t_f}\right)^{1+m}\right)^{\left(1-\frac{n}{\phi+1}\right)}\right\} \tag{3.9}$$

This equation is fitted to a set of creep curves corresponding to uni-axial creep tests over a stress range under isothermal conditions and in conjunction with equation (3.5) the 6 creep constants may be determined in equations (3.2) and (3.3). What follows is a brief discription of a well developed creep curve fitting procedure [49,50,37], for obtaining these material constants.

Othman [50] details the use of a two-parameter creep curve representation, where he defines one parameter as $(1 + m)$ and the other as $\Delta = (1 - (n/\phi + 1))$ in equation (3.9), which gives:

$$\frac{\epsilon}{\epsilon_f} = \left\{1 - \left(1 - \left(\frac{t}{t_f}\right)^{1+m}\right)^{\Delta}\right\} \tag{3.10}$$

Dunne [37] details that the experimental data for each stress level is normalised in the same way as equation (3.9) and equation (3.10) is fitted in turn to each experimental creep curve, using a least squares optimization scheme, where the residuals or errors are minimised with respect to (Δ) and (m). Values of $(K\sigma^n)$ are then obtained using (Δ) and (m) for each creep curve, at each test stress level by rearranging equation (3.6):-

$$K\sigma^n = \epsilon_f(1 + m)\Delta t_f^{-(m+1)} \tag{3.11}$$

The technique described above is used to provide starting values for a further optimization [37,49]. The second optimization minimises the residuals between the experimental creep curve data, and the functional creep curve representation of equation (3.4), with respect to the constant groups (1+m), (Δ) and $(K\sigma^n)$. Therefore obtaining new values of the three constants for each creep test stress level. As stated by Othman [50] (m) and (Δ) should ideally be independent of stress and hence should be constant for the whole stress range. In practice the fitted values vary slightly for creep curves at different stress levels, so the average values are used in a repeat optimisation and the best values of $(K\sigma^n)$ are obtained for each stress level. (K) and

(n) are found by taking the logs. of ($\dot{\epsilon}_s = K\sigma^n$) and fitting a straight line through the data:-

$$log(\dot{\epsilon}_s) = log(K) + nlog(\sigma) \tag{3.12}$$

Referring to Fig. 3.23 ($1/n$) is the gradient of a line on the log(stress) vs. log(min. strain rate) diagram for the experimental data. Having determined the value of (n), (ϕ) is obtained from the value of (Δ). The values of (χ), (A) and (M) are found using equation (3.5) which may be written taking logs as:-

$$log(\sigma) = log\left\{\left(\frac{A(\phi+1)}{1+m}\right)^{\frac{-1}{\chi}}\right\} - \left(\frac{1+m}{\chi}\right) log(t_f) \tag{3.13}$$

by fitting a line through the log(stress) vs. log(rupture time) data, where M is given using: $M = A(\phi + 1)$, as previously. Referring to the stress rupture plot of Fig. 3.22 the gradients of the isothermal stress rupture lines are identified to be $(-(1 + m)/\chi)$. Hence all the constants may be determined. The above procedures have been combined forming a set of subroutines by Dunne [37], forming a robust package which reads a set of digitized creep curves, corresponding to a series of at least two uni-axial creep tests at a particular test temperature, giving the optimized creep constants as output.

Sets of material parameters for creep tests at 150, 250 and 500^oC were obtained using the above procedure. Experimental scatter in the data, as a result of microstructural variation in the test specimens, caused the fitting of curves to the optimum number of tests (5 tests) at each temperature to be downgraded. Some of the experimental creep curves at different test stress levels were close to one another, some even crossed. Material parameters were obtained for data at 150^oC using two creep curves, at 250^oC using two curves and at 500^oC using three curves. Care was taken in choosing the curves to be fitted, so that the stress rupture points corresponding to each curve lay close to the best line fitted through the stress-rupture and stress-minimum strain rate data of Figs. 3.22 and 3.23 respectively.

The material constants for the three test temperatures are presented in Table 3.4. Comparisons between the experimental data and the fitted creep curves are presented in Figs. 3.29(a) to (c).

3.7 The Anisothermal Creep Model.

Having obtained the creep constants at these three discrete temperatures, it is required to interpolate between these temperatures to predict the creep deformation and failure behaviour over the whole temperature range ($150°C$ to $500°C$). Formerly this has been done with the use of an Arrhenius law [51] (equation 2.4), where it is assumed that both the creep strain rate and the damage rate increases exponentially with test temperature. This involves incorporating exponential terms as scalar multipliers in both the damage rate and strain rate equations (3.2) and (3.3) by replacing (K) and (A) by:

$$K = \left(K_0 e^{\frac{-b}{\theta}}\right) \tag{3.14}$$

$$M = \left(A_0 e^{\frac{-a}{\theta}}\right) \tag{3.15}$$

where θ is temperature, K_o, b and A_o, a are constants. Values of m, n, χ and ϕ in equations (3.2) and (3.3) are taken as the average values of those at the three temperature levels. This assumes that the gradients of the stress-rupture and stress-minimum creep rate graphs of Figs. 3.22 and 3.23 do not vary much over the temperature range. Taking the natural logs of (K) and (A) the linear equations are obtained:-

$$\ln(K) = \ln(K_0) - a\left(\frac{1}{\theta}\right) \tag{3.16}$$

$$\ln(A) = \ln(A_0) - b\left(\frac{1}{\theta}\right) \tag{3.17}$$

which may be fitted to the values of (K) and (A) available across the temperature range (Table 3.4), giving the values of the material constants (K_0), (b) and (A_0), (a). Following this procedure it was found that the values of the constants varied so widely (Table 3.4) over the temperature range, that a reasonable representation of the experimental creep curves over the temperature range was impossible. Even when the $150°C$ data was neglected on the grounds that this data is for the power-law breakdown mechanism, allowing a line to be fitted through the values of (A) and (K) corresponding to the $250°C$ and $500°C$ tests, the difference between the average values of m, n, χ and ϕ produced extremely poor creep curve predictions when comparisons were made with the originally fitted curves at $250°C$ and $500°C$. Therefore, though an Arrhenius law has been used successfully for very small temperature ranges [51] and [52] of the order of $50°C$ and $30°C$ respectively, where the variation in the material

constants is small, its use was found to be totally inappropriate over a temperature range of $350°C$, between $150°C$ and $500°C$.

A new approach has been proposed. It was decided to again neglect the $150°C$ test data, as the tests were of the ductile creep failure type, lying in the power-law breakdown region of the Ashby mechanism map. The new fitting procedure would use only the $250°C$ and $500°C$ creep data and data corresponding to $150°C$ test data, would be intuitively extrapolated, to give the correct strain-rate effect observed in the temperate-cyclic plasticity tests of Dunne [47].

It would have been ideal to produce tables of creep constants at smaller temperature intervals for the temperature range, so that the exact functional variation of the constants could be represented. Limitations of time and finance on the project made it impossible to carry out lengthy creep tests at intermediate temperature levels.

The new approach involved fitting exponential functions to all the material constants across the temperature range. As there were only two data points for each constant over the temperature range $250°C$ to $500°C$ the fit is perfect at the discrete temperatures of $250°C$ and $500°C$ (Figs. 3.30(a) to (f)). The extrapolation of material constant data to $150°C$ was done on the basis that a value of (n =1.5) is required to make the strain-rate effect negligibly small at this temperature, as observed in experiments [47]. An exponential function was fitted between n =4.261 at $250°C$ and n =1.500 at $150°C$ (Fig. 3.30(c)). The value of (m) below $250°C$ was kept constant (Fig. 3.30(a)) at the value of (m) at $250°C$, as a reasonable approximation. (m) cannot become much larger than (m) at $250°C$, as it can never reach (-1.0) or $(1+m)$ in the constitutive equation would become zero or negative. It was proposed to make (A) constant at the value of (A) at 250^0C for temperatures below $250°C$ as an approximation (Fig. 3.30(f)); having tried the extrapolated high temperature exponential curve prediction for (A) in the creep strain equation (3.4) and finding it to predict poor creep curve shapes. The values of ϕ and χ at $150°C$ were simply obtained from the extrapolation of the high temperature exponential curves passing through the $250°C$ and $500°C$ data points (Fig 3.30 (b) and (e)). Finally, the value of (K) at $150°C$ was obtained using the creep curve equation (3.4) with different values of (K), starting at the high temperature exponentially extrapolated value, which was modified until similar creep strian levels were obtained to those from creep tests at the

same stress levels. A second exponential function for the temperature range $150°C$ to $250°C$ was fitted to the two values of (K), one at $150°C$ and the other at $250°C$ (Fig. 3.30 (d)). The fitted exponentials through all the material constant data points are shown in figs. 3.30(a) to (f) and their respective equations and temperature ranges are given in Table 3.5. It is noted that a similar procedure of fitting exponential funcitons to material constants over a similar temperature range (200 to $550°C$) has been applied successfully [53] for stainless steel.

Predictions of material constants using the set of exponential equations of Table 3.5 at temperature intervals over the temperature range 150 to $500°C$ were calculated. Using these material constants and equation (3.4) for stress levels similar to those used in the uni-axial creep tests, predicted creep curves are plotted in Figs. 3.31 (a), (b) and (c) at similar temperature intervals. The creep curve predictions at the test temperatures $250°C$ and $500°C$ are the same as those of Figs. 3.29 (a) and (b). From the predicted creep curves it is noticed that as the test temperature decreases the primary creep strain increases, similar to that observed in experiments. The $150°C$ predicted curves give similar failure strains to those of the experimental tests at the same stress levels, though the predicted rupture lives are longer (c.f. Fig. 3.31 (a) and Fig. 3.29 (a)). At lower stress levels the predicted $150°C$ creep curves show the existence of a brittle stress-rupture line, as is thought to exist in practice. Predicted stress-rupture lines, for $50°C$ temperature intervals over the test temperature range, are plotted as dashed lines on a log(stress) versus log(rupture-time) plot in Fig. 3.32. The predicted lines may be judged against the solid lines which represent a best fit through the experimental data. Dashed lines actually lie on top of the solid lines at temperatures of $250°C$ and $500°C$, where a perfect fit to the experimental data is obtained. Similarly Fig. 3.33 shows a comparison between the predicted log(stress) vs. log(min. strain rate) lines (dashed lines) and the experimental lines (solid lines). Again the dashed lines corresponding to the $250°C$ and $500°C$ predicted lines lie on top of the solid experimental lines.

3.8 Conclusions.

(i) Metallurgical examination of a sample of the specimens tested showed a marked difference in grain sizes, both within individual specimens and between different specimens. As great care was paid to machine accuracy, specimen accuracy and

test procedure it seems that in this case material variations did cause some scatter in the results.

(ii) From the experimental stress rupture lines of Fig. 3.22 it is observed that batch-(C) material at $250°C$ has a lower creep strength than batch-(M) material at $250°C$. This is due to the finer grain size of batch-(M) material and highlights the importance of the effects of grain structure on the material properties. Grain size variations can be directly related to the material production methods.

(iii) A metallurgical report, on a sample of microsectioned creep specimens, highlighted a mechanism change from $250°C$ tests to $150°C$ tests. The high stress $150°C$ tests fail in a ductile creep failure mode, showing characteristic neck formation at rupture. Therefore, as Norton's law cannot be used to model this type of deformation and the $150°C$ test data was neglected in the final curve fitting procedure.

(iv) It was concluded that the Arrhenius law could only be applied for small temperature ranges of the order of $50°C$, or so, and is totally inappropriate for temperature fitting over the much larger ranges of $150°C$ to $500°C$.

(v) Good predictions of creep test behaviour over the temperature range 250 to $500°C$ were obtained with the use of exponential functions, which were fitted to each material constant. With the use of some intuitive assumptions and extra data supplied from temperate cyclic plasticity experiments, constitutive data was also obtained to represent low stress brittle creep behaviour at $150°C$.

A summary of this work has also been detailed in [54].

Parameter	Quantity	Sensor Type
t	time in (hrs)	computer clock
T_T	specimen temperature at top protrusion	thermocouple 1
T_b	specimen temperature at bottom protrusion	thermocouple 2
T_R	room temperature	thermocouple 3
δL	displacement of gauge length (L_0) gives the total strain (ϵ_T) in percent.	L.V.D.T.
L_D	load cell reading gives specimen load in (KN).	strain gauge bridge type load cell

Table 3.1: Data Recorded For Each Creep Rig By The Expert System.

Test No.	Batch No.	Test Temp. (^oC)	Stress Level. σ_0 (Mpa)	Failure Time t_f(hrs)	Min. Creep Strain Rate, ϵ_s(%/hr)	Last Recorded Creep Strain,ϵ_f(%)
1	M	250	51.13	684.5	1.301E-3	2.308
2	M	250	46.81	2185.0	5.938E-4	3.00
3	M	250	56.84	123.0	7.392E-3	3.15
4	M	150	130.0	Inst.	-	-
5	M	150	65.0	Stop'd	3.520E-4	-
6*	M	150	80.0	Stop'd	1.410E-4	-
7	M	150	105.03	992.92	2.515E-3	5.939
8	C	150	115.0	0.1	-	-
9	C	150	107.4	16.8	1.657E-1	6.70
10	C	250	56.72	47.0	2.896E-2	6.597
11	C	150	105.94	12.58	-	-
12	C	20	Tens'l	-test	-	-
13	C	250	Tens'l	-test	-	-
14	C	500	Tens'l	-test	-	-
15	C	250	51.13	51.0	1.946E-2	2.492
16	C	500	24.25	0.80	-	-
17	C	500	14.04	85.98	4.197E-2	3.477
18	C	250	45.23	83.11	1.010E-2	2.210
19	C	500	11.88	71.0	6.557E-4	0.433
20	C	250	25.7	Stop'd	-	-
21	C	500	7.94	Stop'd	-	-
22	C	500	10.9	136.80	3.33E-4	1.358
23	C	500	9.1	187.97	3.241E-4	0.791
24	C	500	7.95	533.57	6.284E-5	0.150
25	C	250	38.0	452.6	1.228E-3	1.661
26	C	250	35.4	224.93	1.608E-3	2.346
27	C	150	94.3	426.77	8.340E-3	8.20
28	C	250	32.7	Stop'd	-	-
29	C	150	92.0	152.95	-	-
30	C	150	98.0	284.13	1.216E-2	7.773
31	C	150	92.0	35.98	3.666E-2	2.029
32	C	250	32.7	39.97	1.674E-2	1.865
33	C	250	32.7	64.45	1.231E-2	1.877
34	C	150	91.0	41.66	-	-
35	C	250	44.0	46.0	1.364E-2	1.918

Table3.2: Summary of uni-axial creep and tensile test results for as-cast copper batches (A) and (C).
(Inst.) means specimen failed immediately on loading.
(Stop'd) means the test was aborted.
Test 6* was aborted after 3,500 hrs.

Specimen Stress	106MPa	45MPa	13MPa
Temperature	150°	250°	500°
Etch-Pit Density	Low	High	Low
Voiding	Slight due to grain bdry sliding.	Internal voiding present.	Some Voiding at fracture site.
Cracks	45° and 90° to tensile axis.	Surface cracks present 90° to tensile axis.	Single failure crack 90° to tensile axis.
Climb	None	Climb present	High climb activity.
Oxide	None	Black CuO	Cu_2O
Failure Mode	Creep Ductile	Creep Brittle	Creep Brittle

Table 3.3: Summary of metallographic observations of microsections from uni-axial creep specimens tested at 150, 250 and 500°C, due to Mabutt[48].

Temp.(^oC)	m	n	χ	ϕ	A	K
150	-0.6941	6.991	7.599	20.22	0.2234E-17	0.3194E-14
250	-0.7431	4.261	1.889	4.737	0.965E-5	0.3373E-8
500	-0.0704	7.033	4.562	7.432	0.2397E-7	0.5063E-10

Table3.4: Material constants fitted to batch-(C) Copper at 150^oC, 250^oC, 500^oC. Material constants are calculated such that the variables take the units of Stress in MPa, Strain in (%), and Time in hours.

a)	m = -0.743	150 ≤ θ < 250
	m = -7.8482 exp(- 9.4289E-3 θ)	250 ≤ θ < 500
b)	n = 0.31329 exp(0.010441 θ)	150 ≤ θ < 250
	n = 2.5815 exp (2.0046E-3 θ)	250 ≤ θ ≤ 500
c)	K = 510.48 exp (- 0.10297 θ)	150 ≤ θ < 250
	K = 2.2471E-7 exp (- 0.01680 θ)	250 ≤ θ ≤ 500
d)	ϕ = 3.0199 exp (1.8010E-3 θ)	150 ≤ θ ≤ 500
e)	χ = 0.78218 exp (3.5271E-3 θ)	150 ≤ θ ≤ 500
f)	A = 0.9650E-5	150 ≤ θ < 250
	A = 3.8854E-3 exp (- 0.0240 θ)	250 ≤ θ ≤ 500

Table3.5: Functional variation of the material constants with temperature. Variables take the units of Stress in MPa, Strain in (%), and Time in hours.

Figure 3.1: The three constant-load uni-axial tension creep rigs, as used in tests by the author.

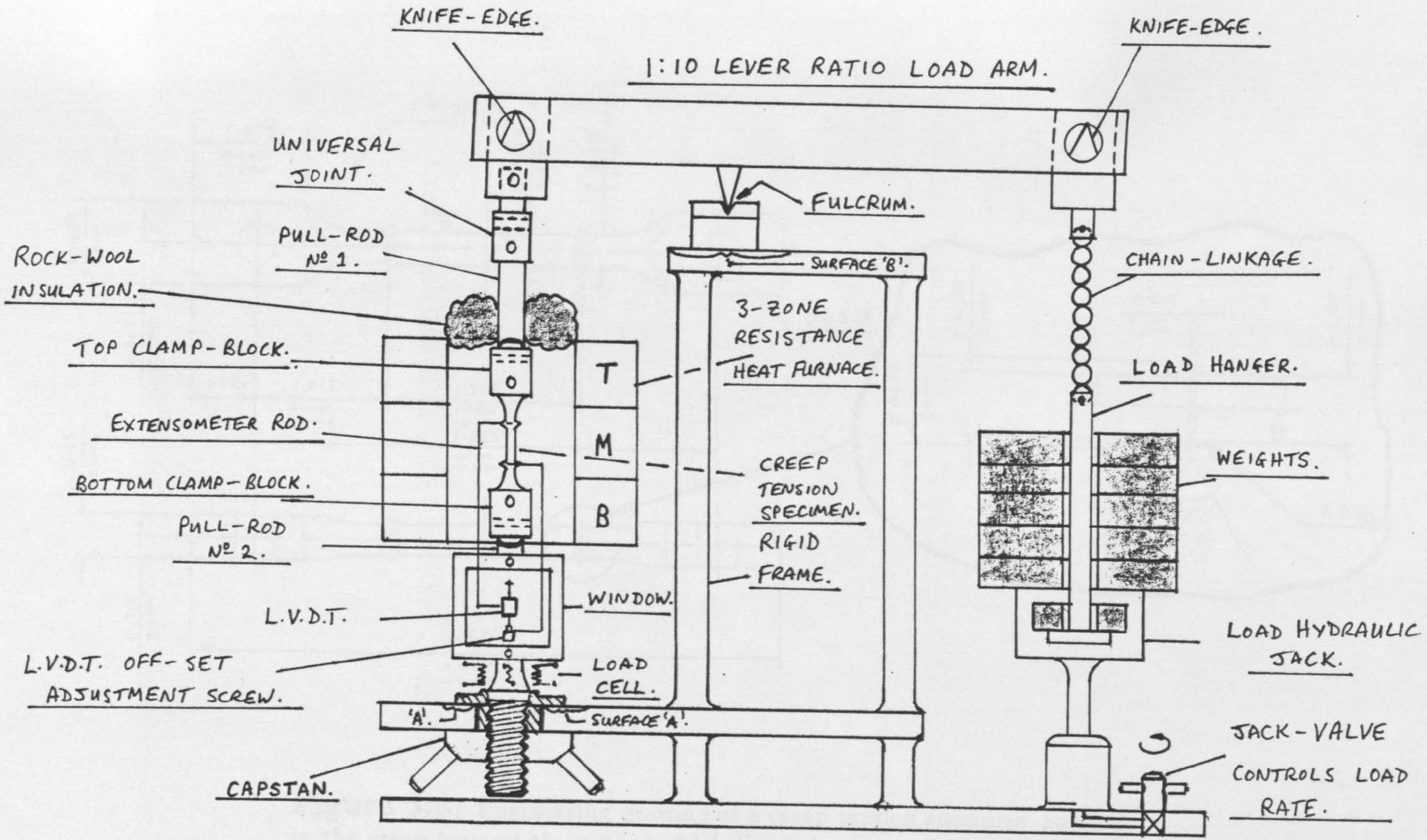

Figure 3.2: Schematic diagram of a constant load uni-axial tension creep rig. N.B. the alignment of the universal joint pins, to provide flexibility in two mutually perpendicular planes.

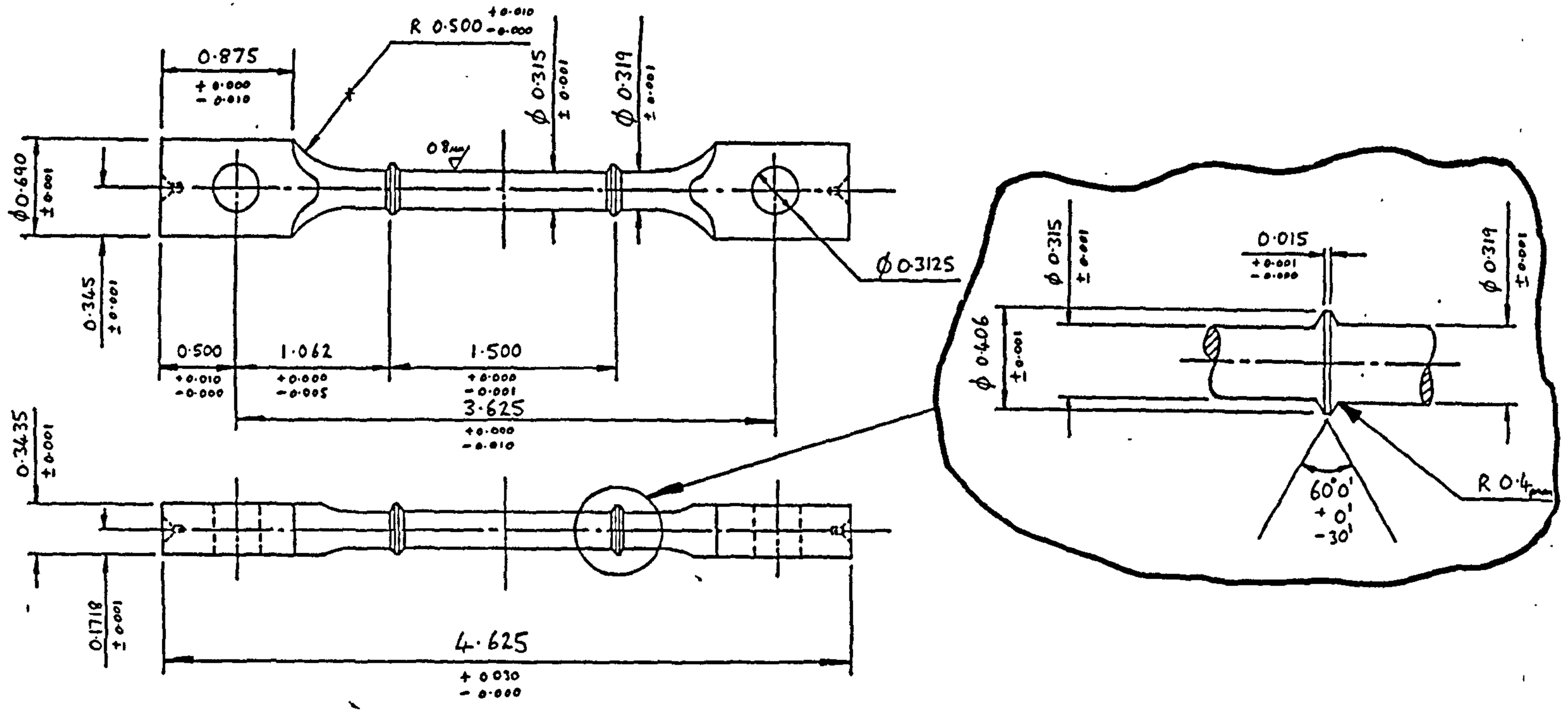

Figure 3.3: Engineering drawing of a creep tension specimen, as used in the creep tests of the author. (All dimensions in inches except where stated).

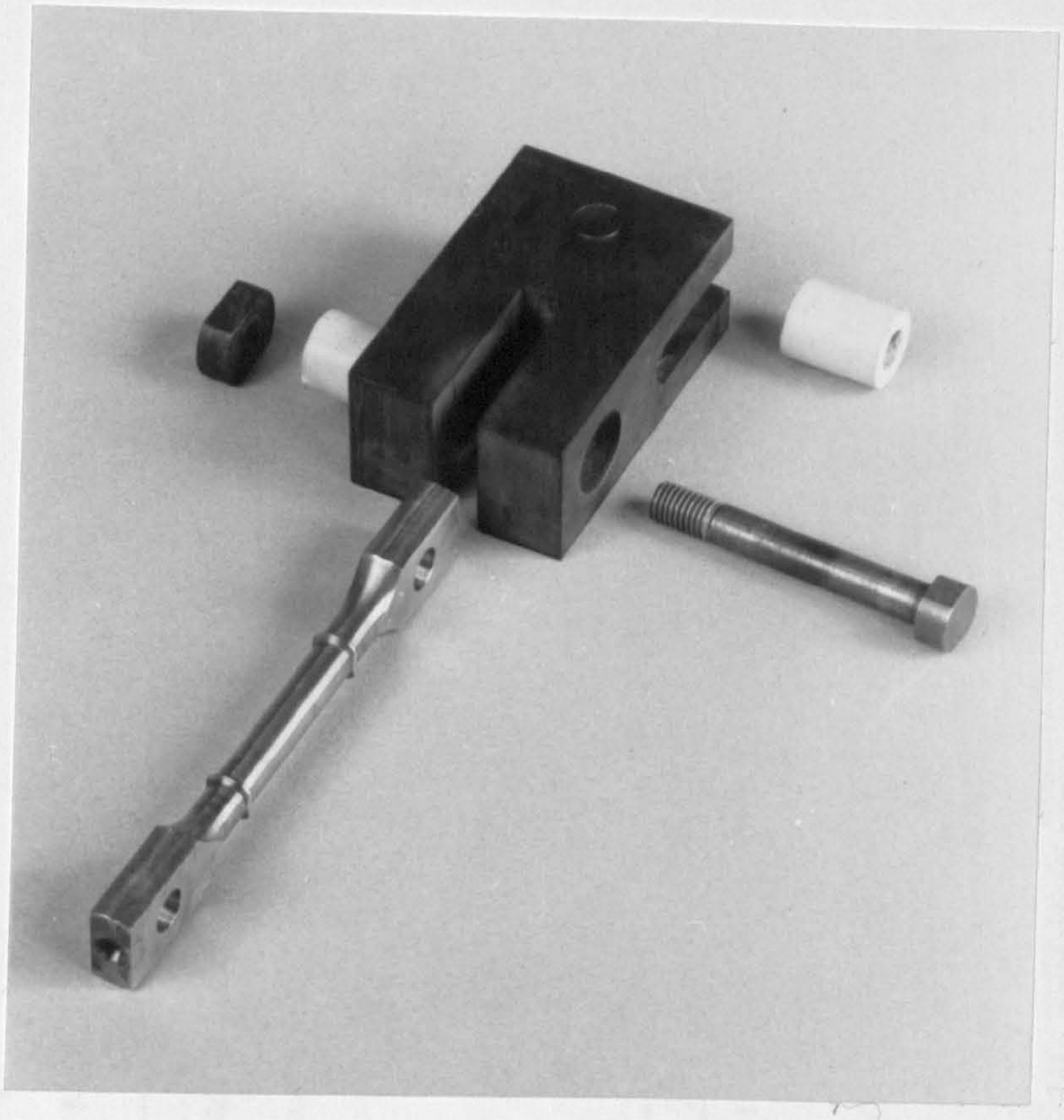

Figure 3.4: The specimen is held in the clamp-block with ceramic collars and a bolt. N.B. the block has two pivots, allowing specimen rotation in two mutually perpendicular directions.

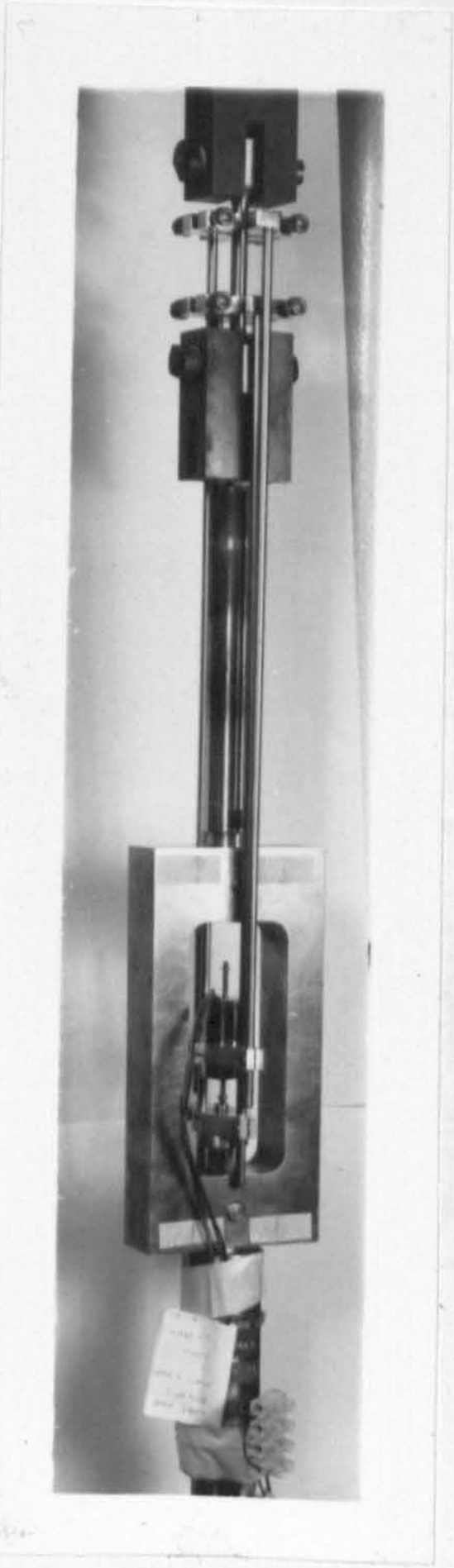

Figure 3.5: Arrangement of the extensometer rods which are connected to the specimen protrusions and the L.V.D.T. for the electrical measurement of gauge length extension with time.

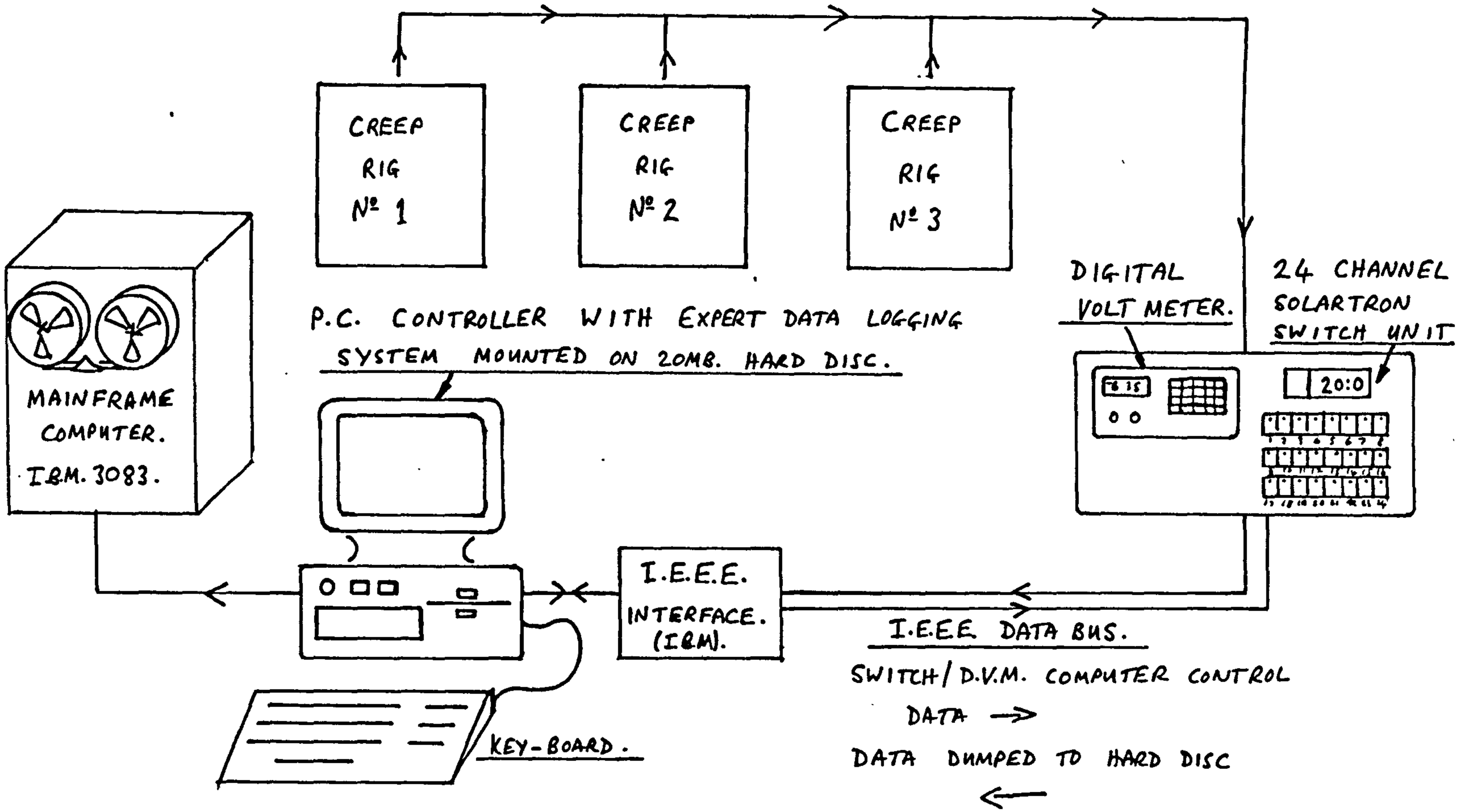

Figure 3.6: Schematic diagram of the laboratory data aquisition system.

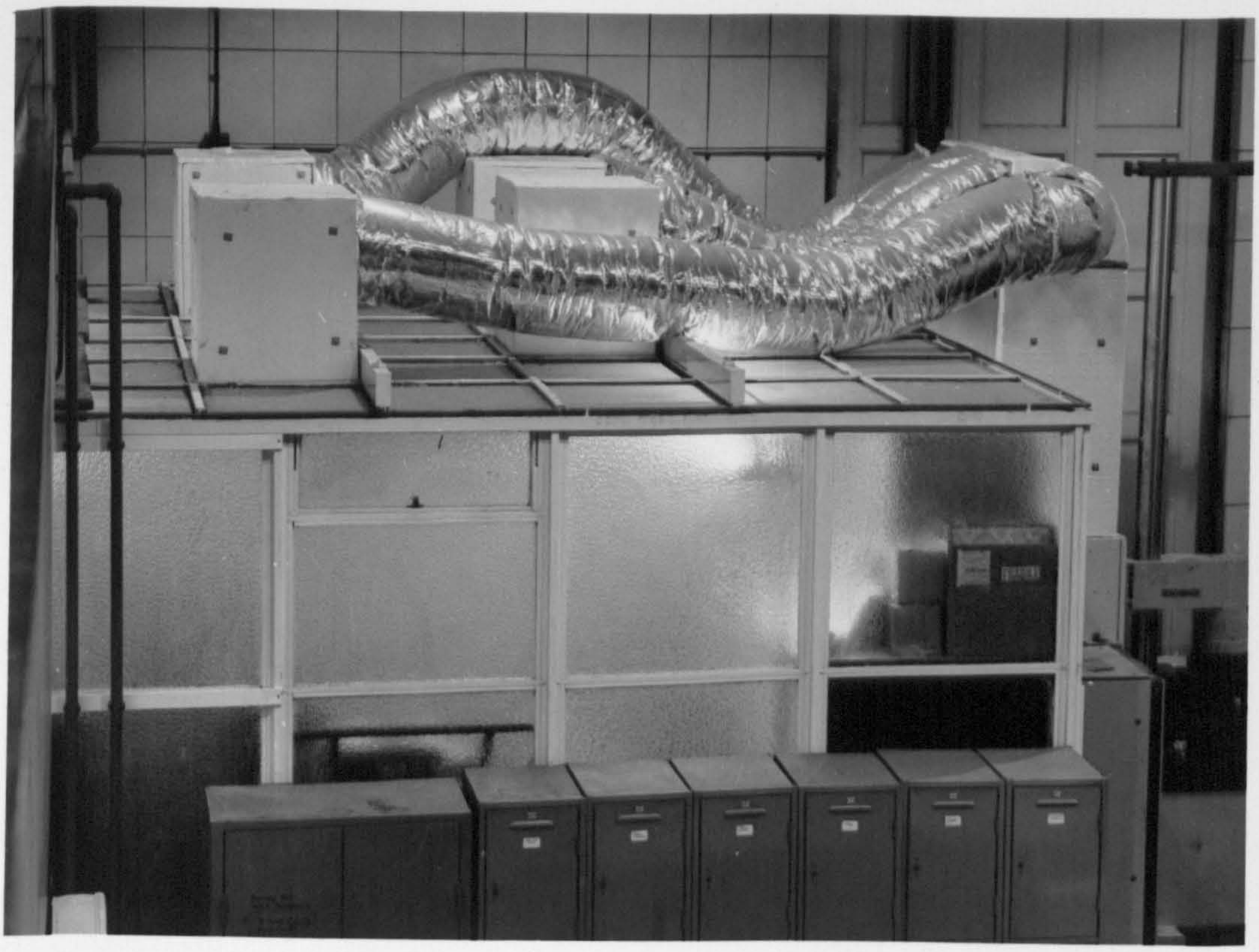

Figure 3.7: The exterior of the testing laboratory, showing the air-conditioning ducting.

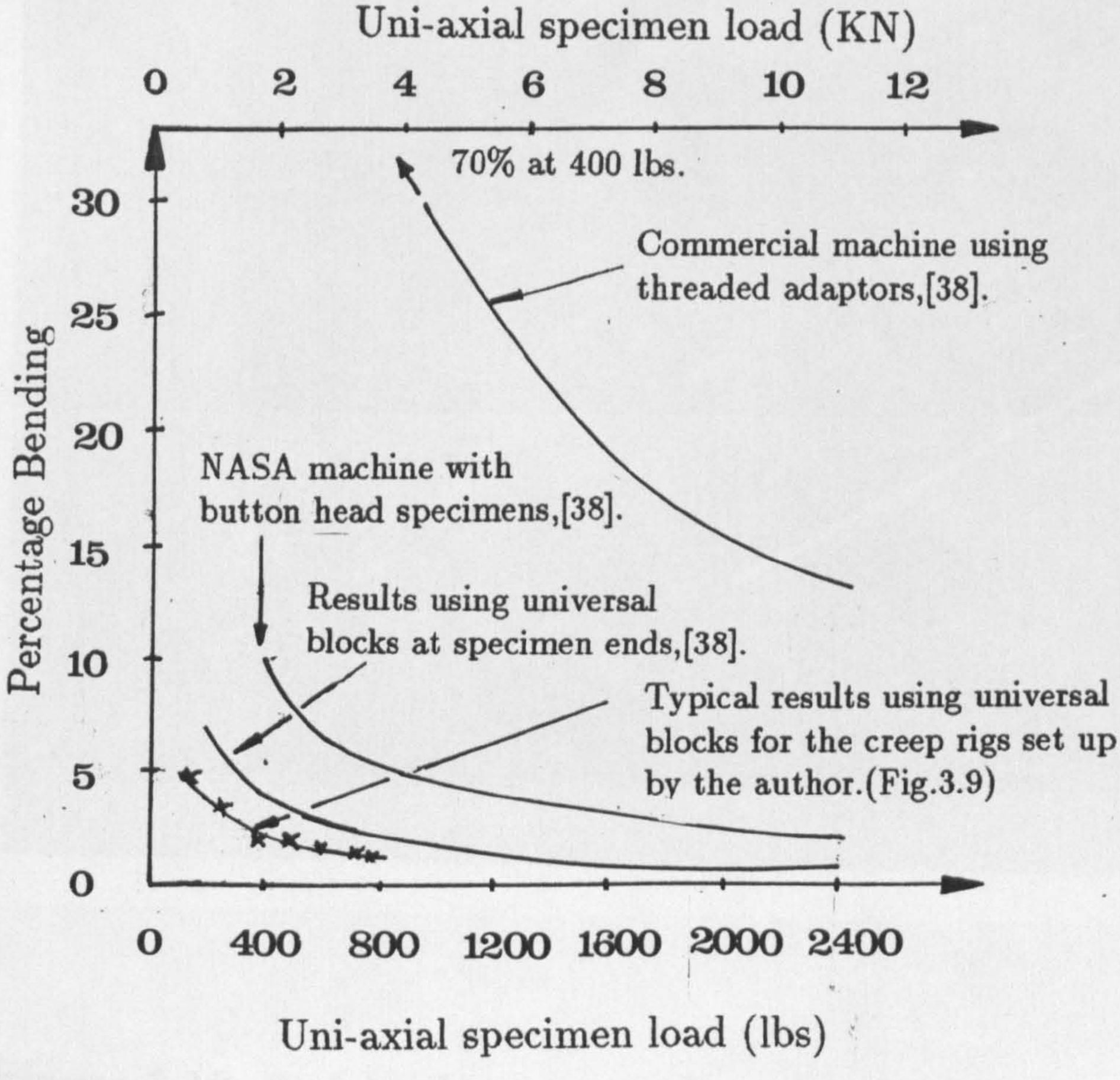

Figure 3.8: Percentage bending (equation 3.1) across a creep specimen as a function of test load, for different test machines.

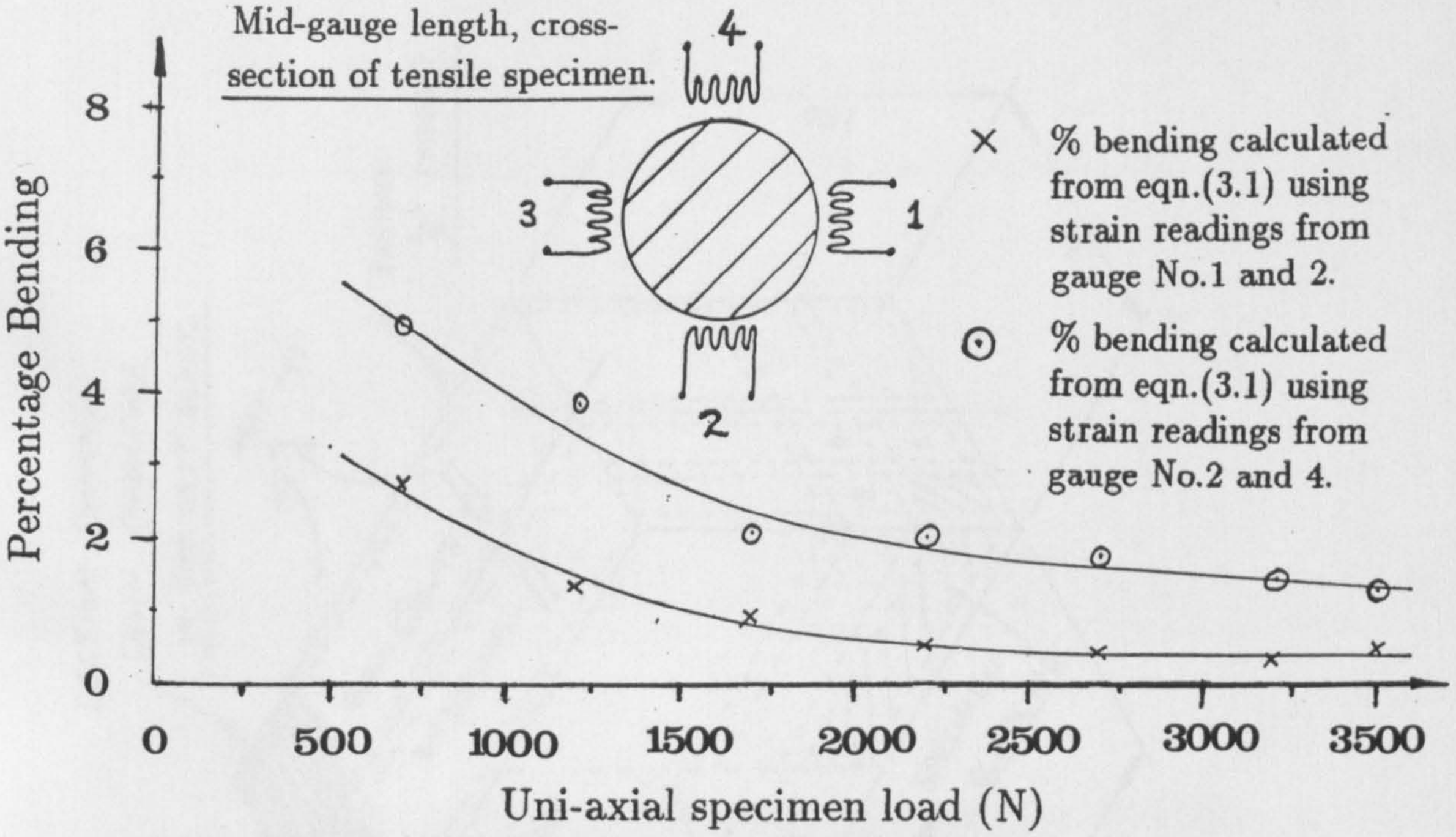

Figure 3.9: The results from a typical bending test, for creep rig No.2.

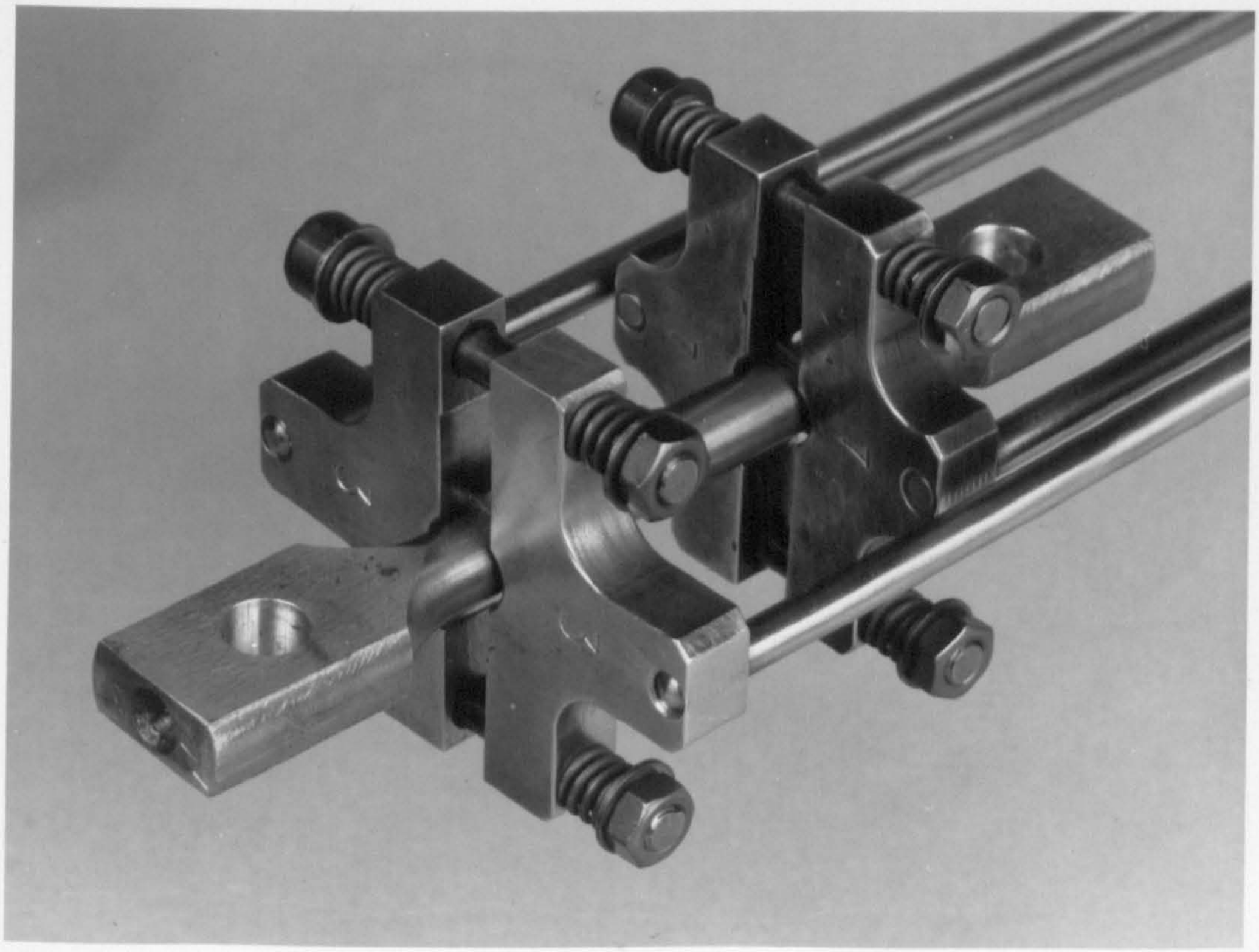

Figure 3.10: Re-designed extensometer clamps, incorporating a four-spring arrangement.

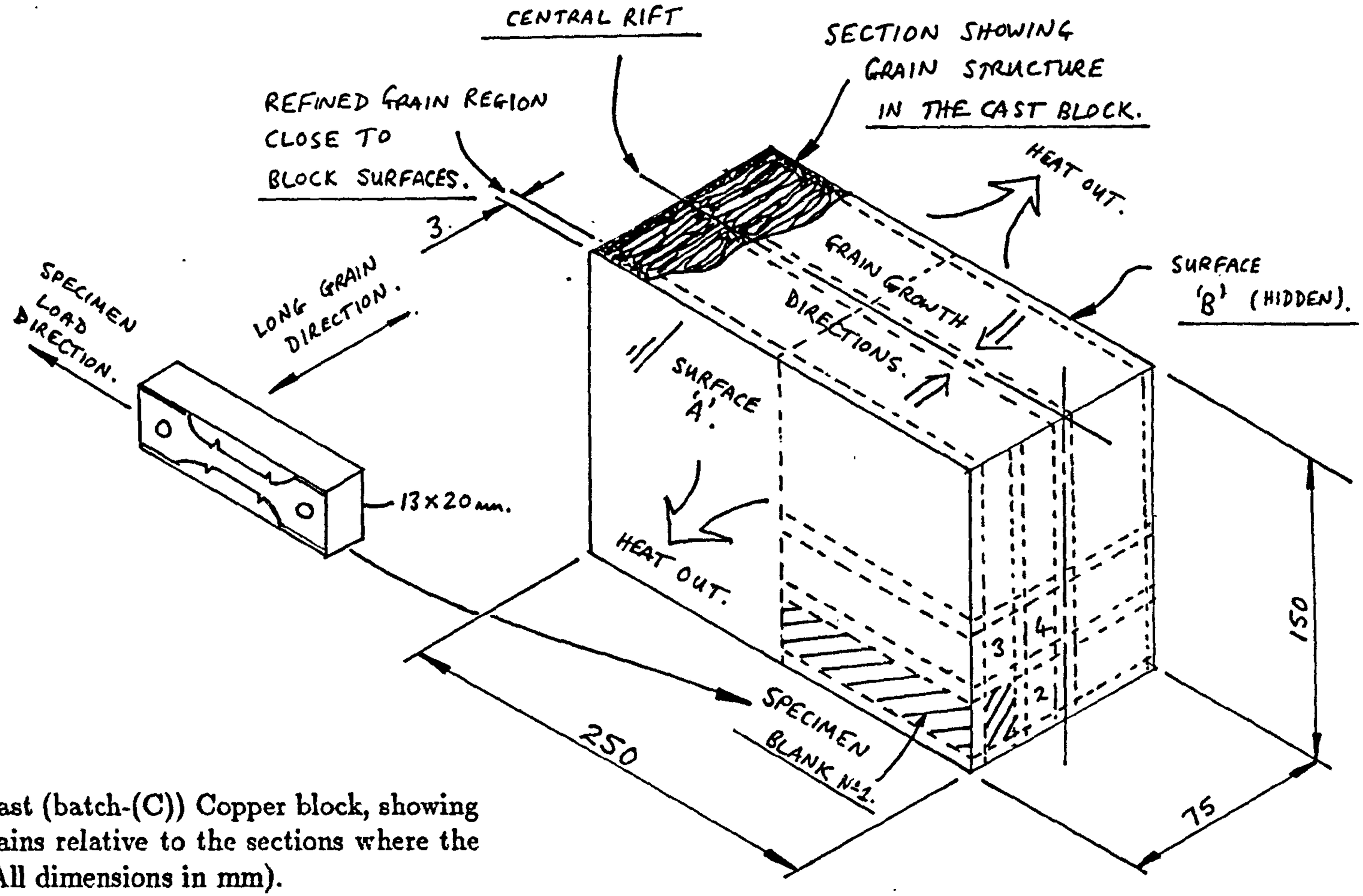

Figure 3.11: Sketch of an as-cast (batch-(C)) Copper block, showing the orientation of the columnar grains relative to the sections where the creep specimen blanks were cut. (All dimensions in mm).

(a)

(b)

Figure 3.12: (a) long-thin columnar grains of Copper in the as-cast condition. Note the grain refinement towards the left-hand side and bottom edge. These edges during casting touched the cast-iron chill and the sand-box of the mould, respectively.
(b) etched microsection cut across the columnar grains, showing a plane 90° to that of (a).

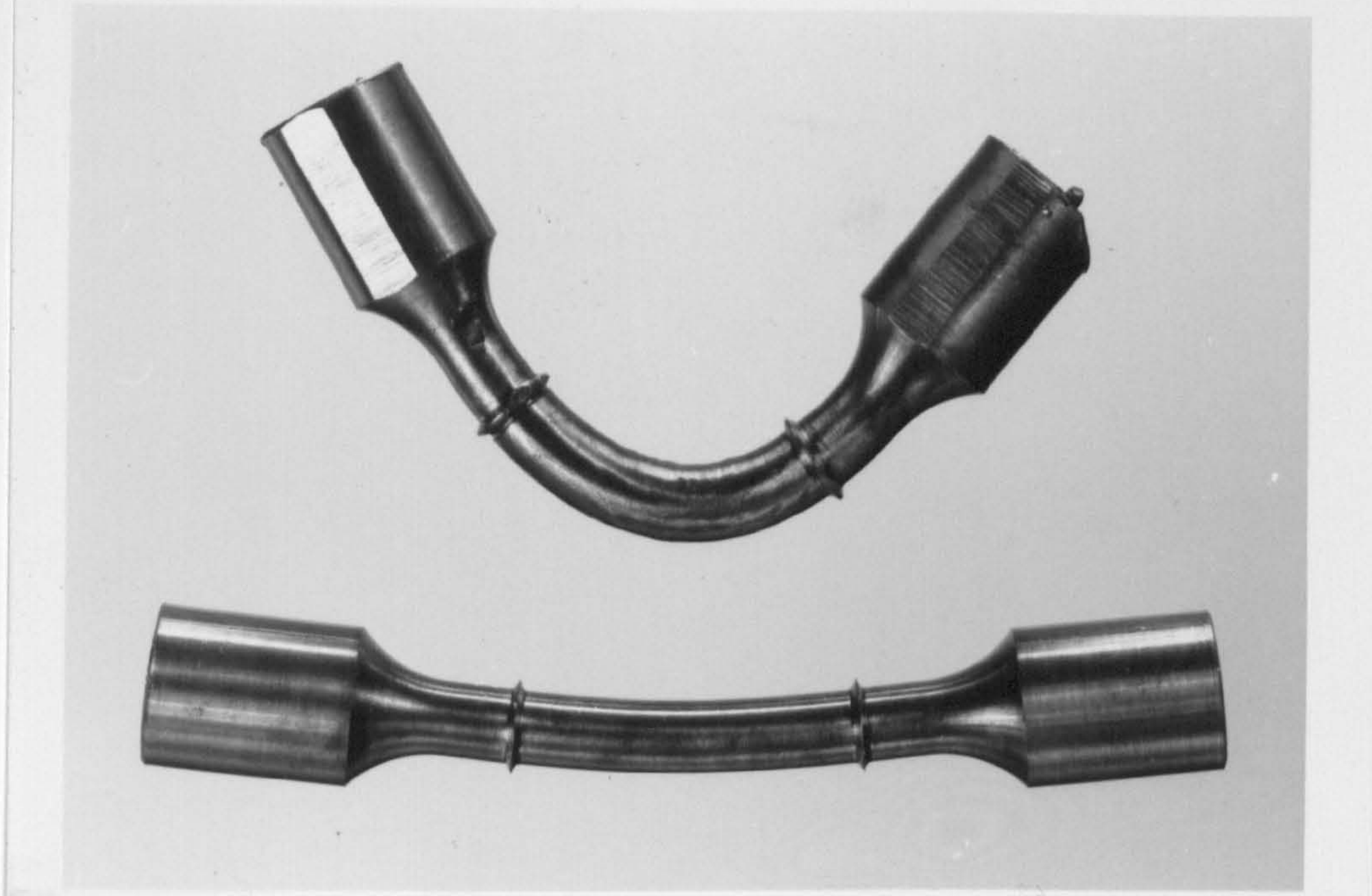

Figure 3.13: Problems encountered with machining soft as-cast Copper. Even at low spindle speeds, taking fine cuts, cutter force is sufficient to bend the specimen, ejecting it from the lathe.

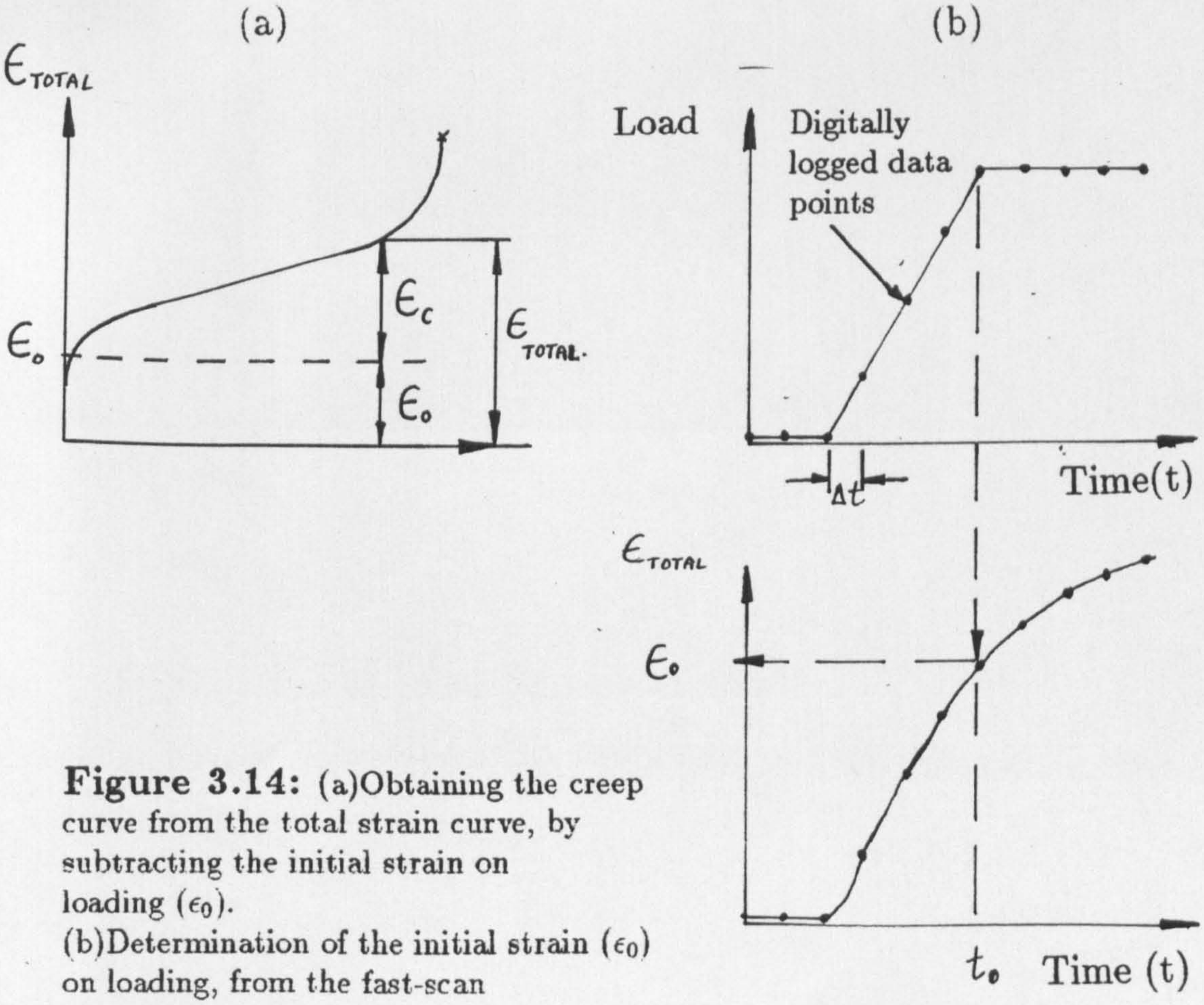

Figure 3.14: (a)Obtaining the creep curve from the total strain curve, by subtracting the initial strain on loading (ϵ_0).
(b)Determination of the initial strain (ϵ_0) on loading, from the fast-scan digitally logged data.

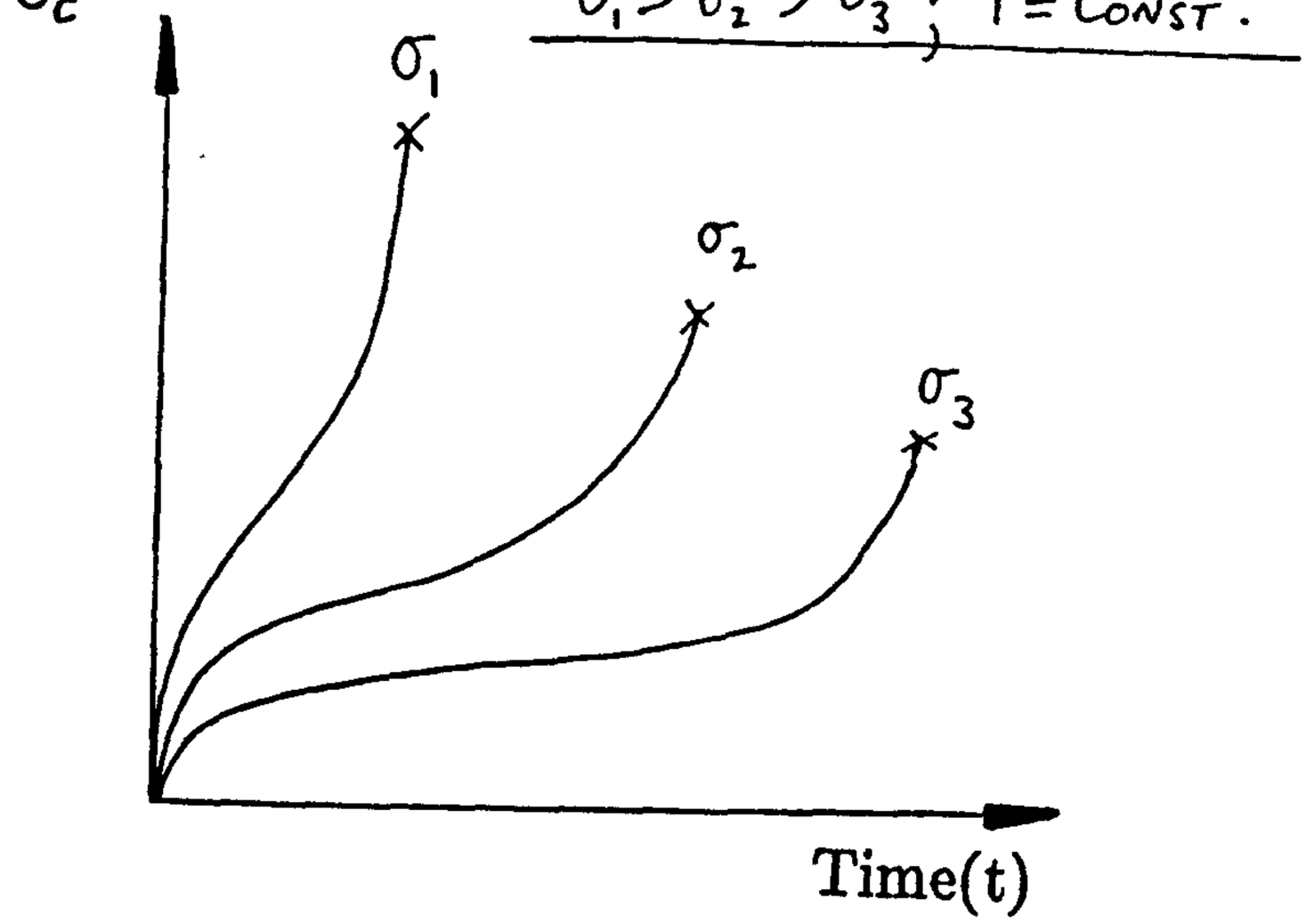

Figure 3.15: A typical series of creep-rupture curves at different test stress levels, required to define the material constants for the constitutive equations at this temperature.

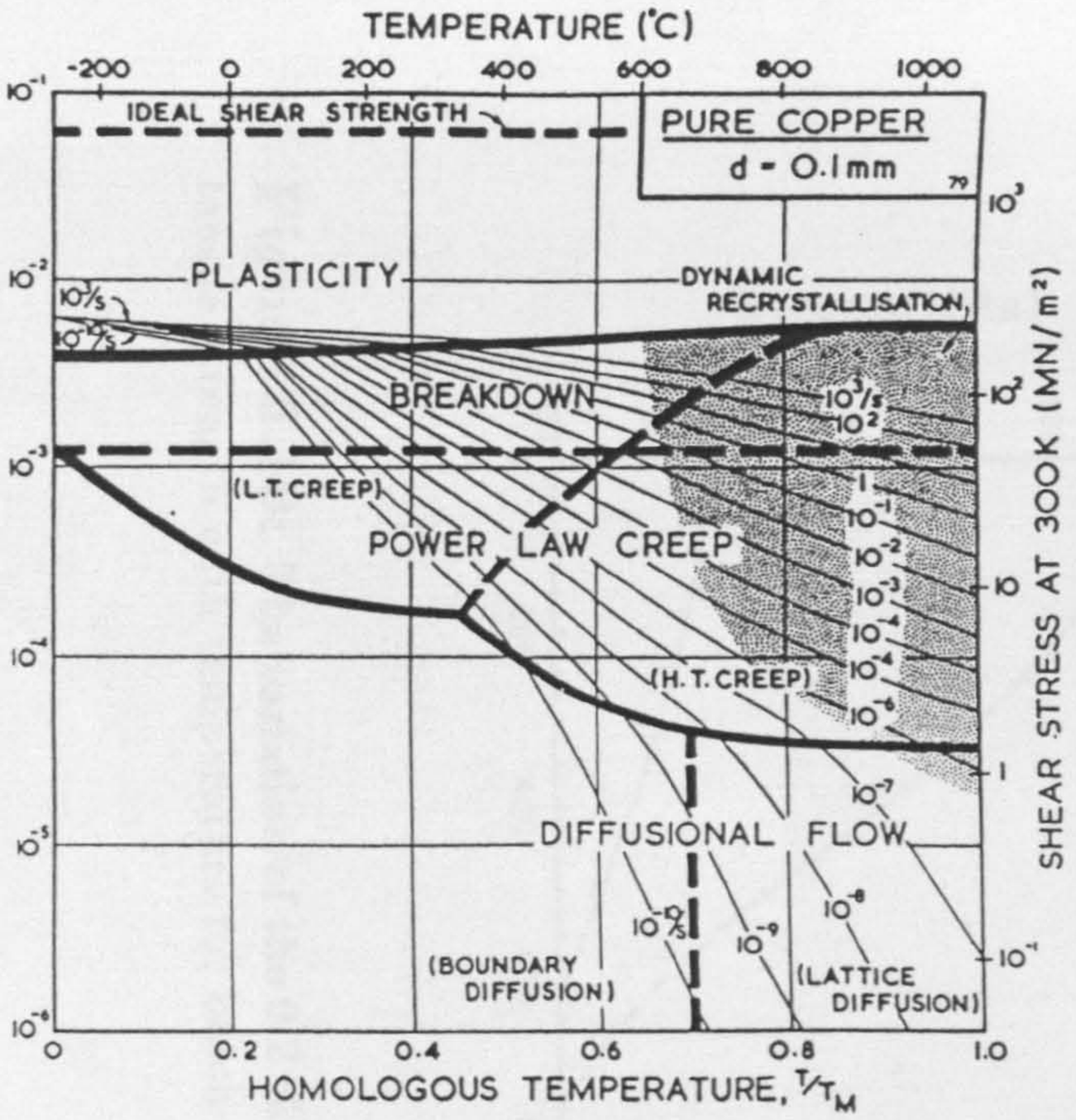

Figure 3.16: Deformation mechanism map for pure Copper, due to Ashby et al [8].

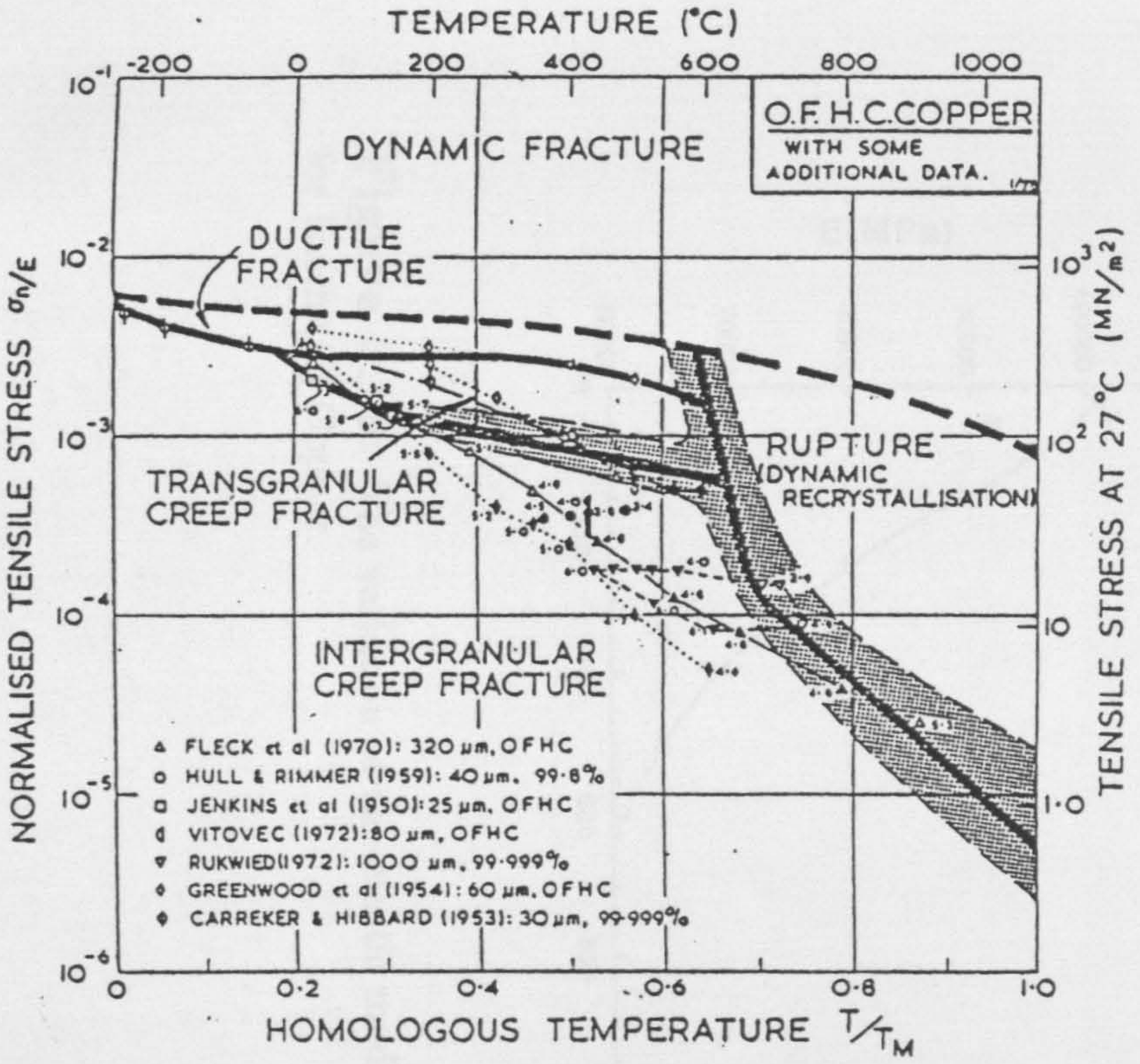

Figure 3.17: Fracture mechanism map for (OFHC) Copper, due to Ashby et al [11].

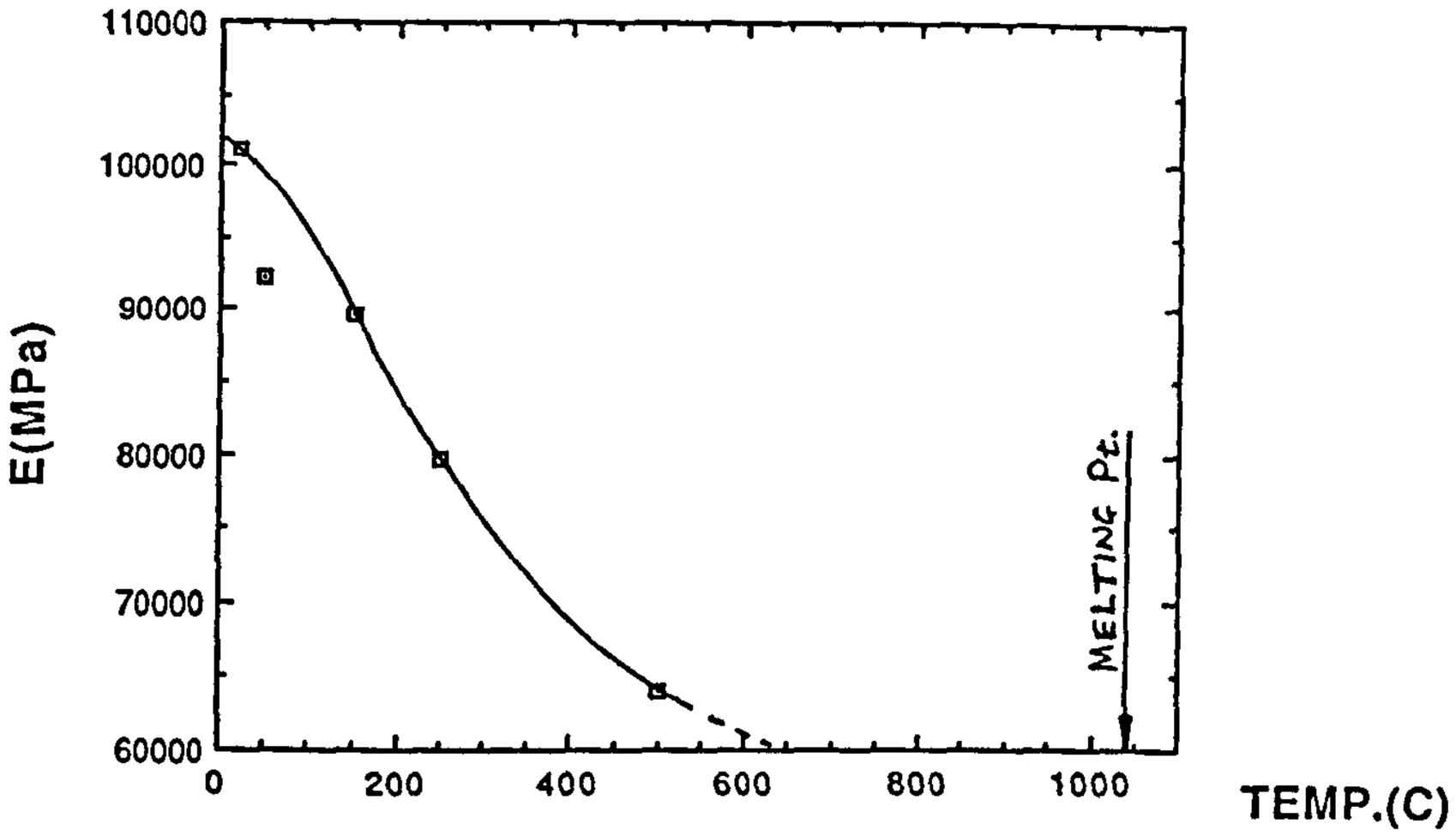

Figure 3.18: The variation of the elastic modulus with temperature for batch-(C) Copper.

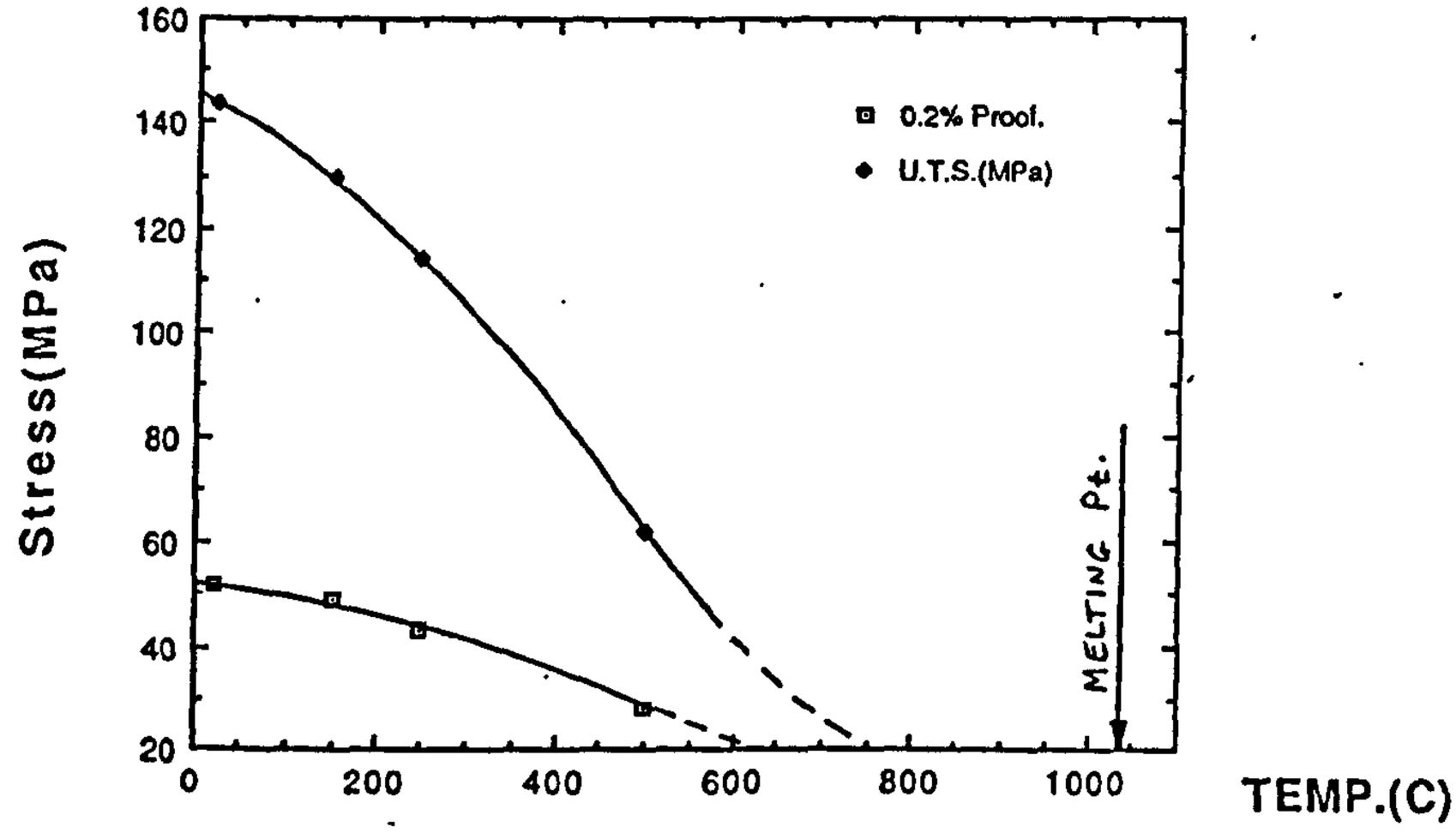

Figure 3.19: The variation of the 0.2 % proof stress and the ultimate tensile strength with temperature for batch-(C) Copper.

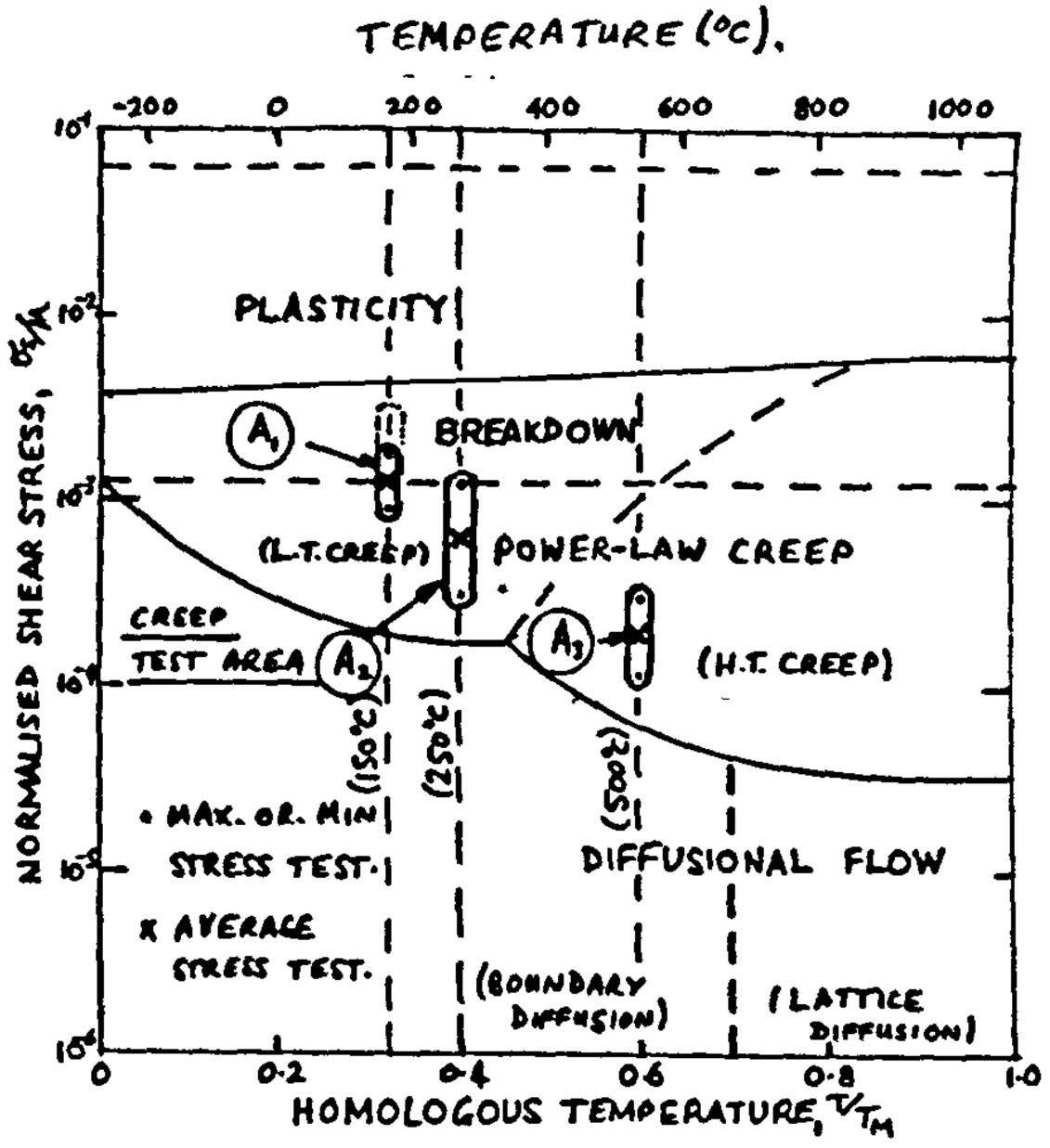

Figure 3.20: Deformation mechanism map for pure Copper, due to Ashby et al [8]. Areas (A1), (A2) and (A3) are identified corresponding to the creep tests performed.

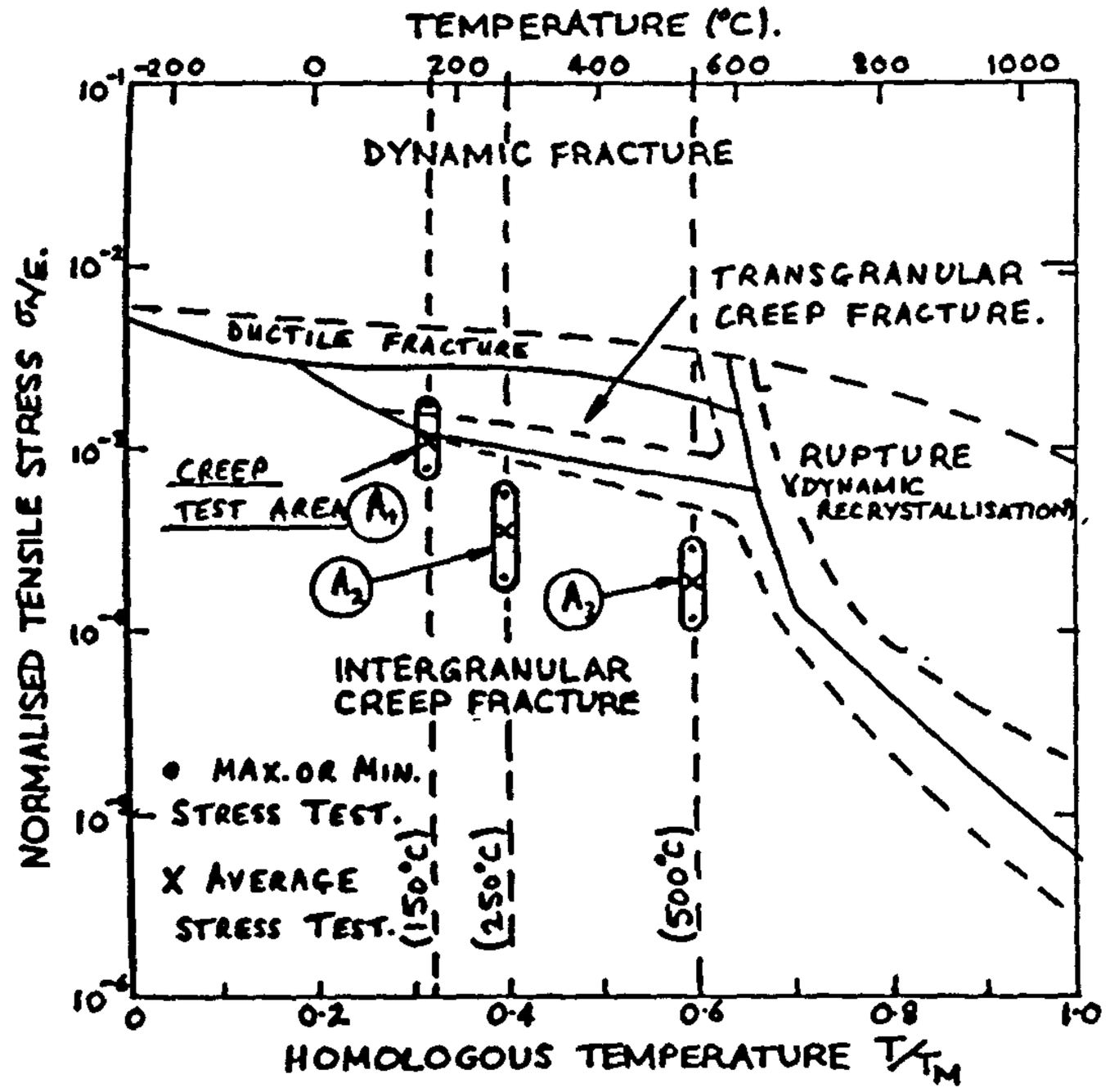

Figure 3.21: Fracture mechanism map for (OFHC) Copper, due to Ashby et al [11]. Areas (A1), (A2) and (A3) are identified corresponding to the creep tests performed.

N.B. (x) indicates the average stress level and (.) indicates the maximum and minimum stress levels of all tests at this temperature.

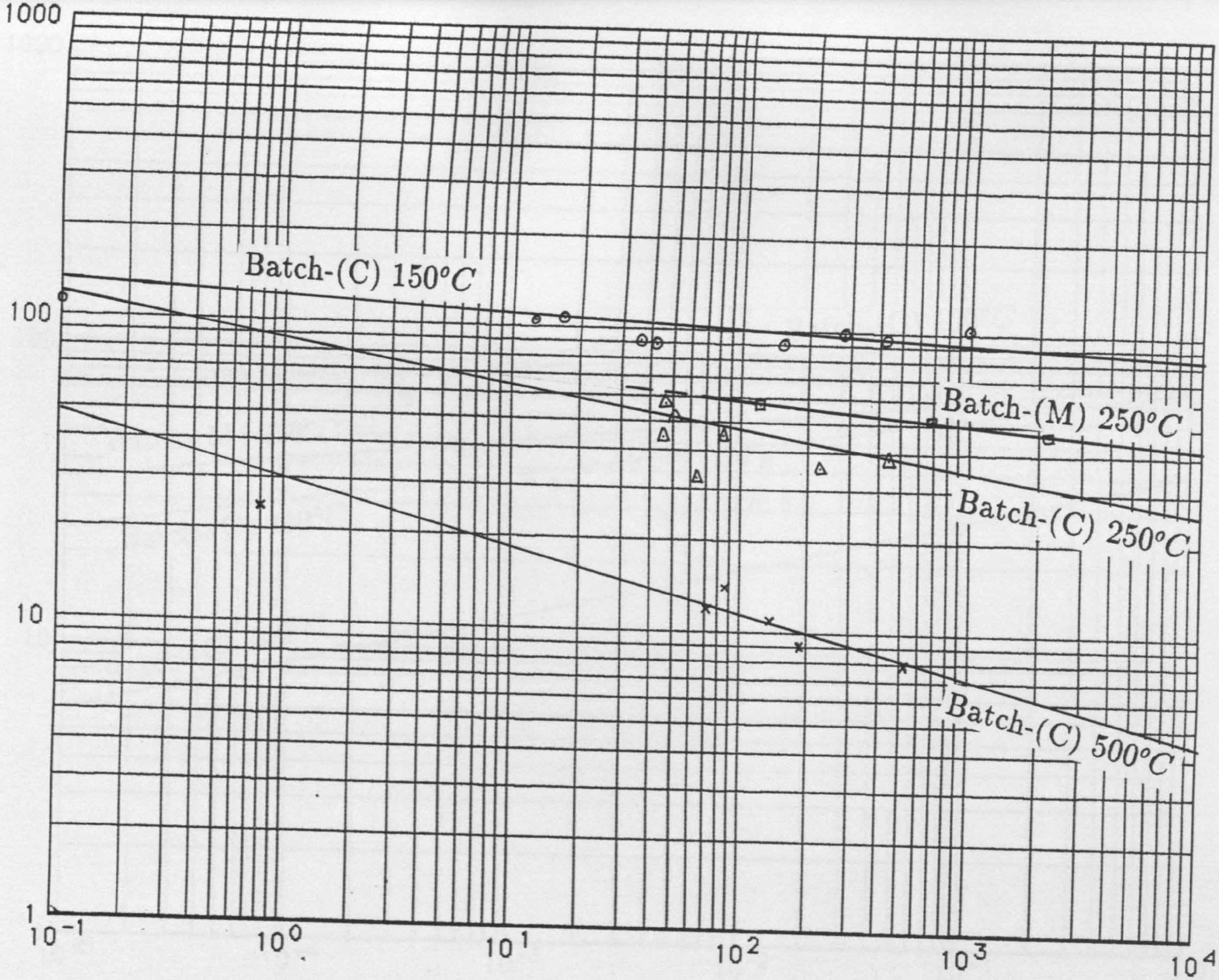

Figure 3.22: Uni-axial stress-rupture creep test results for batch-(M) and batch-(c) as-cast Copper.

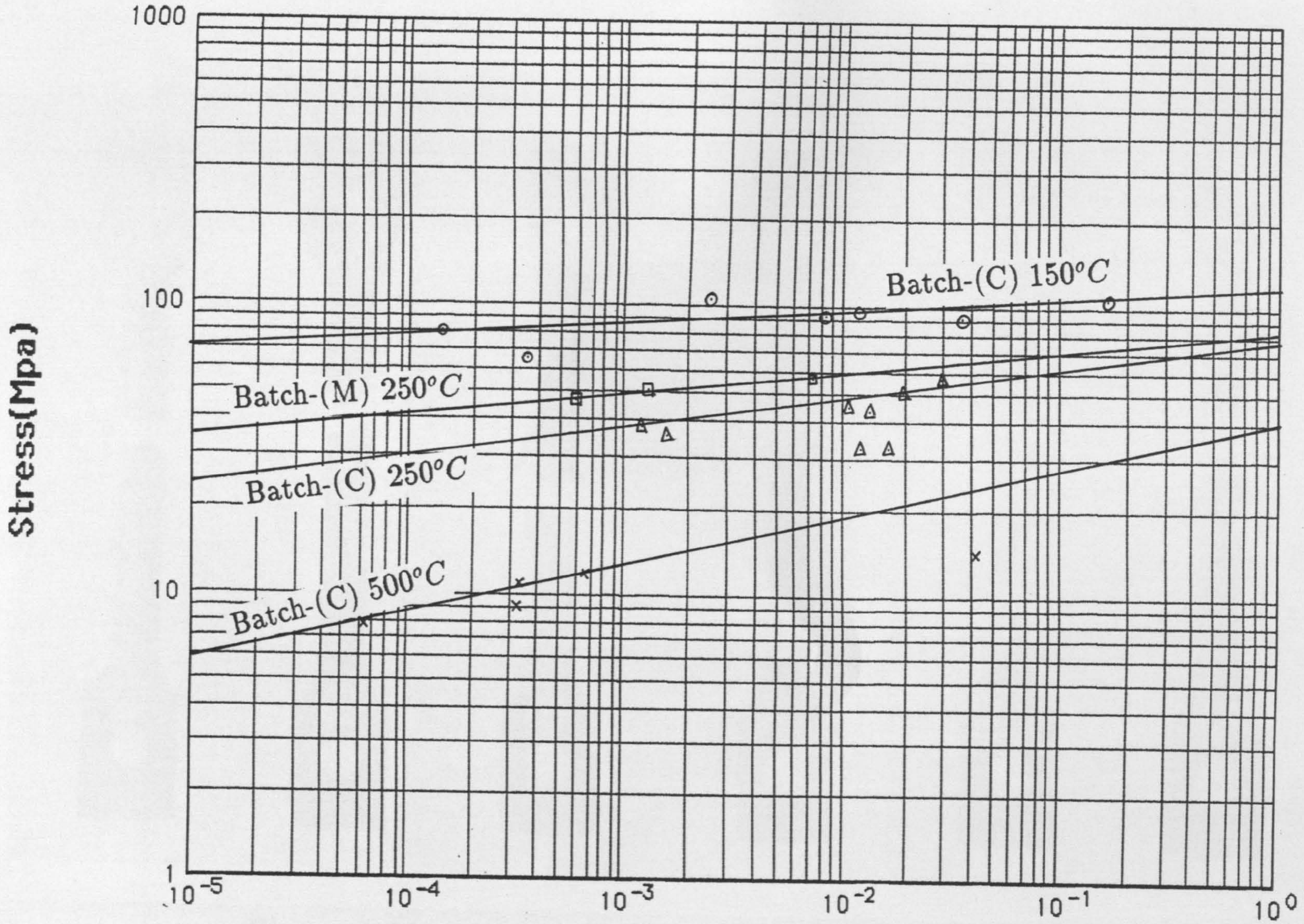

Figure 3.23: Uni-axial stress-min. creep rate test results for batch-(M) and batch-(C) as-cast Copper.

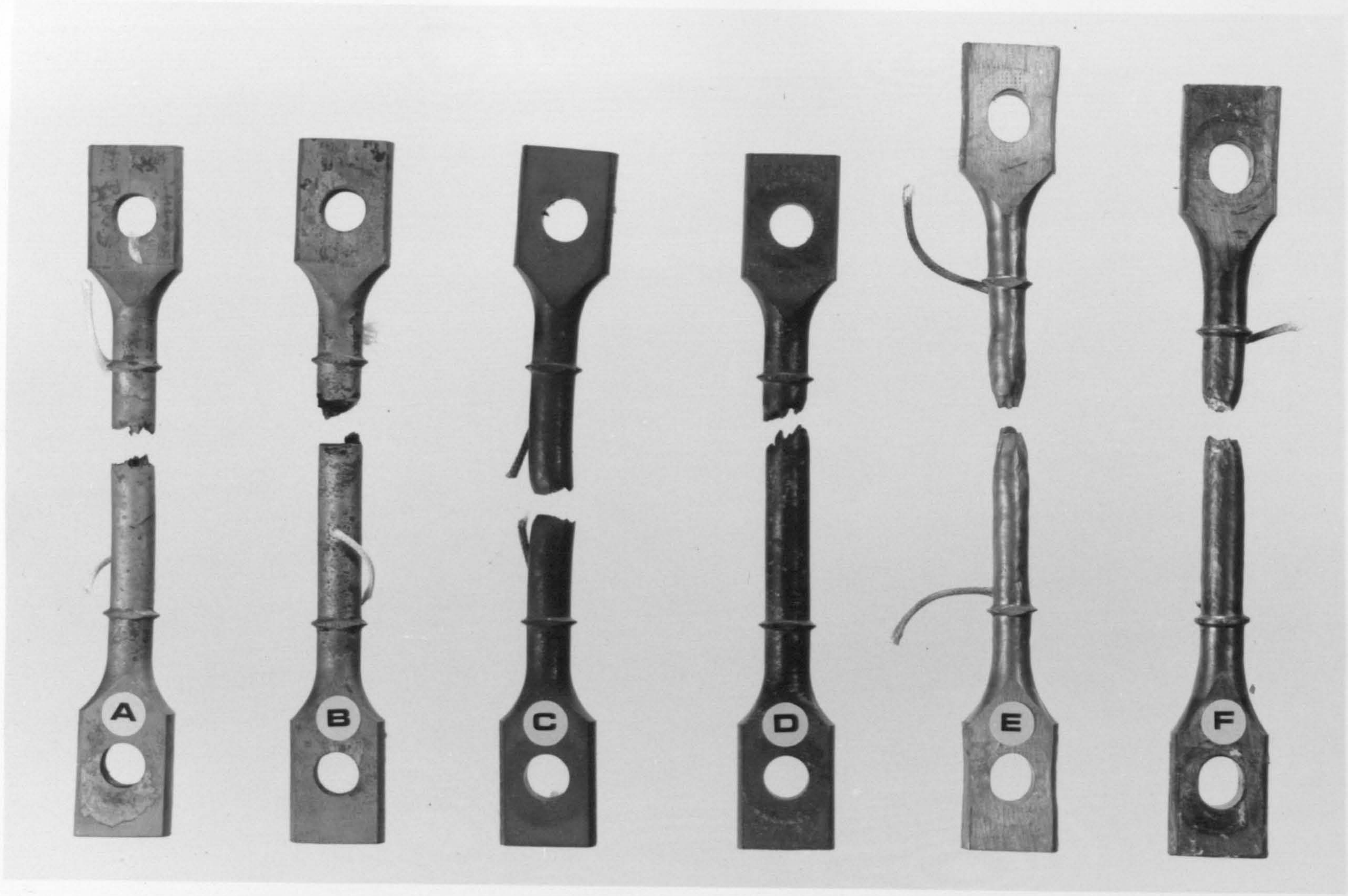

Figure 3.24: Ruptured uni-axial creep test specimens. (A) and (B) tested at $500°C$; (C) and (D) tested at $250°C$; (E) and (F) tested at $150°C$. N.B. Large strain and necking of specimens (E) and (F).

Figure 3.25: Fracture surfaces for specimen (A), Fig.3.24, tested at $500°C$.

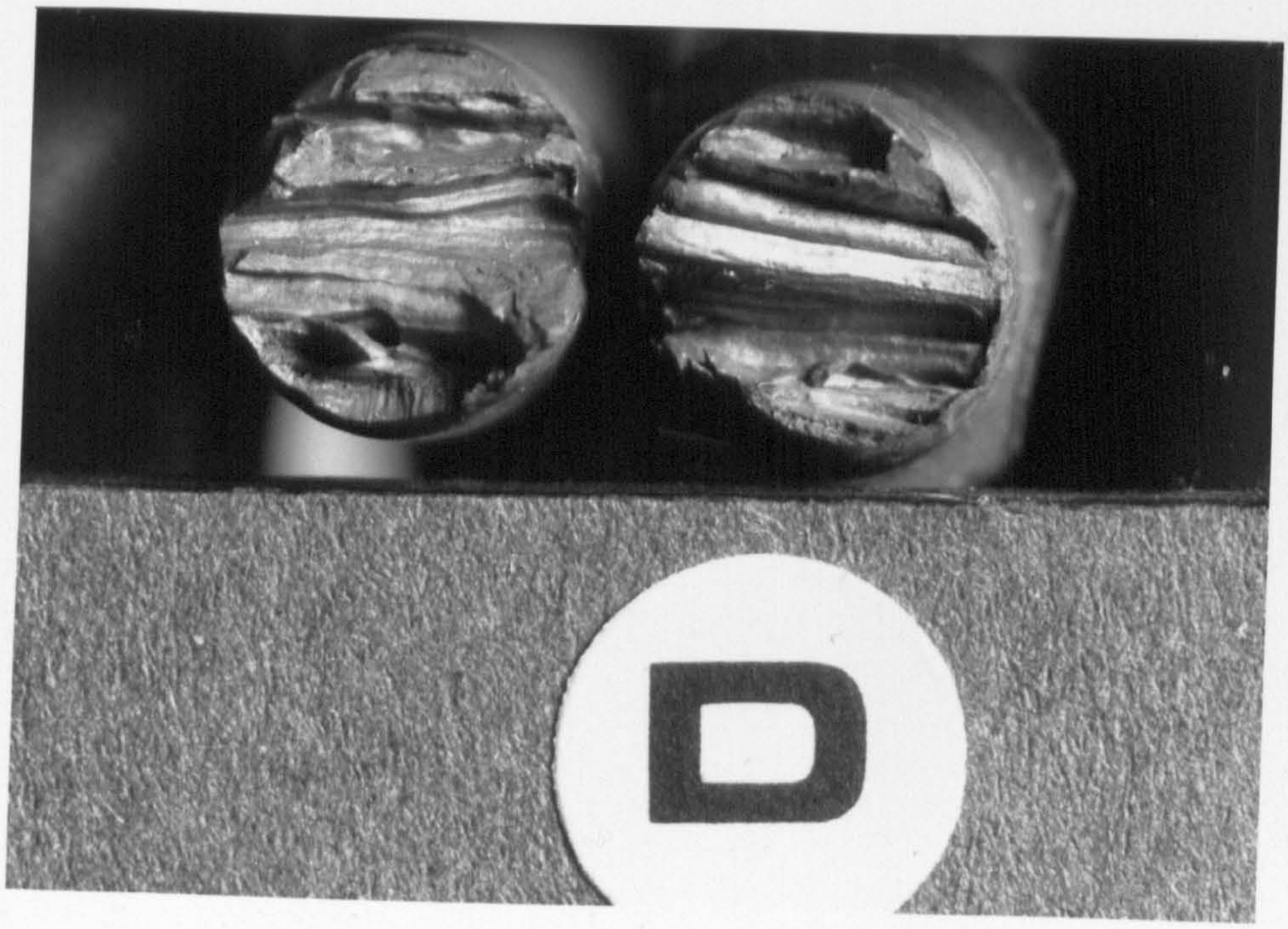

Figure 3.26: Fracture surfaces for specimen (D), Fig.3.24, tested at $250°C$.

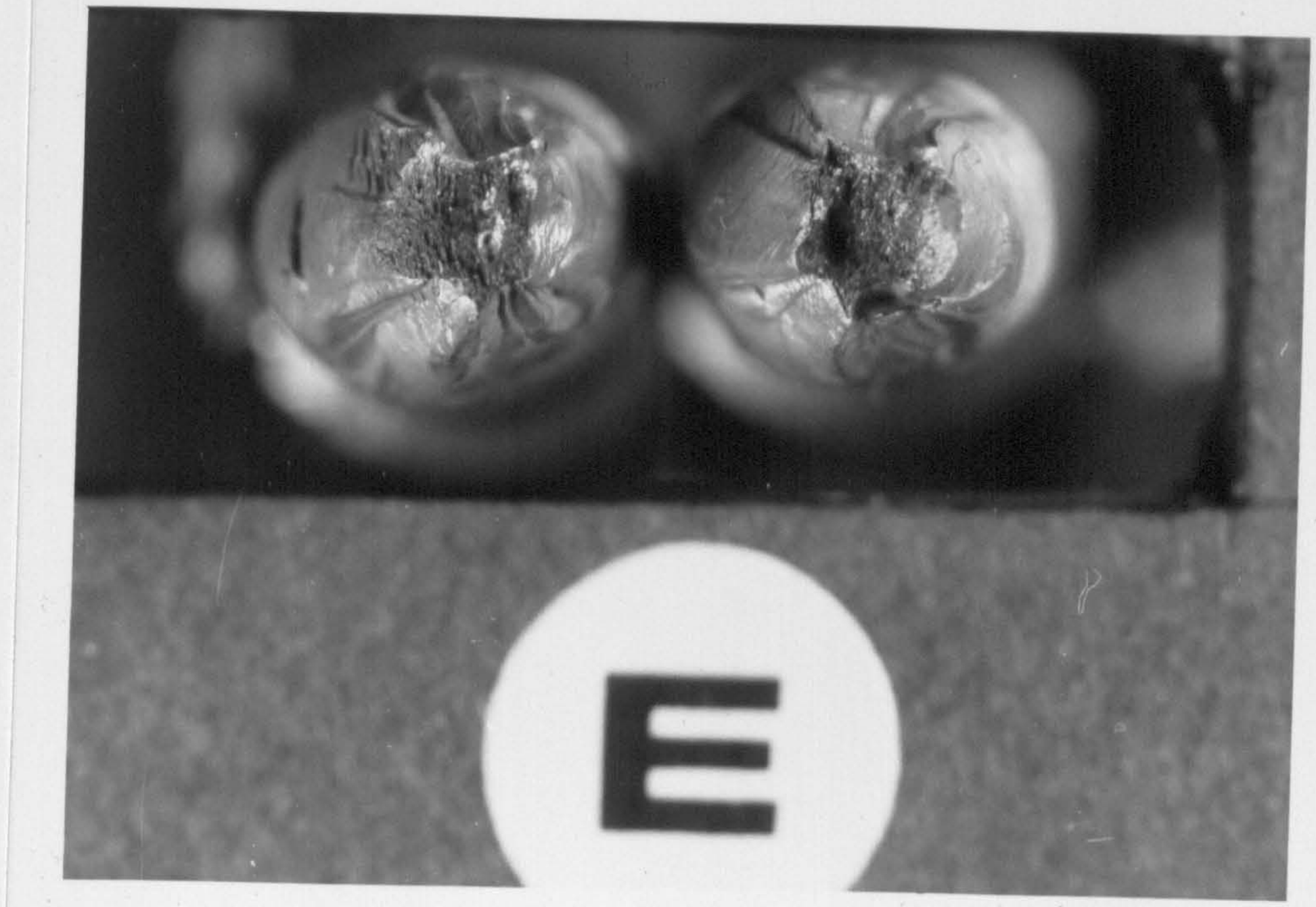

Figure 3.27: Fracture surfaces for specimen (E), Fig.3.24, tested at $150°C$.

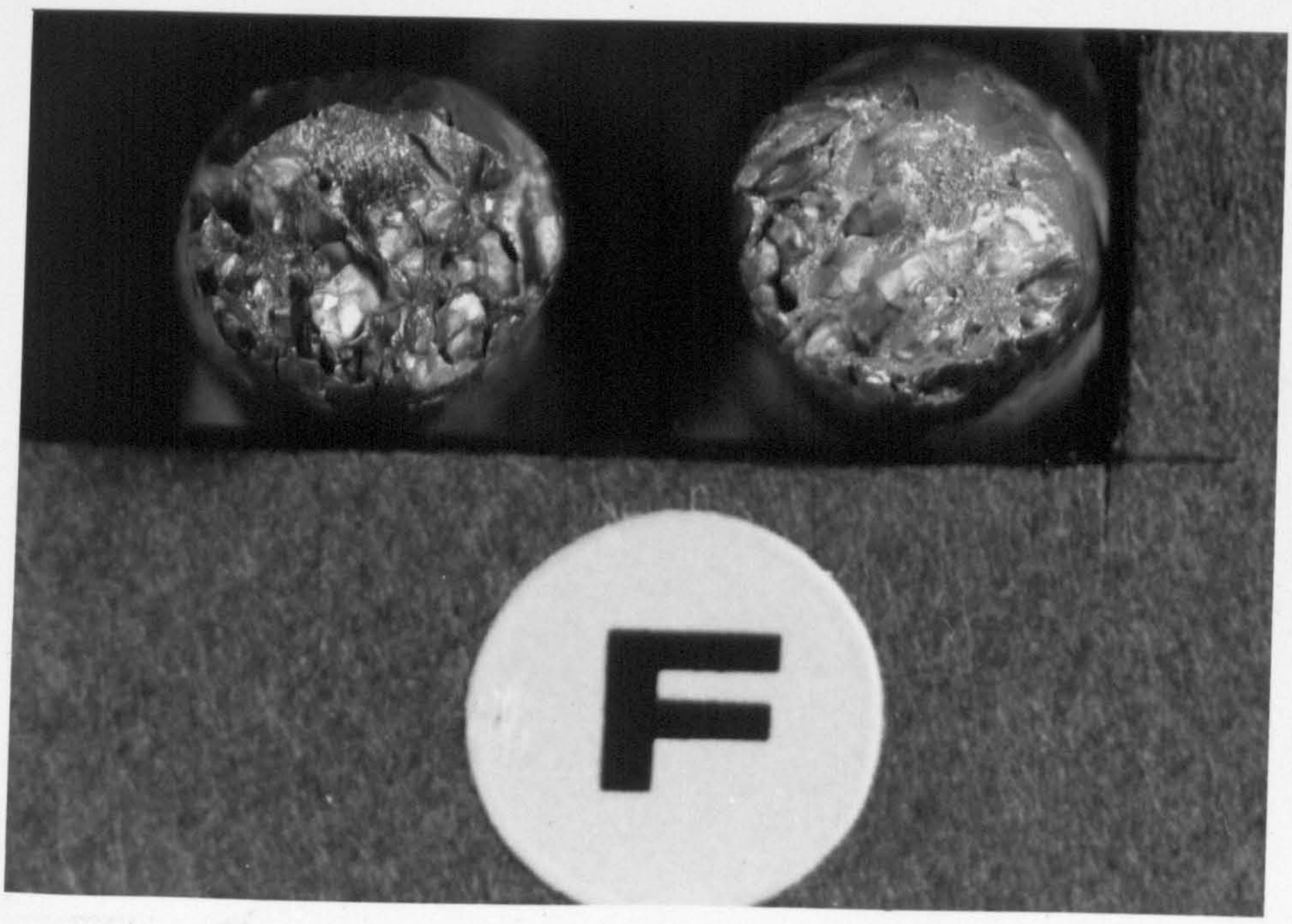

Figure 3.28: Fracture surfaces for specimen (F), Fig.3.24, tested at $150°C$. (Batch-(M) Copper).

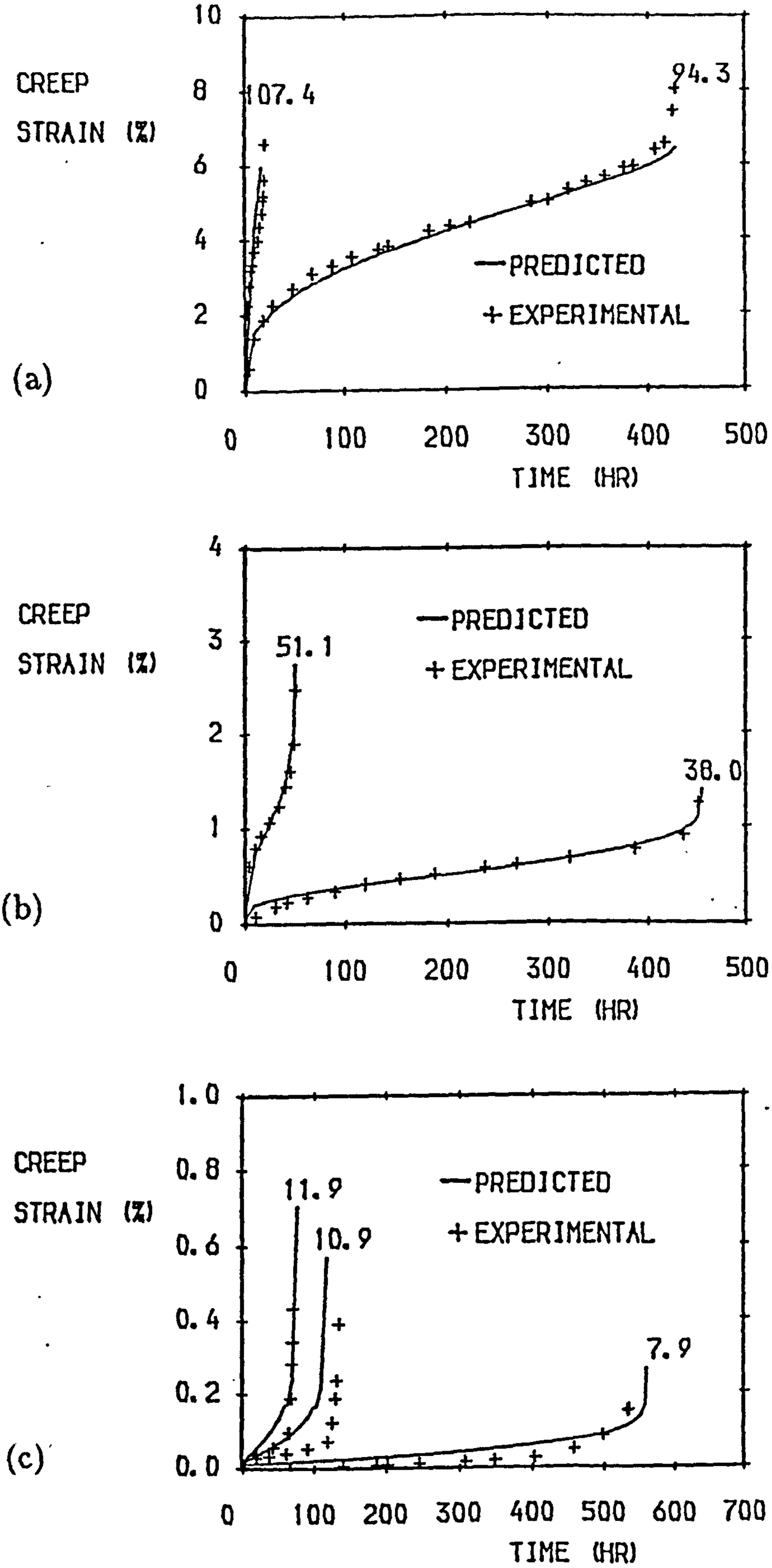

Figure 3.29: Experimental (+) and fitted (-) creep curves for creep tests (a) at 150°C, (b) at 250°C and (c) 500°C and various test stress levels in MPa.

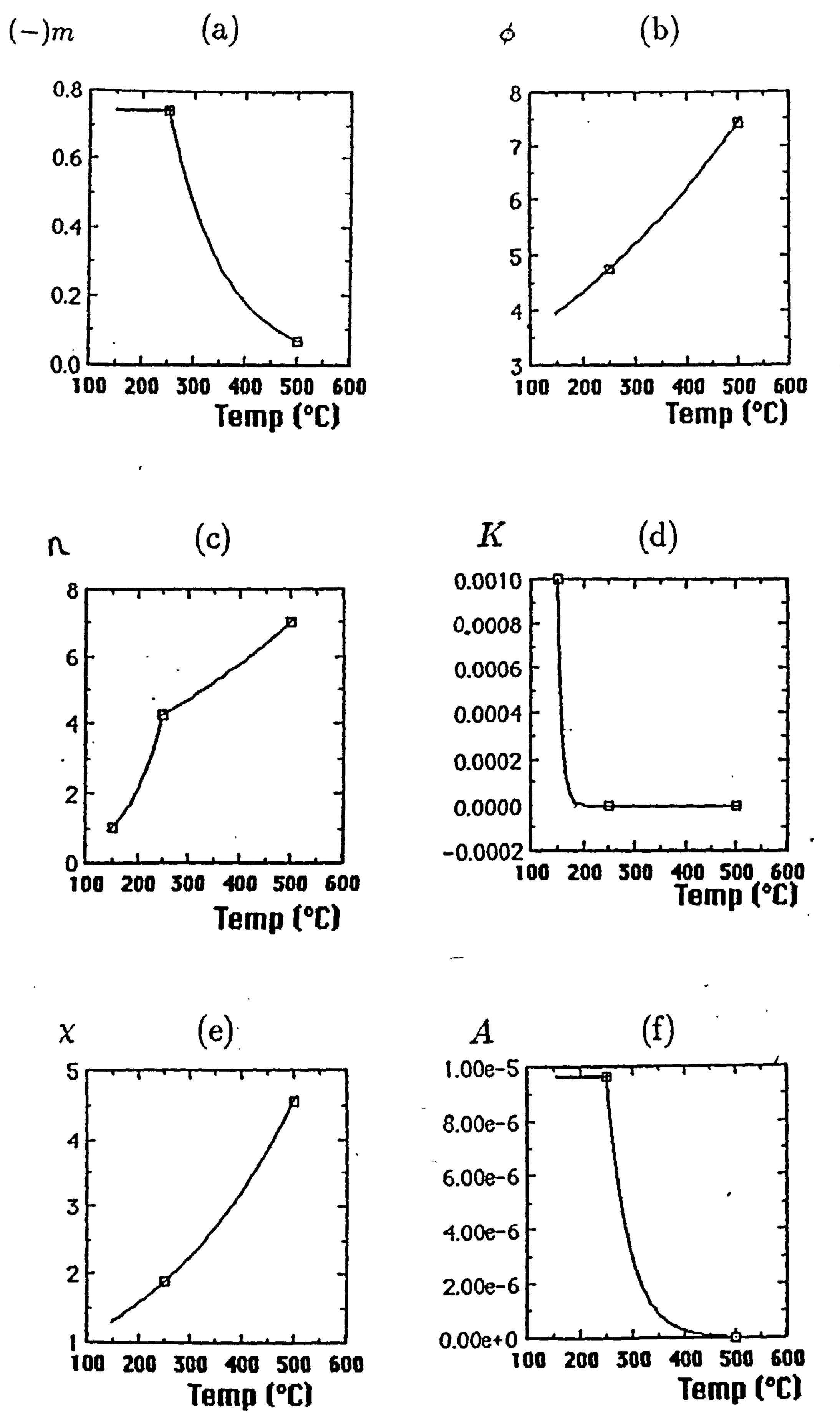

Figure 3.30: Graphs showing the functional variation of material parameters with temperature. Parameter functions are given in Table 3.5.

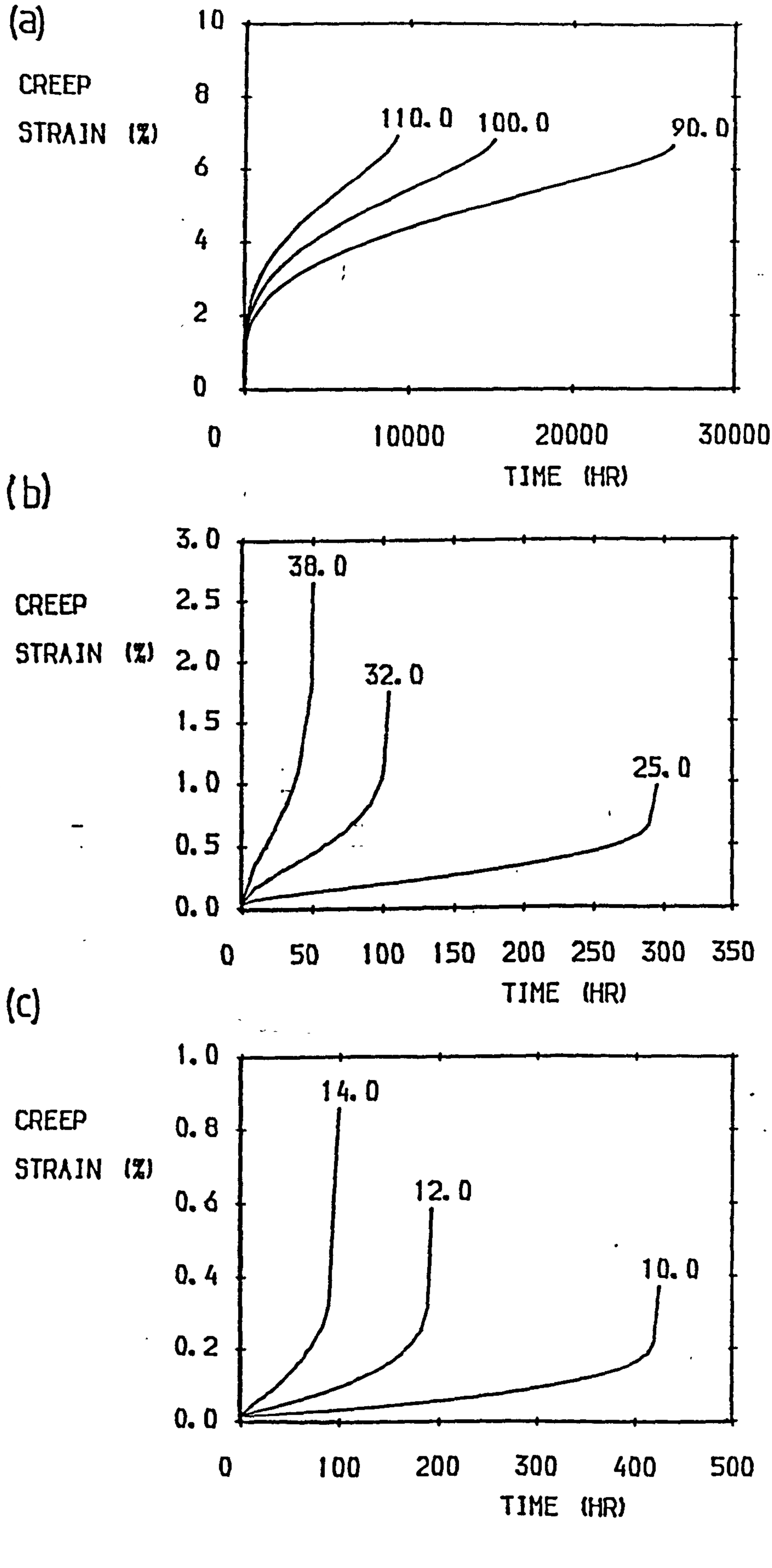

Figure 3.31: Predicted creep curves for Copper at (a) 150°C, (b) 300°C, and (c) 450°C. Stress levels in Mpa. N.B. Creep curves at 250°C and 500°C are the same as the predicted curves of Figs. 3.29 (b) and (c), respectively.

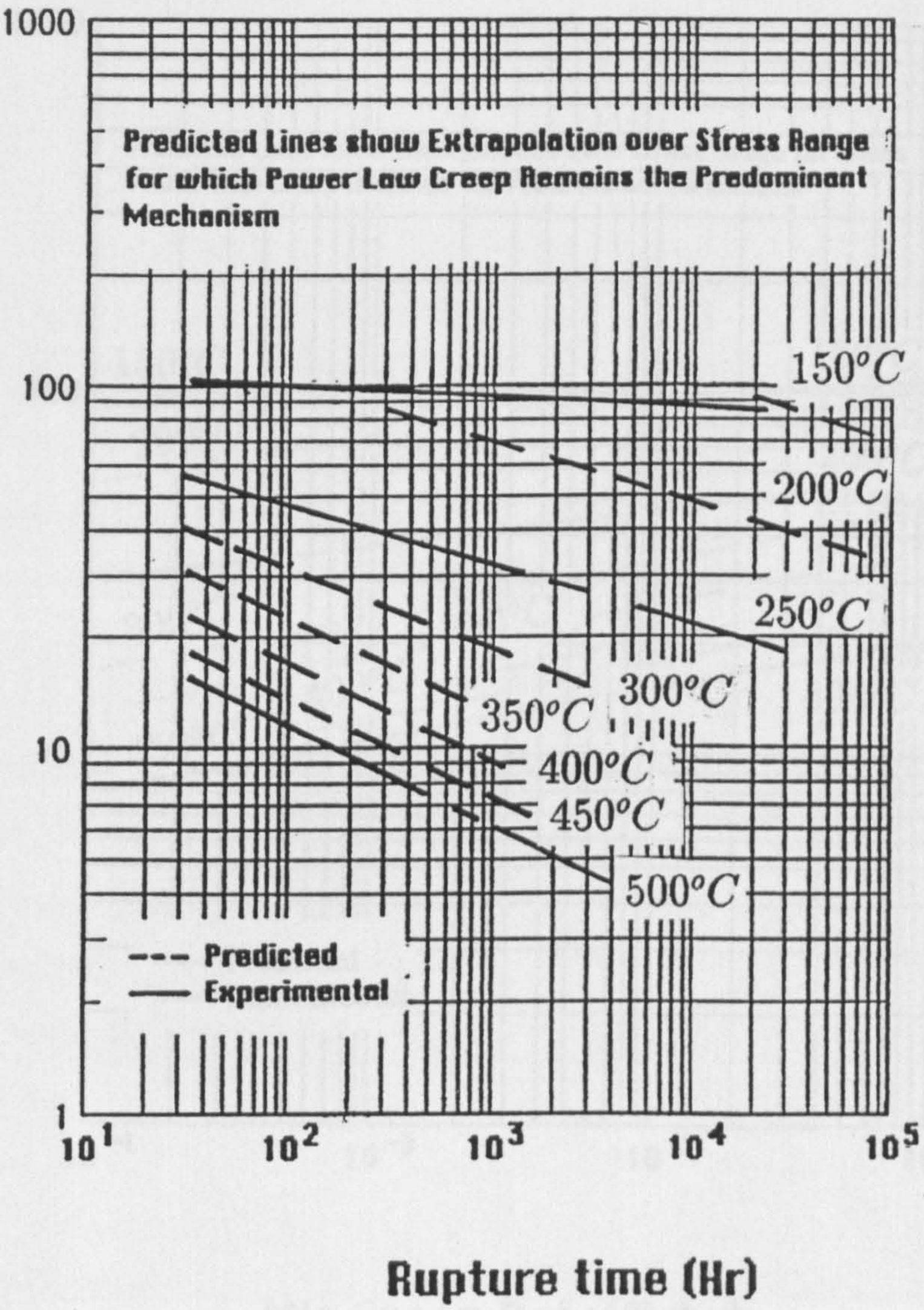

Figure 3.32: Comparison of predicted and experimental variations of log(stress) against log(rupture time) for batch-(c) Copper over the temperature range $150°C$ to $500°C$.

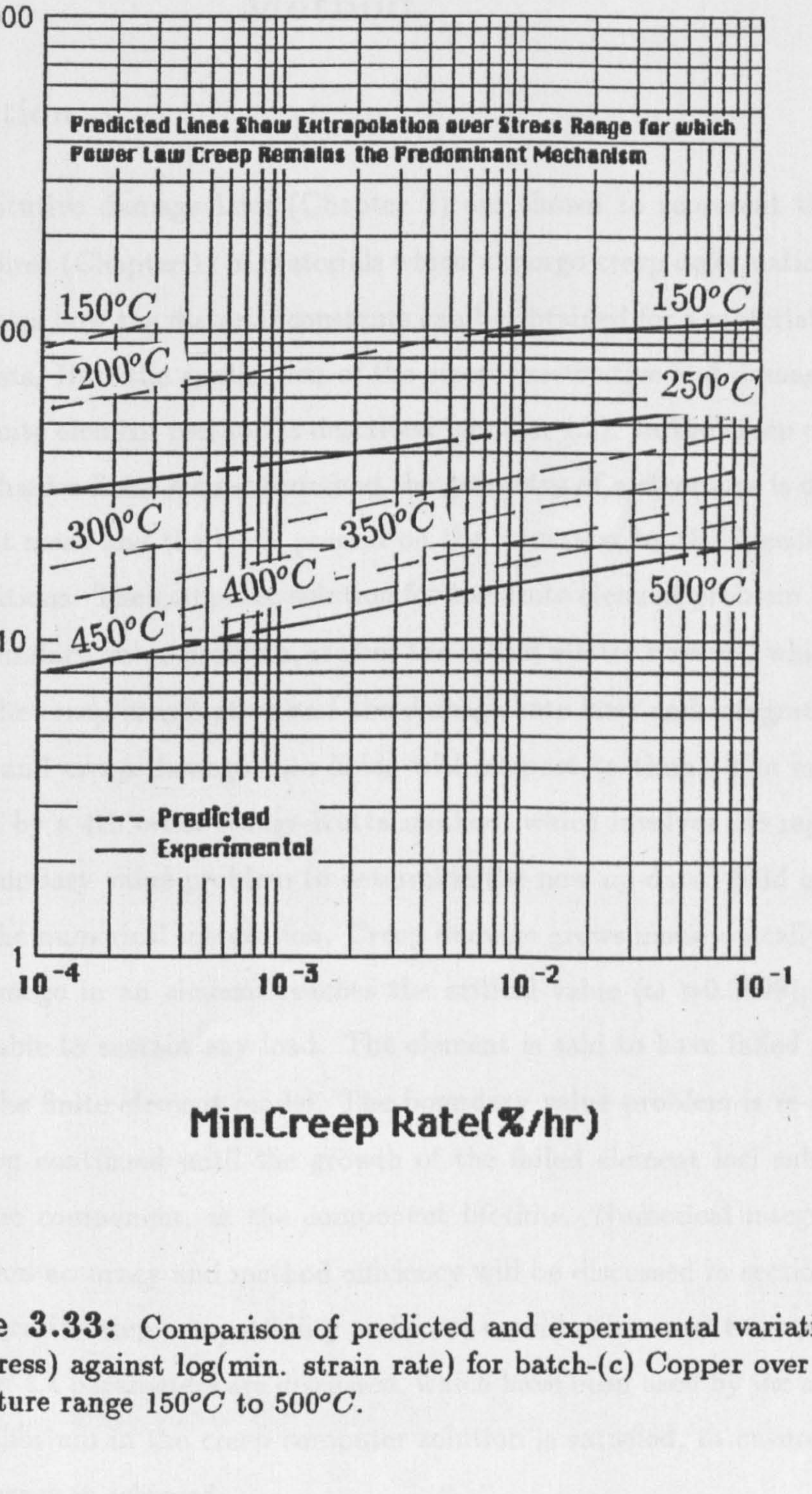

Figure 3.33: Comparison of predicted and experimental variations of log(stress) against log(min. strain rate) for batch-(c) Copper over the temperature range $150°C$ to $500°C$.

Chapter 4.

The Creep Continuum Damage Finite Element Method.

4.1 Introduction.

The constitutive damage laws (Chapter 2) are shown to represent the microstructural features (Chapter 1) of materials which undergo creep deformations. In Chapter 3 it is shown how the material constants can be obtained for a material, from uni-axial creep tests. Here the application of the creep constitutive and damage rate laws within the finite element method is described (section 4.2). In the creep continuum damage mechanics finite element method the geometry of a structure is defined by a finite element mesh and the loads present on the structure, by the specification of boundary conditions. The computer solution for the finite element problem begins by solving the boundary value problem, it uses the initial elastic stresses, which are substituted into the creep constitutive and the damage rate laws and integrates the creep strain rate and creep damage rate fields with respect to time. The integration is carried out by a 4th order Runge-Kutta method, which involves the repeated solution of the boundary value problem to determine the new up-dated field quantities required for the numerical integration. Creep damage grows monotonically with time until the damage in an element reaches the critical value (ω >0.9999), when the element is unable to sustain any load. The element is said to have failed and it is removed from the finite element model. The boundary value problem is re-solved and the integration continued until the growth of the failed element loci subtends the ligament of the component, at the component lifetime. Numerical integration methods, integration accuracy and method efficiency will be discussed in section 4.3.

For each iterative step compatibility and force equilibrium must be explicitly satisfied. In section 4.4 parameters are discussed, which have been used by the author to check that equilibrium in the creep computer solution is satisfied, to ensure that good solution accuracy is achieved.

4.2 The Finite Element Method.

(a) Here particular attention is given to the **Absolute Method** [23] for the solution of structural creep problems. This method has the distinct advantage over the **Rate Method** [55], in that cumulative truncation errors within the iterative technique do not violate the force equilibrium equations [56].

From the principle of virtual work applied to the boundary value problem given elsewhere [23]:-

$$F_e = [K]U - F_c \tag{4.1}$$

where (F_e) is the global elastic, applied force vector, and (F_c) is the global creep force vector; (U) is the global vector of the nodal displacements and $[K]$ is the global stiffness matrix given by the assemblage of the stiffness terms for each individual (k)th. element:

$$[K]_{(k)} = \int_{v(k)} B^T_{(k)} D B_{(k)} dv_{(k)} = \qquad B^T_{(k)} D B_{(k)} A_{(k)} . \hat{t} \tag{4.2}$$

Equation (4.2) is for two dimensional constant strain triangles, as used by the author, where $(\hat{t})$ is the element thickness, which is normalised and taken as unity. (B) is a matrix whose components are dependent upon the nodal co-ordinates of the element and (D) is the isotropic elastic material property matrix derived from the general expression (C_{ijkm})[19].

The boundary conditions are applied in equation (4.1) by setting components of a single dimensioned array vector (called the state vector), to have a value of 1.0 or 0.0. A 1.0 in the state vector fixes a displacement component for a node in the (X) or (Y) direction.

Initially (F_c) is zero and (4.1) is solved by finding the inverse of the global stiffness matrix $[K]$, which is performed using a Choleski square root method:

$$U = [K]^{-1} (F_e + F_c) \tag{4.3}$$

giving the elastic (X) and (Y) nodal displacements. The elastic strains for each element are obtained:

$$\epsilon_{(e)ij(k)} = B_{(k)} U_{(k)} \tag{4.4}$$

where $U_{(k)}$ is from global displacement vector (U).The elastic stress are given by:

$$\sigma_{(e)ij(k)} = D \epsilon_{(e)ij(k)} \tag{4.5}$$

The elastic stress components are substituted into the creep strain rate equation:

$$\dot{\epsilon}_{(c)ij} = \frac{H(\sigma)\sigma_{ij}Kt^m}{(1-\omega)^n} \tag{4.6}$$

where $H(\sigma)$ may be shown [57] to be

$$\Phi^{n-1}(\sigma_{ij}) \begin{vmatrix} 1 & 0.5 & 0 \\ -0.5 & 1 & 0 \\ 0 & 0 & 3 \end{vmatrix} \tag{4.7}$$

and:

$$\Phi(\sigma_{ij}) = \left\{\sigma_{11}^2 + \sigma_{22}^2 + \sigma_{11}\sigma_{22} + 3\sigma_{12}^2\right\}^{\frac{1}{2}} \tag{4.8}$$

Here the creep strains are the engineering strains and plane stress conditions are assumed. Equation (4.6) is the same as Odqvist's equation (2.7), but equation (2.7) is defined in terms of the absolute strains in accordance with the absolute strain tensor [20]. N.B. for brevity future reference to the creep strain rate equations of Chapter 2 is made in preference to equations (4.6) and (4.7).

The elemental damage rates are calculated substituting the elastic stress components into the equation:

$$\dot{\omega} = \frac{Mt^m\Delta^x(\sigma_{ij})}{(1+\phi)(1-\omega)^\phi} \tag{4.9}$$

The creep strain rate and damage rate values obtained from equations (4.6) and (4.9) are numerically integrated with respect to time (t) using a 4th. order Runge-Kutta method, but here for simplicity a Euler 1 scheme is shown, giving the current creep strain and damage values at time $(t+\Delta t)$:-

$$\epsilon_{(c)ij_{(t+\Delta t)}} = \epsilon_{(c)ij_{(t)}} + \dot{\epsilon}_{(c)ij_{(t)}}.\Delta t \tag{4.10}$$

$$\omega_{(t+\Delta t)} = \omega_{(t)} + \dot{\omega}_{(t)}.\Delta t \tag{4.11}$$

for each element (k). The elemental creep stiffness matrices are calculated:-

$$[R]_{(k)} = \int_{v(k)} B_{(k)}^T D dv_{(k)} = B_{(k)}^T D A_{(k)}.\hat{t} \tag{4.12}$$

for plane strain triangles.

The nodal creep force vectors for each element are given by:

$$F_{(c)_{(k)}} = [R]_{(k)}\epsilon_{(c)ij_{(k)}} \tag{4.13}$$

and assembled into the global creep force vector (F_c). (F_c) is used to up-date equation (4.3). Now the solution of (4.3) yields the total displacements due to both creep and elastic forces, giving the total strain:

$$\epsilon_{(Tot.)ij_{(k)}} = B_{(k)}U_{(k)} = \epsilon_{(e)ij_{(k)}} + \epsilon_{(c)ij_{(k)}} \tag{4.14}$$

from which the elastic strain may be obtained, knowing $(\epsilon_{(c)ij_{(k)}})$ from (4.10):

$$\epsilon_{(e)ij_{(k)}} = B_{(k)}U_{(k)} - \epsilon_{(c)ij_{(k)}} \tag{4.15}$$

and the current stress field at time $(t + \Delta t)$ is obtained using (4.5). Then, equation (4.5) to (4.15) may be used iteratively stepping forward in time (t), until the damage values (ω) for an element reaches the critical values (0.9999), when the element is said to have failed. This element is unable to transmit any load and is removed, by removing its element stiffness component $[K]_{(k)}$ and its corresponding creep forces $F_{(c)_{(k)}}$ from equation (4.1). The global stiffness matrix is re-inverted (4.3) and the solution continued until the next element fails, when this procedure is repeated, until the whole finite element mesh ligament is subtended by failed elements. Elements are also forced to fail for special cases, where an element or an island consisting of a number of elements are surrounded by failed elements. Nodes which are not connected to unfailed elements are included within the boundary conditions of equation (4.1). The procedure described is primarily for a plane stress analysis, but is similar to the procedure used for plane strain and axisymmetric analysis; though for each analysis different (B) and (D) matrices are defined [58]. The loading conditions for the axisymmetric analysis are given in section 8.6.1.

(b) In the finite element program Damage-(XX), equation (4.1) is normalised by defining $(\hat{U} = u/e_0)$, $(e_0 = \sigma_0/E)$, $(V_{(c)ij} = \epsilon_{(c)ij}/e_0)$ and $(\hat{D} = D/E)$, to give the applied elastic force vector (F_e) in terms of the leg lengths of the top boundary elements, giving (4.1) as:

$$\hat{F}_{el} = l_{(T.B.)_{(k)}} = [\hat{K}]\hat{U} - \hat{F}_c \tag{4.16}$$

where

$$l_{(T.B.)_{(k)}} = \left\{\int_{v_{(k)}} B^T_{(k)}\hat{D}B_{(k)}dv_{(k)}\right\}\hat{U}_{(k)} - \left\{\int_{v_{(k)}} B^T_{(k)}\hat{D}dv_{(k)}\right\}V_{(c)_{(k)}} \tag{4.17}$$

Using this normalised formulation the normalised creep strain rate and damage rate equations (2.19) and (2.20) are used, which are integrated using the normalised failure time scale defined by equation (2.18). The normalisation improves solution accuracy by not allowing very small and very large numbers into the computer solutions, therefore reducing the effects of numerical rounding errors.

4.3 Numerical Time Integration.

4.3.1 The Initial Value Problem.

The initial value problem may be written as:

$$\frac{dy}{dx} = y^{(1)} = f(x,y); y(x_n) = \eta \tag{4.18}$$

A solution is to be found for (y) in the range $(x_n \leq x \leq x_f)$. It is assumed that (f) has a unique continuously differentiable soution $(y(x))$. (η) is the known starting or the initial value of the solution. (dy/dx) may be identified with the creep strain rate or damage rate, where (x) is the time scale. Considering the Taylor series for $y(x_n + h)$ about the point (x_n):-

$$y(x_n + h) = y(x_n) + hy^{(1)}(x_n) + \frac{h^2}{2!}y^{(2)}(x_n) + \ldots \tag{4.19}$$

where

$$y^{(q)}(x_n) = \left(\frac{d^q y}{d^q x}\right); x = x_n; q = 1,2\ldots \tag{4.20}$$

and (h) is the step length: $h = (x_{n+1} - x_n)$.

The simplest integration technique involves the truncation of (4.19) after the second term:

$$y(x_n + h) \approx y(x_n) + hy^{(1)}(x_n) \tag{4.21}$$

$$= y(x_n) + hf(x_n, y(x_n)) \tag{4.22}$$

from (4.19), which is called the Euler 1 method, as shown in Fig. 4.1. Hence, (4.19), or the creep strain rate and damage rate equations (2.19) and (2.20) respectively, may be numerically integrated forward in time using such an integration scheme.

4.3.2 The Numerial Integration Technique Chosen For Use In The Creep Continuum Damage Finite Element Program.

The time integration technique used in the creep continuum damage program Damage-(XX) is a 4th order Merson's Runge-Kutta method [59,60]. This method is an explicit one step method [60] and has improved accuracy over Euler 1, 2, and 3 methods [60], in that it takes account of higher order derivatives of the Taylor expression (4.19) in the initial value problem, by sacrificing linearity; yet, the method only requires a single starting value. Merson's method provides an easily calculable local truncation error estimate, which forms the basis for the choice of time step, in the time stepping technique of the program Damage-(XX). If the error estimate is large the time step chosen is reduced and vice-versa. The use of high accuracy integration techniques of the implicit multi-step methods, such as predictor corrector methods and the explicit multi-step methods, require additional starting values and usually involve much higher computational effort than the 4th order Runge-Kutta technique. Numerical integration techniques have been reviewed and used by the author [60]; and the 4th order Merson's method, has been found to be particularly suited to its appli-caiton within the creep continuum damage program. This integration method gives reasonably good solution accuracy and stability with a low computational overhead. The use of the 4th order Merson's method and the variable time stepping procedure has been described by Hayhurst et al [23] in (Appendix A1 and A2) respectively.

4.3.3 Time Integration Accuracy And Its Effect On The Finite Element Creep Damage Solution.

The selection of a time step ($\Delta\tau$) is detailed [23] (Appendix A2.1 and A2.2). Having selected a time step, the Merson's error estimate is calculated for each component of creep strain for each element ($V_{(ERR)ij_{(k)}}$), and is normalised by the current component of creep strain ($V_{(c)ij_{(k)}}$). When the creep strains ($V_{(c)ij_{(k)}}$) are very small ($V_{(c)ij_{(k)}}$) is replaced by ($V_{(LIM)} = EPSL \times V_{(Abs.Av.)}$), where (EPSL) is a constant and ($V_{(Abs.Av.)}$) is the minimum absolute average strain for all the elements in the structure. The criterion for the acceptance of the time step is given as: the maximum absolute value of $V_{(ERR)ij_{(k)}}/V_{(c)ij_{(k)}}$ for all elements in the structure must be less than ($EPSR$), where ($EPSR$) is also a constant and for $V_{(c)ij_{(k)}} < V_{(Abs.Av.)} \Rightarrow V_{(c)ij_{(k)}} = V_{(LIM)}$.

The values of $(EPSL)$ and $(EPSR)$ therefore determine the size of the acceptable integration error in creep-strain, in the automatic time stepping integration procedure. If the maximum normalised strain error is larger than $(EPSR)$, then the time step increment is reduced and a new solution obtained and the strain error is judged again. This procedure is continued until an acceptable strain error is obtained. A reduction in the sizes of both $(EPSL)$ and $(EPSR)$ therefore increases the accuracy of the integration and hence the accuracies of the predicted stresses, strains, failure time and failure strain are improved. This increase in accuracy unfortunately involves an increase in the number of iterative time steps for a finite element prediction to run to completion and also involves an increase in the number of unacceptible time steps tested within each iteration. Therefore, requiring an increased computational overhead.

A simple two element, finite element mesh is subjected to a constant uniaxial load, under plane stress conditions, to show the effect of modifying the integration parameters on the predicted normalised failure time (τ_f) and normalised failure strain (V_f) respectively. The top curve in Fig. 4.2 shows how the normalised failure time (τ_f) is reduced with reduced sizes of the integration error parameters $(EPSL)$ and $(EPSR)$, which reduce the integration error. The theoretical value of rupture time obtained by analytical integration of the damage rate law is given by (2.23) as (τ =31.805). It is observed that as the integration error is decreased the number of iterative steps required increases from 22 to 290 steps. Referring to the top curve in Fig. 4.3, it is noticed that creep strain at failure (V_f), is affected to a lesser extent by the integration parameters. The values remain close to the theoretical value of (V_f) for most of the range of the integration parameter values used in these tests. The theoretical value of (V_f) is obtained from the integration of both the creep stain rate and the damage rate equations and is given by equation (2.25) as $(V_f = 7.65\%)$.

The significance of the size of the error in the predicted normalised failure time (τ_f) for a structure must be judged, by obtaining the real error between the numerical and the theoretical values of real failure time (t) using equation (2.27). Referring to this equation the significance of the integration error depends on the size of $(1/(m+1))$. If $(1/(m+1))$ is large then improved integration accuracy will be required, over the integration accuracy required for a material having a small value

of $(1/(m+1))$.

4.3.4 The Z-Transformation Of The Damage Parameter, Coupled With the Runge-Kutta Method.

Here a substitution [61] of:

$$z = (1-\omega)^{(\phi+1)} \tag{4.23}$$

is made in both the creep constitutive and damage law, equations (2.19) and (2.20) respectively. From (4.23):

$$dz = -(\phi+1)(1-\omega)^{\phi} d\omega \tag{4.24}$$

giving:

$$\frac{dV_{ij}}{d\tau} = \frac{\Sigma^{n-1} S_{ij}}{z^{\frac{n}{(\phi+1)}}} \tag{4.25}$$

and

$$\frac{dz}{d\tau} = \frac{d\omega}{d\tau} \times \frac{dz}{d\omega} = \frac{d\omega}{d\tau} \times (-1)(\phi+1)(1-\omega)^{\phi} = (-1)\frac{\Delta^{x}(\Sigma_{ij})}{V_u} \tag{4.26}$$

where at time (τ=0; $\omega = 0$),(z =1.0) and at ($\tau = \tau_f$; $\omega = 1.0$), (z =0) from (4.23). This substitution considerably eases the integration of the damage rate equation, as here (4.26) will be integrated instead of equation (2.19) and (4.26) is now independent of the monotonically increasing damage parameter. Hence (z) increases linearly at constant stress ($\Delta(\Sigma_{ij})$) with the normalised time. The Z-transformation has been included in the program Damage-(XX), by the author in collaboration with Othman [62] and utilises the 4th order Merson's method Runge-Kutta technique. Before entering the Runge-Kutta integration program module (ω) is transformed to (z) using equation (4.23) and the strain rates and damage rates are given by (4.25) and (4.26) respectively. On leaving the module (z) is tranformed back to (ω), so no further program modification is required.

Similar integration accuracy tests were performed to those of section 4.33, for the standard Runge-Kutta technique, using a plane stress two element finite element mesh under uni-axial tension. The results are summarised as the lower curves of Figs. 4.2 and 4.3. Referring to the lower curve of Fig. 4.2 it is noticed that the normalised failure time is almost exactly that of the theoretical failure time, for

all the values of the integration accuracy parameters chosen. This is as a direct result of the simplified integration of the linear equation (4.26) for constant stress conditions. It is noticed that the number of iterative steps required till failure of the structure, is on average approximately 10% smaller for the Z-transformed tests in comparison with the plain Runge-Kutta method tests. Though, the Z-transformation gives much improved lifetime predictions compared with the standard Runge-Kutta solutions (Fig. 4.2), the failure strain predictions are worse than those obtained by the standard Runge-Kutta method (Fig. (4.3)). The value of the strain at failure approaches the theoretical value (V_f=7.65%) as the integration error parameters are reduced.

Therefore, if sufficiently small integration error parameters are chosen the two integration methods should give the same failure time and failure strain predictions, approaching the theoretical values respectively. As the use of small integration error parameters involves a high computational overhead, then if larger values of integration error parameters have to be used, the Z-transformed Runge-Kutta technique will provide the best lifetime predictions and the standard Runge-Kutta technique will provide the best creep deformation (or creep strain) predictions, using the least computational resources. All computer solutions performed by the author and detailed in this thesis used the standard Runge-Kutta method so that consistent comparisons between results and CPU time usage of different finite element problems could be made.

4.4 Mesh Equilibrium And Equilibrium Parameters.

Formerly an equilibrium parameter called SIGREF has been used in the program Damage-(XX). This parameter is defined as the ratio of the total vertical force (i.e. in the (y) direction) on the finite element mesh bottom boundary, to the applied total vertical force on the mesh top boundary:

$$SIGREF = \frac{\sum F_{(y)(B.B.)_{(k)}}}{\sum F_{(y)(T.B.)_{(k)}}} \tag{4.27}$$

which may be written as:

$$SIGREF = \frac{\sum l_{(B.B.)_{(k)}} \Sigma_{(y)_{(k)}}}{\sum l_{(T.B.)_{(k)}}} \tag{4.28}$$

where $(l_{(k)})$ are the leg lengths of the elements on the bottom boundaries $(B.B.)$ and the top boundaries $(T.B.)$ and $(\Sigma_{(y)(k)})$ are the stresses in the bottom boundary elements. The stress applied to the top boundary is usually normalised to unity in the program and hence the force on the top boundary of the finite element mesh is equal to the length of the top boundary (equation (4.16) and (4.17)), as the mesh has unit thickness for plane strain and plane stress conditions. For perfect force equilibrium SIGREF should equal unity throughout the creep solution, until a line of failed elements forms along the effective cross-sectional area of the mesh, when SIGREF becomes zero. Though, SIGREF only includes the force contribution to the bottom boundary of elements with a side on the bottom boundary, and does not include the contributions of other elements connected to bottom boundary nodes. For example in Fig. 4.4(a) only element No. 2 contributes force to the bottom boundary in the calculation of SIGREF; the contributions of elements No. 1 and 3 are neglected. This results in the parameter SIGREF giving erroneous values, particularly when crossed-triangular finite element meshes are used. This is exemplified by the situations which may occur when modelling crack growth along a crossed-triangle finite element mesh boundary. Examination of one crossed triangular element set taken from the larger mesh, shown in Fig. 4.4(a), shows that if the element at the bottom boundary fails first (Fig.4.4(b)) then the value of SIGREF becomes zero, as the applied force is taken by the elements (1) and (3). Yet in Fig. 4.4(c) if element No. 1 fails first, the value of SIGREF becomes 2.0. Though, for both cases, from the summation of the nodal forces, force equilibrium, is satisfied. In a large structure smaller changes in SIGREF are noticed, but the parameter is still erroneous.

The author has used a new parameter to check mesh equilibrium is satisfied throughout the creep continuum damage solution. The parameter is called FREF, defined:

$$FREF = \frac{\sum F_{(B.B.)(y)_{(n)}}}{\sum F_{(T.B.)(y)_{(m)}}} = \frac{\sum \left\{ \int_{v_{(k)}} B^T_{(k)} \Sigma_{(e)(y)_{(k)}} dv_{(k)} \right\}_{(n)}}{\sum F_{(APP)(y)_{(m)}}} \tag{4.29}$$

where (k) indicates the element numbers of elements having finite element mesh bottom boundary nodes, (n), and the top boundary nodes are termed (m). Therefore, FREF is the summation of the vertical (y) forces at the bottom boundary nodes, obtained from the elemental stresses in the bottom boundary elements (connected to the bottom boundary nodes), divided by the total force applied to the top boundary

in the vertical (y) direction. When an element fails (ω >0.9999) at the bottom boundary its force contribution is not included in the calculation of FREF. The value of FREF should be explicitly satisfied at every iterative time step of the finite element creep damage solution and should remain at a value close to -1.0000, usually FREF = -0.9999, indicating that an almost perfect state of equilibrium is maintained.

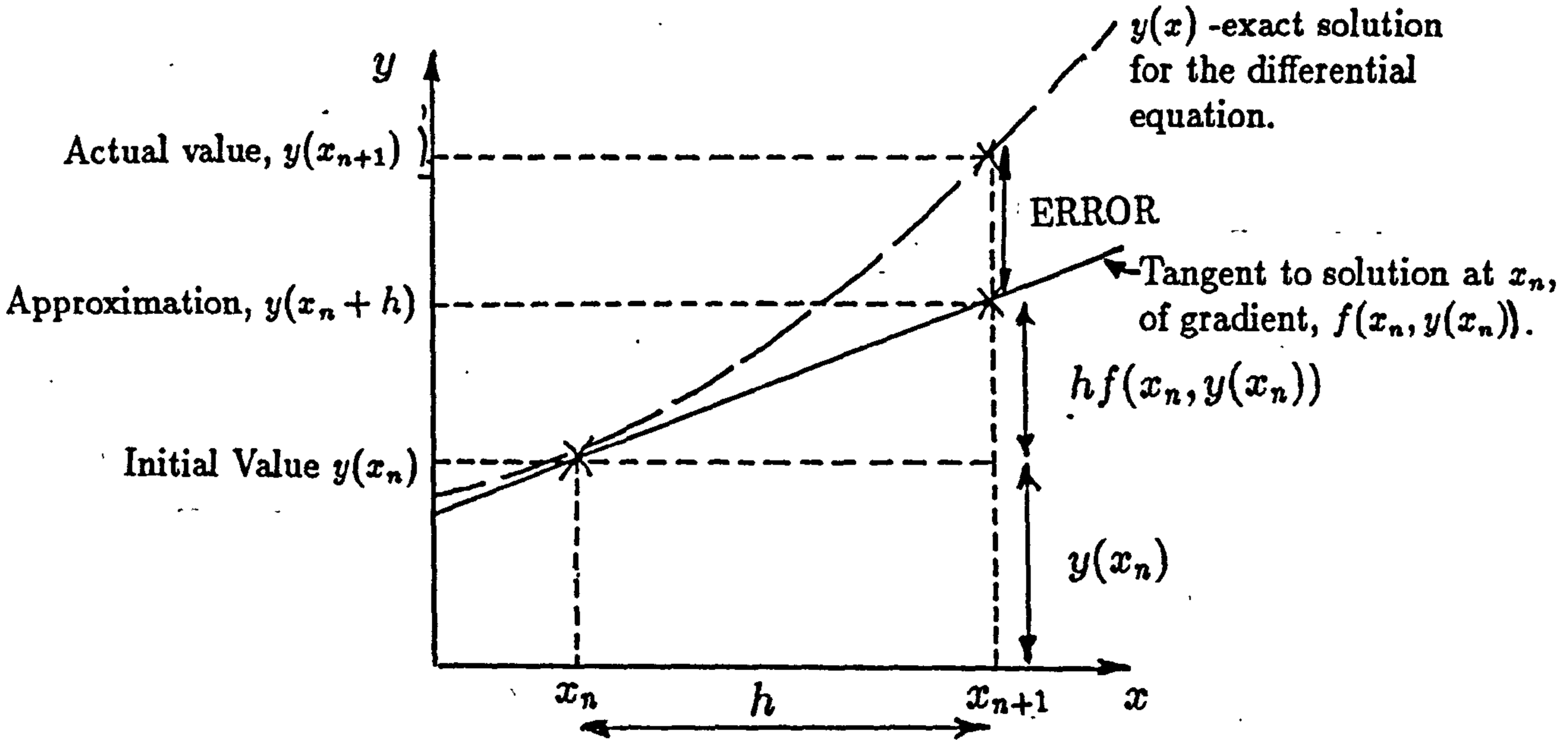

Figure 4.1: Graphical representation of the solution to the initial value problem using the Euler 1 integration scheme, equation (4.22).

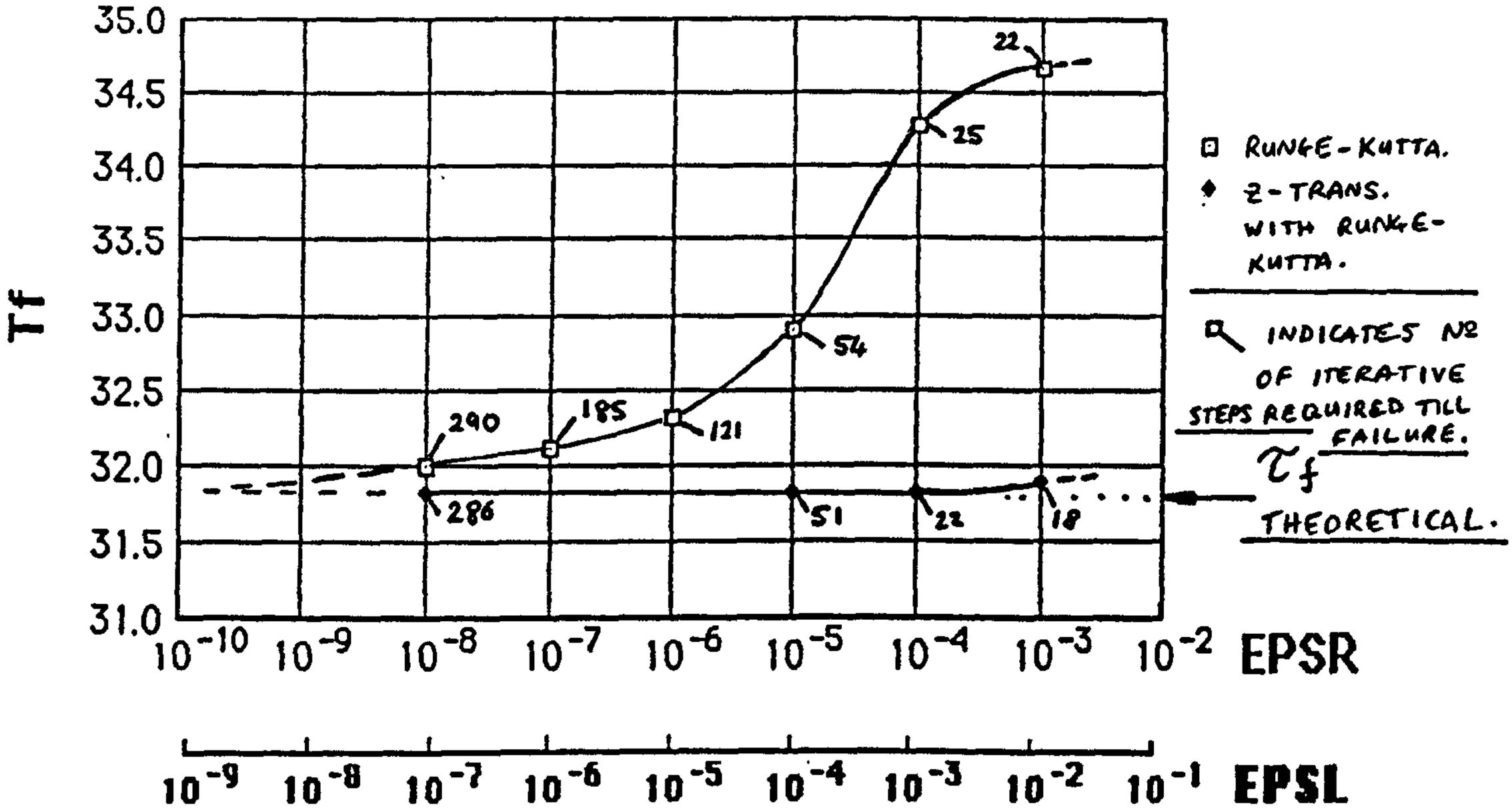

Figure 4.2: Graph showing the increased accuracy of the numerical prediction of the normalised failure time (τ_f) for the finite element problem of Fig.4.4(a) as the allowable integration error parameters (EPSL) and (EPSR) are reduced.

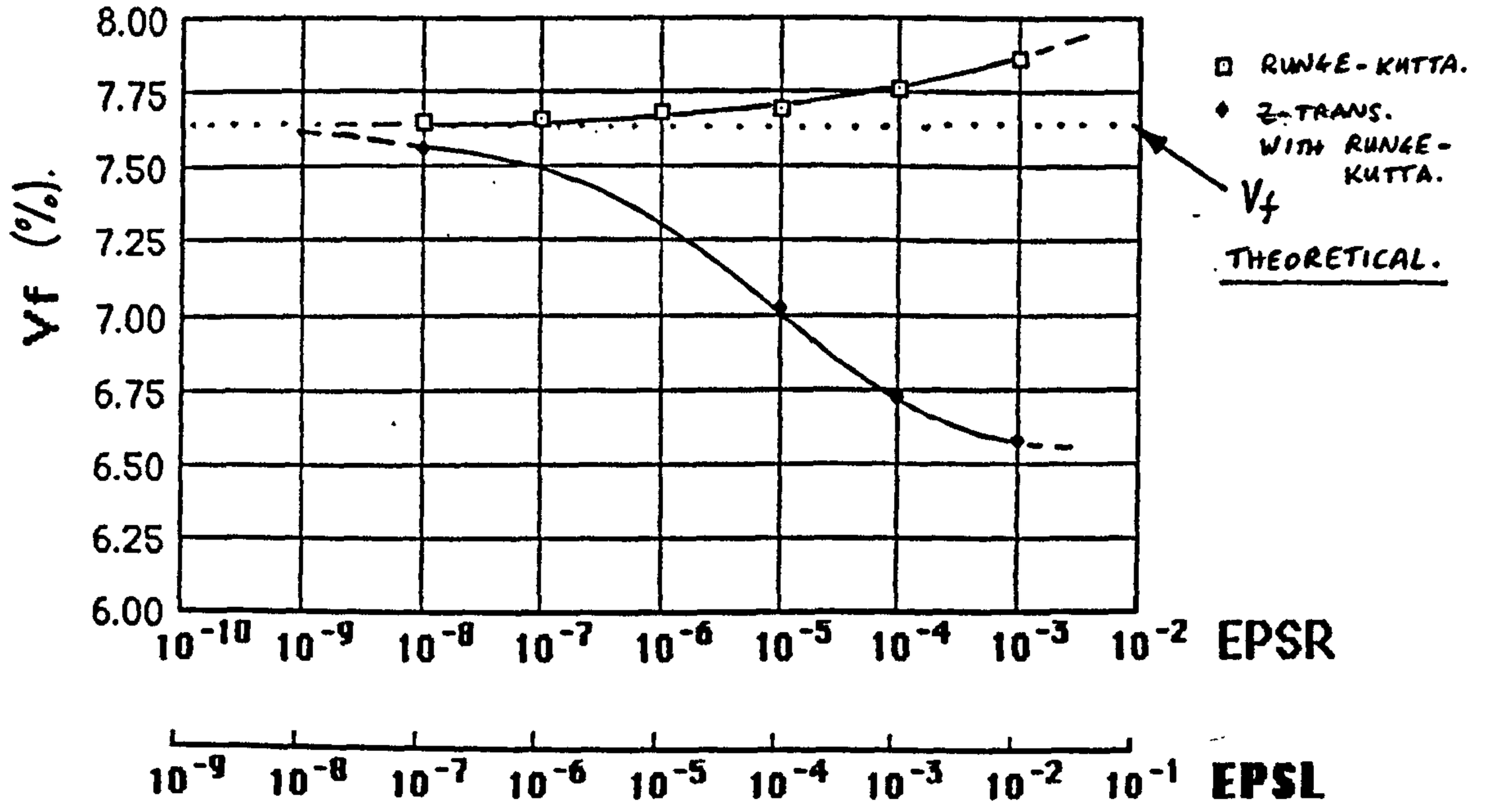

Figure 4.3: Graph showing the increased accuracy of the numerical prediction of the normalised failure strain (V_f) for the finite element problem of Fig.4.4(a) as the allowable integration error parameters (EPSL) and (EPSR) are reduced.

(a)

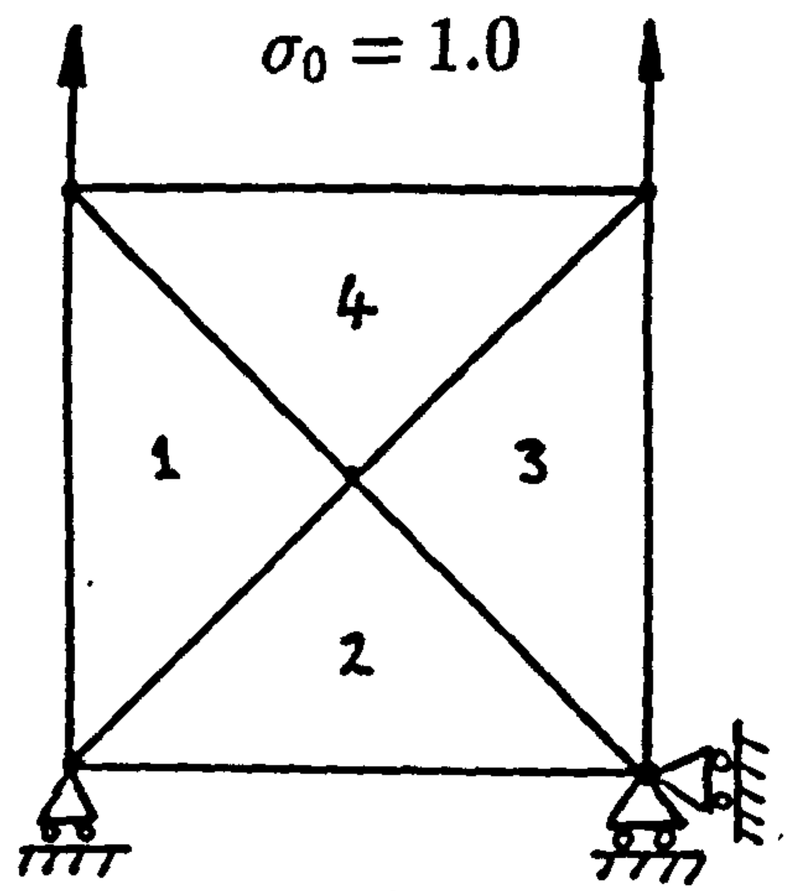

$\sigma_{(1)} = 1.0$
$\sigma_{(2)} = 1.0$
$\sigma_{(3)} = 1.0$
$\sigma_{(4)} = 1.0$

SIGREF=1.0

(b) Horizontal element No.2 force to fail.

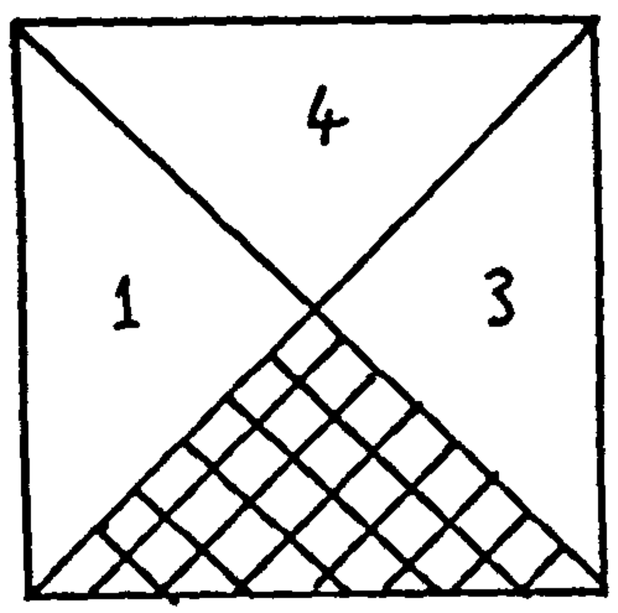

$\sigma_{(1)} = 2.0$
$\sigma_{(3)} = 2.0$
$\sigma_{(4)} \approx 0.0$

SIGREF=0.0

Stress from 4 elements is taken by 2 elements $\Rightarrow$ stress increases by a factor of 2x.

(c) Vertical element No.1 forced to fail.

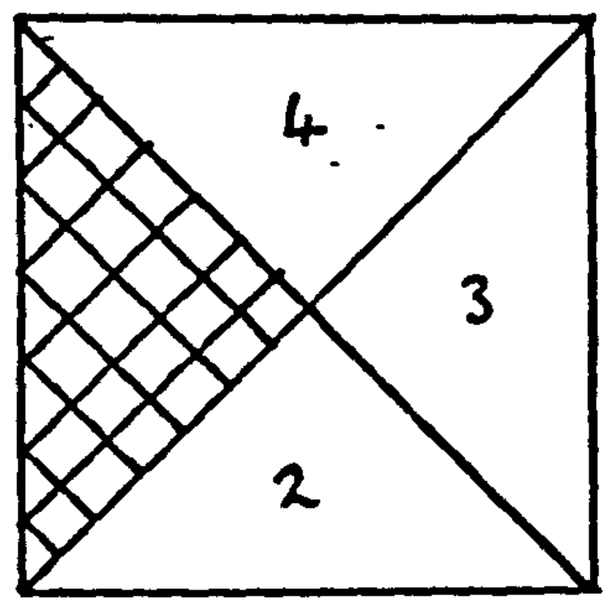

$\sigma_{(2)} = 2.0$
$\sigma_{(3)} \approx 0.0$
$\sigma_{(4)} = 2.0$

SIGREF=2.0

Fig.4.4: The effect of failing boundary elements in a crossed-triangle element set, on the value of the equilibrium parameter SIGREF given by equations (4.27) and (4.28).

Chapter 5.

Modelling Creep Deformation And Failure In Regions Of High Stress Gradient.

5.1 Introduction.

In modern power generating plant operating at high temperatures many components of complex geometry are fabricated from creep resistant alloys, using welded joints. During the component service life cracks may occur in or close to the weld heat affected zone. Subsequent creep crack growth has two main characteristics:

(i) High levels of constraint, due to the high local tri-axial stress gradient, caused by the presence of the crack tip, and by the material property mismatch across the heat affected zone.

(ii) Bending stresses across the crack plane in Mode I loading, causing compressive as well as tensile stress in the ligament.

In this chapter the compact tension specimen (CTS) is studied as representative of these two characteristics. Previously the failures of structures, containing moderate tri-axial stress states such as notched bars [23] and centre and edge cracked plates (Chapter 6 and [63]), have been predicted using the creep constitutive and damage laws, equations (2.19) and (2.20) in the finite element program Damage-(XX). Reasonably good agreement has been obtained between the predictions and the experimental tests. The modelling of the CT-specimen is complicated by the specimen having a high tri-axial stress state at the crack tip, together with a superimposed bending stress. Brown [64] tried to model the creep failure of the compact tension specimen using the same program and analysis technique used for both the notched bars [23], and the cracked plates [63], with little success. The predicted failure time and damage distributions were both much larger than the results expected from experiment.

This chapter describes systematically new computer methods and modelling modifications which have been introduced to try to obtain an improved failure prediction for the CT-specimen. The initial sections 5.2 to 5.6 detail the specification of the finite element model, the constitutive equations and material constants to be

used including the assumption for the growth of damage in compression; together with the calculation of the expected normalised experimental failure time for the AISI 316 stainless steel compact tension specimen, using the creep-rupture data of Myers and Pilkington [65] and the uni-axial creep rupture data of Hayhurst [23] for AISI 316 stainless steel. This experimental failure time is used as a means of assessing the appropriateness and accuracy of the finite element model predictions. A similar solution to that of Brown [64] for the CT-specimen has been obtained by the author and the results are presented in section 5.7. New computational techniques to remove elemental stiffness and creep forces, when an element fails (ω >0.9999), are presented in section 5.8 . These techniques are used to try and promote improved stress redistribution ahead of the crack tip in the computer model for the CT-specimen. A plane stress CTS solution is detailed in section 5.9. The constitutive model is modified in section 5.10 to a full bi-linear model (Chapter 2, section 2.6) and a new plane stress solution is obtained for the CT-specimen model in section 5.11. A large deformation and rotation analysis is performed and discussed in section 5.12 and the effects of mesh refinement on the solution are considered in section 5.13. Section 5.15 concentrates on the modification of both the creep constitutive and the damage rate laws in line with the physically based model of Cocks and Ashby [66], to allow for the effects of the tri-axial stress state on constrained void growth (section 1.3.2.(ii)), during the creep fracture process. New isochronous rupture surfaces are defined and a new computer failure prediction for the compact tension specimen is obtained, giving improved results.

5.2 Creep Testing The Compact Tension Specimen.

The geometry and dimensions of the compact tension specimen are shown in Fig. 5.1. The notch is machined into the specimen and a sharp crack is grown to a distance (a) from the tip of the notch, by fatigue loading the specimen at room temperature. This is done by cycling the specimen load, which is applied to the specimen through the load-holes by the load-pins. In a CT-specimen creep test the specimen is heated to the constant test temperature and subjected to a constant load. Creep tests for a range of applied constant loads (W), have been carried out at a constant temperature of $550°C +/- 2°C$ by Myers and Pilkington [65] for 1Cr

0.5Mo - ferritic steel compact tension specimens. When the reference stress (σ_{Ref}), defined by equation (A5.2), is calculated for each compact tension specimen tested and is plotted against the specimen failue time (t_f), on a stress-rupture diagram, Myer's and Pilkington's data falls close to their uni-axial creep test, stress-rupture line.

5.3 The Compact Tension Specimen Problem Specification.

5.3.1 Determination Of A Test Load And A Specimen Failure Time For Comparison With Finite Element Predictions.

The constants in the creep constitutive equations (2.19) and (2.20) are not available for the 1Cr 0.5Mo - ferritic steel used by Myers and Pilkington [65], and so a direct comparison cannot be made between CT-specimen lifetimes predicted from uni-axial data, using Damage-(XX), and the results of experiment. However material creep constants are available, for a batch of AISI 316 stainless steel, which have been obtained from the uni-axial and multi-axial creep tests of Hayhurst et al [23,63]. This AISI 316 stainless steel material has similar uni-axial creep curve shapes, has similar ductility and multi-axial behaviour to the 1Cr0.5Mo material used in the tests by Myers and Pilkington; but it has a different stress rupture character. It will therefore be assumed that the relationship between the log. stress vs.log. rupture time behaviour for the CT-specimen and the uni-axial specimen, for the material data due to Hayhurst, is the same as that for the material tested by Myers and Pilkington; the same specimen geometry will be assumed. The lifetime of a compact tension specimen test carried out at a test load of (W=19,620 N), having a reference stress ($\sigma_{Ref} = 164.808$ MPa, (equation A5.2)) , has been determined from the data due to Hayhurst, (Fig. 5.2), and is shown to be 4×10^4 hours. This approach is justified on the grounds that Myer's and Pilkington's CT-specimen rupture test results when plotted on log. reference stress, (σ_{Ref}), and log. rupture time, (t_r), axes lie close to his uni-axial creep rupture line, plotted on the same axes. This rupture time of 4×10^4 hours gives a normalised rupture time of ($\tau_f = 31.8$), which will be taken as the basis for comparison with compact tension specimen finite element lifetime

predictions. While this approach may not be strictly correct, it gives results of the correct order which are useful in assessing the numerical methods and the constitutive equations to be developed in this chapter.

5.3.2 Finite Element Mesh Discretization Of The Compact Tension Specimen.

Only half of the compact tension specimen is modelled due to symmetry. The simplest finite element mesh generated [64], together with two exploded views of the refinement at the crack tip are shown in Fig. 5.3. The finite element mesh has 544 elements and 296 nodes. The smallest elements at the crack tip are arranged to be of a similar dimension to the size of an average grain of the specimen material ($d \approx 0.055mm$). Nodes on the lower boundary of the mesh are restricted not to move in the (y) direction. The crack is modelled by allowing the lower boundary nodes up to a distance (a) away from the notch (Figs. 5.1 and 5.3) to have freedom in both the (x) and (y) directions. The node marked (F) in Fig.5.3(a) is fixed in both the (x) and (y) directions, to effectively fix the whole mesh in space. The load hole is also modelled, as the specimen geometry is such that the hole may affect the stress state at the crack tip [67].

The finite elements used are linear displacement three noded triangles, which are used in plane strain or plane stress. This mesh uses the crossed-triangle arrangement of elements, which have been observed to give improved creep solutions over standard triangular arrangements of elements [68].

5.3.3 Finite Element Mesh Loading.

The true loading of the compact tension specimen at the load hole is best represented by a distributed pressure load along the upper surface of the load hole. Brown [64] performed computer solutions using both distributed and a single point load at the load-hole of the finite element mesh and concluded that the method for loading had little effect upon the solution. For simplicity a single point load (P) is used by the author (shown in Fig. 5.3(a)), where (P) is the normalised finite element mesh load (given in section 5.4 and calculated in Appendix A5.1) corresponding to a real test load of W=19,620 N.

5.4 Normalisation, AISI 316 Stainless Steel Creep Data And Creep Constants.

The stresses, strains, applied load and the time scale are normalised in the finite element program to minimise rounding errors in the solution (section 2.4.4). It was decided to predict the failure time for a compact tension specimen having a test load of W=19,620 N. The normalised load (P) and the normalising stress (σ_o) are calculated in the Appendix A5.1 for the compact tension specimen finite element mesh, using a specimen called the moment specimen shown in Fig. A5.1. The moment specimen has a similar ligament length and load position to the CT-specimen, but does not have a notch, or a crack, or load-holes. It allows the calculation of the stress distribution in the compact tension specimen due to pure tension and bending alone (i.e no stress concentration is present due to the notch,load-hole and crack). From the calculations for the moment specimen (Appendix A5.1), the reference stress is defined and the applied finite element mesh load (P) is given as 4.76190, which gives a normalised maximum tensile stress of unity in the moment specimen, with a normalising stress equal to the reference stress for the CT specimen (i.e. σ_o=164.808 MPa).

The material constants of the creep constitutive and damage laws, equations (2.19) and (2.20), for the batch of AISI 316 stainless steel have been determined elsewhere [23,63], from uni-axial constant load creep tests. A summary of the material parameters and the value of (V_u) for the normalised stress used for this specimen are given in Table 5.1. The uni-axial stress rupture data is given in Fig. 5.2 reproduced from Fig. 5, [63] and is observed to be bi-linear. This bi-linear material behaviour is represented with the use of two damage evolution laws (equation (2.53) and (2.54)) subscripted (I) and (II) for high and low stress behaviour respectively. Only low stress creep curves are available from the uni-axial tests and are given in Fig. 5.4 from Fig. 2, [23]. Figure 5.4 shows the comparison between the uni-axial creep curves, computed using the creep constants of Table 5.1, in equation (3.4) and the experimental creep curves. The theoretical representation of the experimental data is observed to be good.

The AISI 316 stainless steel tested by Hayhurst et al [23,63] had an average grain size of diameter 0.055 mm. Figures 5.5(a) and (b) show Ashby deformation

mechanism maps [69] for AISI 316 stainless steel of a similar grain size to that used in tests by Hayhurst et al [23] and [63]. Using the bulk shear modulus for the stainless steel given by ($\mu = E/2(1+\nu)$), where (E) and (ν) are obtained from Table 5.1, and the relationship between the shear stress and the tensile stress ($\sigma_s = \sigma_T/\sqrt{3}$); region (A) is determined on the Ashby map of Fig. 5.5(a), representing the creep tests of Hayhurst et al, for a range of uni-axial stresses at a constant homologous temperature of ($T/1810^{o}K$=0.455). The high and low stress points within area (A) represent the highest and lowest test stress levels of 500 MPa and 162 MPa respectively (Figs. 5.2 and 5.4). From Fig. 5.5(a) it is clearly seen that a mechanism change occurs as the test stress level is increased, from the mechanism of dislocation creep (section 1.2.1) to that of dislocation glide (section 1.2.3). The boundary between these two mechanisms occurs at a tensile stress of approximately 440 MPa from the mechanism map. The boundary between the low and high stress behaviour from the creep tests of Hayhurst et al is in close agreement with this, occurring at the break stress of 441.28 MPa. Comparisons between the predicted strain rates for various test stress levels using the constitutive data of Table 5.1, in equation (2.19) with the lines of constant strain rate of Fig. 5.5(a), also agree reasonably well in the dislocation creep region. High stress comparisons (σ >441.28 MPa) gave creep strain rates which were lower than the constant strain rate line values given in Fig. 5.5(a), but comparisons are not easy due to the closeness of the constant strain rate lines on the mechanism map in the dislocation glide region.

5.5 The Elastic Solution And Solution Convergence.

The stresses in the (y)-direction at the centroids of elements on the lower boundary of the compact tension specimen mesh are plotted with distance from the crack tip in Fig. 5.6. In Fig. 5.6 this stress distribution is compared with that for a more refined compact tension specimen finite element mesh (Fig. 5.7), having 844 elements, to show convergence. The stress concentrations for the finite element meshes of Fig. 5.3 and the more refined mesh of Fig. 5.7 are 5.135 and 13.086 respectively. The stress distributions are noted to be similar until very close to the crack tip. This difference in stress concentration at the crack tip is not important

since within a very short time (a few hours) this peak stress is redistributed due to the fast creep strain accumulation and damage growth at the crack tip. The refined finite element mesh required much more computational effort to obtain a full creep damage solution than the less refined compact tension specimen mesh. It was decided not to run the refined mesh problem to completion, as initial damage plots around the crack tip showed similar damage distributions for both meshes. Figure 5.8 shows the distribution of the normalised first stress variant ($\tilde{I}_1 = I_1/\sigma_0$), equation (5.11), the normalised effective stress ($\Sigma_{ef} = \sigma_{ef}/\sigma_0$), equation (5.12) and the ratio of the former and the latter ($\tilde{I}_1/\Sigma_{ef}$), which gives some measure of the severity of the tri-axial stress state in the compact tension specimen.

Referring to Fig. 5.6 note the compressive stress which occurs in the compact tension specimen ligament furthest from the crack tip, due to the bending moment produced by the applied load. The next section dicusses the assumptions made to model damage growth in this compressive stress region of the CT-specimen.

5.6 Damage In Compression.

Hayhurst et al [70] have performed both tensile and compressive creep tests for both Copper and Aluminium. The compressive creep curves show the presence of primary, secondary regions, with compressive creep strains which are much smaller than the strains in tensile tests for both materials. For Copper no tertiary creep has been observed after 5 times the lifetime of the uni-axial tension test at the same test stress level. For Aluminium the lifetimes in both tension and compression are similar. Therefore, as Aluminium and Copper are materials which have bi-axial rupture criteria which are dependent upon the effective stress (Σ_{ef}) and the maximum principal stress (Σ_1) [22], respectively, it is reasonable to suggest that only the effective (Σ_{ef}) contributes to the growth of creep damage in compression. This asumption is included within the finite element creep continuum damage analysis in making the maximum principal stress zero in equation (2.20) and the damage rate purely dependent upon the effective stress when stresses become compressive . Therefore, when ($\Sigma_1 \leq 0$) for a finite element (k), the damage rate equation (2.20) in compression becomes:-

$$\omega_{(k)} = \frac{\left\{(1-\alpha)\Sigma_{(e)_{(k)}}\right\}^{\chi}}{V_u(1+\phi)(1-\omega_{(k)})^{\phi}} \tag{5.1}$$

5.7 The First Finite Element Creep Continuum Damage Solution For The Compact Tension Specimen In Plane Strain.

This solution used the material constants given in Table 5.1 with the finite element mesh shown in Fig. 5.3. As the compact tension specimen is 25 mm thick, through thickness deformation will be assumed to be negligibly small and hence a plane strain finite element solution will be performed. The stress field close to the crack tip rises above the break stress ($\hat{\sigma}$), making it necessary to model both high stress, ductile, and low stress, brittle, material behaviour, which is observed as a change in the gradient of the stress-rupture diagram of Fig. 5.2. As no creep strain rate data was available for high stress tests, due to very short rupture times (<16 hours), the first solution is assumed to be bi-linear only in damage growth laws. The same low stress, creep strain rate equation is assumed to represent both low and high stress creep deformation behaviour.

From the finite element solution, the first element fails (ω >0.9999) almost immediately on loading the specimen. The window sizes for the failed element distribution diagrams are given in Fig. 5.9 against the outline of the compact tension specimen finite element mesh. Further elements fail in the element fan at the crack tip; followed by elements failing forwards of the crack tip (Fig.5.10(a)). Figure 5.10(b) shows the growth of the failed element zone into the body and across the ligament of the specimen. Figure 5.10(c) shows the distribution of failed elements (ω >0.9999) at a normalised time close to failure. Damaged elements are observed around the load-hole and the damage distribution around the crack-tip is seen to grow towards the hole, close to the specimen failure time. The specimen fails quickly across the ligament at a normalised lifetime of (τ_f =48.04)(Table 5.2). This normalised failure time gives a real life prediction of 38.89×10^6 hours. The expected experimental lifetime is 4.0×10^4 hours (τ_f =31.8). Therefore, the finite element solution over-estimates the real failure time of the CT-specimen by a factor of approximately 1000.

During the finite element computer solution the parameter FREF (Section 4.4 equation (4.29)) remained constant at -0.9999 indicating that force equilibrium based on the boundary element stress is satisfied throughout the solution. Reduction in the automatic time stepping error bound parameters EPSL and EPSR (section 4.3.3)

from 10^{-3} and 10^{-4} to 10^{-4} and 10^{-5} only produced a 6% reduction in the normalised lifetime for the compact tension specimen solution.

The finite element model is therefore well conditioned in that equilibrium calculated from the boundary element stresses is satisfied, yet the model yields an inaccurate lifetime prediction. From the failed element plots of Figs. 5.10 it is observed that the damage distribution is not forward growing, as would be expected in practice, but seems to spread out equally in all directions. It was thought that this may be caused by the poor promotion of stress redistribution ahead of the crack tip. This may be caused by a loss of strain energy from the immediate removal of failed element stiffness components and the respective creep forces, within one iterative step in the finite element computer technique (section 4.2), causing poor off-loading of stress to neighbouring unfailed elements. Typically a finite element close to a crack-tip, with an initial elastic normalised stress of 3.0, off-loads stress to its neighbouring elements with time and has a normalised stress of approximately 0.3 when ($\omega > 0.9999$) and the element is removed from the solution. These values of stress are dependent upon the material parameters used and hence may vary for different materials in the finite element model. This method of instantaneous element removal when (ω) reaches the critical value of ($\omega > 0.9999$), will be term the instantaneous technique.

Other researchers such as Chaboche [71] and Tvergaard [72] use different methods of removing the components of stiffness and creep force, whereby the effects of failed elements removed from the finite element solution are spread out over a number of iterative steps. The techniques of Chaboche and Tvergaard are thought important for achieving an accurate solution for the compact tension specimen, it was expected that they might promote improved stress redistribution ahead of the crack tip; and decrease the size of the failed element distribution, hence localizing failure into a narrow cracked zone growing across the ligament, therefore, reducing the predicted failure time of the specimen. These techniques are explained; and they are used to predict the failure of the compact tension specimen in the following two sections.

5.8 Evaluation Of Techniques For The Removal, From The Solution Procedure, Of Element Stiffness And Creep Forces For Failed Elements (ω >0.9999).

5.8.1 The Elastic Modulus Technique Of Chaboche.

Chaboche [71] details that damage may be represented in structural mechanics by a decrease in the elastic modulus (E). He relates the elastic modulus for an undamaged material element (E) to that of a damaged material element ($\tilde{E}$) through the damage parameter (ω):-

$$\tilde{E} = E(1-\omega) \tag{5.2}$$

Instead of removing the stiffness of a fully damaged finite element from the global stiffness matrix and reducing the element creep forces to zero in one step, it may be more representative of continuous void growth within a material to reduce the value of the modulus of elasticity (E) for this element as the damage grows. This is done within the finite element creep damage program Damage-(XX) by pre-multiplying (E) for an element by $(1-\omega_{(k)})$, where $(\omega_{(k)})$ is the damage parameter for the element (k) in the creep strain rate and damage rate laws, equations (2.19) and (2.20). Therefore the value of $(1-\omega_{(k)})$ varies from 1.0 at $(\tau = 0)$ to 0 at $(\tau = \tau_f)$. The modifications to the finite element creep damage program are summarised as follows:-

From equation (5.2):

$$\tilde{E}_{(k)} = E_{(k)}(1-\omega_{(k)}) \tag{5.3}$$

$$\Rightarrow \tilde{D}_{(k)} = D_{(k)}(1-\omega_{(k)}) \tag{5.4}$$

then:

$$[\tilde{K}]_{(k)} = [K]_{(k)}(1-\omega_{(k)}) \tag{5.5}$$

and

$$\tilde{F}_{c_{(k)}} = F_{c_{(k)}}(1-\omega_{(k)}) \tag{5.6}$$

$[\tilde{K}]_{(k)}$ and $\tilde{F}_{c_{(k)}}$ are assembled to replace the global stiffness matrix $[K]$ and the global force vector F_c in the boundary problem equation (4.1). The solution to the

boundary value problem (equation (4.3)) is found by determining the inverse of the stiffness matrix $[\tilde{K}]$:

$$U = [\tilde{K}]^{-1}(F_e + \tilde{F}_c) \tag{5.7}$$

and the solution procedure described previously (equations (4.4) to (4.15)) is followed except that a new global stiffness matrix $[\tilde{K}]$ its inverse, together with the global force vector $\tilde{F}_c$ are assembled, and equation (5.7) is solved for each iterative time step, using the current values of (ω) in equations (5.5), (5.6); also equation (4.5) now becomes:

$$\sigma_{(e)ij_{(k)}} = D(1 - \omega_{(k)})\epsilon_{(e)ij_{(k)}} \tag{5.8}$$

Instead of removing $[K]_{(k)}$ and $F_{c_{(k)}}$ when $(\omega_{(k)} = 0.9999)$ for element (k), as in the instantaneous technique, both $[K]_{(k)}$ and $F_{c_{(k)}}$ are reduced in magnitude as the damage parameter $(\omega_{(k)})$ grows, until $(\omega_{(k)} = 1.0)$ at failure, when $[K]_{(k)}$ and $F_{c_{(k)}}$ will be completely removed as $((1 - \omega_{(k)})=0)$, (in equations (5.5) and (5.6)). This method is expensive in the usage of computer time because it involves inversion of the stiffness matrix and re-solution of the equation (5.7) at each iterative step. Implicit in the formulation is that as $(\omega_{(k)})$ tends to unity, the elastic stress in the failing element tends to zero (equation (5.8)), allowing the full redistribution of stress from damaged elements to less damaged elements within the finite element mesh. As the finite element formulation is a dynamic one, (i.e. as the creep forces are modified, these creep forces affect the stresses, which affect the creep and damage rates, which affect the creep strains, damage values and creep forces at the next time step and so on). Such a modification in the formulation may therefore produce significantly different solutions.

The program Damage-(XX) has been modified by the author to include this technique, which will be termed the Chaboche technique [71]. The results for the compact tension specimen problem using the Chaboche technique and the constants given in Table 5.1 are summarised in Figs 5.11 and Table 5.3. Referring to Figs. 5.11 the failed element distributions at similar times to those of the previous instantaneous method given in Fig. 5.10, are very similar. The first element to fail in the structure at the crack-tip occurs at a greater normalised time than that obtained using the instantaneous technique; indicating that slightly more stress redistribution from the crack tip is allowed in the Chaboche technique. Though, the failure times of both

techniques are very similar. Therefore there seems to be little difference between the two procedures.

Research work recently published by Rides et al [73],(after these results were obtained), where a simple two bar structure is analysed to assess the effect of including the variation of the elastic properties with the growth of creep damage, within the structural analysis; also indicates that the variation of the elastic properties with damage does not strongly affect the structural response.

5.8.2 The Tvergaard Technique.

Tvergaard [72] uses a totally different technique to those of the instantaneous technique used by Hayhurst et al and the technique used by Chaboche. His technique is not explicitly documented, but what follows is a technique founded on what can be inferred from the descriptions of his method. This technique has also been included within the program Damage-(XX) by the author.

When the damage parameter (ω) becomes greater than 0.9999 and the element is said to have failed, the elastic forces at the nodes of this element (Fig.5.12(b)), due to the stress in the element, are opposed by equal and opposite tractions (Fig. 5.12(c)). The creep forces at this stage are still present (Fig.5.12(d)). This causes the displacements at the nodes of the failed element to be due to the permanent creep deformation only. The elastic displacements are reduced to zero by the opposing forces. The stiffness components of this element may then be removed with the creep forces during the next iterative step, with the element containing zero stress due to the elastic forces (5.12(d),(e)). The opposition forces are then relaxed over 6 further iterations, by multiplying by a factor (R), which varies from 1.0 to 0 in steps of 0.2 (5.12(e),(f)). This involves re-solving the stiffness solution equation (4.3) at every relaxation step for each failed element which is expensive in computer time (CPU-time). The creep solution may then continue as usual until the next element fails. This method is supposed to ensure that all the strain energy in the failing element is re-distributed gradually to its neighbouring elements.

The results obtained using the Tvergaard approach are summarised in Figs. 5.13 and Table 5.4. The failed element loci (Figs. 5.13) are similar to those the previous two methods (Figs. 5.11 and 5.10), though the failure pattern seems to

be influenced to a lesser extent by the hole. The predicted failure time is slightly reduced from the former two approaches, (τ_f) is 2% lower than the instantaneous approach value. Therefore, both the techniques of Chaboche and Tvergaard seem to give similar results to the instantaneous technique and hence provide no advantage over the instantaneous technique in the prediction of the true creep deformation and failure behaviour of the compact tension specimen.

In the next section the effect of changing the plane strain assumption for the CT-specimen model to one of plane stress will be studied, where the through thickness stress is set to zero, yet through thickness deformation is allowed.

5.9 The Plane-Stress Creep Continuum Damage Finite Element Solution For The Compact Tension Specimen Using The Instantaneous Technique.

The finite element creep continuum damage program Damage-(XX) has been suitably modified by the author to include plane stress conditions. The material constants of Table 5.1 are used again. The finite element results are summarised in Table 5.5 and the form of failed element (ω >0.9999) distributions throughout the life of the specimen in Fig. 5.14. It is noticed that the stress concentration at the crack tip is 7.97 which compares with that of 5.135 for the previous plane strain solution. The failed element distributions of Fig. 5.14 are observed to be similar to those of the previously described instantaneous plane-strain solutions (compare Figs. 5.14 with Figs. 5.10), but the failed element element distribution does seem to be directed slightly more in the horizontal direction. The hole seems to influence the damage growth to a lesser extent than that for the plane strain solution (Fig. 5.10(c)). The predicted normalised failure time from the plane-stress solution for the compact tension specimen is (τ_f =46.90) giving a real lifetime of 26.06×10^6 hours, which may be compared with that of 48.04 and 38.89×10^6 hours respectively, for the plane-strain solution.

This result does not agree with the results of Webster [74], who details both experimental and theoretical results using the creep fracture parameter (C^*) and shows that crack growth rates are faster in plane strain than in plane stress. In his

theoretical models the differences between the plane stress and plane strain results are predicted by modifying the available fracure ductility at the crack tip (ϵ_f^*). He states that for plane stress conditions(ϵ_f^*) is taken to be equal to the uni-axial creep ductility (ϵ_f); and, for plane strain (ϵ_f^*) is taken as ($\epsilon_f/50$).

The results obtained from the finite element calculations, giving a smaller failure time for a plane-stress solution than the plane-strain solution, are consistent with the decrease in the effective stress term (Σ_{ef}) in the damage rate equation for plane strain conditions. For plane strain (Σ_{ef}) for a uni-axial tension specimen under unit load (σ_o) is 0.866 or ($\sqrt{3}/2$), whereas for plane stress (Σ_{ef}) is 1.0. This causes reduced damage rates in equation (2.20) for plane strain conditions and hence increased life predictions.

At this stage is was not clear how to apply Webster's modification to the failure ductility within the finite element procedure to model plane strain and plane stress conditions.

5.10 The Accuracy Of The Constitutive Model And Its Modification To A Full Bi-Linear Damage Rate And Strain Rate Model.

The theoretical uni-axial stress-rupture characteristics for the AISI 316 stainless steel material have been calculated, using equation (2.23) which is substituted into (2.27), and the material constants of Table 5.1, for a range of stresses above and below the break stress ($\hat{\sigma}$). The theoretical stress-rupture lines are compared with the experimental stress-rupture lines of Hayhurst et al [63] in Fig. 5.15. The theoretical fit is reasonable, though the high stress line is slightly low.

The theoretical creep strains at failure are obtained from equation (2.24) for uni-axial plane stress conditions using the material constants of Table 5.1 for ranges of stress above and below the break stress (Fig. 5.16).

Tests on a simple two element finite element mesh under uni-axial tension for plane-stress conditions gave stress-rupture and creep strains at failure close to those obtained theoretically in Figs. 5.15 and 5.16 respectively. When the allowable integration error parameters EPSL and EPSR of section 4.3 are made very small of the order (10^{-9}) and (10^{-10}) exact correlation between theoretical and finite element

results are obtained. Similar tests under plane strain conditions have slightly longer predicted lifetimes and slightly higher creep strains at failure for all uni-axial test stress levels, which is to be expected from the explanation of section 5.9.

Therefore the high stress-rupture line for the AISI 316 stainless steel material is adjusted using equations (2.56) and (2.47), so that the line passes through the exerimental point in Fig. 5.15 at a stress of 500 MPa having a rupture time of 1.0 hour; giving values of (χ_I) and (M_I) for the high stress line, as explained in section 2.6.

The constitutive model used by Hayhurst et al [23,63] for AISI 316 stainless steel is bi-linear only in damage rate, with a single creep strain rate constitutive equation representing both high and low stress creep deformation behaviour. With reference to Fig.5.5(b) it is noticed that the gradient of the lines on the shear strain rate vs. stress diagram, for AISI 316 stainless steel, changes across the mechanism map boundary between dislocation creep and dislocation glide. (see the lines of Blackburn (1973) in Area (B) on the diagram at a temperature of $538°C$, which is close to the $550°C$ temperature used in the tests of Hayhurst et al). The constitutive model for the AISI 316 stainless steel should therefore be bi-linear in creep strain rate as well as damage rate. Bi-linear strain rate behaviour is represented with two creep strain rate equations (2.42) and (2.43).

It is known [75] that many bi-linear materials have high (I) and low (II) stress constants (χ_I), (χ_{II}), (n_I), (n_{II}) such that:

$$\frac{\chi_I}{\chi_{II}} \approx \frac{n_I}{n_{II}} \tag{5.9}$$

Therefore, as there is no minimum creep rate data available to give the true high stress value of (n) for the AISI 316 stainless steel material, this equation is used to given a approximate value of (n_I). (K_I) may be obtained from equation (2.37). For the new high stress constitutive equation to have a compatible failure strain at the break point with that of the low stress constitutive equation (2.57) must be satisfied. Hence (ϕ_I) is obtained using (n_I) and the low stress constitutive parameters of Table 5.1, as detailed in section 2.6. Therefore, all the new high stress constants can be derived. The new constants are summarised in Table 5.6 and are used in the bi-linear representation constitutive and damage laws of equations (2.42), (2.43) and (2.53),(2.54).

A graph of theoretical creep strains at failure for a range of uni-axial test stress levels using the new high stress constitutive parameters in the full bi-linear model are given in Fig. 5.17. If the new failure strain graph of Fig. 5.17 is compared with that of the old constitutive model, Fig. 5.16, it is noticed that the rupture ductility of the material above the break stress increases with increasing stress. Nishida et al [76] have shown that the variation of creep ductility with stress affects the crack growth rate and hence the failure time of cracked specimens. The effect of this high stress ductility change, (modelled using the full bi-linear representation with the material constants of Table 5.6), on the failure prediction for the CT-specimen under plane stress conditions is detailed in the results of the following section:

5.11 The Plane Stress Creep Continuum Damage Finite Element Solution For The Compact Tension Specimen Using The Instantaneous Technique With The New Bi-Linear Damage Rate And Strain Rate Model.

The results are summarised in the Table 5.7 and the failed element diagrams of Figs. 5.18. Comparing the failed element plots of Figs. 5.18(a) and (b) with those obtained for the plane-stress solution using the material constants of Table 5.1, given in Figs. 5.14(a) and (b); it is observed that the initial failed element distributions are smaller due to increased stress redistribution away from the crack tip. The failed element distribution close to failure, Fig. 5.18(c), is also much more compact than that of Fig. 5.14(c). The solution became numerically stiff close to failure at a normalised lifetime of ($\tau = 44.45$); as a result of the automatic time step control choosing infinitely small time steps at the point where platic collapse of the specimen occurs. The normalised failure time of the specimen is taken as (τ =44.45) which less than that of the previous solution and gives a predicted failure time of 10.66×10^6 hours; which is still much larger than the expected experimental value of approximately 4×10^4 hours, having a normalised life of (τ_f =31.80).

5.12 Large Deformation And Rotation Finite Element Analysis For The Compact Tension Specimen.

The previous finite element analyses used a small deformation finite element method, where the effects of geometry changes and rotation of the finite elements within the structure, on the stress states are not allowed for; with all the calculations based on the initial non-deformed finite element mesh. A large deformation and rotation version of the finite element program Damage-(XX) has been developed by Othman [77]. This same program was modified by the author to produce a large deformation and rotation finite element creep continuum damage solution for the compact tension specimen, as rotations of 15° to 20° or so are observed in the compact tension specimen at failure (Fig. 5.19). It was thought that a large deformation and rotation analysis would model the increased stresses close to the crack-tip caused by the change of thickness of the specimen section and would also model the stress field rotations, which might influence the damage distibutions and the hence failure time prediction.

Constant load uni-axial finite element tests using the creep constants of Table 5.6, with the large deformation formulation, gave larger failure strains at high stress ($\sigma > \tilde{\sigma}$). A 10% increase in strains at failure was observed at a uni-axial stress level of 500 MPa, over the strains at failure obtained using the previous small strain analysis at the same stress level. This is caused by the mesh geoemtry changes in the large deformation solution at high stress, modelling the decreasing cross-sectional area of the uni-axial specimen and the formation of a neck. This raises the net section stress causing increased strain values at failure, because strain at failure increases with stress in the model (Fig. 5.17).

The high stress value of the creep exponent (n_I) is therefore adjusted to (n_I =2.5) and new values of (K_I) and (ϕ_I) calculated as in the last section, to give similar failure strain values at the same stress levels as were obtained (Fig. 5.17) using the constants of Table 5.6, in the small strain analysis. The new high stress constants are summarised in Table 5.8.

The damage distribution close to failure is shown in Fig. 5.20, for the compact tension specimen from the large deformation and rotation finite element solution under plane strain condtions. The red, most highly damaged zones show the

regions where elements have failed (ω >0.9999), which may be compared with the plane-strain (small strain) failed element distribution of Fig. 5.10(c) at a similar normalised time. Distinct similarities are observed. With reference to Fig. 5.20, the large displacements and rotations are predicted in the compact tension specimen. The displacements shown in this figure are scaled down by a factor of 0.694. The normalised lifetime of the specimen is predicted to be ($\tau_f = 49.95$) which corresponds to real life prediction of 73.25×10^6 hours. This life prediction is slightly larger than that of previous predictions, which is thought to be caused as a result of crack tip blunting, enabling the reduction of the stress concentration at the crack tip and therefore reducing the damage rates here. Therefore the large deformation and rotation analysis also fails to model the correct failure mode of the CT-specimen.

Next the effects of using a constant mesh refinement across the ligament is examined, as it was thought that a possible reason for the diversity of the predicted damage distribution for the CT-specimen, using the finite element mesh of Fig.5.3, could be due to the mesh refinement increasing with distance from the crack-tip.

5.13 Compact Tension Specimen Solution Using Constant Finite Element Mesh Refinement Across The Ligament Length.

A new finite element mesh for the compact tension specimen has been generated by the author, where a constant node spacing along the bottom boundary is used, giving less mesh refinement at the crack tip than the mesh of Fig. 5.3, but a more uniform mesh refinement along the ligament length. The new mesh is shown in Fig. 5.21. The finite elements are crossed-triangles. The damage distribution close to failure of the plane strain small deformation solution for the compact tension specimen problem using the new mesh and the constants of Table 5.6 is given in Fig. 5.22. It is seen that the most severely damaged zone (red) is not significantly different from the failed element distribution of the previous plane-strain solution (Fig. 5.10(c)), but the shape of this region has a smoother periphery. The predicted normalised failure time is approximately ($\tau \approx 45.0$); as in the previous solution the numerical procedure became stiff, close to ultimate plastic collapse when infinitely small time steps were selected by the automatic time stepping subroutine. The lifetime pre-

diction is 13.08×10^6 hours which is still very large in comparison with the expected experimental life of 4×10^4 hours.

Therefore, although improved mesh refinement across the ligament will reduce the predicted lifetime, and, the definition of the damage distributions will be improved, mesh refinement does not fully explain the difference between the expected and predicted lifetimes differing by a factor of at least two orders of magnitude.

5.14 Brief Summary Of Results So Far.

New computational techniques; constitutive models with improved accuracy; allowances for large deformations and rotations; and, the effects of mesh refinement, have all been shown not to be responsible for the poor lifetime predictions of the CT-specimen. All the previous solutions yield very similar damage distributions; and, the failure time predictions are at least two orders of magnitude greater than the experimental.

5.15 Allowance For The Effects Of The Tri-Axial Stress State On Rupture.

Ductility is the ability of a material to deform under an applied load without fracture. Manjoine [78] states that ductility is a function of the state of stress, because of the constraint to plastic flow. Under equal tri-axial tension no plastic flow can occur. Manjoine presents a diagram showing how ductility ratio varies as a function of the tri-axiliaity factor (Fig. 5.23); the diagram is compiled from his own tests and data from other published data for ductile materials. He suggests an empirical relationship between the multi-axial to uni-axial failure ductility ratio and the Davis Triaxiality Factor (TF_D)

$$\frac{\epsilon_{ef}}{\epsilon_1} = 2^{(1-TF_D)} \tag{5.10}$$

where (TF_D) is identified to be the first stress invariant (I_1) divided by the Von Mises effective stress (σ_{ef}), where:

$$I_1 = \sigma_1 + \sigma_2 + \sigma_3 \tag{5.11}$$

and

$$\sigma_{ef} = \frac{1}{\sqrt{2}}\left\{(\sigma_1-\sigma_2)^2 + (\sigma_2-\sigma_3)^2 + (\sigma_3-\sigma_1)^2\right\}^{\frac{1}{2}} \tag{5.12}$$

Equation (5.10) shows how the ductility of the material decreases with increasing tri-axiality factor (I_1/σ_{ef}). N.B. equations (5.11),(5.12) and (5.10) may be normalised giving ($\tilde{I}_1 = I_1/\sigma_0$), ($\Sigma_{ef} = \sigma_{ef}/\sigma_0$) and ($TF_D = \tilde{I}_1/\Sigma_{ef}$), respectively.

Hayhurst [22] allows for the effects of the tri-axial stress state on the rupture behaviour of materials using a time to rupture versus stress relationship given in equation (2.29), where the representative rupture stress of the material (σ_{Rup}), is a linear combination of the maximum principal stress (σ_1), the hydrostatic stress (I_1) (the first stress invariant), and the effective stress(σ_{ef}), equation (2.28). The isochronous rupture surfaces (section 2.4.7) in principal stress space are given in Fig.2.2 for extreme values of (α, β, γ).

For the AISI 316 stainless steel this expression (equation (2.29)) is simplified equating (β_H =0):

$$t = A\left\{\alpha\Sigma_1 + (1-\alpha)\Sigma_{ef}\right\}^{\frac{-\chi}{m+1}} = A\Sigma_{Rup}^{\frac{-\chi}{m+1}} \tag{5.13}$$

where (α) has been determined by Hayhurst et al [23,63] to be (α =0.75) and its isochronous rupture surface is defined by equation (2.32) for plane stress conditions and is shown in (Σ_1, Σ_2) principal stress space in Fig.5.24 . Similarly the isochronous rupture surface for plane strain conditions is defined by equation (2.33) and is shown graphically in Fig.5.25. Close to the crack tip (Fig.5.8) of the CT-specimen (I_1), is the largest stress term in equation (2.29); however, its effect on rupture life has not been previously allowed for. If (β_H) is non-zero, then the rupture surface will be lowered from that of Fig.5.24 towards the hydrostatic stress line (line-(a)) of Fig.2.2 in the tension-tension quadrant. Therefore, in regions of high triaxial tension the allowance for this hydrostatic term (I_1) in the rupture criterion will have the effect of decreasing failure times of crack-tip finite elements, decreasing the size of the creep-strains allowed to accumulate at failure. Therefore representing lower rupture ductility at high tri-axial states of stress.

Cocks and Ashby [66] detail the use of a β-term, which will be termed β_{CA} to be different from that of Hayhurst's β-term, β_H.

$$\beta_{CA} = \sinh\left\{\frac{2(n-\frac{1}{2})}{(n+\frac{1}{2})}\frac{I_1}{\sigma_{ef}}\right\} \tag{5.14}$$

and allows for accelerated void growth due to hydrostatic tension, through the the ratio (I_1/σ_{ef}), which is included in their creep constitutive and damage rate laws for

void growth controlled by power-law creep:

$$\frac{1}{\dot{\epsilon}_0}\frac{df_h}{dt} = \beta_{CA}\left\{\frac{1}{(1-f_h)^n} - (1-f_h)\right\}\left(\frac{\sigma_{ef}}{\sigma_0}\right)^{\chi} \tag{5.15}$$

$$\frac{1}{\dot{\epsilon}_0}\frac{d\epsilon}{dt} = \left\{1 + \frac{2r_h}{d}\beta_{CA}\left(\frac{1}{(1-f_h)^n} - 1\right)\right\}\left(\frac{\sigma_{ef}}{\sigma_0}\right)^{n} \tag{5.16}$$

where (f_h) is a damage parameter and (χ) is assumed equal to (n) in equation (5.15).

Cocks and Ashby [66] state that for transgranular creep fracture, the diameter of a growing void $(2r_h)$, replaces the grain diameter (d) in the strain rate equation (5.16) and the equation becomes:

$$\frac{1}{\dot{\epsilon}_0}\frac{d\epsilon}{dt} = \left\{1 + \beta_{CA}\left(\frac{1}{(1-f_h)^n} - 1\right)\right\}\left(\frac{\sigma_{ef}}{\sigma_0}\right)^{n} \tag{5.17}$$

and the damage rate equation (5.15) remains unaltered.

These two equations (5.15) and (5.16) are analogous to the equations due to Kachanov, Rabotnov and Hayhurst, (2.19), (2.20), as used in the program Damage-(XX) when $(n = \chi)$. Uni-axial plane stress conditions imply that β_{CA} =1; and that the area fraction of voids (f_h), is taken in the range 0.001 to 1.0 from $(t = t_i \approx 0)$ to $(t = t_f)$, which are similar to the limits used for the damage parameter (ω) in (2.20).

By analogy with (2.19) and (2.20) equations (5.15) and (5.16) may be rewritten as:

$$\frac{df_h}{dt} = \beta_{CA}M'\left\{\frac{1}{(1-f_h)^{\phi}} - (1-f_h)\right\}\sigma_{ef}^{\chi}t^m \tag{5.18}$$

$$\frac{d\epsilon}{dt} = K\left\{1 + \beta_{CA}\left(\frac{1}{(1-f_h)^n} - 1\right)\right\}\sigma_{ef}^{n}t^m \tag{5.19}$$

where (t^m) includes the Andrade term to represent the shape of the primary creep region, (M') and (K) are constants. The terms (ϵ_0) and (ω_0) do not appear as the equations are now not normalised. The equations are written in general form with $n \neq \chi$, and (ϕ) is introducted for consistency with the equation (2.20) due to Hauhurst [23,63].

The equations (5.18) and (5.19) are normalised consistently in a similar manner to equations (2.19) and (2.20) by defining the normalised strain as $V_{ij} = \epsilon_{ij}/e_0$, where $(e_0 = \sigma_0/E)$, and the normalised stress as $\Sigma_{ij} = \sigma_{ij}/\sigma_0$; and, by allowing for multi-axial stresses and creep strains in a manner consistent with equation (2.7) due to Odqvist. Equation (5.19) then becomes:-

$$\frac{dV_{ij}}{dt} = \frac{3}{2}KE\sigma_0^{n-1}\left\{1 - \beta_{CA} + \frac{\beta_{CA}}{(1-f_h)^n}\right\}\Sigma_{ef}^{n-1}S_{ij}t^m \tag{5.20}$$

where $S_{ij} = s_{ij}/\sigma_0$. Introduction of the normalised time scale, defined by equation (2.18), (5.20) becomes:

$$\frac{dV_{ij}}{d\tau} = \frac{3}{2}\left\{1 - \beta_{CA} + \frac{\beta_{CA}}{(1-f_h)^n}\right\}\Sigma_{ef}^{n-1} S_{ij} \tag{5.21}$$

Similarly, normalisation of equation (5.18) gives:

$$\frac{df_h}{dt} = \frac{M\beta_{CA}\sigma_0^{\chi}}{(1+\phi)}\left\{\frac{1}{(1-f_h)^{\phi}} - (1-f_h)\right\}\Sigma_{ef}^{\chi} t^m \tag{5.22}$$

where $(1+\phi)$ is introduced to simplify the later integration of (5.22) and $M' = M(1+\phi)$. Introduction of the same normalised time scale (2.18) leads to the expression:

$$\frac{df_h}{dt} = \frac{M\beta_{CA}\sigma_0^{\chi}}{KE\sigma_0^{n-1}(1+\phi)}\left\{\frac{1}{(1-f_h)^{\phi}} - (1-f_h)\right\}\Sigma_{ef}^{\chi} \tag{5.23}$$

and:

$$\frac{df_h}{d\tau} = \frac{\beta_{CA}}{V_u(1+\phi)}\left\{\frac{1}{(1-f_h)^{\phi}} - (1-f_h)\right\}\Sigma_{ef}^{\chi} \tag{5.24}$$

where V_u is given by equation (2.21). For equations (5.21) and (5.24), the equation for the β_{CA}-term (5.14) is re-written in normalised for as:

$$\beta_{CA} = \sinh\left(F\frac{\tilde{I}_1}{\Sigma_{ef}}\right) \tag{5.25}$$

where (F) has been introduced to give (β_{CA} =1.0) for uni-axial plane-stress conditions (i.e. F =0.8814) and the strain rate equation becomes exactly the same as the equation (2.19). The Cocks and Ashby equations (5.21), (5.24) and (5.25) are now written in a similar form to the equations (2.19) and (2.20) due to Hayhurst, and may now be compared for uni-axial plane-stress conditions where (β_{CA} =1.0) and ($\alpha\Sigma_1 + (1-\alpha)\Sigma_{ef} = \Sigma_1 = \Sigma_{ef}$). It may be observed that the creep strain rate equation (5.21) is identical to that of (2.19) when (β_{CA} =1.0). The damage rate equation (5.24) has a damage rate of zero for (f_h=0), at (τ =0), whereas (2.20) has a finite damage rate. The results of the Cocks and Ashby equations differ under uni-axial plane stress conditions from those of the Hayhurst equations because of the inclusion of the $(-(1-f_h))$ term in the damage rate equation (5.24). This causes differences in the damage rates, failure times and failure strains. Though for large (f_h) equations (5.24) and (2.20) have approximately the same damage rates as $(-(1-f_h))$ can be neglected in equation (5.24).

Integration of equation (5.24) for conditions of constant uni-axial stress gives:

$$\tau - \tau_i = V_u\left\{\ln(1-(1-f_h)^{(\phi+1)}) - \ln(1-(1-f_i)^{(\phi+1)})\right\}\left(\frac{\sigma_1}{\sigma_0}\right)^{-\chi}. \tag{5.26}$$

where (f_i) is the initial volume fraction of voids at normalised time ($\tau_i \approx 0$), which is taken to be small (0.001) and (f_h) is the volume fraction of voids at some normalised time ($\tau_i < \tau < \tau_f$) which gives:

$$\tau = V_u \left\{ \ln(1-(1-f_h)^{(\phi+1)}) + 5.8392 \right\} (\Sigma_1)^{-\chi} \tag{5.27}$$

Similarly integration of (2.20) for conditions of constant uni-axial stress between the limits (ω_i=0) at (τ_i =0) and (ω) at ($\tau_i < \tau < \tau_f$) gives:

$$\tau - \tau_i = V_u \left\{ (-)(1-\omega)^{(\phi+1)} - (-)(1-\omega_i)^{(\phi+1)} \right\} (\Sigma_1)^{-\chi} \tag{5.28}$$

$$\tau = V_u \left\{ 1-(1-\omega)^{(\phi+1)} \right\} (\Sigma_1)^{-\chi} \tag{5.29}$$

The normalised times at failure, for the Cocks and Ashby equation (τ_f) at ($f_h = 1.0$) and for the Hayhurst equation (τ_f) at (ω =1.0) are given from equations (5.27) and (5.29) as:

$$\tau_f = V_u (5.8392) \Sigma_1^{-\chi} \tag{5.30}$$

and

$$\tau_f = V_u \Sigma_1^{-\chi} \tag{5.31}$$

respectively.

The predicted normalised failure time from the Cocks and Ashby equations is 5.8392 times that of the Hayhurst equations. If equations (5.27) and (5.29) are normalised by their respective normalised failure times equations (5.30) and (5.31), the increase of damage with normalised time, divided by the normalised time at failure, may be obtained as shown in Fig. 5.26, using ϕ =1.914 as determined for (2.19) and (2.20) and shown in Table 5.1.

These differences in the damage growth rates caused by the inclusion of (−(1−f_h)) term in equation (5.24) will not occur if the material constants in the Cocks and Ashby equations are fitted to the same creep curves, as were used to obtain the creep constants in the Hayhurst equations (2.19) and (2.20), Different constants (ϕ), (χ), (M), (K) will be obtained for both sets of equations. This may be exemplified by Fig. 5.27 which shows that the damage evolution law of Hayhurst eqn. (2.20) if adjusted, using a (ϕ) value of 11.5901 may have a damage evolution curve close to that of the Cocks and Ashby model. Obviously other parameters would have to be adjusted to obtain exact compatibility of normalised failure times and damage curves. However,

for simplicity and since the material constants have already been determined from the Hayhurst damage evolution law, the term $(-(1-f_h))$ will be removed from the Cocks and Ashby damage rate law and (5.24) becomes:

$$\frac{df_h}{d\tau} = \frac{\beta_{CA}}{V_u(1+\phi)}\left\{\frac{1}{(1-f_h)^{\phi}}\right\}\Sigma_{ef}^{x} \equiv \frac{d\omega}{d\tau} \tag{5.32}$$

which now becomes directly compatible with the Hayhurst equation (2.20), where (β_{CA} =1.0) for uni-axial conditions and ($f_h \equiv \omega$).

Taking ($f_h = \omega$) equation (5.32) can be integrated in the range ($0 < \omega < 1.0$) at ($0 < \tau < \tau_f$) with the initial conditions ($\omega = 0$), ($\tau = 0$) to give:

$$\left\{1-(1-\omega)^{(\phi+1)}\right\} = \frac{\beta_{CA}}{V_u}\Sigma_{ef}^{x}\tau \tag{5.33}$$

$$\Rightarrow (1-\omega) = \left\{1-\frac{\beta_{CA}}{V_u}\Sigma_{ef}^{x}\tau\right\} \tag{5.34}$$

At failure ($\tau = \tau_f$) and (ω =1.0) this equation gives:

$$\tau_f = \frac{V_u}{\beta_{CA}\Sigma_{ef}^{x}} \tag{5.35}$$

From (5.21) the effective creep strain rate equation may be written as:

$$\frac{dV_{ef}}{d\tau} = \left\{1-\beta_{CA}+\frac{\beta_{CA}}{(1-\omega)^n}\right\}\Sigma_{ef}^{n} \tag{5.36}$$

Substituting for $(1-\omega)$ from (5.34) into (5.36), integrating, then using (5.35) gives:

$$V_{ef} = \Sigma_{ef}^{n}\left\{\tau(1-\beta_{CA})+\frac{\beta_{CA}\tau_f}{(1-\frac{n}{\phi+1})}\left(1-\left(1-\frac{\tau}{\tau_f}\right)^{(1-\frac{n}{\phi+1})}\right)\right\} \tag{5.37}$$

where

$$\beta_{CA} = \sinh\left\{0.8814\left(\frac{\tilde{I}_1}{\Sigma_{ef}}\right)\right\} \tag{5.38}$$

The modification to the Cocks and Ashby damage rate equation (5.24) neglecting the $(-(1-f_h))$ term considerably simplifies the integration of the constitutive and damage rate laws to give the equation (5.37) for the creep strain variation with time.

At failure ($\tau = \tau_f$) and ($V_{ef} = V_{ef}^{(f)}$):-

$$V_{ef}^{(f)} = \Sigma_{ef}^{(n-x)}V_u\left\{\left(\frac{1-\beta_{CA}}{\beta_{CA}}\right)+\left(1-\frac{n}{\phi+1}\right)^{-1}\right\} \tag{5.39}$$

The uni-axial tensile elongation at failure is given by substituting ($\beta_{CA} = 1.0$) and $\Sigma_{ef} = \Sigma_1$ into (5.39), for uni-axial plane stress conditions:

$$V_1^{(f)} = \frac{\Sigma_1^{(n-x)} V_u}{(1 - \frac{n}{\phi+1})} \tag{5.40}$$

The uni-axial tensile elongation at failure is used to normalise the strain versus tri-axiality factor diagram of Fig. 5.23, due to Manjoine [78]

Normalising the multi-axial effective strain at failure equation (5.39) by the uni-axial tensile elongation at failure, equation (5.40), gives:

$$\frac{V_{ef}^{(f)}}{V_1^{(f)}} = \left\{ \Delta \left(\frac{1 - \beta_{CA}}{\beta_{CA}} \right) + 1 \right\} \left(\frac{\Sigma_{ef}}{\Sigma_1} \right)^{(n-x)} \tag{5.41}$$

where (β_{ca}) is given by (5.38) and $\Delta = 1 - (n/\phi + 1)$.

Equation (5.41) is used to plot the multi-axial rupture ductility predicted by the new constitutive and damage laws, using the (β_{CA})-term, to allow for the influence of the tri-axial stress state on the rupture ductility and is compared against the empirically obtained curve of Manjoine [78] in Fig. 5.28. The points plotted (Fig.5.28) represent (a) uni-axial tension (ζ =0); (b) equal-biaxial tension (ζ =1.0); (c) un-equal bi-axial tension (ζ =1/2); (d) tension-compression (ζ =-1/2); (e) tension-compression (ζ =-1/3); where (ζ) is the ratio (Σ_2/Σ_1). The curve predicted by equation (5.41) compares reasonably well for ($\tilde{I}_1/\Sigma_{ef}$) > 1.0, with the empirical curve of Manjoine. For ($\tilde{I}_1/\Sigma_{ef}$) < 1.0, it is noticed that as ($\tilde{I}_1/\Sigma_{ef}$) or the Davis Triaxiality Factor tends to zero the ratio of the effective strain at failure to the tensile elongation at failure predicted by equation (5.41) becomes infinite. Manjoine in Fig. 5.23 uses constant value of ($V_{ef}^{(f)}/V_1^{(f)}$ =2.0) given by a dotted line for (TF_D <0).

From the integration of (5.32), using (2.18) to give the real time (t), the rupture time may be shown to be:

$$t = \left\{ \left(\frac{m+1}{M} \right) \beta_{CA}^{-1} \sigma_{ef}^{-x} \right\}^{\frac{1}{m+1}} \tag{5.42}$$

If (5.42) is written in full, for the principal bi-axial stresses in plane-stress:

$$t = \left(\left\{ \left(\frac{m+1}{M} \right) \sinh \left(\frac{0.8814(\sigma_1 + \sigma_2)}{(\sigma_1^2 + \sigma_2^2 - \sigma_1\sigma_2)^{\frac{1}{2}}} \right) \right\}^{-1} (\sigma_1^2 + \sigma_2^2 - \sigma_1\sigma_2)^{\frac{-x}{2}} \right)^{\frac{1}{m+1}} \tag{5.43}$$

Defining (t_0) as time to rupture in a uni-axial test (i.e.β_{CA} =1.0) at a stress (σ_0) from (5.42):

$$t_0 = \left\{ \left(\frac{m+1}{M} \right) \sigma_0^{-x} \right\}^{\frac{1}{m+1}} \tag{5.44}$$

Writing ($T = t/t_0$) and ($\Sigma_i = \sigma_i/\sigma_0$), (5.43) is re-written as:-

$$T = \frac{t}{t_0} = \left(\left\{ \sinh \left(\frac{0.8814(\Sigma_1 + \Sigma_2)}{(\Sigma_1^2 + \Sigma_2^2 - \Sigma_1\Sigma_2)^{\frac{1}{2}}} \right) \right\}^{-1} (\Sigma_1^2 + \Sigma_2^2 - \Sigma_1\Sigma_2)^{\frac{-\chi}{2}} \right)^{\frac{1}{m+1}} \tag{5.45}$$

By expressing (Σ_2) as the ratio (ζ) of (Σ_1), ($\zeta = \Sigma_2/\Sigma_1$), (5.45) may be re-written as:

$$T^{m+1} = \left\{ \sinh \left(\frac{0.8814(\zeta + 1)}{(\zeta^2 - \zeta + 1)^{\frac{1}{2}}} \right) \right\}^{-1} \left((\zeta^2 - \zeta + 1)^{\frac{1}{2}} \right)^{-\chi} \Sigma_1^{-\chi} \tag{5.46}$$

Setting (T =1.0) the equation for the isochronous rupture surface in bi-axial principal stress space is determined for different values of the bi-axiality ratio (ζ):-

$$\Sigma_1 = \left\{ \sinh \left(\frac{0.8814(\zeta + 1)}{(\zeta^2 - \zeta + 1)^{\frac{1}{2}}} \right) \right\}^{\frac{-1}{\chi}} \left((\zeta^2 - \zeta + 1)^{\frac{1}{2}} \right)^{-1} \tag{5.47}$$

Similarly for plane strain conditions the equation for the isochronous rupture surface corresponding to equation (5.32), using the (β_{CA})-term may be shown to be:

$$\Sigma_1 = \left\{ \sinh \left(\frac{0.8814(\frac{3}{2} + \frac{3}{2}\zeta)}{(\frac{3}{4} - \frac{3}{2}\zeta + \frac{3}{4}\zeta^2)^{\frac{1}{2}}} \right) \right\}^{\frac{-1}{\chi}} \left(\left(\frac{3}{4} - \frac{3}{2}\zeta + \frac{3}{4}\zeta^2 \right)^{\frac{1}{2}} \right)^{-1} \tag{5.48}$$

It may be observed from equations (5.47) and (5.48) that the rupture surfaces are dependant on the value of (χ), whereas the equations (2.32) and (2.33) used by Hayhurst [22] are independant of (χ).

The isochronous rupture surface defined by the plane stress equation (5.47) with (χ=5) is given in Fig. 5.29. It may be observed that the effect of the inclusion of the (β_{CA})-term, drops the rupture surface below that of the rupture surface defined by ($\alpha\Sigma_1 + (1-\alpha)\Sigma_{ef}$) of Fig. 5.24, in the tension-tension quadrant. The corresponding isochronous rupture surface using the Ashby/Cocks model represented by equation (5.48) for plane strain conditions is shown in Fig. 5.30. Here it may be observed that the rupture life is zero for the equi-tri-axial tension (ζ =0) case. This may not be explicitly true for real materials, but is accepted here whilst the new model is evaluated. The Cocks and Ashby constitutive model is for growth of voids due to the surrounding material deforming by the mechanism of power-law creep (section 1.3.2 (ii)). In this model voids do not grow in pure shear, but are elgonated by the shear processes. Therefore, the model predicts infinite life in pure shear, as shown by the (ζ)-ratio of (-1.0) on the dotted line shown in Fig. 5.29; whereas the Hayhurst model

(Fig.5.24) based on experimental data from tension-torsion tests in plane stress, shows a reduction in life, below the uni-axial life in the same region. For this reason the Hayhurst damage law and creep strain rate constitutive equations will be used for principal stresses in all the quadrants of the (Σ_1, Σ_2) principal stress space, except the tension-tension quadrant, where the Cocks and Ashby model equations will be used allowing for the effect of the tri-axial stress state on rupture life. Both low and high stress behaviour using a bi-linear model similar to that of section 2.6, will also be incorporated in the Cocks/Ashby equations.

The new creep damage model may be represented graphically using the schematic diagram of Fig. 5.32. Here the shaded plane represents the original uni-axial stress-rupture diagram as shown in Fig.5.2, which is selected for compatibility of the new multi-axial model with plain stress uni-axial conditions. The axes for this plane are log(stress) vs. log(rupture-time). The third axis is the ratio of the normalised hydrostatic stress $(\tilde{I}_1)$, to the normalised effective stress, (Σ_{ef}). For $(\tilde{I}_1/\Sigma_{ef}) \geq 1.0$, the high and low stress-rupture lines extend into plane surfaces (C) and (D) (Fig.5.31) in 3-D space. The gradients of the lines in the shaded plane which are related to, (χ_1) and (χ_2), remain constant as $(\tilde{I}_1/\Sigma_{ef})$ increases, but their levels in planes parallel to the shaded plane drop with increasing $(\tilde{I}_1/\Sigma_{ef})$. This models the effect of decreasing rupture-life with increasing tri-axiality. The break point line (Fig.5.2) is assumed to lie on the plane $(\Sigma_{ef} = \hat{\Sigma})$, where $(\hat{\Sigma})$ is the normalised break stress $(\hat{\sigma}/\sigma_0)$. The high and low stress rupture planes for $(\tilde{I}_1/\Sigma_{ef}) \geq 1.0$ will be represented by the Cocks/Ashby model equations (D2) and (C2) (Fig.5.32) respectively. Their isochronous rupture surfaces are only defined in the tension-tension quadrant by equation (5.47) for plane stress and (5.48) in plane strain.

For $(\tilde{I}_1/\Sigma_{ef}) \leq 1.0$ the equations due to Hayhurst (B2) and (A2) (Fig.5.32) will be used to represent the surfaces (B) and (A) respectively. Their isochronous rupture surfaces are only defined for compressive stress quadrants by the rupture criterion in equation (5.13) shown for plane stress and plane strain conditions in Figs.5.24 and 5.25 respectively.

Under uni-axial plane stress conditions ($\beta_{CA} = 1.0$), the equations (A), (B), (C) and (D) have been formulated to be compatible giving the same creep strain rates and rupture times, at the break stress point on the shaded plane ($(\tilde{I}_1/\Sigma_{ef})=1.0$), shown

in Fig. 5.31. The isochronous rupture surfaces must also be compatible in both principle plane stress and plane strain space, moving from the tension-tension quadrant represented by the Cocks and Ashby equations (C2) and (D2), to compressive stress quadrants, represented by the Hayhurst equations (A2) and (B2).

The material constants of Table 5.8 are used in the new model, in preference to the equations of Table 5.6 as these constants produced slightly lower failure strains at high stress (as for the large deformation solution), requiring much fewer iterative steps to solution completion and hence reduced computational effort. It required 6,852 iterative steps to solve the plane stress instantaneous technique CT-specimen problem (Table 5.7), which may be compared with 983 iterations (Table 5.5) for the same solution using the material constants of Table 5.1. The failure strain predictions using the constants of Table 5.8 increases monotonically with stress similar to that shown in Fig.5.17, and the stress-rupture characteristics are the same as those modelled by the constants of Table 5.6.

The equations (5.47) and (5.48) show the dependence of the form of the isochronous rupture surfaces on the value of (χ). As the values of (χ) given in the table of material constants (Table 5.8), have been determined for the normalised time scale and the correct value of (χ) must be used in equations (5.47) and (5.48) corresponding to the real time scale in hours, for the (β_{CA})-term to have the correct effect on the multi-axial rupture behaviour, in line with the Cocks/Ashby mechanism; (m+1) is therefore included in a new definition of the (β_{CA})-term:-

$$\beta'_{CA} = \left\{ \sinh\left(0.8814 \frac{\tilde{I}_1}{\Sigma_{ef}}\right) \right\}^{m+1} \tag{5.49}$$

this carries through to give the true value of (χ) in the equations (5.47) and (5.48), as $(\chi_T = \chi/(m+1))$, which is identified as the material constant (ν) which defines the true gradient $(-1/\nu)$ of the stress-rupture diagram given equation (2.12).

By plotting the isochronous rupture surface in both plane stress and plane stress space, it is found that the plane stress isochronous rupture surfaces produced by the Cocks/Ashby equations (Fig.5.29) will always match up with those of the Hayhurst equations (Fig.5.24) at the points $(\star(a))$ and $(\star(b))$ (Fig.5.29) giving a smooth transition reasonably independent of the value of (χ_T) in equation (5.47). The matching of the surfaces Fig.5.25 and Fig.5.30 in plane strain is dependent upon the value of (χ_T) in equation (5.48). It has been found by the author that a reasonably

good match of rupture surfaces at the points (⋆(a)) and (⋆(b)) Fig.5.30 in plane strain between the Cocks/Ashby (low stress) isochronous rupture surface, and that of the Hayhurst rupture surface may be obtained using:-

$$\beta''_{CA} = \left\{ \sinh\left(0.8814 \frac{\tilde{I}_1}{\Sigma_{ef}} \right) \right\}^{n(m+1)} \tag{5.50}$$

where (n) is the creep exponent. Using this (β''_{CA}) instead of (β_{CA}) equations (5.47) and (5.48) representing the isochronous rupture surfaces are modified by replacing $(-1/\chi)$ by $(-n(m+1)/\chi)$. Equation (5.50) has been used to give the isochronous rupture surfaces for the final constitutive model, which are shown in Figs.5.33(a) and (b) for low and high stress values of (n) and (χ), respectively in plane stress, principal stress space and Figs.5.34(a) and (b) for low and high stress values of (n) and (χ), respectively in plain strain, principal stress space. The new constitutive model only uses the solid lines of the rupture surfaces in the tension-tension quadrant and the dotted lines in the other quadrants of Figs.5.33 and 5.34.

The new constitutive model is therefore defined using the four strain rate equations, the four damage rate equations of Fig.5.32 and the material constants of Table 5.8, with (β_{ca})-term given by equation (5.50). The results from the use of this new model in the creep continuum damage program Damage-(XX) to predict the failure of the CT-specimen are summarised in the following section.

5.16 Results From The New Creep Continuum Damage Model Allowing For The Effect Of The Tri-Axial Stress State On Rupture.

The first solution used the finite element mesh of Fig. 5.3, as used by Brown [64] to model the compact tension specimen under the plane strain conditions. The finite element solution showed the growth of the failed element (ω >0.9999) loci in a localised band along the bottom boundary of the mesh, as shown in Fig. 5.35. The finite element solution became numerically stiff after the formation of the damage distribution shown in Fig.5.36 close to failure, giving a normalised lifetime prediction of (τ_f =41.3).

A second solution was performed for a finite element mesh (Fig.5.21) having an almost constant mesh refinement across the ligament. This finite element solution

also, as was the case for the previous, became numerically stiff, giving a predicted normalised lifetime of (τ_f =34.4). This normalised failure time prediction lies close to the expected experimental value of (τ_f = 31.80), giving an error of 8% in the normalised lifetime prediction for the CT-specimen using the new tri-axial constitutive model. The damage distribution as shown in Fig.5.37, is much more localised, which is as expected in practice. The damage distribution is seen to grow only forward of the crack tip, with very little damage at the crack-flanks. The damage around the load holes is seen to be much reduced in comparison with the earlier damage distributions of Fig.5.22. It is seen that the damage distribution becomes slightly more localised, where the vertical element refinement becomes more refined, at about half way across the mesh ligament.

The allowable integration error parameters for both these two solutions using the new model were set at quite large values; EPSL and EPSR were 10^{-2} and 10^{-3} respectively (section 4.33), due to the restriction on computational resources. The refined mesh required approximately 3 hours dedicated CPU time for the whole solution.

5.17 Discussion.

The results obtained for the failure predictions of the compact tension specimen are summarised in Table 5.9. Referring to Table 5.9 (No. 1) it is seen that the original continuum damage solution performed by the author similar to that by Brown [64], grosly over-estimates the expected normalised failure time expected in experiments by approximately 50%. The crack tip failed element zone was much larger than that expected in experiments [65,79].

New finite element techniques to remove the elements and creep forces gradually, as used by Chaboche (Table 5.9, No.2) and Tvergaard (Table 5.9 No.3) did not provide significant improvements in the computer solution for the CT-specimen, giving predicted failure time and damage distributions similar to those of (Table 5.9, No.1). The techniques of Chaboche and Tvergaard both used more CPU time than the instantaneous element removal method as used by Hayhurst et al and in the CT-specimen solution of Brown [64]; in that the stiffness matrix has to be inverted for every iterative time step of the Chaboche technique and new displacements have to

be evaluated for every new force vector during the relaxation of the creep forces in the Tvergaard technique.

The Chaboche technique gave a slightly longer life prediction in comparison with that predicted by the instantaneous technique as used by Hayhurst [23,63], which is consistent with the comparisons of Sanouri [80]. Sanouri [80] also compared the damage distributions at the crack tip for the different methods, which show distinct similarlities, to that of the instantaneous approach; the instantaneous approach having a slightly larger failed element region, due to this method allowing less stress re-distribution away from the crack tip. As the solutions progress, and damage grows across the ligament, the differences in the failed element distributions become less obvious and to all intents and purpose, both the solutions are the same. The results of Rides [73] also support this conclusion, that the inclusion of the coupling between the damage parameter and the elastic modulus has little effect on the structural analysis.

From the tests and comparisons made by the author, the instantaneouos element removal technique compares favourably with the Tvergaard and Chaboche techniques, as the stresses in the elements decay, becoming quite small before they are said to fail (i.e. before ω >0.9999) and are removed with their respective creep forces; which results in a negligibly small loss of strain energy. The instantaneous approach is also attractive, as it is more computationally efficient than the former two methods.

Performing a plane-stress solution reduces the normalised life prediction for the compact tension specimen (Table 5.9, No. 4) in comparison with the corresponding plane strain solution (Table 5.9, N0.1), which is consistent with the expected increase in the damage rates due to the larger values of the effective stress present under plane stress conditions in equation (2.20). This is inconsistent with the experimental results of Webster [74], who shows that creep crack growth in plane stress specimens is slower than in a plane strain specimens. He includes this difference in his crack growth rate expressions using (C^*) by defining the available ductility at the crack tip (ϵ_f^*) as equal to the uni-axial creep ductility (ϵ_f) for plane stress conditions and equal to ($\epsilon_f/50$) for plane strain conditions. Therefore, fracture occurs at the crack tip at a rupture strain of (1/50)th of the uni-axial rupture ducitlity (ϵ_f) for a plane-strain specimen, which causes the plane strain specimen to have a considerably shorter lifetime than

a plane-stress specimen.

Nisheda et al [76] show that ductility may affect the creep crack growth rates and hence lifetimes of cracked specimens. The constitutive model was re-defined in terms of a full bi-linear strain rate and damage rate model (section 2.6), which was modified to represent the high stress rupture data more accurately and to have a continuously increasing failure strain with increasing stress. The new bi-linear model had the effect of producing a more localised damaged element distribution at the crack-tip under plane-stress condtions, giving a slight reduction in the predicted normalised lifetime (Table 9, No. 5).

A large deformation and rotation solution was performed in plane-strain which produced an larger normalised lifetime prediction, (Table 5.9, No. 6), than the comparable small deformation solution, (Table 5.9, No. 1). This is caused by increased stress re-distribution, caused by the allowance of crack-tip blunting in the model, producing larger damage distribution at the crack-tip spreading into the body of the CT-specimen mesh.

The effect of mesh refinement was also considered and a mesh with almost constant refinement across the ligament length was used to provide a new plane strain solution for the CT-specimen. The new lifetime prediction is given in Table 9, No.7 which is smaller than that predicted from the previous solution (Table 9, No. 1), using a mesh with fine refinement close to the crack-tip and coarse refinement elsewhere.

Therefore, all the model modifications performed still give a minimum normalised life prediction somc 40% greater than that expected, which corresponds to a lifetime prediction approximately 300 times larger than that expected by experiment of 4×10^4 hours.

Having explored almost all available avenues to explain the differences between predicted and the exerimental life times, the effect of the tri-axial stress-state on rupture life was considered. Cocks and Ashby [66] derived damage rate and strain rate equations for the mechanism transgranular creep fracture due to constrained void growth. Included within their equations is the term (β_{CA}), (equation (5.14)), which modifies the damage rate and strain rate equations, to model the increased damage and strain rates due to the effect of the hydrostatic stress, which in turn models

accelerated void growth. These new equations have been modified to give similar equations to the creep rate and damage rate equations used by Hayhurst et al, [23,63], but including the (β_{CA})-term . They have been shown to reproduce, reasonably well, the empirically obtained ductility curve of Manjoine [78], (Fig.5.28) relating the decrease in the multi-axial rupture ductility with increasing tri-axiality measured by (I_1/σ_{ef}). The new constitutive model produced modified isochronous rupture surfaces in the tension-tension quadrants of (Σ_1, Σ_2) principal-stress space. The new isochronous rupture surfaces for plane stress conditions (Figs.5.33 (a) and (b)) are similar but more rounded than those of the previously used constitutive equations of Hayhurst (Fig.5.24) which are more vee-shaped. These rupture surfaces should produce broadly similar compact tension specimen failure predictions to the solutions previously obtained for plane stress conditions. Though, isochronous rupture surfaces for plane strain conditions using the new constitutive model allowing for the effect of tri-axiality on rupture (Fig.5.34 (a) and (b)) are considerably different in the tension-tension quadrant from those of the previously used constitutive equations of Hayhurst shown in Fig.5.25. The trough along the equal bi-axial tension line (Fig.5.34(a)) is caused by the accelerated growth of voids under tri-axial stress states. If the (β_H)-hydrostatic term in the rupture criterion (equation (2.28)) defined by Hayhurst [22] is allowed for in the in the damage rate equation (2.20), the isochronous rupture surface in plane-stress will become more rounded than that of Figs.5.24 depending on the value of (β_H). This is consistent with the Cocks/Ashby model (Fig.5.29); but for plane-strain conditions the rupture criterion of Hayhurst cannot represent the same isochronous rupture surface of the Cocks/Ashby model Fig.5.30(b). It is this behaviour, unique to the plane-strain stress state of the Cocks/Ashby model, which will predict the factor of 50 decrease in the available ductility at the crack tip, $(\epsilon_f/50)$, observed by Webster [74] and has been shown to predict the rupture ductility curve Fig.5.23, observed by Manjoine [78], to produce reduced life of material elements at the crack tip in this region of high tri-axial stress state.

The modified (β_{CA})-term (equation (5.50)) is observed to be raised to the power (n) and is a multiplier on the power law in equation (5.21). It may be that with the inclusion of the power (n) in the (β_{CA})-term, an exponential stress dependence of the strain rate is modelled, possibly producing increased strain rates particularly at

high stress in the glide controlled flow region of the Ashby mechanism map Fig.5.5(a). Strain rates in this region were previously predicted to be too small by the equations (2.19) and (2.20) using the bi-linear representation (section2.6). These equations due to Hayhurst et al, are based on the Norton's power-law, which breaks-down at high stress in the dislocation glide region [8].

The results under plane stress conditions using the new constitutive model allowing for the effects of the tri-axial stress state on rupture, are given in Table 5.9,No.8 and No.9 for the original finite element mesh and a refined mesh with constant refinement across the ligament length respectively. The predicted normalised failure times are significantly reduced and the damage distributions are seen to grow forward of the crack-tip along the liagement length,(Fig.5.37), consistent with the observations of Riedel [79]. The effects of this mesh refinement on the solution is more pronounced for the new constitutive model, giving approximately 20% reduction in the ratio $(\tau/\tau_{e_{(f)}})$ between solutions No.8 and No.9, Table 5.9, compared with a 10% reduction in the same ratio between the solutions No.1 and No.7. The integration error parameters corresponding to the two computer solutions given in Table 9, No.8 and No.9, were set quite large due to the refined mesh requiring a large computational effort. If the integration parameters were refined from EPSL and EPSR values of (10^{-2}) and (10^{-3}) to values of (10^{-4}) and (10^{-5}), one would expect a reduction in normalised life to $(\tau_f \approx 33.0)$, from the graph of Fig.4.2 which was formulated using the same AISI 316 stainless steel material constants used here. In this same figure, as the life prediction for the CT-specimen $(\tau_f = 34.4)$ lies approximately on this curve, and predicted life of the CT-specimen with no integration error could be infered to be $(\tau_f = V_u = 31.805)$, which is consistent with the expected normalised life for the compact tension specimen on the basis of the tests by Myers and Pilkington [65].

These preliminary results in plane strain using the new constitutive model with the inclusion of the modified (β_{CA})-term look very promising, in that a comparable failure time prediction with the expected value by experiment should be possible if the time stepping integration accuracy is improved and a refined mesh such as that of Fig.5.38 is used to given an accurate damage growth prediction.

It may be that the plane-stress solutions detailed in this chapter will approximately represent the failure behaviour of a plane stress CT-specimen (with thickness

$t < 5$ mm or so, with a proportionally reduced test load to maintain the same net section stress); as the new model allowing for the tri-axial stress state gives isochronous rupture surfaces, which are not too dis-similar to those produced by the rupture criterion (equation (5.13)) used in the Hayhurst equations. This would give agreement with the observations of Webster [74], in that the plane stress solution lifetime prediction is larger than the plane strain prediction (c.f. normalised lifetimes Table 9 solution No. 9 for plane strain, with solution No. 5 for plane stress).

Ideally if the exact form of the bi-axial isochronous rupture surfaces could be determined by experiment, for both plane-stress and plane-strain stress states, the (β_{CA}) term could be used to fit the damage rate rate equation to the experimental data. Though it is questionable whether purely bi-axial tests will suffice, and possibly tri-axial rupture behaviour should be studied by reproducing similar stress states which occur in the compact tension specimen by testing notched bars. Although notched bars are not able to reproduce the high tri-axial stress states present at the crack tip of the compact tension specimen.

Therefore, recommendations for future work include the use of the developed finite element model allowing for the effect of tri-axiality on rupture, with further experimental compact tension specimen results for CT-specimens of various crack geometries under plane strain and plane stress conditions. More detailed experiment investigations of bi-axial and tri-axial rupture behaviour are required to verify and/or improve the new multi-axial constitutive model developed in this chapter, so that it may be applied to other crack growth problems with confidence. Further investigations into the validity of using the bi-linear representation in the power-law breakdown region needs to be carried out, together with investigations into the ability of the (β''_{CA}) term and other modifications to the constitutive equations to model creep in the power-law breakdown region.

	For $\sigma \leq \hat{\sigma}$	For $\sigma > \hat{\sigma}$
$\sigma_0 = 164.808MPa$	$n_{II} = 1.7371$	$n_I = n_{II}$
$\hat{\sigma}_0 = 441.28MPa$	$K_{II} = 1.3826 \times 10^{-5}$	$K_I = K_{II}$
$E = 169.617 \times 10^3 MPa$	$\chi_{II} = 0.4776$	$\chi_I = 4.00$
$\nu = 0.300$	$M_{II} = 2.7726 \times 10^{-3}$	$M_I = 4.3033 \times 10^{-11}$
$m = -0.940$	$\phi_{II} = 1.9136$	$\phi_I = \phi_{II}$
$\alpha = 0.750$	$V_u = 31.805$	

Table5.1: Summary of material constants for AISI 316 Stainless Steel in units of megapascals, percentage creep strain and hours, due to Hayhurst et al [23], [63].

Failed Element Plot Fig.No.	Normalised Time (τ)	Iteration No.	No. of Elements Failed (ω >0.9999)
5.10(a)	24.97	380	54
5.10(b)	36.66	664	112
5.10(c)	47.40	1100	211
At failure	48.04	1159	224

Table5.2: Summary of numerical results for the CT-specimen, in plane strain using the **instantaneous technique** of elemental removal and creep constants of Table 5.1.(1st element failure at τ=1.48)

Failed Element Plot Fig.No.	Normalised Time (τ)	Iteration No.	No. of Elements Failed (ω >0.9999)
5.11(a)	24.31	210	51
5.11(b)	36.80	349	122
5.11(c)	47.52	525	213
At failure	48.94	571	243

Table5.3: Summary of numerical results for the CT-specimen in plane strain, using the **Chaboche technique** and creep constants of Table 5.1.(1st element failure at τ=3.30).

Failed Element Plot Fig.No.	Normalised Time (τ)	Iteration No.	No. of Elements Failed (ω >0.9999)
5.13(a)	24.60	420	63
5.13(b)	36.76	819	122
5.13(c)	46.89	1554	231
At failure	46.89	1554	231

Table5.4: Summary of numerical results for the CT-specimen in plane strain, using the Tvergaard technique and creep constants of Table 5.1.(1st element failure at τ=1.47)

Failed Element Plot Fig.No.	Normalised Time (τ)	Iteration No.	No. of Elements Failed (ω >0.9999)
5.14(a)	24.37	396	50
5.14(b)	36.55	609	111
5.14(c)	46.90	983	226
At failure	46.90	983	226

Table5.5: Summary of numerical results for the CT-specimen in plane stress using the instantaneous technique and creep constants of Table 5.1.

	For $\sigma \leq \hat{\sigma}$	For $\sigma > \hat{\sigma}$
$\sigma_0 = 164.808MPa$	$n_{II} = 1.7371$	$n_I = 4.8215$
$\hat{\sigma_0} = 441.28MPa$	$K_{II} = 1.3826 \times 10^{-5}$	$K_I = 9.6206 \times 10^{-14}$
$E = 169.617 \times 10^3 MPa$	$\chi_{II} = 0.4776$	$\chi_I = 1.3257$
$\nu = 0.300$	$M_{II} = 2.7726 \times 10^{-3}$	$M_I = 1.5835 \times 10^{-5}$
$m = -0.940$	$\phi_{II} = 1.9136$	$\phi_I = 7.0789$
$\alpha = 0.750$	$V_u = 31.805$	

Table5.6: Summary of material constants for AISI 316 Stainless Steel, with new high stress constants giving a full bi-linear model, in units of megapascals, percentage creep strain and hours. (Low stress constants are the same as in Table 5.1)

Failed Element Plot Fig.No.	Normalised Time (τ)	Iteration No.	No. of Elements Failed (ω >0.9999)
5.18(a)	24.39	4685	46
5.18(b)	36.39	4875	118
5.18(c)	44.45	6852	190
At failure	44.45	6852	190

Table5.7: Summary of numerical results for the CT-specimen in plane stress using the instantaneous technique and the new creep constants of Table 5.6, representing full bi-linear strain rate and damage rate behaviour.

	For $\sigma \leq \hat{\sigma}$	For $\sigma > \hat{\sigma}$
$\sigma_0 = 164.808 MPa$	$n_{II} = 1.7371$	$n_I = 2.50$
$\hat{\sigma_0} = 441.28 MPa$	$K_{II} = 1.3826 \times 10^{-5}$	$K_I = 1.3267 \times 10^{-7}$
$E = 169.617 \times 10^3 MPa$	$\chi_{II} = 0.4776$	$\chi_I = 1.3257$
$\nu = 0.300$	$M_{II} = 2.7726 \times 10^{-3}$	$M_I = 1.5845 \times 10^{-5}$
$m = -0.940$	$\phi_{II} = 1.9136$	$\phi_I = 3.1934$
$\alpha = 0.750$	$V_u = 31.805$	

Table5.8: Summary of material constants for AISI 316 Stainless Steel, in units of megapascals, percentage creep strain and hours. As used for large deformation and rotation solution.

Solution No.	Solution Method Discription.	Normalised Failure Time (τ_f)	Ratio of (τ_f) to experimental (τ_f) ($\tau_f/\tau_{e(f)}$) In (%)	Damaged Element Distribution At (τ_f) In Fig.No.
1	1st soln. as Brown [64] (plane strain)	48.04	151.1	5.10(c)
2	Technique of Chaboche (plane strain)	48.94	153.9	5.11(c)
3	Technique of Tvergaard (plane strain)	46.89	147.5	5.13(c)
4	(plane stress) solution	46.90	147.5	5.14(c)
5	(plane stress) full bi-linear representation	44.45	139.8	5.18(c)
6	large deformation and Rotation (plane strain)	49.95	157.1	5.20
7	constant mesh refinement across ligament (F.E.mesh Fig.21) (plane strain)	45.0	141.5	5.22
8	new tri-axial constitutive model. (F.E.mesh Fig.5.3) (plane strain)	41.3	129.9	5.36
9	as 8 with constant mesh refinement across ligament. (F.E.mesh Fig.21)	34.4	108.2	37

Table5.9: Summary of the finite element results obtained for the prediction of the failure of the CT-specimen. (Expected experimental normalised lifetime of the CT-specimen for comparison with the finite element results is $\tau_f = 31.8$).

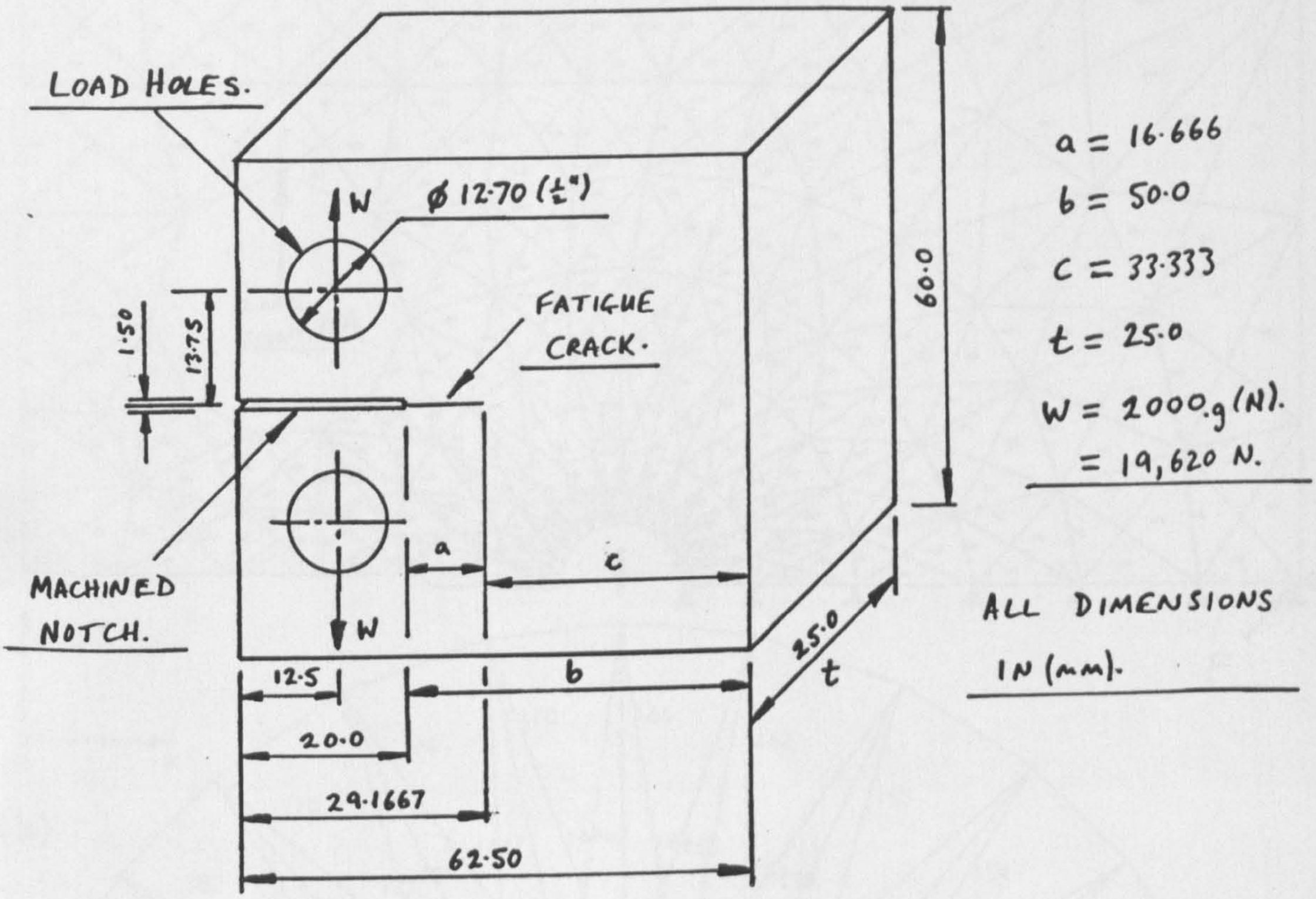

Figure 5.1: Geometry and dimensions of the compact tension specimen.

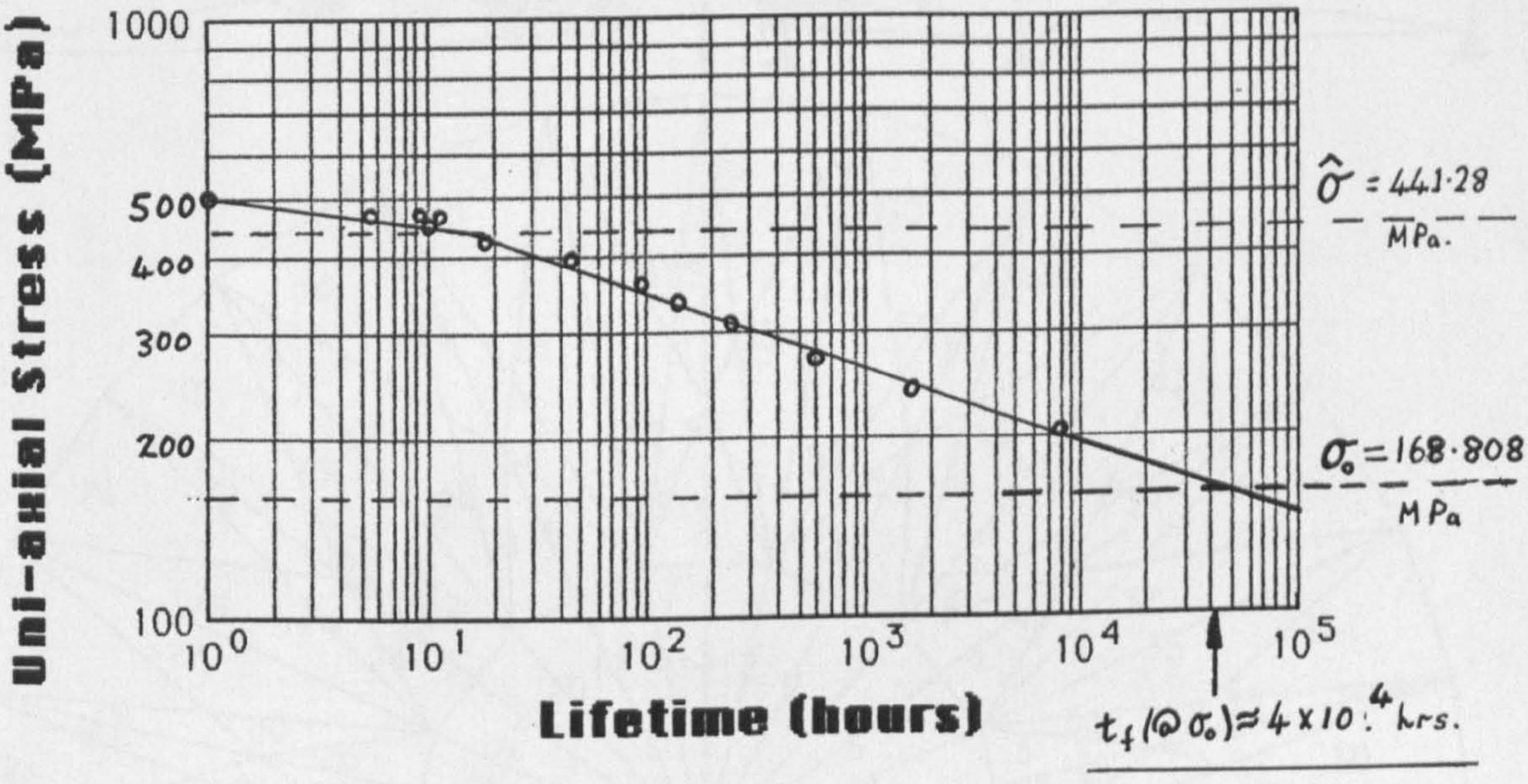

Figure 5.2: Uni-axial stress rupture data for AISI 316 stainless steel, at 550°C, after Hayhurst et al, [23].

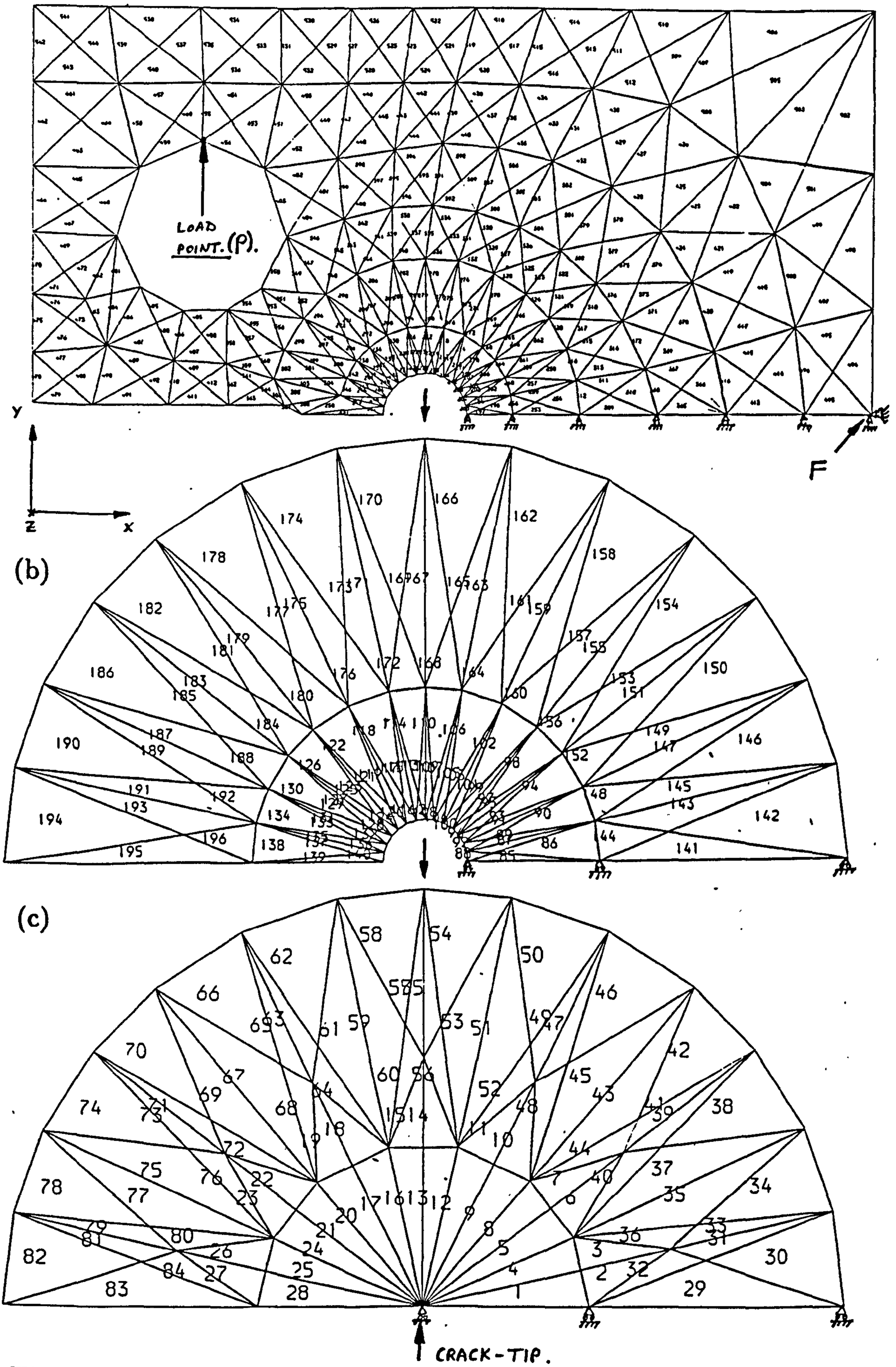

Figure 5.3: The finite element mesh for the CT-specimen generated by Brown, [64], showing the mesh refinement at the crack tip. The mesh has 544 elements and 296 nodes.

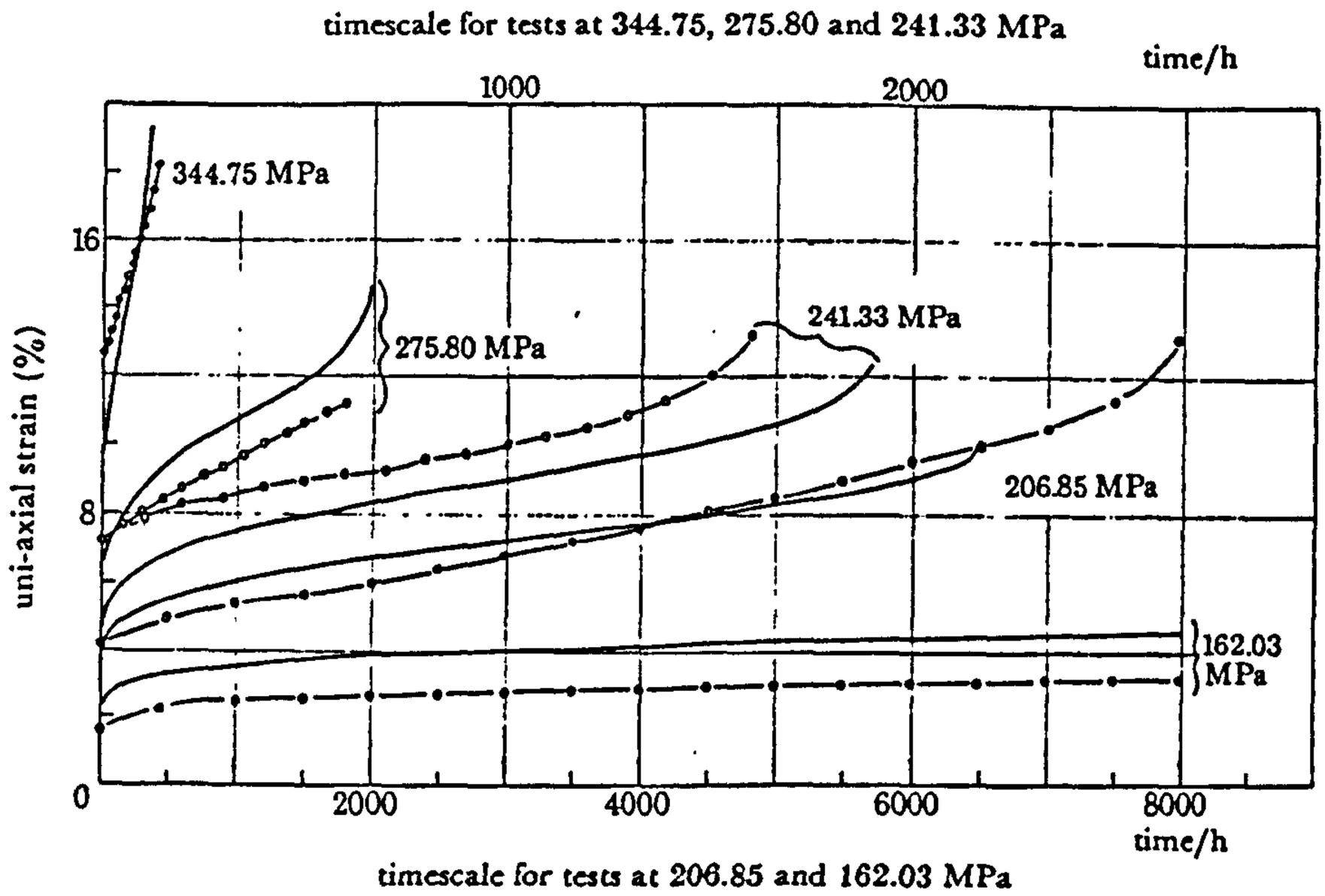

Figure 5.4: Comparison between the theoretical (—) and experimental (-o-) creep curves for AISI 316 stainless steel, at low stress levels ($\sigma < \hat{\sigma}$), after Hayhurst et al [23].

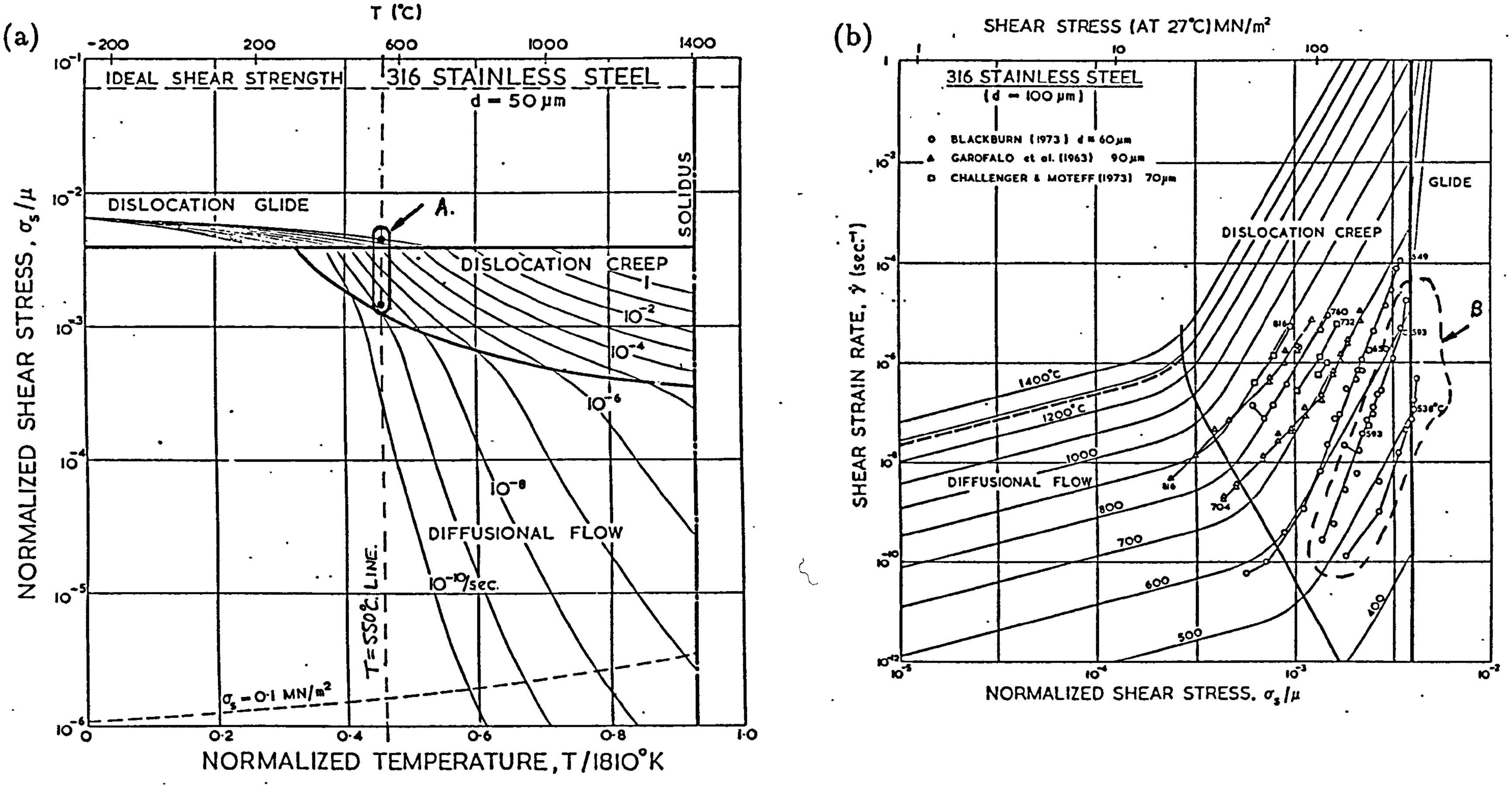

Figure 5.5: Ashby mechanism maps for ASI 316 stainess steel after Frost and Ashby [69].

(a) shows the region (A) corresponding to the creep tests performed (Figs 5.2 and 5.4).

(b) shows contours of constant test temperature on the axes of strain-rate versus normalised stress, and shows region (B) where data from the creep tests performed would lie. The line of Blackburn at $538°C$ is closest to the test data (Fig. 5.2 and 5.4).

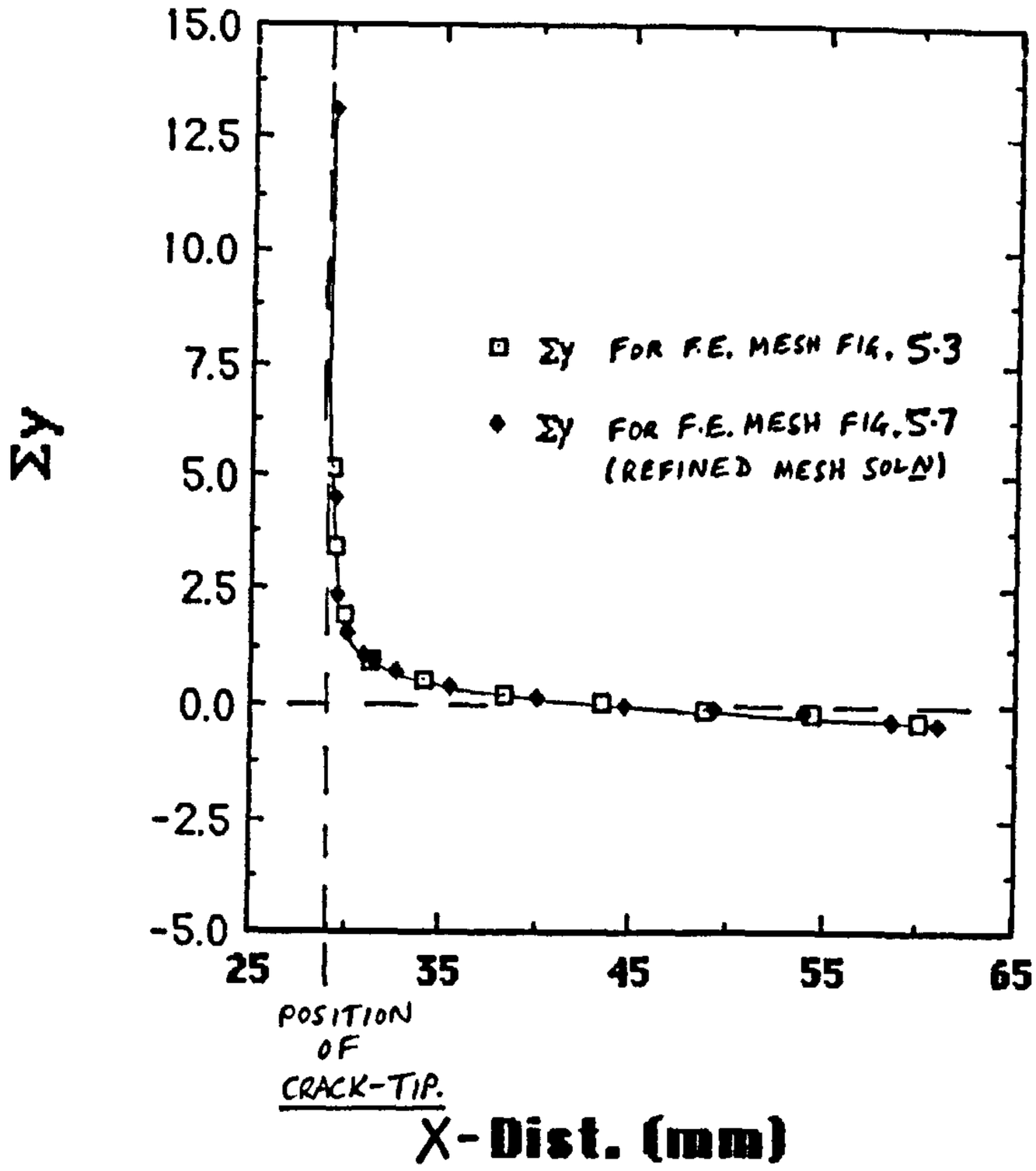

Figure 5.6: Elastic stress in the (y)-direction versus distance from the crack-tip, for the finite element mesh shown in Fig.5.3 and a more refined mesh shown in Fig.5.7.

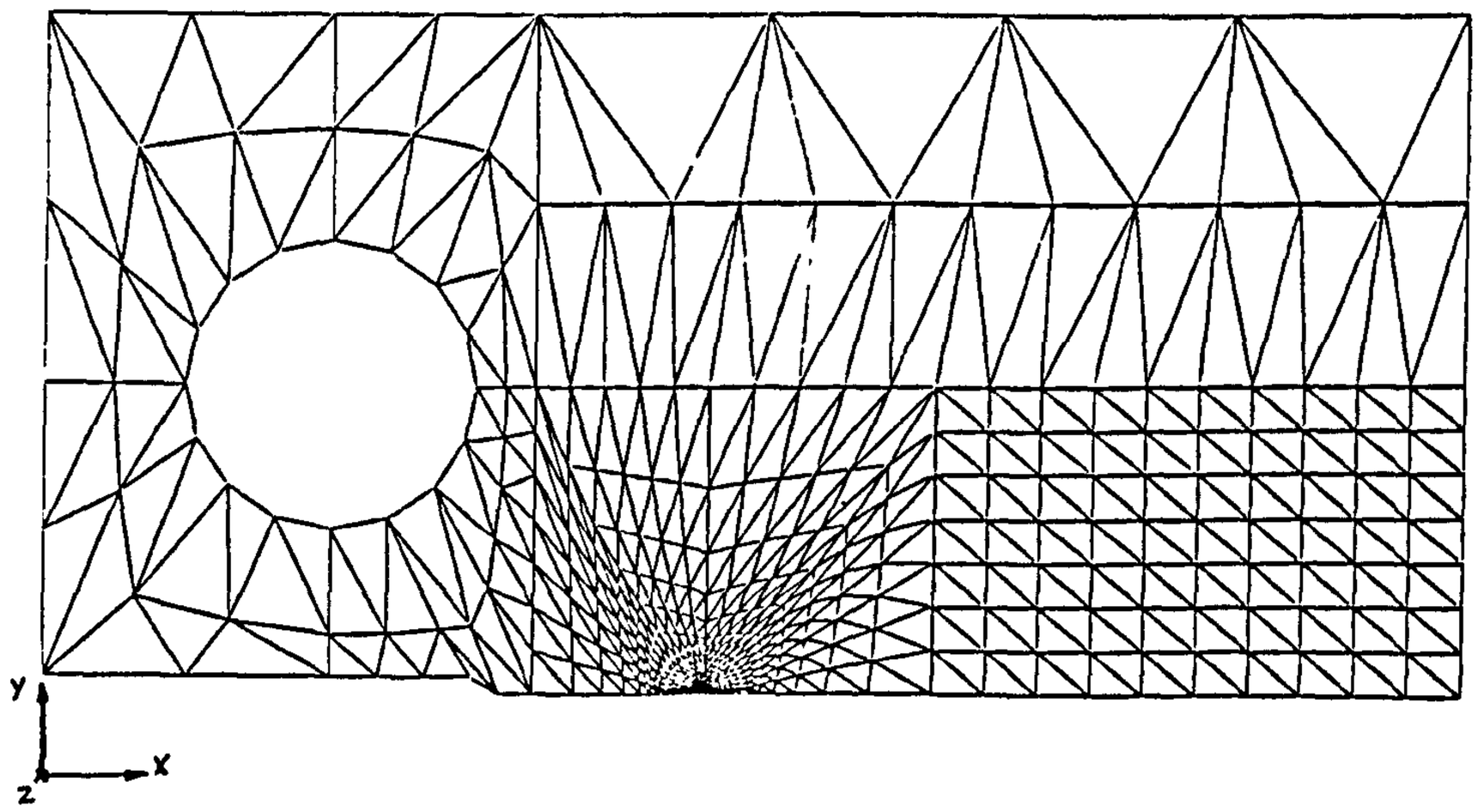

Figure 5.7: Refined compact tension specimen finite element mesh, having 844 elements.

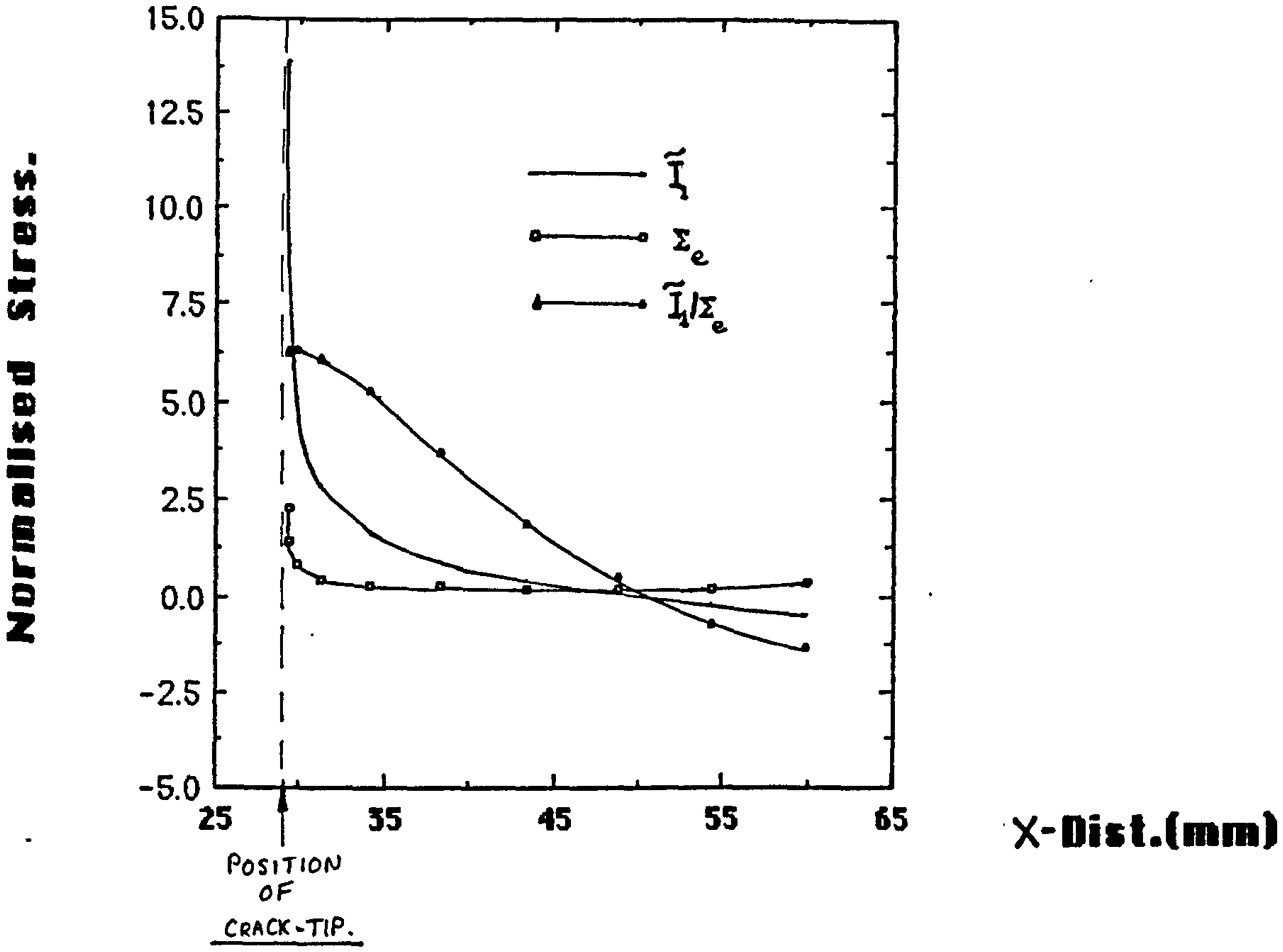

Figure 5.8: The variation of measurements of tri-axial stress state with distance from the crack-tip, from the elastic finite element solution for the mesh shown in Fig.5.3.

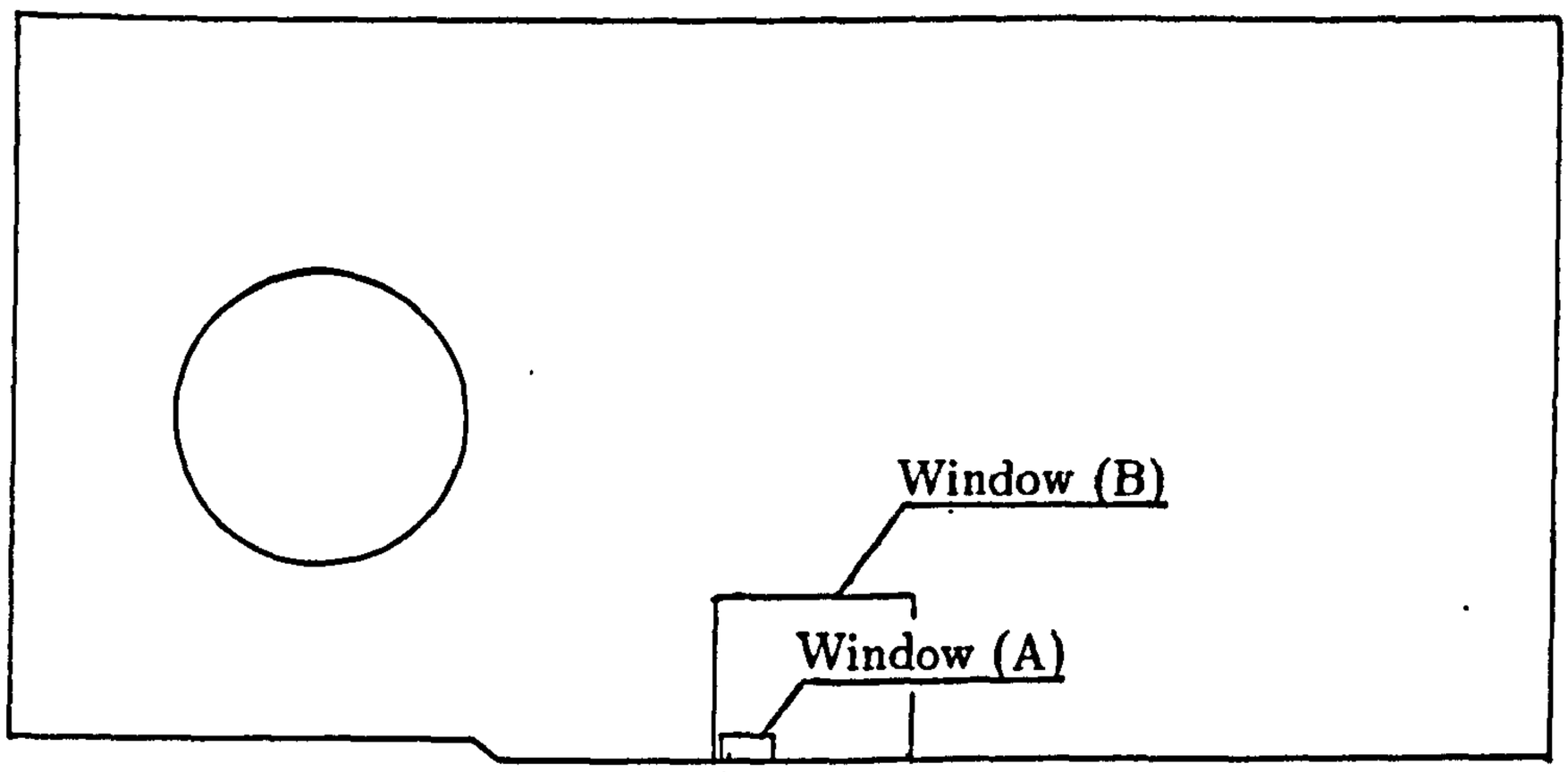

Figure 5.9: Window sizes for the failed element ($\omega > 0.9999$) plots shown in Figs. 5.10, 5.11, 5.13, 5.14, 5.18, against the outline of the compact tension specimen.
Window (A) is 2.15mm wide by 1.30mm high.
Window (B) is 8.00mm wide by 6.50mm high.

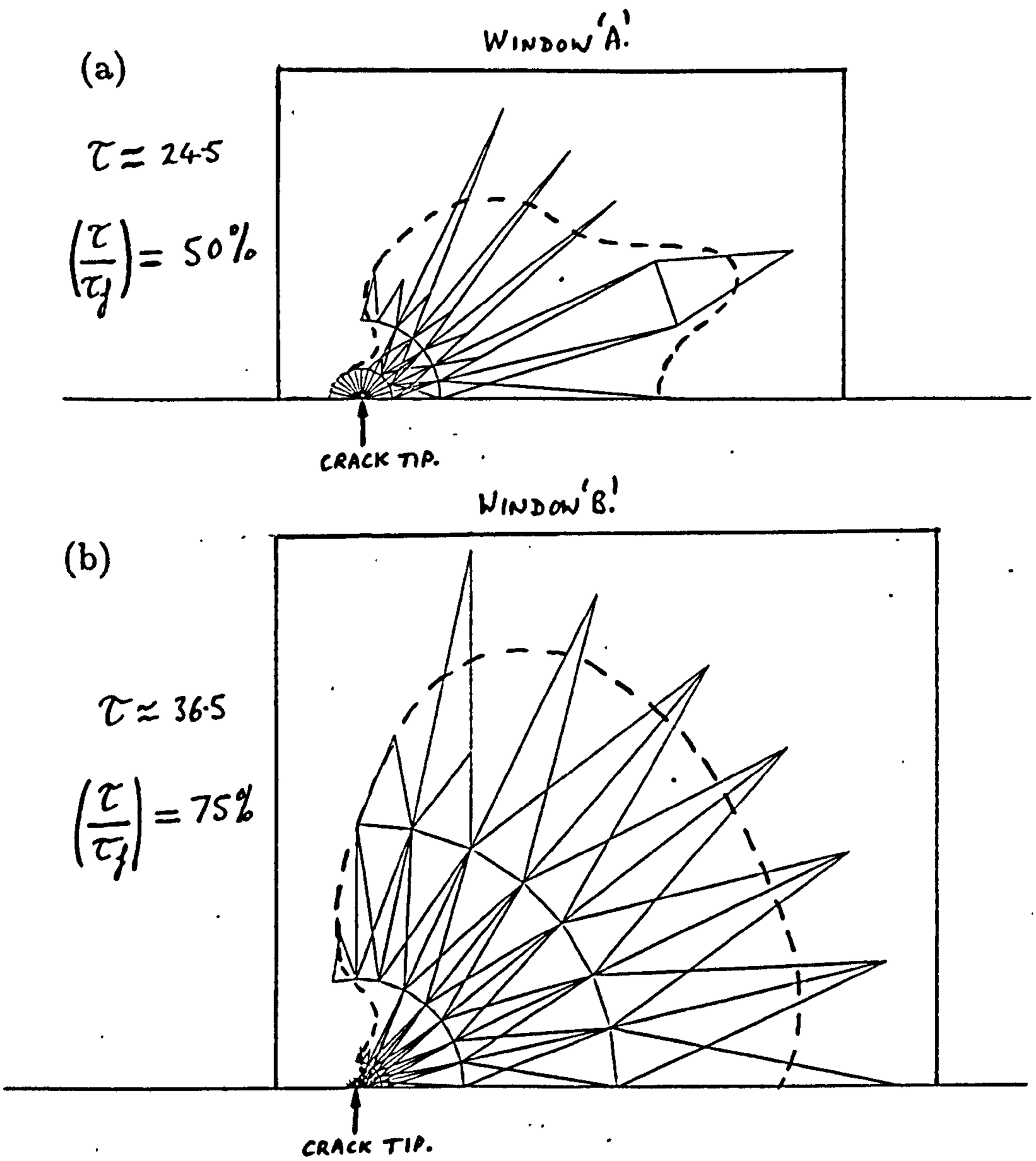

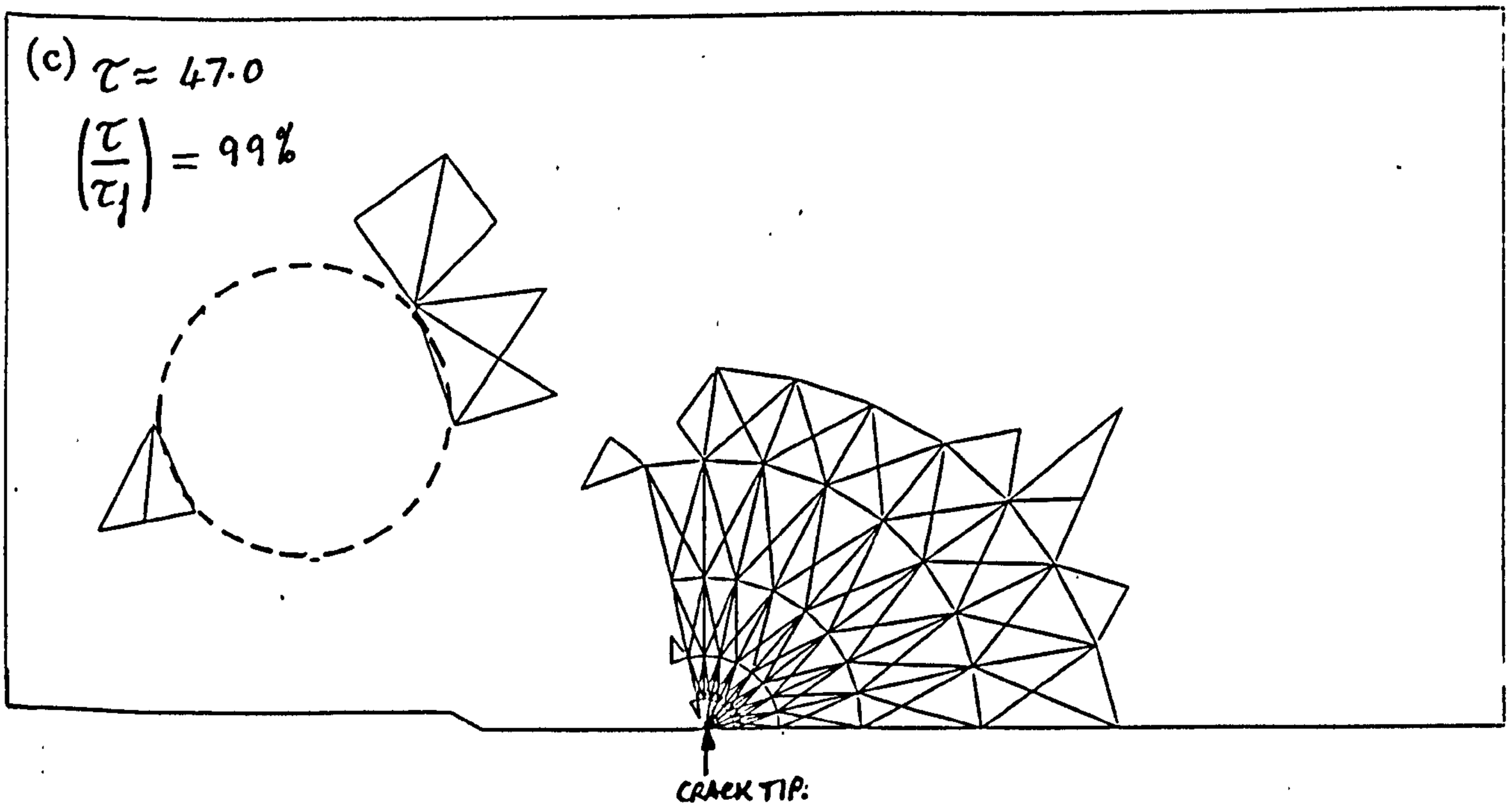

Figure 5.10: Failed element ($\omega > 0.9999$) plots, for the failure prediction of the CT-specimen in plane strain using the instantaneous method and the creep constants of Table 5.1.

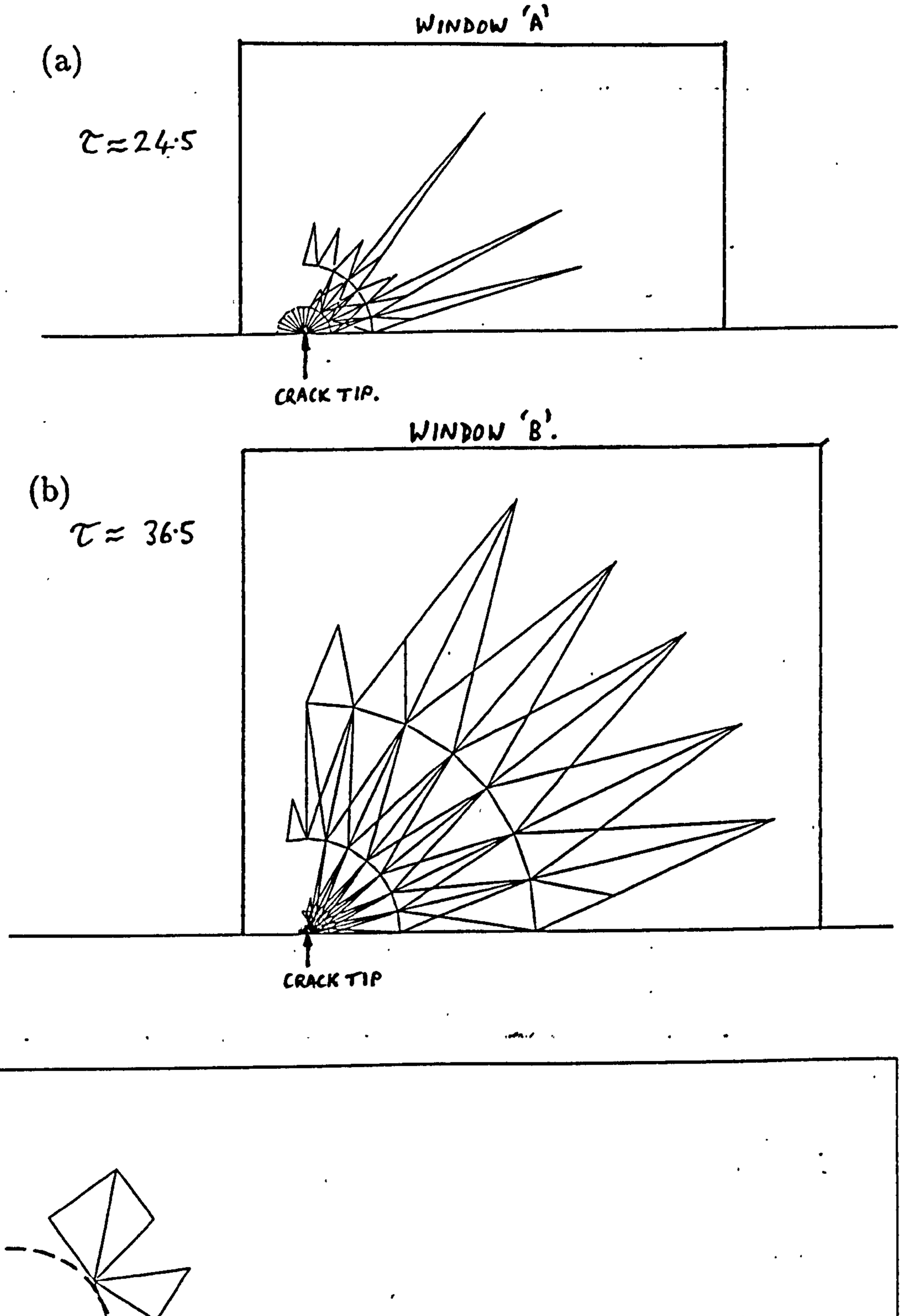

Figure 5.11: Failed element ($\omega > 0.9999$) plots, for the failure prediction of the CT-specimen in plane strain using the technique of Chaboche and the creep constants of Table 5.1.

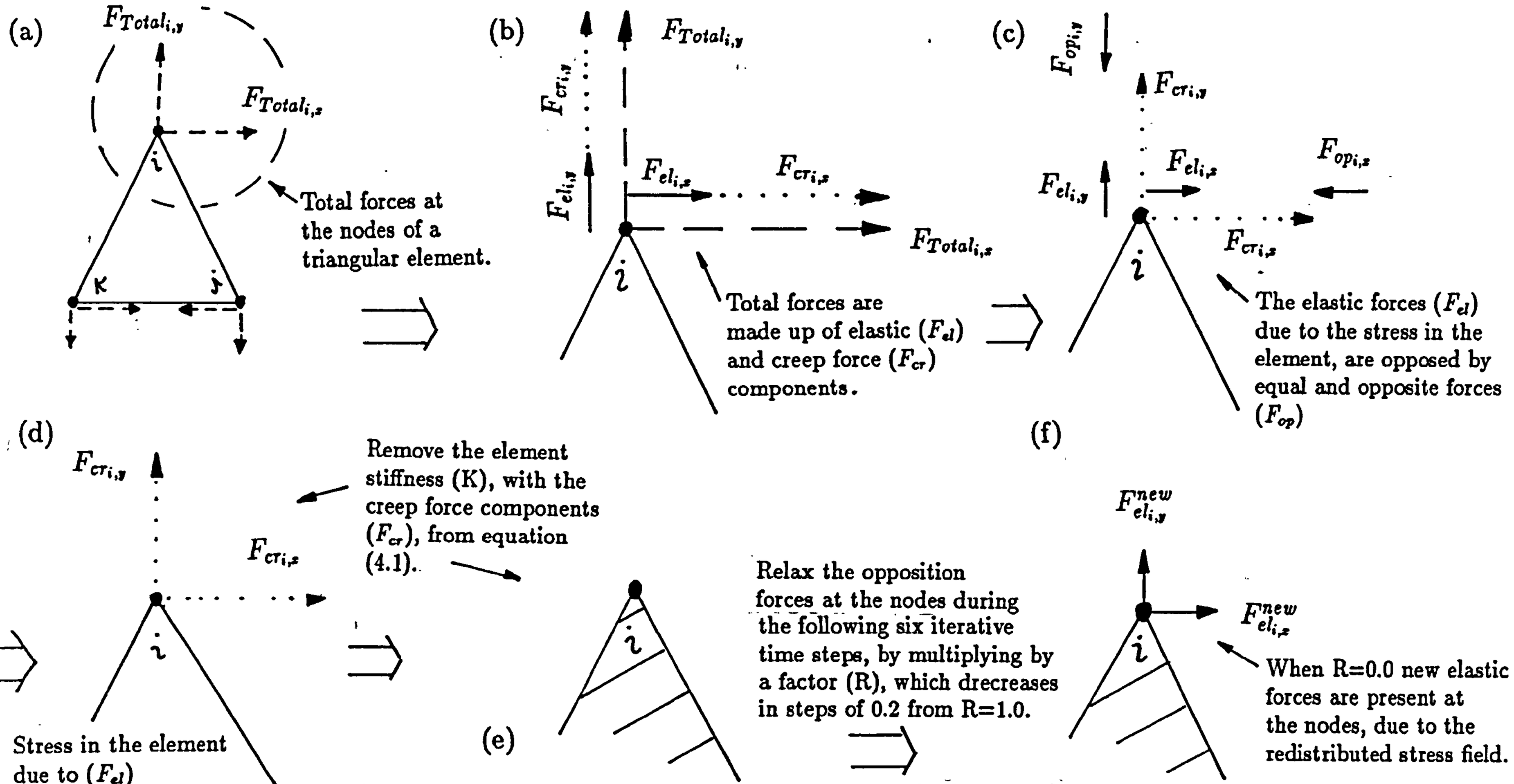

Fig.5.12: The technique of Tvergaard, showing how the forces at the nodes of a failed ($\omega > 0.9999$) triangular element are treated during the removal of the element stiffness and creep forces from equation (4.1). The circled region in (a) and the forces at node (i) are studied in (b), (c), (d), (e) and (f).

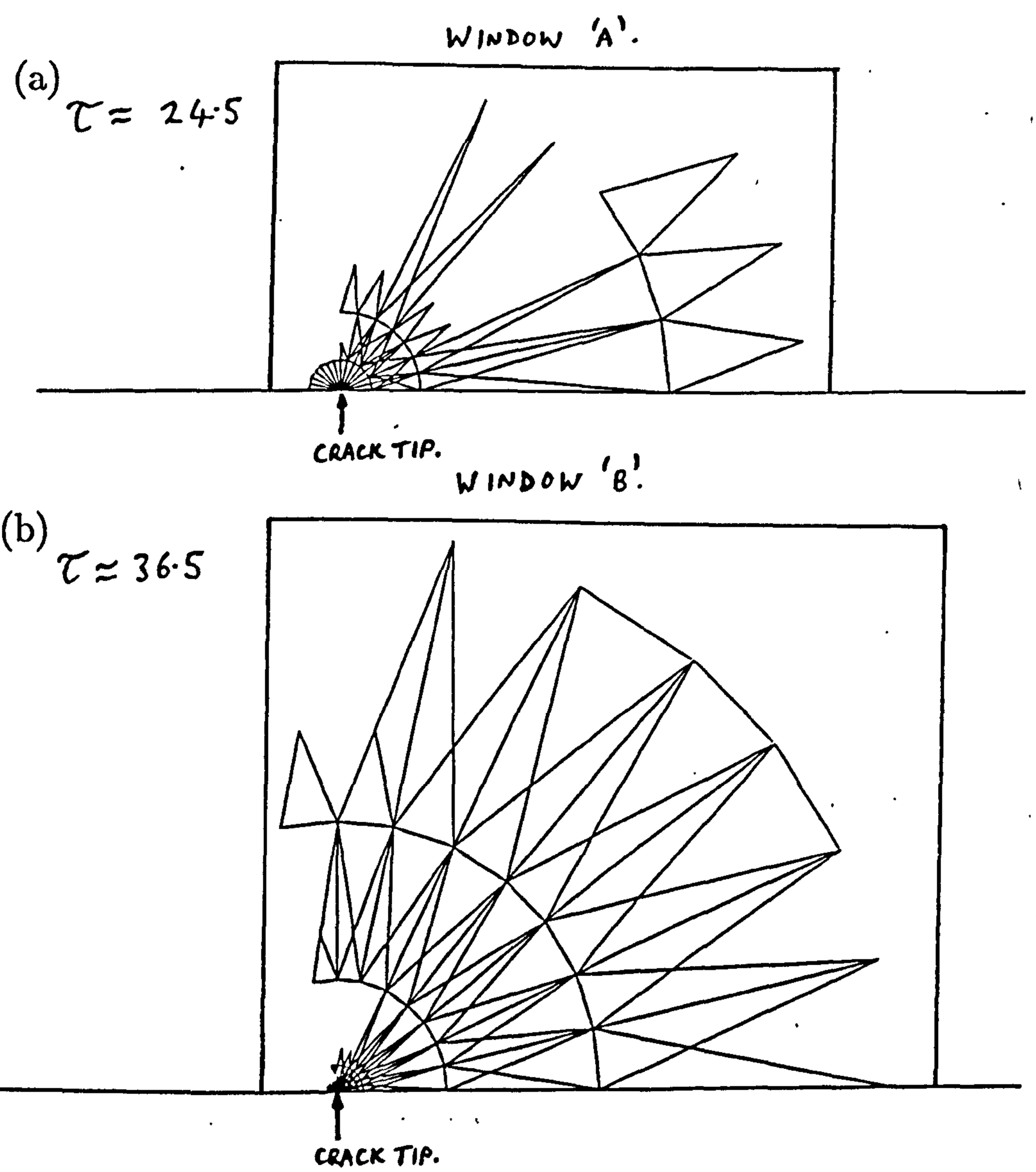

Figure 5.13: Failed element ($\omega > 0.9999$) plots, for the failure prediction of the CT-specimen in plane strain using the technique of Tvergaard and the creep constants of Table 5.1.

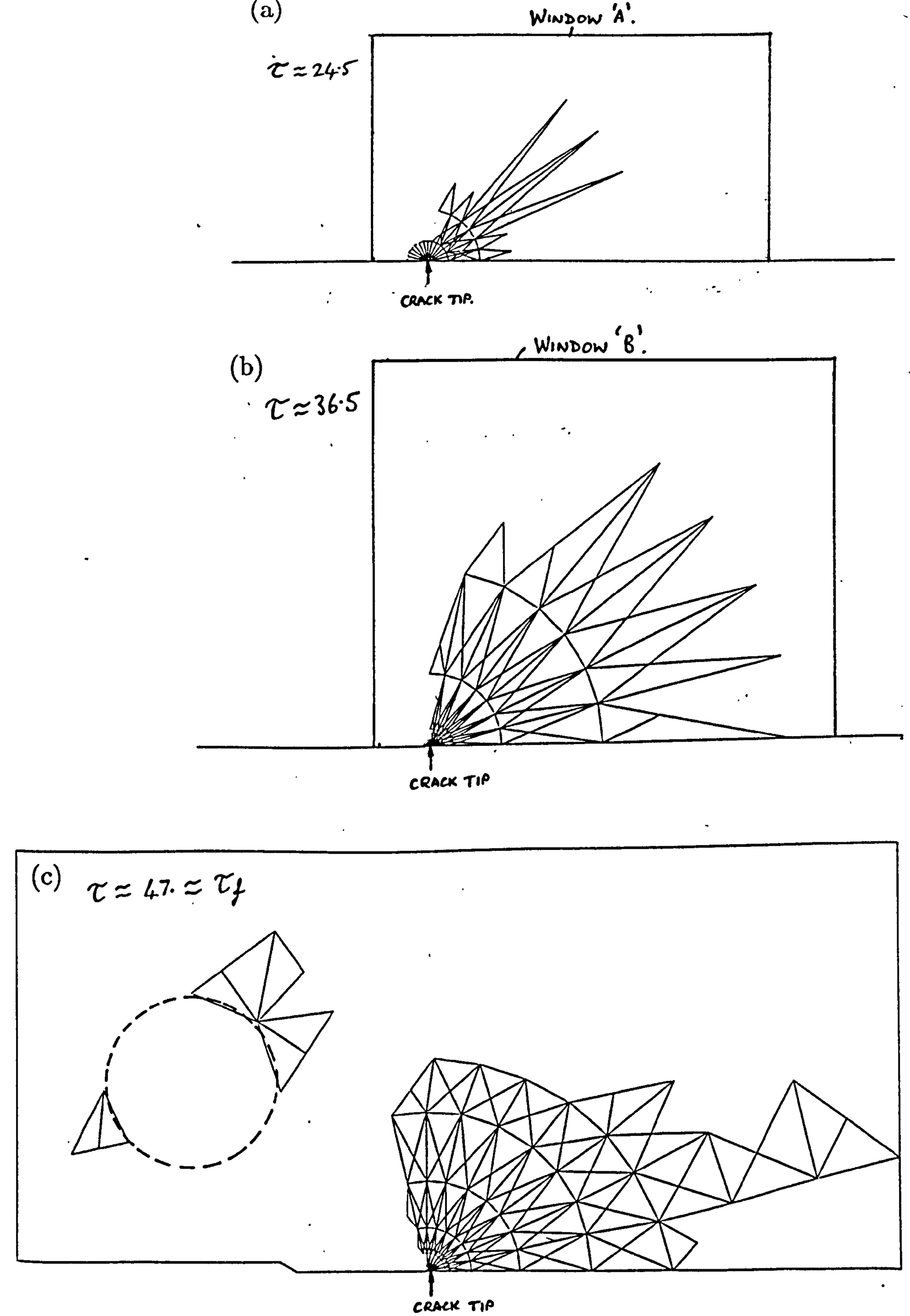

Figure 5.14: Failed element ($\omega > 0.9999$) plots, for the failure prediction of the CT-specimen in plane stress using the instantaneous technique of element removal and the creep constants of Table 5.1.

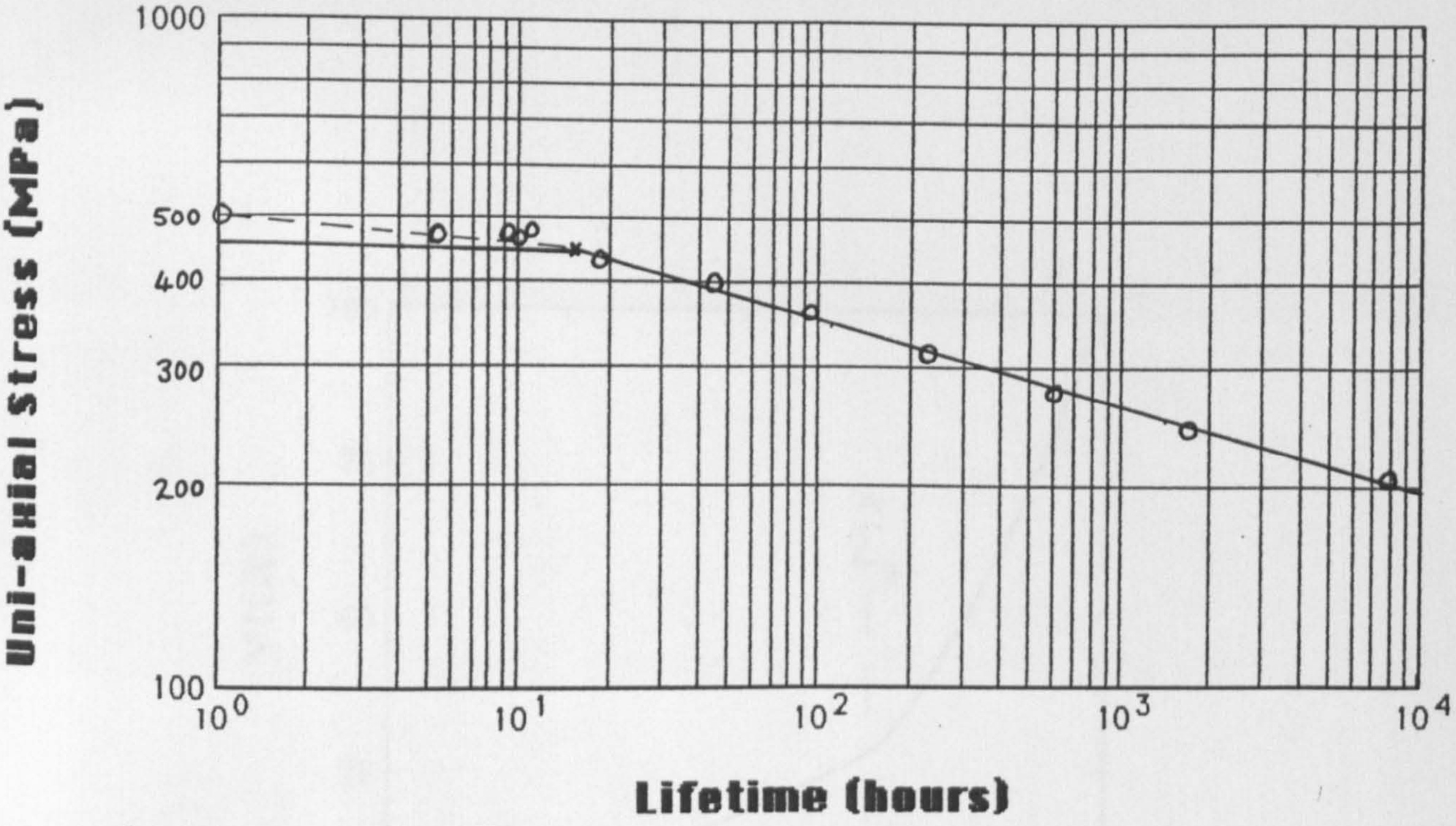

Figure 5.15: The theoretical uni-axial stress rupture lines fitted to the experimental data points (o), given by the constants of Table 5.1 and the new high stress rupture line (- -), given by the constants of Table 5.6.

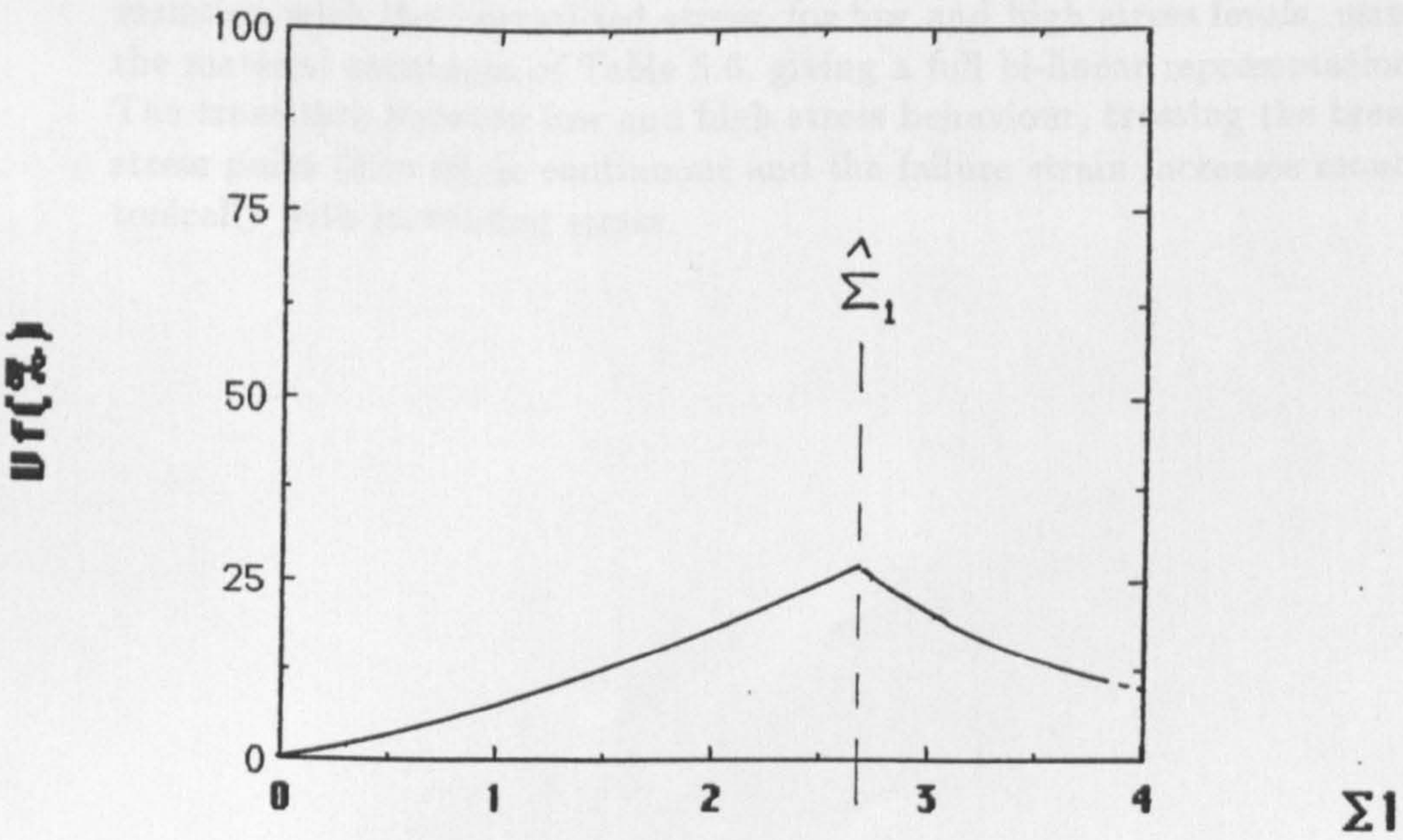

Figure 5.16: Plot of the theoretical normalised uni-axial failure strain variation with the normalised stress, for low and high stress levels, using the material constants of Table 5.1.

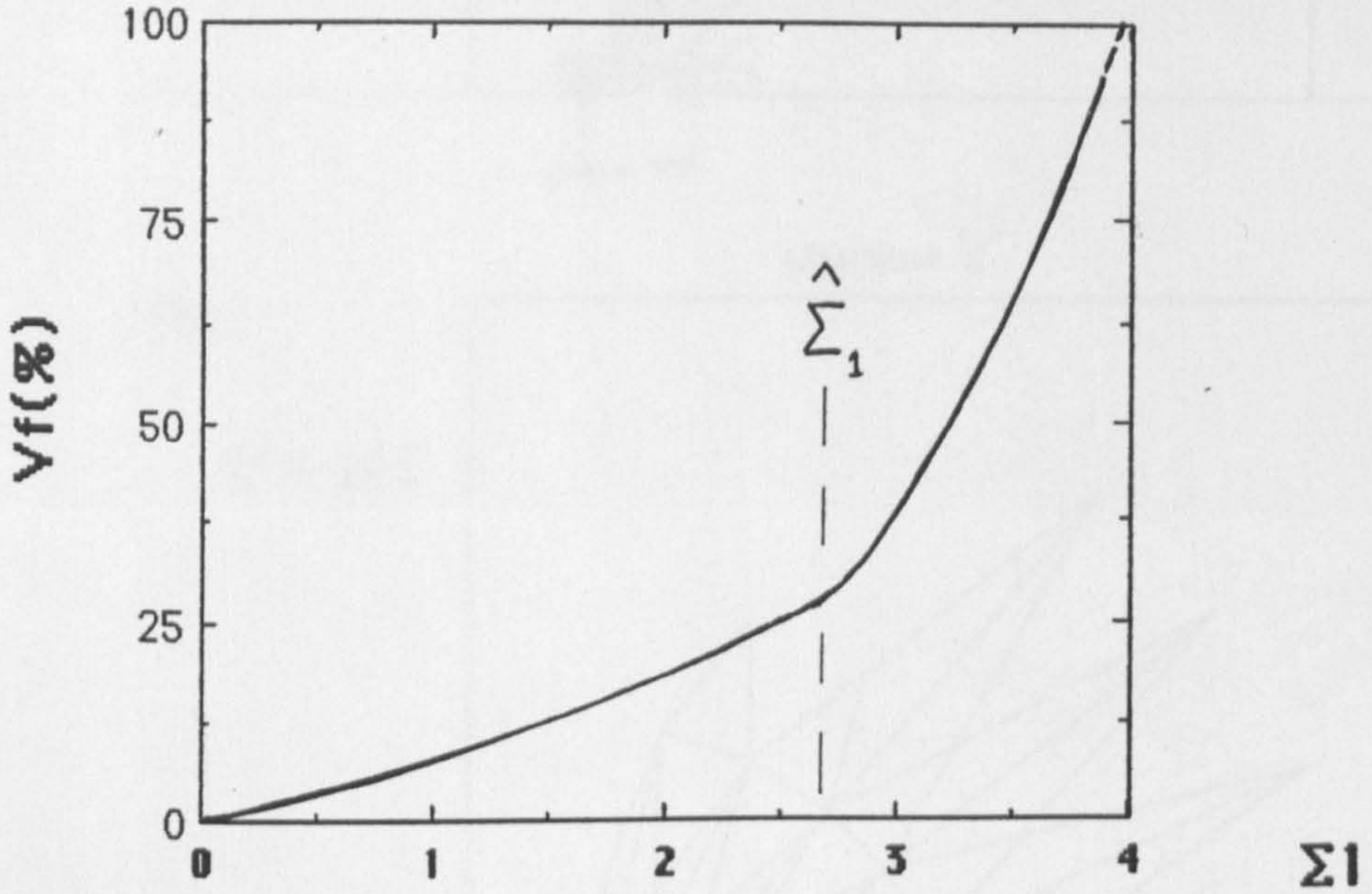

Figure 5.17: Plot of the theoretical normalised uni-axial failure strain variation with the normalised stress, for low and high stress levels, using the material constants of Table 5.6, giving a full bi-linear representation. The transition between low and high stress behaviour, crossing the break stress point ($\sigma = \hat{\sigma}$), is continuous and the failure strain increases monotonically with increasing stress.

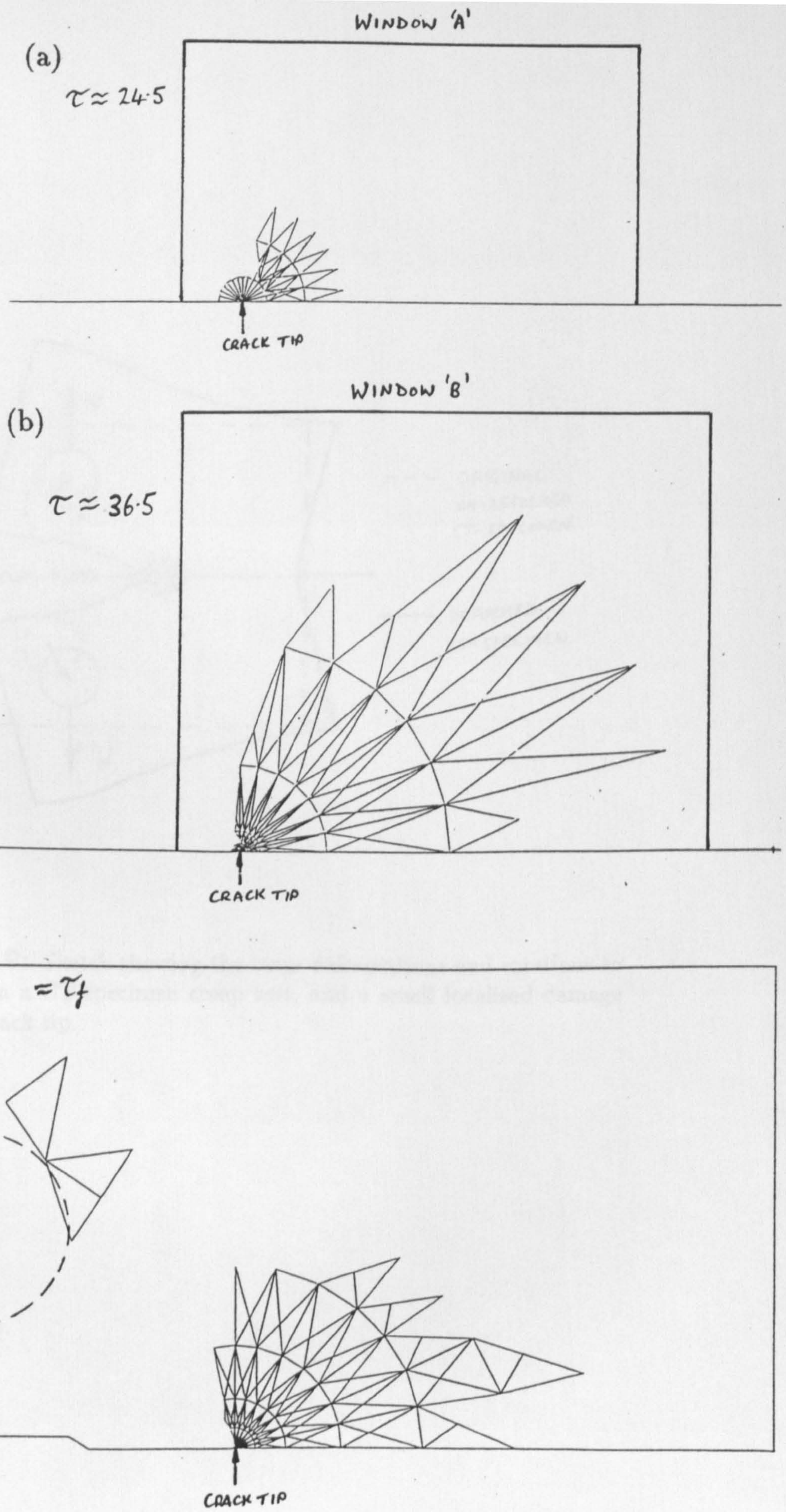

Figure 5.18: Failed element ($\omega > 0.9999$) plots, for the failure prediction of the CT-specimen in plane stress using the instantaneous technique of element removal and the new creep constants of Table 5.6, giving a full bi-linear representation of material behaviour.

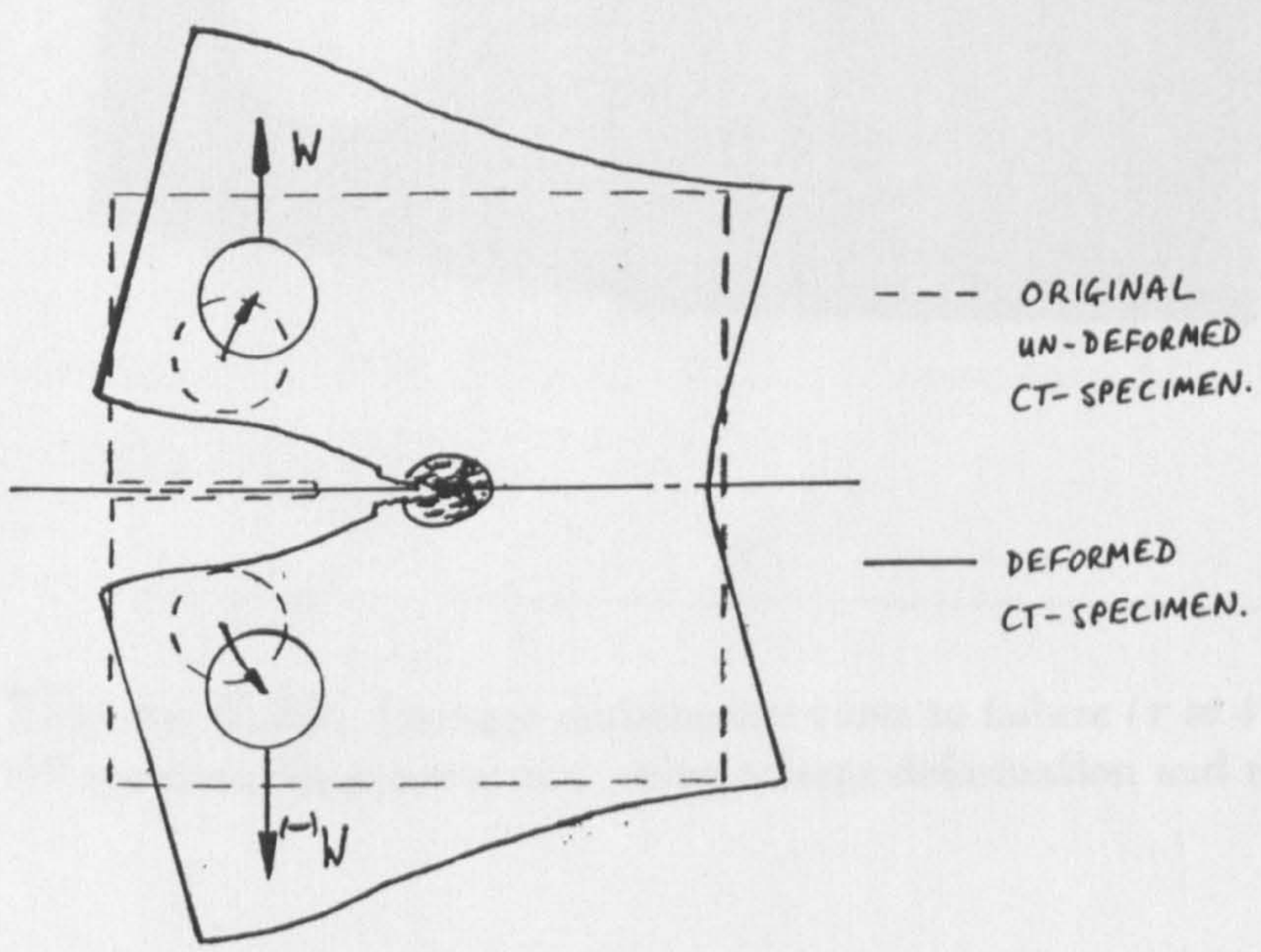

Figure 5.19: Sketch showing the large deformations and rotations to be expected in a CT-specimen creep test, and a small localised damage zone at the crack tip.

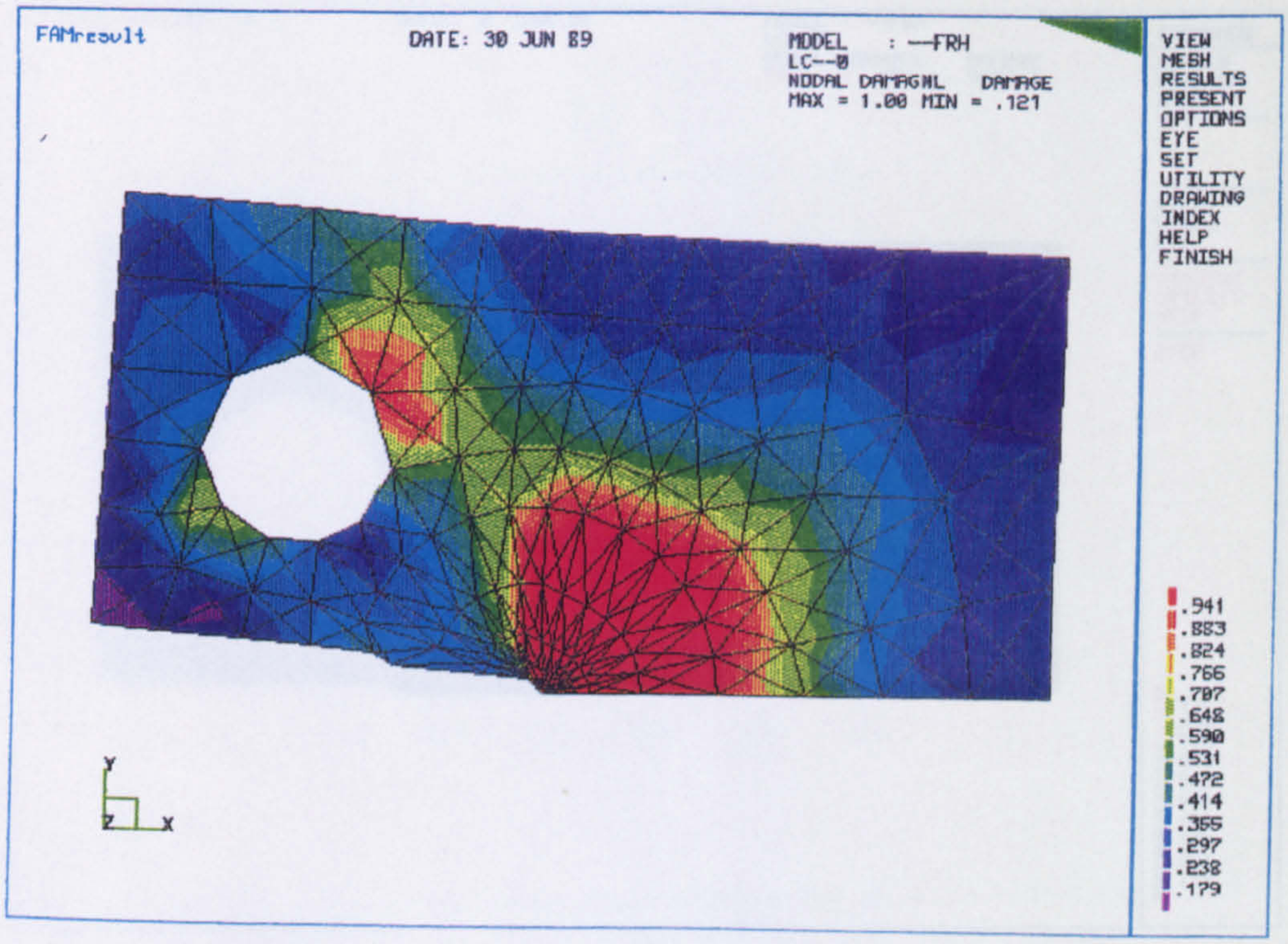

Figure 5.20: Damage distribution close to failure ($\tau \approx 47.0$) for the CT-specimen in plane strain, using a large deformation and rotation analysis.

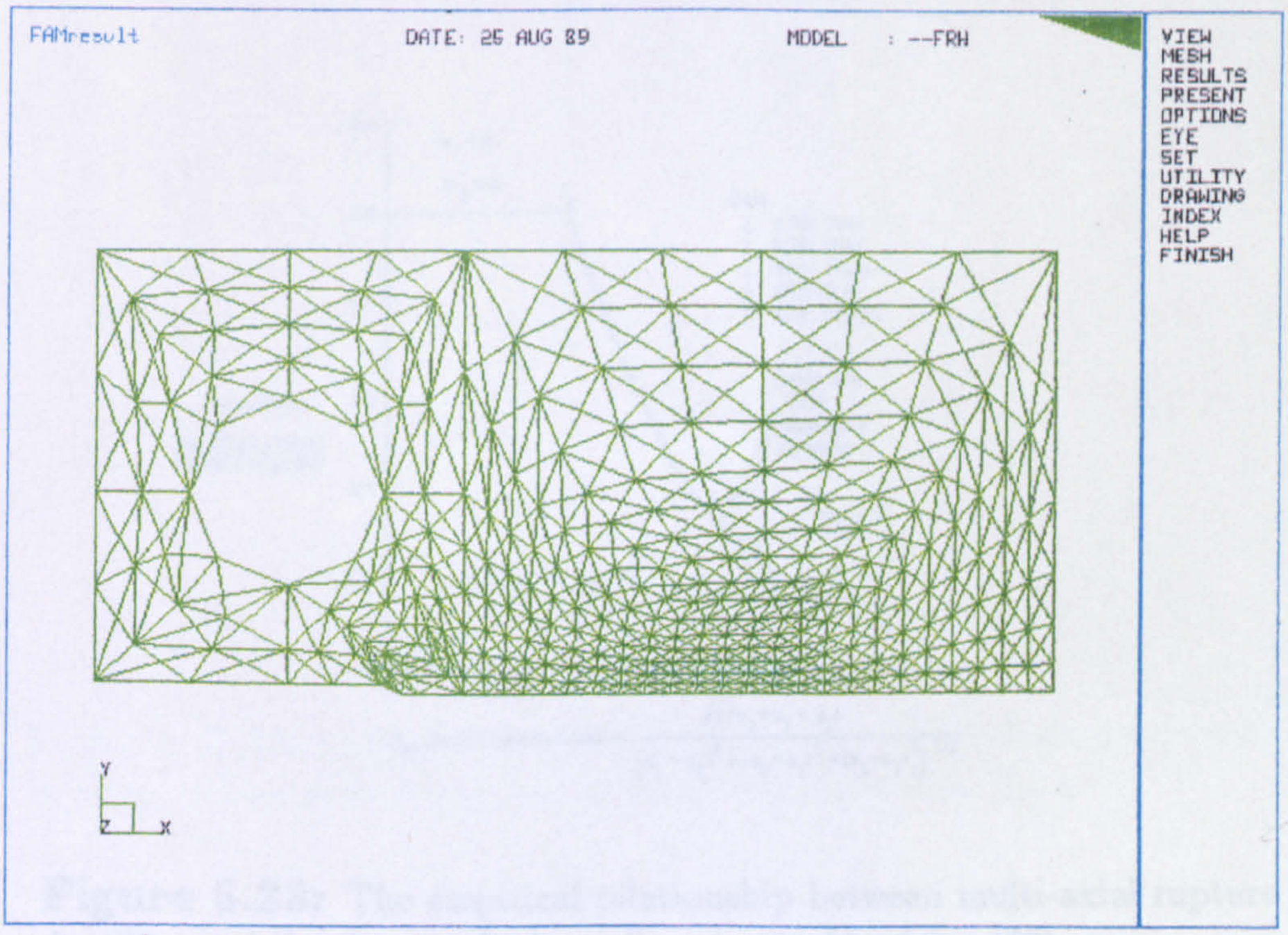

Figure 5.21: Finite element mesh generated to represent the CT-specimen and has a constant mesh refinement across the ligament.

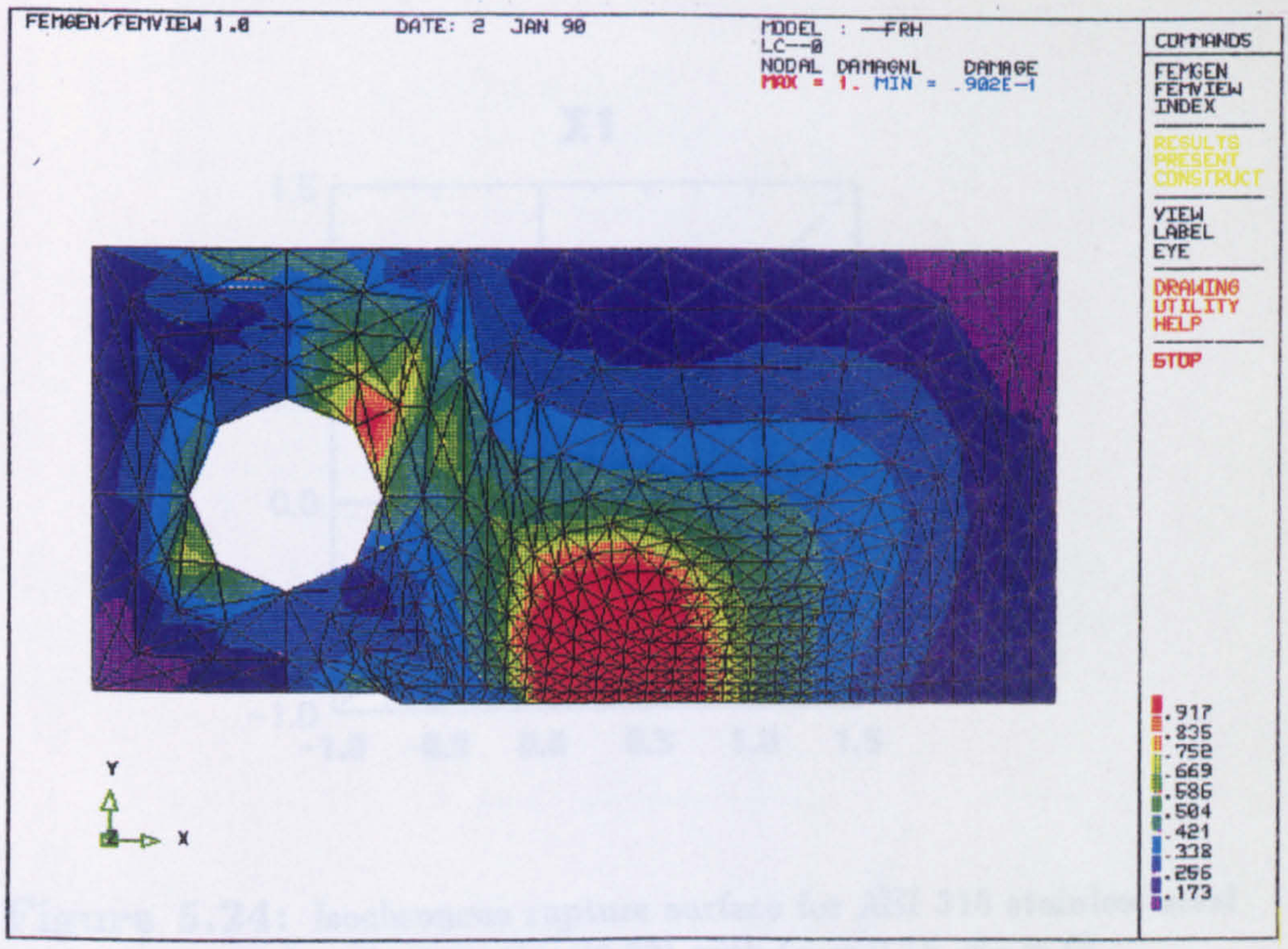

Figure 5.22: Damage distribution close to failure ($\tau = 44.1$) for the CT-specimen, using the finite element mesh of Fig.5.21, in plane strain.

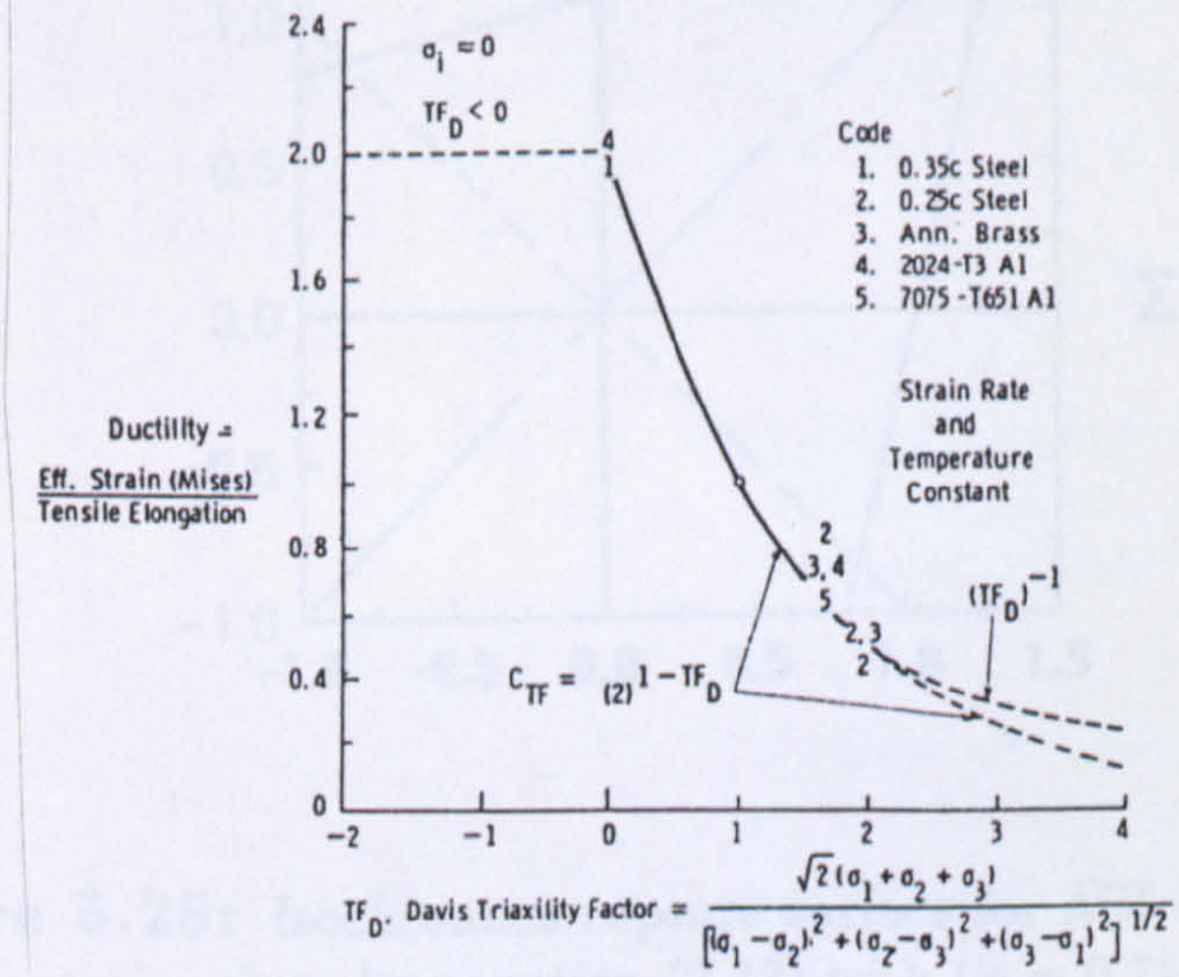

Figure 5.23: The empirical relationship between multi-axial rupture ductility and the degree of tri-axiality, due to Manjoine [78].

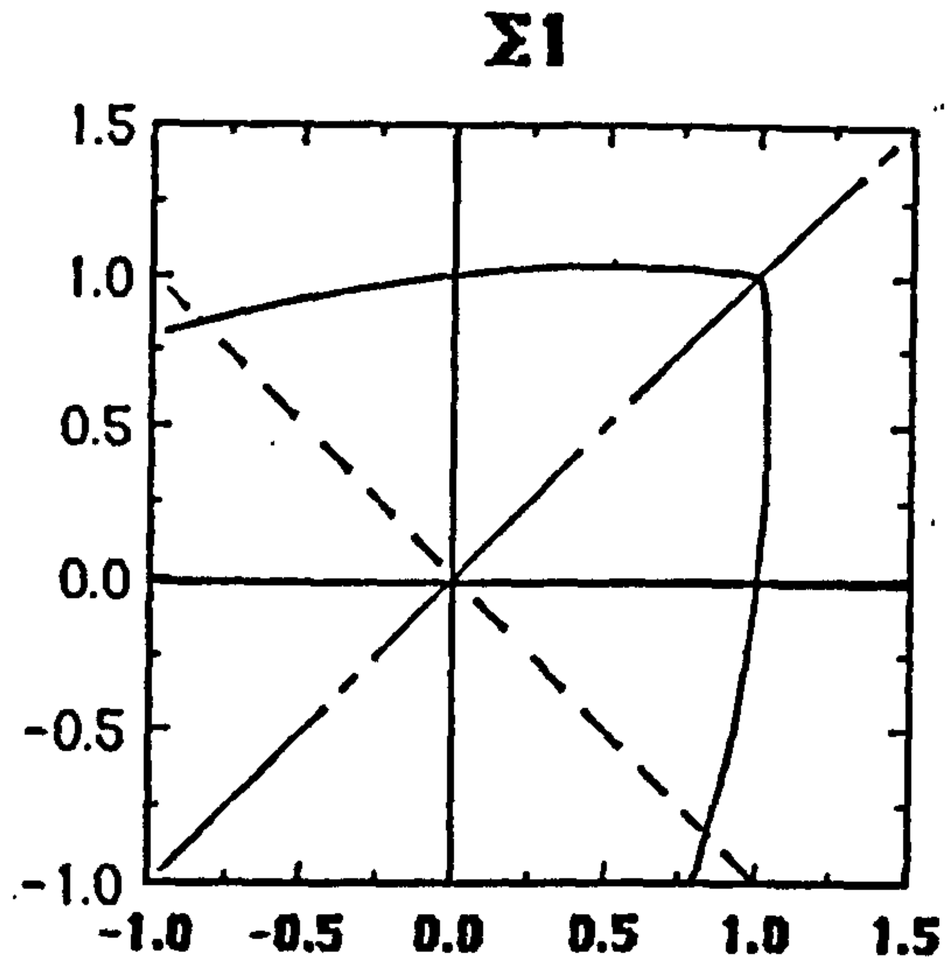

Figure 5.24: Isochronous rupture surface for AISI 316 stainless steel in plane stress, given by equation (2.32) with ($\alpha = 0.75$, $\beta_H = 0$).

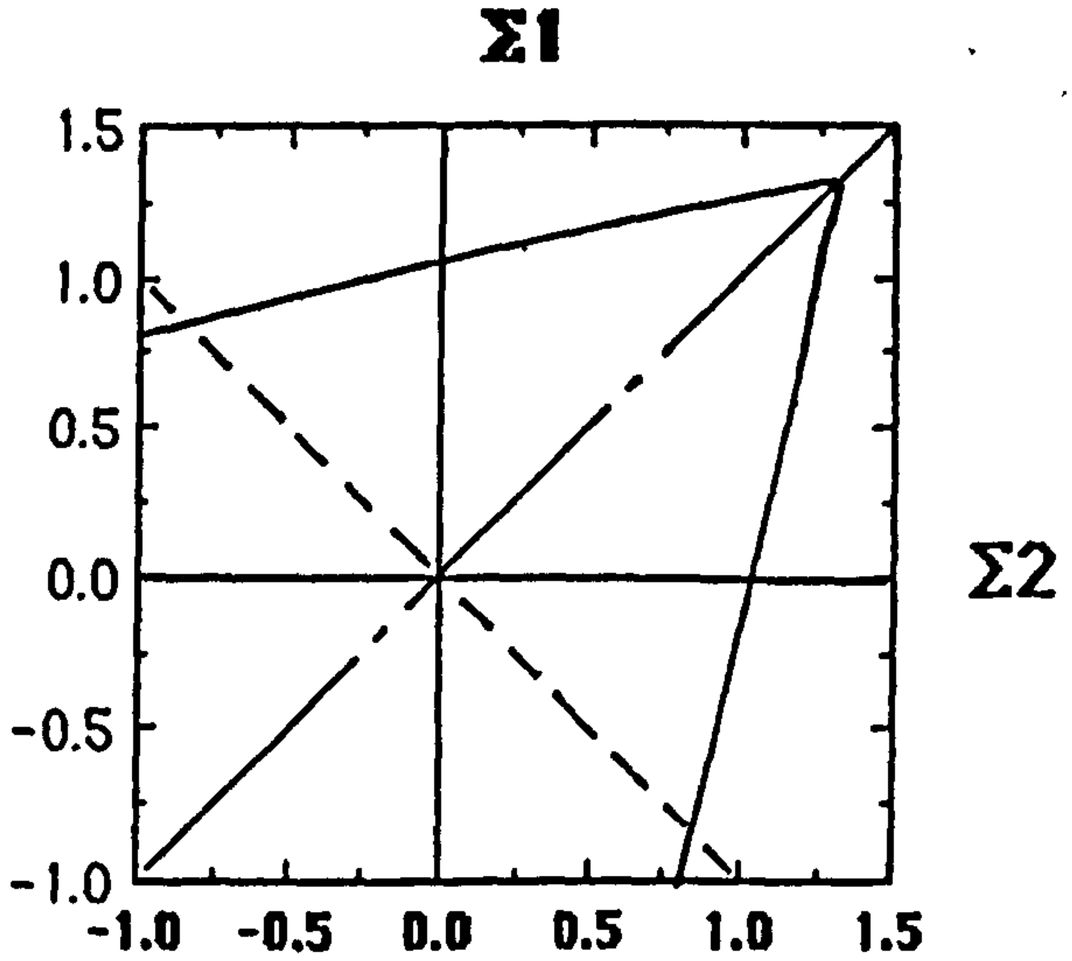

Figure 5.25: Isochronous rupture surface for AISI 316 stainless steel in plane strain, given by equation (2.33) with ($\alpha = 0.75$, $\beta_H = 0$).

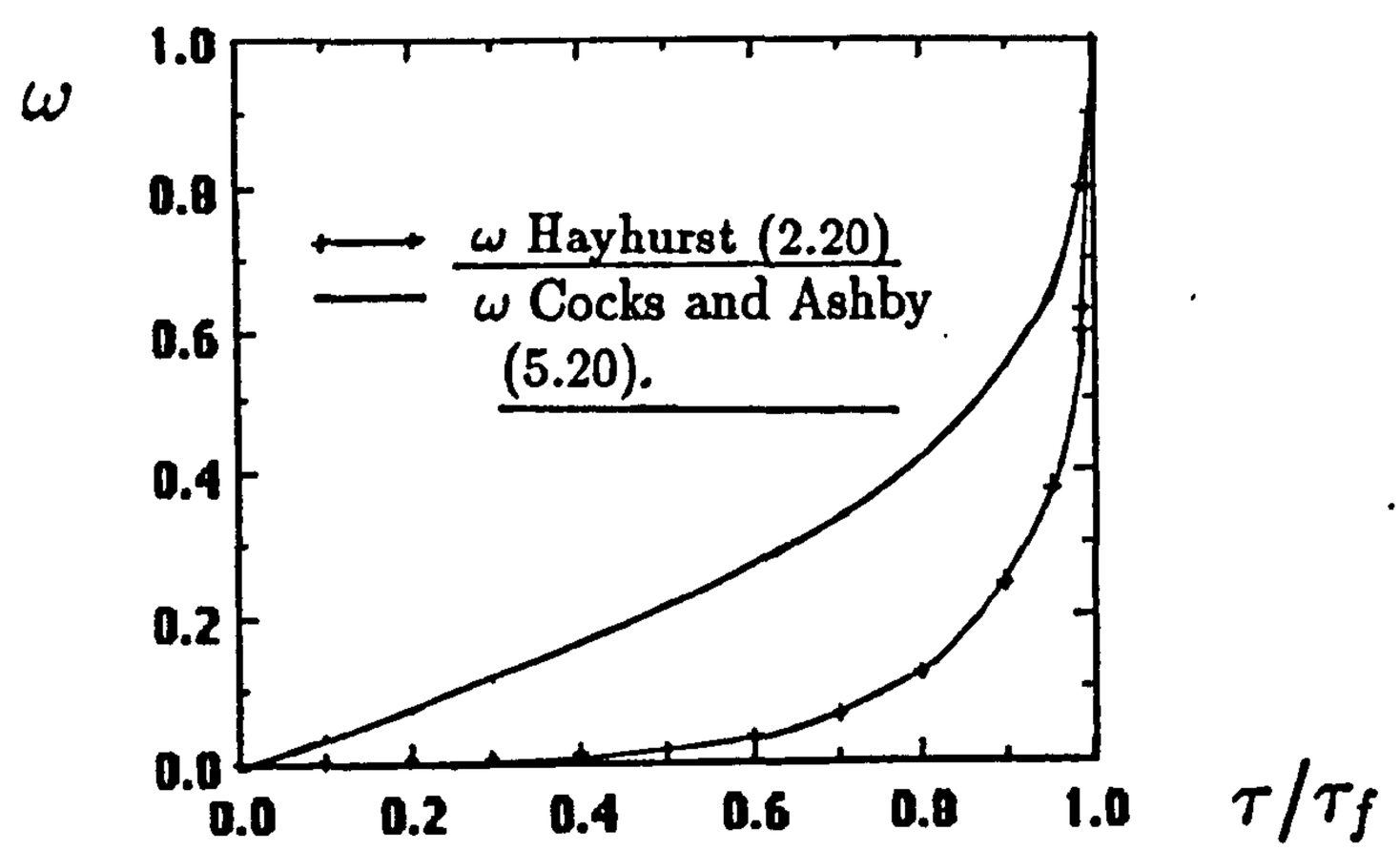

Figure 5.26: Graph showing the differences in the damage evolution rates predicted by the equation of Hayhurst (2.20) and that of the Cocks and Ashby model (5.24).

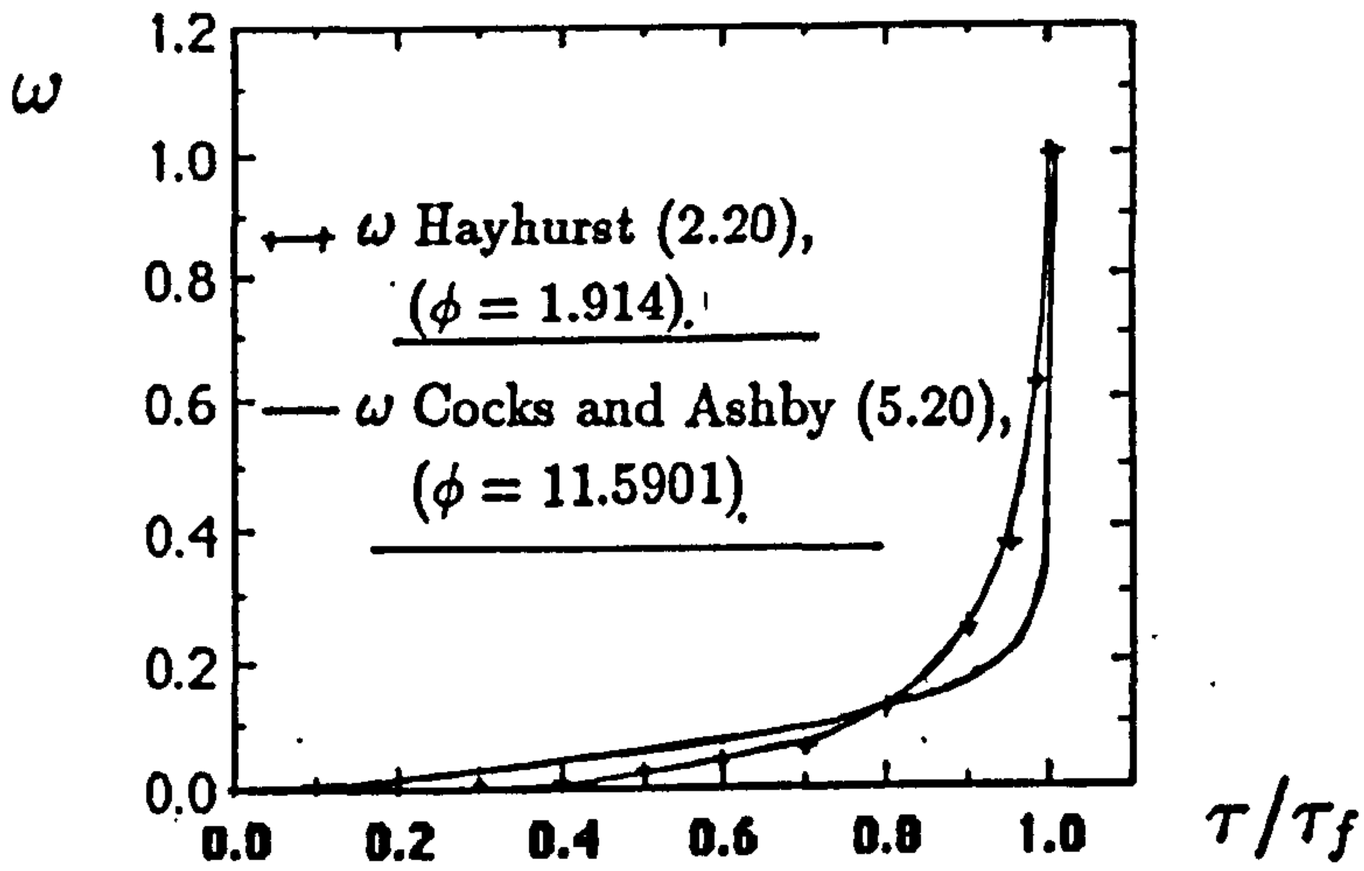

Figure 5.27: Graph showing the comparison between the damage rates predicted by the equation of Hayhurst (2.20) and that of the Cocks and Ashby model (5.24), when the creep constant (ϕ) is changed from 1.914 to 11.590 in the former equation.

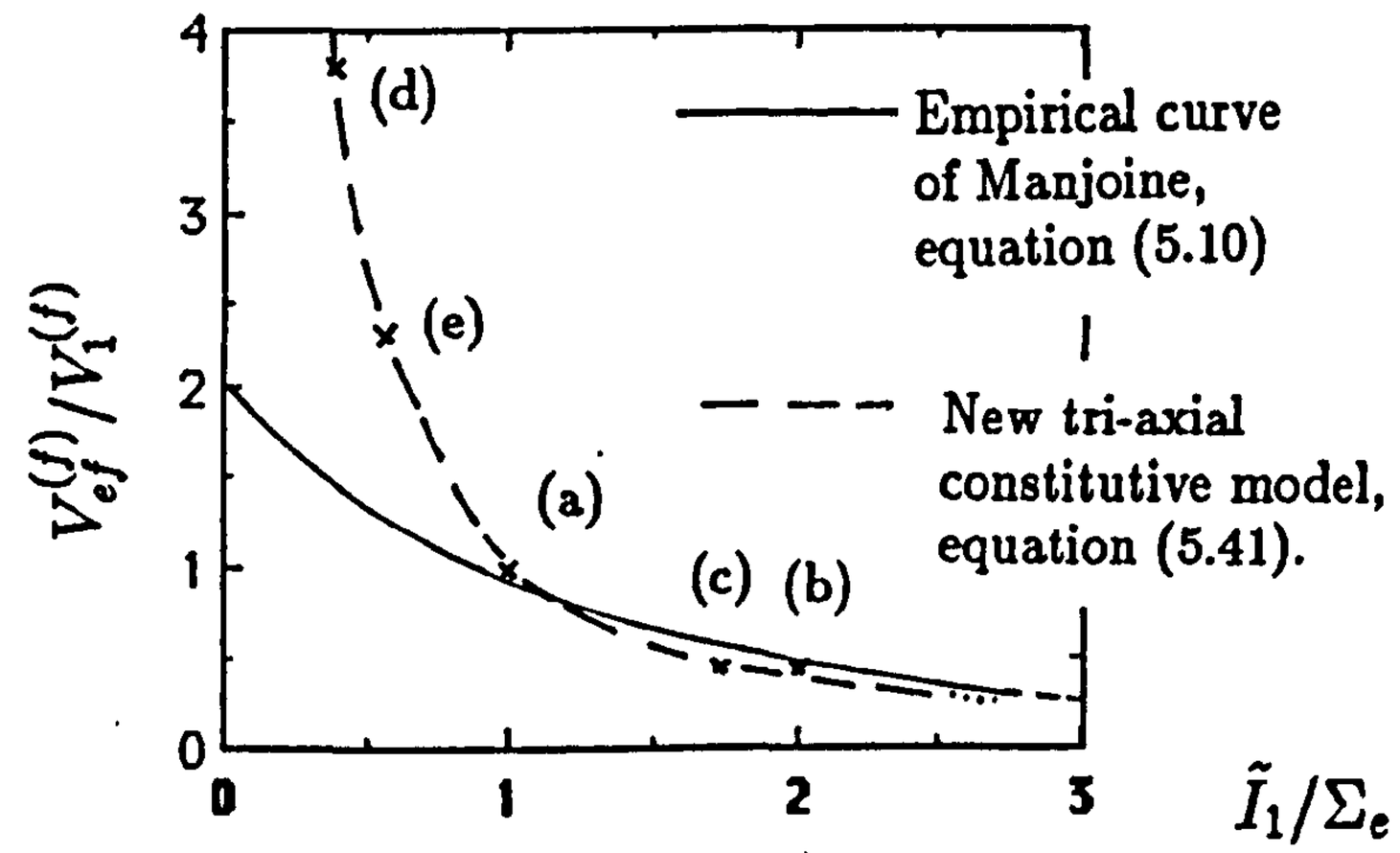

Figure 5.28: Comparison of the multi-axial rupture ductility predicted by the new constitutive model (equation(5.41)) with the empirical curve of Manjoine [78], Fig.5.23.

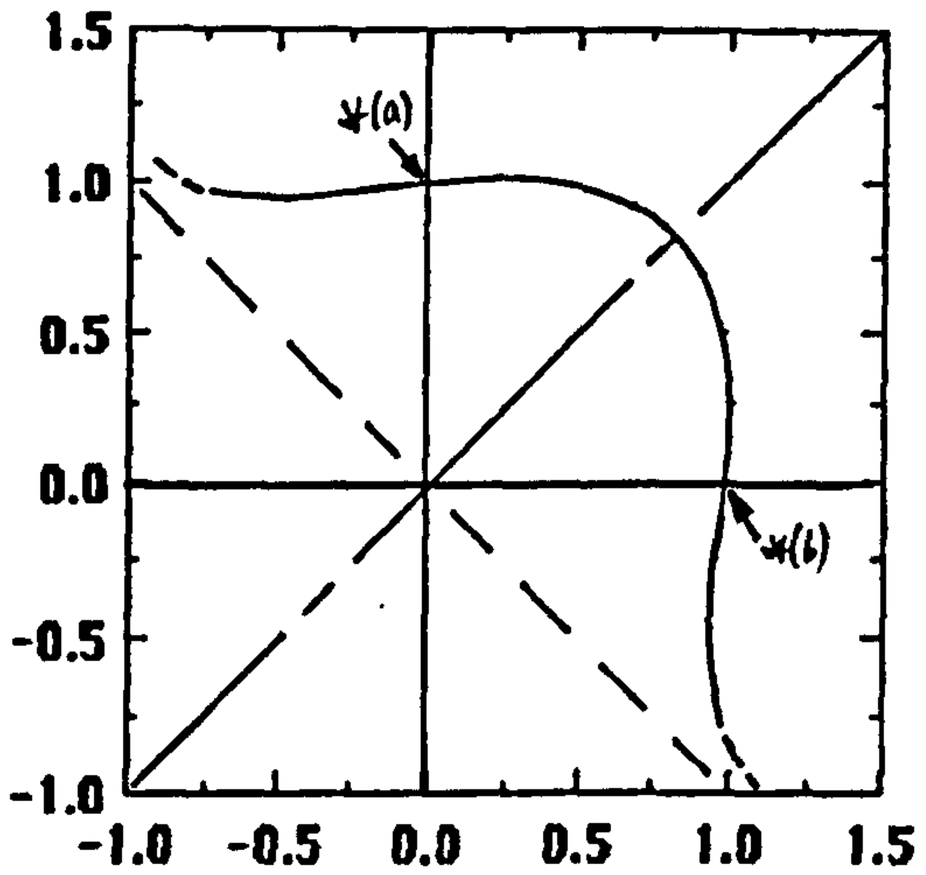

Figure 5.29: Isochronous rupture surface in plane stress for a material with a value of ($\chi = 5$), using equation (5.47).

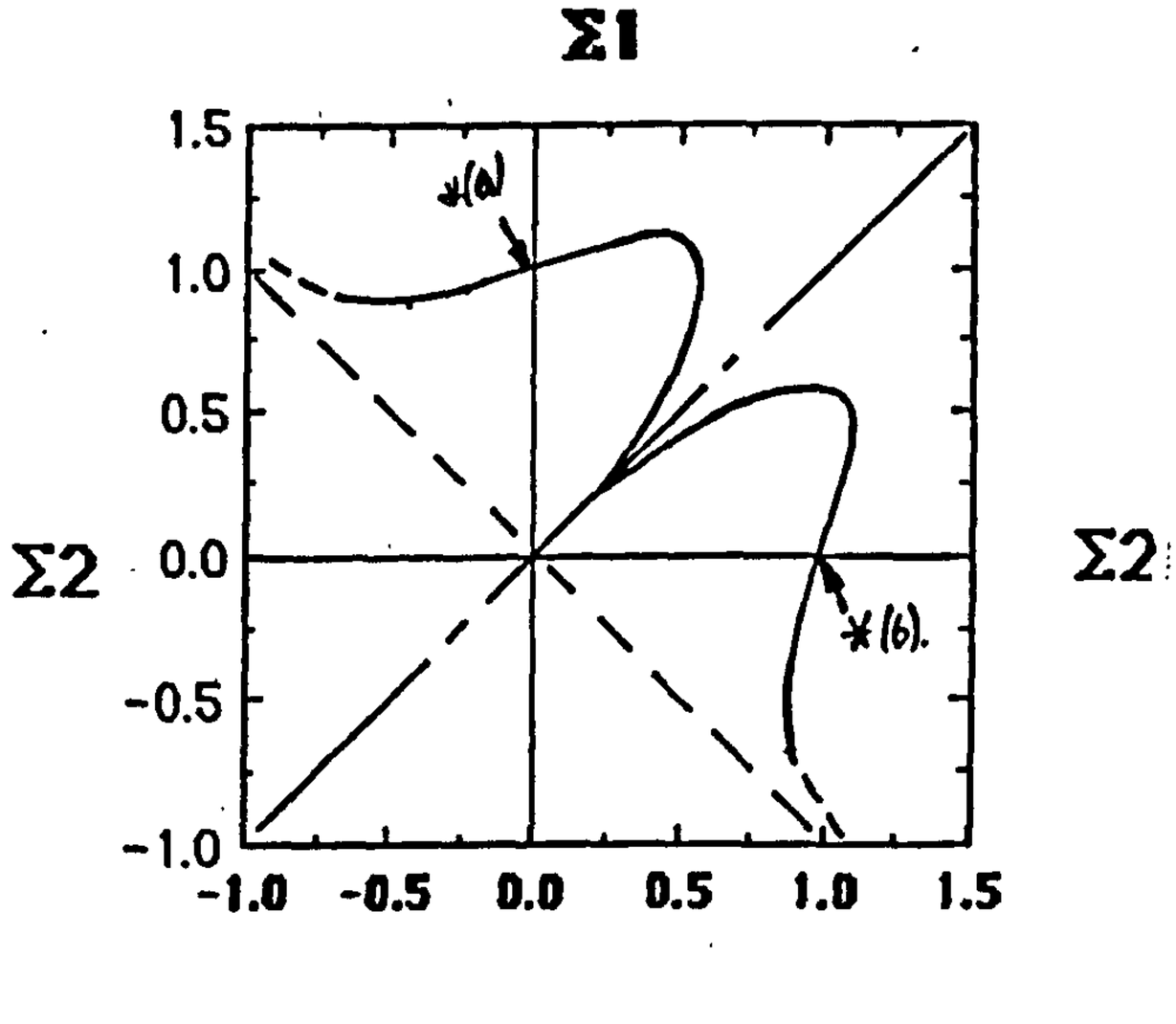

Figure 5.30: Isochronous rupture surface in plane strain for a material with a value of ($\chi = 5$), using equation (5.48).

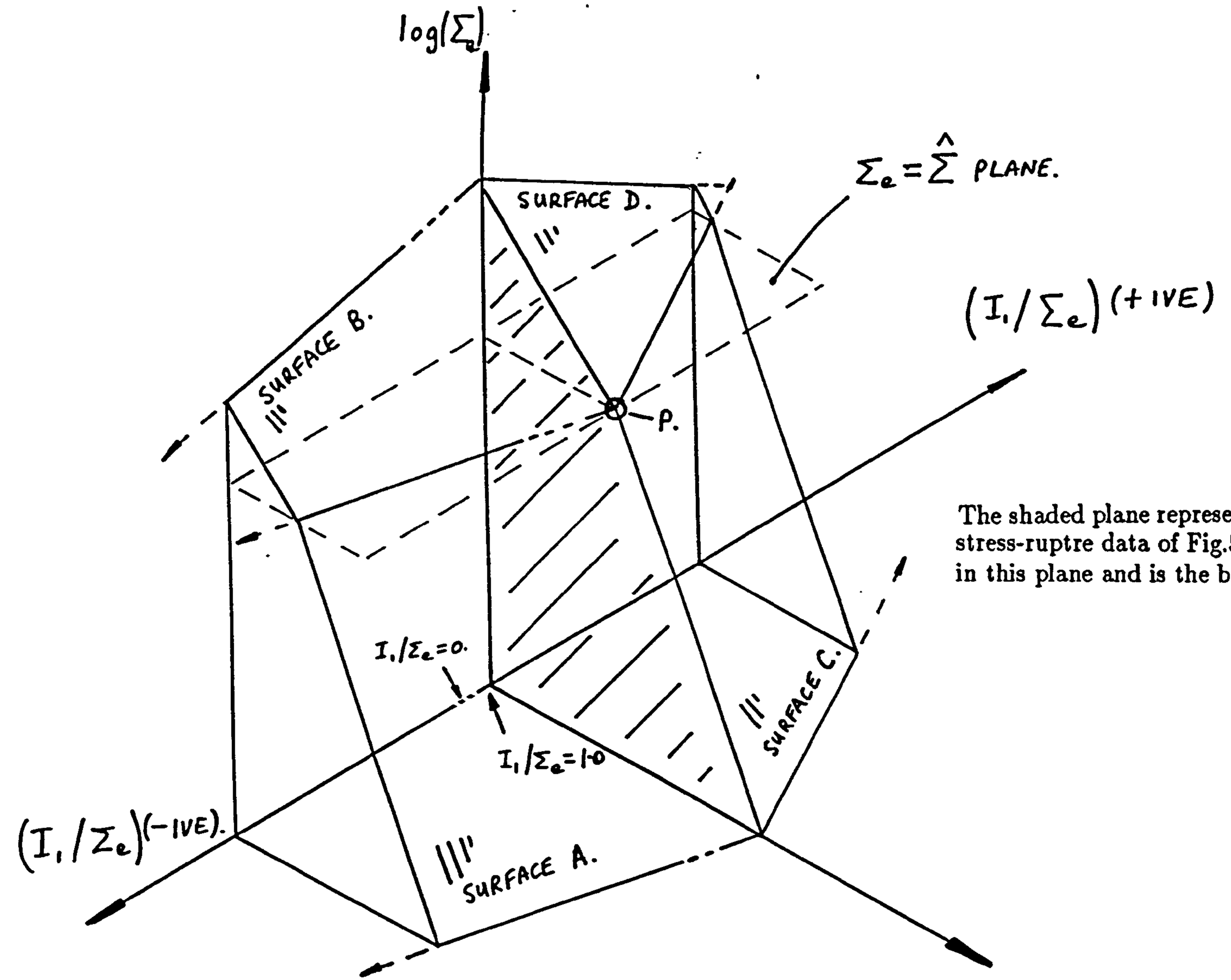

The shaded plane represents the uni-axial stress-ruptre data of Fig.5.2. Point (P) lies in this plane and is the break-stress point.

Figure 5.31: Graphical 3-D rupture surface representation of the new creep continuum damage model, using both the equations of Hayhurst and the Cocks/Ashby model (Fig.5.32), to allow for the effects of the tri-axial *stress state on rupture.*

Low Stress.

Equations (A).

$$\frac{dV}{d\tau} = \frac{3}{2}\frac{\Sigma_{ef}^{n_{II}-1}}{(1-\omega)^{n_{II}}}S_{ij} \quad \text{(A1)}$$

$$\frac{d\omega}{d\tau} = \frac{\{\alpha\Sigma_1 + (1-\alpha)\Sigma_{ef}\}^{\chi_{II}}}{V_u(1+\phi_{II})(1-\omega)^{\phi_{II}}} \quad \text{(A2)}$$

High Stress.

Equations (B).

$\Sigma_{ef} > \tilde{\Sigma}$ or $\{\alpha\Sigma_1 + (1-\alpha)\Sigma_{ef}\} > \tilde{\Sigma}$

$$\frac{dV}{d\tau} = \frac{3}{2}\frac{\hat{\Sigma}^{(n_{II}-n_I)}\Sigma_{ef}^{n_I-1}}{(1-\omega)^{n_I}}S_{ij} \quad \text{(B1)}$$

$$\frac{d\omega}{d\tau} = \frac{\hat{\Sigma}^{(\chi_{II}-\chi_I)}\{\alpha\Sigma_1 + (1-\alpha)\Sigma_{ef}\}^{\chi_I}}{V_u(1+\phi_I)(1-\omega)^{\phi_I}} \quad \text{(B2)}$$

Σ_1 or $\Sigma_2 \leq 0$

Equations (C).

$$\frac{dV}{d\tau} = \frac{3}{2}\left\{1 + \frac{\beta''_{CA_{II}}}{(1-\omega)^{n_{II}}} - \beta''_{CA_{II}}\right\}\Sigma_{ef}^{n_{II}-1}S_{ij} \quad \text{(C1)}$$

$$\frac{d\omega}{d\tau} = \frac{\beta''_{CA_{II}}\Sigma_{ef}^{\chi_{II}}}{V_u(1+\phi_{II})(1-\omega)^{\phi_{II}}} \quad \text{(C2)}$$

$$\beta''_{CA_{II}} = \left\{sinh\left(0.8814\left(\tilde{I}_1\right)\right\}^{n_{II}(m+1)} \quad \text{(C3)}$$

Σ_1 or $\Sigma_2 \leq 0$

Equations (D).

$\Sigma_{ef} > \tilde{\Sigma}$

$$\frac{dV}{d\tau} = \frac{3}{2}\hat{\Sigma}^{(n_{II}-n_I)}\left\{1 + \frac{\beta''_{CA_I}}{(1-\omega)^{n_I}} - \beta''_{CA_I}\right\}\Sigma_{ef}^{n_I-1}S_{ij} \quad \text{(D1)}$$

$\Sigma_{ef} > \tilde{\Sigma}$

$$\frac{d\omega}{d\tau} = \frac{\beta''_{CA_I}\hat{\Sigma}^{(\chi_{II}-\chi_I)}\Sigma_{ef}^{\chi_I}}{V_u(1+\phi_I)(1-\omega)^{\phi_I}} \quad \text{(D2)}$$

$$\beta''_{CA_I} = \left\{sinh\left(0.8814\left(\tilde{I}_1\right)\right\}^{n_I(m+1)} \quad \text{(D3)}$$

For $\Sigma_1 \leq 0 \Rightarrow \Sigma_1 = 0$ and only Σ_{ef} contributes to the damage rate.

Figure 5.32: The series of constitutive and damage laws defining the new continuum damage model, used to represent the rupture surfaces (A),(B),(C) and (D) in Fig.5.31.

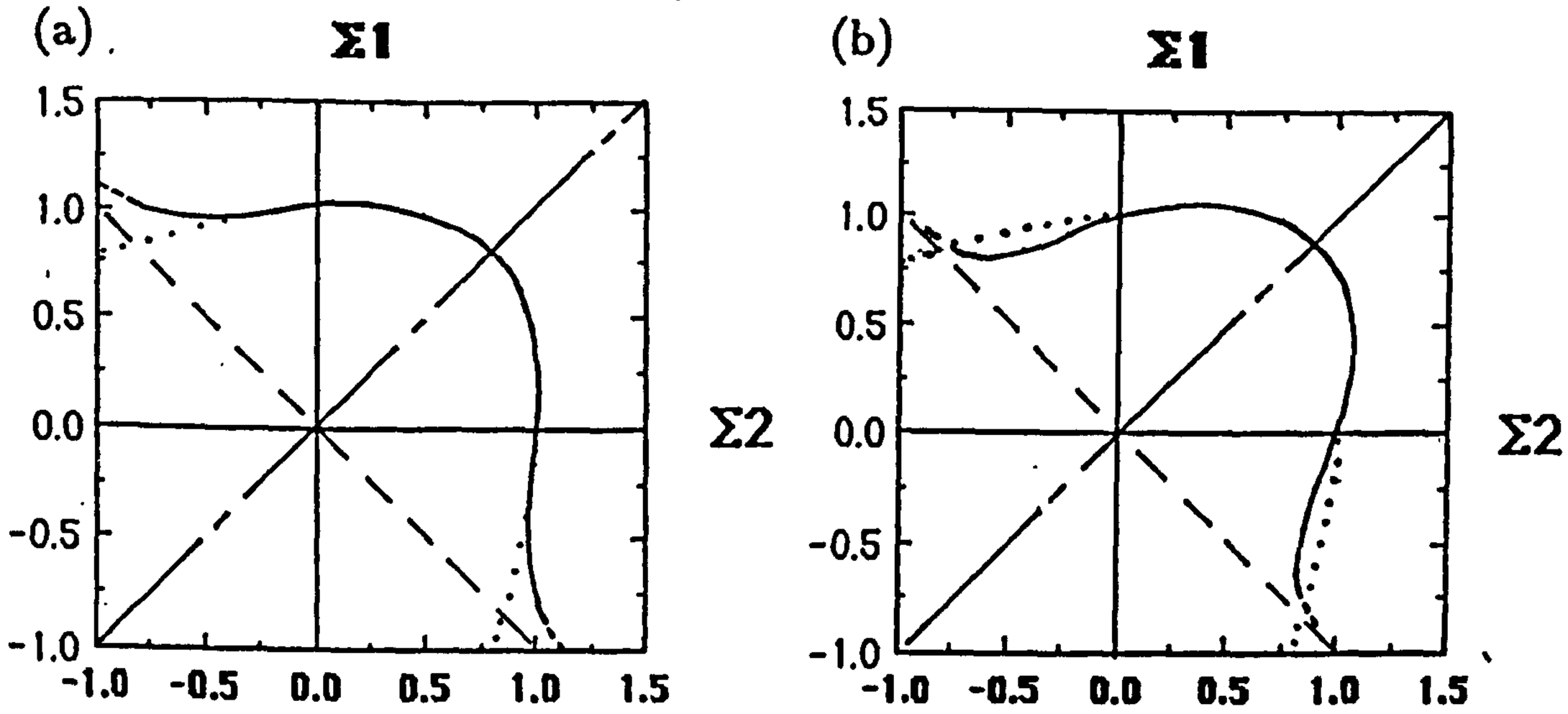

Figure 5.33: Plane stress isochronous rupture surfaces for the new continuum damage model allowing for the effects of the tri-axial stress state. Solid lines represent the Cocks/Ashby rupture surfaces (equation (5.47)) and the dotted lines the Hayhurst rupture surfaces (equation (2.32)) for low (a) and high stess (b) values of (β''_{CA}).

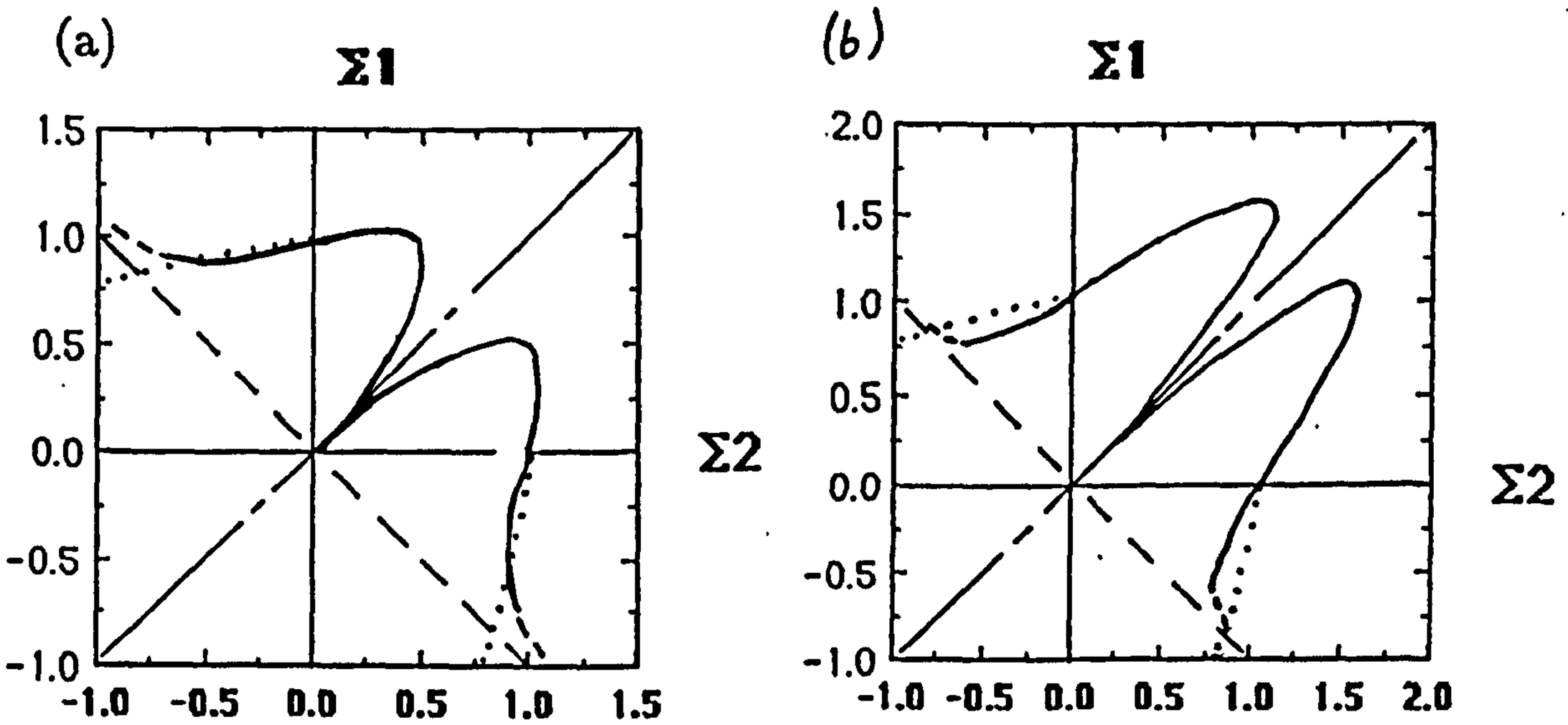

Figure 5.34: Plane strain isochronous rupture surfaces for the new continuum damage model allowing for the effects of the tri-axial stress state. Solid lines represent the Cocks/Ashby rupture surfaces (equation (5.48)) and the dotted lines the Hayhurst rupture surfaces (equation (2.33)) for low (a) and high stess (b) values of (β''_{CA}).

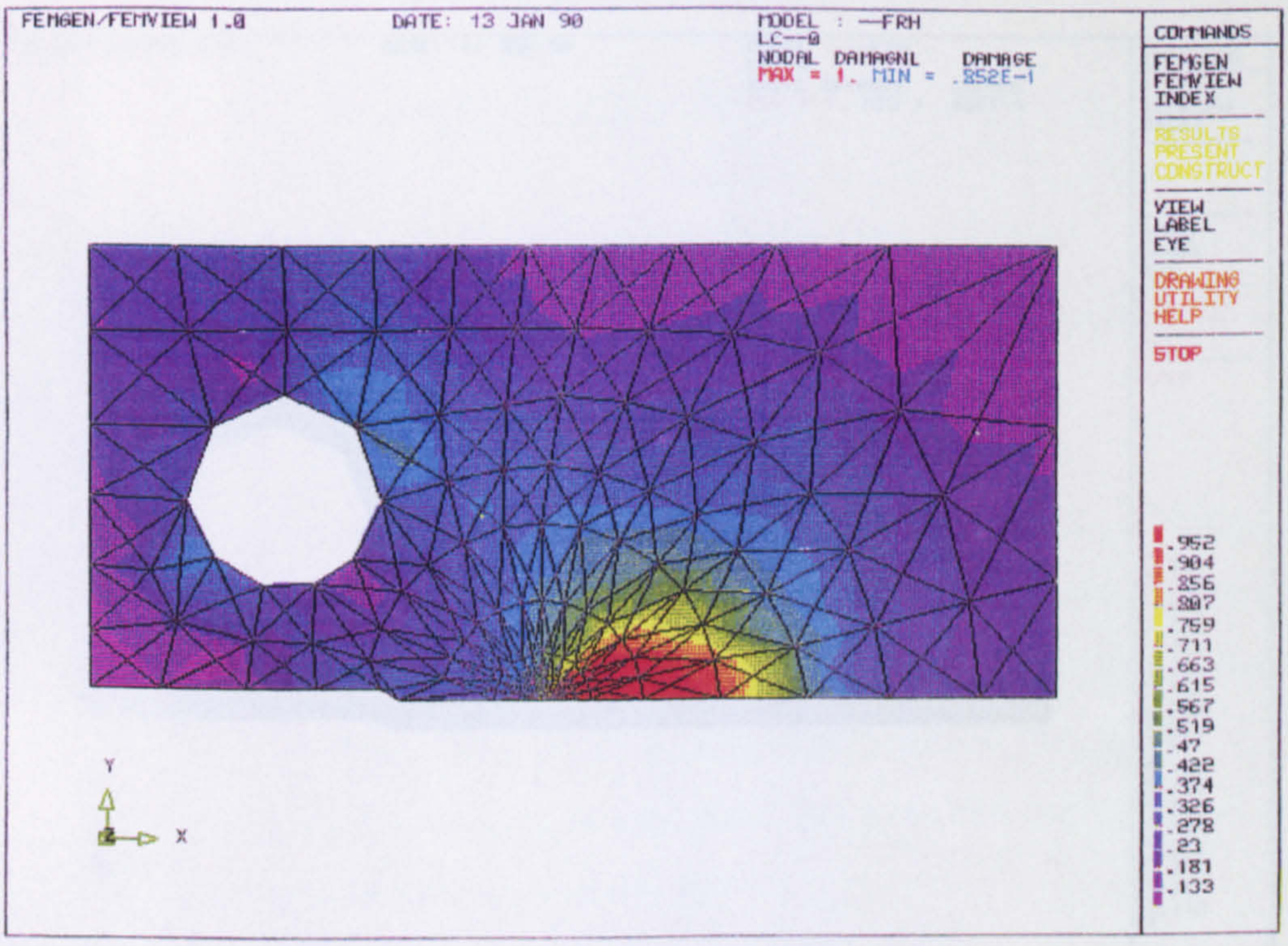

Figure 5.35: Damage distribution at ($\tau = 36.06$), for the simplest CT-specimen finite element mesh (Fig.5.3) in plane strain, using the new continuum damage model allowing for the effects of tri-axiality on rupture and deformation.

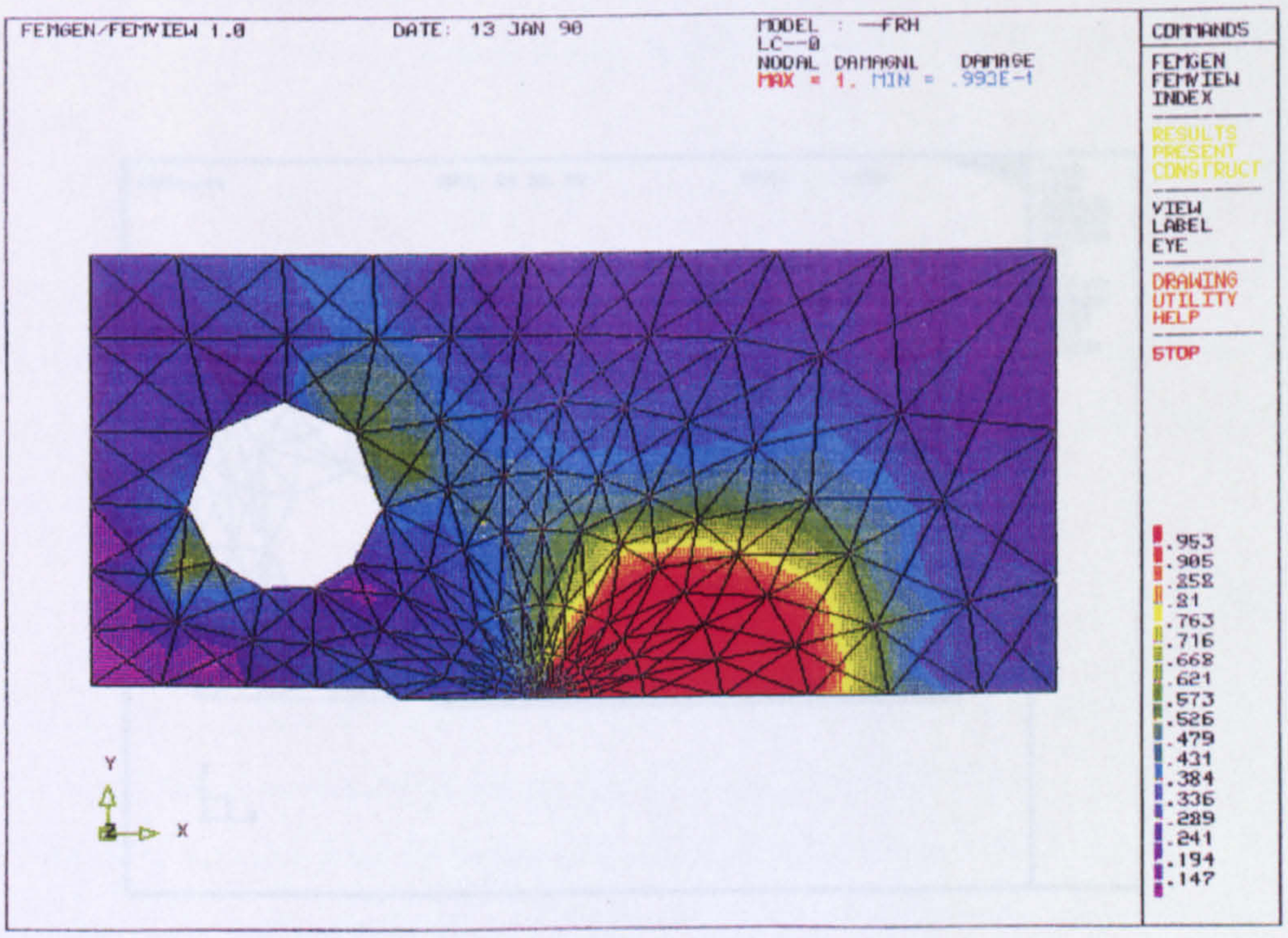

Figure 5.36: Damage distribution at ($\tau = 41.3$) close to failure, for the simplest CT-specimen finite element mesh (Fig.5.3) in plane strain, using the new continuum damage model allowing for the effects of tri-axiality on rupture and deformation.

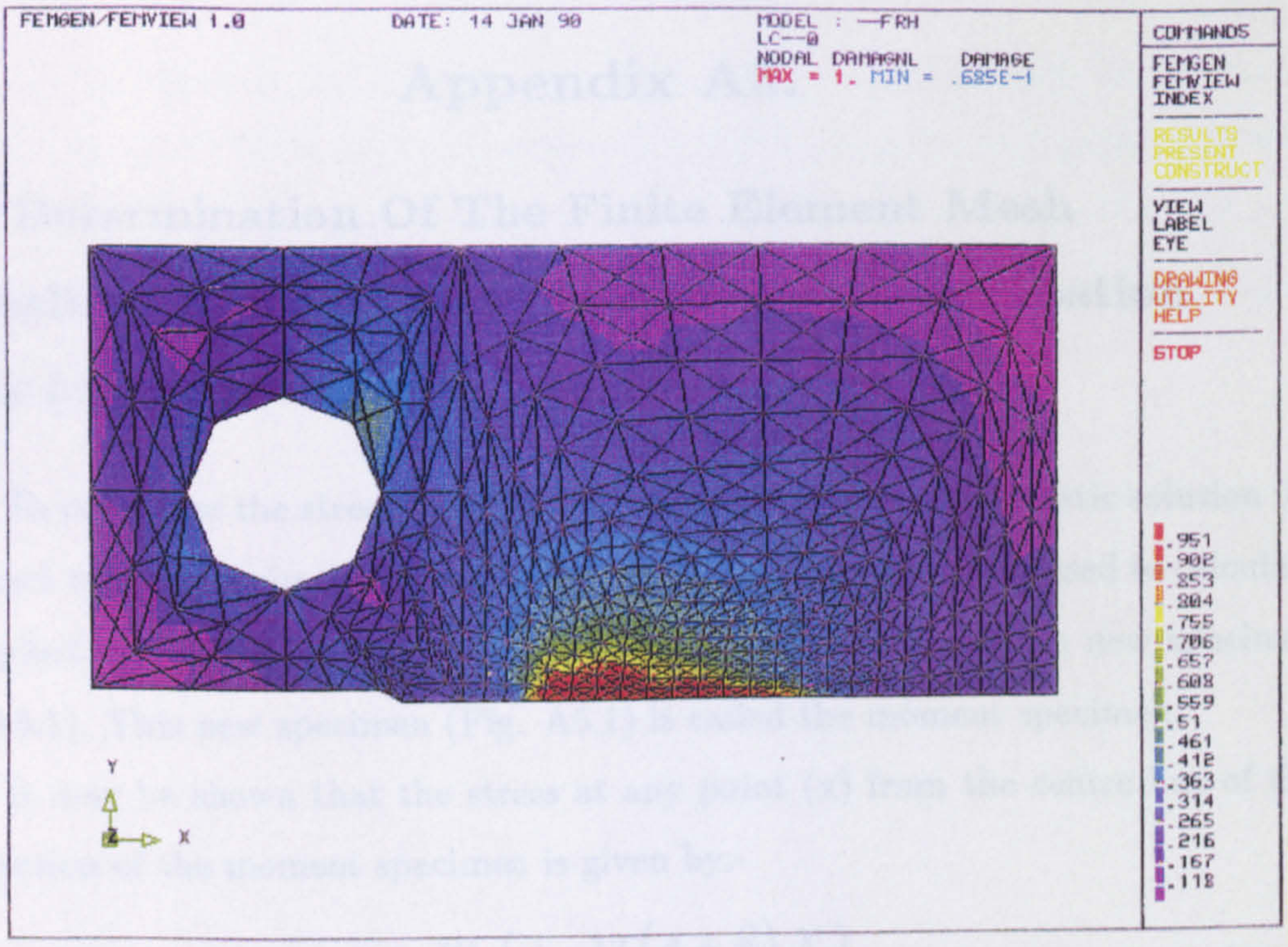

Figure 5.37: Damage distribution at ($\tau = 34.3$) close to failure, for the CT-specimen finite element mesh (Fig.5.21) in plane strain, having a constant mesh refinement across the mesh ligament; using the new continuum damage model allowing for the effects of tri-axiality on rupture and deformation.

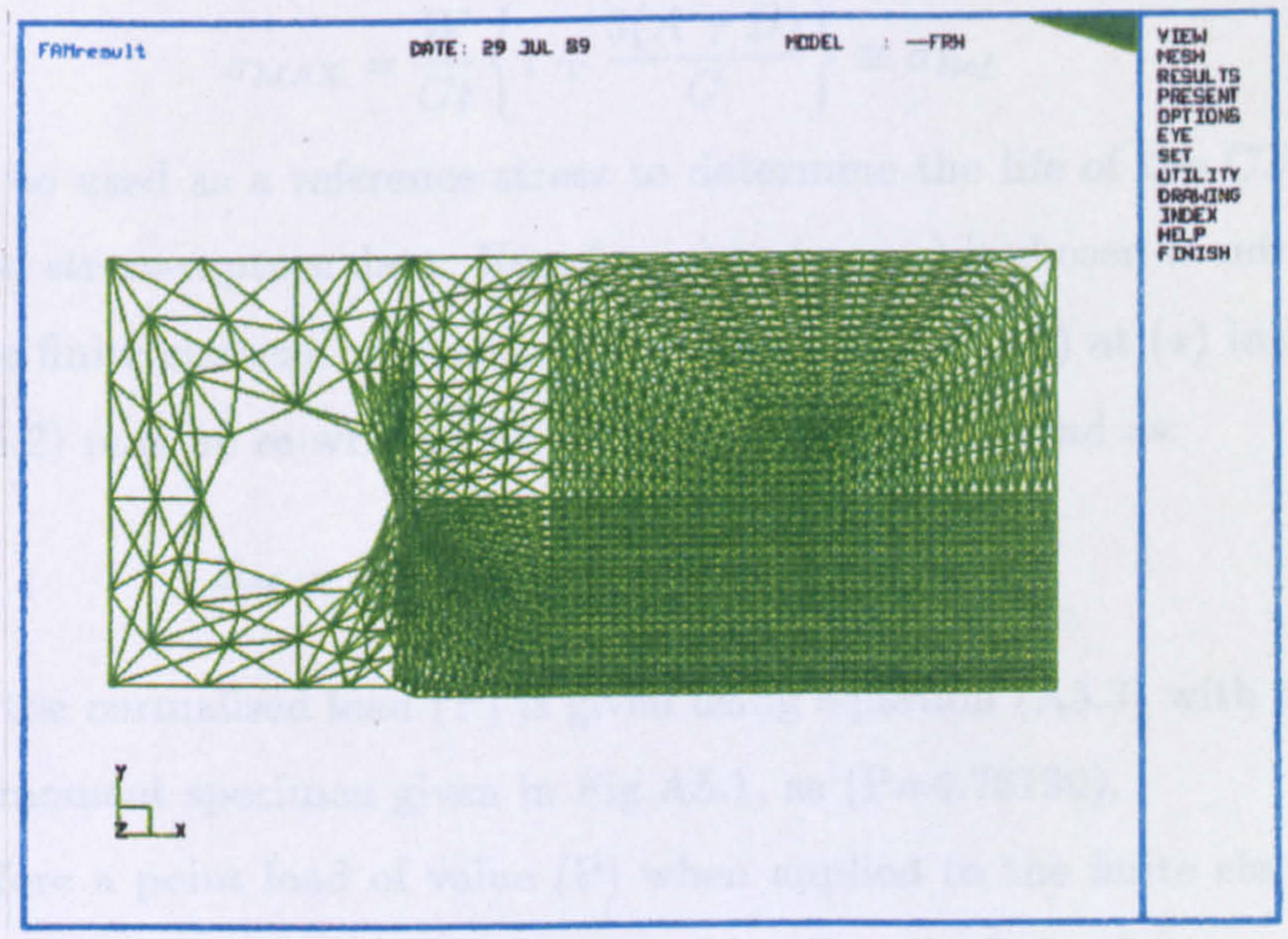

Figure 5.38: A refined compact tension specimen finite element mesh, having approximately 150,000 degrees of freedom, necessary to accurately model the damage distribution of crack growth across the ligament length.

Appendix A5.

A5.1 Determination Of The Finite Element Mesh Normalised Applied Load (P) And The Normalisation Stress (σ_0).

To normalise the stresses in the finite element program the elastic solution for a compact tension specimen without a notch, a crack, or load-holes is used to calculate the applied normalised load (P) to produce unit stress at ($\star$) in the new specimen (Fig. A5.1). This new specimen (Fig. A5.1) is called the moment specimen.

It may be shown that the stress at any point (x) from the centre line of the cross-section of the moment specimen is given by:-

$$\sigma = \frac{W}{Ct}\left\{1 + \frac{12\left(A + \frac{C}{2}\right)X}{C^2}\right\} \qquad \text{(A5.1)}$$

where (t) is the thickness of the specimen and (W) is the applied load in Newtons. In the finite element program the thickness (t) is constant and is normalised out of the procedure. (t) is therefore taken as unity.

As the maximum stress occurs at ($\star$), substitution of ($X = C/2$) into equation (A5.1) gives:

$$\sigma_{MAX} = \frac{W}{Ct}\left\{1 + \frac{3(A+B)}{C}\right\} \equiv \sigma_{Ref} \qquad \text{(A5.2)}$$

(σ_{MAX}) may be used as a reference stress to determine the life of the CT-specimen using uni-axial stress-rupture data. Here (σ_{Ref}) or (σ_{MAX}) is chosen to normalise the stresses in the finite element program, so that ($\sigma_{MAX}/\sigma_0 = 1.0$) at ($\star$) in Fig. A5.1. Equation (A5.2) may be re-written for normalised stress and load as:

$$\Sigma_{MAX} = \frac{\sigma_{MAX}}{\sigma_0} = \frac{P}{C}\left\{1 + \frac{3(A+B)}{C}\right\} \qquad \text{(A5.3)}$$

The value of the normalised load (P) is given using equation (A5.3) with the dimensions for the moment specimen given in Fig.A5.1, as (P=4.76190).

Therefore a point load of value (P) when applied to the finite element mesh representing the moment specimen will produce a normalised elastic stress (Σ) in the vertical direction at ($\star$), in Fig.A5.1, of unity. The normalising stress (σ_0) is calculated using equation (A5.2) to calculate the real stress at ($\star$), using ($t = 25 \times 10^{-3}$m) with

the dimensions given in Fig.A5.1 in meters. (σ_0) is calculated as 8400.W Pa. As the real specimen load (W) is 2000.g Newtons = 19,620 N this gives (σ_0) as 164.808 MPa.

A finite element mesh representation of the moment specimen was also used to confirm these calculations and check the normalisation procedure for the compact tension specimen problem [64]

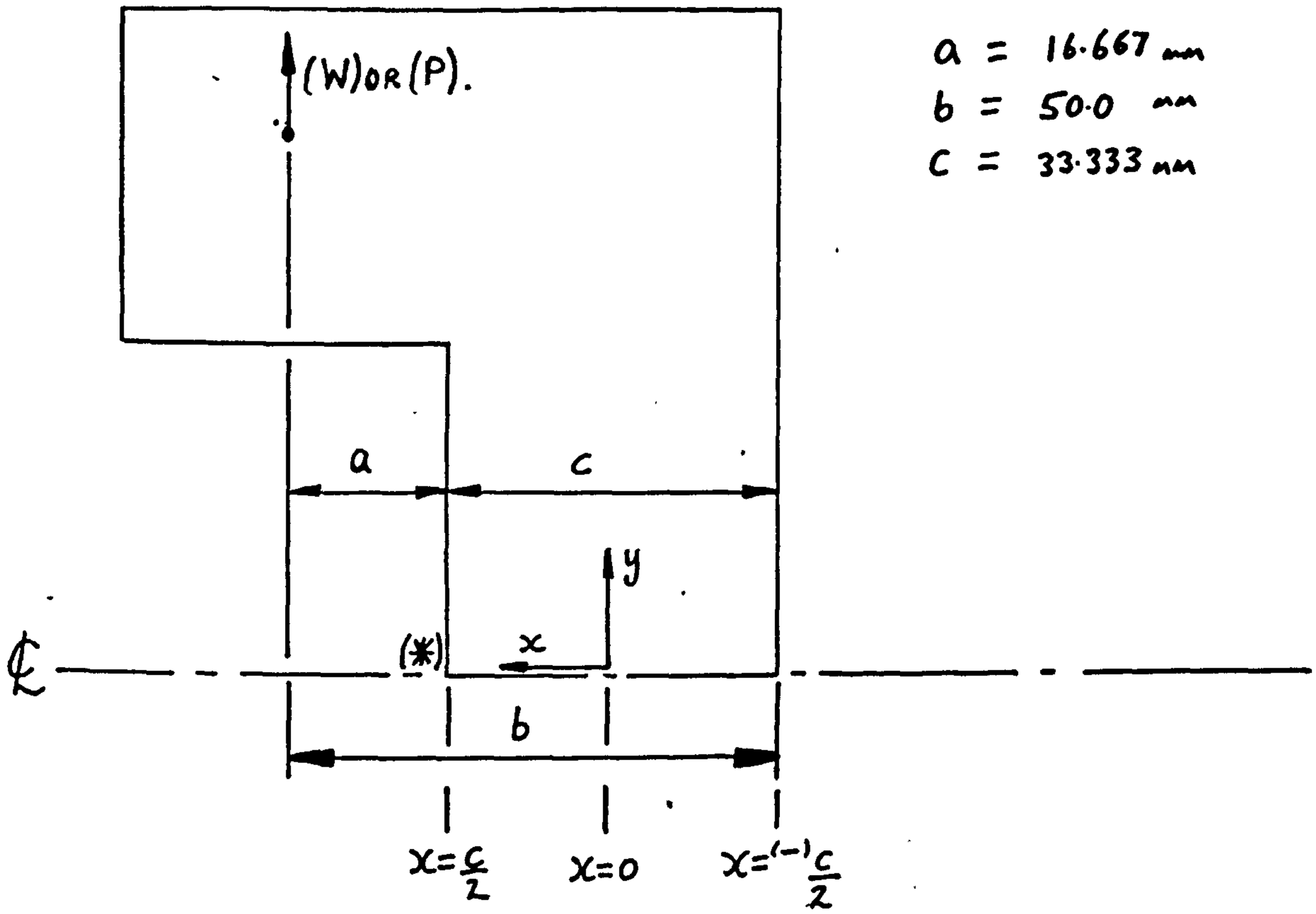

a = 16.667 mm
b = 50.0 mm
c = 33.333 mm

Figure A5.1: The moment specimen, for the compact tension specimen problem normalisation. Only the top half of the specimen is shown due to symmetry.

Chapter 6.

Modelling The Size Effect Due To Grain Characteristic Dimension, Through A Non-Local Damage Approach.

6.1 Introduction.

Hayhurst [81] observed a size effect in the experimental failure times of two different sizes of both centre and edge cracked plates, tested under tensile creep conditions at $250°C$. The plates are made from Copper and their geometries are shown in Figs 6.1(a) and (b). The dimensions of the large plates are twice those of the small plates, (a/b) ratios being preserved. Plate dimensions are given in Tables 6.1(a) and (b) which refer to Figs 6.1(a) and (b) respectively. Plane strain conditions are achieved by making $(\hat{t})$ large compared with (a). All the plates were machined from the same batch of Copper, having the same average grain size. The nominal stress is defined as:

$$\sigma_n = \frac{P}{2(b-a)\hat{t}} \tag{6.1}$$

where (P) is the tensile load on the specimen load-pins. The nominal stress (σ_n) is plotted against the specimen failure time for external and internal cracked specimen tests in figures 6.2(a) and (b) respectively. The uni-axial stress-rupture data for the same material is also plotted on the same axes for comparison.

The size effect on the rupture time for the externally cracked specimen is clearly seen in Fig. 6.2(a). The small externally cracked specimen demonstrates higher notch strengthening character than the large externally cracked specimen. The terms notch weakening/strengthening character and the representative rupture stress have been introduced by Hayhurst et al [23]. Hence at the same nominal stress level, a large external cracked specimen will fail before a correspondingly small specimen.

The size effect on the rupture time for the internal cracked specimen is much smaller (c.f. Fig. 6.2(b)). The failure points lie within the experimental scatter band ($\pm$ 8%), showing slight notch weakening ($\Sigma_{Rup} = 1.01$).

Formerly finite element creep continuum damage analyses carried out by the author have shown that such a size effect cannot be predicted, due to the assumption

that the model has homogenous and continuous material properties, and is independent of the geometrical scale of the microstructure. It is thought by the author that the observed size effect only occurs where a correspondingly similar stress gradient acts over two different microstructural fields (i.e. the crack tip stress gradient may initially act over a smaller number of grains, for a small specimen, compared to a larger number of grains, of the same size, for a large specimen). Therefore, it is proposed to use the non-local damage method to spacially average the damage state variable over a discrete characteristic volume, which may be related to a characteristic microstructural cell size, to model the grain size effect using a modified finite element creep damage analysis. If the size effect on creep lifetimes can be predicted then such a non-local damage technique may be applied to other problems in structural mechanics such as the microstructural modelling of the spatial grain size variations across a weld heat affected zone, in which it is known that microstructures and their distribution have important effects on the weld failure.

The size effect due to grain characteristic dimension will be modelled by averaging the damage rate parameter, ($\dot{\omega}$), spatially over a characteristic area of the microstructure through a non-local damage rate formulation, where all other variables remain local within the finite element technique. The non-local concept was first introduced to continuum mechanics by Kroner [82], Krumhansl [83] and Eringen [84], and has been successfully applied for strain-softening materials by Bazant et al [85-87]. Chaboche [88] used non-local continuum damage to overcome localisation in creep problems, but the non-local damage concept has not been adopted to model microstructural effects of size. What follows is an account of the use of non-local damage finite-domain methods, developed by the author, followed by the use of a general non- local damage infinite domain method similar to that used by Chaboche [88], to attempt to predict the size effect between the large and small, externally and internally cracked specimens. Finally, the problems of localization, convergence and spurious mesh refinement are studied with reference to the use of the non-local damage concept in finite element creep damage solutions.

First the standard creep damage solutions for both the external and internal cracked specimens are presented.

6.2 The Standard Creep Continuum Damage Finite Element Solutions For The Centre And Edge Cracked Plates.

The discretized internal and external cracked specimen finite element meshes are detailed in Figs. 6.3 and 6.4 respectively. The boundary conditions are also given in these figures. The batch of Copper used for the experimental tests by Hayhurst et al [81] was also used by Hayhurst in uni-axial creep tests to give constitutive parameters for this material at $250°C$, [63]. These parameters are summarised in Table 6.2 . . (V_u) was calculated for a mid-stress level uni-axial test having the value of ($\sigma_0 = 48.76MPa$). The material constants are used in the creep strain rate and damage rate equations (2.19) and (2.20) within the creep continuum damage finite element program Damage-(XX), to provide computer predictions of the deformation and failure of the cracked plate specimens.

The finite element meshes for the cracked plate specimens are scaled to give the dimensions of the test specimen to be modelled. Each (1/4)-plate mesh is loaded only on the top boundary with a uniform unit normalised stress ($\sigma/\sigma_0 = 1.0$). Values of the normalised stress concentration at the crack tips at normalised time ($\tau = 0$) are given in Table 6.3. The results from the plain-strain finite element creep continuum damage mechanics solutions for both internally and externally cracked specimens are also summarised in this table and the damaged element failure loci of Figs 6.5 and 6.6 respectively. The integration parameters defined in section 4.3.3, EPSL and EPSR, were set at 10^{-3} and 10^{-4} respectively, for these computer solutions . The results almost exactly agree with those obtained by Hayhurst et al [23]. The failure loci may be compared with the micrographs taken from failed Copper internal and external cracked specimens which are given in Figs 11(a) and 11(b) of the paper by Hayhurst et al [23].

6.3 The Development Of Non-Local Damage Methods Using A Square Cell Having A Characteristic Grain Dimension.

6.3.1 The Finite Domain Non-Local Damage Method.

Bazant [87] has proposed that damage may localize into one single crack, but more usually cracking is distributed over a characteristic volume. When such distributed damage reaches a critical level, one large crack may form through the smaller cracks, leading to the failure of the whole structure; this type of cracking has been observed, c.f. Figs 6(a) and 6(b) [23], during the creep tests for both the internally and externally cracked Copper specimens by Hayhurst et al [23], also refer to [81]. It is proposed here that materials have a characteristic volume over which cracking is almost uniform. This characteristic volume is related to grain size, or to the distribution of material inhomogeneities, and is thought to be characterised by a multiple of one of these dimensions. Therefore, the definition of a characteristic material volume will be used to determine if damage will be allowed to localized or whether damage will grow in a more distributed manner in the finite element model. Localization will be allowed to occur for a small characteristic volume (relative to the specimen size), but the damage will be forced to distribute for a large characteristic volume.

For the case of Copper it is postulated that the single state damage variable or its rate of change is constant within such a characteristic volume, which will be described by a cell having a characteristic dimension which is some multiple of the grain size of the Copper. It is convenient to define the cells as cubes, so that a sequence of such cubes in 2D may be represented as a mesh of squares, which may be overlayed on a 2D-finite element mesh representing the material specimen, as shown in Fig. 6.7.

The objective of the analysis is to seek a spatially averaged damage value, (ω), or a damage rate value, ($\dot{\omega}$), within each cell, from the corresponding elemental damage values, which when used in the continuum damage theory models the observed physical behaviour of non-local damage. Using such an analysis one can investigate its potential to describe the size effect observed in Section 6.1. The spatial averaging

will be performed on an area basis for a 2D finite element mesh, as the thickness of the cracked plates is constant; and, as the damage parameter, (ω), represents an area fraction of damaged material.

The spatially averaged damage rate parameter for each square cell is defined non-locally as:-

$$\dot{\omega}_{cell} = \frac{1}{A_{cell}} \int_{A_{cell}} \dot{\omega}_{el} dA \tag{6.2}$$

where

$$A_{cell} = \int_{A_{cell}} dA \tag{6.3}$$

and where the subscripts (el) and ($cell$) denote a parameter which refers to a triangular element and a parameter which refers to a square cell, respectively. For example ($\dot{\omega}_{el}$) is the damage rate at the centroid of a triangular finite element.

The integrals in equations (6.2) and (6.3) are evaluated numerically. The area weights (dA) of the damage rate, ($\dot{\omega}$), are calculated prior to the finite element analysis by precise calculation of the element intersection areas within each cell. This is done by determining if the sides of each element triangle lie either totally inside the cell, or cross the cell boundary. If the element triangle is contained wholly within the square cell then (dA) is the total area of the element. If the triangular element lies outside the square cell region, then (dA) and ($\dot{\omega}_{el} dA$) for this element is not included in the numerical summation. If the sides of the triangular elements cross the cell boundary then the intersection coordinates of each element side with the sides of the cell are calculated and stored. These coordinates are then subtended by lines only around the extreme points to form a convex polygon, which is termed forming the convex-hull [Appendix A6.1]. The resultant polygon is then split into triangles whose areas are calculated and summed to give the overlap area of the element within the cell concerned. Such a procedure is repeated for all triangular elements and all material cells, giving the area weights which are stored in a single dimensional array. Two additional arrays are used; one stores the element numbers of the elements contained in such a cell; and the other stores the number of elements contained in the same cell. They are used to locate the area weight corresponding to a particular cell and element intersection, for repeat evaluation of equation (6.2). A detailed description of the weight factor calculation algorithm is given in Appendix A6.1.

The integral (6.3) is used to allow for cell area extending beyond the boundaries

of the triangular finite element mesh and for elements which have failed ($\omega > 0.9999$). This area is automatically not included in the integrals of (6.2) by the use of (6.3), which maintains the sum of all area weights over each cell as unity:

$$\frac{1}{A_{cell}} \int_{A_{cell}} dA = 1.0 \tag{6.4}$$

Here it is also noted that elements which have failed automatically have their damage rates set to zero, as the elements are removed from the finite element solution in the instantaneous method (section 4.2).

During the finite element damage analysis for each time step iteration a new spatially averaged non-local damage rate ($\dot{\omega}_{cell}$) is determined using equations (6.2) and (6.3) from the local damage rates ($\dot{\omega}_{el}$), and the area weights (dA). Each element contained within a cell is then forced to have this new spatially averaged damage rate ($\dot{\omega}_{cell}$). This is imposed in one of two ways:-

Firstly:

$$\dot{\omega}_{el_{(NEW)}} = \dot{\omega}_{cell} \tag{6.5}$$

applies if the area of the triangular element within a cell is greater than the area of the triangular element outside the cell; otherwise ($\dot{\omega}_{el}$) remains unchanged from that determined by the single state variable damage evolution law. The non-local damage method using this procedure will be known as Method 1.

Secondly:

$$\dot{\omega}_{el_{(NEW)}} = \frac{1}{A_{el}} \int_{A_{el}} \dot{\omega}_{cell} dA \tag{6.6}$$

This is in effect a double weight method, in which reverse-weights are calculated for cells intersecting elements. This procedure will be known as the non-local damage Method 2. This procedure does not force the damage rate parameter to be the same for all elements within a cell. Here the damage rate parameter for an element crossing a cell boundary, or boundaries, will be calculated from area weighted values of ($\dot{\omega}_{cell}$) for all cells associated with the element. Therefore, smoothing the elemental damage rate step which occurs across cell boundaries using Method 1. For an element contained within a cell (6.6) reduces to (6.5).

The computer algorithms were written in modular form using double precision arithmetic to achieve the accuracy required for the area calculations. Many tests were performed during their development to check the program formulation and numerical accuracy of intersection area and area summation calculations.

A simple quadrilateral mesh generator was written by the author to generate the overlay cell meshes. Both cell mesh and triangular mesh data are input to the area intersection module,(described in Appendix A6.1), prior to the finite element analysis. The number of elements, and the numbers of the elements, which lie in each cell, together with the respective intersection area weights, are calculated and stored. These data are accessed by the finite element creep continuum damage program during each iteration to obtain the new non-local damage rate values for each triangular element. If it is necessary to make use of the restart facility in the program then the intersection area calculations need not be performed again, since the area weights are stored on disc and are read in directly to the finite element program, to minimise CPU time.

A boundary element number may be specified, where for element numbers beyond the boundary number no spatial averaging of the damage values is performed. This is achieved by arranging the triangular element numbers to increase with distance away from the crack tip. Hence, as the element size approaches the cell size, with increasing distance from the crack tip, the original continuum damage solution may be used to save CPU time.

6.3.2 Results Of Finite Domain Non-Local Damage Method Tests.

Many tests were performed in the development of the finite domain non-local damage methods. One such test is the symmetric loading of a rectangular finite element mesh in plain strain, as shown in Fig. 6.8. Only part of the left-hand side of the mesh defined by the region ABCD is analysed non-locally using the double weight Method No.2. Plots of elemental damage and stress values at the centroids of elements in the bottom row of the mesh, are plotted against horizontal distance along the mesh boundary in Fig. 6.9(a) and (b) respectively. The plotted curves are jagged due to the properties of the crossed triangle arrangement of the elements. The

elements with edges on the vertical sides of the quadrilaterals have peaks and troughs in the damage and stress distributions. The elements with edges on the horizontal sides of the quadrilaterals have damage and stress values between these peaks and troughs. It is of interest to note that the damage profile across the non-local damage analysis region is smoother, and slightly lowered. Though the corresponding stress profile over the this same region region is perturbed slightly. This is thought to be caused by the spatially averaged damage parameters becoming smaller than the local damage values, due to the spatial averaging, hence causing stress to be off-loaded from the local damage analysis regions of the finite element mesh. The distributions of stress and damage, in the case of a full local damage analysis of the same structure, are symmetrical about the mesh centre-line. Method 1 may be shown to have similar properties to Method 2, but requires increased triangular element size refinement than is used here.

Methods 1 and 2 have been used with damage rates ($\dot{\omega}$) replaced by damage values (ω) and essentially the same results have been obtained; but, with a higher level of computational complexity. For this reason the damage rates have been used for the non-local damage solutions detailed in this chapter.

6.3.3 Finite Domain Non-Local Continuum Damage Mechanics Analysis Of Internally And Externally Cracked Tension Members.

For the prediction of the size effect between large and small, external and internal cracked specimens a characteristic cell dimension has to be determined. For Method 1, numerical solutions showed that the failure time increased from that of the local damage analysis value as the cell size increased. Hayhurst [89] suggested a cell dimension of 6 or 7 grain diameters from his observations of the damage growth in this Copper material. The average grain diameter of the Copper is 0.15mm, which results in a cell dimension of approximately 0.9mm, and is the cell dimension chosen for the size effect tests. The characteristic cell dimension (C) may be normalised relative to the ligament length (L), giving the normalised cell dimension ($\gamma_c = L/C$), for square cells, as defined in Fig. 6.10.

Details of the cell meshes used to overlay the finite element meshes (Figs.6.3

and 6.4) for both the small and large, external and internal cracked specimens are shown in Fig.6.11 and Fig.6.12 respectively. The same cell dimension is used for both large and small meshes. The finite domain non-local finite element results are given in Table 6.4. The corresponding damaged element ($\omega > 0.9999$) failure loci are shown in Figs.6.13 and 6.14 for external and internal cracked geometries respectively. Figures 6.13(a) and 6.14(a) are for Method 1 and Figures 6.13(b) and 6.14(b) are for Method 2. From Figs. 6.13 and 6.14 it may be clearly seen that the extent of the damage distributions close to the crack tips are greater for the small specimens than for the large. This is caused by each cell covering more triangular elements for the small specimens, thus increasing the strength of the spatial averaging and delocalization of the damage over a larger region than for the large specimens. If the non-local damage failure patterns are compared with the local damage analysis failure patterns of Figs. 6.5 and 6.6, the non-local damage plots show increased spread of damage, blunting the crack tip, yet the failure loci is confined more to the initial notch plane. The large specimen failure loci are seen to deviate more from the initial notch plane than do the loci for the small specimens. This behaviour may be observed particularly in Figs.6.14(a).

Colour plots of elemental damage values over the finite element mesh relating to the solution for the small externally cracked non-local damage Methods 1 and 2, at a time just before the first element fails, are shown in Figs. 6.15 and 6.16 respectively. The large square cell mesh, representing the cells of side 0.90mm, may be overlayed on these figures, to show the non-local damage analysis cellular regions in the finite element mesh. The differences in the way elements which cross cell boundaries are treated by each method may be observed. Fig.6.15 shows how Method 1 causes a sharp discontinuity in the elemental damage values as the cell boundary at the crack tip is crossed. Fig. 6.16 shows how Method 2 averages the damage values of an element on the cell boundary, (on an area basis), between the damage values of the cells it subtends. This is seen as the intermediate colouring of elements crossing the cell boundary at the crack tip, between the red and blue colours, of the crack tip cell and the surrounding cells, respectively. Both methods 1 and 2 show similarities, in that elements totally contained within each square cell have the same colour and hence damage value.

The colour contour plots of Figs. 6.17, 6.18, 6.19, and 6.20 relate to the results for the small externally cracked specimen, using the finite domain non-local damage Method 2, at a time just before the first element failure. These figures show how the damage values are non-local, through the cellular spacial averaging (Fig.6.17), whilst the stresses (Figs. 6.18 and 6.19) and strains (Fig.6.20) remain local to the triangular elements. The maximum principal stress is shown (Fig. 6.18) to be re-distributed out of the most damaged cellular region, which is shown as the red damaged zone at the crack tip in Fig. 6.17. Figs. 6.19 and 6.20 show how the Von-Mises stress and creep strain are distributed and that both have maximum values at the crack tip. Corresponding plots to Figs. 6.17 to 6.20 for the small specimen, are shown in Figs. 6.21 to 6.24 for the large externally cracked specimen, also using Method 2. Care must be taken when comparing corresponding plots since both plots are at an instant in time just before the failure of the first element, but correspond to different life fractions (t/t_f).

The small square cell mesh, representing cells of side 0.90mm, may be overlayed with the plot of Fig. 6.21, to show the cellular damage regions. The damage contour plots of Figs. 6.17 and 6.21 may be compared to show the difference in the spatial distribution of damage at the crack tips of the large and small cracked specimens.

Figs. 6.25 and 6.26 show damage contour plots at various fractions (t/t_f) of specimen lifetime (t_f), for small and large external cracked specimens respectively using the non-local damage Method 2. These figures show the differences in the shapes of the most damaged (or cracked) regions for small and large specimens, and also how these damaged regions grow, and eventually cover the whole ligament length of the specimen, to produce failure. Enlargements of the damaged contour plots at specimen failure for the small and large specimens (Figs. 6.25(c) and 6.26(c)) are given in Figs. 6.27 and 6.29 respectively. The figures 6.27 and 6.29 may be compared with the photo-micrographs of figures 6.28 and 6.30 respectively. The micrograph of Fig. 6.28 is at a life fraction of ($t/t_f = 0.94$) and that of Fig. 6.30 is at specimen failure. The computed damage plots give a reasonable representation of the damage distributions in the real specimens. The damage distributions for the small specimen (Fig. 6.27) are restricted to a narrow band, whereas in the large specimen the damage distributions (Fig. 6.29) spread out away from the cellular damaged zone at the crack tip, to form a

more curved damage envelope. The computed damaged zones at the crack tips seem slightly larger than the cracked zones observed in the photo-micrographs, possibly indicating that a slightly smaller non-local damage analysis cell size could have been chosen, with a more refined triangular finite element mesh.

Referring to the results of Table 6.4 it may be seen that the number of time iterations taken by the program to achieve failure of the structure, is reduced significantly for non-local damage Method 1 compared with the local damage computer solutions. More elements fail during the same iteration, hence requiring fewer stiffness matrix inversions to be performed; this caused a considerable saving in computer time when using Method 1. No real saving in computer time has been observed for Method 2. This method required more iterations to achieve failure of the specimen compared with the local damage solution. The normalised times to failure of the first finite element, during all the non-local damage runs are greater than those of for the local damage runs.

The real failure times of the specimens may be obtained from the normalised failure times for a nominal specimen stress of ($\sigma_n = 40MPa$), using equation:

$$t_f = \left\{ \frac{(m+1)\tau_f}{V_u \sigma_0^x M} \right\}^{\frac{1}{m+1}} \tag{6.7}$$

where

$$\sigma_0 = \left\{ 1 - \frac{a}{b} \right\} \sigma_n \tag{6.8}$$

The predicted failure times may be compared with the experimental stress rupture lifetimes of Fig. 6.31(a) and (b), for external and internal cracked specimens respectively. For the externally cracked specimens, the non-local damage Method 1 predicts a size effect of a difference in the failure lifetimes between, 1830 hours for the large and 2110 hours for the small specimens, a difference of approximately 280 hours at a nominal stress of 40 MPa. This may be compared with the experimentally measured difference of approximately 500 hours. The predicted failure times for large and small specimens made using the non-local damage Method 1 lie to the right of the experimental lines of Fig.6.31(a), therefore predicting failure times which are slightly too large. The corresponding prediction for the externally cracked specimens by Method 2 gives an improved prediction for the size effect, of a difference in the failure lifetimes, between 1390 hours for the large and 1850 hours for the small specimen

of approximately 460 hrs at the same nominal stress level. This compares favourably with that of the experimentally measured difference of 500 hrs. The corresponding failure points are also shown in Fig.6.31(a) for the externally cracked specimens and lie only marginally to the right of the experimental lines. Referring to figure 6.31(b) for the internally cracked specimens both homogenization procedures show very little difference between the failure times for the large and small specimens, which is consistent with the experimental results. The Method 1 again predicts failure times which are slightly longer than the experimental values; and, the Method 2 predicts failure times close to the unhomogenized solution. Therefore, the non-local damage Method 2 correctly predicts the difference between the failure times for the large and the small externally cracked specimens; and, correctly predicts very little relative difference between the failure times of the internal cracked large and small specimens; but, the absolute failure times for the external cracked specimen solutions are slightly larger due to the characteristics of the spatial averaging technique. From tests performed using non-local damage Method 1 and 2 as the cell size is decreased the failure time of the specimen is shown to decrease until the original local damage analysis failure time is approached; and, conversely as the cell size is increased the failure time of the structure is increased. If a slightly smaller cell size is used for the externally cracked specimen and the finite element mesh is refined constantly from the crack tip to the left-hand side of the mesh (Fig.6.4), then it would be expected that this may reduce the magnitude of the predicted failure times and the size of the damage distributions, bringing them into line with those of the experimental, yet maintaining the size of the difference in failure times between large and small specimens.

6.4 The Infinite Domain Non-Local Continuum Damage Mechanics Analysis For Externally Cracked Tension Members.

The infinite domain non-local damage method detailed here is similar to that used by Chaboche [88], although the technique has been specifically adapted by the author for use with the creep continuum damage mechanics program Damage-(XX). In the method the damage rate parameter ($\dot{\omega}$) is assumed to be non-local and the

new spatially averaged damage rate parameter ($\tilde{\omega}$) is defined as:

$$\tilde{\omega}_{(x)} = \frac{1}{V_{r(x)}} \int_V \vartheta(s-x)\dot{\omega}_{(s)} dV_{(s)} \tag{6.9}$$

where

$$V_{r(x)} = \int_V \vartheta(s-x) dV_{(s)} \tag{6.10}$$

and is the characteristic or representative material volume defined in Fig.6.32. For a two dimensional finite element mesh this characteristic volume is represented as the area of a circular cell. The weighting function is defined according to a Gaussian normal distribution as:

$$\vartheta(R) = exp\left\{-\left(\frac{K|R|}{l}\right)^2\right\} \tag{6.11}$$

where

$$|R| = \left(\Delta x^2 + \Delta y^2\right)^{\frac{1}{2}} \tag{6.12}$$

as shown also in Fig.6.32. The term (x) in equations (6.9 and 6.10) represents an element centroid which forms the centre of a circular cell. The term (s) represents the centroids of the triangular elements whose damage rates are to be averaged within the bounds of the circular cell. (V) is the volume of a finite element which reduces to the area of a triangular element for the case of a two dimensional mesh. The constant (K) in equation (6.11) takes the value $(K = 2)$ for circular cells used by Bazant [86], and the cell diameter is $(4l)$. It can be seen from Fig.6.31, that for each triangular element (x), all elements whose centroids lie within distance $(2l)$ from (x), (i.e. $|R| \leq 2l$), have their weights calculated using (6.11), which are multiplied by their respective elemental areas. For those elements whose centroids lie outside the distance $(2l)$ from (x), $(\vartheta(R))$ is set to zero, due to the rapid decay of the Gaussian normal distribution defined by (6.11). The numerical sum of all the weights multiplied by the elemental areas over the whole circle gives $(V_{r(x)})$ as in (6.10); $(V_{r(x)})$ allows for the boundaries of the finite element mesh and for elements which have failed $(\omega > 0.9999)$. The areas beyond the boundaries and of failed elements are simply deleted from the integration in (6.10), therefore maintaining the sum of the weights $(\vartheta(x,s) = \vartheta(s-x)/V_{r(x)})$, over each circular cell, equal to unity for any (x). The integrals (6.9) and (6.10) are therefore calculated as finite sums and a new spatially averaged damage parameter $(\tilde{\omega})$ is calculated. The closer an element is to the centre of the cell then the greater the influence the damage rate value will have on the spatially averaged value. The new

non-local damage rates ($\tilde{\omega}$) for each triangular element may be substituted directly for the local damage rate parameter ($\dot{\omega}$) in the continuum damage finite element solver. A new damage parameter is calculated for each element at every subsequent iteration.

When an element fails ($\omega > 0.9999$) the damage rate for this element is automatically set to zero by the program and hence this element will not contribute to the non-local solution in (6.9).

The area weights and Gaussian weights are calculated before the finite element creep continuum damage solution is performed; and, are stored for subsequent access, if the creep solution is re-started, to save computer time. When the finite element mesh is coarse, so that the cell size is smaller than the element size the spatial averaging of the local damage values may be stopped by specifying a boundary element number, as before in the finite domain technique. The infinite domain method is considerably simpler than the finite domain methods as intersection areas do not have to be calculated. This is due to the use of the Gaussian normal distribution where the damage rate contributions due to elements at the boundaries of a cell are weighted to zero. The larger the value of (l) in (6.11) the flatter the Gaussian normal distribution, and hence the damage, or damage rate values of surrounding elements become more influential in determining the damage rate for a particular element.

As before the normalised cell dimension (γ_l) is defined relative to the ligament length of the external crack specimen as shown in Fig. 6.10. As the size effect was observed to be most significant in the external cracked specimen, only this specimen has been studied with the infinite domain technique. The numerical results obtained using the infinite domain non-local damage method are given in Table 6.5 for the externally cracked Copper specimen for a wide range of normalised cell dimension (γ_l) values. The failed element ($\omega > 0.9999$)) distributions are given in Fig. 6.33 at final rupture. The numerical results in Table 6.5, and the corresponding failure plots in Fig.6.33, are for a range of normalised cell sizes including those for the large and small externally cracked Copper specimens; a cell size of ($C = 0.6mm$) has been taken for the (c) large and for the (d) small specimens respectively. The failure times for all the computations performed do not differ significantly, showing an inability to predict the change of failure times between large and small externally cracked

specimens. The failure times all lie close to the local damage solution time. It may be clearly seen from Fig.6.33(a) to (c) that as the normalised cell dimension decreases (i.e. the cell size relative to ligament length increases) the damage region close to the crack tip becomes less localised.

No significant saving in computer time was observed, Table 6.5, as was reported by Chaboche [88] in the non-local damage solution of a uni-axial tension specimen , because either more or a similar number of iterations were required for each solution, compared with the requirements of the local damge analysis solutions; but, a larger number of elements failed within single iterations, reducing the number of stiffness matrix inversions required and the associated computational overhead.

6.5 Non-Local Continuum Damage And The Problems Of Localisation, Convergence And Spurious Mesh Refinement.

Localisation of stress and/or strain occurs in finite element solutions which involve softening due to the formation of damage, where the energy dissipation rate due to imminent element failure is incorrectly predicted to be zero and subsequently the solutions converge to a physically meaningless solution as the mesh is refined further. Localisation effects have been observed and detailed by Bazant [85-87] and by Chaboche [88]; and they occur where the finite element mesh is most refined, e.g. at a crack-tip. As the finite element mesh is refined further to achieve convergence of the field variable to the required solutions, the stresses and/or strains increase in such regions, inducing increased local deformation. When the effects of material degeneration, damage, or softening are included it is therefore possible to induce highly localised failure mechanisms or zones, in regions of high mesh refinement. The solution to the finite element structural model therefore becomes totally mesh dependent.

With reference to Fig.6.34 and 6.35 it may be seen that the normalised time to the failure of the first finite element, at the crack-tip, is increased as the normalised cell dimension is decreased. This result effectively shows the power of the non-local damage techniques as localisation limiters. Formerly, the minimum size of the mesh refinement at the crack tip is chosen arbitrarily to be that of one grain of the material to be modelled. Such a choice is a localisation limiter itself, but is dependent upon

the material chosen to be modelled; depending upon the physics of the process being modelled this minimum homogenous damage region may in fact be much larger than a grain. This minimum homogenous damage region is the characteristic volume or cell, for the material, which has a size determined by how material defects nucleate, grow and form macrocracks.

It is important to notice that, although the cell size effects the stress and/or strain localisation around the crack tip and produces different times to failure of the first element, the infinite domain non-local damage method of Chaboche shows little if any effect on the overall lifetime of the whole structure. This is thought to be due to the fact that the energy dissipation for the delocalised cracking, in the case of the external and internal cracked specimens, using the non-local damage method of Chaboche is the same for the different cell sizes chosen. Bazant shows [87] that the non-local damage concept is equivalent to providing an energy dissipation rate control, where the energy dissipation rate due to damage evolution is independent of the degree of mesh refinement.

Spurious mesh refinement may also cause problems which may be thought of as localisation problems; for instance, where a fine zone finite element mesh interacts with a coarse zone, or where a line of elements coincides with a plane of maximum shear. One such example is shown in Fig.6.36, which shows part of the damage failure loci for a heavily refined cracked tension specimen mesh. By using a non-local damage analysis such localisations may be smoothed, producing a more realistic deformation and failure pattern.

6.6 Discussion.

The difference between the failure times of the large and small external cracked specimens has been predicted with finite domain non-local damage Method 2 to be approximately 460hrs, whereas experiments give a difference of 500hrs. A difference between the failure times of large and small internal cracked specimens is predicted to be small, which is also in agreement with the experimental data. Though the actual magnitude of the failure times predicted for the external cracked specimens are slightly higher than the experimental values, and than the values predicted by the local damage method. The results of Method 2 gave an improved prediction in

comparison with the results of the finite domain non-local damage Method 1, though the results highlighted distinct similarities between both methods. The difference in the two methods is due to the different treatment of the elements which cross a cell boundary.

The computations performed using the infinite domain non-local damage method of Chaboche [88] did not predict the size effect; the failure times for externally cracked specimens were almost constant for a large range of normalised cell dimensions.

It is thought that the ability of the finite domain non-local damage method to model such effects of size is due to distinct regions of material being constrained to have the same spatially averaged damage rate value. These distinct regions may be directly related to a material characteristic volume, which are observed to damage uniformly in experiments [87]. The characteristic volume is also advocated by material scientists and is consistent, for the cell located at the crack tip, with the concept of a crack-tip process zone of finite size [90], (Fig.6.21).

In contrast the infinite domain non-local damage technique of Chaboche shows an independence of the cell characteristic dimension on the failure lifetime of the structure. This is possible due to the energy dissipation due to damage evolution being constant for this delocalized cracking model for arbitrary cell size or mesh refinement. Even so the cell characteristic dimension does limit the amount of localization for all the techniques used and hence determines the deformation processes local to the crack tip.

It is possible that the exact failure times could be obtained by using the finite domain non-local damage Method 2, with a slightly smaller cell dimension and constant mesh refinement across the ligament of the externally cracked specimen; with the elements smaller than the cells close to the left-hand mesh boundary shown in Fig.6.4. This will involve large computer resources and hence has not yet been studied.

Many researchers have modelled grain, or inhomogeneity, effects in material; with reference to creep and plasticity the most noteworthy are Eringen [91], Giessen and Tvergaard [92]. Tvergaard's analysis involves modelling grain facets by the sides of polygons where damage may grow along grain boundaries. To model a whole structural specimen with such grains will require a vast amount of computer re-

source. Hence, to develop models based on a characteristic material dimension is all important, to relate the behaviour of small scale test specimens to large structures.

Besides the prediction of grain or inhomogenity effects the non-local damage theory is necessary to restrict stress or strain localisation into small regions of refined meshes as shown by Bazant [85-87], by Chaboche [88] and by Tvergaard [93,94]; they have observed localisation effects both experimentally and computationally. Tvergaard [93] has used constitutive equations suggested by Gurson [95] to model the material properties of a porous ductile medium using the finite element technique. Tvergaard [94] produced solutions showing plastic flow localisation into shear bands between voids in the material. He notes that the prediction of localisation is very sensitive to mesh design and that shear bands may localise along lines of nodes preferentially orientated within the mesh. Therefore localisation effects depend on the constitutive equations used, and also the mesh geometry and refinement close to stress raisers. Through the use of non-local concept, problems associated with localisation, convergence and spurious mesh refinement may be overcome and failure behaviour predicted which is more closely allied to that observed in practice.

The concept of non-local damage used in the finite domain Methods 1 and 2 show an ability to model the magnitude of the size effect due to a grain or inhomogenity characteristic dimension. The results show the validity of such a model and the potential to predict the size effect in the specimens considered. Through the work of Bazant and Chaboche a non-local procedure has been developed by the author to restrict localisation, improve convergence of solutions and to overcome the problems associated with spurious mesh refinement; with the aim of obtaining more physically related finite element solutions through a characteristic material volume.

	TYPE	d	2a	2b	C	$\hat{t}$
INTERNAL CRACKED	SMALL	4.762	8.382	25.4	38.10	22.225
SPECIMEN	LARGE	9.525	16.764	50.8	63.5	38.10

Table 6.1(a): Dimensions of the small and large internally cracked specimens shown in Fig. 1(a).

	TYPE	a	2b	$\hat{t}$
EXTERNAL CRACKED	SMALL	6.35	19.05	38.10
SPECIMEN	LARGE	12.70	38.10	38.10

Table 6.1(b): Dimensions of the small and large externally cracked specimens shown in Fig. 1(a).

σ_o	48.76
E	66.24×10^3
ν	0.30
m	-0.79
α	0.70
n	2.97
K	1.28×10^{-6}
χ	1.21
M	6.02×10^{-4}
ϕ	3.83
Vu	27.02

Table 6.2: Material creep constants for Copper at 250^oC in units of MPa, % creep strain and hours, after Hayhurst et al [63].

Specimen Type	Stress Concentration @ Crack tip (r=0)	Normalised Failure Time r_f	Representative Rupture Stress $\Sigma_r = \sigma_r/\sigma_o$
External Cracked Specimen (Small and Large)	17.99	8.309	0.884
Internal Cracked Specimen	14.26	16.372	1.014

Table 6.3: Finite element local continuum damage solution results for externally and internally cracked specimens.

Finite domain non-local damage, finite element, (CDM) solutions.

Cracked Specimen Type	Specimen Size	Finite Domain Homogen-ization Method	Normalized Cell Dimension γ_c	Damaged Element Failure Loci In Fig.	Failure of 1st Element @		AT THE INSTANT OF SPECIMEN LIGAMENT FAILURE			
					Normalized Time τ	Iteration No.	Normalized Time τ_f	Real Time t_f(hrs)	Iteration No.	No. of Elements failed in total
EXTERNAL	SMALL	1	3.53	13(a)	7.493	367	8.888	2107.4	709	136 (141)
EXTERNAL	LARGE	1	7.06	13(a)	6.097	291	8.632	1833.6	908	130 (132)
EXTERNAL	SMALL	2	3.53	13(b)	7.581	379	8.649	1850.9	1,324	148 (144)
EXTERNAL	LARGE	2	7.06	13(b)	6.146	297	8.146	1391.5	1,556	132 (132)
INTERNAL	SMALL	1	9.46	14(a)	11.238	350	16.817	791.2	830	212 (225)
INTERNAL	LARGE	1	18.91	14(a)	8.850	274	16.838	795.9	1,236	179 (179)
INTERNAL	SMALL	2	9.46	14(b)	11.387	361	16.357	693.3	3,929	218 (221)
INTERNAL	LARGE	2	18.91	14(b)	8.973	279	16.263	674.6	2,550	200 (203)

Compare: standard finite element local (CDM) solutions.

EXTERNAL	BOTH(L&S)	- NONE	-	6	2.936	174	8.309	1529.4	1,259	63 (64)
INTERNAL	BOTH(L&S)	- NONE	-	5	3.7201	105	16.372	696.4	1,139*	102 (102)

NOTE:
i) ( ) - Indicates total no. of elements failed, including those forced to fail at time of last failure.
ii) Cell size 'C' = 0.90mm; All integration parameters EPSL/EPSR set @ $10^{-3}/10^{-4}$, EXCEPT for *
iii) * (EPSL/EPSR = $10^{-2}/10^{-3}$).

Table 6.4: Summary of results from the finite domain non-local damage methods which may be comared with the results from the standard local-damage finite element method, for both large and small, internally and externally cracked specimens.

Infinite domain non-local damage, finite element, (CDM) solutions.

Specimen Size	Normalized Cell Dimension γ_ℓ	Damaged Element Failure Loci in Fig.	Failure of 1st Element @		No. of 1st Element to Fail	AT THE INSTANT OF SPECIMEN LIGAMENT FAILURE				Integration Parameters set @: EPSL/EPSR
			Normalized Time τ	Iteration No.		Normalized Time τ_f	Real Time t_f(hrs)	Iteration No.	No. of Elements Failed in Total	
	66.63	6.33(a)	2.951	122	24	8.327	1545.0	890	65 (66)	$10^{-2}/10^{-3}$
	16.66	6.33(b)	3.581	210	23	8.323	1541.4	1,393	69 (70)	$10^{-3}/10^{-4}$
LARGE	10.56	6.33(c)	3.807	189	23	8.339	1555.6	1,151	80 (81)	$10^{-2}/10^{-3}$
SMALL	5.29	6.33(d)	4.467	247	23	8.342	1558.3	1,513	101 (102)	$10^{-2}/10^{-3}$
	2.78	6.33(e)	5.465	356	55	8.355	1569.9	2,586	145 (159)	$10^{-2}/10^{-3}$

Compare: standard finite element local (CDM) solutions.

BOTH(L&S)	-	6.6	2.936	174	24	8.309	1529.4	1,259	63 (64)	$10^{-3}/10^{-4}$

NOTE: ( ) - Indicates total no. of elements failed, including those forced to fail at time of last failure.

Table 6.5: Summary of results from infinite domain non-local damage methods for a range of externally cracked specimen sizes; including those corresponding to large and small specimen sizes. These results may be compared with the results from the standard local-damage finite element method for the externally cracked specimen.

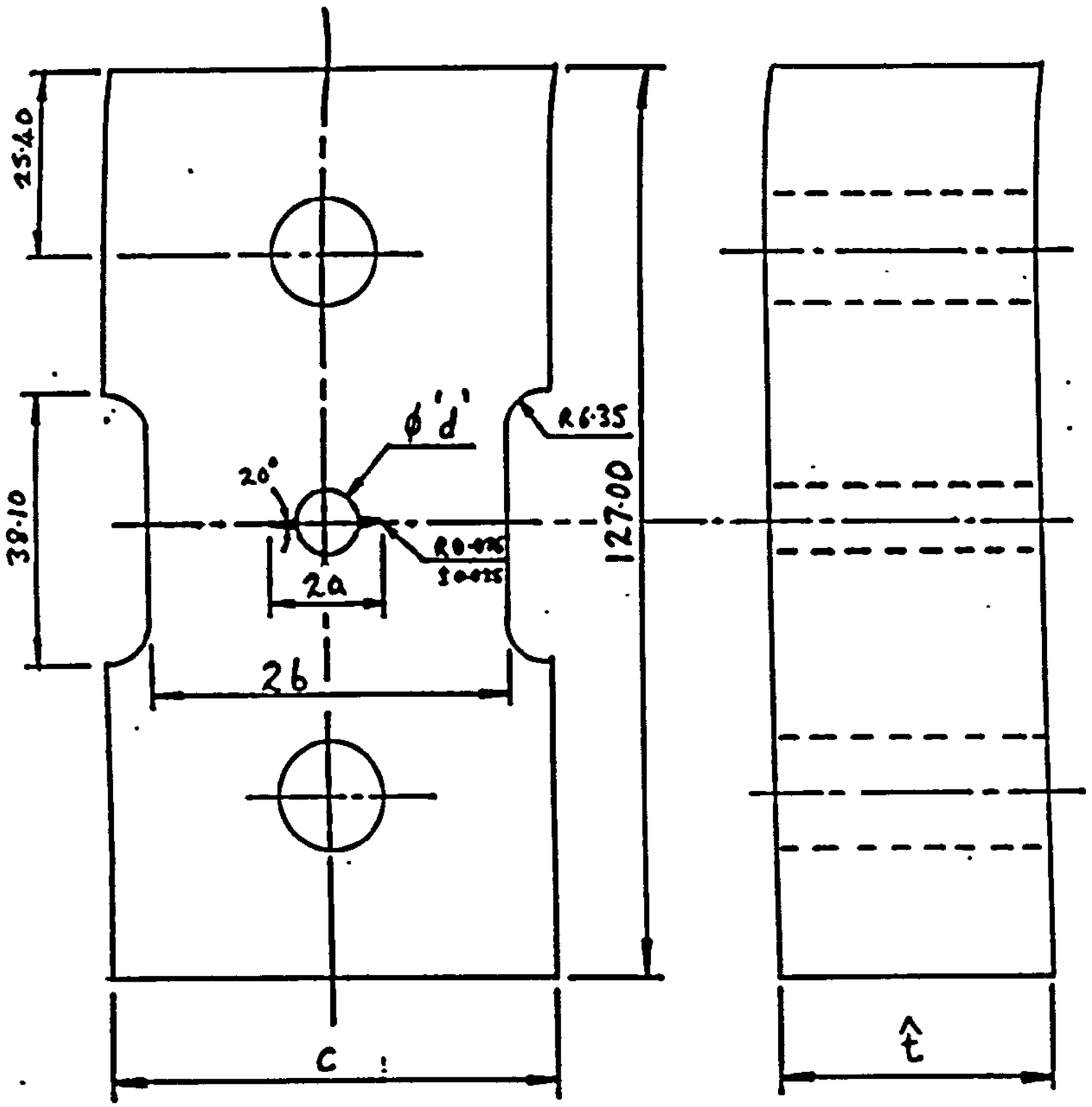

(a)

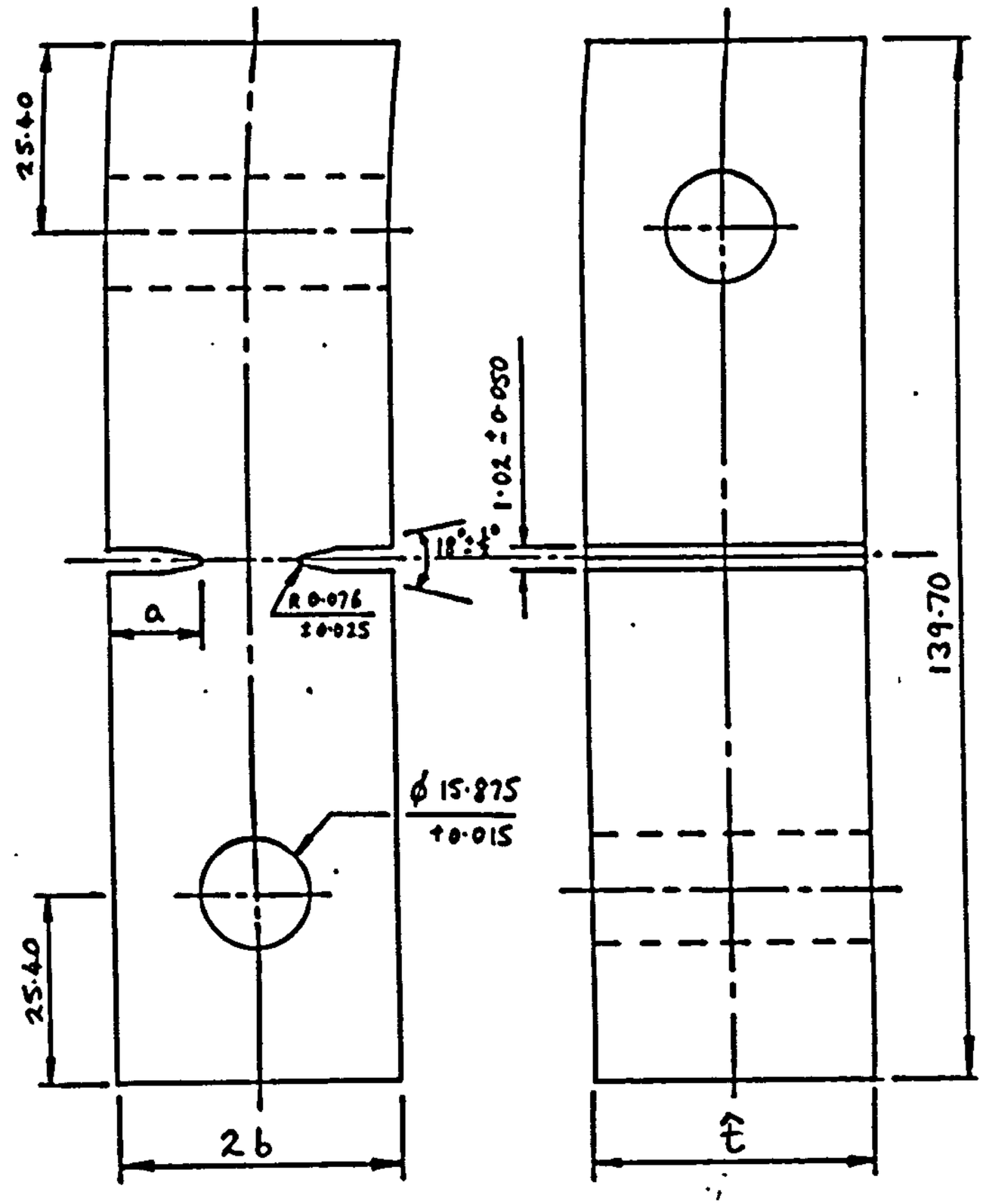

(b)

Figure 6.1: The plane strain (a) internally cracked specimen and (b) externally cracked specimen. (all dimensions in mm).

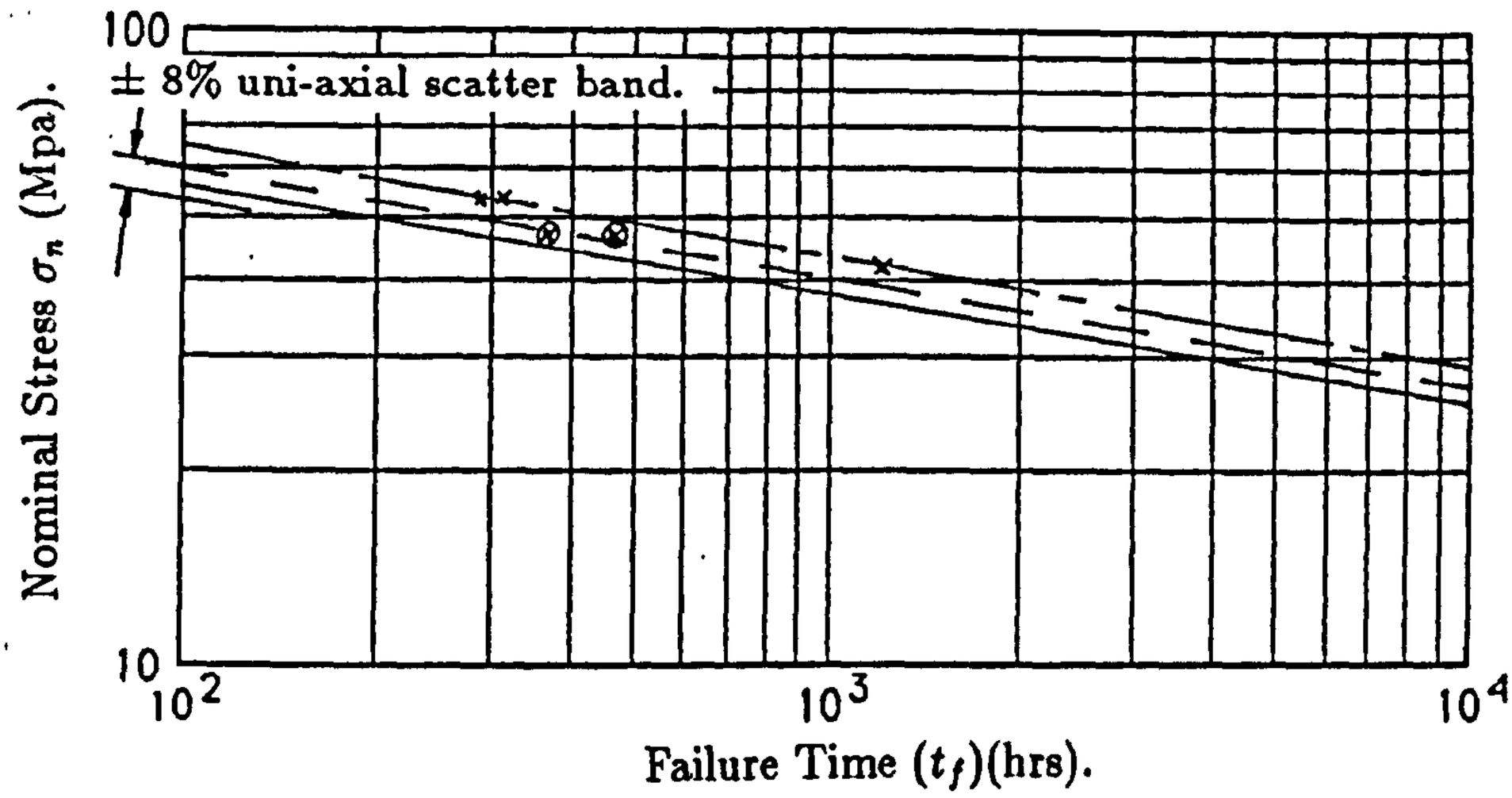

Figure 6.2(a): Specimen nominal stress-rupture diagram showing creep data from tests on both large and small, externally cracked plates.
(×) small sized specimen.
(⊗) large sized specimen.
—— Uni-axial specimen test line.

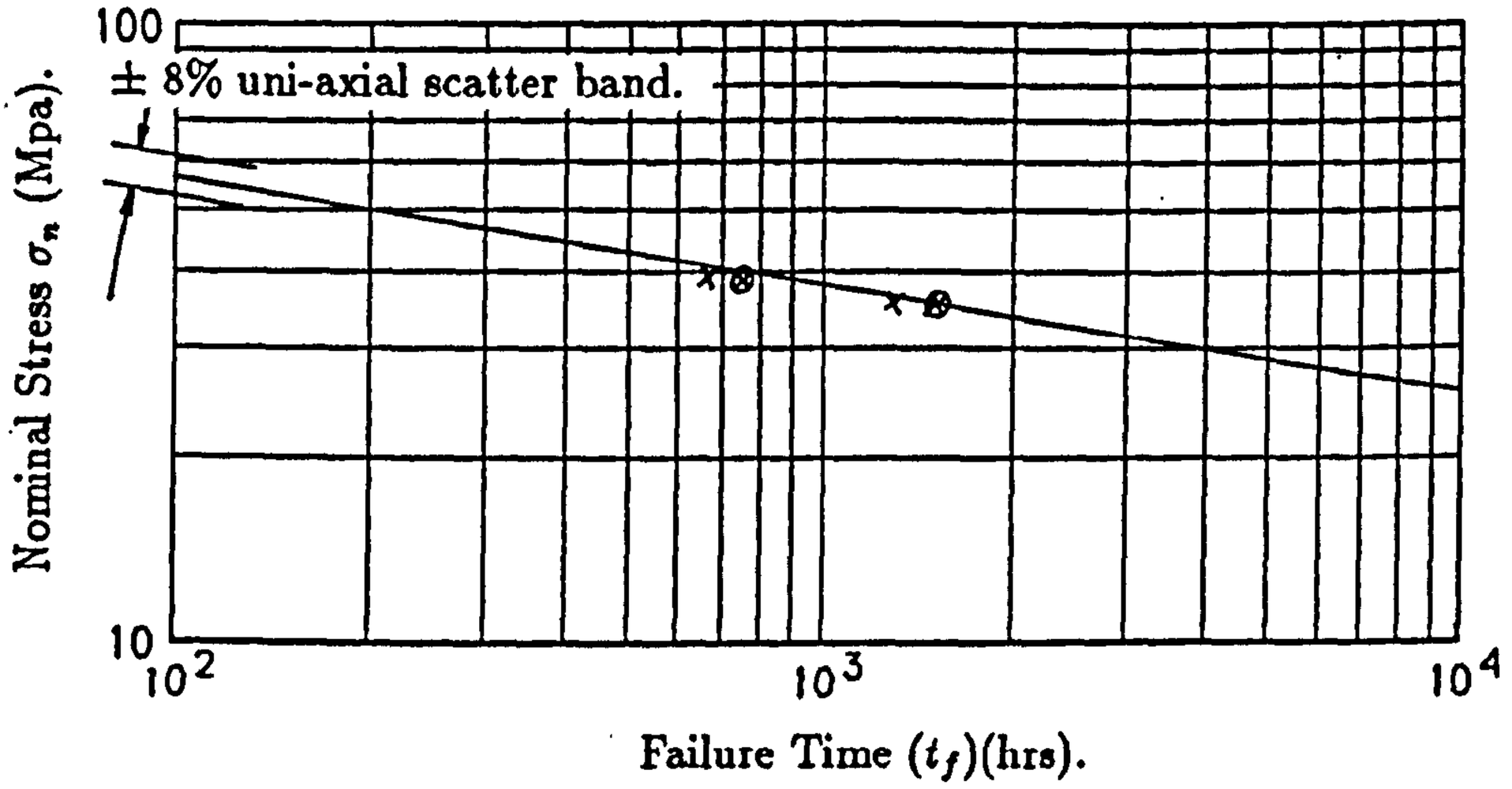

Figure 6.2(b): Specimen nominal stress-rupture diagram showing creep data from tests on both large and small, internally cracked plates.
(×) small sized specimen.
(⊗) large sized specimen.
—— Uni-axial specimen test line.

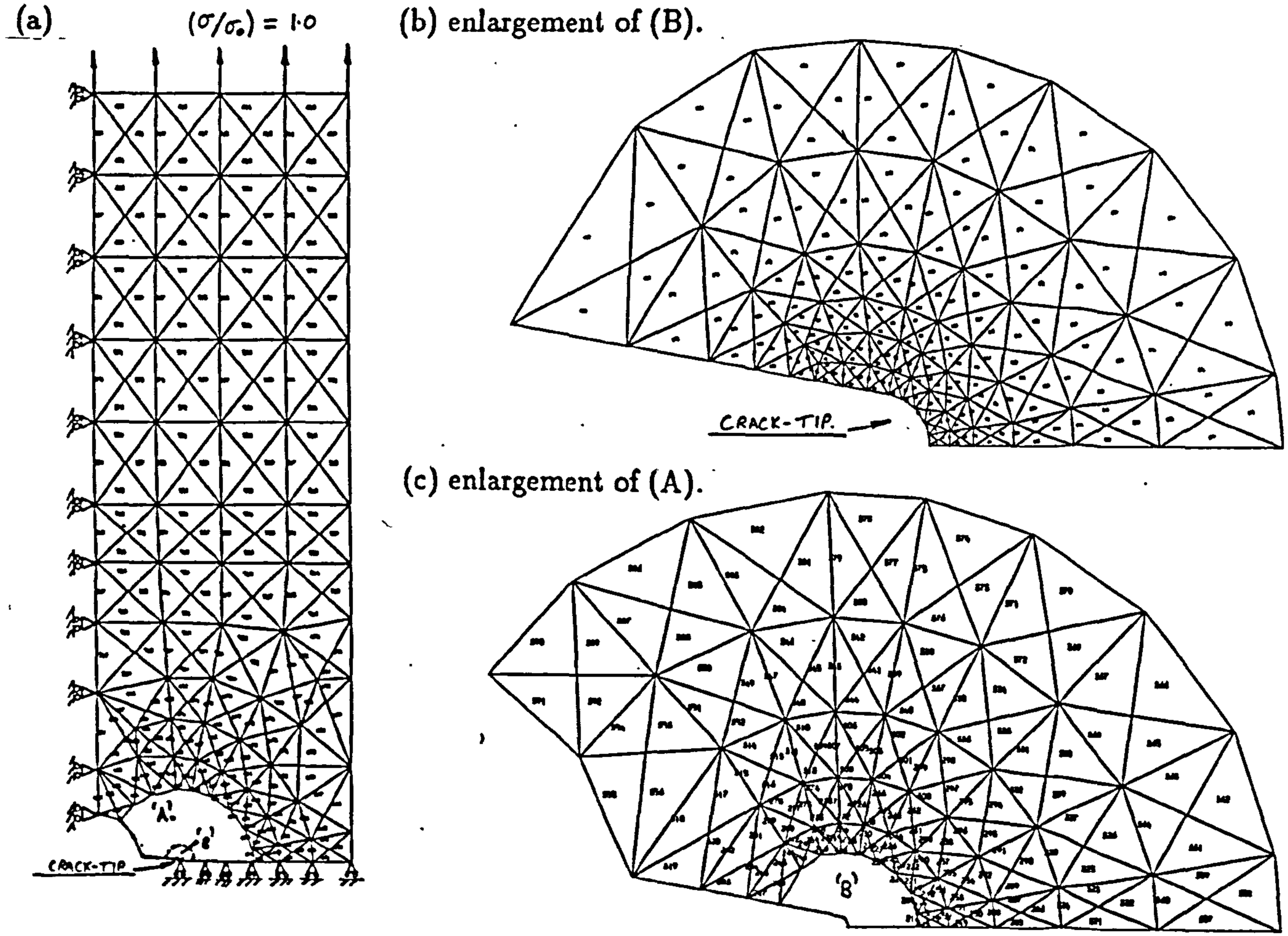

Figure 6.3: Finite element mesh for the internally cracked specimen (1/4)-plate, (a), with the applied bounday conditions. Enlargements of the mesh detail close to the crack-tip are given in (b) and (c).

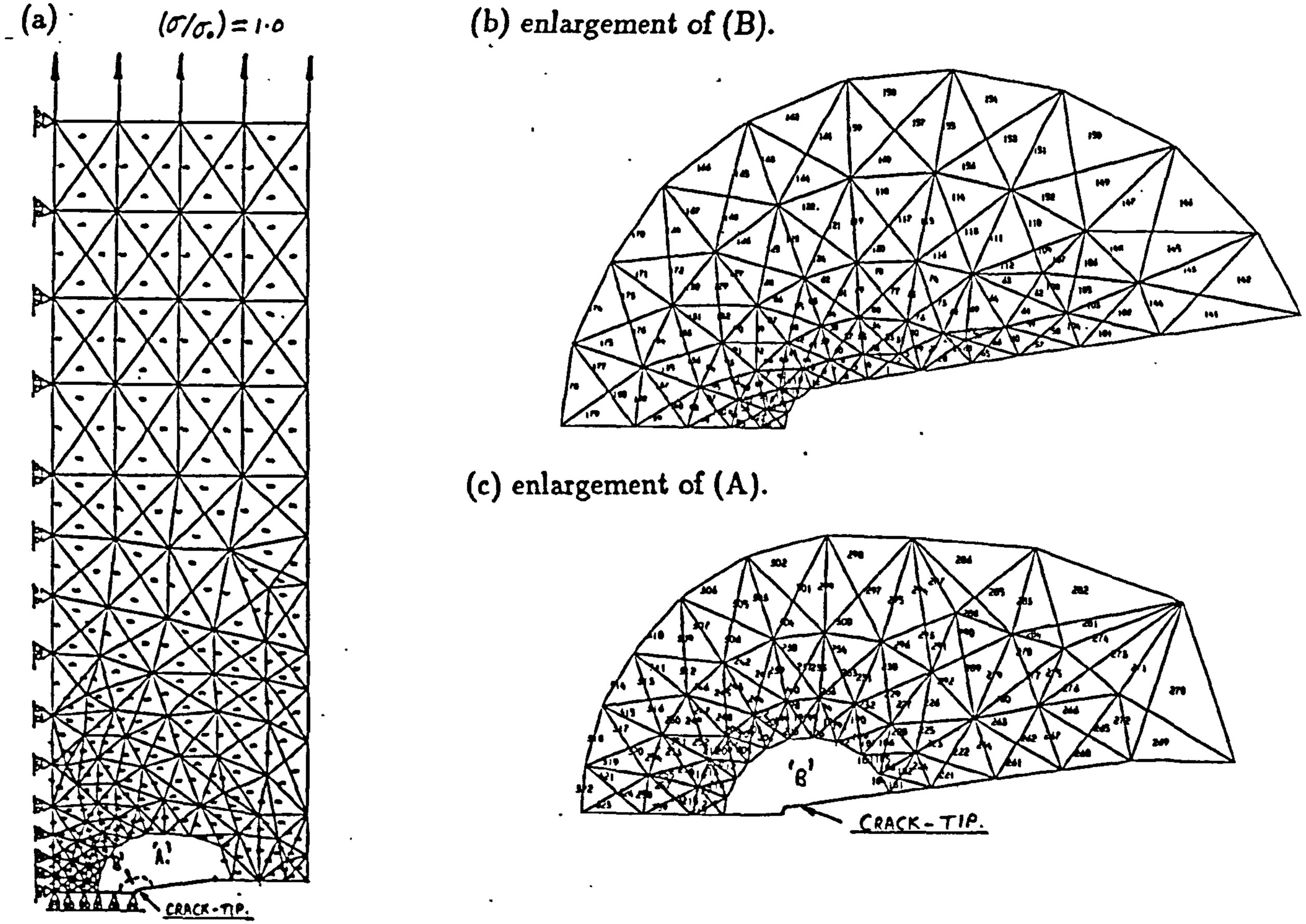

Figure 6.4: Finite element mesh for the externally cracked specimen (1/4)-plate, (a), with the applied bounday conditions. Enlargements of the mesh detail close to the crack-tip are given in (b) and (c).

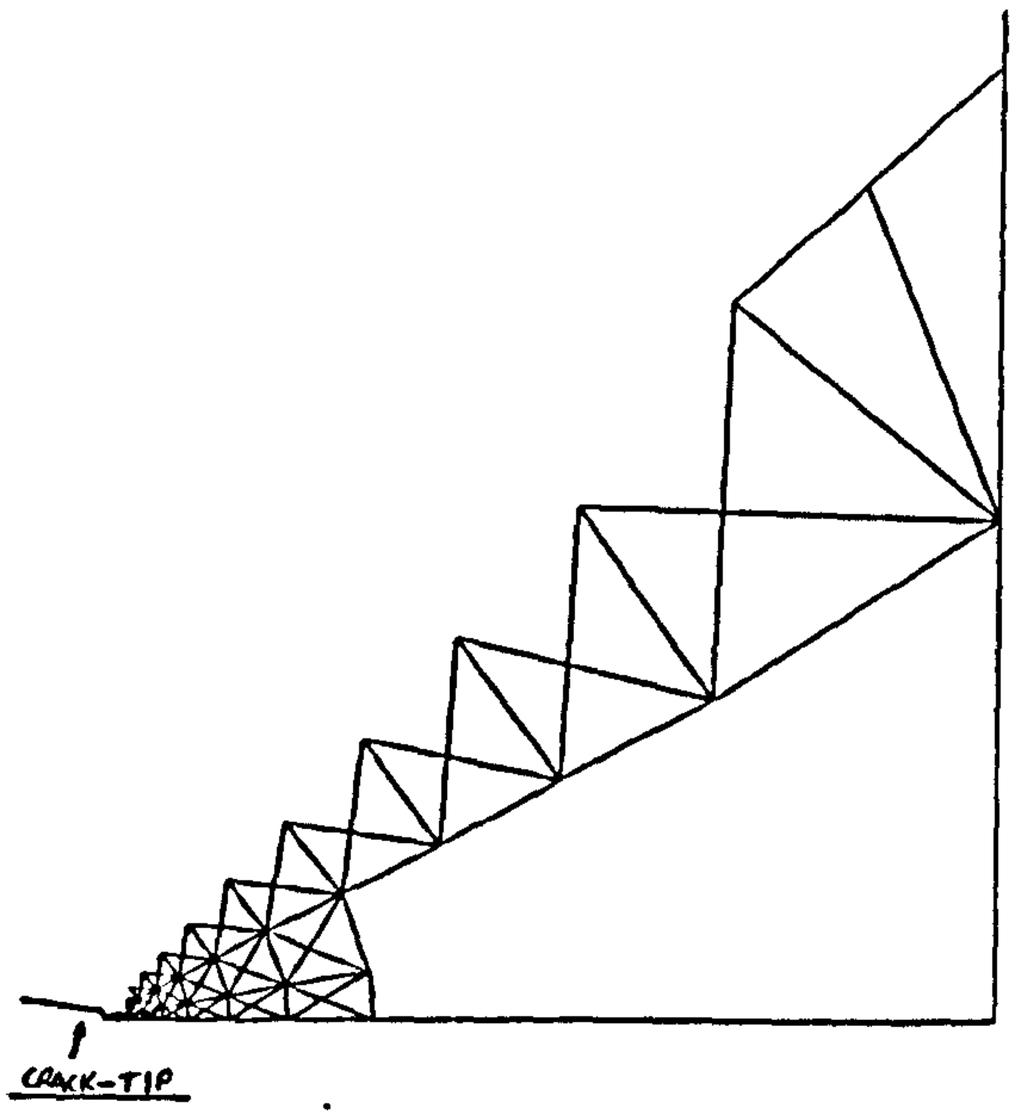

Figure 6.5: Failed element ($\omega > 0.9999$) distributions across the ligament of the internally cracked Copper specimen, using the standard local damage tequnique.

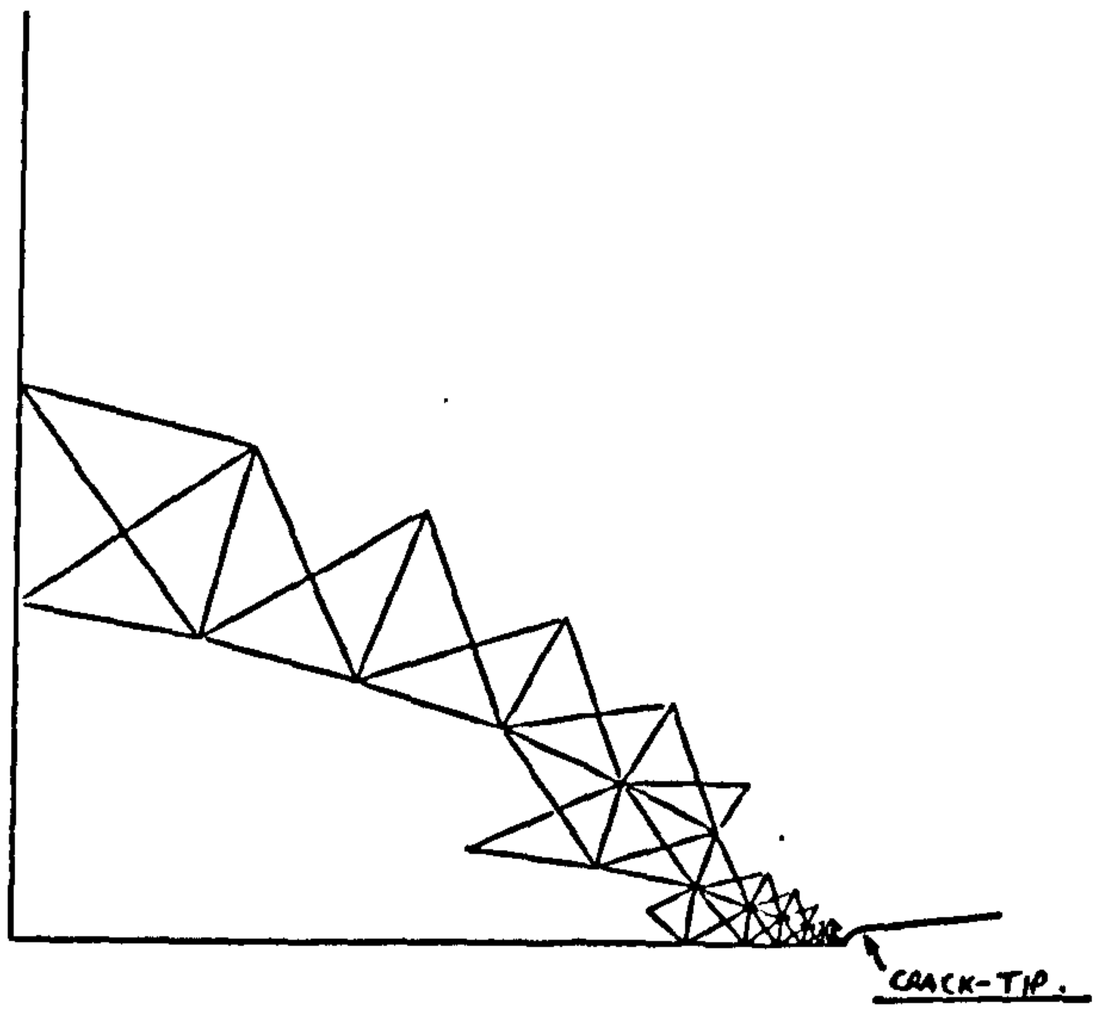

Figure 6.6: Failed element ($\omega > 0.9999$) distributions across the ligament of the externally cracked Copper specimen, using the standard local damage teqnique.

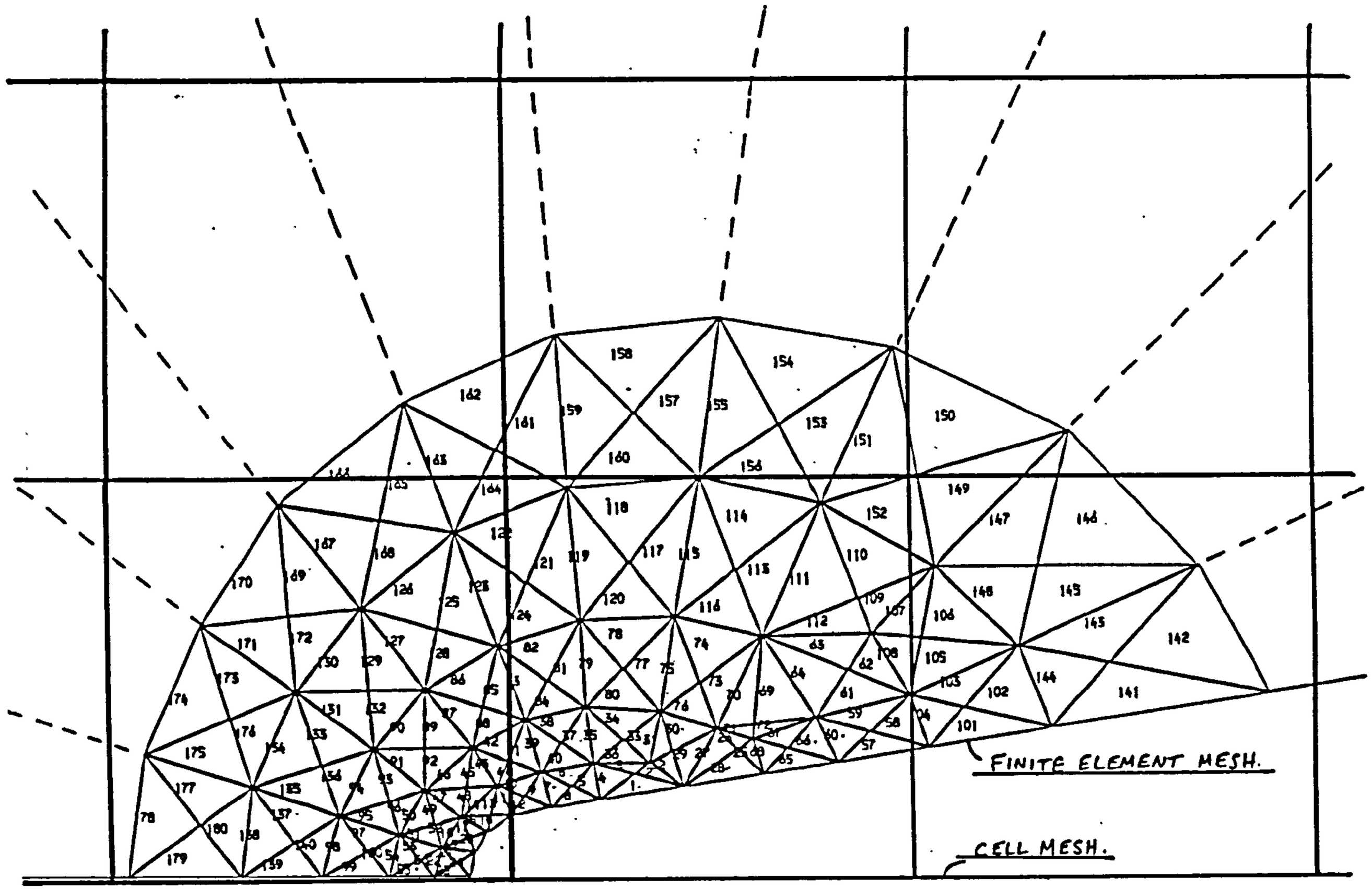

Figure 6.7: Cell mesh overlapping the triangular finite-element mesh for the externally cracked specimen. Only the region close to the crack-tip is shown.

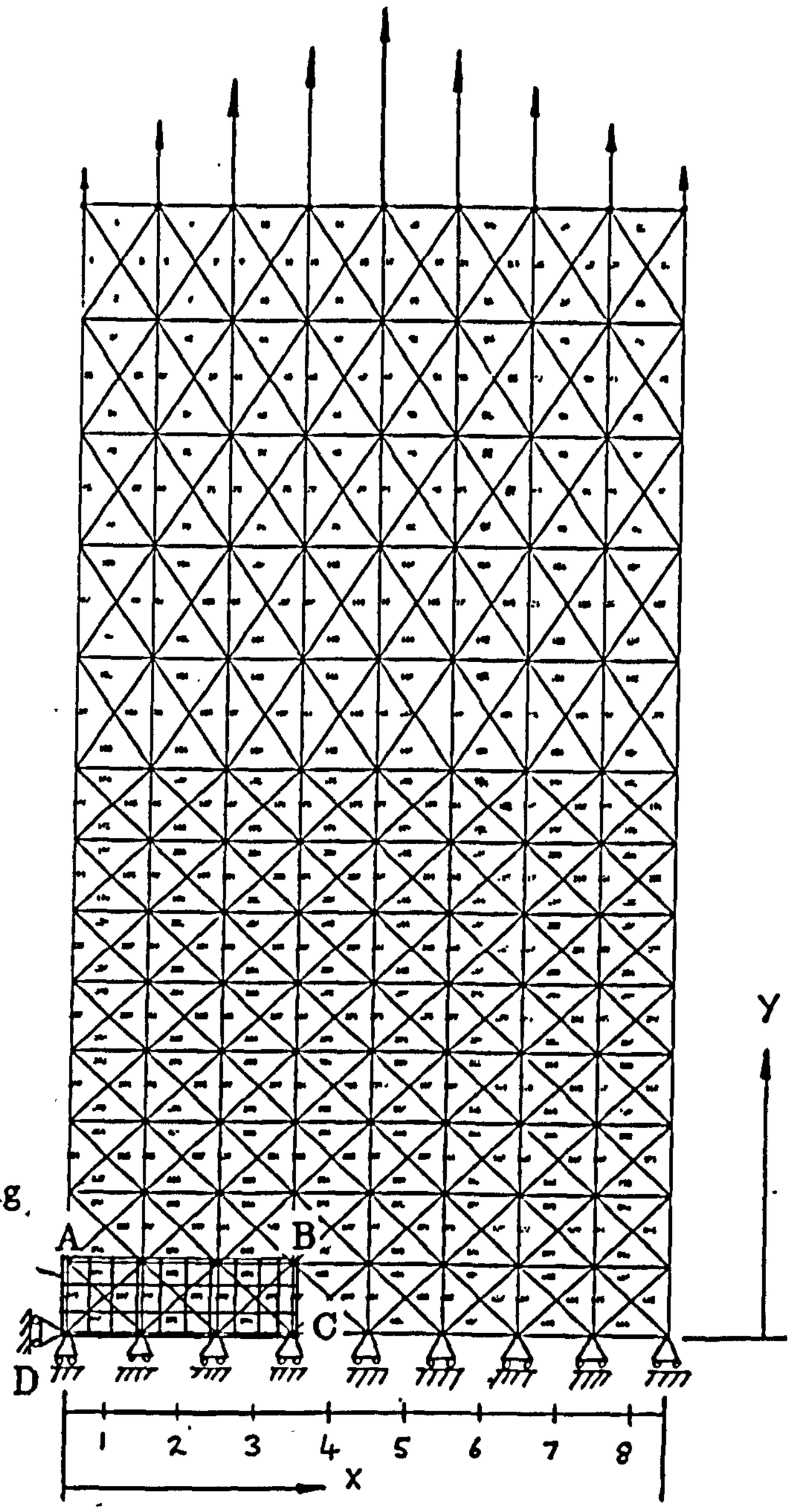

Figure 6.8: Finite-domain, non-local damage analysis, test problem, showing a symmetrically loaded oblong mesh with region A B C D overlapped with a cell mesh. In this region the non-local damage technique is applied, the rest of the mesh is solved using the standard local damage technique.

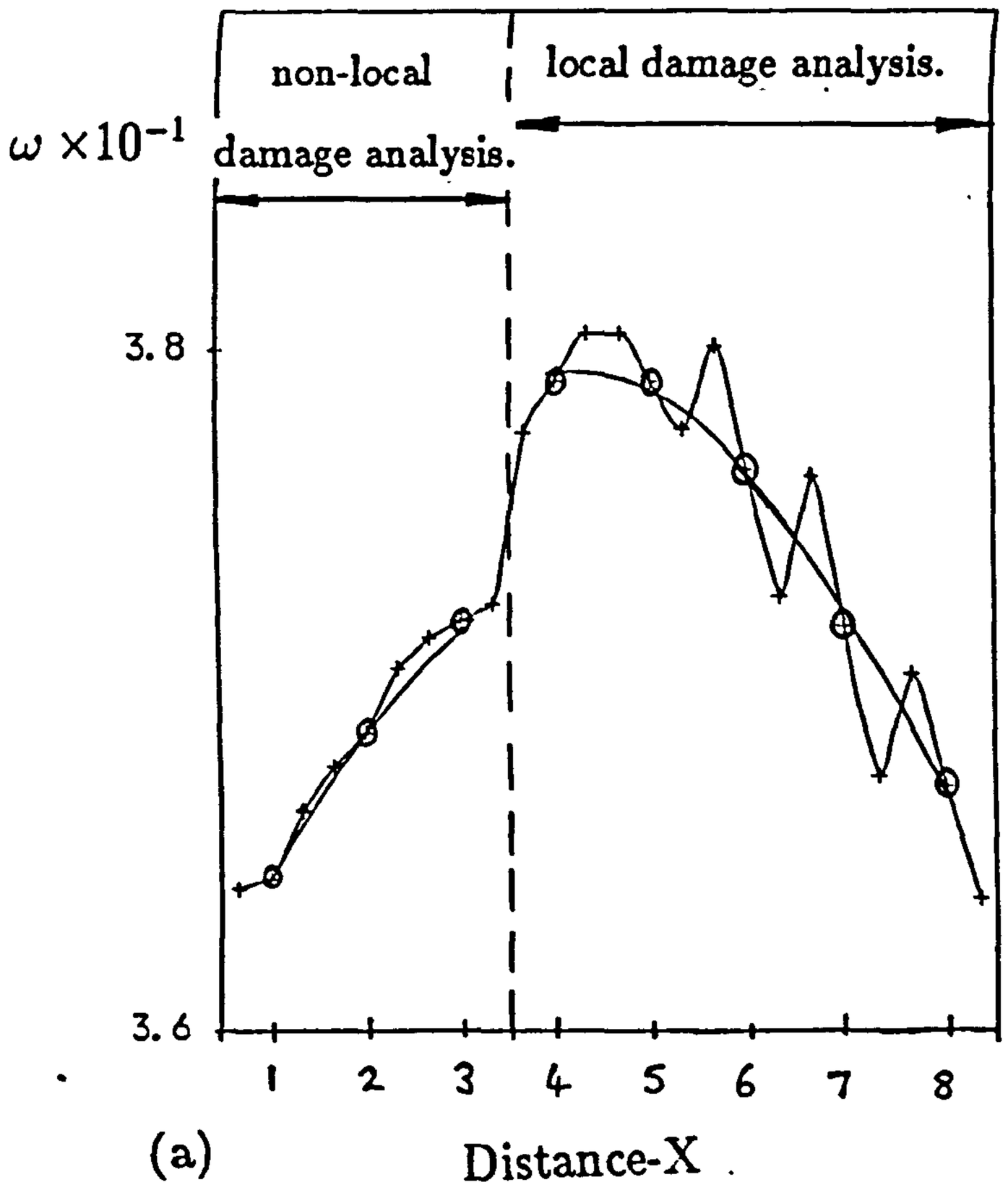

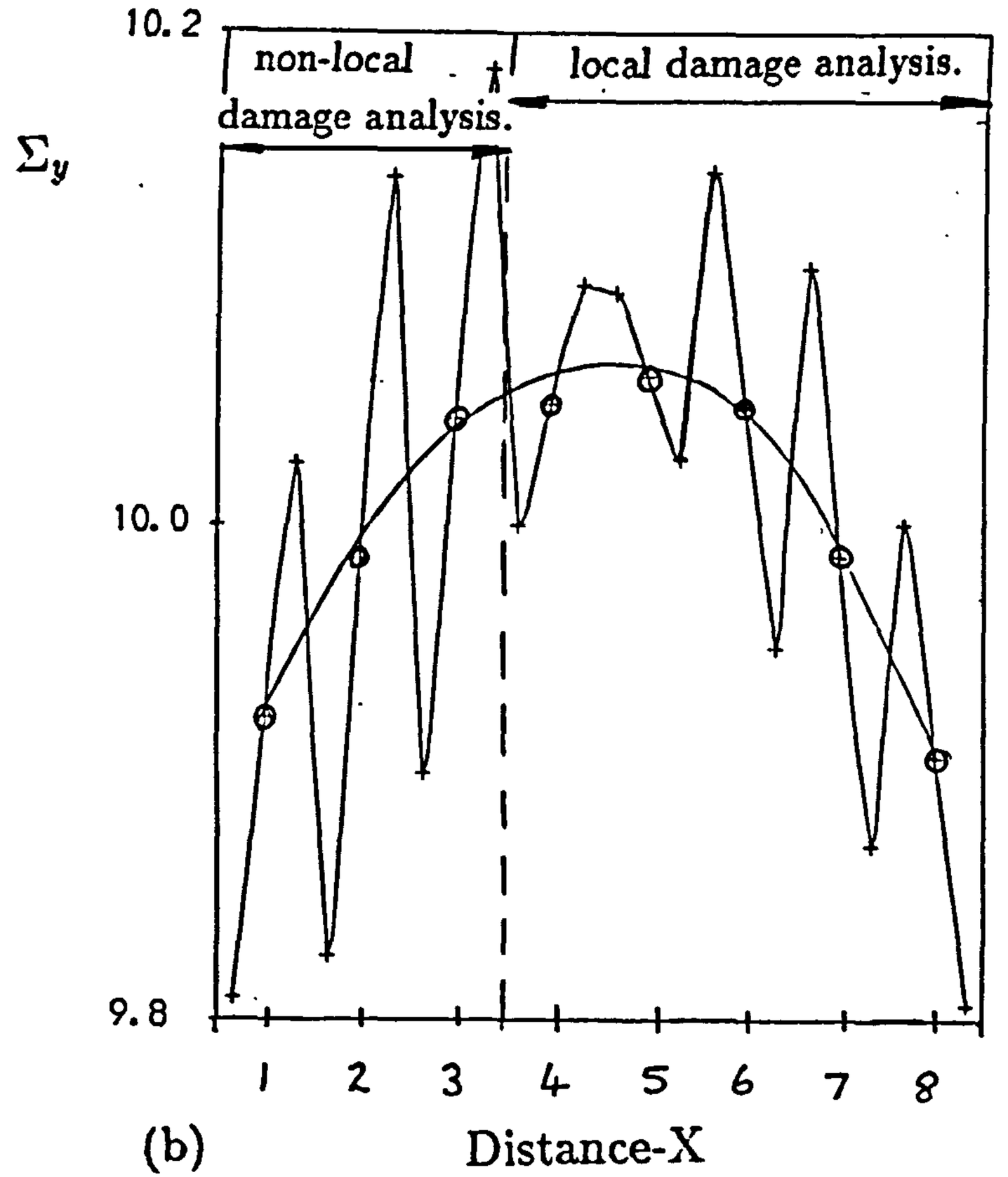

Figure 6.9: Elemental (a) damage and (b) stress values at the centroids of elements of the finite element mesh (Fig.6.8), lower boundary. Notice how the damage values are smoothed, and the stresses values are perturbed in the region, where the damage analysis is non-local.

(⊕) indicates bottom boundary elements :

(+) indicates bottom boundary elements:

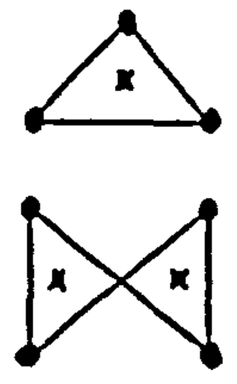

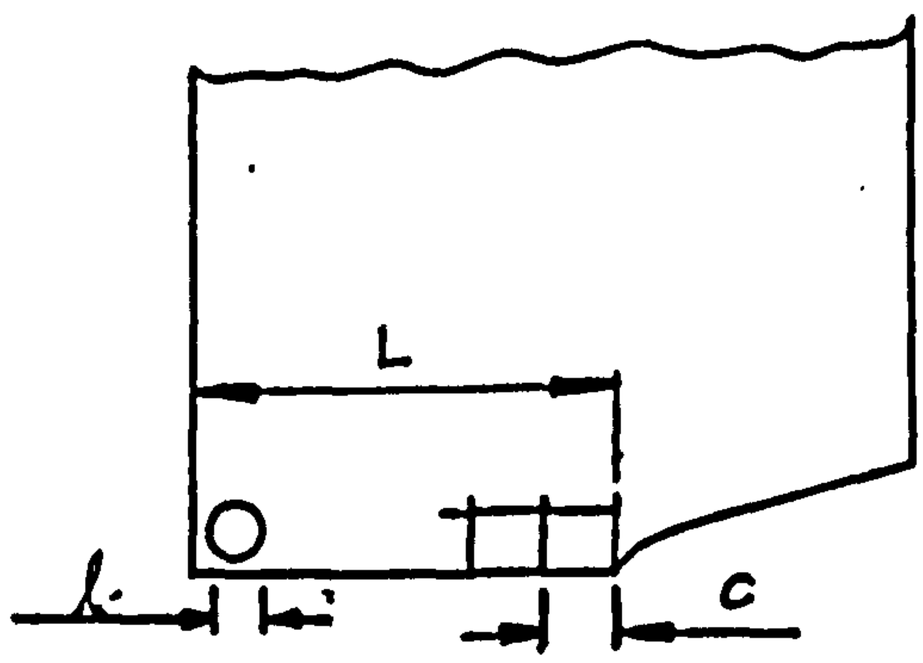

Figure 6.10: Definition of the normalised cell dimensions (γ_c) and (γ_l).
L is the ligament length.
C is length of the side of a square cell, in the overlapping cell mesh for the finite domain non-local damage technique.
l is the diameter of a circular cell for the infinite domain non-local damage technique.

$$\gamma_c = \left(\frac{L}{C}\right)$$

$$\gamma_l = \left(\frac{L}{l}\right)$$

(a) Small

(b) large

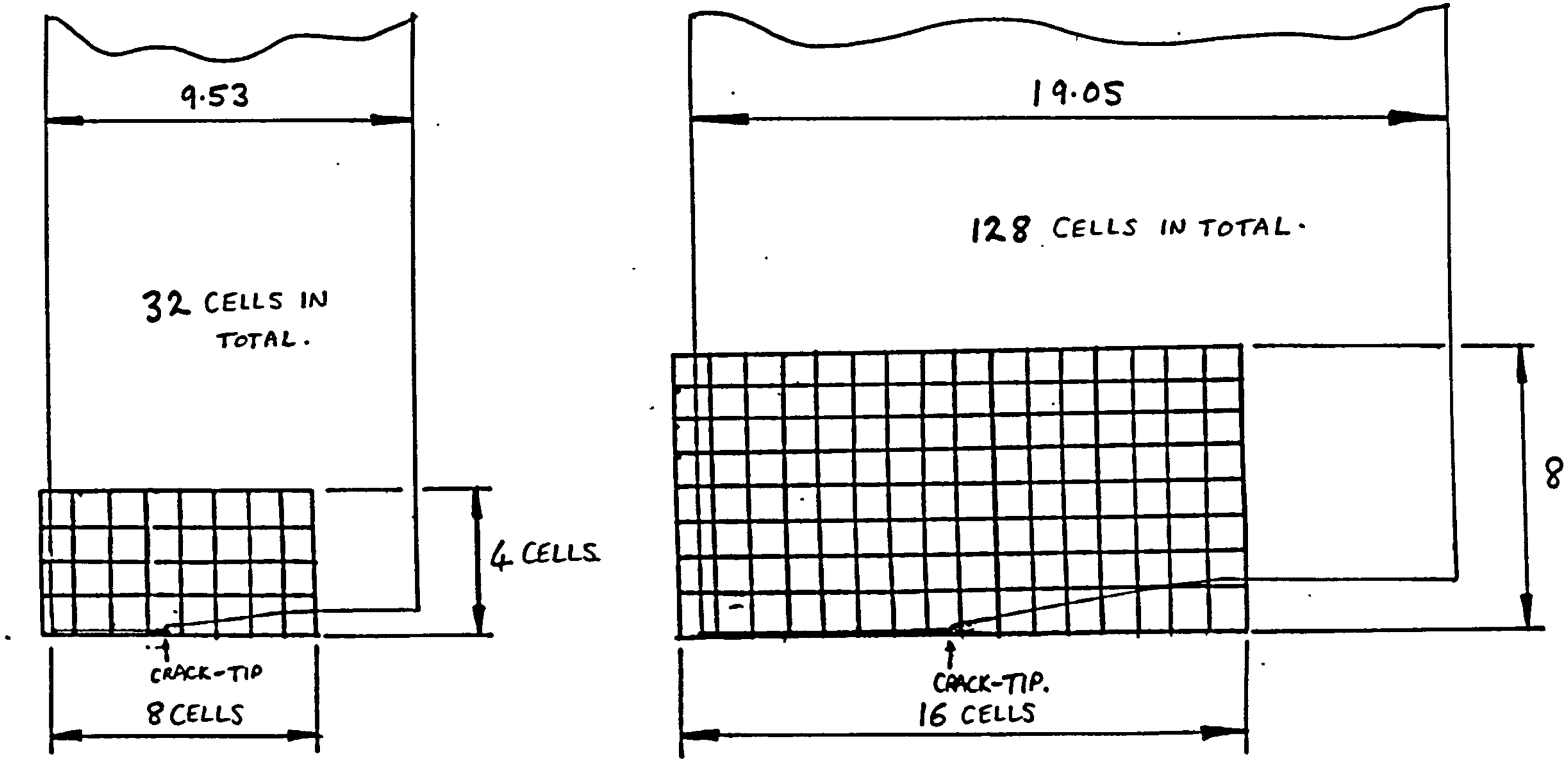

Figure 6.11: Diagrams showing the positions and sizes of the cell meshes used to overlap the finite element meshes representing the small (a) and the large (b) externally cracked specimens. The square cells are of side 0.9mm.

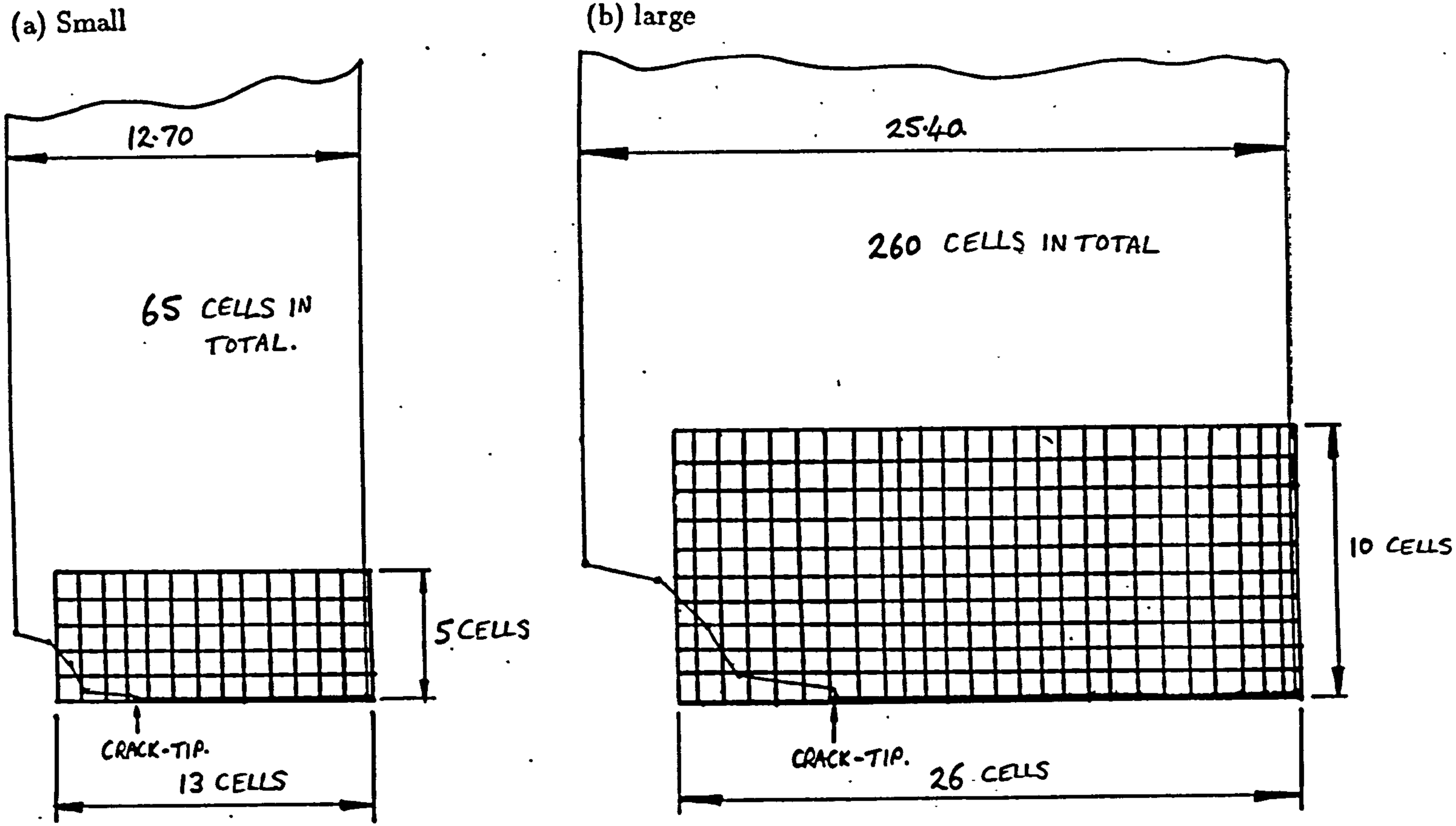

Figure 6.12: Diagrams showing the positions and sizes of the cell meshes used to overlap the finite element meshes representing the small (a) and the large (b) internally cracked specimens. The square cells are of side 0.9mm.

(a) *Method No.1.*

Small Sized Specimen.

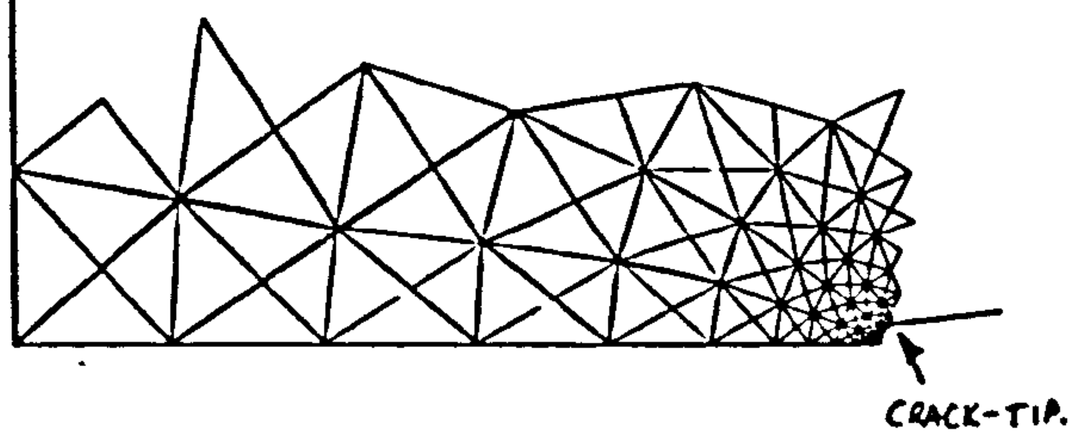

Large Sized Specimen.

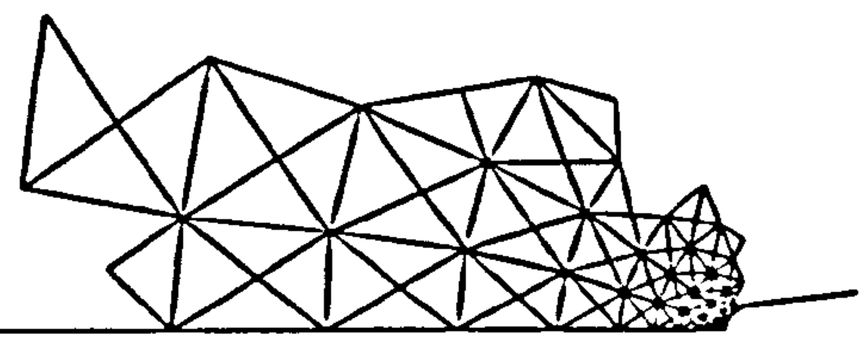

(b) *Method No.2.*

Small Sized Specimen.

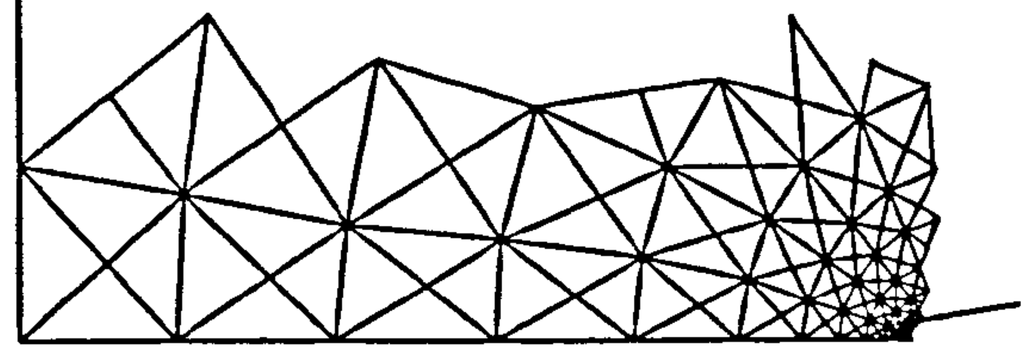

Large Sized Specimen.

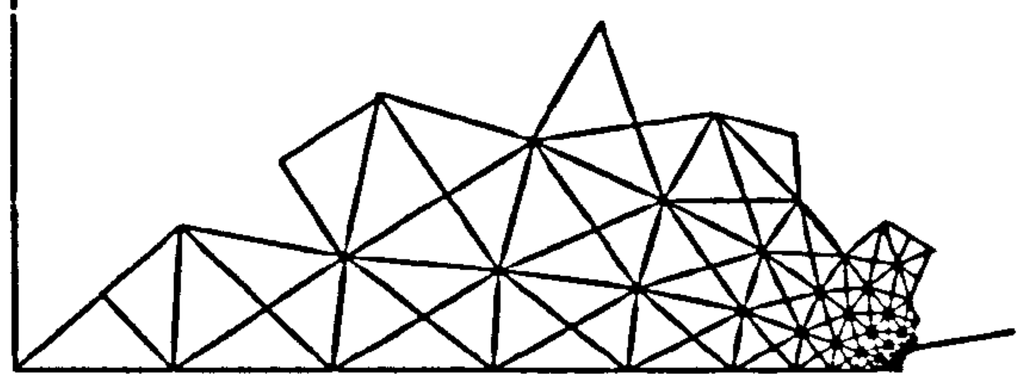

Figure 6.13: Predicted failed element ($\omega > 0.9999$) distributions across the ligaments of the externally cracked large and small specimens using finite domain non-local damage: (a) method 1 and (b) method 2. (cell size used, C=0.9mm).

(a) Method No.1.

Small Sized Specimen.

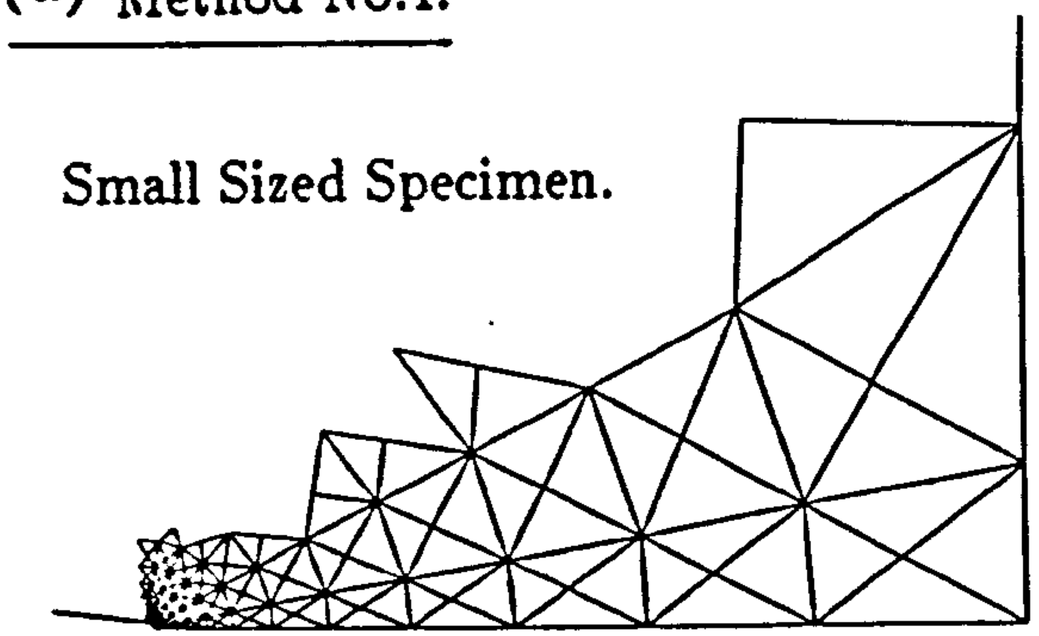

Large Sized Specimen.

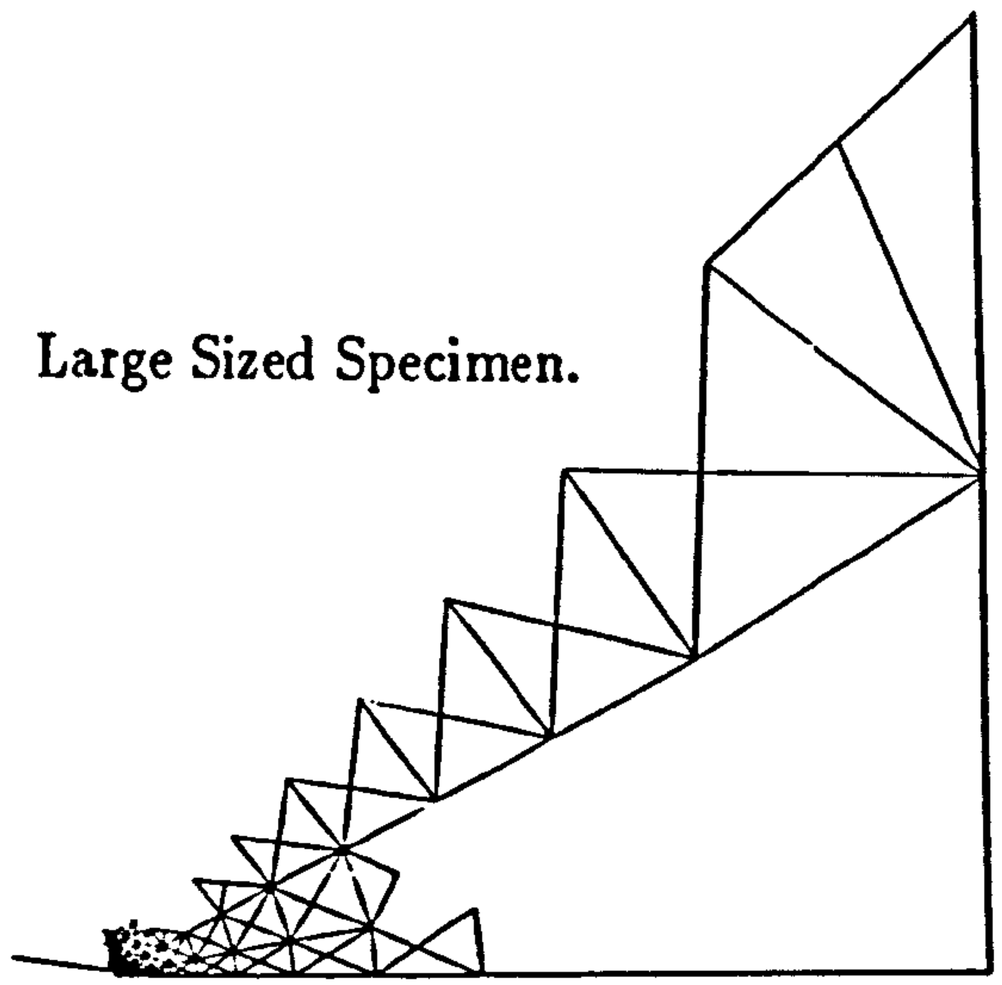

(b) Method No.2.

Small Sized Specimen.

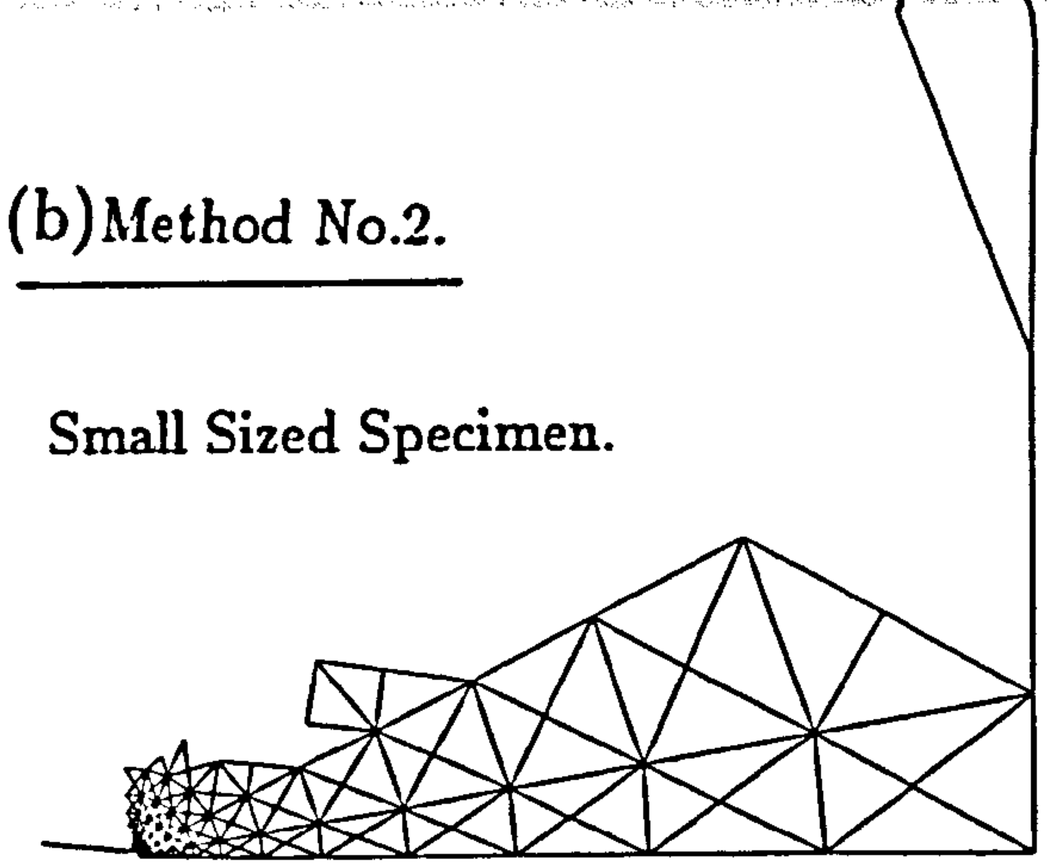

Large Sized Specimen.

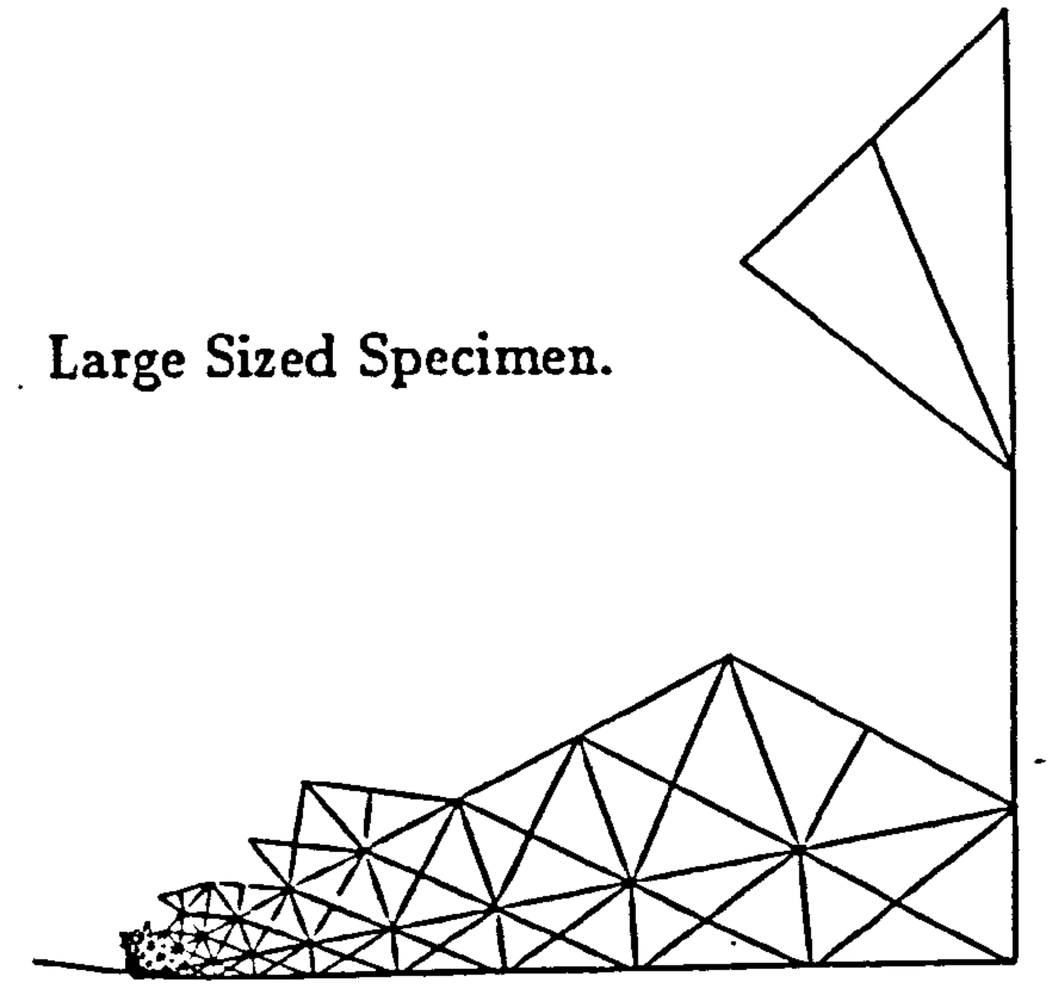

Figure 6.14: Predicted failed element ($\omega > 0.9999$) distributions across the ligaments of the internally cracked large and small specimens using finite domain non-local damage: (a) method 1 and (b) method 2. (cell size used, C=0.9mm).

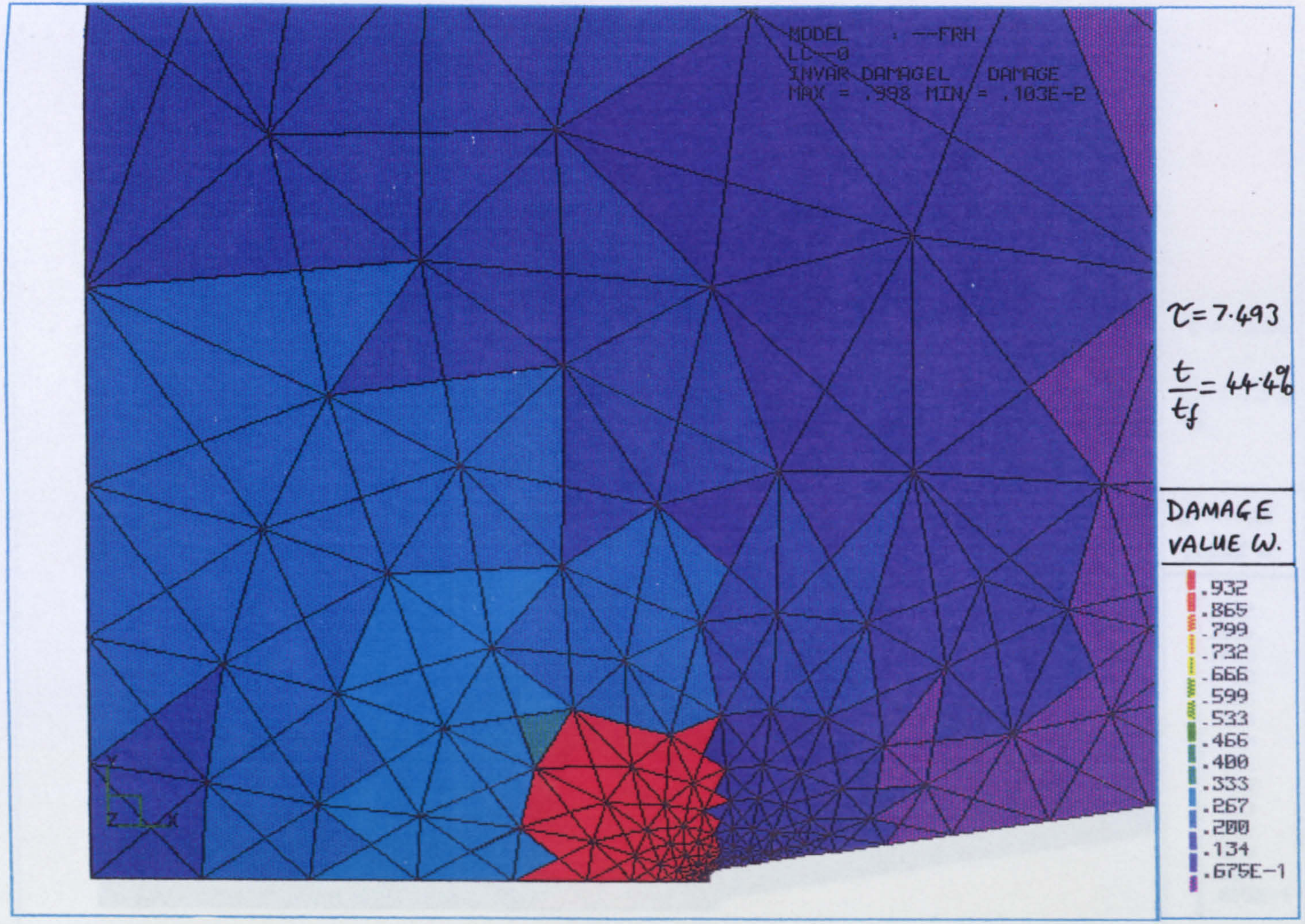

Figure 6.15: Colour plot showing elemental damage values, for the small externally cracked specimen using finite domain non-local damage method No. 1, at a time just before the failure of the first element. Transparency shows part of the cell mesh used.

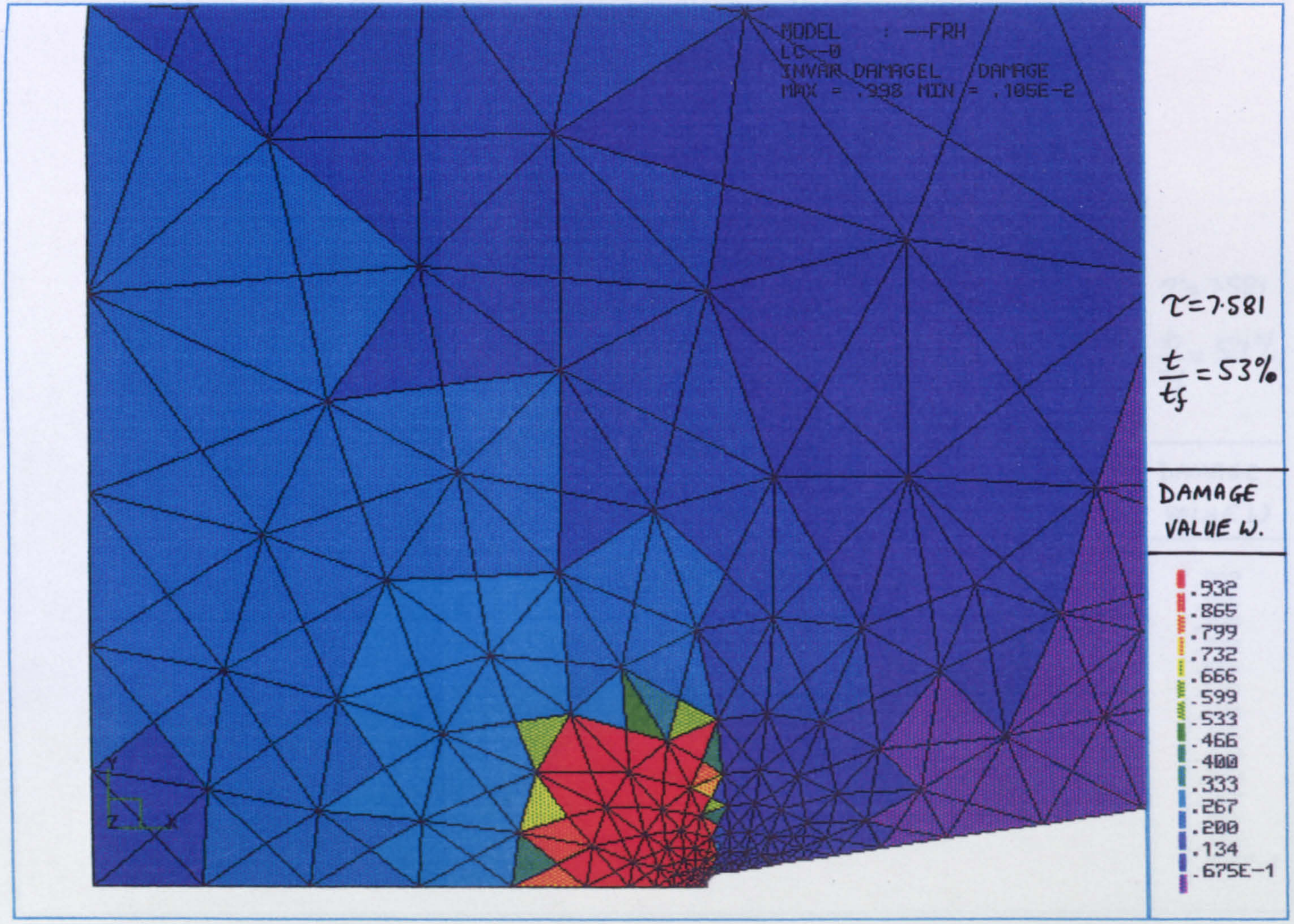

Figure 6.16: Colour plot showing elemental damage values, for the small externally cracked specimen using finite domain non-local damage method No. 2, at a time just before the failure of the first element. The cell mesh transparency given at Fig.6.15 may be overlapped with this fig-

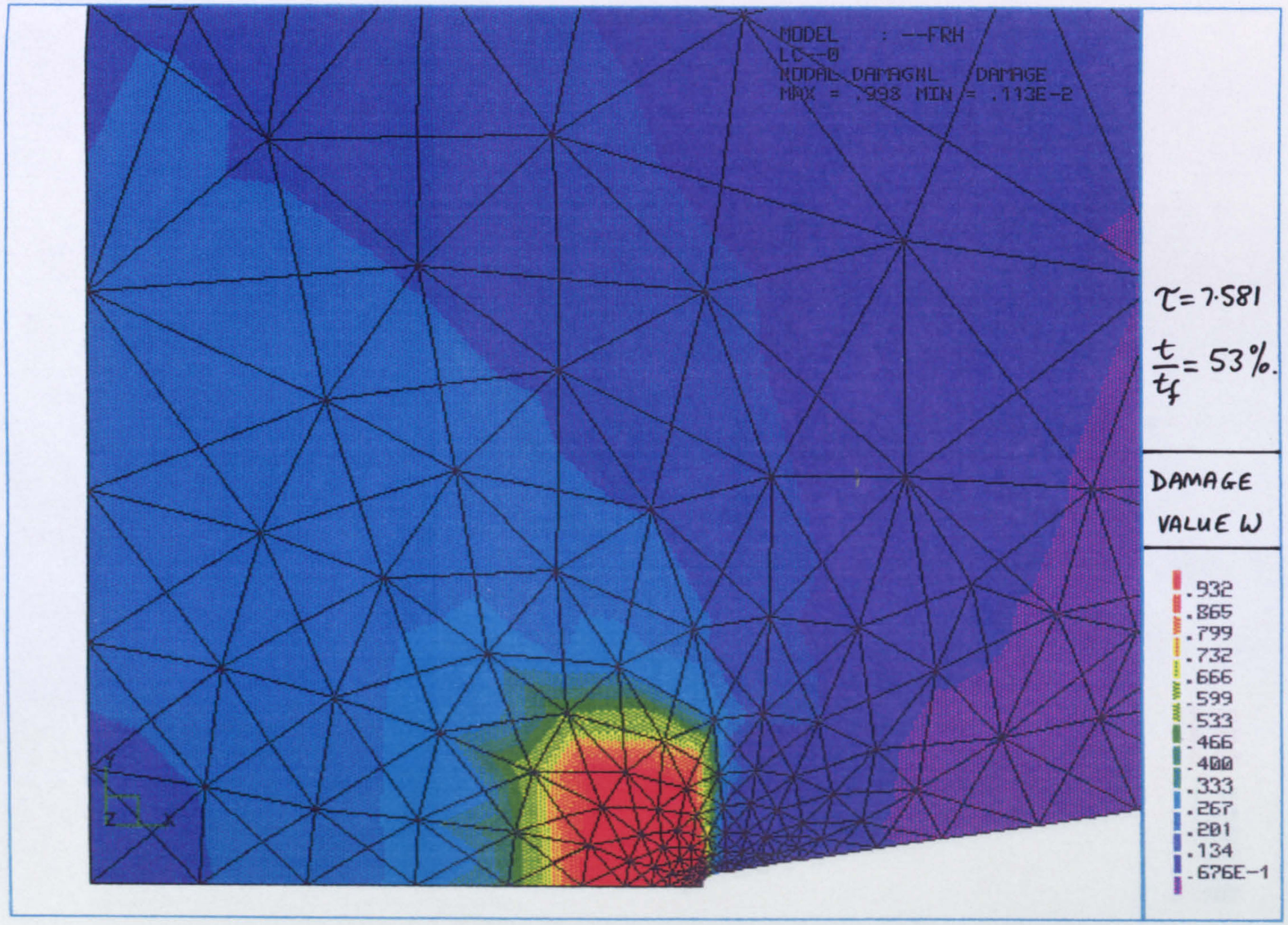

Figure6.17: Damage distribution at a life fraction of (t/t_f=53%) for the small externally cracked specimen using finite domain non-local damage method No.2.

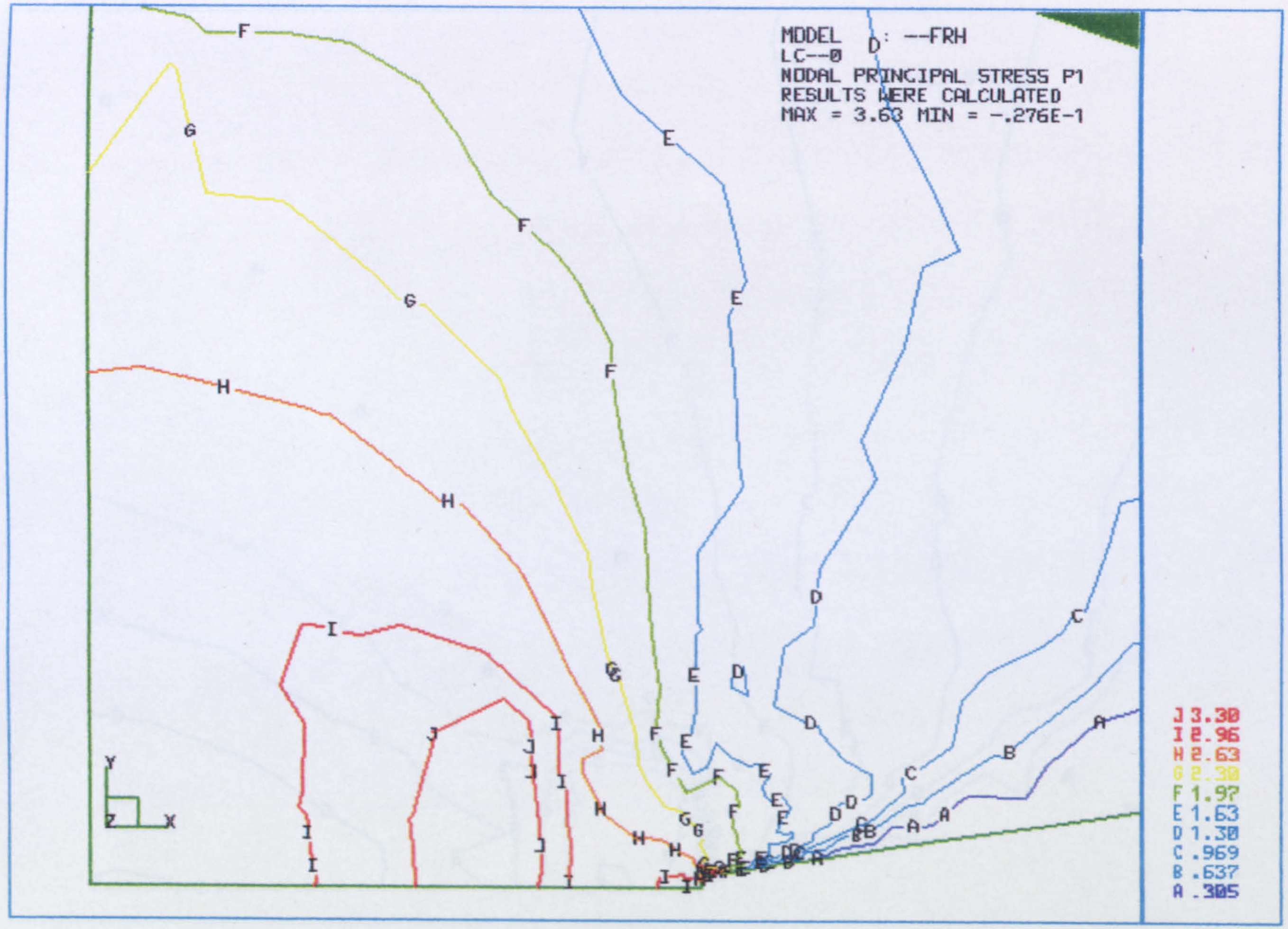

Figure 6.18: Normalised maximum principal stress contour plot at a life fraction (t/t_f=53%) for the small externally cracked specimen using finite domain non-local damage method No.2.

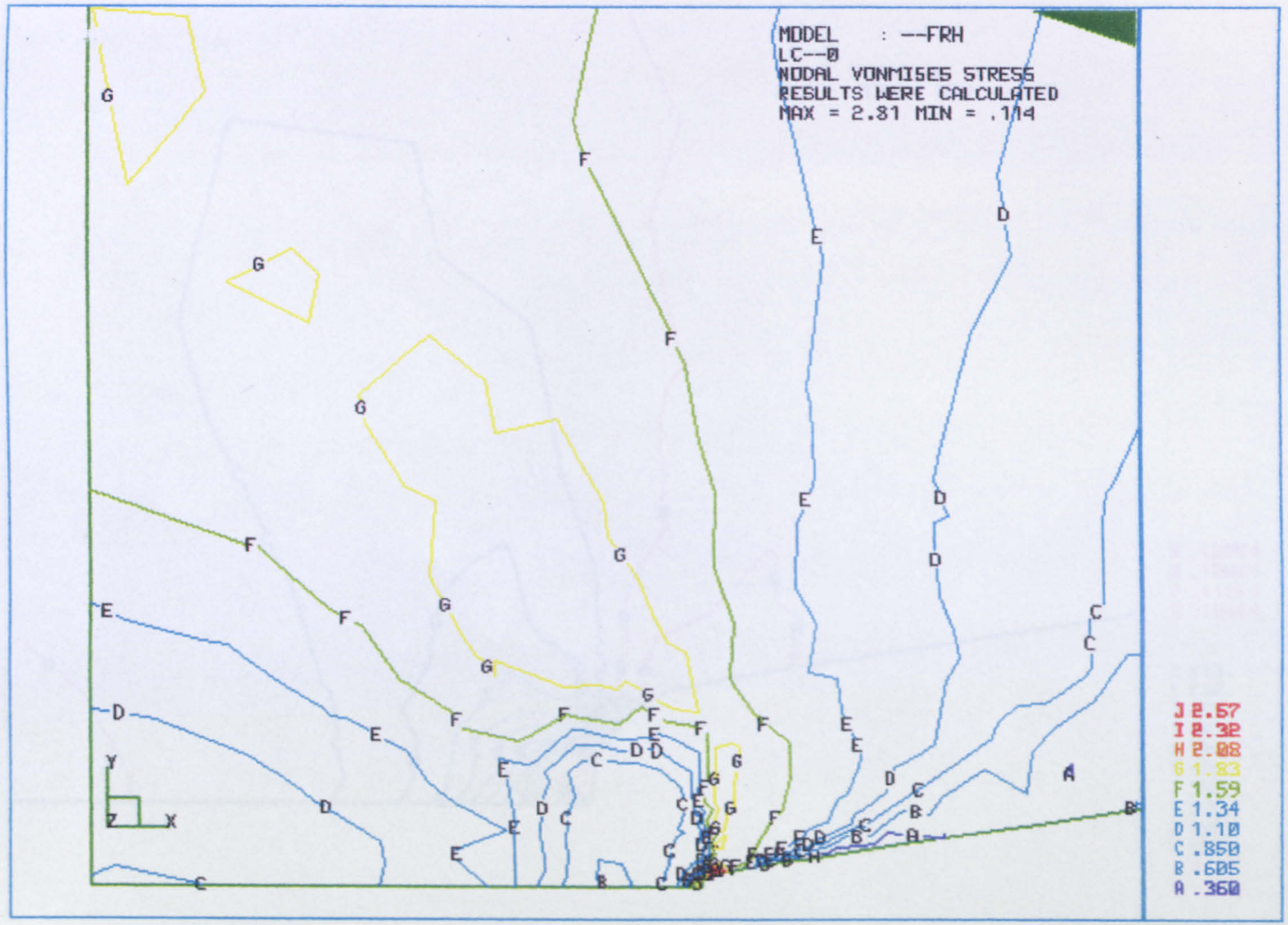

Figure 6.19: Normalised effective stress contour plot at a life fraction of (t/t_f=53%) for the small externally cracked specimen using finite domain non-local damage method No.2.

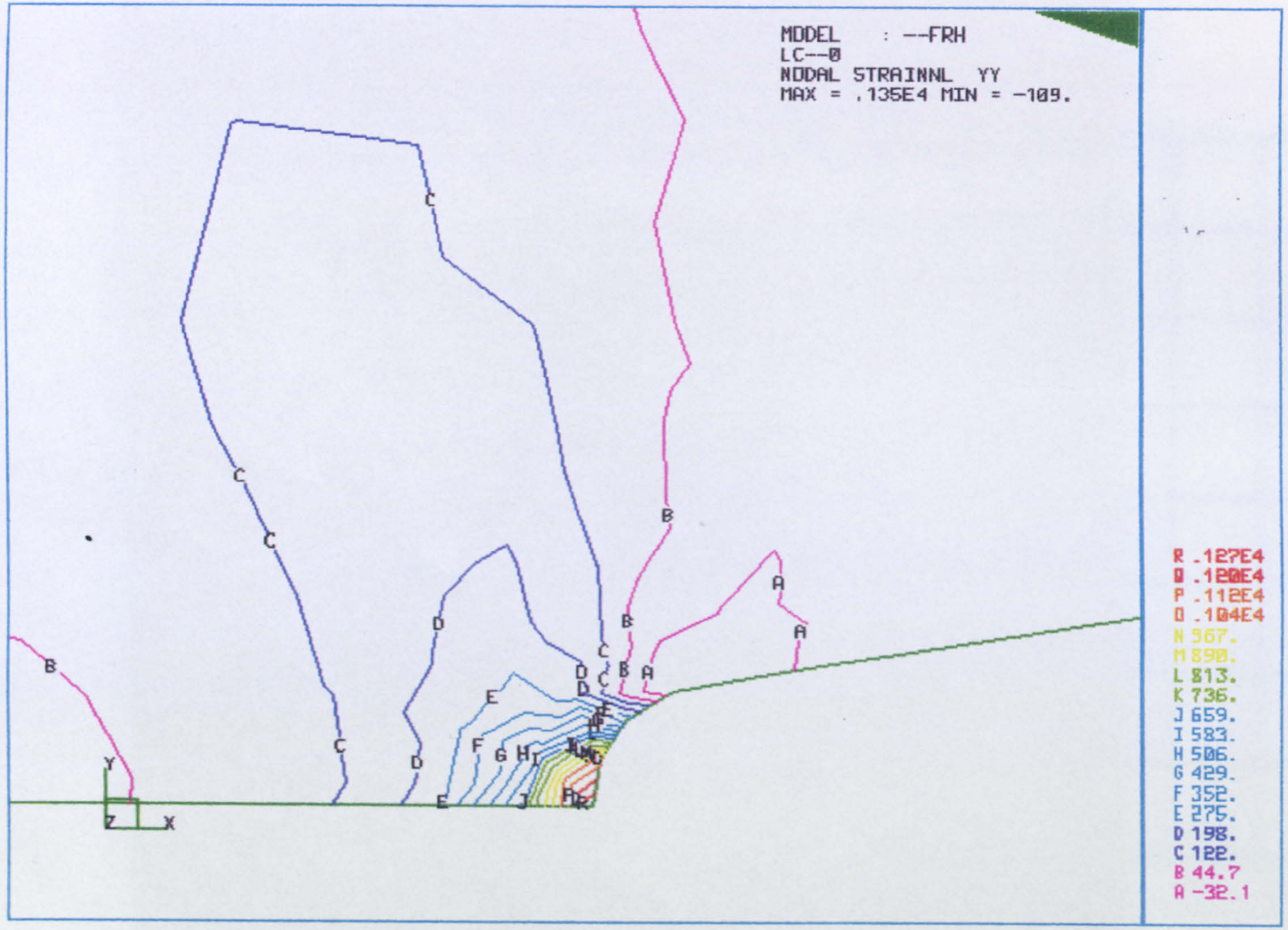

Figure 6.20: Normalised creep strain in the (y)-direction at life fraction (t/t_f=53%) for the small externally cracked specimen using finite domain non-local damage method No.2.

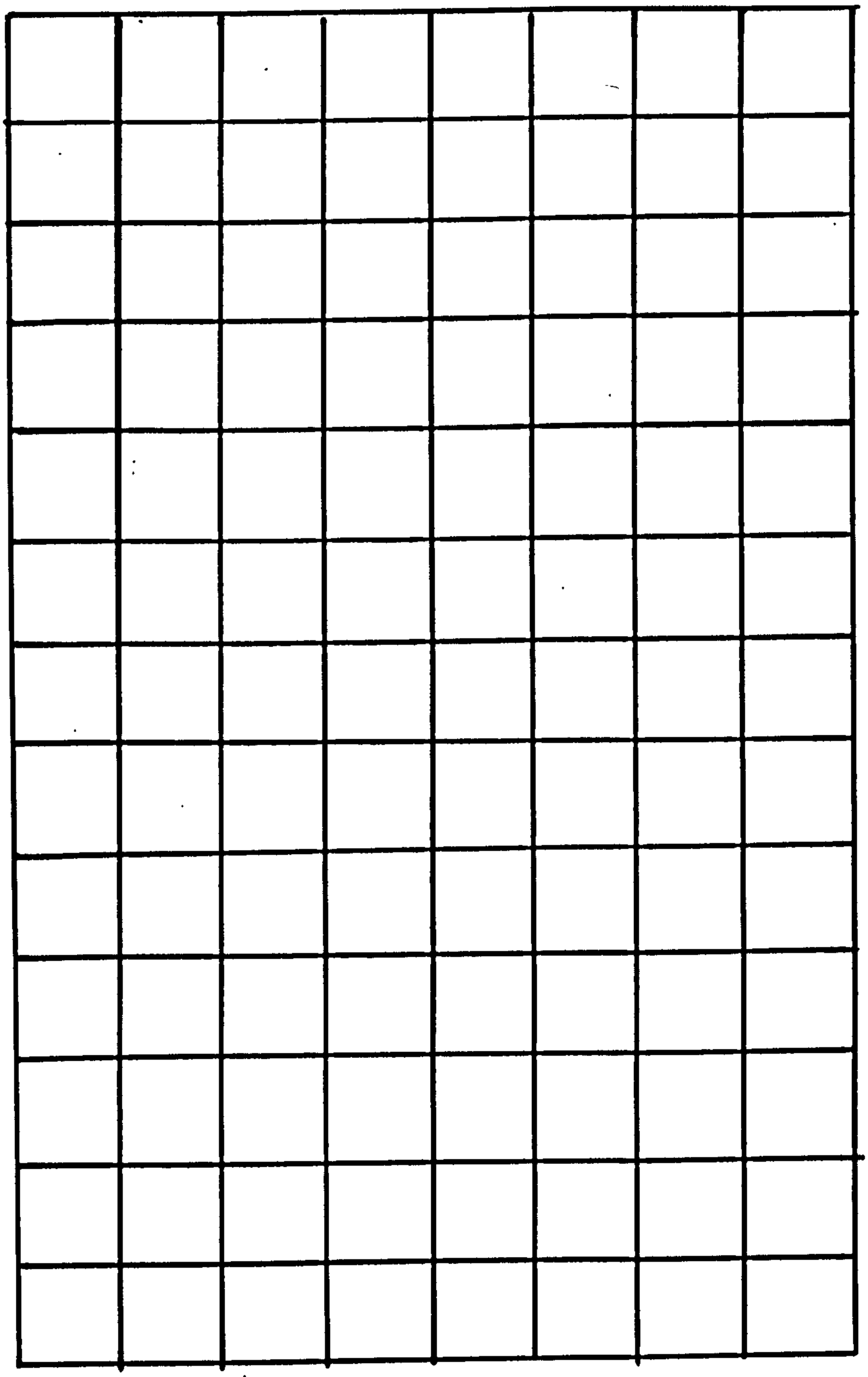

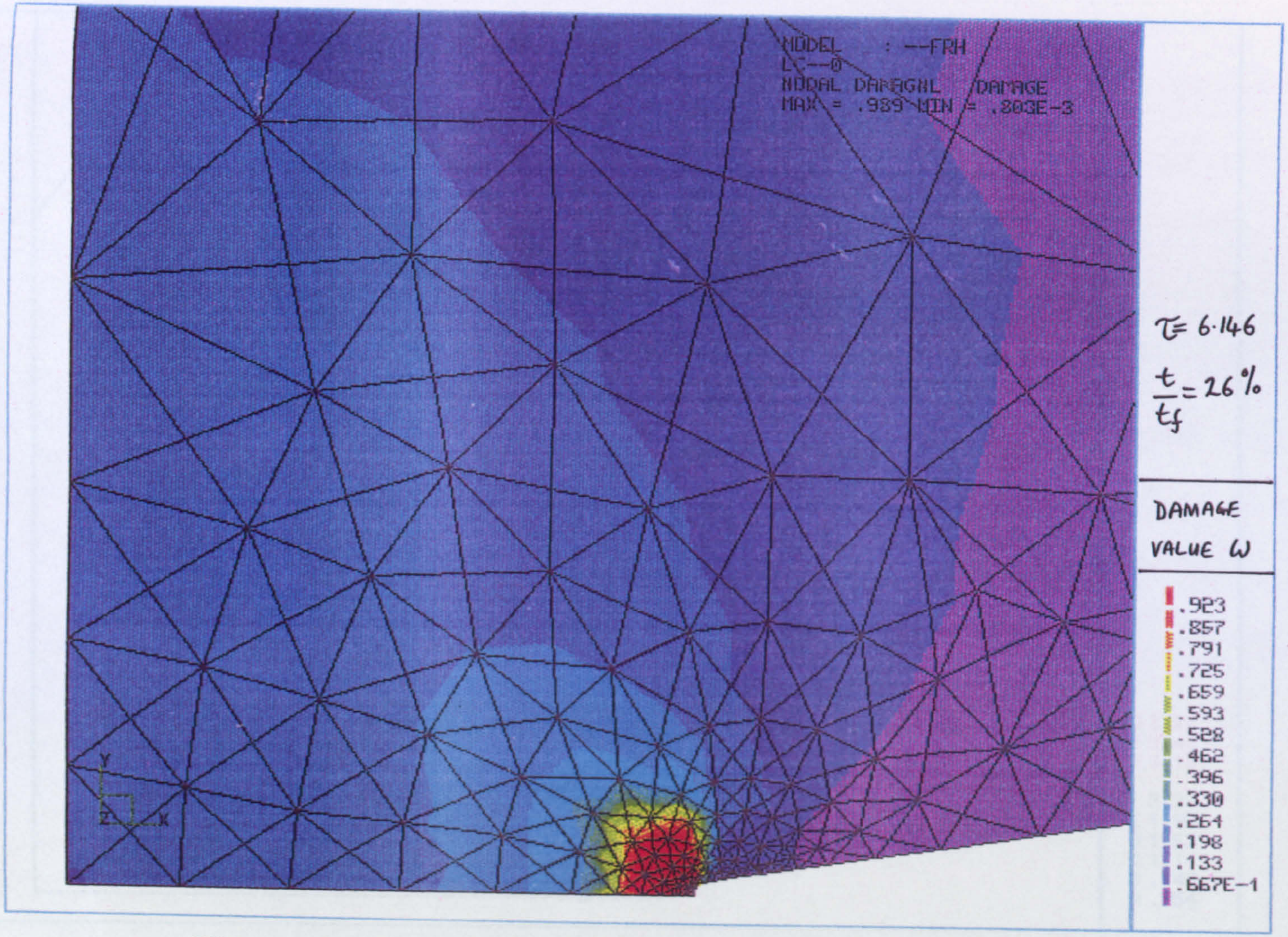

Figure6.21: Damage distribution at a life fraction of (t/t_f=26%) for the large externally cracked specimen using finite domain non-local damage method No.2.

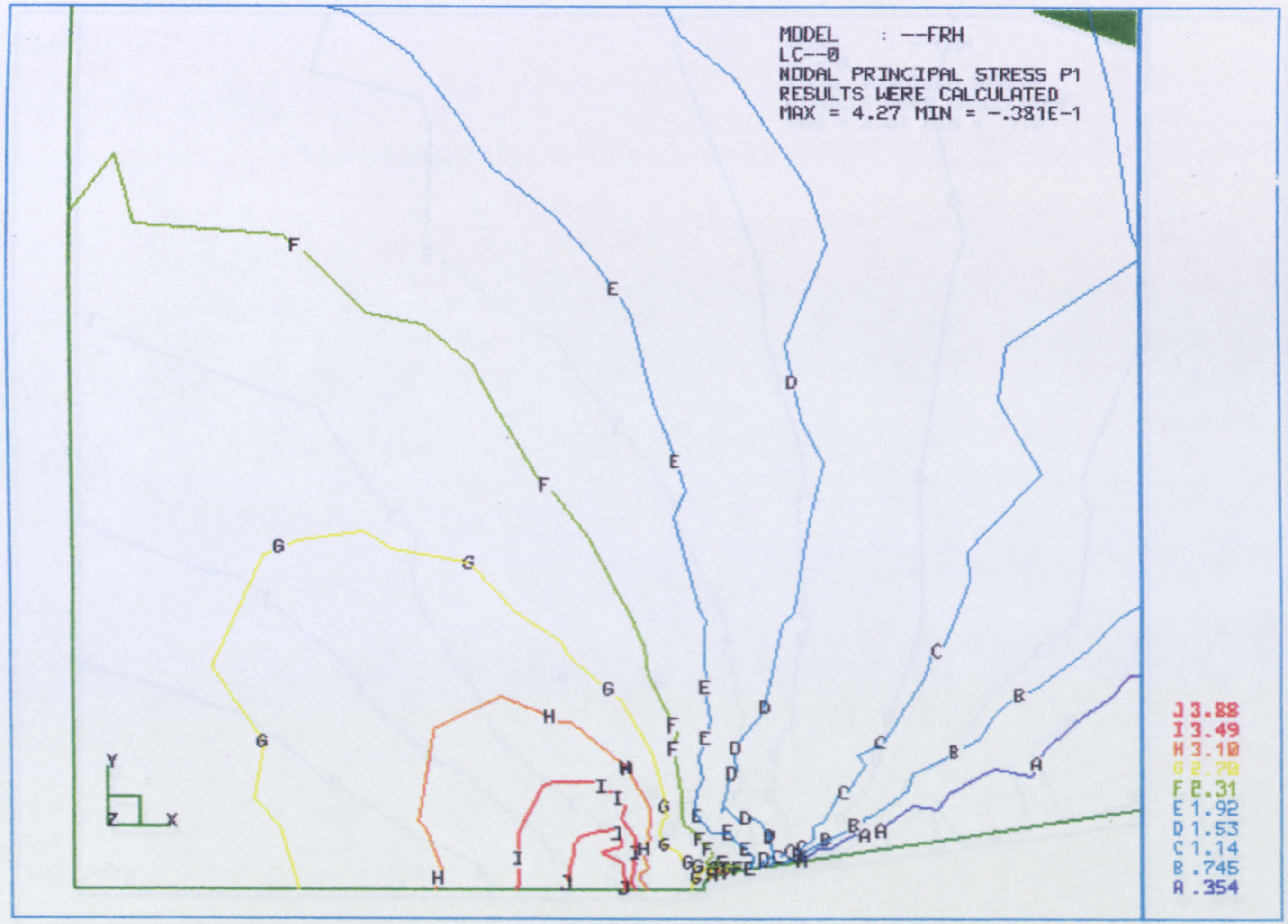

Figure 6.22: Normalised maximum principal stress contour plot at a life fraction (t/t_f=26%) for the large externally cracked specimen using finite domain non-local damage method No.2.

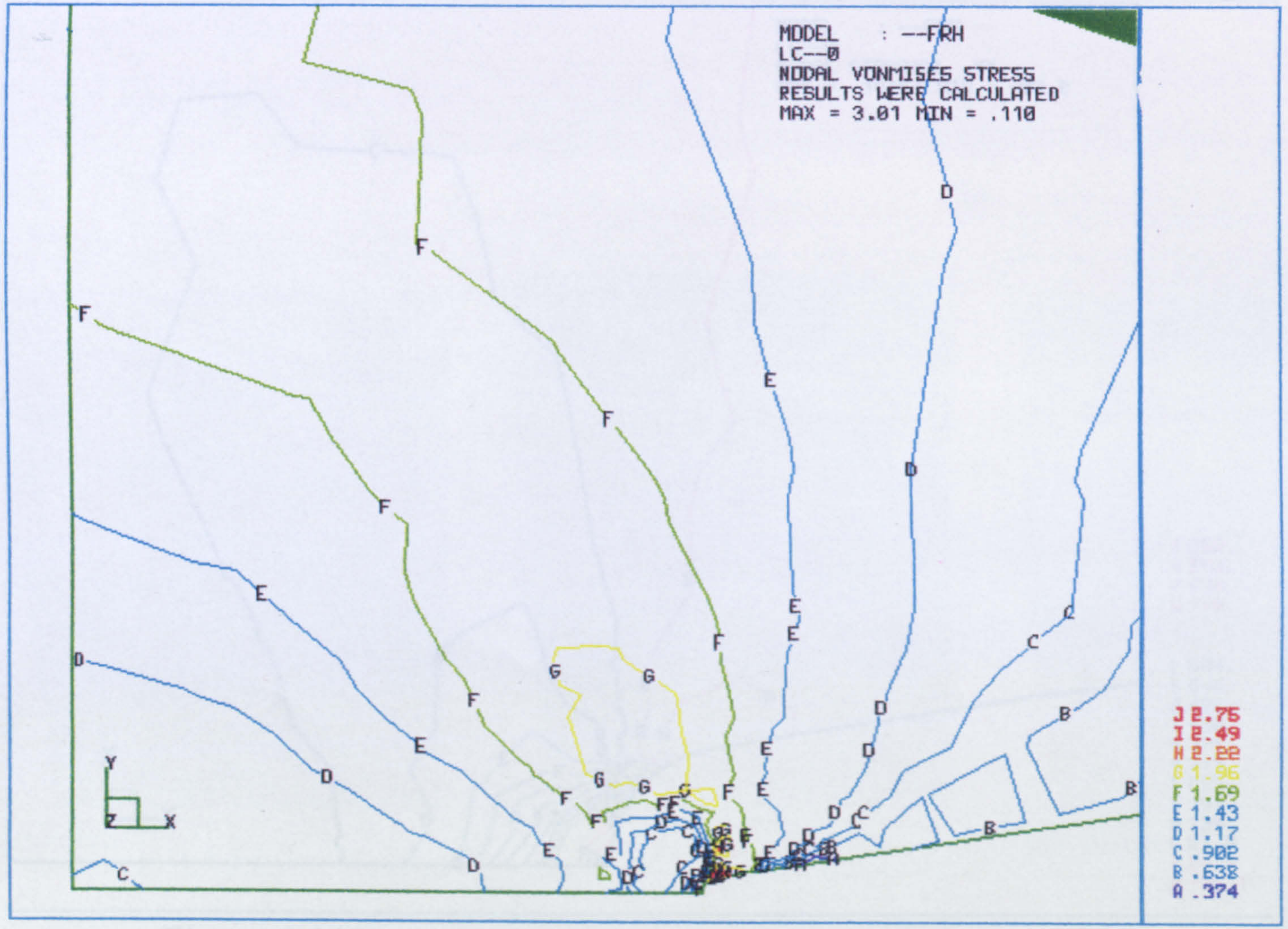

Figure 6.23: Normalised effective stress contour plot at a life fraction of (t/t_f=26%) for the large externally cracked specimen using finite domain non-local damage method No.2.

Figure 6.24: Normalised creep strain in the (y)-direction at life fraction (t/t_f=26%) for the large externally cracked specimen using finite domain non-local damage method No.2.

(a)

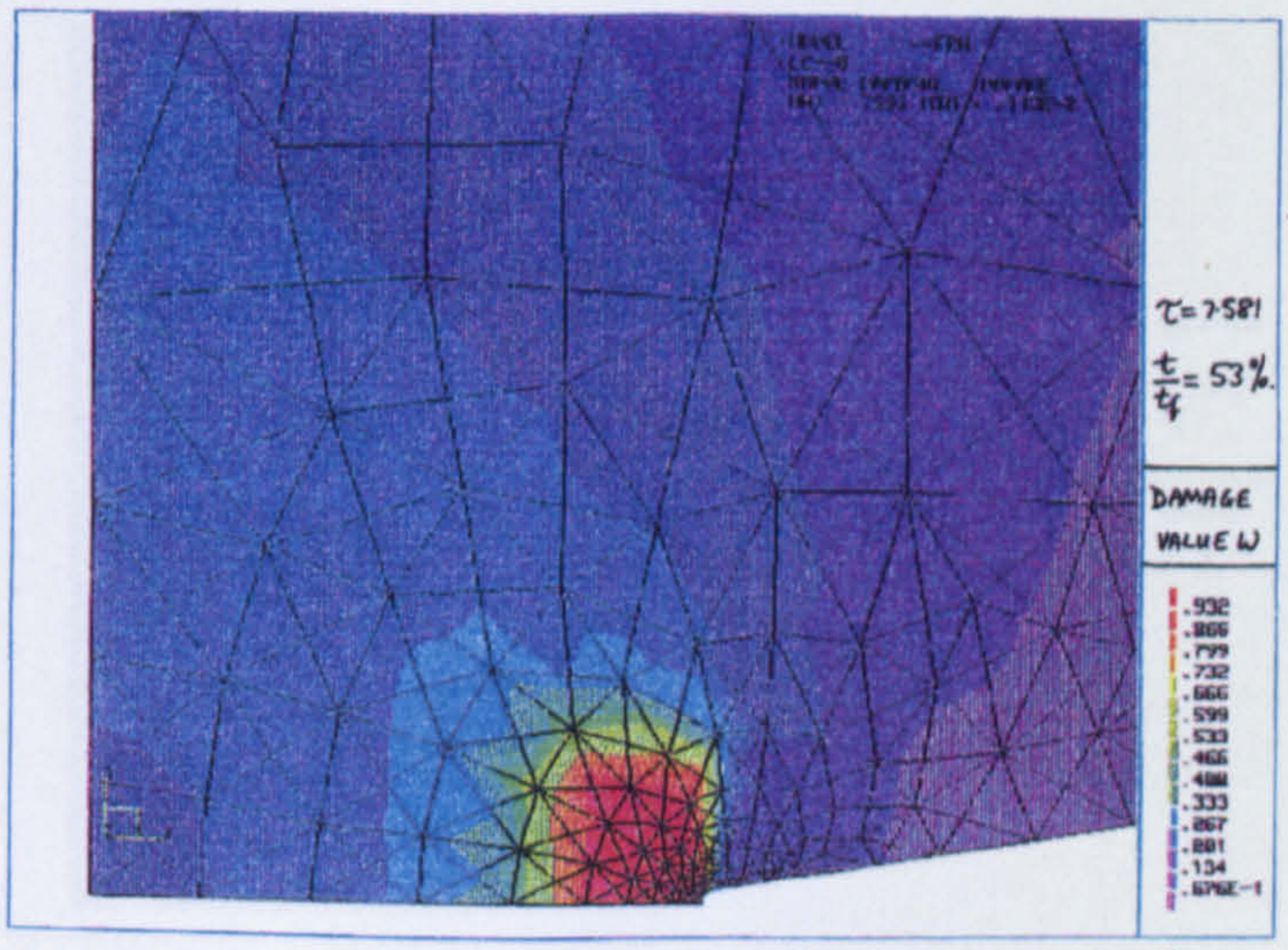

(b)

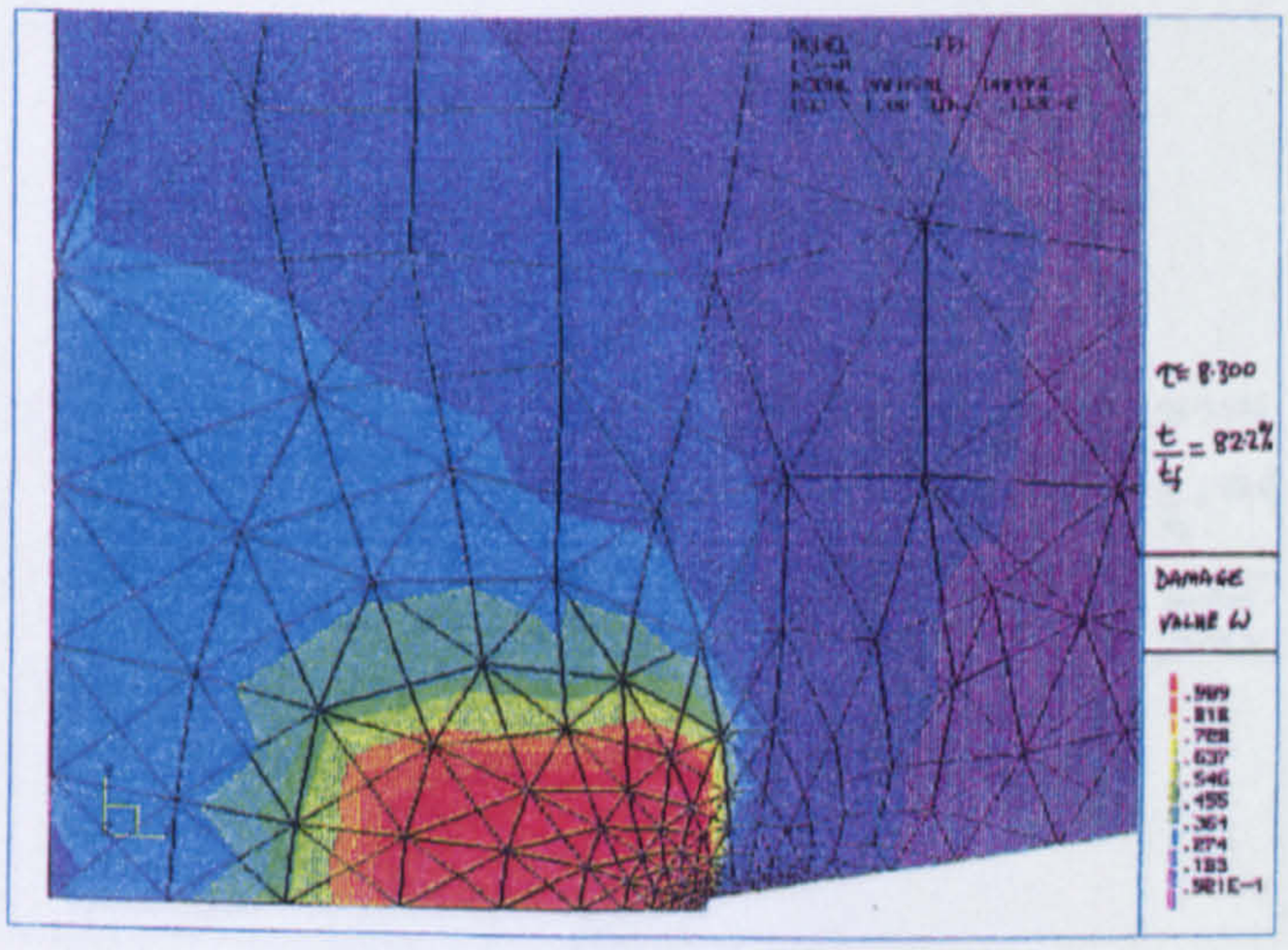

(c)

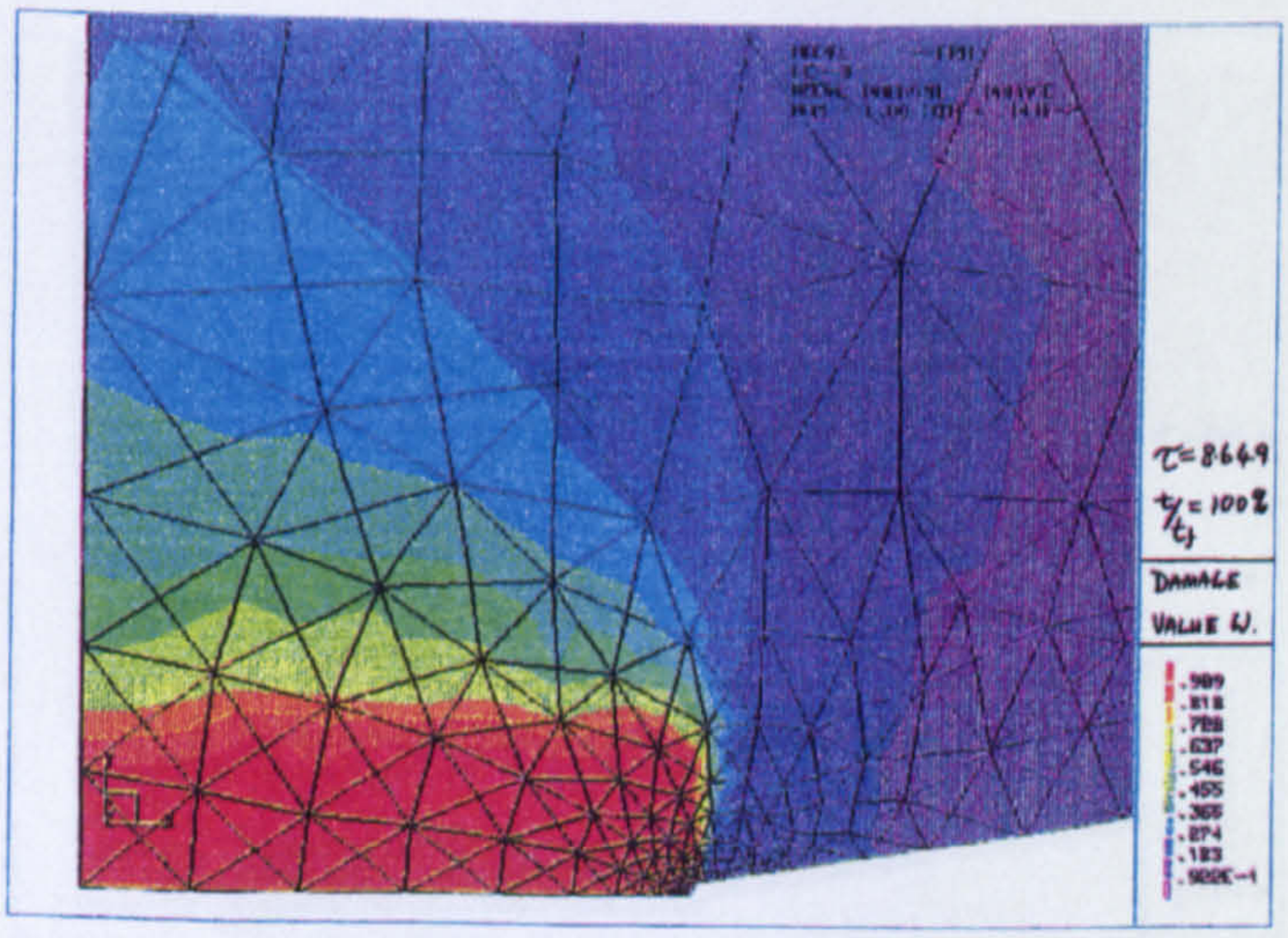

Figure 6.25: Damage distribution contour plots for the small externally cracked plate at life fractions (t/t_f) of: (a)53%; (b)82.2%; (c)100%., using the finite domain non-local damage method No.2.

(a)

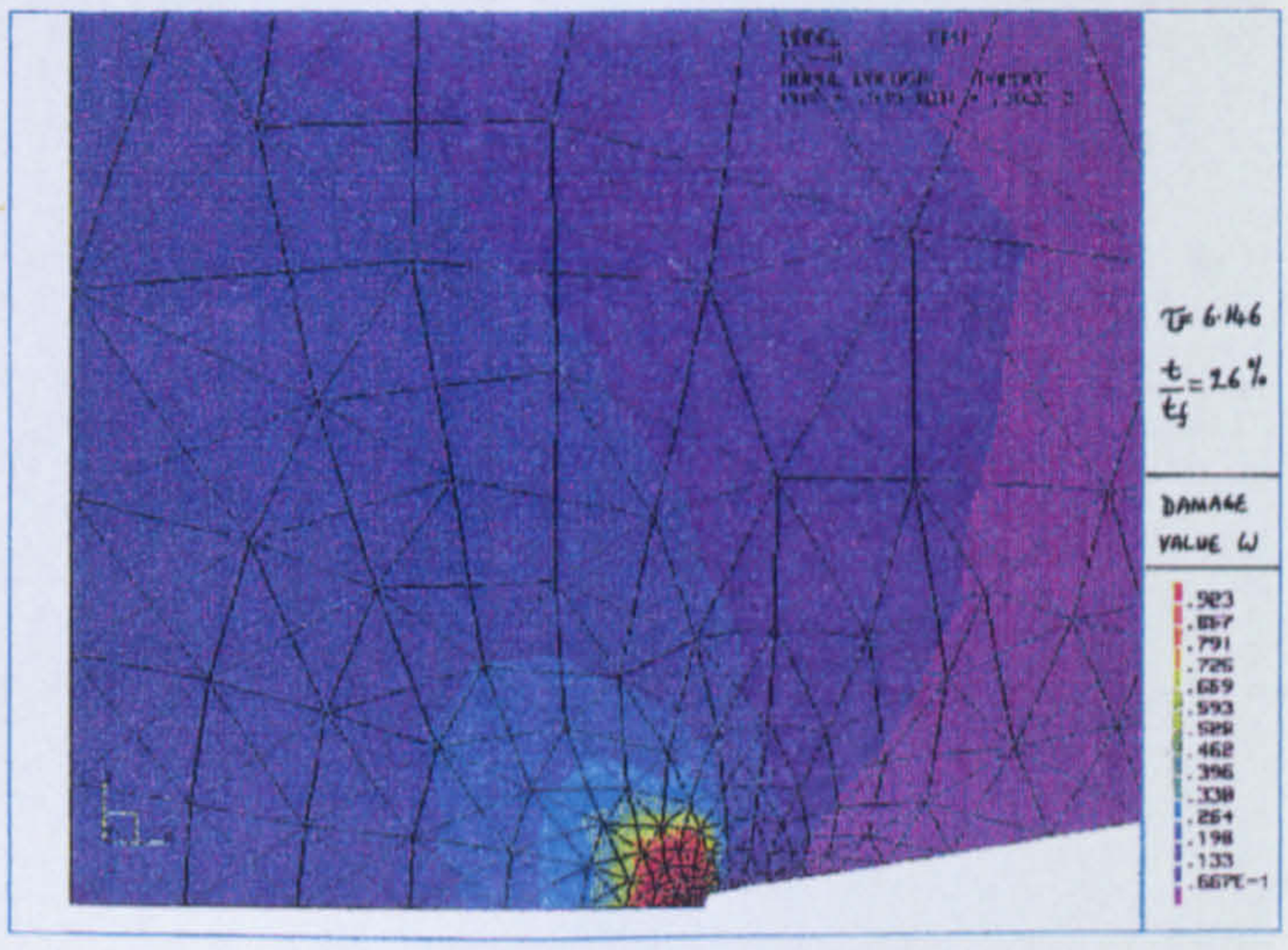

(b)

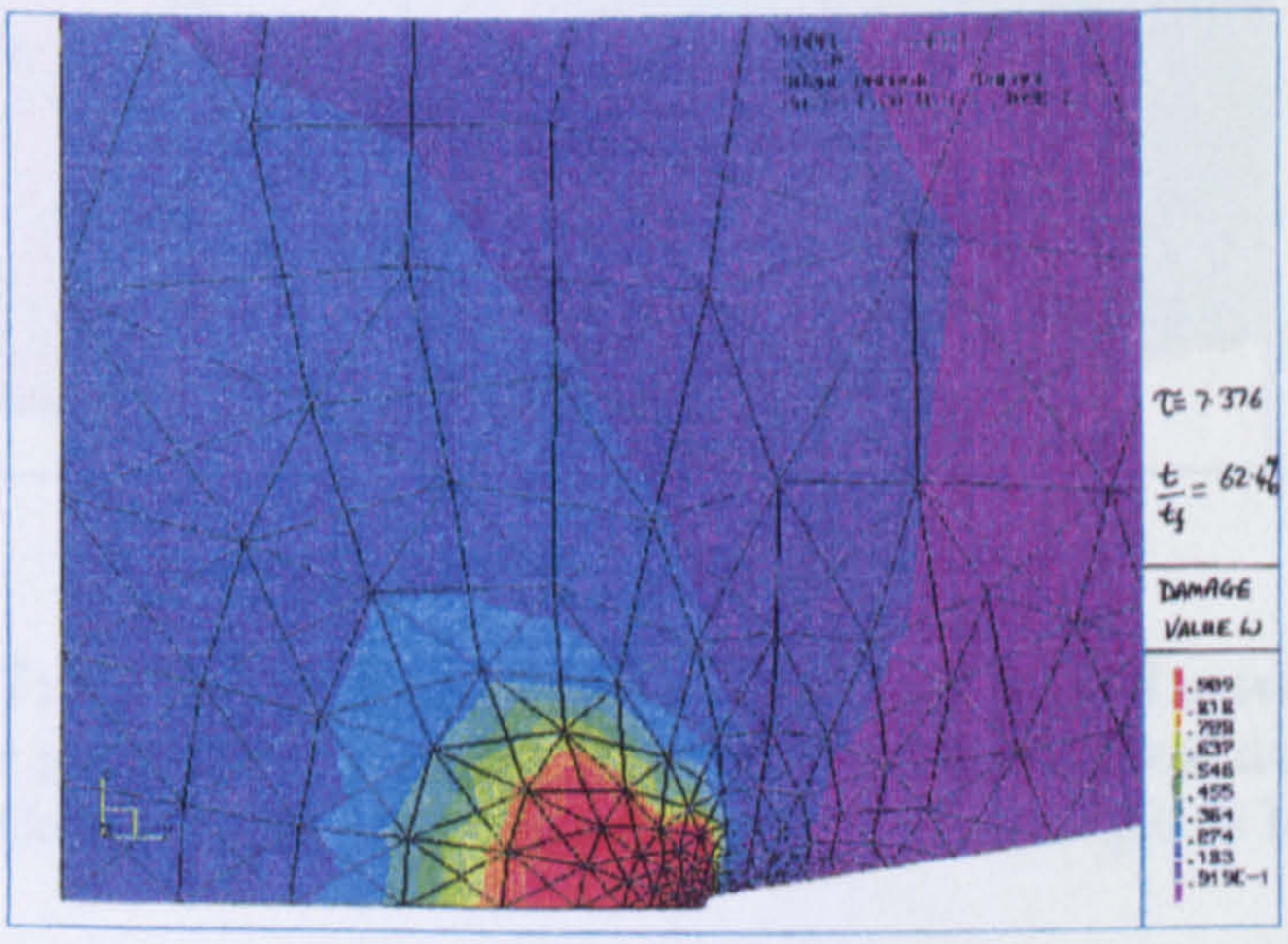

(c)

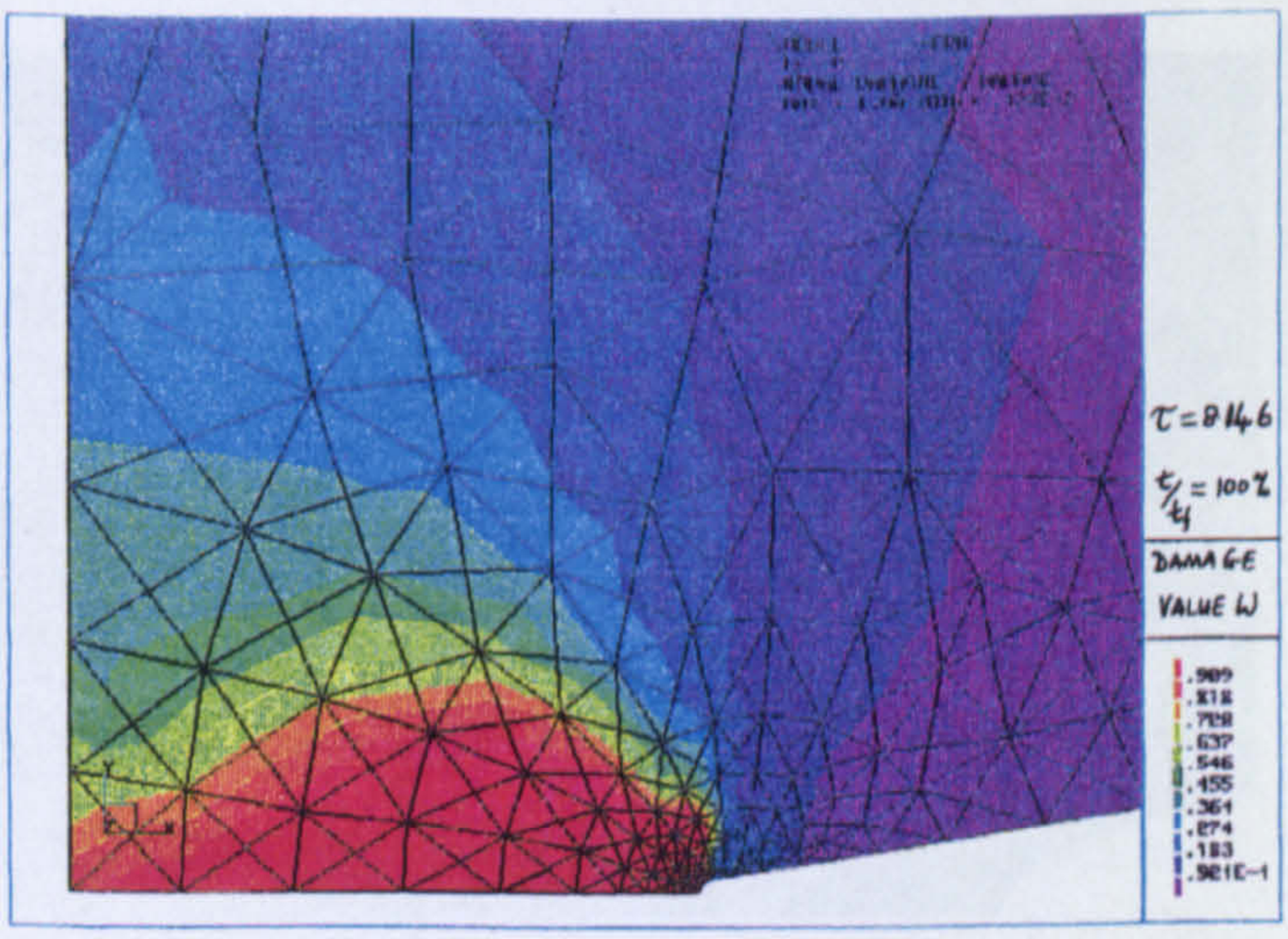

Figure 6.26: Damage distribution contour plots for the large externally cracked plate at life fractions (t/t_f) of : (a)26%; (b)62.4%; (c)100%, using the finite domain non-local damage method No.2 .

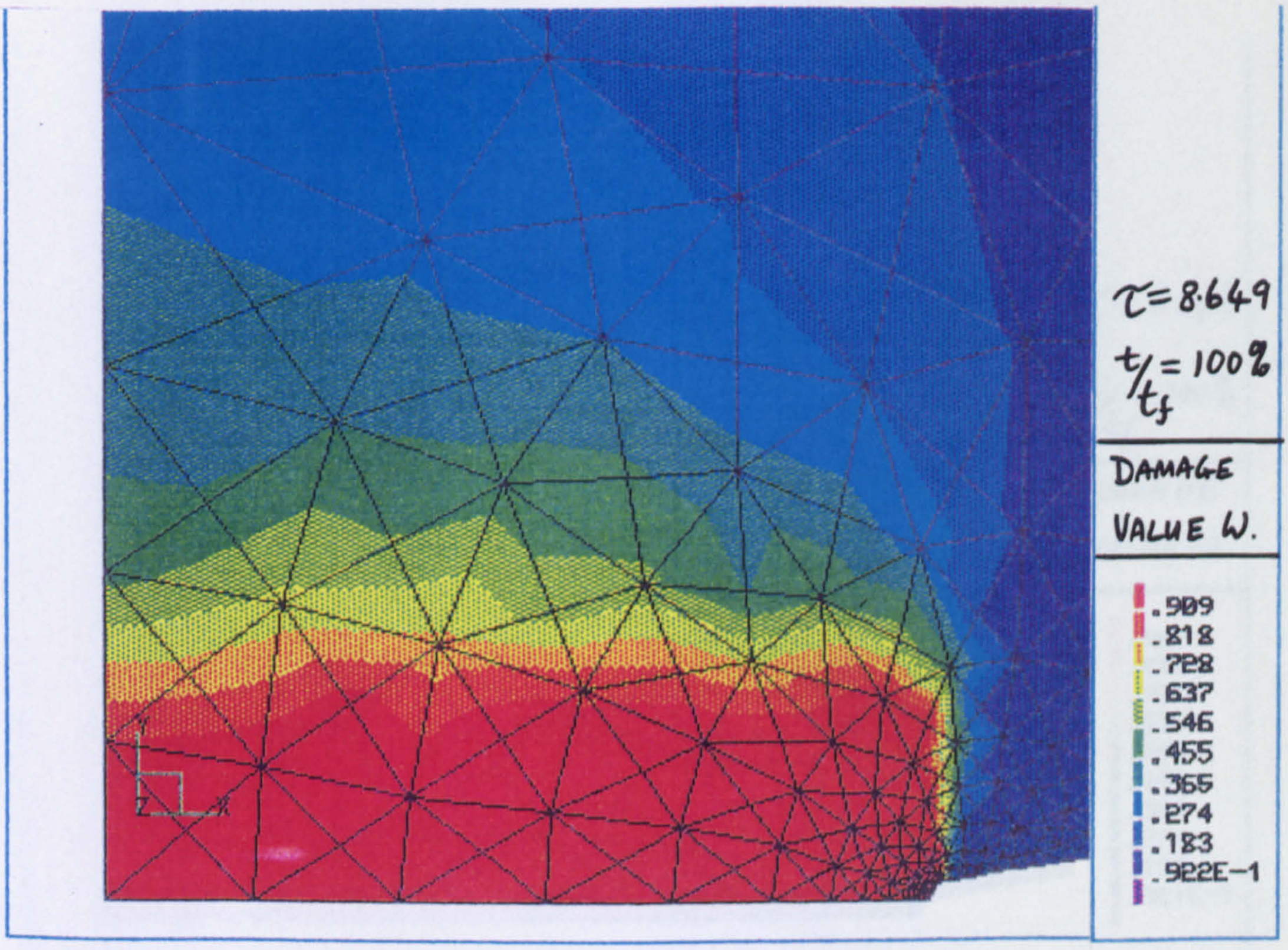

Figure 6.27: Predicted damage distribution for the small externally cracked Copper plate at failure, using the finite domain non-local damage method No.2. Compare this figure with the micrograph in Fig.6.28 below.

Figure 6.28: Mid-thickness micrograph taken from the minimum section of a small externally cracked Copper plate specimen at a life fraction of (t/t_f=94%).

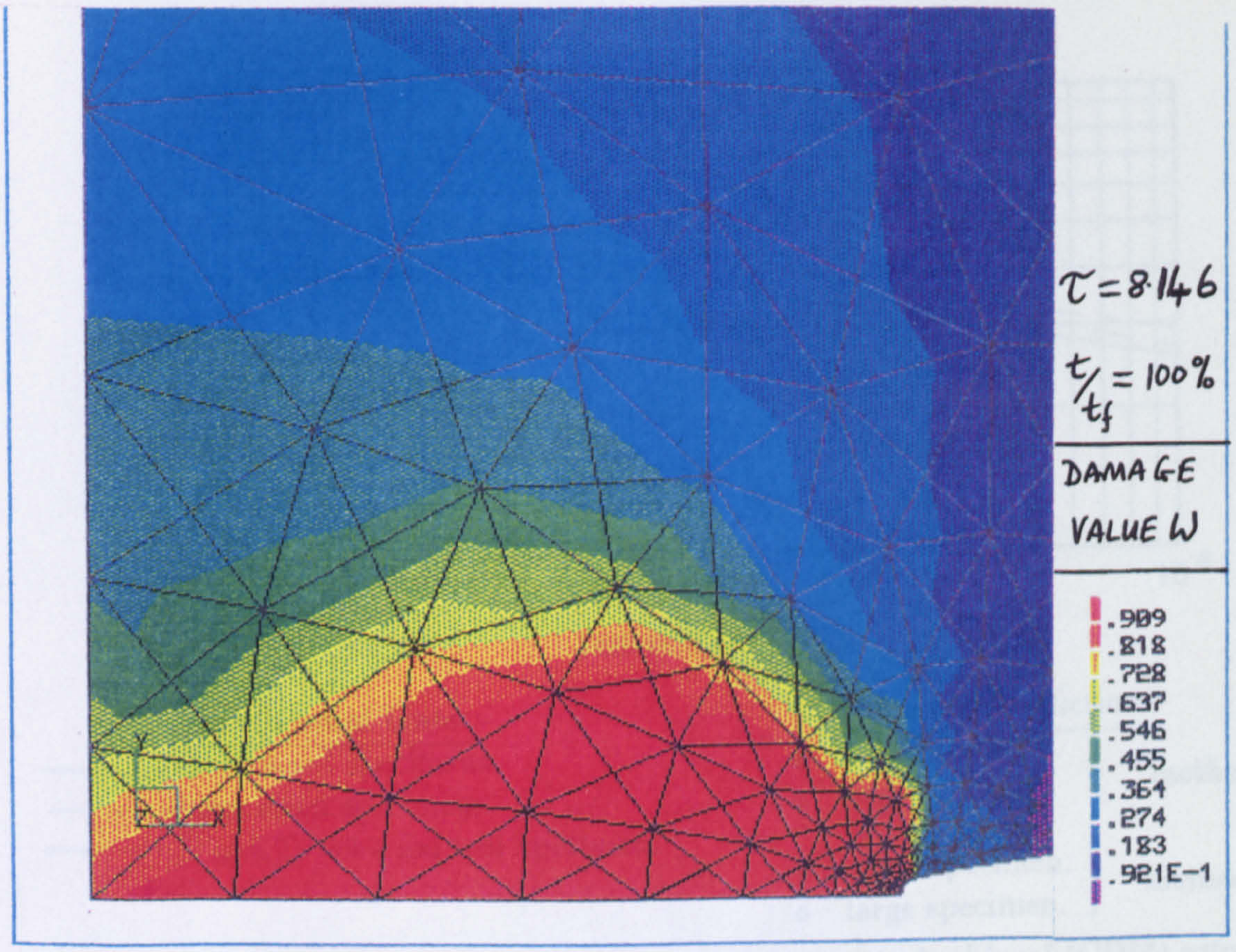

Figure 6.29: Predicted damage distribution for the large externally cracked Copper plate at failure, using the finite domain non-local damage method No.2. Compare this figure with the micrograph in Fig.6.30 below.

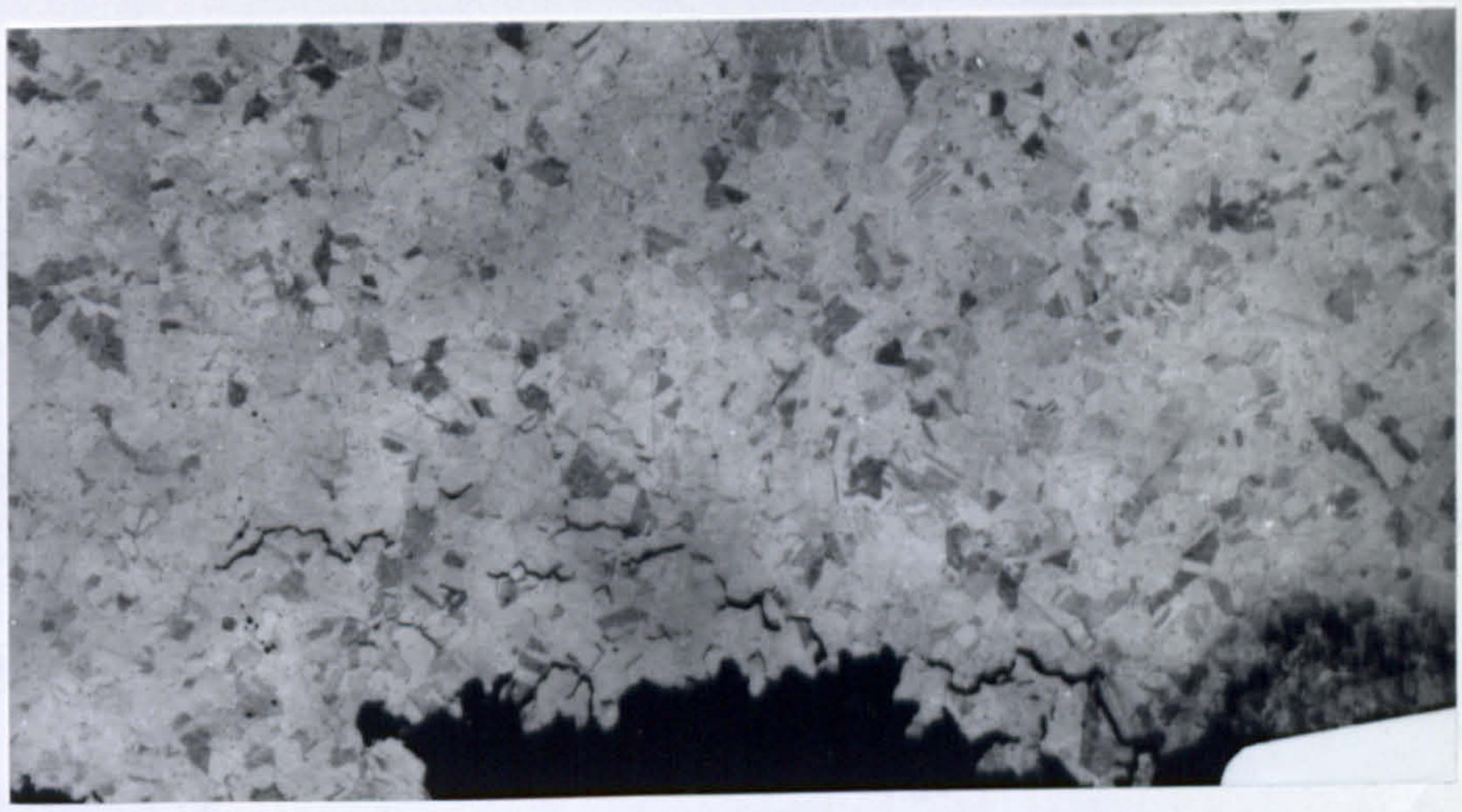

Figure 6.30: Mid-thickness micrograph taken from the minimum section of a large externally cracked Copper plate specimen at failure.

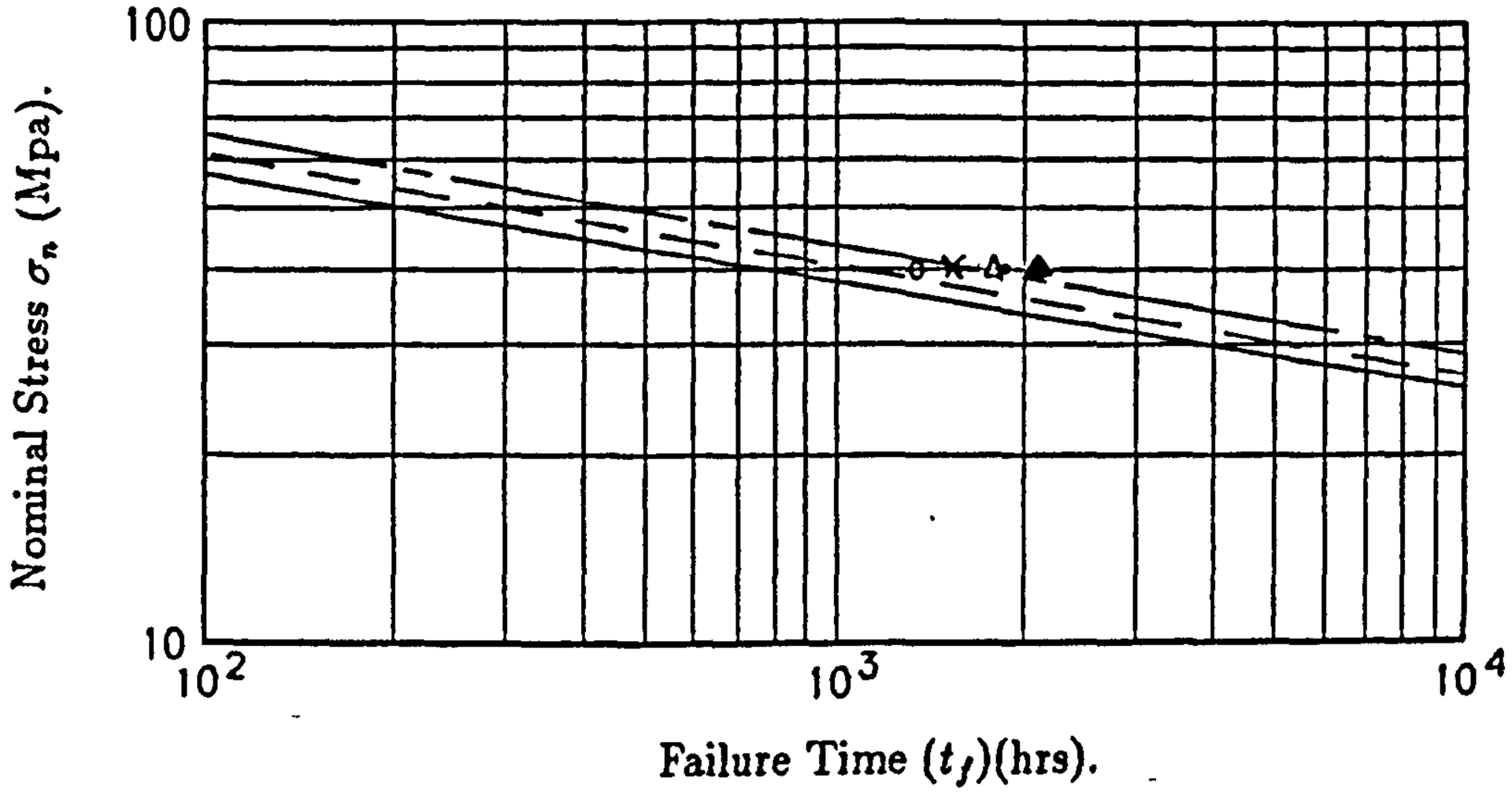

Figure 6.31(a): Comparison between experimental and predicted lifetimes for large and small externally cracked Copper plate specimens, using the developed finite domain non-local damage methods:

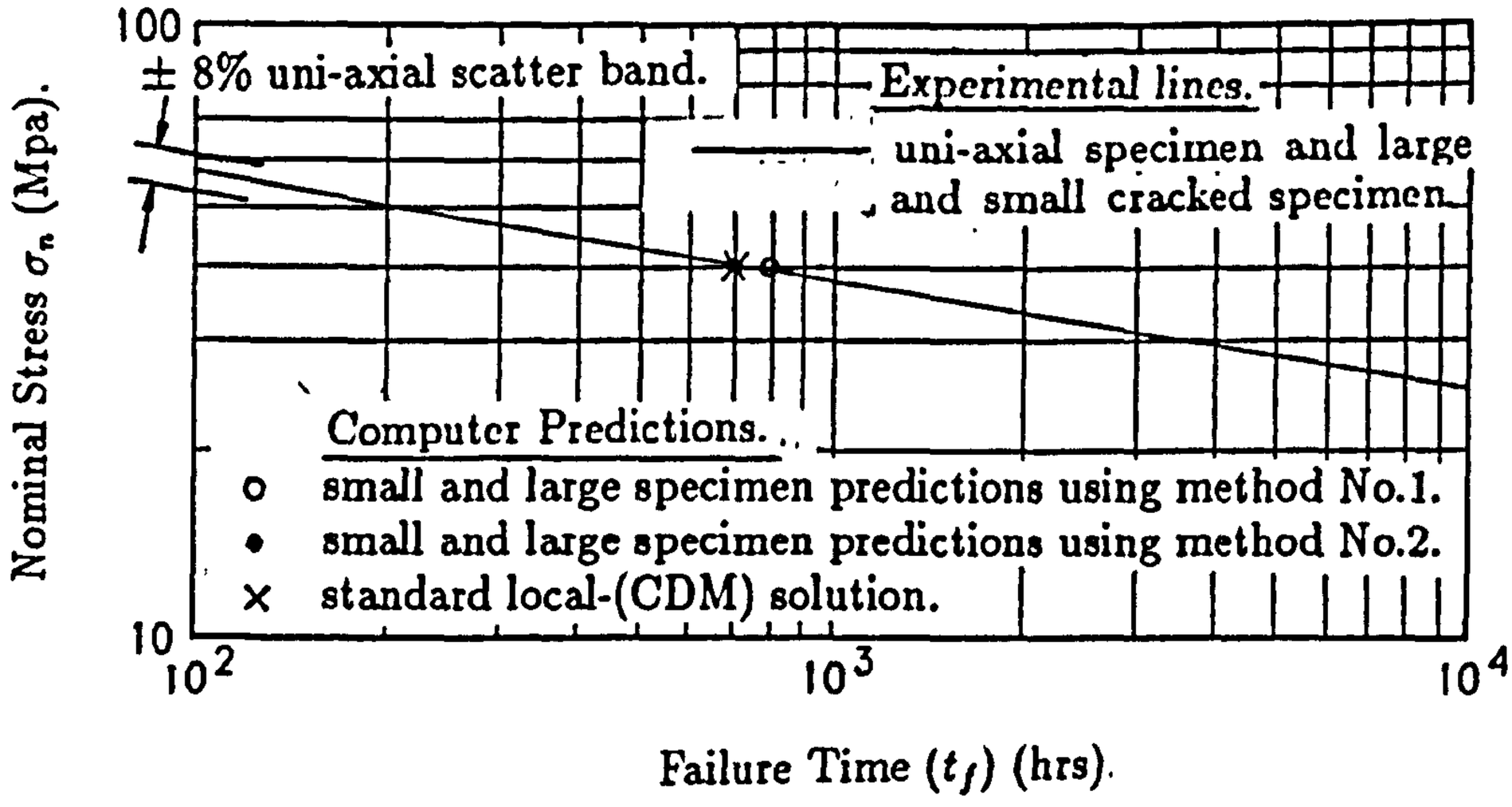

Figure 6.31(b): Comparison between experimental and predicted lifetimes for large and small internally cracked Copper plate specimens, using the developed finite domain non-local damage methods. Note that both small and large specimen experimental lines lie on the uni-axial stress-rupture line.

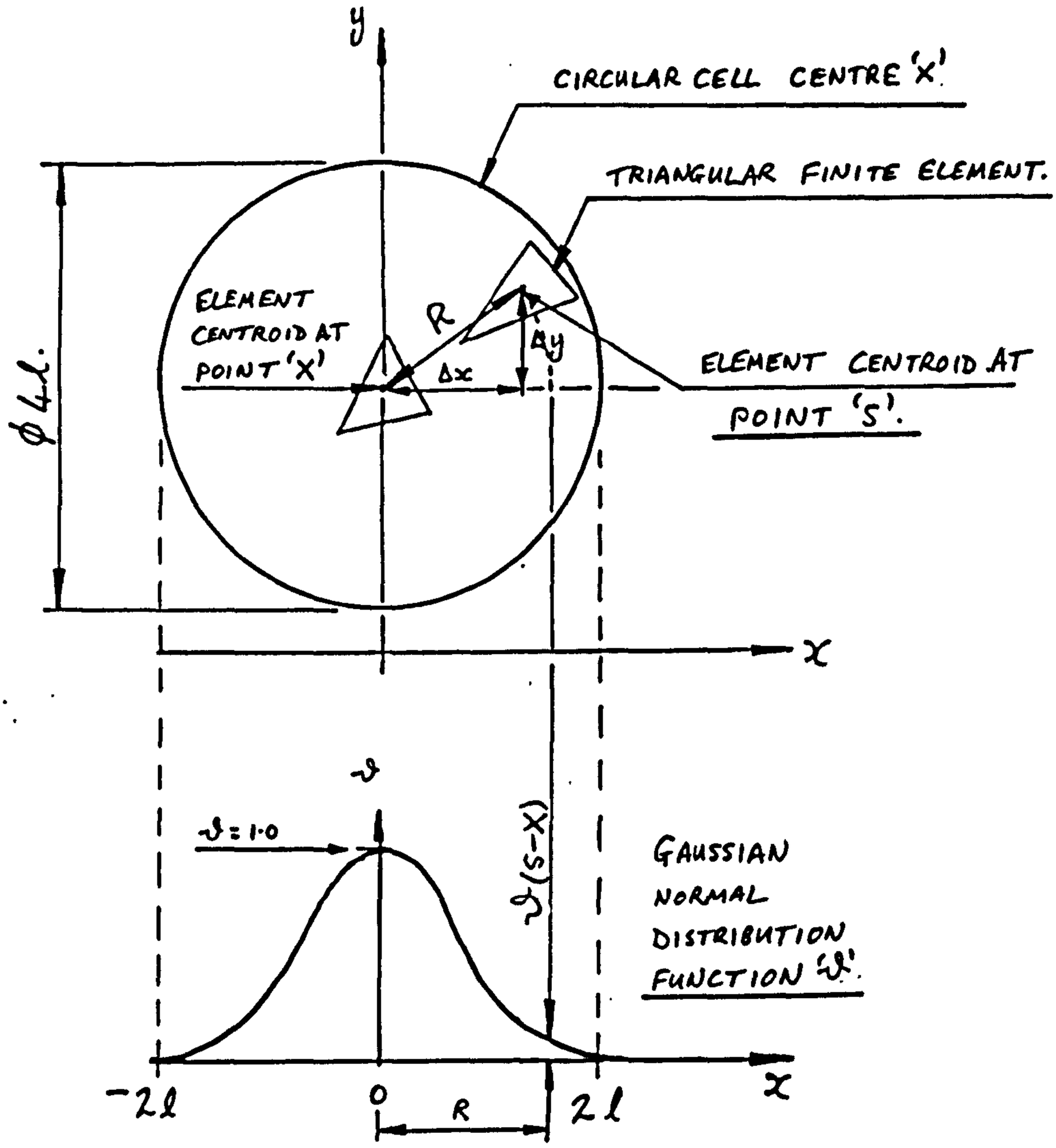

Figure 6.32: Schematic representation of the circular cell used in the infinite domain non-local damage method, which is centered on an element centroid (x). The damage values (ω) of other element centroids within radius ($2l$) are scaled by the height of the gaussian normal distribution at distance R along the (x)-axis in the lower graph.

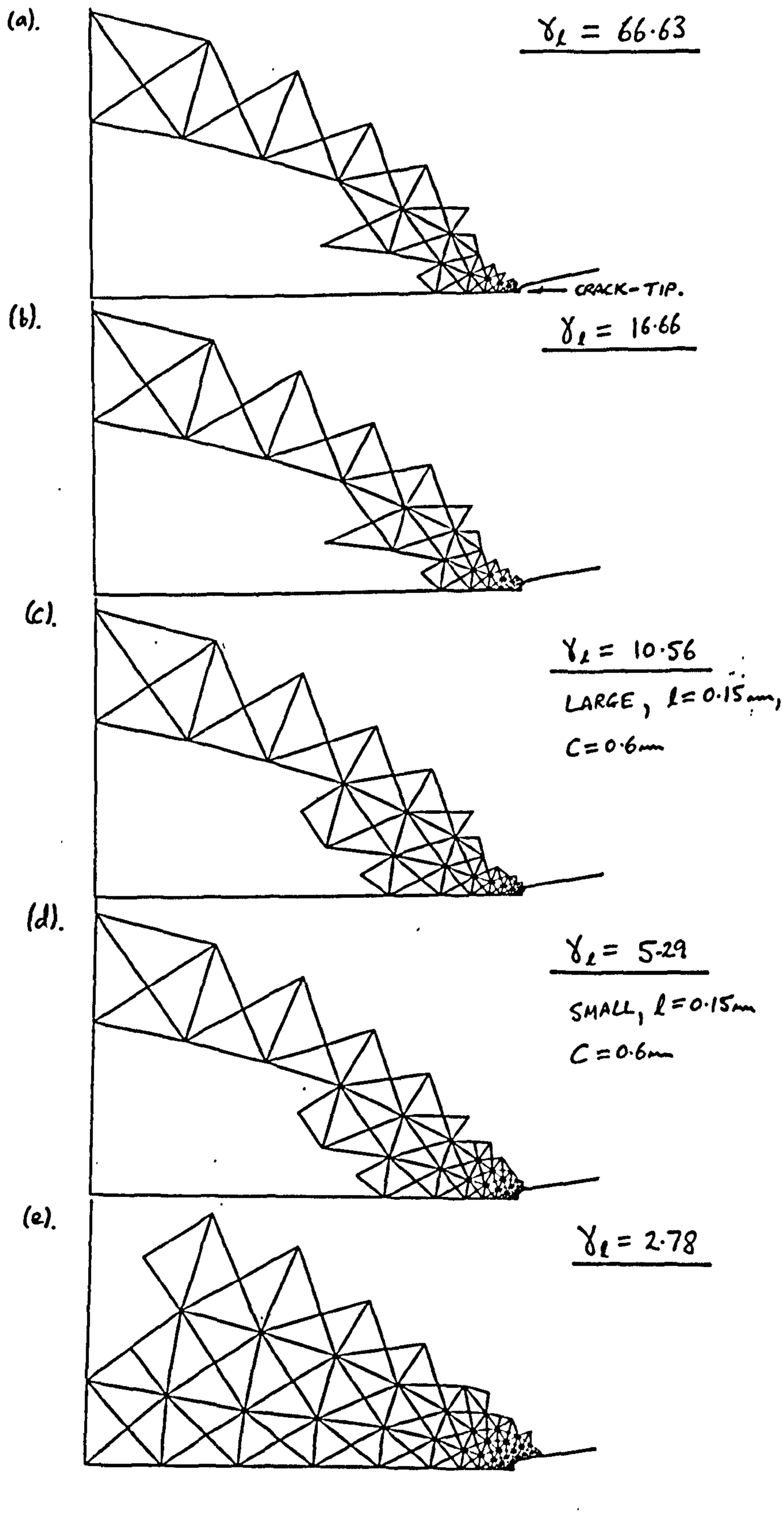

Figure 6.33: Failed element ($\omega > 0.9999$) distributions for externally cracked Copper specimens, predicted by the infinite domain nonlocal damage method, for a wide range of normalised cell sizes (γ_l). (γ_l) is defined in Fig.6.10, and figures (c) and (d) have cell sizes corresponding to large and small specimen sizes, respectively.

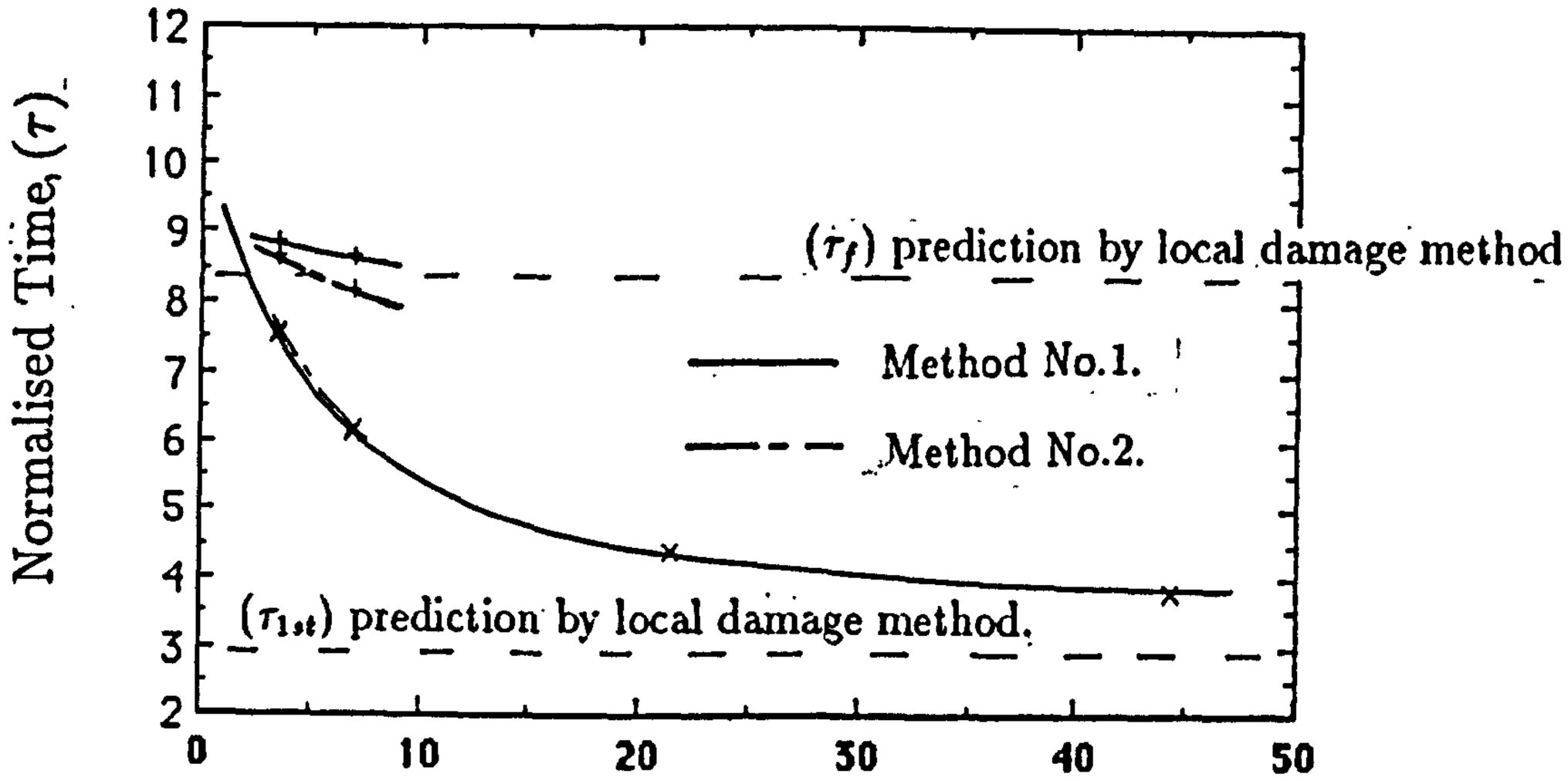

Figure 6.34: Graph showing the variation of the normalised time to the failure of the first element in the structure ($\tau_{1,t}$), (points-×), and the normalised time to the failure of the specimen (τ_f), (points-+) with the size of the normalized cell dimension (γ_c), for the externally cracked Copper specimen, using the finite domain non-local damage methods No.1 and No.2.

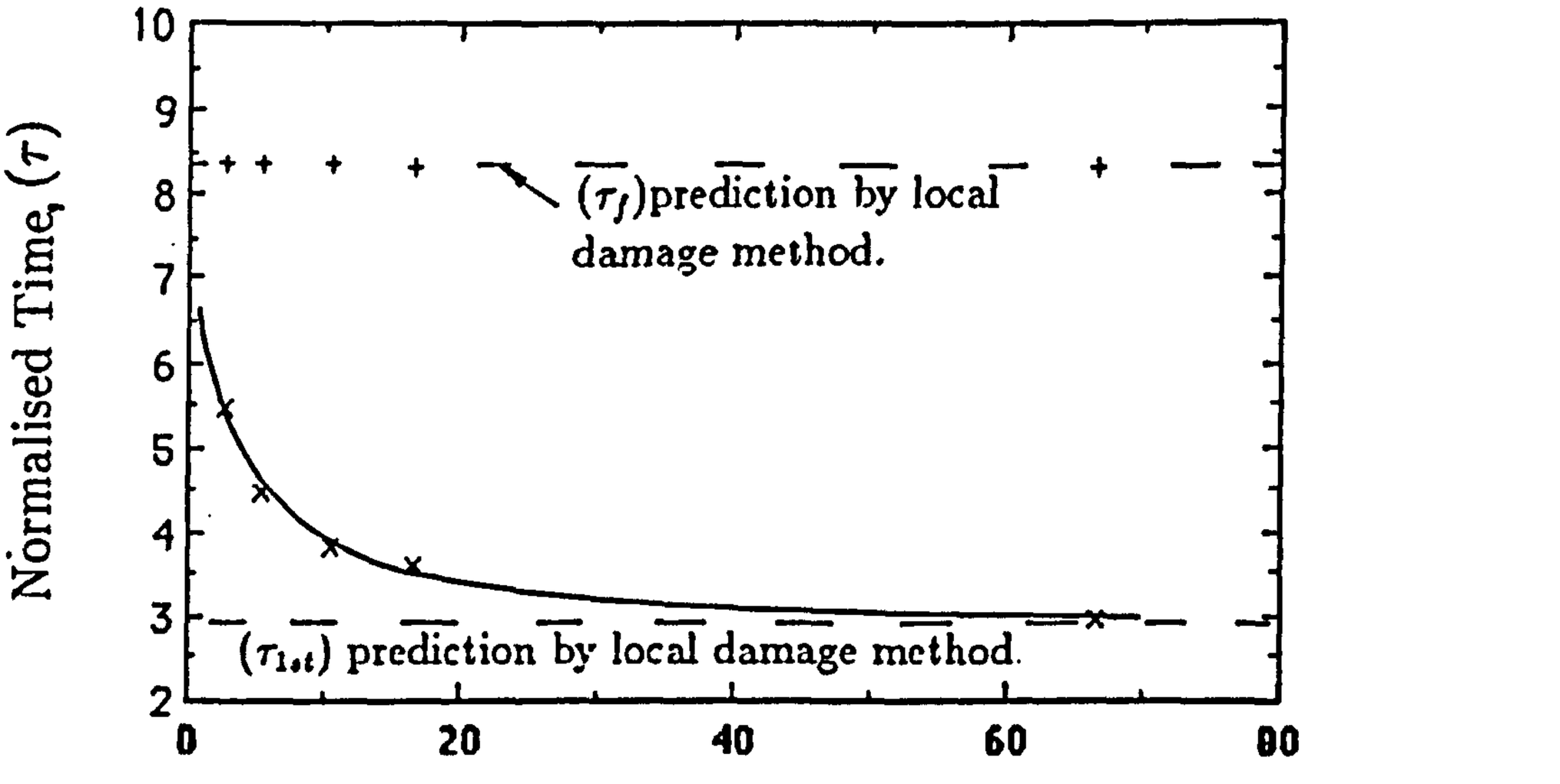

Figure 6.35: Graph showing the variation of the normalised time to the failure of the first element in the structure($\tau_{1,t}$), (points-×), and the normalised time to the failure of the specimen (τ_f), (points-+), with the size of the normalized cell dimension (γ_l), for the externally cracked Copper specimen, using the infinite domain non-local damage method.

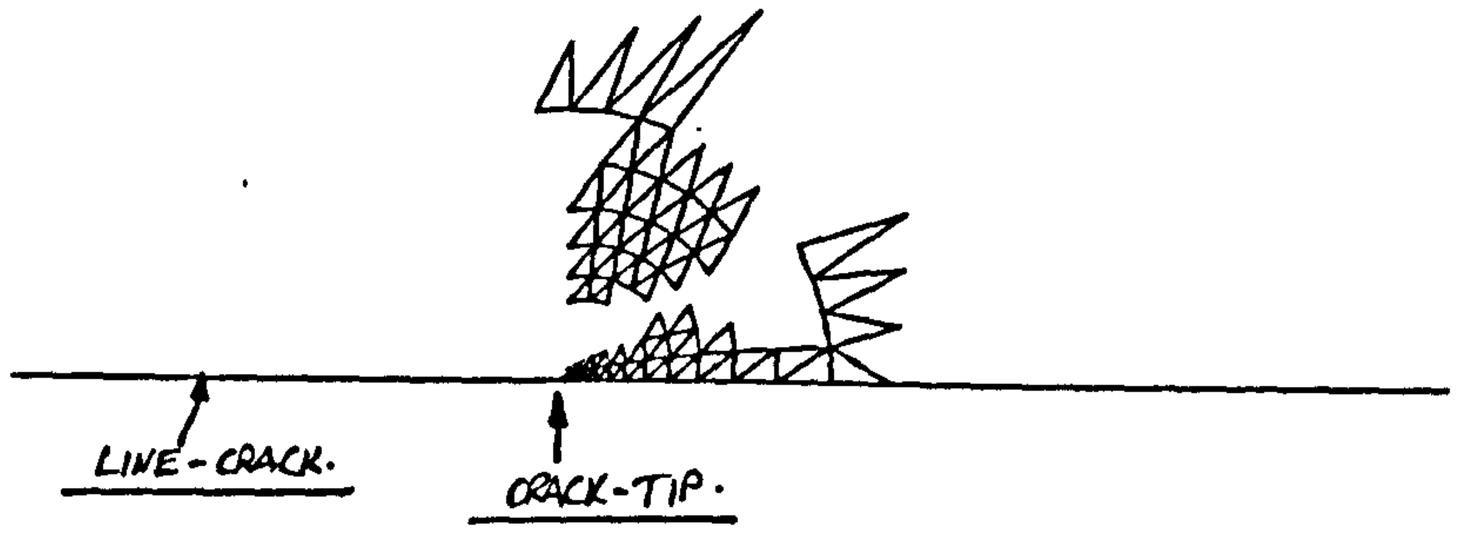

Figure 6.36: Example of localization due to spurious mesh refinement at the crack-tip of a finite element mesh representing a cracked specimen.

Appendix A6.

A6.1 Algorithms Used For The Calculation Of Area Weight-Factors In The Finite Domain Non-Local Damage Methods.

In the following description, reference is made to the Area Weight-Factor flow chart presented in figure A6.1 on three separate pages of Fig.A6.1. Referring to the section of the flow chart marked (A) to (B), the coordinates and topolgies for both triangular finite element mesh and the square cell mesh are read into stores within the computer program. Test 1 is performed to determine if any of the first cell's sides (CL1, CL2, CL3, CL4) intersect with any of the first triangular element's sides (L1, L2, L3). This is done with the subroutine INTR, which requires the end coordinates of each pair of line segments PQ and RS (Fig. A6.2); one line segment belonging to a triangular element, the other to a square cell respectively. The subroutine uses a property of the calculation for the area of a triangle from its coordinates, that if the nodes of the triangle are numbered in a clockwise order, the area calculated will be of opposite sign, to that calculated for a triangle with nodes numbered in an anti-clockwise direction. It is observed that the areas of the triangles formed by the points RPQ, SQP, QRS and PSR are all positive, when the line segments intersect, (Fig. A6.2(a)). When the line segments do not intersect (Fig. A6.2(b)) negative and positive signs are produced whose signs cancel. Therefore, a (one) is used to denote line segments which intersect and a (zero) is used to denote non-intersecting line segments. If the nodes at the ends of the line segments touch or the lines are colinear a (zero) is given by the algorithm, but the intersection, if there is one, will be spotted by later tests. If two line segments intersect the coordinates of the point of intersection are calculated from the solution of two simultaneous equations for the lines. The intersection coordinates are stored in the single dimension arrays XNST and YNST. When all three sides of the triangular element have been tested for intersection with all sides of the square cell, Test 2 is performed, (see section (B) in the flow chart, Fig.A6.1). Here the nodes are stored of any triangular element nodes which lie inside the square cell area under consideration. This is done using two inequalities defined by two IF-statements, one with upper and lower bounds as the

x-coordinates of the vertical cell sides and the other with bounds as the y-coordinates of the horizontal cell sides. If all the nodes of a triangular element lie within the square cell, then the whole area of the triangular element is the intersection area, which is then calculated. If the number of nodes contained within the square cell is less than three, Test 3 is performed, (see section (C) of the flow chart, Fig.A6.1). Here, in Test 3 a more complicated set of inequalities is used, with bounds provided by a side of the triangle and a parallel line through the opposite node to the side, to define the triangular element region, (Fig. A6.3). Any cell nodes lying within the triangular element region are stored. If more than three nodes lie within the triangular region, then the area of intersection is the area of the square cell, which is then used as the area weight factor for this cell/triangular element pair. If no overlap is present between the triangular element and square cell pair then ITTI = 0, ISQ = 0 and ITR = 0 and no area weight calculation will be performed. The next triangular element and cell pair will then be tested for intersection. If an intersection is present then ACTION 1 is performed (see section (D) of the flow chart, Fig.A6.1). At this stage the trivial intersections of all the shaped intersections possible (many of which have been summarised in Fig. A6.4), have had their area weights calculated. Now the areas of more complex intersections must be calculated. This involves the use of a general technique called forming the Convex-Hull, to order the intersection coordinates, as previously stored. The method takes the lowest point having the smallest y-coordinate and the largest x-coordinate as its starting datum point No. 1. (See Fig.A6.5(a)). A horizontal line is drawn through this starting point and lines are also drawn between this point and every other intersection point. The angles between the horizontal line and the other lines are calculated and the coordinate point having a line which forms a minimum angle with the horizontal line is stored. This newly stored coordinate point then becomes the new datum coordinate No.2 and a line may be drawn from the previous datum point to it. The angles between this current line and lines adjoining the new datum point with all other points are calculated and the next point chosen, as that of a line which forms the minimum angle with the current line, (Fig.A6.5(b)). This procedure continues until points are stored in an anti-clockwise order, which define a peripheral convex shape enclosing all the intersection coordinate points, (Fig.A6.5(c)); hence the term, forming the Convex-

Hull. This convex shape is then segmented into triangles using ACTION 2. (See section (E) in the flow chart, Fig.A6.1). This is done by noting a simple number pattern for the triangles forming the convex shape, i.e. 1,2,3 - 1,3,4 - 1,4,5 etc..(See Fig.A6.5(d)). The areas of each triangle are calculated from the coordinates of its nodes and each area is summed giving the area of the convex hull intersection shape, which is the area weight-factor for this particular cell/triangular element pair.

These procedures are repeated for every square cell and each triangular element up to the finite domain non-local damage analysis boundary element number, yielding three single dimension stores AR(I), NEL(I) and NIN(I). (See section (F)in the flow chart, Fig. A6.1). AR(I) contains the area weight factors, NEL(I) contains the numbers of the elements in each cell and NIN(I) contains the total number of elements contained in each cell. NEL(I) and NIN(I) are used to locate the intersection area of a particular cell/triangular element intersecting pair in the array AR(I), which will be used to weight the relevant elemental damage rate parameter in the finite element, finite domain, non-local damage program.

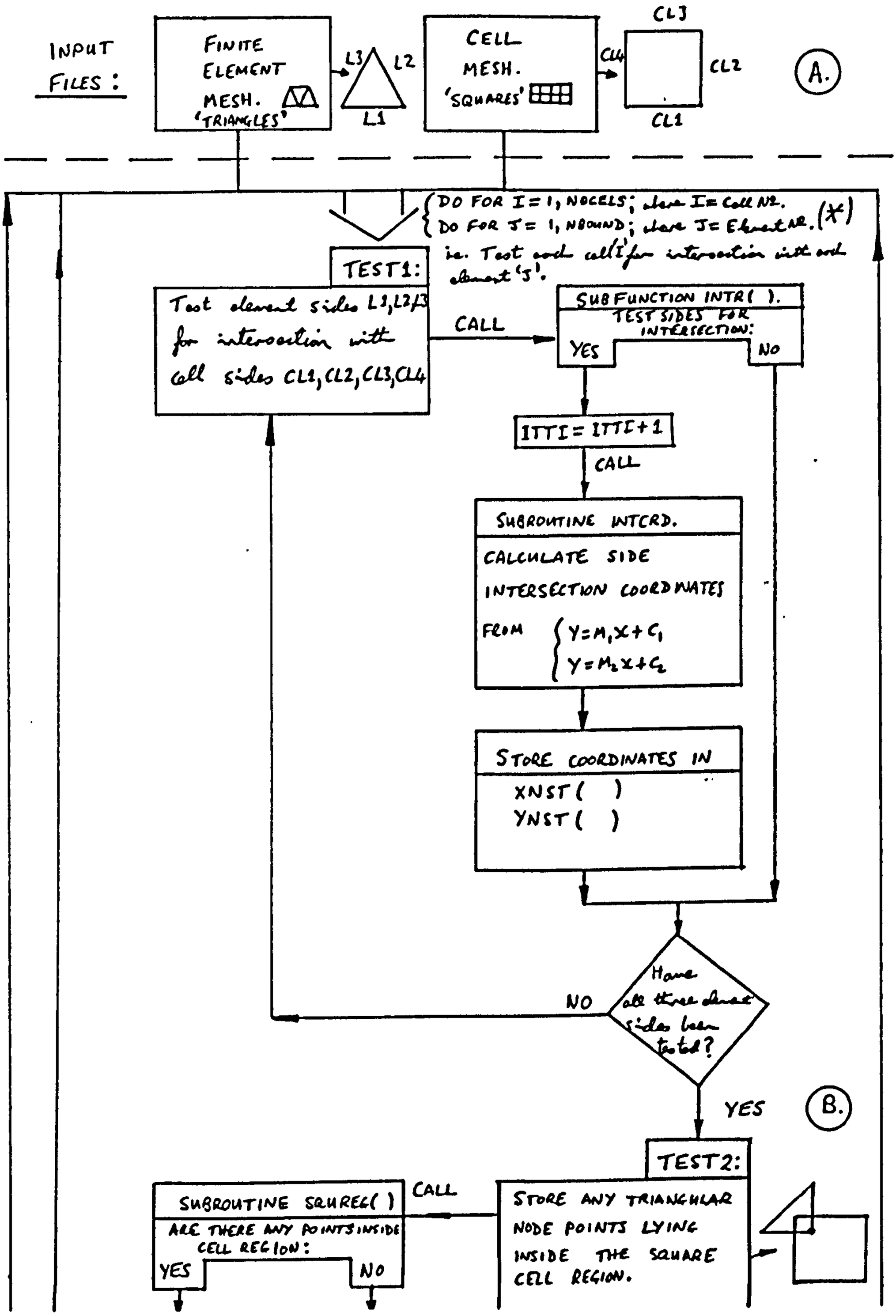

Figure A6.1: Flow chart for the calculation of the Area Weight Factors (dA) in (equations (6.2) and (6.3), for the finite domain non-local damage analysis.

YES

STORE NODE COORDS IN:
XNST( )
YNST( )

NO

Have all three element nodes been tested?

NO

YES

ISQ=?
(ISQ IS Nº OF NODES IN REGION).

ISQ=3 CALL

FUNCTION AREA( )
INTERSECTION AREA = TOTAL AREA OF ELEMENT!
AR( ) = AREL( ).

ISQ<3

TEST3:
STORE ANY SQUARE CELL NODES LYING INSIDE THE TRIANGULAR ELEMENT REGION.

CALL

SUBROUTINE TRIREG( )
ARE THERE ANY POINTS INSIDE THE ELEMENT REGION:

YES

NO

STORE NODE COORDS IN:
XNST( )
YNST( )

Have all four cell nodes been tested?

NO

YES

(ITR>3)

ITR=?
(ITR IS Nº OF NODES IN REGION).

IF ITTE=0
ISQ=0
ITR=0
THEN

(0≤ITR≤3)

SET: INTERSECTION AREA = TOTAL AREA OF CELL.
AR( ) = ACELL.

ACTION 1:
FORM THE "CONVEX-HULL" AROUND THE STORED POINTS STORED IN XNST( ), YNST( ). NUMBERING NODES IN ACW ORDER

CALL

SUBROUTINE CONHUL( ).

CONVEX HULL.

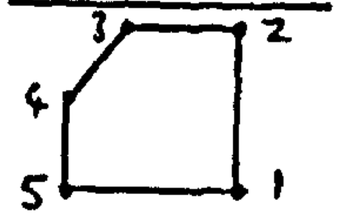

e.g.

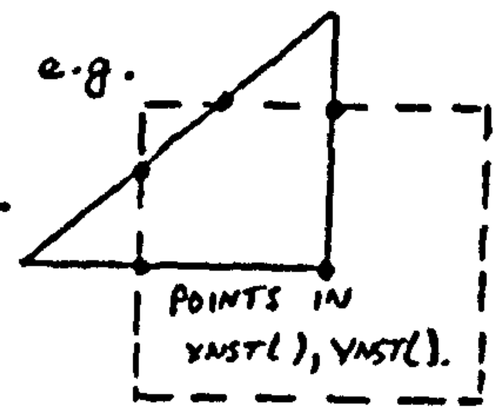

POINTS IN XNST( ), YNST( ).

C

D

(E)

ACTION 2:

CUT-UP POLYGON FORMED INTO TRIANGLES, AND SUM THE AREAS TO GIVE TOTAL INTERSECTION AREA.

CALL

SUBROUTINE CUT( )

CALL

FUNCTION AREA( ).

TOTAR = AREA + TOTAR.

N.B:- Not area to be calculated if area of 1,5,1 ⇒ AREA=0 ⇒ FINISH.

AREA = 0 ?

NO

YES.

SET: AREA OF INTERSECTION AR( )=TOTAR

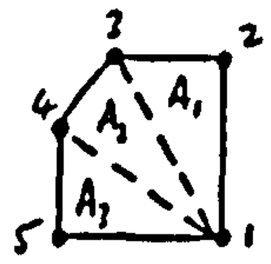

TOTAR = $A_1+A_2+A_3$.

(F)

I= NOCELS.

YES

J= NBOUND

YES

NO

NO

DUMP :

(i) Dump area weight store AR(I).

(ii) Dump NEL(I) containing the numbers of the elements contained in each cell.

(iii). Dump. NIN(I) containing the number of elements contained in each cell.

STOP!

N.B:- NEL(I) and NIN(I) are obtained from the indicies of (*) after the results of test 1, 2 and 3 are known.

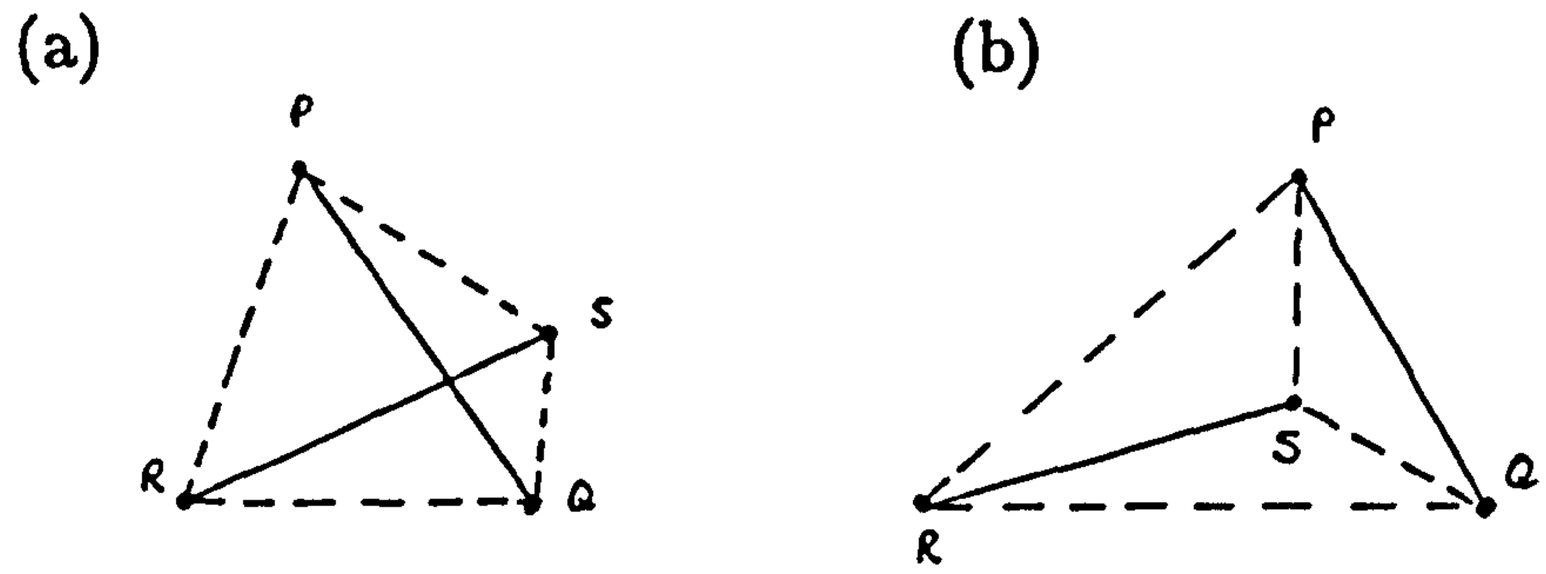

Figure A6.2: Two line segments, one from a triangular finite element, the other from a square cell which (a) intersect and (b) do not intersect, forming triangular arrangements which may be used to identify if an intersection of line segments has occured.

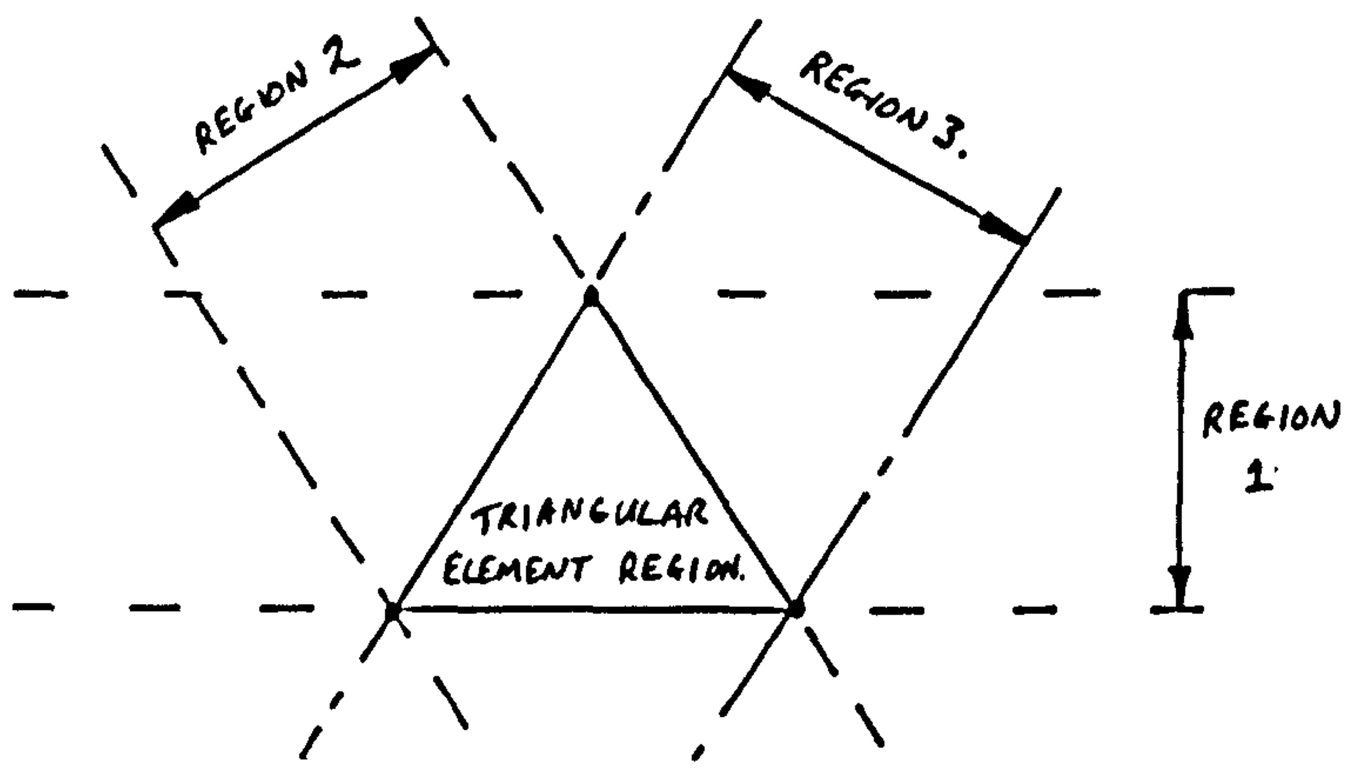

Figure A6.3: Inequalities are used to define regions 1, 2 and 3, which intersect forming the triangular element region for Test No.3 in the flow chart of Fig.A6.1.

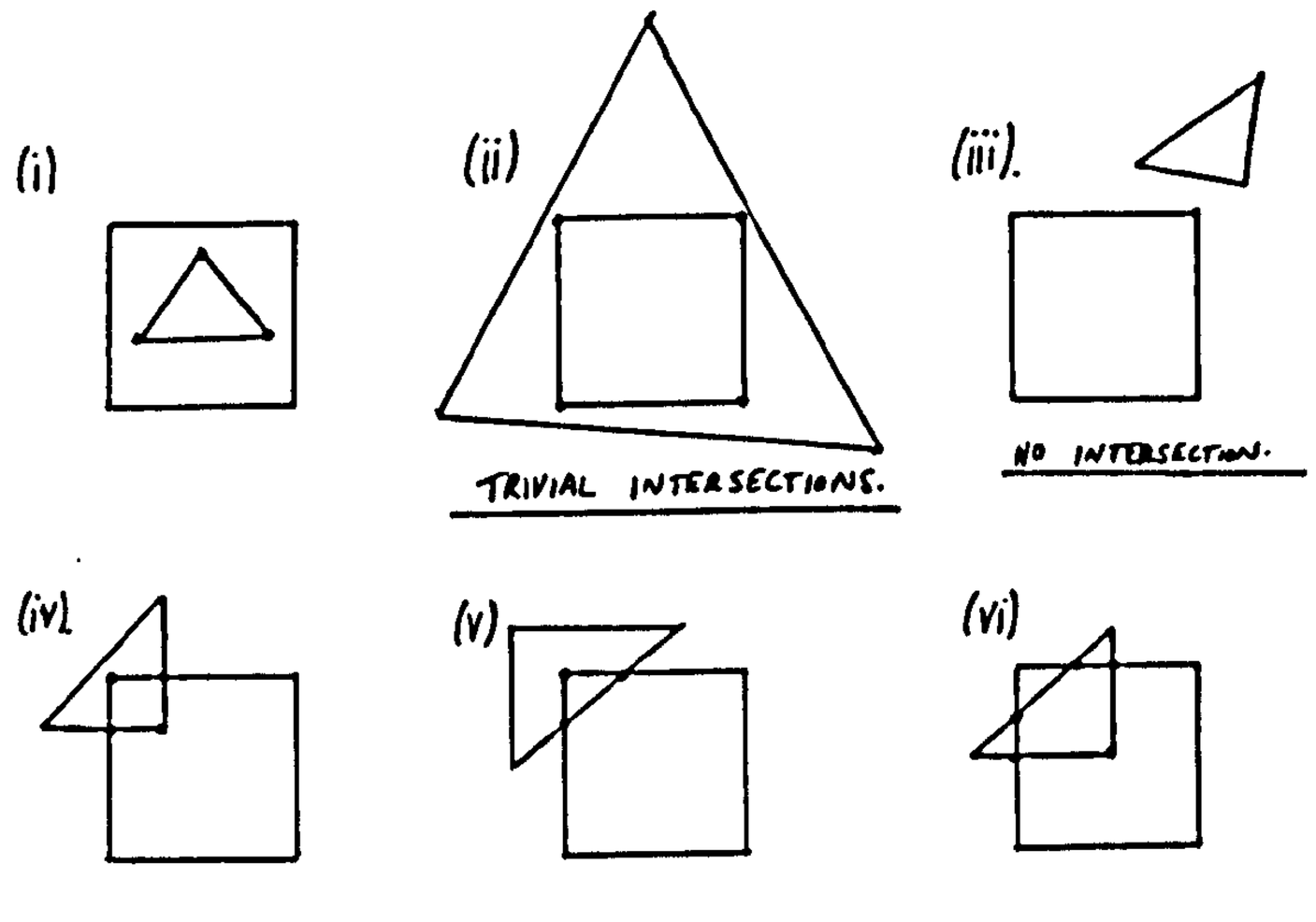

Figure A6.4: Some of the possible intersection shapes which may occur between overlapping triangular elements and square cells.

(•)- are the stored intersection points of the sides of a cell with the sides of a triangular element. (Fig.A6.2).

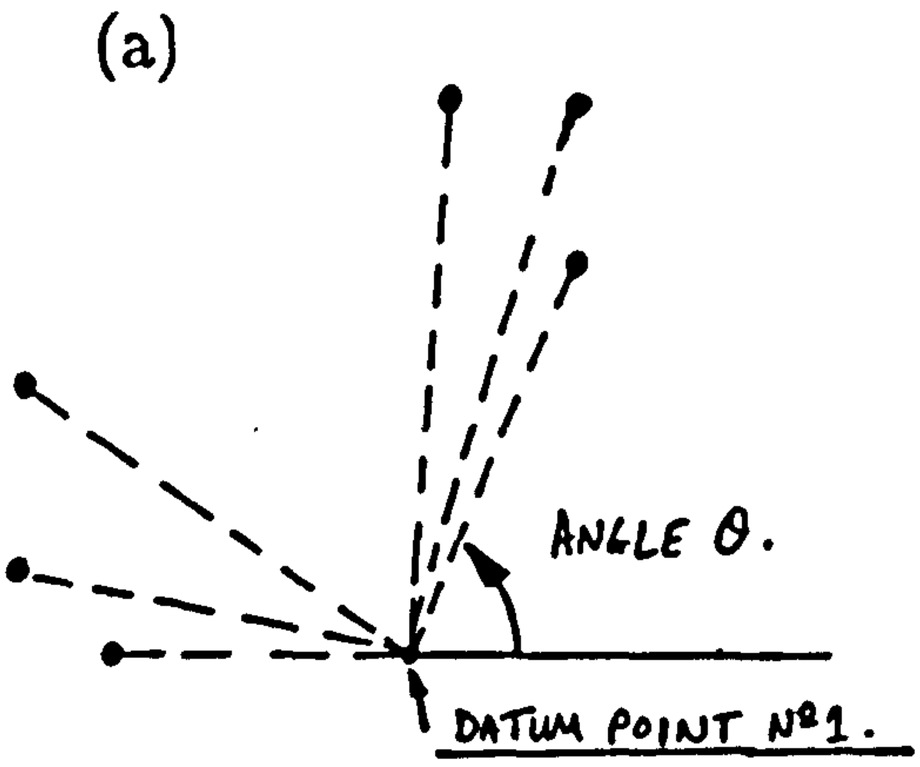

Final convex shape with coordinate points ordered 1 to 7 as shown.

Area of triangle 1,2,3 = A_1
Area of triangle 1,3,4 = A_2
Area of triangle 1,4,5 = A_3
Area of triangle 1,5,6 = A_4
Area of triangle 1,6,7 = A_5

Area of overlap for cell and triangular element pair = $dA = A_1 + A_2 + A_3 + A_4 + A_5$

Figure A6.5: Figures showing the procedure for the calculation of non-trivial square cell and triangular element areas of overlap, using the intersection coordinates of line segments, by forming the Convex-Hull, then segmenting the convex shape into triangles, whose areas are calculated and summed to give the area weight (dA) for this cell and element pair.

Chapter 7.

Creep Deformation And Failure Of Weldments.

7.1 Introduction.

Welded joints are used extensively in the construction of electrical power plant. Welding provides a strong, yet simple and cost effective joint between components, alleviating the need for bolted flanges and seals. There are many methods available for producing a welded joint, the most important method for high temperature power plant is fusion welding.

The Central Electricity Generating Board (C.E.G.B.) use the Manual Metal Arc technique for a large proportion of their fusion welds, to form joints in 0.5Cr 0.5Mo 0.25V main steam pipes using 2.25Cr 1Mo weld metal. Such steam pipes and joints are designed in accordance with British Standard Codes (BS 806, BS 1113 and BS.5500) to have a high temperature design life in excess of 100,000 hours, based on the stress-rupture properties of the parent material and the mean diameter hoop stress level in the parent pipe. However in practice lifetimes are not limited by the behaviour of the parent metal pipe but by the formation of macroscopically large cracks in the weld, which can occur early in the service life of the component [96,97]. This cracking is observed to be as a direct result of creep damage accumulation within certain microstructural regions of the weld metal or heat affected zones of the joint. The large cracks observed in steam pipes, although not usually resulting in catastrophic failure, produced concern for safety in the continued operation of the power plant past its initial 20 years design life. In the early 1970's the CEGB proposed a collaborative research program for the high temperature design of weldments. Together with independent researchers a significant amount of literature is now available from the past 20 years intensive research into the creep behaviour of weldments. What follows is a review of the past research and a statement by the author of the current understanding of weld metallurgy, design and weld modelling. The next chapter (No.8) covers the advancements made by the author for the prediction of the creep deformation and failure of welded components operating at high temperature.

7.2 Welding Methods.

Currently the main methods of fusion welding used in power plant construction are the Manual Metal Arc, the Gas Metal Arc and the Submerged Arc Processes. The Manual Metal Arc process uses a high current discharge, which melts the core wire of the electrode and bridges the gap between the two components to be joined. The electode flux coating melts and provides protection of the weld pool against atmospheric elements, which may adversely affect the quality of the weld. The Gas Metal Arc process uses an inert gas shroud. The gas shroud may be tungsten inert gas (T.I.G.), which uses an Argon shroud or metal inert gas (M.I.G.), which uses a Carbon Dioxide inert shroud and may have force fed filler wire. This method produces a metallurgically clean weld having low absorbed gas and inclusion content with no surface slag. The Submerged Arc Process has a separate slag feeding process. It is a high energy production process and is automated to weld large steel constructions. Other specalist fusion welding methods exist such as the electroslag process for joining large castings and forgings, but are not covered here.

Non-fusion techniques include friction welding, electron beam welding, diffusion bonding, laser-beam welding and explosive welding. These specialist processes can be costly, but may impart the required properties of the materials and provide the most appropriate production method for a particular component. For example electron-beam welding and laser welding provide very small heat affected zones due to very localised heating and hence cause low distortion in the vicinity of the weld.

7.3 Weld Types And Preparations.

Typical high temerature ferritic steel steam pipes and pressure vessels use 0.5Cr 0.5Mo 0.25 V parent metal with 2.25Cr 1Mo, 1Cr 1Mo, 0.5Cr 0.5 Mo 0.25V or mild steel weld metal. Dissimilar metal welds, or transition joints as they are sometimes called, are used where a corrosion and creep resistant steel is joined to a less resistent ferritic steel for economic reasons. For example a joint is made between AISI type 316 austenitic steel and 2.25Cr 1Mo ferritic steel welded with a Nickel based weld metal, e.g. an Inconel weld metal. The relatively expensive austenitic steel is used only where it is required and the cheaper ferritic steel is used where lower creep resistance and corrorsion resistance is adequate. New designs of power plant now use

high alloy ferritic steels in transition joints such as the 9Cr 1Mo and the 12Cr Mo V series of steels.

Within transition joints thermal expansivity differences between the different materials connected produce detrimental interfacial stresses, resulting in additional creep strains which contribute to failures occurring early within the design life of the component. New weld materials and graded composition joints reduce the severity of these differences (section 7.7 and [98]).

Weld preparations are made by machining and or grinding the parent metal surfaces before welding. Weld preparation geometries are designed to improve weld penetration, by making it easy for the weld metal to reach the lower parts of the joint and produce good fusion contact with the parent metal. The weld preparation should also be such that the weld may be easily built up by the successive layering of weld beads in a neat and consistent manner, to provide uniformity of material strength across the joint. Three popular weld preparations are shown in Figs.7.1(a) to (c). Figure 7.1(a) details a general vee-weld preparation for thin plates and Fig. 7.1(b) shows a 'J' type preparation used for thick steam pipes. Figure 7.1(c) shows a narrow gap preparation which has nearly parallel sides in which the weld beads are deposited, one or two per layer, in an automated process. The narrow gap weld preparation provides a quicker and cheaper method for connecting thick pipes than the 'J' type preparation, but care has to be taken to ensure good side wall fusion. Other weld preparations include the use of a backing strip to hold the first layer of weld beads into the weld cavity, and the use of a back preparation where the weld is completed from both back and front of the plate, alleviating the need for a backing strip. The most commonly used weld preparation for thick pipes is that of the 'J' type preparation of Fig.7.1(b).

The weld preparation has to be filled with weld metal in a controlled and systematic order, where small diameter rods are used initially and the size of the rod is increased as the weld is filled. This layering procedure is called buttering or multipassing. An ideal filler metal geometry is shown in Fig. 7.2. The geometry of the weld preparation, the overlapping of the buttered layers of weld, the weld bead size, the heat input and corresponding thermal cycle heating and cooling rates determine the final microstructures and their distribution in the weld and hence determine the

creep properties of the joint.

7.4 The Weld Thermal Cycle.

Rosenthal [99,100] calculated theoretical temperature distirbutions produced by a point heat source moving with velocity V, similar to that produced by arc welding (Fig.7.3(a)). Figure 7.3(b) shows a 3D temperature distribution in mild steel thick plate produced by a point heat source, calculated from heat flow equations by Rosenthal. (n-n) in the figure represents the locus of the boundary between rising and falling temperatures. As the heat source moves forwards with velocity V it rapidly heats the parent material at a point ahead of it and as it passes this point the point cools at a slower rate, the point is then left behind in the wake of the heat source, 3D-thermal cycle. Kohno and Jones [101] measured the temperature at such points in the parent metal heated by a weld thermal cycle. Figure 7.4 shows the temperature variation with time for various points in the weld preparation and highlights the severity of the heating and cooling rates in the weld thermal cycle. It is these severe heating and cooling rates which cause phase transformations, grain growth and refinement in the region close to the weld metal fusion boundary called the heat affected zone (HAZ).

7.5 Weldment Metallurgy.

The following analysis is primarily concerned with low alloy ferritic weld materials and base metals. During welding the parent plate material is heated to its melting point by the severe weld thermal cycle, enabling the weld metal and parent metal to fuse together. The parent metal further from the fusion boundary experiences lower peak temperatures and heating and cooling rates of the thermal cycle than parent metal at the fusion boundary, which produces different material microstructures of varying degrees of grain refinement in the heat affected zone (Fig.7.5). The type of microstructure and grain refinement produced are dependent on the severity of the weld thermal cycle, the base material phase transformation characteristics and grain growth kinetics.

A detailed investigation of a 0.5Cr 0.5Mo 0.25V:2.25Cr 1Mo weld by Middleton and Cane [102] has identified 13 separate microstructures in the heat affected

zone alone. Coleman [96] details simplified microstructural observations of both a single weld bead and a multipass ferritic weld. With reference to Fig.7.6(a), (b) and 7.7, each weld bead produces a repeatable microstructural distribution if the welding parameters such has heat input and bead dimensions are kept constant. The microstructure of the cast weld metal has coarse columnar grains and is almost fully bainitic. Referring to Fig.7.6(a) and Fig.7.5, crossing the fusion boundary the first microstructural region in the heat affected zone is the coarse grained region. Here the parent material has been fully austenitised by the weld thermal cycle peak temperature, and on cooling, the cooling rate is such that the austenite is fully transformed to bainite. Moving further away from the fusion boundary the grain structure becomes more refined, with the prior austenite grain size decreasing almost linearly with decreasing peak temperature of the thermal cycle. This is represented as the fine grain zone in Fig.7.6. Moving still further away from the fusion boundary is a region where the peak temperature reached by the parent metal is only sufficient for partial transformation to austenite to occur (Fig.7.5); the resulting microstructure in this region is a mixture of ferrite and bainite. The partially transformed zone is predominantly ferrite at the cold end of the heat affected zone and predominantly bainite at the hot end. The next zone experiencing lower peak temperatures than the partially transformed zone is termed the tempered or overtempered zone (Fig.7.5), which has a microstructure similar to that of the parent metal. It does show some degradation in structure having precipitates of vanadium carbide and is 95% ferritic, 5% bainitic. The partially transformed zone and overtempered zones are included in Fig. 7.5, but for simplicity only the partially transformed zone is represented in Fig. 7.6(a) and (b) as the intercritical zone, because the overtempered zone has a microstructure very similar to the parent metal.

Microstructural distributions in the heat affected zone have been predicted by Allerry and Jones [103] using heat flow equations to define the weld thermal cycle, knowing the continuous cooling transformation diagram for the parent metal.

In multipass welds layers of weld are built up on top of each other. Figure 7.7 shows a section through a 'J' type preparation Manual Metal Arc weld in a low alloy ferritic steel thick pipe section, showing how the weld beads are arranged to fill the weld cavity. Each weld bead laid down is tempered by the weld thermal cycle of the

next adjacent weld bead, which recrystallises the previous coarse and fine bainite (Fig. 7.6(b)) in the previously laid down weld bead. The heat cycle of each weld bead also tempers the heat affected zones in the parent metal produced by the previously laid down weld bead. The last layer of weld beads to be laid down are called the capping beads, they remain fully coarse and have a columnar grain structure (Fig.7.6(b)).

Multiple layers of weld beads are found in many thick pipe welds, where the extent of the overlap, bead dimensions, heat input and other welding parameters controls the proportion of the final microstructures in the weld metal and heat affected zones. Allerry and Jones [104] developed a computer program which is capable of predicting the heat affected zone microstructures and their distribution from the welding conditions, so that optimum conditions can be established to produce the most beneficial microstructural distributions to improve weld performance. For low alloy ferritic steel weldments the promotion of refined bainitic microstructures gives good creep strength, rupture ductility and weld performance. Highly refined heat affected zone and weld metal structures are obtained by overlaying small weld beads produced by small diameter electrodes with larger weld beads produced by large diameter electrodes [105].

Krutz and Segerlind [106] detail a finite element thermal model where certain welding parameters can be varied to optimise joint strength by promoting certain beneficial metallurgical structures in the weld.

Further modification of weldment microstructures can occur due to any post weld heat treatment, or in-service heating due to plant temperature, or due to ageing.

7.6 Properties Of Weld Microstructures.

The mechanical testing of thin zones of microstructures from welds cannot be carried out, as insufficient quantities of each microstructure can be isolated to make uni-axial creep specimens. However, weld simulation apparatus [107] are available, where a thermal cycle analogous to that which occurs in the welding process is applied to a specimen of the parent material, producing larger quantities of microstructures analogous to those observed in the real weld [108]. Furnace heat treatments of parent metal specimens may also be used to reproduce bulk quantities of the heat affected zone microstructures, if the prior austenite grain size and cooling rate through the transformation temperature range are carefully controlled.

Middleton and Cane [102] have identified the microstructures within a 0.5Cr 0.5Mo 0.25V:2.25Cr 1Mo weld and have obtained their mechanical properties [109]. For welds in general the coarse grained heat affected zone material has the strongest creep resistance and is the most brittle structure. The parent metal has a relatively good creep strength with a medium to high ductility. The weld metal is weaker in creep than the parent metal and has a lower ductility. The partially transformed and over-tempered regions have the lowest creep strength and the highest ductility. The properties of the weld metal coarse and fine zones have not been determined, but the weld metal coarse grained bainitic regions can be thought of as stronger in creep and more brittle than the refined weld metal zones [110].

Figure 7.8 shows the relative creep properties for weld metal, parent metal and heat affected zone microstructures at the same uni-axial test stress level for a transition weld due to Roode, Etienne and Van Rossum [111]. In transition joints sometimes the weld metal can be arranged to be stronger than the parent metal. The property changes across transition welded joints is complicated as dissimilar parent metals are welded together, for example 2.25Cr 1Mo ferritic alloy is joined to AISI 316 austenitic steel with a Nickel based weld metal. Different heat affected zones are observed on either side of the weld which are produced by the different responses of the two base materials to the same weld thermal cycle.

7.7 Weldment Failure.

Cracking and failure of ferritic pipe weldments occurs primarily in three modes: either through the formation of circumferential cracks in the coarse heat affected zone; or by transverse cracks forming in the weld metal; or by circumferential cracks forming in the soft over-tempered and partially transformed region. These cracking modes may initiate during post weld stress relief heat treatment or early within the life of the welded component. Cracks form due to the accumulation of creep strain, which leads to the nucleation and subsequent growth of cavities, which coalesce to form macroscopic damage reducing the effective cross-section of the component till failure.

Circumferential heat affected zone cracking occurs in the coarse grained bainitic region adjacent to the fusion boundary. Cracks start to grow in the outer 1/3 of the pipe wall thickness and may subtend the whole circumference of the pipe, growing

inwards towards the internal bore (Fig.7.9). Cracking can arrest in refined bainitic region of the HAZ [112] and re-initiate ahead of the main crack in a coarse bainite region of a neighbouring weld bead. This shows the ability of the refined bainitic regions to arrest crack growth. Gooch and King [113] have shown that creep crack growth is an order of magnitude smaller in the HAZ refined zones in comparison to crack growth rates in coarse grained zones. The final failure of the component usually involves brittle fracture or plastic collapse leading to steam leakage in a safe manner.

Transverse weld metal cracking usually initiates in the coarse columnar bainite regions of the outermost weld beads. The cracks, oriented transversely across the circumferential weld, extend radially inwards. In extreme cases the cracks may extend across the heat affected zones into the more ductile parent metal where crack growth usually arrests. Initially the transverse cracks are confined within the creep brittle, coarse grained regions of each weld bead, surrounded by more ductile fine grained weld metal. Stress off-loading from the hoop to the axial direction due the transverse cracking ,can sometimes change the cracking mode from transverse to circumferential. Final failure is through steam leakage through the weld metal, although the possibility of a longitudinal pipe split resulting in a catastrophic failure does exist.

Circumferential cracks may also form in the partially transformed and overtempered regions of the heat affected zone, close to the parent metal. This cracking is termed type IV cracking which originates from the German classification of weld cracking [114]. This type of cracking usually occurs due to additional system loading on the joint such as bending caused by pipe supports or reactions of internal fluid at bends or close to pipe geometry changes where stress raisers may exist [115].

With reference to Fig.7.10 several failure modes may occur within one weld; here types IV and associated circumferential IIAZ cracking occur together.

Premature heat affected zone and weld metal cracking may occur as a result of the relaxation of residual welding stresses due to inadequate post weld stress relief heat treatment.

Though these main failure modes have been reported to occur prematurely before the design life of the welded component has elapsed, failures similar to these basic modes are also observed close to the design life of the component.

The failure of transition joints are usually associated with the coarse grained

heat affected zone of the ferritic steel parent metal close to the fusion boundary [116,117]. Cracking results because of the material inhomogeneity across the dissimilar weldment, which is aggrevated by thermal gradients and the incompatibility of thermal strains between the parent metals and the weldment. Failure modes at high stress may be associated with the soft partially transformed zones of the HAZ in the ferritic steel parent metal [117]. Nicholson et al [118] detail thermal cycling and creep loading of a transition joint, where the failure mode is complicated by the competing failure processes of cracking associated with a narrow zone of interfacial carbides close to the fusion boundary in the 2.25Cr 1Mo pipe as well as coarse heat affected zone cracking. Interfacial carbide precipitates have also been observed to cause failure of transition joints after long term service. Graded composition joints alleviate some of the problems of the severe change in mechanical and thermal properties across the ferritic to austenitic fusion interface, where most in-service failures occur; by arranging for the material and thermal properties to gradually change across an elongated welded joint. This results in improved joint life and low crack susceptibility [98].

7.8 Design Codes For High Temperature Weldments.

In Britain the current design codes used to design high temperature pipe and pressure vessels fabricated using welds are BS 806, BS1113 and the most recent BS5500. These design codes are based on the stress-rupture properties of the parent material using the mean diameter hoop stress and no allowance is made for the effects of the material inhomogeneity in the region of the weld on the design lifetime of the component.

In the design of a pressure vessel or pipe the internal diameter is calculated to give the required volume for a pressure vessel or steam flow for piping. The thin pressure vessel formula for the mean diameter hoop stress is :-

$$\sigma_{mdh} = \frac{P_r D_m}{2\hat{t}} \tag{7.1}$$

where the mean diameter is given by

$$D_m = D_{ID} + \hat{t} \tag{7.2}$$

and (D_{ID}) is the internal pipe diameter. This formula is used to calculate the pressure vessel thickness ($\hat{t}$) required to sustain the internal pressure load (P_r), to give a mean

diameter hoop stress (σ_{mdh}), which when multiplied by a safety factor of 1.2 to 1.5, and compared to ISO uni-axial creep rupture data for the parent material, gives a rupture life in excess of 10^5 hours design life.

Having determined the pipe thickness, ($\hat{t}$), a further 10% is added to the thickness to allow for bending, which may occur due to additional loads at bends, junctions, or pipe supports. In practice there is no evidence of plain pipes failing by creep within their design life using these British Standard codes and hence this approach is conservative. Though early failures associated with cracking in weldments occur early in the design life of some components. With the need for the accurate appraisal of the remenant life of conservatively designed pipework in power plant, which has passed its initial design lifetime, so that it may continue to operate safely into the future, and with new high performance and safety standards required by the nuclear power industry; the understanding and prediction of welded component deformation and failure is important.

The United States nuclear (high temperature) code N47 allows for the presence of the weld in the design of pipework by defining the maximum allowable creep strain which can accumulate in the locality of the weld under service conditions.

Researchers have considered the use of stress, strain based approaches, the use of the reference stress, the mean diameter, the maximum principal stress, the effective stress, the skeletal stresses and weld performance factors, to define the failure mode and the failure times of the welded component with reasonable success. These approaches will be discussed in more detail in the following sections.

7.9 High Temperature Weld Deformation And Failure Predictions And Their Comparison With Experimental Test Results, In The Search For An Improved Design Methodology.

7.9.1 Analysis Of Cross-Welds.

Clark and Allerry [119] and Clark [120] presented results from uni-axial creep tests of specimens containing heat affected zone microstructures produced by weld

thermal simulation in ferritic steel parent metal. The simulated weld was perpendicular to the tensile axis. Failures occurred in the coarse grained bainite regions of the heat affected zone. Homogeneous specimens of the heat affected zone microstructures produced by furnace heat treatment gave rupture lives of an order of magnitude greater than those of corresponding tests on specimens produced by weld simulation in the same parent material. They concluded that this is due to a complex interaction between the mismatched creep properties of each component microstructure along the gauge length of the specimens produced by the weld thermal simulation.

A simple two material model is presented [119] where coarse and fine heat affected zone material have different creep rates in both the axial and radial directions; but at the interface between these structures, due to compatibility of strain, both structures are forced to creep at some intermediate strain rate. A more realistic model is that of the Nicol model [121]. This model uses Cosserat Plate theory and Norton's law to predict the steady state strain rate distributions in a composite plate, containing a zone of different mechanical creep properties under uni-axial tension (Fig.7.11). Referring to figure 7.11, the plate is assumed to be infinitely wide in the (z) and (y)-directions. Plane strain conditions are used, where no displacement is allowed in the (y)-direction. The plate contains a zone of material (B), of thickness (T), and width (h); with different creep properties to the zones of material (A).

The model assumes that the creep deformation of each zone is governed by Norton's law:-

$$\dot{\epsilon}_A = A\sigma^{n_A} \tag{7.3}$$

$$\dot{\epsilon}_B = B\sigma^{n_B} \tag{7.4}$$

and that the creep exponents for each zone are the same. (i.e.$n_A = n_B$), allowing the relative creep rate ratio of the two materials to be defined as a constant:-

$$\frac{\dot{\epsilon}_A}{\dot{\epsilon}_B} = \left(\frac{A}{B}\right) \tag{7.5}$$

Numerical solutions were obtained using (B/A) values from 0.01 to 1,000 and creep exponent (n) from 1 to 10, for a zone width ratio (T/h) from 0.5 to (∞), corresponding to a thin zone (B) and an infinitely thick zone (B) respectively. For the infinitely thick zone (B) only one interface is present at $(z = 0)$, (Fig.7.11).

The change in the secondary creep strain rate in the (z)-direction across a single interface (i.e $T/h = \infty$) is shown in Fig.7.12, due to Nicol and Williams [122], for ($n = 4$) and (B/A) ratios form 1 to 10. It is noticed that the creep rates remote from the interface are the same as would be expected in individual uni-axial specimens of each homogeneous zone of material, as the interface is approached the creep strain rate varies smoothly from the remote values, with a compatibile creep strain rate intermediate at the interface itself, which is consistent with the Clark and Allerry model [119].

A zone width ratio ($T/h < \infty$) represents two interfaces and a significant interaction occurs once (T/h) becomes less than one. Nicol and Williams [122] show the effect on the secondary creep axial strain rate of varying the creep exponent (n) for a very soft zone (B), with a (B/A) ratio of 200 for various zone width ratios (T/h), (Figs.7.13 (a) to (c)). As (n) increases the strain rate at the interface is increased, but the rate of change of strain rate near the interface decreases. Figures 7.14 (a) and (b) show the effect of reducing the zone width for hard and soft zones respectively due to Nicol [121]. It is observed that for a soft zone (Fig.7.14(b)) as the zone width is reduced relative to the specimen width (i.e. T/h changes from ∞ to 0.25) the strain rate is reduced below that of a homogeneous soft zone material subject to the same loading conditions. The maximum strain rate is at the centre of the soft zone. For a hard zone, which is analogous to a heat affected zone in a weld (Fig.7.14(a)), as the zone width ratio (T/h) is reduced the creep strain rate in the harder zone (B) is increased over that of the homogeneous hard zone material under the same loading conditions. Now the maximum strain rate in the hard zone is at the zone interface. It is thought that as the zone width ratio (T/h) is reduced the constraint on the deformation of the zone (B) by the deformation of the parent material (A) increases, forcing the zone (B) to creep closer to the rate of the parent material (A).

On the basis of these results it may be concluded that soft zones will have a small effect on the weld behaviour, as for small zone width ratios the strain rates in the soft zone are reduced. Yet, for hard zones with narrow zone width ratios, strain rates are increased, which is a detrimental effect. Though in both cases increased strain rates are observed in the harder material and decreased strain rates in the softer material at the zone interfaces, relative to the respective creep strain rates of

samples of each homogeneous material for the same loading condition. This is caused as a direct result of stress redistribution from the softer zone material to the harder zone material in close proximity to the interface.

Therefore on the basis of these secondary state analyses maximum strain rates occur at the intefaces in the hard zone material, which is where final failure should occur and this is consistent with circumferential heat affected zone failures in weldments.

From the predicted maximum strain rates within the zone material, Nicol and Williams [122] were able to propose equations for an apparent reference stress for such a composite, to predict the approximate failure lifetimes of cross welds knowing the secondary creep rate ratios of the microstructural zones within the weldment.

Experimental cross welded specimen tests involve the uni-axial creep testing of a specimen machined from a blank cut from a welded joint (Figs.7.15). The specimen will contain parent metal, weld metal and heat affected zone regions. These specimens can give information of which zone will fail under particular uni-axial stress levels and may also be used to observe damaged microstructures and fracture surfaces analogous to those obtained in practice [123]. Williams [124] details that care has to be taken when testing and interpreting the results of cross-weld specimen tests as the ratio of the specimen diameter to the weld metal zone thickness influences the failure times of the specimens and may in some extreme cases influence the zone in which microstructural failure occurs. Another drawback in using cross-weld specimens to determine the deformation and failure behaviour of larger components is that the stress-state in most standard cross-welded specimens produces a maximum principal stress at right angles to the weld direction, whereas in pressure vessels and pipe welds the maximum principal stress usually lies in the same direction as the circumferential direction along the weld and hence is 90° to that of the cross welded specimen. Geometry and loading differences together with effects of size make the multi-axial stress-states significantly different in the uni-axial cross-weld specimen to those in a pipe weld. This causes great difficulty in relating the test results from cross-welds to real structures containing welds.

Etienne, Von Rossum and Roode [125] performed uni-axial creep tests on weld metal, two heat affected zone microstructures and the parent metal of an austenitic

weld in a thick plate. The uni-axial creep data for each material weld zone was represented by Blackburn's formula (similar to that of Garofalo, equation (2.3) using (2.2)) to represent both primary and secondary creep behaviour; tertiary creep is neglected. Multi-axial creep strains are represented using Odqvists generalisation given in section 2.3. A finite element study of the creep deformation of both a circular section cross-weld and a thick plate were performed using a four material model [111]. The cross-weld was modelled with an axisymmetric finite element analysis and the thick plate by a plain strain analysis. The finite element meshes used to analyse sections of the cross-weld specimen (Fig.7.16(b)) and the thick plate (Fig.7.16(d)), are shown in Figs.7.16 (a) and (c) respectively. Both specimens were subjected to the same uni-axial stress of $(165MNm^{-2})$ at a constant temperature of $600°C$. The predicted longitudinal creep strains and the Von Mises surface stresses for the cross-weld and the thick plate weld specimens are given in Figs.7.17 (a),(b) and (c),(d) respectively. Experimental values of creep strain obtained from a cross-weld specimen test compare favourably well with the finite element results in Fig.7.17(a). Comparing creep strain distributions for the cross-weld specimen (Fig.7.17(a)) with those for the thick plate weld Fig.7.17(b), significant differences in the creep strain levels are observed. The longitudinal creep strain is maximum in the parent metal for the cross-weld specimen, yet the maximum longitudinal creep strain is a maximum in the weld metal for the thick plate weld. This behaviour may be explained as a direct result of the difference in the multi-axial stress states present in each specimen (Figs. 7.17(c) and (d)). It is clearly seen in both figures 7.17(c) and (d), that on initial loading, a uniform stress is produced in all the zones of the welds, but stress is redistributed with test time from the softer weld metal and base metal (parent metal) into the harder heat affected zone (HAZ), close to the fusion boundary and the (HAZ)/parent metal boundary. (See Fig.7.8 for the relative creep strengths of each material zone). Futher stress redistribution may occur in practice as a result of the formation of tertiary creep damage in one or more of the weld zones, which is not allowed for in this model. Though the axial stresses are the same the Von Mises stresses in the thick plate weld are much lower than those in the cross-weld specimen; hence the creep strain rates in the thick plate will be smaller than that in the cross-weld specimen. Roode et al [111] concludes that it is not possible to use the test data from a cross-weld compos-

ite specimen to assess the creep resistance of a complete structure containing a weld. Structural creep analysis will be possible with a finite element analysis using experimental data from uni-axial creep tests on the various weld microstructural zones. To make accurate predictions of rupture life and failure mode it will be necessary to incorporate tertiary creep into the calculations.

Evans and Wilshire [117] also studied the failure of cross-welded test pieces taken from a transition weld between 2.25Cr 1Mo steel and AISI 316 austenitic steel parent plates, joined with 17Cr 8Ni 2Mo austenitic weld metal, tested at a temperature of 838K ($565°C$). Uni-aixal tests performed at high stress ($250 MNm^{-2}$) showed ductile creep failures in a region of the 2.25Cr 1Mo steel outside the heat affected zone several millimeters from the fusion boundary. At low stress ($100 MNm^{-2}$) cross-weld test pieces replicated long term failures in most transition welded tubes, with creep damage accumulating in the coarse heat affected zone of the 2.25Cr 1Mo material some 75 to 150 μm from the fusion boundary. Evans and Wilshire performed an axisymmetric secondary creep finite element analysis of the transition weld under a uniform axial stress using a five material model. The multi-axial creep constitutive equation of Odqvist (2.7) is used to model the creep deformations of each material zone and no allowance for the effects of tertiary creep damage on the secondary creep stress state. The model used uni-axial creep strain data from tests on homogeneous specimens of the parent metal, weld metal and simulated heat affected zone microstructures in the 2.25Cr 1Mo parent metal; namely the coarse grained bainitic, fine grained bainite and intercritical zone microstructures. The uni-axial creep strain data provided creep constants in equation (2.7), to represent the multi-axial minimum secondary creep strain rates of each material zone in the finite element model. Results from the finite element analysis gave maximum principal stress and effective stress contour plots in the welded joint, which showed a stress concentration at the interface between the intercritical zone and the 2.25Cr 1Mo parent metal for a cross-weld uni-axial specimen pressure load of $250 MNm^{-2}$. Corresponding results for a cross-weld subjected to uni-axial pressure load of $100 MNm^{-2}$ showed stress concentrations in a region close to the fusion boundary in the coarse heat affected zone of the 2.25Cr 1Mo plate. The positions of maximum stress were consistent with the final experimental failure positions of the cross-weld specimens.

Life reductions of 2.5 and 60 were calculated for the high and low stress tests respectively, using the maximum stress level and the stress-rupture properties of the material zone (where this maximum stress level occured), to calculate a rupture time. This was compared to the rupture life of the same zone under the same applied specimen stress level to give the life reduction factor. These values were also in agreement with experimental tests.

Creep strain values were plotted along the length of the cross-weld specimen surface from the finite element analysis results (Fig.7.18). In addition measurements taken from the distortion of a strain grid scribed on the surface of the cross-weld test specimens were included in the paper and compared with the finite element results. The comparisons were good showing the localisation of creep strain at the positions where final failure occurred.

Evans and Wilshire also showed that from the good correlation of the finite element results with the results from cross-welded specimens, the finite element techniques using uni-axial creep strain data for each weld zone material could be applied to real component geometries. Thermal stresses, non-steady loading and temperature cycling could also be included in the finite element analysis, to replicate the actual in-service conditions.

Evans and Wilshire also state that the exact material properties of in-service component heat affected zone microstructures cannot be determined accurately using weld simulation by furnace heat treatment of the parent material, as a result of compositional changes in microstructure which occur at elevated temperature during service. Elements in the weld metal alloy such as Cr, Ni and Mo diffuse into the parent metal and Carbon migrates into the weld metal. Ageing may also affect the material properties of each weld zone due to Carbide dispersion. The Evans and Wilshire model makes no allowance for stress redistribution during the primary and tertiary creep regions of the weld materials and the effects of the multi-axial stress state on the failure of the material, which are of equal if not more importance to the prediction of weldment failure than these microstructural effects.

Therefore, although good correlations have been obtained between cross-weld test behaviour and finite element predictions, the data obtained from cross-weld tests cannot be related to full size component geometries, due to differences in the multi-

axial stress states. Hence, laboratory tests and finite element studies must be performed on the actual weld geometries encountered in practice. Therefore small scale tube burst tests and expensive full size pressure vessel tests on steam pipes containing welds have to be performed to obtain meaningful results.

7.9.2 Creep Testing Butt Welded Tubes.

Ivarson and Sandstrom [126,127] studied the creep deformation and rupture of thin butt welded tubes of cold worked AISI 316 stainless steel with an external to internal diameter ratio less than 1.1. Uni-axial creep data was obtained for the parent metal, weld metal and heat affected zones using samples of the parent metal, weld metal and furnace heat treated parent metal respectively. The appropriate heat treatment was chosen to give a microstructure and microhardness values of a heat affected zone in the pipe weld. Properties of other heat affected zone microstructures were interpolated from the previously determined HAZ data using the hardness measurements in the pipe weld HAZ as weight functions [127]. Using the material data for each weld zone a secondary creep finite difference computer simulation was performed for the butt welded tube containing an internal pressure of 24.5 MPa. The calculated hoop stress distributions as a function of time are shown in Fig.7.19. This figure clearly shows the severe off-loading of hoop stress from the weld metal into the heat affected zone. Reasonably good agreement was obtained between the finite difference and the creep strain results from the tube burst tests, after a primary creep representation was included in the finite difference analysis. In the tube burst tests failure of the tube occurred in the weld heat affected zone with the formation of through thickness axial cracks, which is consistent with the finite difference results if one assumes that the maximum principal stress (the hoop stress) is the stress which controls the failure of the tube; with cracking occurring at 90° to this principal stress direction (i.e. in the axial direction).

It was concluded that the creep life of the tube was reduced by a factor of 15 to 30 dependent on the test stress level in comparison with the lives of homogeneous cold worked tubes. Invarson et al [126] suggest that in order to decrease the loss in creep strength caused by the presence of a weld, the creep deformation and rupture properties of the different material zones in the weld should be arranged to be similar,

to prevent the severe stress redistribution of stress from soft zones to harder ones, as the increased stress carried by hard zones (such as the HAZ) is not usually outbalanced by the increased rupture strength of this hard zone.

Invarson and Sandstrom [126] present a simplified graphical method based on the stress rupture diagrams for the parent metal and the weld metal, with the use of an estimation of how stress is redistributed from the weld metal. The maximum stresses in the weld metal and parent metal are used to give the minimum life of the welded joint. Though failure of the tube burst tests occurs in the heat affect zone, the stress rupture properties of the HAZ are not allowed for in the calculations and no allowance for the effects of the multi-axial state of stress on the failure life of the welded tube is made. The life predictions therefore are reasonable but conservative.

Browne et al [128] also studied the failure of butt welded tubes. The butt welded tubes were scaled down versions of real thick walled steam pipes having an internal to external diameter ratio of 1.52. The parent pipe was 0.5Cr 0.5Mo 0.25V which was welded with a range of different weld metals: mild steel, 1Cr Mo, 2.25Cr 1Mo and 0.5Cr 0.5Mo 0.5V. Tube burst tests were conducted at two internal pressures of 45.3 MPa and 51.5 MPa at the constant temperature of $565^{o}C$. All failures in the tubes were through axial heat affected zone cracks, with some welds showing circumferential and transverse weld metal cracking close to the fusion boundary. The longest tube life was obtained using the 0.5Cr 0.5Mo 0.25V weld metal having the same creep properties as the parent metal.

An axisymmetric finite element analysis was performed using the secondary creep rate data from uni-axial tests on the parent metal, weld metal and a weld simulated heat affected zone material. The constitutive model of Garofalo (equation (2.3)) was used with the use of Norton's law (equation (2.2)) with the use of Odqvist's multi-axial generalisation (section 2.3) to model multi-axial creep strains in the finite element program. The three material finite element mesh representation of the weld is shown in Fig.7.20. In the analysis the three materials in the weld model were assumed to have the same Norton's law steady state creep exponent of n=4. The different secondary creep strain rates of each material zone are represented as a ratio of the Norton's law constants (A) with respect to the parent material constant (B) (equations (7.3), (7.4) and (7.5)). The weld metal to parent metal ratio (A/B) for

mild steel, 1Cr Mo, 2.25Cr 1Mo and 0.5Cr 0.5Mo 0.25V were 1690, 14, 5 and 1 respectively and the heat affected zone to parent metal ratio of 0.25 was used for all the weld metals.

The stationary state stresses in the weld from the finite element analysis of an internally pressurised tube with weld metal: parent metal : HAZ creep rate ratios of 10:1:0.25 are summarised in the graphs of Fig.7.22(a), (b) and (c) across various various sections of the weld Fig. 7.21. Referring to Fig.7.22(a) stresses are redistributed from the weld metal into the heat affected zone. Figure 7.22 (b) and (c) show that the maximum hoop and axial stress occur at the outer surface of the tube and the maximum equivalent or Von Mises stress occurs at the inner surface of the tube, when the steady state creep conditions are achieved.

Using the maximum principal and equivalent stresses obtained from the finite element weld model stress distributions, estimates of the minimum life of the pipe welds were obtained, using the larger of the former two stresses and the experimental uni-axial stress-rupture diagrams for each material zone. The zone having the shortest lifetime prediction is said to define the region where final tube failure occurs, with the orientation of cracks perpendicular to the maximum principal tension stress direction. Referring to the results of such calculations (Table 7.1) the minimum lifetimes are predicted for the heat affected zone in column No.4 and No.10, which correctly defines the zone where failure of the tubes occurred in the experimental tube burst tests. The calculated failure time predictions for the heat affected zone gives a poor prediction of the life of the tubes giving generally shorter life predictions than those obtained in practice (column No. 2) except for the 2.25Cr 1Mo weldment test at a presure of 51.5MPa. In order to allow for the effects of the multi-axial stress state on the rupture behaviour of the material zone where most tube failures occurred, a stress rupture criterion due to Cane [129] was used:

$$t_{Rup} = \frac{C}{\sigma_1^q \sigma_{ef}^{(r-q)}} \tag{7.6}$$

where (σ_1) is the maximum principal stress, (σ_{ef}) is the Von Mises effective stress; (q) is the principal stress exponent of rupture, determined from torsion/tension creep rupture tests; (r) is obtained from the gradient $(-1/r)$ of the uni-axial stress-rupture diagram and (C) is a constant. (r) and (q) were obtained from rupture tests on the heat affected zone material as 3.0 and 8.5 respectively. Having determined (q) and

(r) the representative rupture stress may be defined from (7.6):-

$$\sigma_{Rep} = \sigma_1^{\frac{q}{r}} \sigma_{ef}^{\frac{(r-q)}{r}} \tag{7.7}$$

which when applied to the uni-axial stress-rupture data will predict the life of the structure.

Improved rupture time calculations were performed for each tube burst test (Table 7.1, column No.9) using equation (7.7) and the uni-axial stress rupture data for the heat affected zones. The rupture times are seen to be greater than those of column No.4 giving improved lifetime predictions. The lifetime predictions using the British Standard codes BS 806 and BS 1113 are given in columns No.s 6, 7 and 8 of Table 7.1, using the mean diameter hoop stress and the parent material uni-axial stress rupture properties, with and without safety factors. The life predictions using the safety factors (Table 7.1, column No.s 7 and 8) are extremely conservative when compared to the experimental rupture times (column No.2). The life predictions without the use of a safety factor in general are poor, overestimating the rupture lifetimes except for the 0.5Cr 0.5Mo 0.25V weld metal test. The use of the mean diameter hoop stress with the parent material uni-axial stress rupture properties does not predict the trends in the failure lifetimes of tubes welded with different weldmetals.

Therefore, the use of the representative rupture stress does imporove the lifetime predictions of welded tubes and goes someway to predicting the relative trends in the rupture times for tubes having different weldmetals. Though life predictions are in general smaller than the experimental lifetimes due to the finite element analysis neglecting the stress redistribution occurring during the primary creep and particularly during the tertiary creep region.

7.9.3 Experimental Testing And Predictions Of The Creep Deformation And Failure Of Full Size Welded Steam Pipes.

In order to study the actual creep strains and failure of full size steam pipes, pressure vessels constructed from welded sections of thick steam pipes were tested by the C.E.G.B. in their collaborative programme on The Correlation of Test Data for High Temperature Design of Steam Pipes. Early research within this research programme by Coleman, Parker, Walters and Williams was concerned with the effects of

through thickness inhomogeneity in the parent metal steam pipes on the outer diameter steady state creep rate and the validity of simple uniform property steady state strain rate calculations. When the parent pipe is mechanically formed, differences in metallurgical structure are caused by localised working variations, through thickness temperature gradient and cooling rate differences. These variations can typically cause a difference between the secondary creep strain rates of uni-axial test specimens taken from the inner and the outer pipe wall, of a factor of 10 to 20. Coleman et al [129] used a simple finite element model of a pipe consisting of three concentric material cylinders, having different creep properties, where the constant (A) in Norton's law (Equation (7.3)) was varied by a factor of 10 between the inner and outer ring (Fig. 7.23). From the finite element results the effect of the through thickness material inhomogeneity produced a difference of less than 20% in the surface strain rate in comparison with the surface strain rates for a homogeneous pipe with mid wall thickness creep properties.

Williams [130] used an analytical technique which incorporated a smooth power law functional variation of pipe through thickness creep properties which is closer to the material property variation expected in practice. Coleman's model [129] described above used three discrete regions with different creep properties and a sharp transition between one region and the next. Williams showed that within an error of ($\pm$11 %) a skeletal point stress exists for a wide range of creep exponent (n) and the material through thickness property variation index (x) and if (n) is kept constant close to the values obtained in practice, the skeletal stress predictions result in negligible tangential surface strain rate calculation error, in comparison with surface strain rate calculations based on the homogeneous pipe of mid wall creep properties. Therefore these results suggest that the steady state outer surface tangential creep strain rate may be represented by the average creep properties of the parent metal pipe at the mid wall position, with an assumption in calculations that the pipe has homogeneous creep properties. This suggests that through thickness parent pipe material variations are of secondary importance when modelling the creep behaviour of welded pipes, in that the mid wall properties will suffice.

Coleman et al [131] performed full size creep tests of 0.5Cr 0.5Mo 0.25V steam pipe at a temperature of $565°C$. Two pressure vessels were constructed from thick

section steam pipe of external to internal diameter ratio 1.52. The pressure vessels were subjected to the same test conditions, and were pressurised to 455 bar, to give a failure life a factor of 10 shorter than the expected service life of the steam pipe. Circumferential welds of mild steel, 1Cr Mo, 2.25Cr 1Mo and 0.5Cr 0.5Mo 0.25V weld metals were used to connect 0.5Cr 0.5Mo 0.25V parent pipe in the pressure vessels, using a standard multipass weld with a standard J-type preparation (Fig.7.1(b)). The weldments were all post weld heat treated for 3 hours at $700°C$ prior to testing, to relieve any welding residual stresses.

The details of the pressure vessel tests, weld specifications and experimental measurements are made elsewhere [131] and in the following chapter, section 8.2, while here the test results, modelling and conclusions which can be gained from the analysis, are of primary importance. It suffices to say that all strain measurements were surface strain measurements either across the weld or parent metal pipe, or locally at the weld metal centre line and the parent metal center line in both the hoop and axial directions. On pressurisation of the vessels, at temperature, the initial loading strains were elastic for both the welds and the parent pipe materials, which were shown to be compatible with those calculated from the Lame equations, giving a hoop stress to axial stress ratio of 2:1. Permanent creep strains were then measured with time, the parent pipe showing primary creep in the hoop direction lasting for some 4,000 hours with no axial creep strain accumulation. All weld metals showed primary and secondary creep strain accumulation in both the hoop and axial directions of varying degrees due to the different creep strengths of the weld metals. The creep strains and strain rates measured across the mild steel weld metal were much higher than those of the other weld metals, showing high ductility and low creep strength. The hoop strain rates measured across the 1Cr Mo, 2.25Cr 1Mo and 0.5Cr 0.5Mo 0.25V welds are all similar to that of the parent metal. The mild steel weld has a hoop creep strain rate approximately three times that of the parent pipe and an axial strain rate which was approximately ten times that of the parent pipe hoop strain rate (from the measurements across the weld metal and parent metal regions).

Local strain gauge data taken at the centre of the welds indicates that the same hoop creep strain rate occurs at the center of all the welds as that in the remote parent pipe, irrespective of weld strength. This indicates that stress must be off-

loaded from the soft weld metal into the heat affected zone to retain hoop strain rate compatibility in the weld with that of the parent metal.

Coleman et al [129] showed that the steady state creep rate observed in a thick walled 0.5Cr 0.5Mo 0.25V steam pipe is best described using the Von Mises equivalent stress and the strain rates in a given direction are obtained from the generalised Norton's law, due to Odqvist, given in equation (2.7). Where the creep deformation may be calculated using the stationary state stresses, predicted by the Bailey [132] equations (8.15), (8.16) and (8.17).

Coleman et al [131] states that the presence of the weld inhomogeneity in the parent pipe invalidates the use of the Bailey equations due to stress redistribution between different material zones. Though if hoop and the axial strain rates are known at a point on the surface of the vessel, equation (2.7) can be used to calculate the hoop to axial stress ratio and therefore the stresses within the weld, if the Norton's law constants (K) and (n) are known for the weld metal. Calculations were performed using the ratios of hoop to axial strain rates at the weld, from the pressure vessel tests with (A) and (n) values for each weld metal obtained from uni-axial creep tests [109], giving hoop to axial stress ratios and actual stress values for each weld (Table 7.2). It is noticed that the 0.5Cr 0.5Mo 0.25V weld has the same stress ratio as the parent pipe ($\sigma_H/\sigma_A = 2.$), which is identical to that predicted by the Bailey equations. The stress ratios for the 1Cr 1Mo and 2.25Cr 1Mo welds show that significant stress redistribution has occurred, in having an almost equi-bi-axial stress ratio ($\sigma_H/\sigma_A \approx 1.$). For mild steel ($\sigma_H/\sigma_A < 1.$) indicating that the axial stress is greater than the hoop stress, showing that for this weld the hoop stress off-loads into the axial direction.

Creep strain measurements therefore can be made on components in the power plant to give the surface stress ratios in the vicinity of the weld, from which life estimates can be made, but due to the large numbers of welds in a power station this may not be economic. Another drawback to this method is that it will only give data local to where the strain measurements have been made and this region may not be the position where the component fails, as many failures are associated with narrow regions of coarse grained microstructure in the weldment and heat affected zones. A finite element stress analysis may provide a full description of stresses and strains

throughout the zones of a welded joint.

A three material secondary creep finite element solution was performed by Coleman et al [131] for different ratios of the weld metal to parent metal creep rate ratios of 1, 3, 10, 15 and 1690, giving the properties of the whole range of different weld materials which can be used to make joints in the 0.5Cr 0.5Mo 0.25V parent metal. The creep rate ratios for the 0.5Cr 0.5Mo 0.25V, 1Cr 1Mo and 2.25Cr 1Mo and mild steel welds are 1, 5, 14 and 1690 respectively, after Browne et al [128]. The stationary state hoop stresses on the pipe surface at the weld metal centre, the heat affected zone and in the parent pipe from the finite element analysis are summarised for the range of weld properties in Fig.7.24(a). As the weld metal to parent metal creep rate ratio increases the hoop stress at the weld metal centre decreases. The hoop stress in the heat affected zone is greatest but only increases marginally with the increase in the creep rate ratio. The remote parent metal hoop stress is insensitive to the variation in the creep rate ratio. The variation in the corresponding axial stresses at the pipe surface are shown in Fig.7.24(b), which shows that a peak HAZ stress exists for a creep rate ratio of about 15. Figure 7.24(c) shows the variation of the Von Mises equivalent stress with the weld metal to parent metal creep rate ratio.

The secondary creep strain rates on the pipe surface at the positions detailed in Fig.7.25 from the finite element analysis are shown in Table 7.3. It is noticed that the hoop strain rates are all approximately the same at the weld metal centre line and are similar to the parent metal hoop strain rates remote from the weld, which is consistent with the observations made in the experiments. The axial creep strain rates at the pipe surface at the centre of weld are dependent upon the weld metal to parent metal creep rate ratio and increases with increasing weld metal to parent metal creep rate ratio (Fig.7.26). The magnitudes of the surface strain rates from the finite element analysis are in general approximately 30% larger than those of the experimentally measured values.

The axial strain rates (Table 7.3) increase with distance from the weld metal centre line (A) reaching a peak value in the heat affected zone then decreasing into the parent metal tending to a zero axial strain rate, which is consistent with the Nicol and Williams uni-axial model (section 7.9.1). This effect is most pronounced for mild steel weld metal with the largest weld metal to parent metal creep rate ratio.

The hoop strain rates (Table 7.3) are relatively constant with distance from the weld metal centre line (A) except for very large weld metal to parent metal creep rate ratio. Since reasonable agreement of the hoop strain rates measured locally at the weld metal centre, non-locally across the weld and in the parent metal was obtained in the experimental tests, the consistency of the hoop creep strain rate at the pipe surface across different microstructures of the weldment during secondary creep is considered to be a real effect. The weaker, initially faster creeping material zones shed load to the harder, slower creeping zones, decreasing the creep rates in soft zones and increasing the creep rates in harder ones, to maintain a hoop strain rate compatible with that of the parent material. Stress redistribution is much easier in the hoop direction in comparison to the axial direction and the creep rates in the axial directions reflect the relative creep strengths of the weld metals.

The predicted life of the pressure vessel using BS 806 and BS 1113 codes with a maximum allowable stress of $110 MNm^{-2}$ gave a life of 20,000 hours, which may be compared to the final failure life of 46,000 hours detailed by Coleman [133] using the pressure vessels of [131] tested to failure. The British Standard codes are therefore conservative. Similar indications have been obtained from damage measurements of sections removed from real components having reached their design life. The results indicate that less than 50% of safe operational life of the components had expired. Other methods were therefore sought to determine the life of welded pipe sections. Using the mean diameter hoop stress underestimates life and using net section stress grosely overestimates life. When the life estimates were based on the surface principal stresses at the weld metal centre line from experimental tests, or from the finite element analysis, calculations using the appropriate weld uni-axial stress-rupture data gave lifetimes in excess of 50,000 hours for the three low alloy ferritic welds. A life estimate of 35,000 hours was calculated for the mild steel weld on the basis of the axial stress at the pipe surface, since the axial stresses were greater than the hoop stresses for this weld metal. This may be compared with the actual life of the mild steel weldment of 23, 671 hours, which failed by circumferential creep cracking in the weld metal [134,135] close to the fusion boundary. These calculations provide obvious improvements in life prediction for welds, but the analysis has assumed that failures occur in the weld metal and no allowance has been given to the effects of the

multi-axial stress state on rupture or the stress redistribution due to tertiary creep. Modelling tertiary creep in the life prediction analysis is important as the growth of creep cracks and damage may occupy a significant proportion of the total life of the weldment.

A recommendation is given on the basis of the reported results [131] that due to the 0.5Cr 0.5Mo 0.25V weld metal having no axial creep rate, similar to that of the parent metal this weld metal has the best properties to give the longest service life.

It is noted that Walters and Coleman [137] performed a large strain tertiary creep finite element analysis of a homogeneous 0.5Cr 0.5Mo 0.25 thick section steam pipe, using parent metal uni-axial creep data represented by a simplified form of Rabnov-Kachanov creep damage relationship. Reasonable agreement was obtained between hoop and axial strain predictions from the finite element analysis in comparison with experimental results from a full size pipe test containing a 0.5Cr 0.5Mo 0.25V weld [131]. Up to 10,000 hours life there was a one to one correlation with the calculated and experimental hoop strains, thereafter the calculated stresses were larger than the experimental values; the difference never exceeding a factor of 2. The axial strains gave good correlations up to 35,000 hours after which the experimental strains were more compressive. The analysis may have been improved by the inclusion of both the primary and secondary creep regions. Unfortunately improved life predictions cannot be obtained from the analysis as the material is assumed to be homogeneous and therefore does not attempt to model the stress redistribution which occurs between different material zones of the weldment, from which new life predictions can be obtained using uni-axial stress-rupture data.

7.9.4 Improved Life Prediction And Design Of Welded Pipes for High Temperature Applications.

Current British Standard codes used for the design of pressure vessels and piping use the mean diameter hoop stress and the uni-axial stress rupture properties of the parent pipe to determine a safe design life of the component, which has been described in detail in section 7.8. The British codes have been shown to give conservative estimates of life. The use of the net section stress with parent pipe uni-axial

stress rupture properties grossly over-estimates the welded tube life.

The through wall thickness stress distribution at a stationary state for a homogeneous pipe under internal pressure has been determined analytically by Bailey [132]. Fairburn and Mackie [138] have extended the work of Bailey, in the derivation of a skeletal stress point, (which is a point in the pressure vessel where the stress remains invariant as the stresses redistribute during creep deformation) and Johnson [139] defined the reference stress, which has been used to define improved deformation and failure predictions of homogeneous pipes at uniform pressure and temperature. None of these analyses include any allowance for stress redistribution and the different stress-rupture characteristics associated with the material inhomogeneity in the region of the weld.

Coleman et al [131] used Bailey's analysis in conjunction with Odqvists equation (2.7) to represent multi-axial steady state strain rates, to obtain hoop and axial stresses at the weld metal centre line on the surface of the pipe, using experimental strain rate data measured at the same surface positions. With the use of the weld metal uni-axial stress-rupture data this gave improved life predictions, but assumed that failure would occur in the weld metal. Therefore surface strains can be measured for in-service weldments to give an estimate of remnant life.

Browne et al [128] used a three material finite element solution to model tube-burst tests, which failed in the heat affected zones. The representative rupture stress based on a multi-axial rupture criterion was used in conjunction with uni-axial stress rupture data for the heat affected zone material using the surface stresses obtained from the finite element analysis to predict lifetimes of different welds in the tube burst tests. The correlation of predicted and experimental test lifetimes was improved, in comparison with the design code lifetime predictions and in general were slightly conservative, but showed the relative trends between the lifetimes of tubes containing different weld metals.

Williams [140] developed simple weld performance factors (WPF) which allow for the effects of stress redistribution from the weld metal to the heat affected zone, on the basis of the stresses obtained from a finite element parametric study by Browne [128]. The weld performance factor is defined as the fraction by which the required pipe stress must be reduced to obtain the required life in the weld metal or the heat

affected zone. If the weld performance factor is less than unity then the operating pipe pressure must be reduced or the pipe thickness increased. If the WPF is greater than unity then the weld or heat affected zone will have a life greater than the design life of the parent pipe. Weld performance factors were obtained for different weld metal and parent metal combinations for both the weld metal and heat affected zone. Material failure ductility is allowed for in the weld performance factor by the use of the Monkman-Grant relationship [141]. In using the weld performance factors the rupture ductilities of the heat affected zone and the weld metal are defined, which may be useful to compare with measured surface strains from the in-service component to judge remnant life.

The use of weld performance factors provides a simple design criterion with improved predictive capabilities over the British Standard codes and other homogeneous stress based approaches. The effects of primary and tertiary creep stress redistribution have been neglected and the effect of the multi-axial stress state on rupture have not been allowed for. These may be allowed for in future development and evaluation of weld performance factors.

The United States nuclear code N47 already allows for the presence of the weld and uses a stress based approach together with strain limits, which dictate the maximum allowable strains which may accumulate near the weld in-service. It is clear that the B.S. codes must be improved, at least, to take into account the material creep ductilities in the region of the weld with the use of strain limits.

Improvements to current design codes must allow for the stress redistribution in the region of the weld from soft to harder zones. Allowance for the effects of the stress redistribution during the primary, secondary and tertiary creep regions on the weld design and performace should also be incorporated. From the improvements in the life prediction of butt welded tubes reported by Browne et al [128] allowing for the multi-axial stress rupture characteristics of the heat affected zone, the effects of the multi-axial stress state on the rupture lives of each material zone in the weld must also be included in improved life calculations. Finally, though the behaviour of most of the ferritic weld materials is bi-linear in stress-rupture character (observed in the data of Cane [109]) and only the low stress-rupture line has been considered in the life predictions of parent and weldment materials, the inclusion of a bi-linear

representation (section 2.6) of stress-rupture behaviour will have an effect on life prediction accuracy and design, particularly for the high redistributed stress levels in the heat affected zone.

7.10 The Effect Of Residual Stresses On Weld Deformation.

Residual stresses are caused by the weld thermal cycle producing local expansion of the weld metal and parent metal, which is opposed by the material further away from the heat source (Fig.7.27(b) and (c)), resulting in the formation compressive stresses in the plate section. As the section cools the surrounding material resists the contraction of the weld material and the previously heated parent metal, and a tensile stress is set up in the weld, with the surrounding material in compression (Fig.7.27(d)). This simplified analysis is complicated by the effects of local changes in the modulus of elasticity, Poisson's ratio, the accumulation of plastic strains and phase transformations of the materials which may cause dilatation in steels. Phase transformations from (γ) to (α)-phase in steel where the structure changes from face centred cubic (F.C.C.) to body centre cubic (B.C.C.) can cause a dilatation of about 4% corresponding to a linear variation of 1.4% strain. Such phase transformation effects interact with temperature effects to produce the total residual stress pattern shown in Fig.7.28. Plastic strains and dilatation may cause distortion particularly in welded thick sections. Residual stresses in thick joints can equal the yield stress of the material dependent on the rigidity of the structure, but multipassing may significantly relieve such stresses.

Coleman and Parker [136] studied the creep deformation of welds made in heavy section 0.5Cr 0.5Mo 0.25V parent pipe using 2.25Cr 1Mo weld metal, which was tested in the as-welded or stress relieved condition, at pressures up to 455 bar at a constant temperature of $565°C$. The aim of the tests were to examine the effects of residual welding stresses on the creep behaviour of the pipe weldments. In these tests the variation of creep strain in the hoop and axial directions were measured across both as welded and stress relieved welds (Figs.7.29 and 7.30). Elastic displacements were the same for both as-welded and stress relieved welds. It is clearly seen that the creep deformation of the as-welded pipe is much faster than that of the stress relieved welds in both the hoop and axial directions.

In all tests performed the hoop and axial steady state creep rates were always greater in the as-welded pipe by up to a factor of four. The differences in the observed behaviour was reported not to be related to mechanical property differences, since uni-axial tests performed on both stress relieved and as-welded weld metals showed little difference in creep properties. The increased deformation rates were therefore directly attributed to residual welding stresses of the order of 10 to 20 MNm^{-2}. These welding stresses relieve during service at temperature, but may lead to low ductility failures due to cavitation damage early in the design life of the component.

7.11 Narrow Gap Welds.

Fidler [142,143] performed finite element analyses of narrow gap welds (Fig 7.1(c)) in ferritic pipe work using a two material weld model representing parent metal and weld metal properties [142] and a three material model [143], where the properties of the heat affected zone were included. The analysis is restricted to secondary creep. The results from the three material model suggests that narrow gap welds will have slightly shorter lives than comparable single vee-preparation welds, with failure initiating in the weld heat affected zone at the bore. The results from the two material model indicates that weld metal widths may significantly alter the life of the welded joint; though small variations in weld width over the practical narrow gap weld ranges of 8 to 12 mm produces only small differences in redistributed peak stresses and hence minimal variations in life. Fidler [143] also states that replacing 2.25Cr 1Mo weld metal by 0.5Cr 0.5Mo 0.25V weld metal, with similar properties to the parent metal does not significantly alter the stress redistribution and life of the joint. This is possibly due to the constraint on the narrow soft zone of 2.25Cr 1Mo weld metal by the stronger parent material, forcing it to deform at the lower creep rate of the parent pipe, as was observed in the Nicol model (section 7.9.1).

7.12 Concluding Remarks.

Failures of welded pipework operating at high temperatures under internal pressure have been shown to occur in microstructural regions associated with the weld. British design codes make no allowance for the presence of the weld, with the

design life of the component determined from parent metal uni-axial stress-rupture data. The life predictions have been shown to be conservative and inaccurate.

Many researchers have studied the deformation and failure of cross-weld specimens, although the problem exists of how to relate the results to the deformation and failure of welded pipes due to differences in the multi-axial stress states. Simple composite models under uni-axial tension containing hard and soft zones of material have been analysed theoretically and have highlighted the effects of stress redistribution from soft zones into harder zones. In such models the creep strain rate distributions are seen to vary smoothly from a high value in the soft zone to a lower value in a hard zone, having an intermediary compatible strain rate at the zone interface.

The uni-axial creep properties of the weld metal, parent metal and thermally simulated heat affected zone microstructures have been obtained successfully. This uni-axial creep data has been used in primary and secondary creep finite element weld models in both plane strain and axisymmetric analyses to represent creep deformations of plates and circular cross-welds or steam pipes respectively. The finite element results show reasonably good agreement with the creep strain measurements from experimental specimens and full size pipe welds. Both experimental and finite element results for the surface hoop strains across the various material zones of pipe weldments show that the hoop creep strain rate remains approximately compatible with that of the parent metal for a range of weld metals. This result also suggests that significant stress redistribution occurs from softer, faster creeping material, to harder heat affected zone, slower creeping material, to maintain this compatibility of the hoop strain rate across the various material zones.

It has been shown that creep strain rate measurements made on the surface of pipes in-service can give the surface stresses from which life estimates can be made, using uni-axial stress-rupture data for the material zone where the measurements were made. Failure predictions have also been made using the stationary state surface stresses from finite element weld models, giving reasonable but still conservative predictions. Better predictions are obtained when the effects of the multi-axial stress state on rupture are allowed for using a multi-axial stress rupture criterion through a representative rupture stress which is applied to uni-axial stress rupture data.

As a result of the complexity of the interactions of the material zones within

the weld and the way in which they off-load stress, enabling various failure modes to occur, advancements in our understanding of the behaviour of weldments has relied heavily on the results of weld models. Due to the problems of relating inexpensive cross-weld specimen tests to real components, expensive full size welded components have to be tested. Therefore the use of uni-axial creep data within the finite element method becomes an attractive alternative. With the new demands for remnant life prediction together with the requirements for safe designs by the nuclear power industry, component deformation and failure predictions at the design stage must be improved. This can be achieved in one of two ways: either by the use of simplified weld performance factors developed from the results of finite element parametric studies, or through actual finite element analyses performed for the actual component design geometry. Both these alternatives rely on finite element model predictions, which have to be accurately verified by experimental test data before they will be accepted, which may take many years of development. Certainly there is now enough data available to include creep strain limits (section 7.9.4) within the British Standard codes to bring them into line with the American N47 code.

To be able to use the finite element technique as a research and/or design tool to develop new design methodologies for welds requires a full primary, secondary and tertiary creep analysis of a weld model containing at least three material zones. Incorporating a full bi-linear material representation of stress-rupture behaviour and a multi-axial stress rupture criterion for each weld zone material. A continuum damage mechanics finite element solution will predict damage distributions showing where failure initiates in the weldment and will also show how the weldment cracks grow until final failure ensues at a rupture time given by the program. The development of a weld model along these lines will be studied by the author in the next chapter.

Weld Metal	Internal Pressure MPa	Observed Rupture Life h.	Life Prediction, h						Maximum Rupture Stress HAZ	Maximum Principal Stress HAZ
			Maximum Equivalent Stress			Mean Diameter Hoop Stress				
			Weld Metal	HAZ	Parent	σ_{mdh}	$1.25\,\sigma_{mdh}$	$1.5\,\sigma_{mdh}$		
Mild Steel	45.3	14,691	23,000	5,000	40,000	31,000	5,200	1,500	8,000	17,000
1CrMo	45.3	18,774	50,000	14,000	40,000	31,000	5,200	1,500	17,000	28,000
2¼CrMo	45.3	22,039	50,000	18,000	40,000	31,000	5,200	1,500	18,000	26,000
¼CrMoV	45.3	43,871	40,000	21,000	40,000	31,000	5,2001	1,500	24,000	24,000
Mild Steel	51.5	7,752	18,000	2,000	18,000	11,000	1,900	300	3,500	10,000
1CrMo	51.5	7,712	36,000	7,500	18,000	11,000	1,900	300	11,000	13,000
2¼CrMo	51.5	9,285	28,000	10,000	18,000	11,000	1,900	300	12,500	15,000
¼CrMoV	51.5	16,511	18,000	12,000	18,000	11,000	1,900	300	14,500	18,000

Column No.	1	2	3	4	5	6	7	–	8	9	10

Table 7.1: Comparisons of experimental rupture lifes with those predicted, using uni-axial stress-rupture data with various stress criteria, after Browne et al [128].

Weld metal	*Experimental measurements*					*Calculated stresses*		
	Uniaxial creep constants		*Pressure vessel strain rates* $\times 10^{-8}\ h^{-1}$		$\dot{\varepsilon}_H/\dot{\varepsilon}_A$	σ_H/σ_A	σ_H (MNm^{-2})	σ_A (MNm^{-2})
	A	*n*	*Hoop*	*Axial*				
Mild steel	$5{\cdot}4 \times 10^{-12}$	4	6	70	0·086	0·60	14·1	23·5
1CrMo	$4{\cdot}5 \times 10^{-14}$	4	8	5	1·60	1·17	44·2	37·8
2CrMo	$1{\cdot}6 \times 10^{-14}$	4	5	4	1·25	1·08	49·0	45·4
¼CrMoV	$3{\cdot}2 \times 10^{-15}$	4	8	0	—	2	95·0	47·5

Table 7.2: Measured steady state strain rates,calculated stress ratios and stresses, at the weld center line on the outer surface of four pipe welds, in a 0.5Cr 0.5Mo 0.25V thick pipe, after Coleman et al [131].

		Weld metal				*HAZ*	*Parent material*		
Position		A	B	C	D	E	F	G	H
Distance from weld centreline (mm)		0–10	14·5	18	22	28	53	140	235
'A' ratios (WM:PM:HAZ) and direction:									
1:1:0·25	Hoop	11	11	11	11	11	11	11	12
	Axial	−1	−1	−1	−1		−1	0	0
3:1:0·25	Hoop	12	12	12	12	13	12	12	12
	Axial	2	2	2	3		0·7	0	0
10:1:0·25	Hoop	13	14	14	14	14	13	12	12
	Axial	5	6	8	9		3	0	−1
15:1:0·25	Hoop	14	14	14	14	15	14	12	12
	Axial	7	9	11	13		4	−1	−1
1690:1:0·25	Hoop	12	13	16	22	37	31	19	17
	Axial	58	61	190	340		100	−6	−1

All creep rates $\times 10^{-8}\,h^{-1}$, with constant $n = 4$.

Table 7.3: Hoop and axial steady state creep rates at the pipe surface positions shown in Fig.7.25 calculated in the finite element analysis of Coleman et al [131], for various creep rate ratios of WM:PM:HAZ.

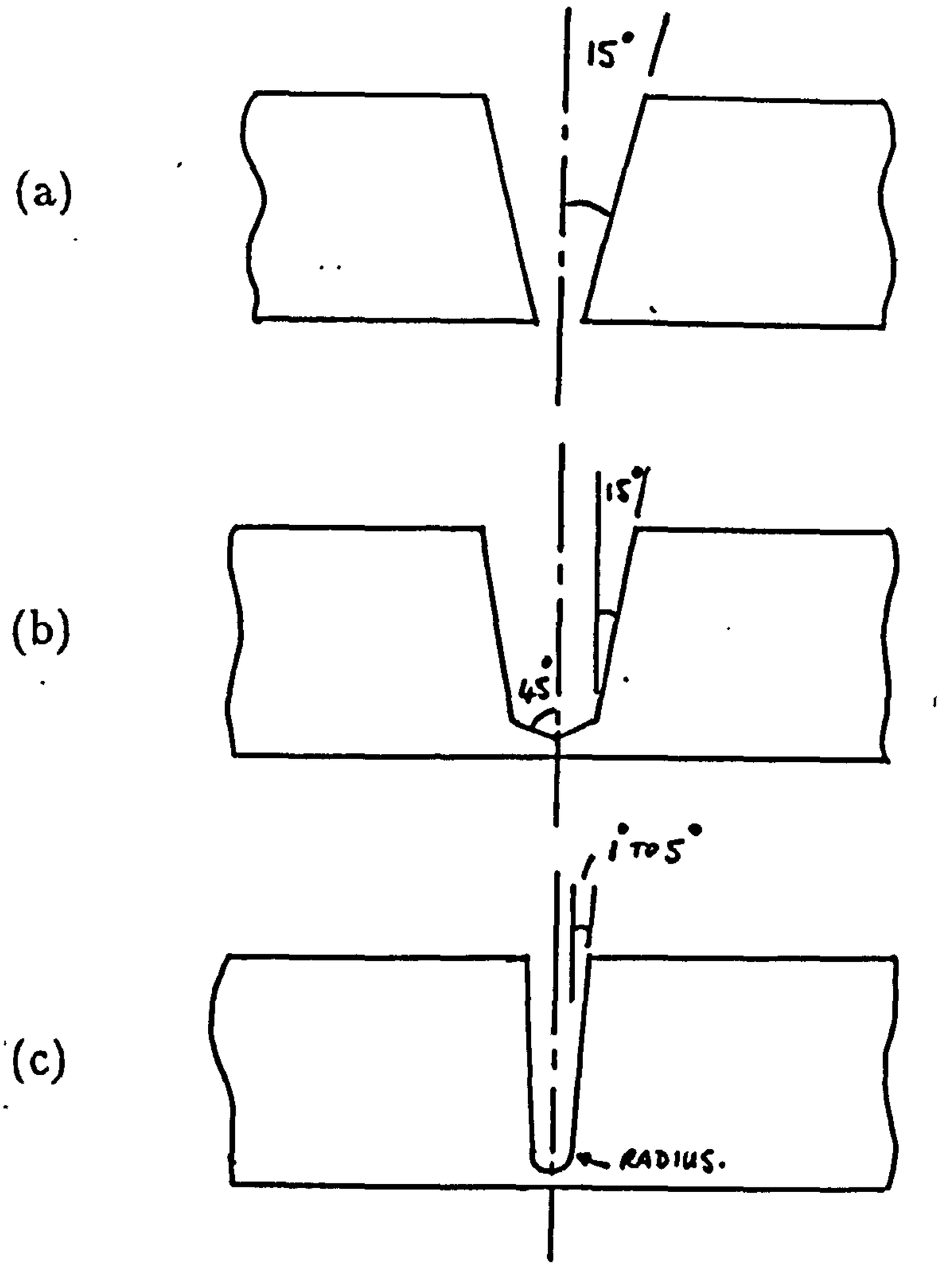

Figure 7.1: cross-sections of commonly used weld preparations in plates to be joined.
(a) General Vee-Preparation.
(b) J-type Thick-Plate Preparation.
(c) Narrow Gap Technique Preparation.

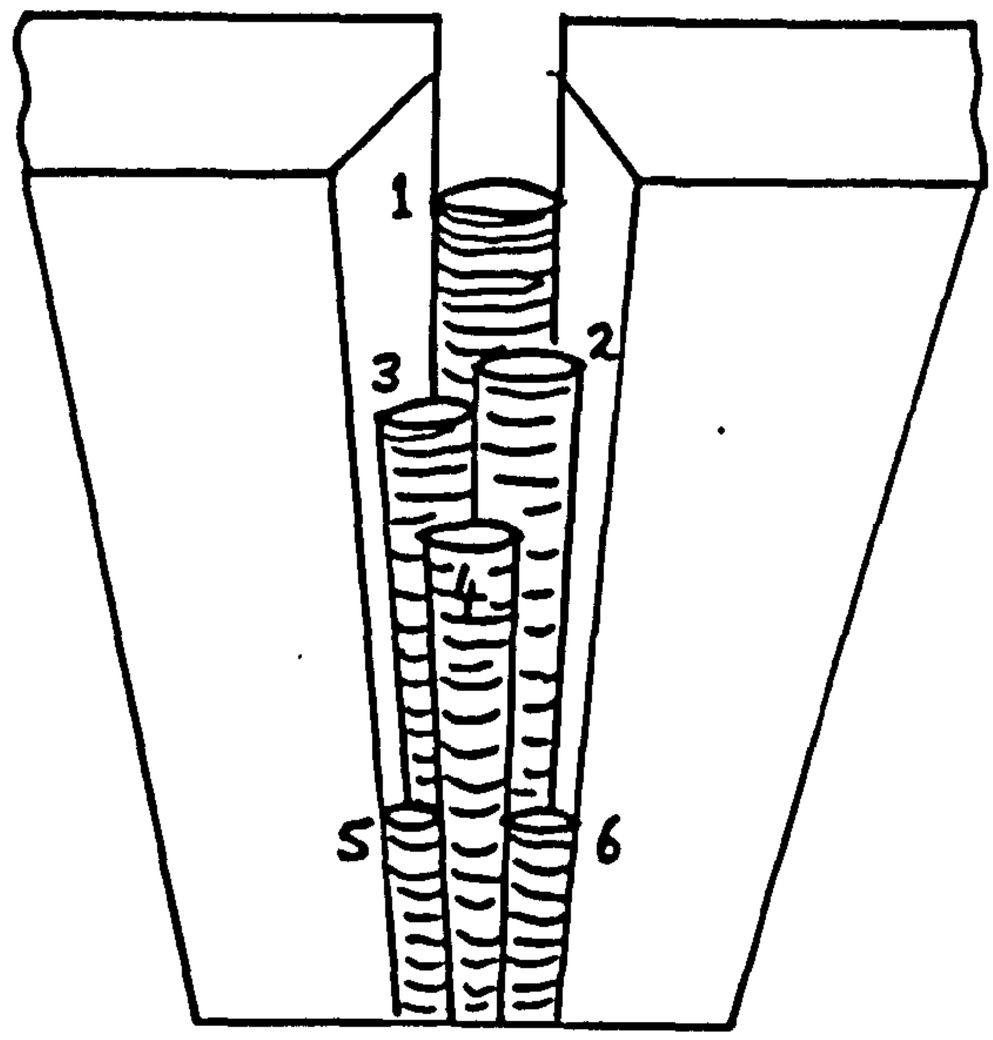

Figure 7.2: Ideal weld filler geometry, showing multipass welding. The first weld bead to be layed is No.1 and the last is No.6.

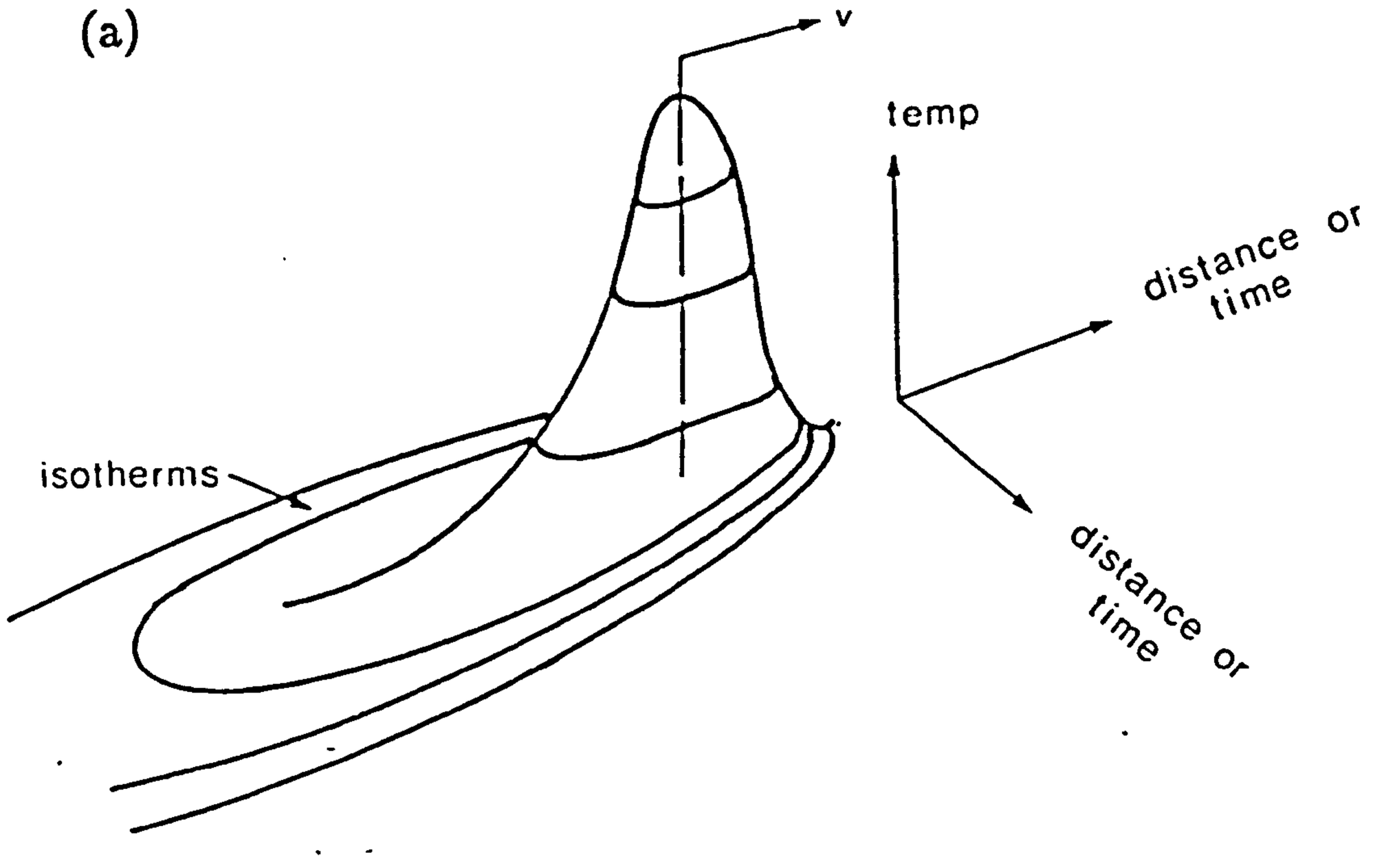

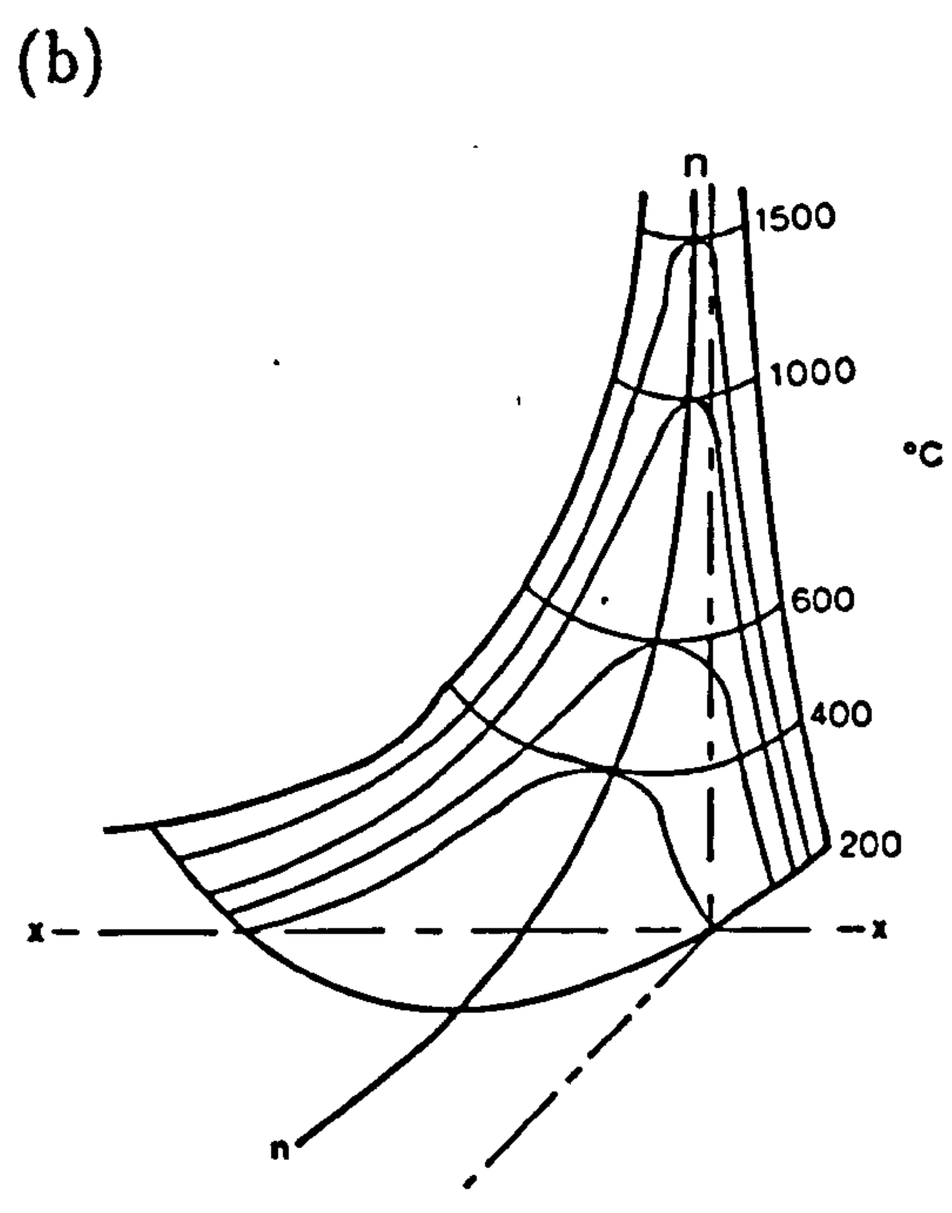

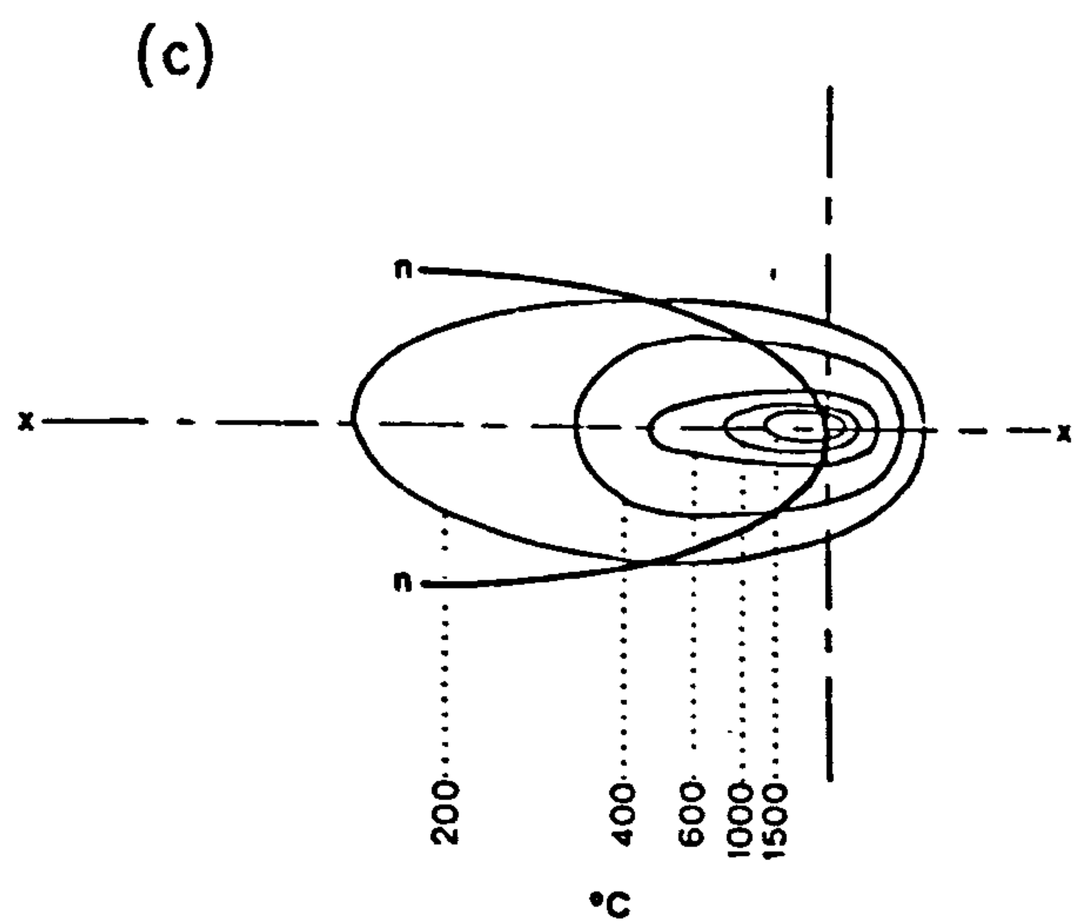

Figure 7.3: Calculated 3D temperature distributions in thick plate mild steel produced by a point heat source, after Rosenthal [99] and [100]. (c) shows a plan section of the isotherms in (b).

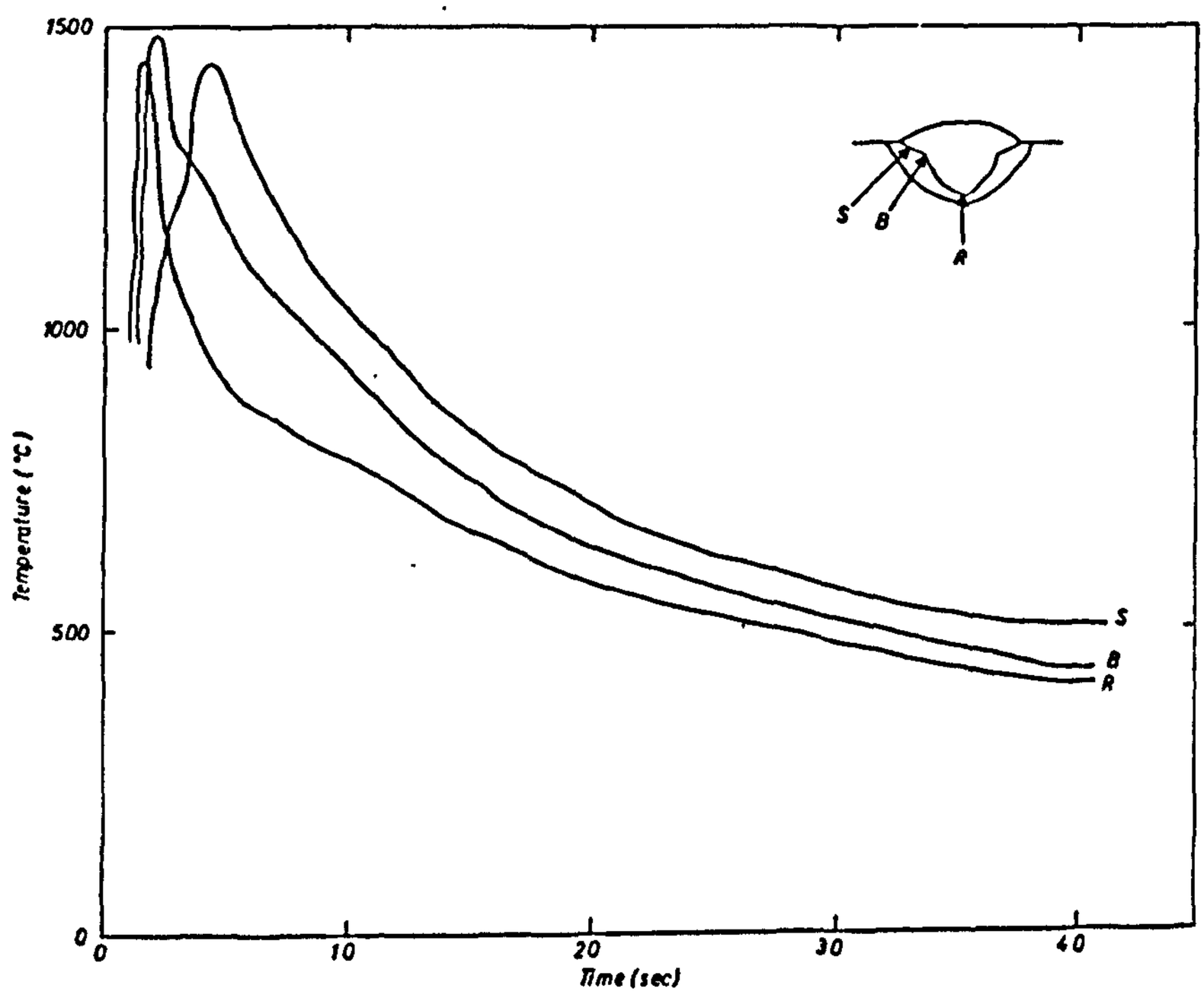

Figure 7.4: Experimentally measured weld thermal cycle at various points in a steel weld preparation after Kohno and Jones [101].

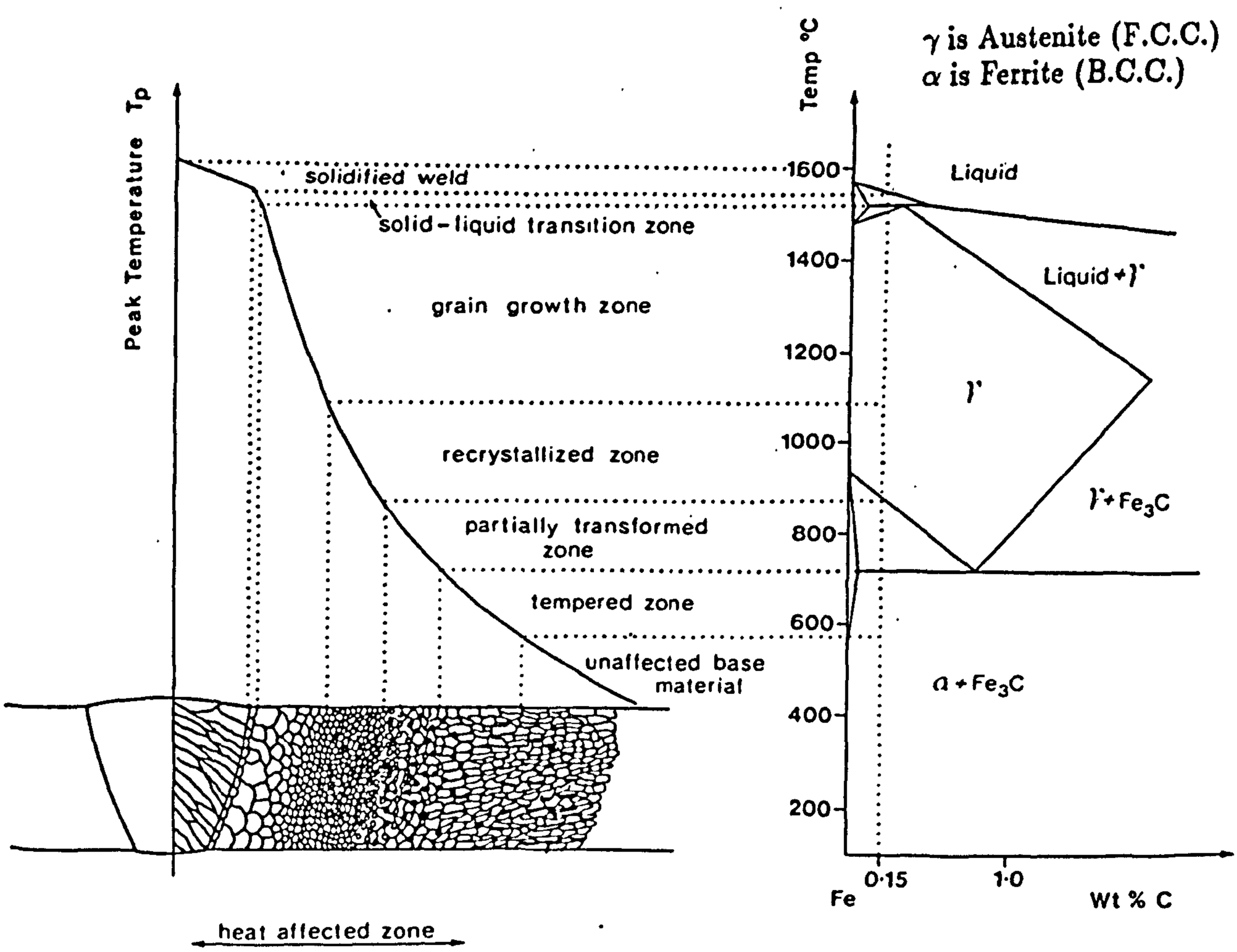

Figure 7.5: Schematic diagram showing the microstructural regions of the a weld in a 0.15% Carbon steel, caused by the weld thermal cycle peak temperatures reached in each zone and the phase transformation characteristics of the material, [144].

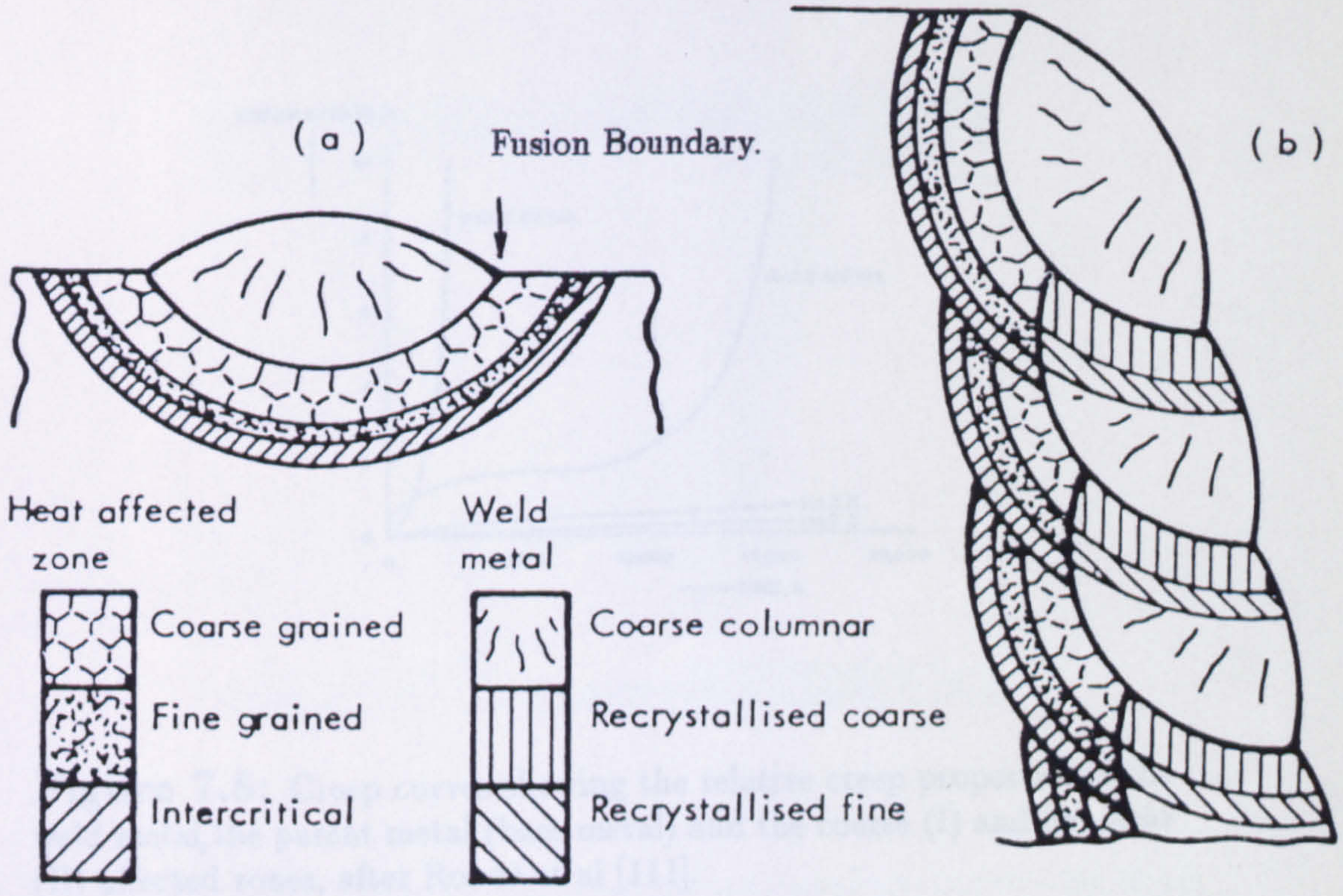

Figure 7.6: A simplified representation of the microstructures in a ferritic (a) weld bead and (b) a multipass weld, after Colman [96].

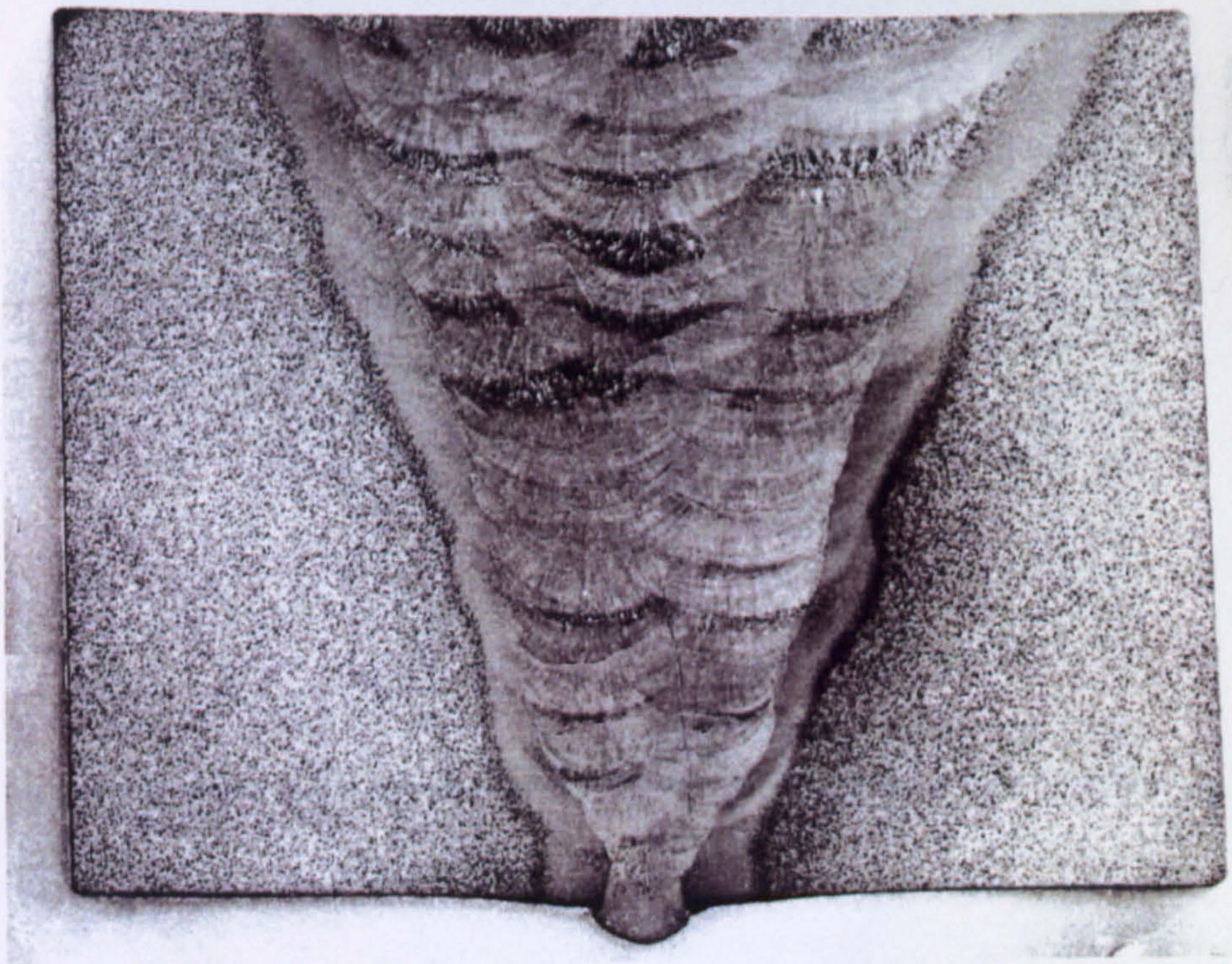

Figure 7.7: Micrograph of a section taken through a 1Cr 1Mo:0.5Cr 0.5Mo 0.25 V multipass weld, the heat affected zone regions and the weld metal recrystalised coarse and fine grained regions can be identified with reference to Fig.7.6. Micrograph courtesy of Coleman [96].

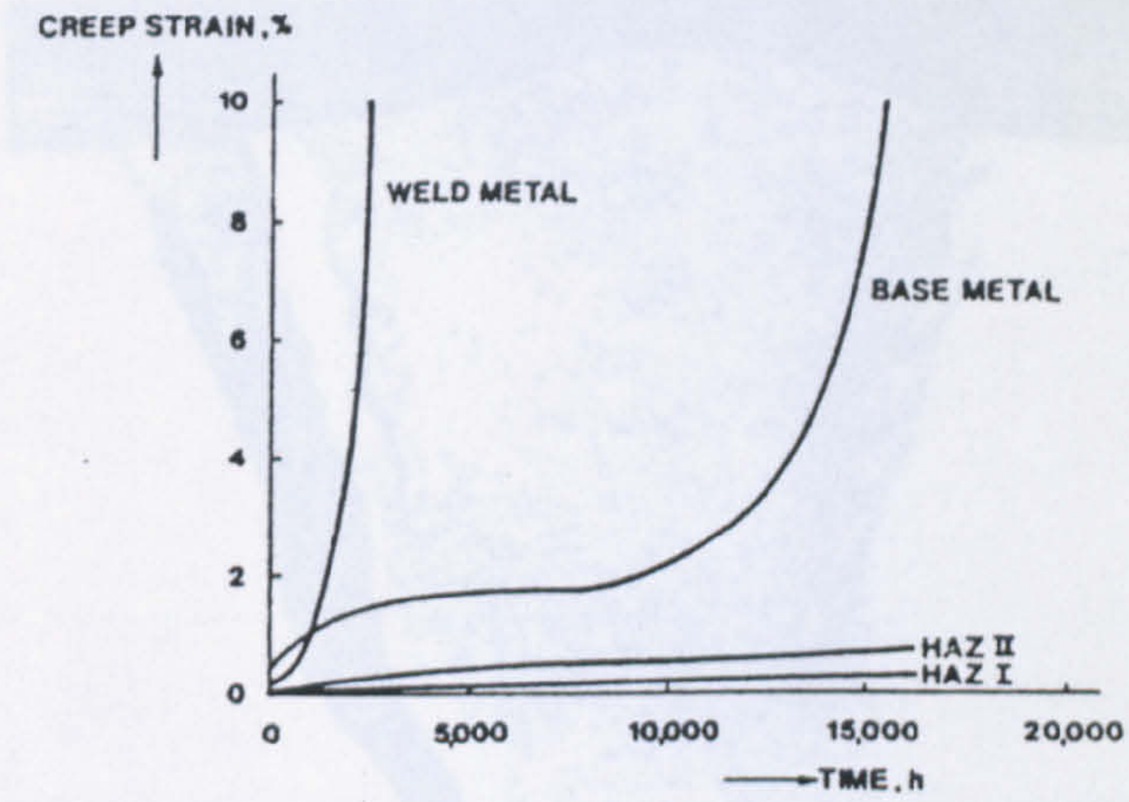

Figure 7.8: Creep curves showing the relative creep properties of the weld metal, the parent metal (base metal) and the coarse (I) and fine heat (II) affected zones, after Roode et al [111].

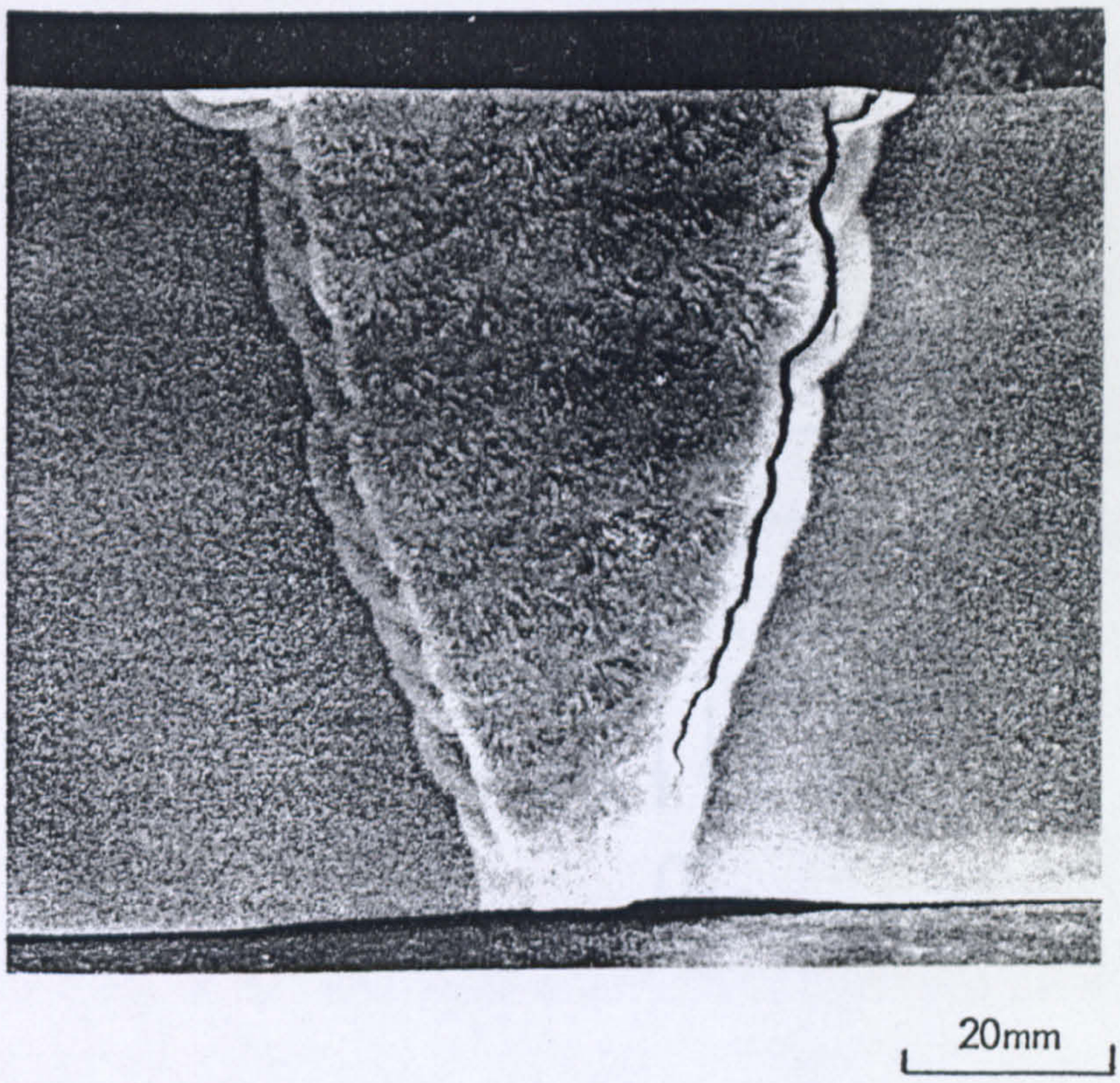

Figure 7.9: Circumferential coarse heat affected zone cracking in a ferritic steel weldment after Coleman [96].

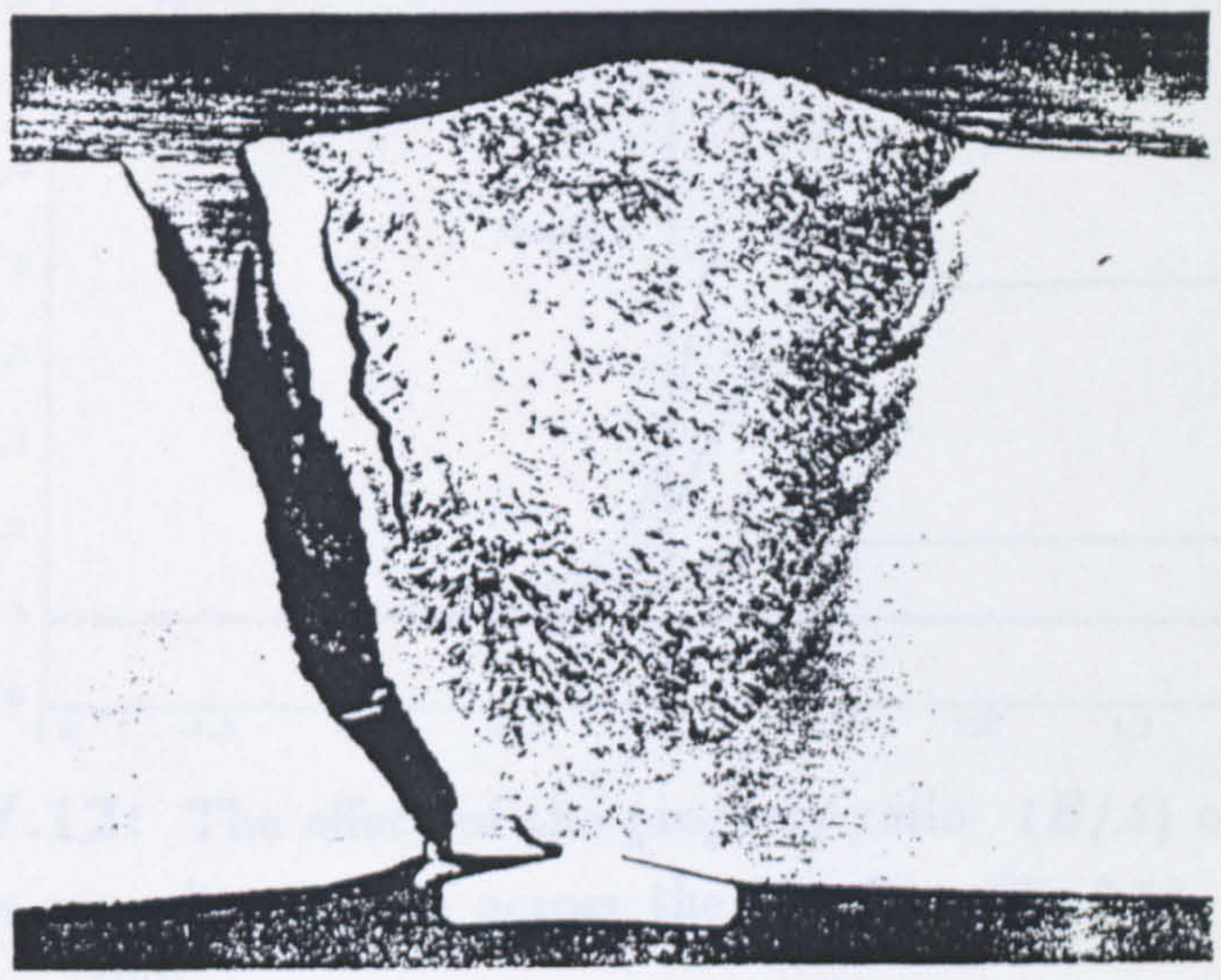

Figure 7.10: Type IV cracking and associated circumferential cracking in the coarse grained region of the heat affected zone, after Yeldman et al [145].

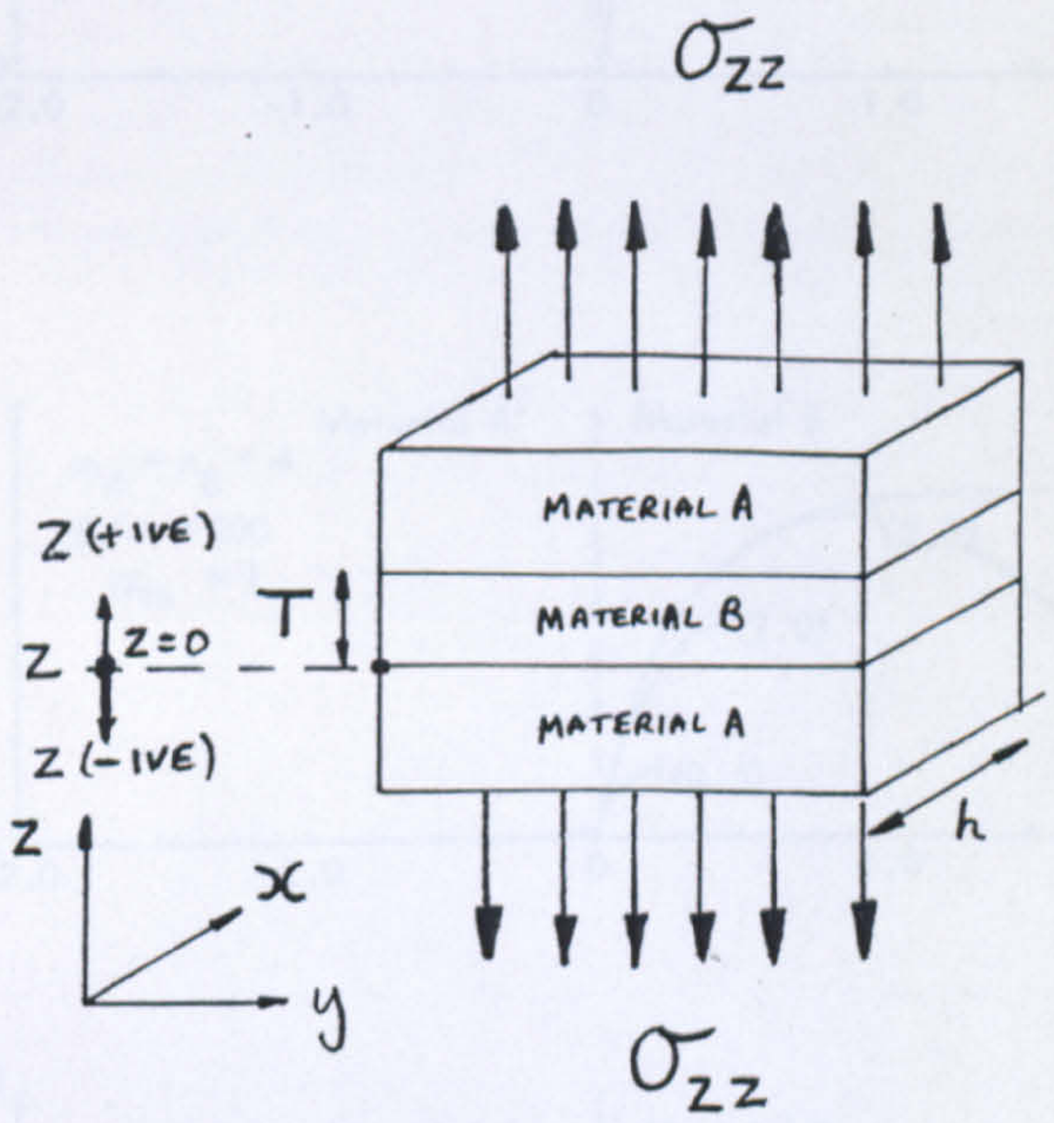

Figure.7.11: Schematic diagram of the Nicol composite plate model [121]. The plane strain direction is coincident with the y-axis.

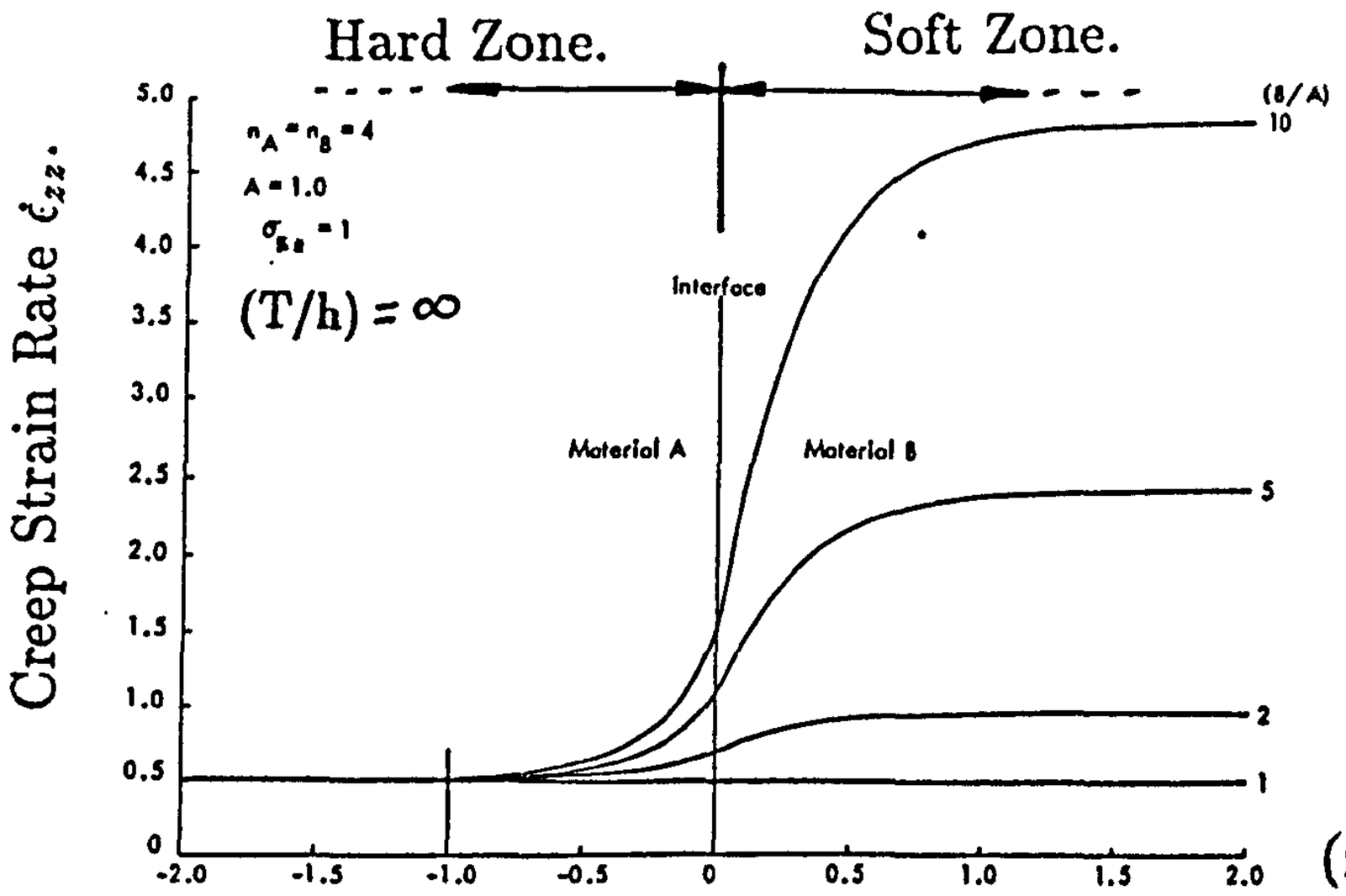

Figure 7.12: The effect of the property ratio (B/A) on the axial creep strain rate distribution across the interface, Fig.7.11, after Nicol and Williams [122].

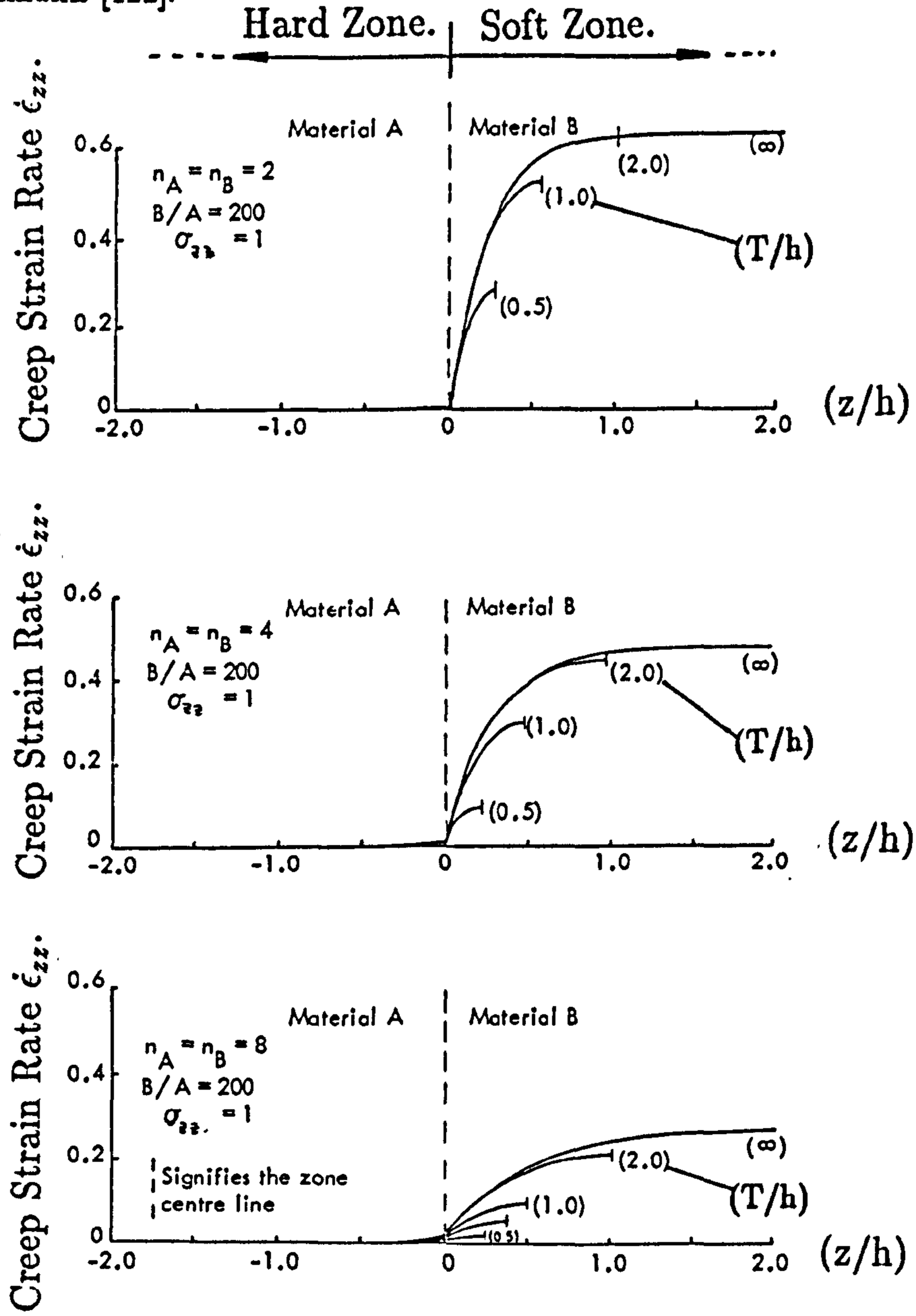

Figure 7.13: The effect of the creep rate index (n) on the axial creep strain rate distribution for a soft zone (material B in Fig.7.11) composite, after Nicol and Williams [122].

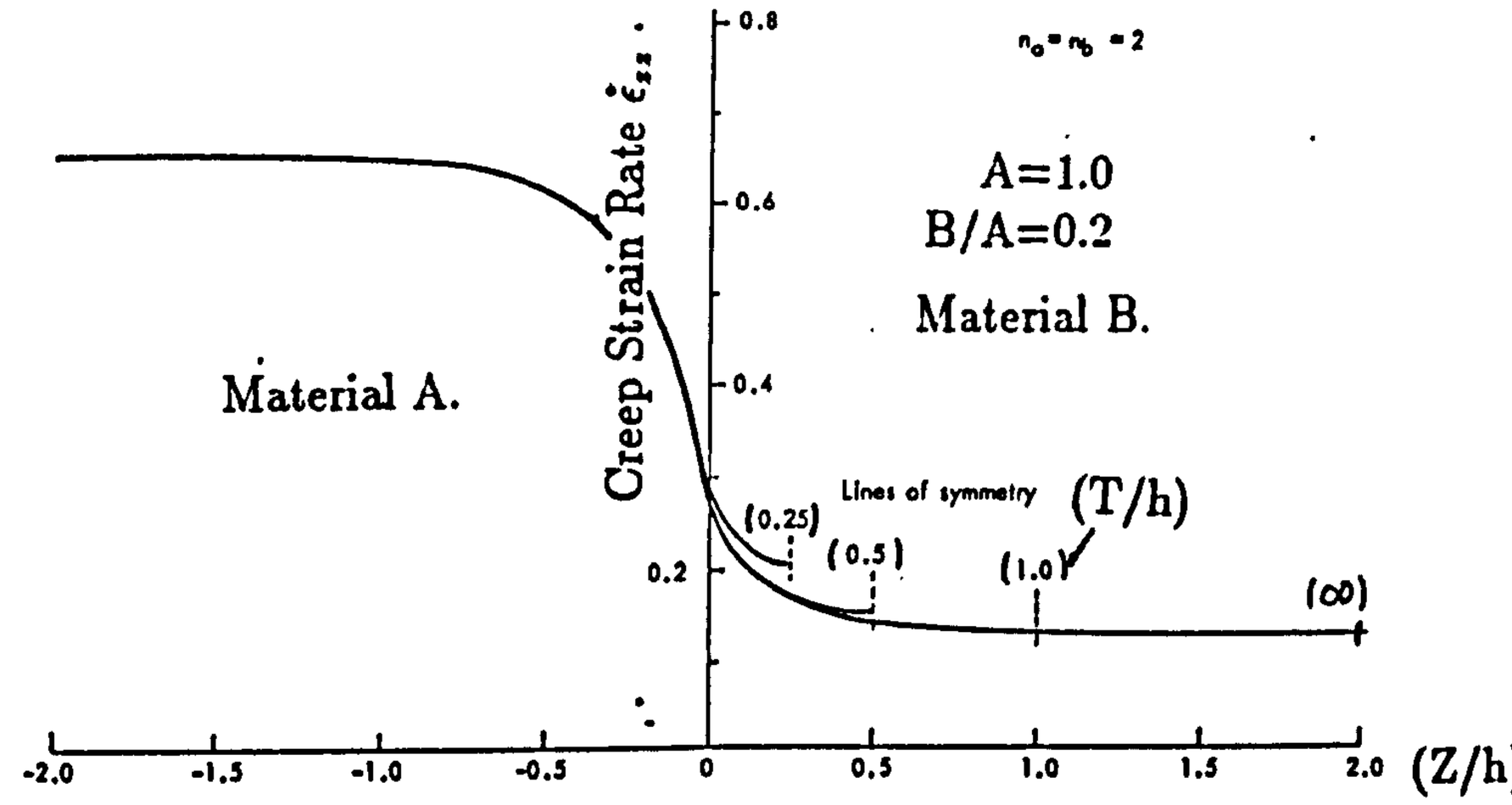

Figure 7.14(a): Axial creep strain rate distibutions across an interface, for a hard central zone (material B in Fig.7.11) composite, after Nicol [121].

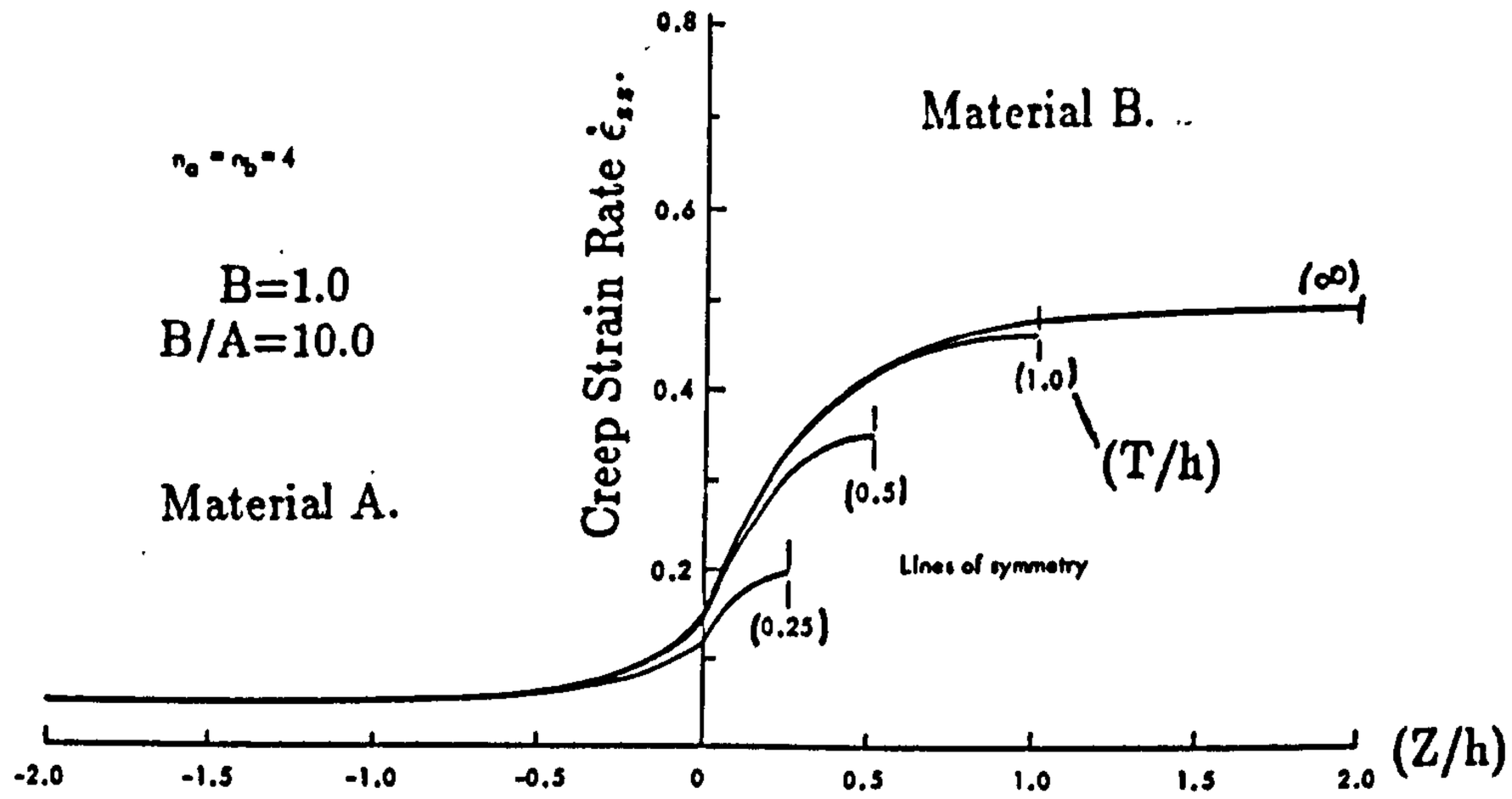

Figure 7.14(b): Axial creep strain rate distibutions across an interface, for a soft central zone (material B in Fig.7.11) composite, after Nicol [121].

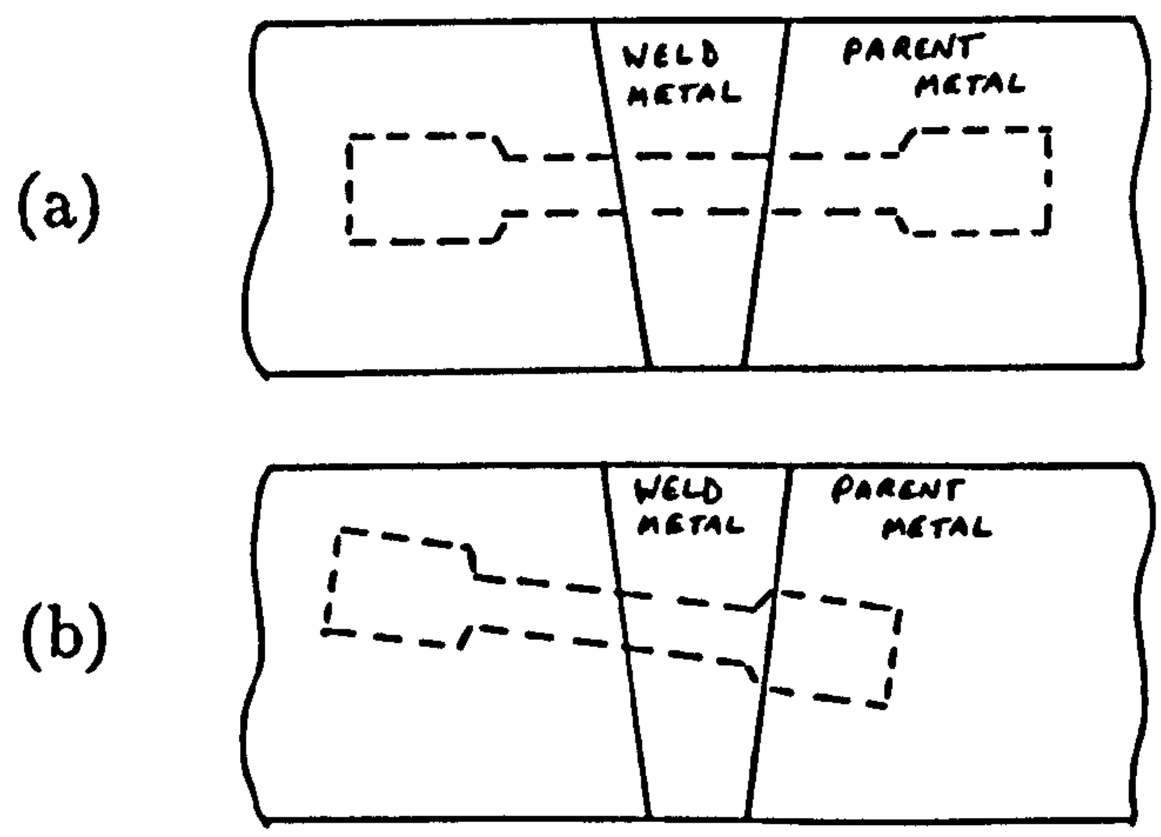

Figure 7.15: Diagram showing how specimens are cut from welded components to form (a) a standard cross-weld specimen and (b) a 45° fusion boundary cross-weld specimen.

(a) The axisymmetric finite element mesh used to model this weld specimen.

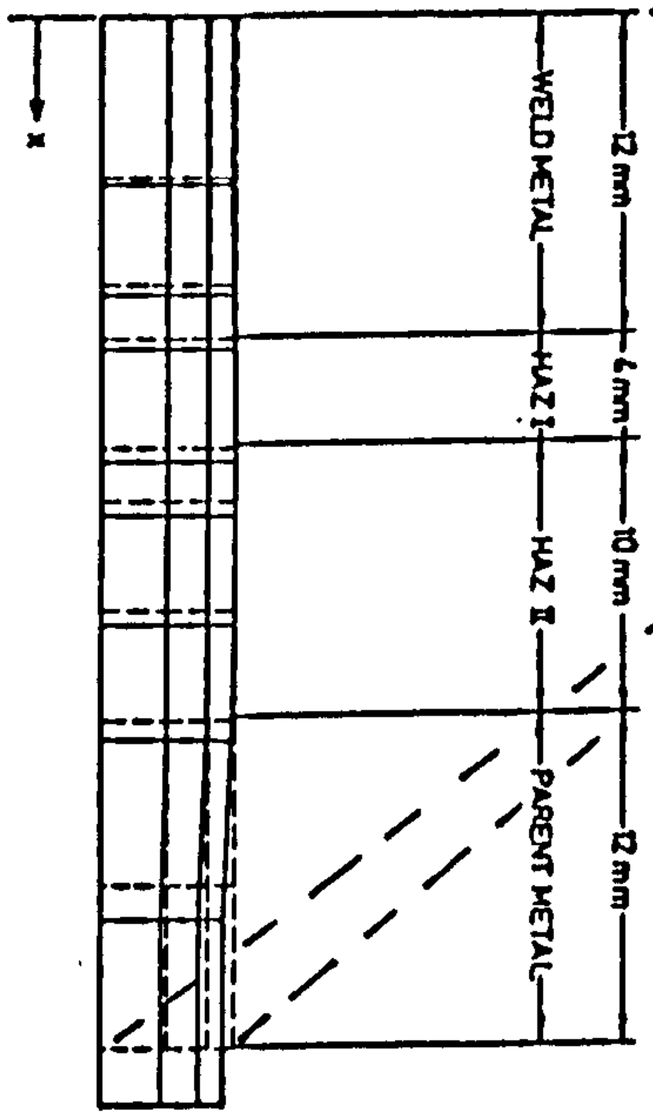

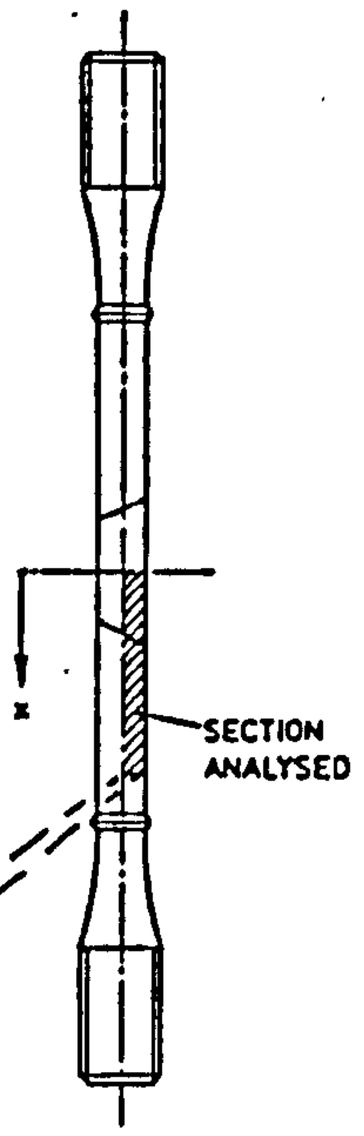

(b) AISI 316 cross-weld specimen, diamenter 10mm.

(d) AISI 316 thick plate containing a weld under uni-axial tension.

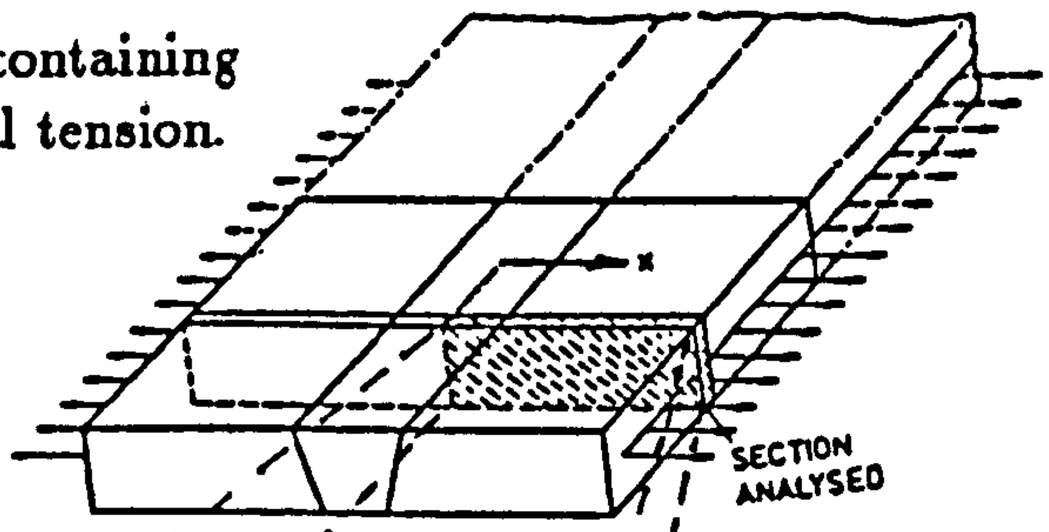

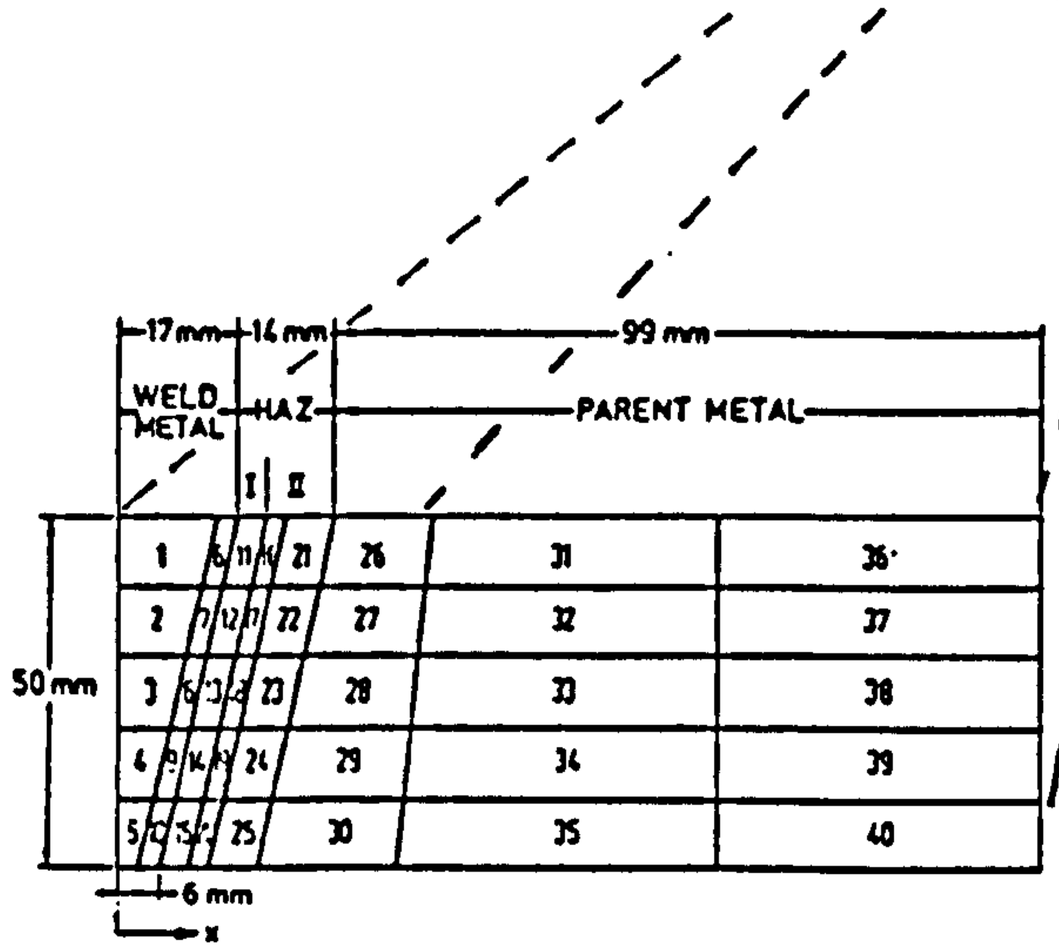

(c) Plain strain finite element mesh used to analyse the thick plate weld in (d).

Figure7.16: AISI 316 specimens analysed by Roode et al [111].

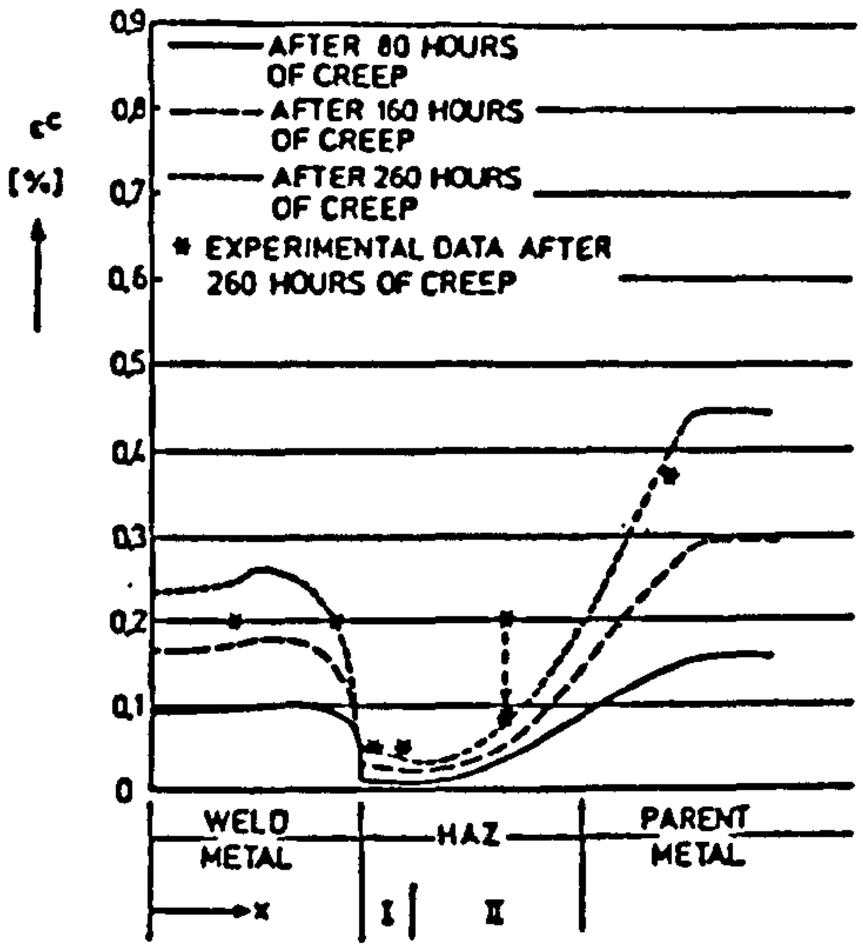

(a) Predicted longitudinal creep strain along the cross-weld center line (i.e. in the x-direction Fig.7.16 (a),(b)), at various creep times.

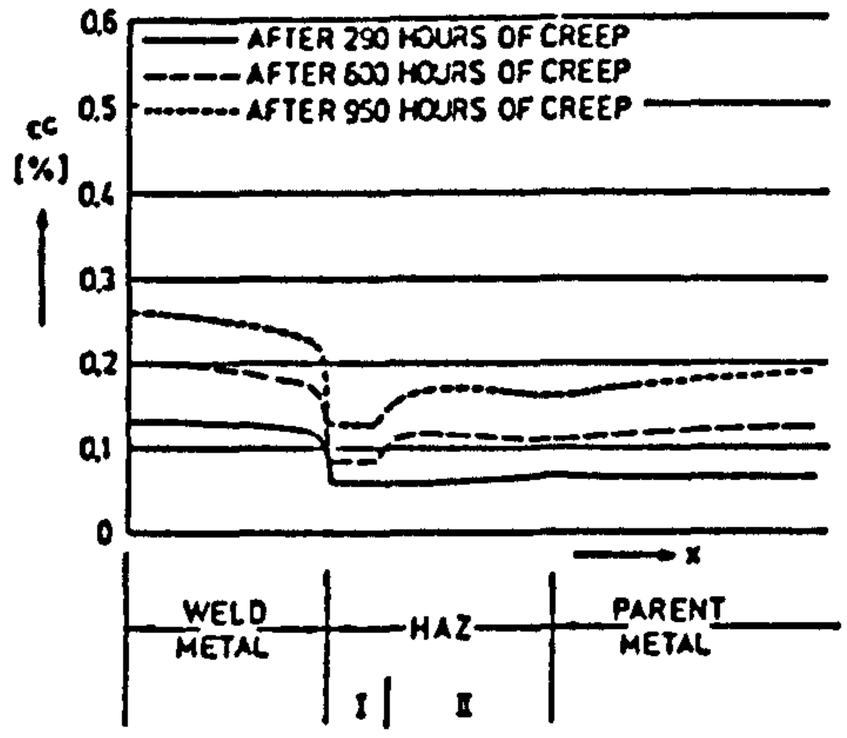

(b) Predicted logitudinal creep strain along the weld plate near the center line of the analysed section (Fig.7.16 (c),(d)), at various creep times.

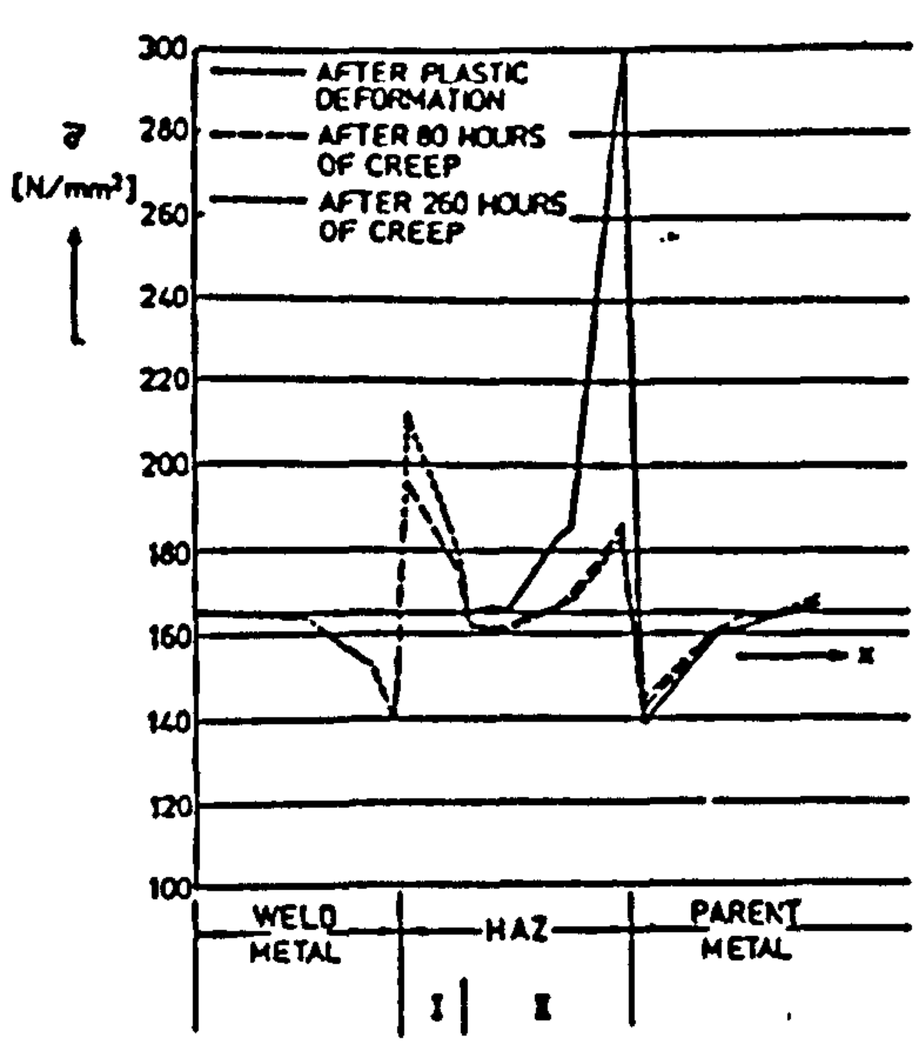

(c) Von-Mises equivalent stress along the outer surface of the cross-weld center line at various creep times.

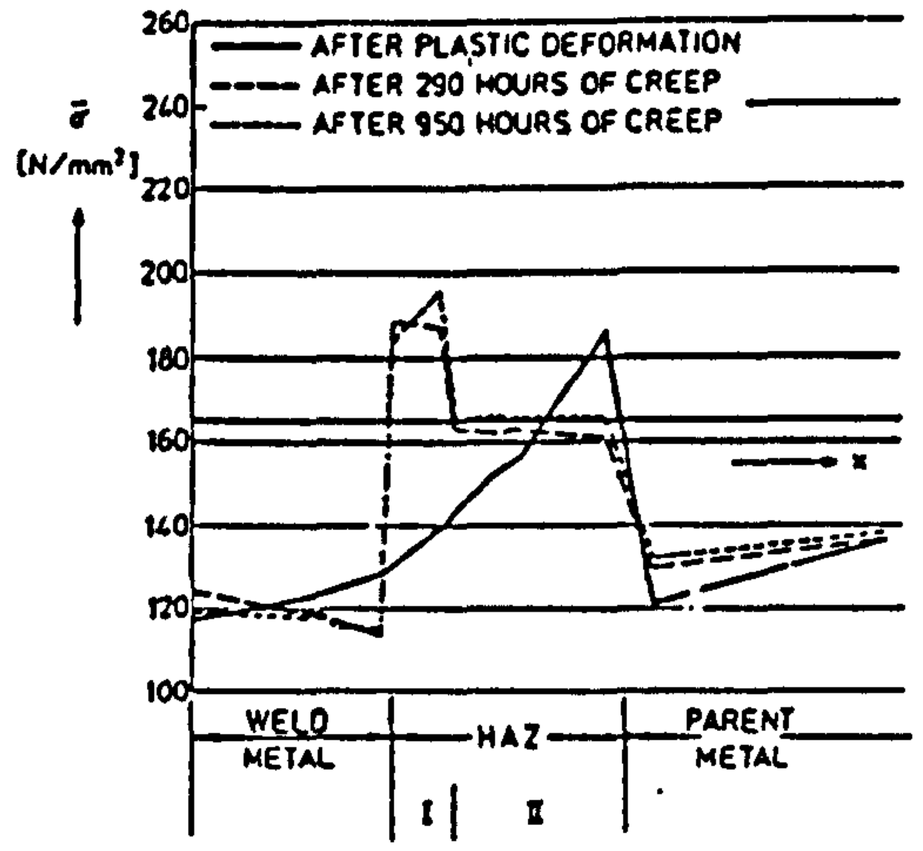

(d) Von-Mises equivalent stress along the outer surface of the plate weld near the center of the analysed section at various creep times.

Figure 7.17: Experimental and finite element predictions for the AISI 316 cross-weld and welded thick plate of Figs.7.16 after Roode et al [111].

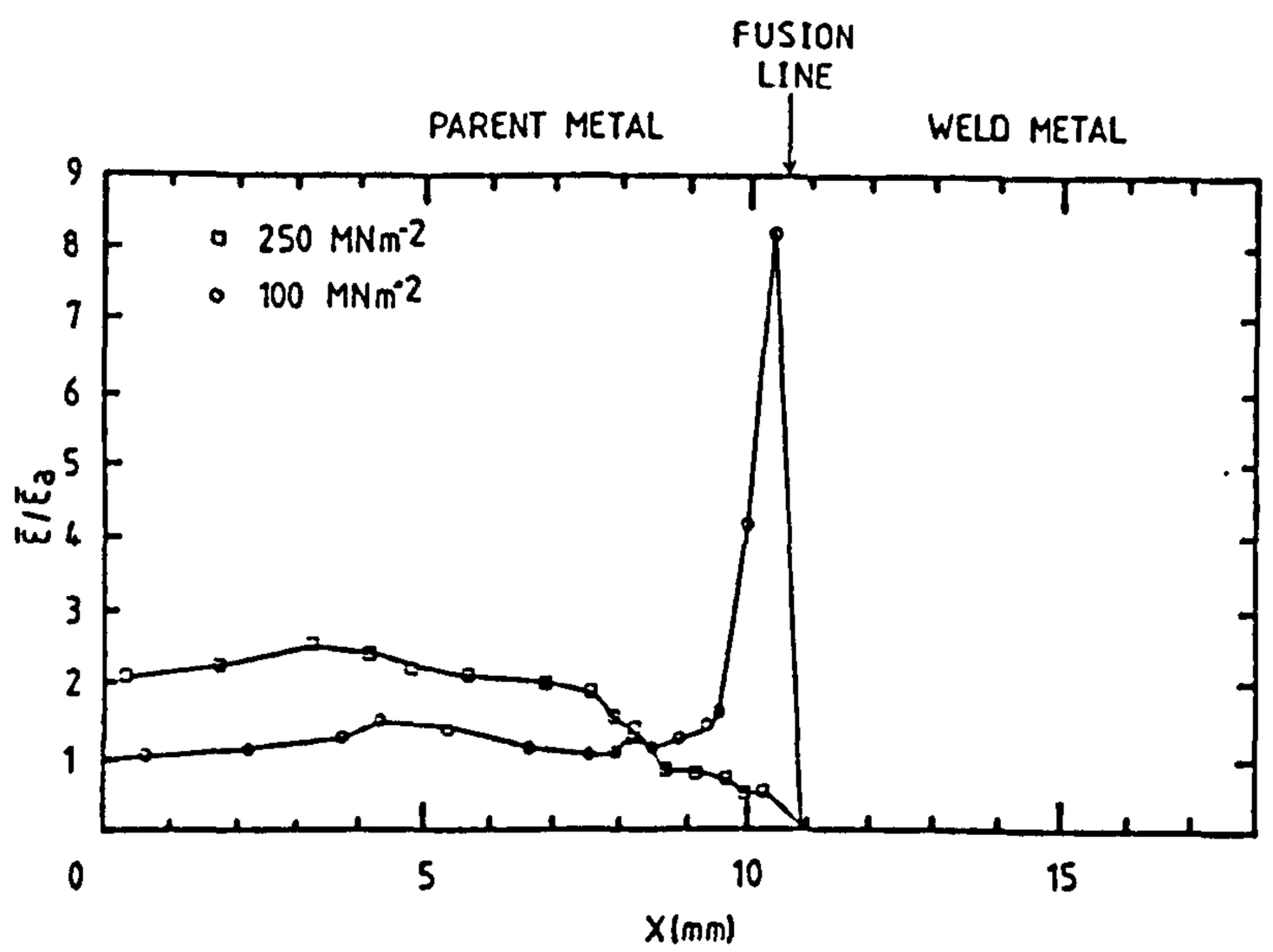

Figure 7.18: Ratio of the average effective strain ($\bar{\epsilon}$) to the overall average strain ($\bar{\epsilon}_a$) as a function of distance (x) along the gauge length of a transition weld, (cross-welded), test piece from an axisymmetric finite element analysis for two specimen test stress levels, after Evans and Wiltshire [117].

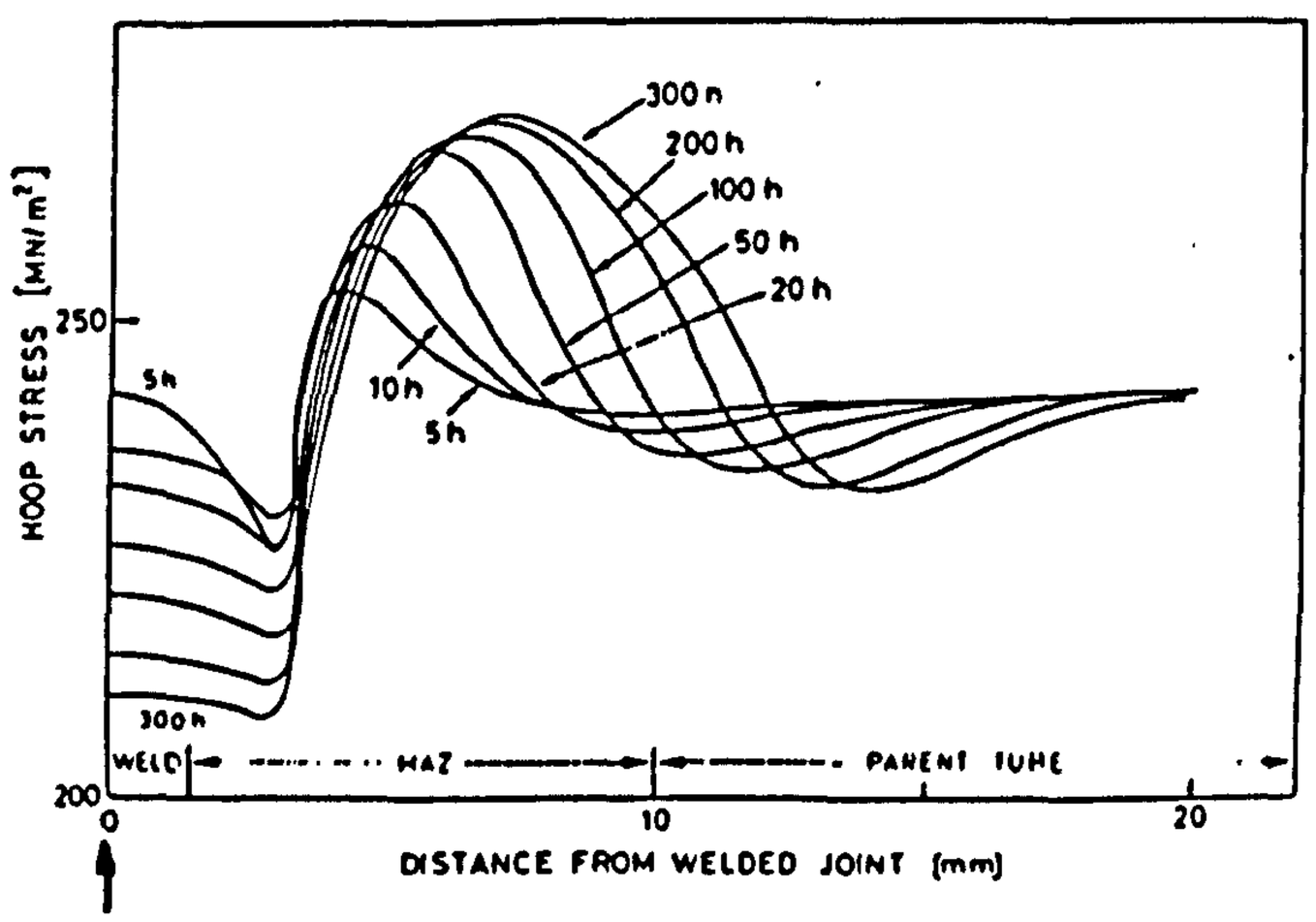

Figure 7.19: Hoop stress distributions at various times across the surface of a stainless steel circumferential pipe weld, from a finite difference analysis, after Ivarson and Sandstrom [127].

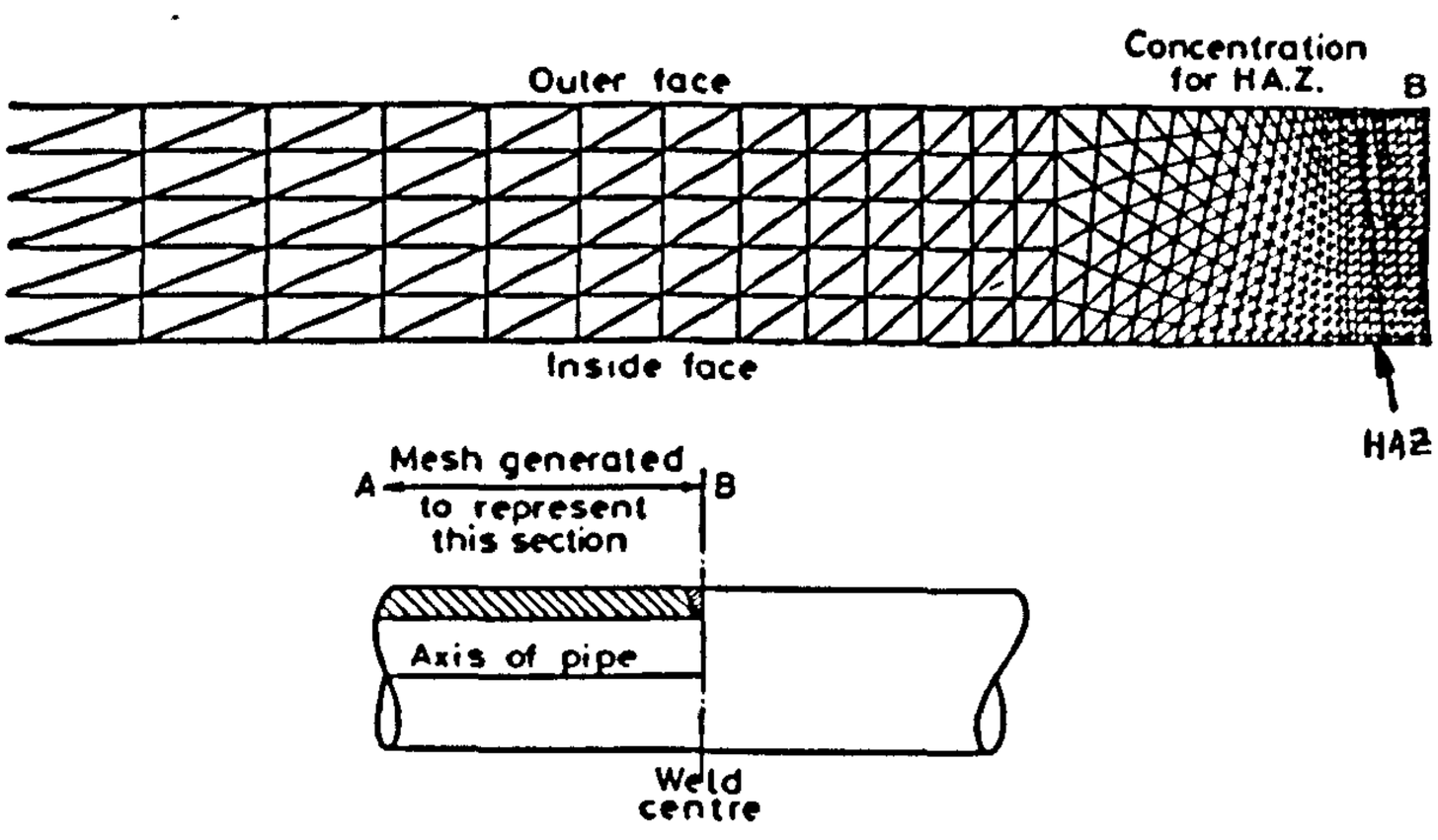

Figure7.20: The three material finite element weld model of a circumferential thick pipe weld, after Browne et al [128]

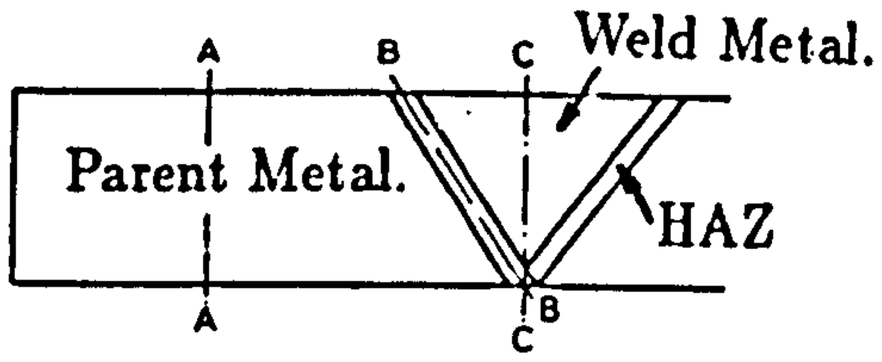

Figure 7.21: Lines BC, BB and CC across an axial section through the weld model (Fig.7.20) pipe wall along which the stress distributions of Fig.7.22 are obtained.

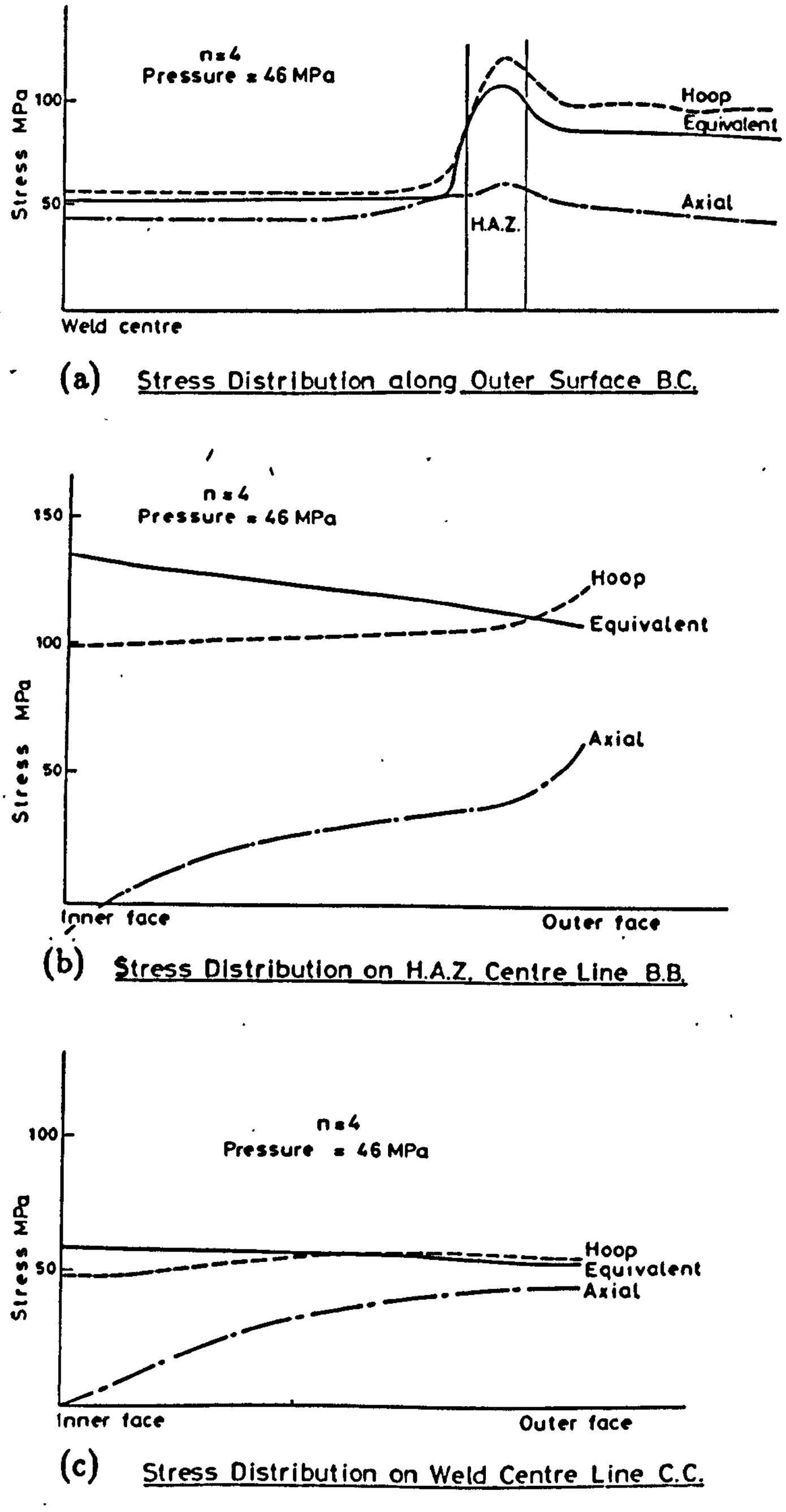

Figure 7.22: Predicted Steady state stress distributions along the lines across the weld model section given in Fig.7.21, after Browne et al [128].

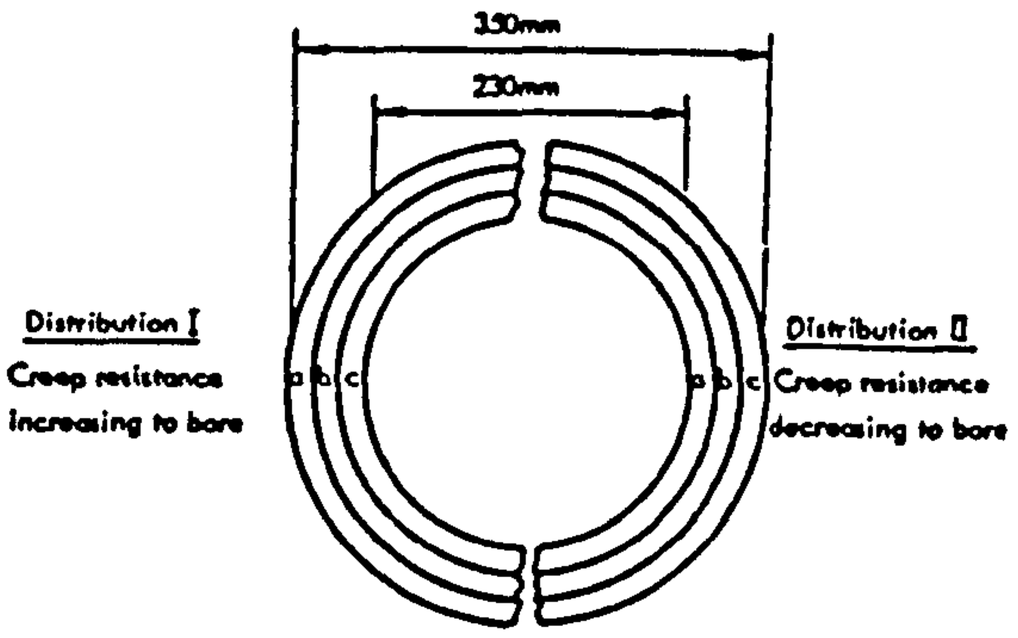

Material	Creep Constants	
	A	n
a	7.4×10^{-19}	6.0
b	2.4×10^{-19}	6.0
c	7.4×10^{-20}	6.0
a	2.4×10^{-11}	2.1
b	8×10^{-12}	2.1
c	2.4×10^{-12}	2.1

Figure 7.23: Three concentric cylinder composite model used to model the through thickness inhomogeneity of material properties in the parent pipe, by Coleman et al [129].

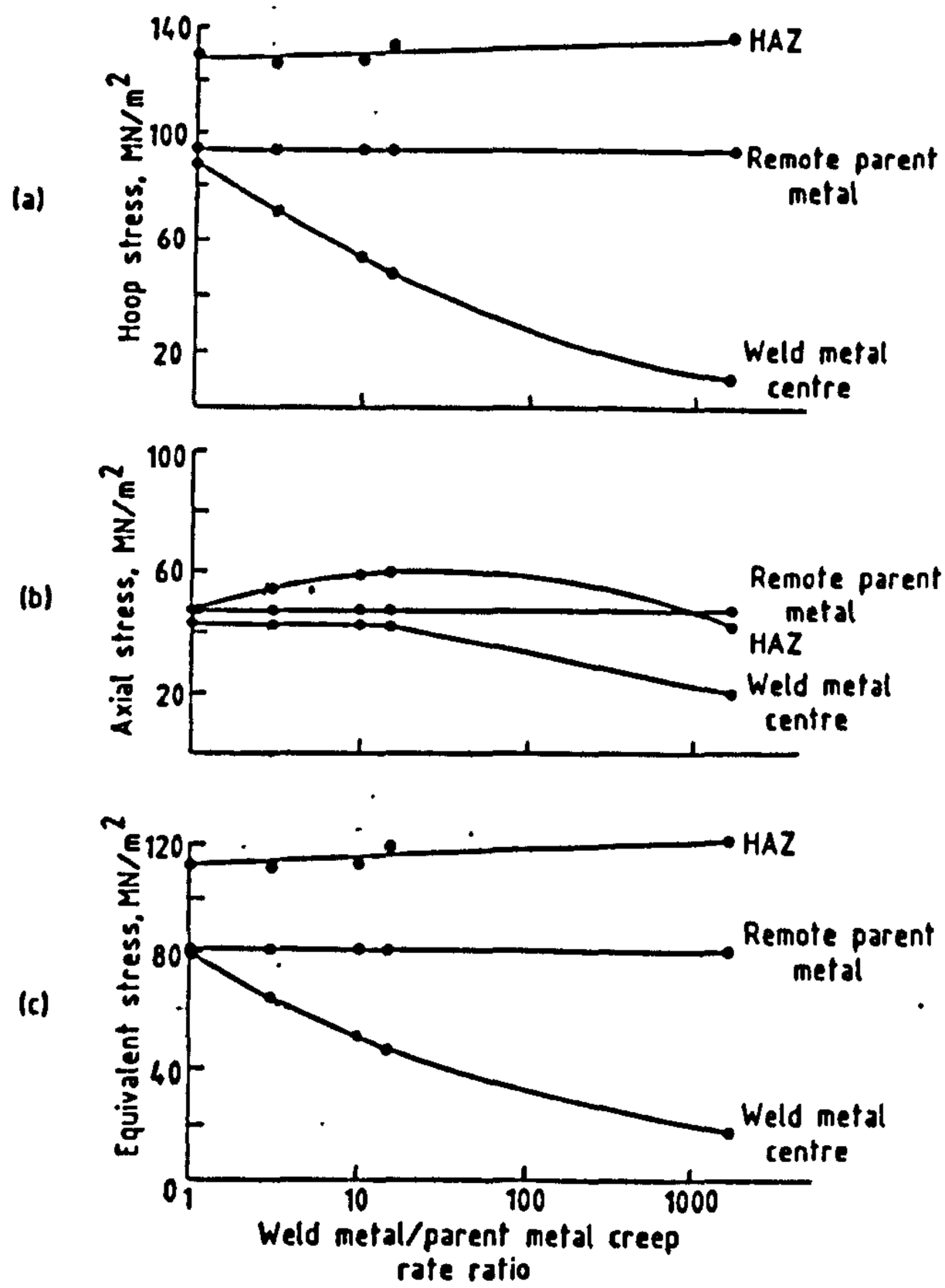

Figure 7.24: The variation of surface stationary state (a) hoop stress, (b) axial stress and (c) equivalent stress with weld metal/parent metal creep rate ratios. After Coleman et al [131].

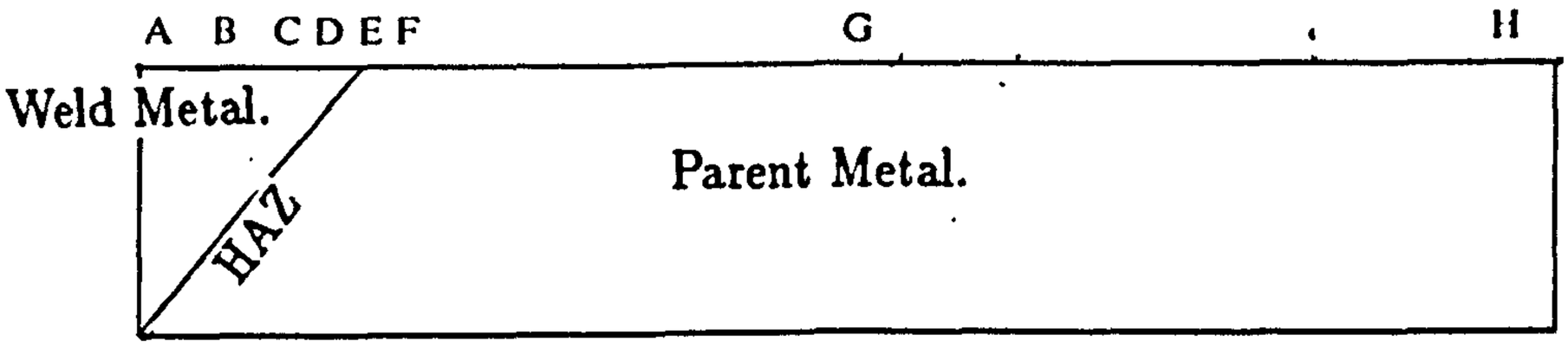

Figure 7.25: Diagram showing the surface positions where creep strain rates given in Table No.7.3 were calculated in the finite element analysis of Coleman et al [131].

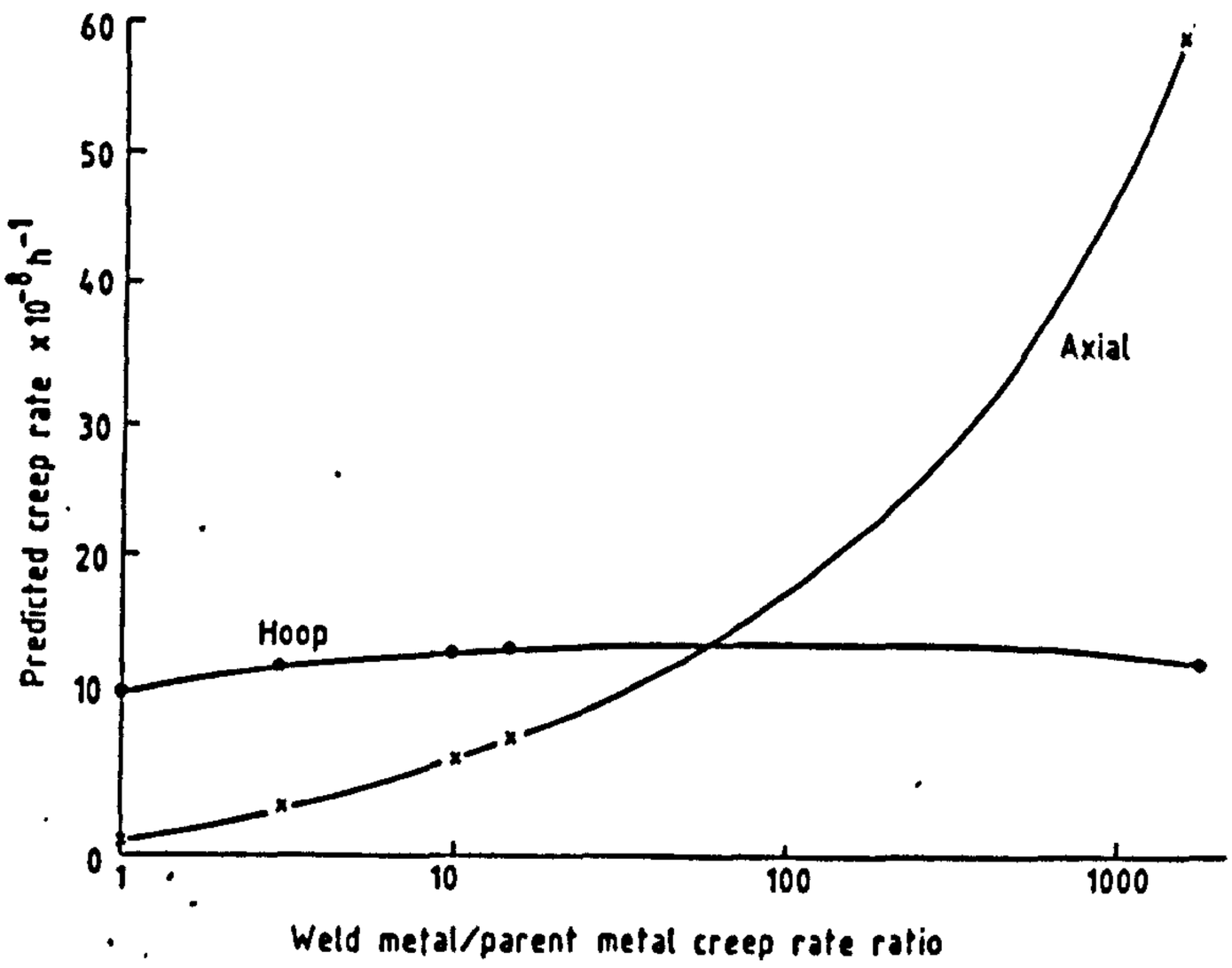

Figure 7.26: Surface hoop and axial steady state creep rates at the weld metal center from the finite element analysis, as a function of the weld metal/parent metal creep rate ratio. After Coleman et al[131].

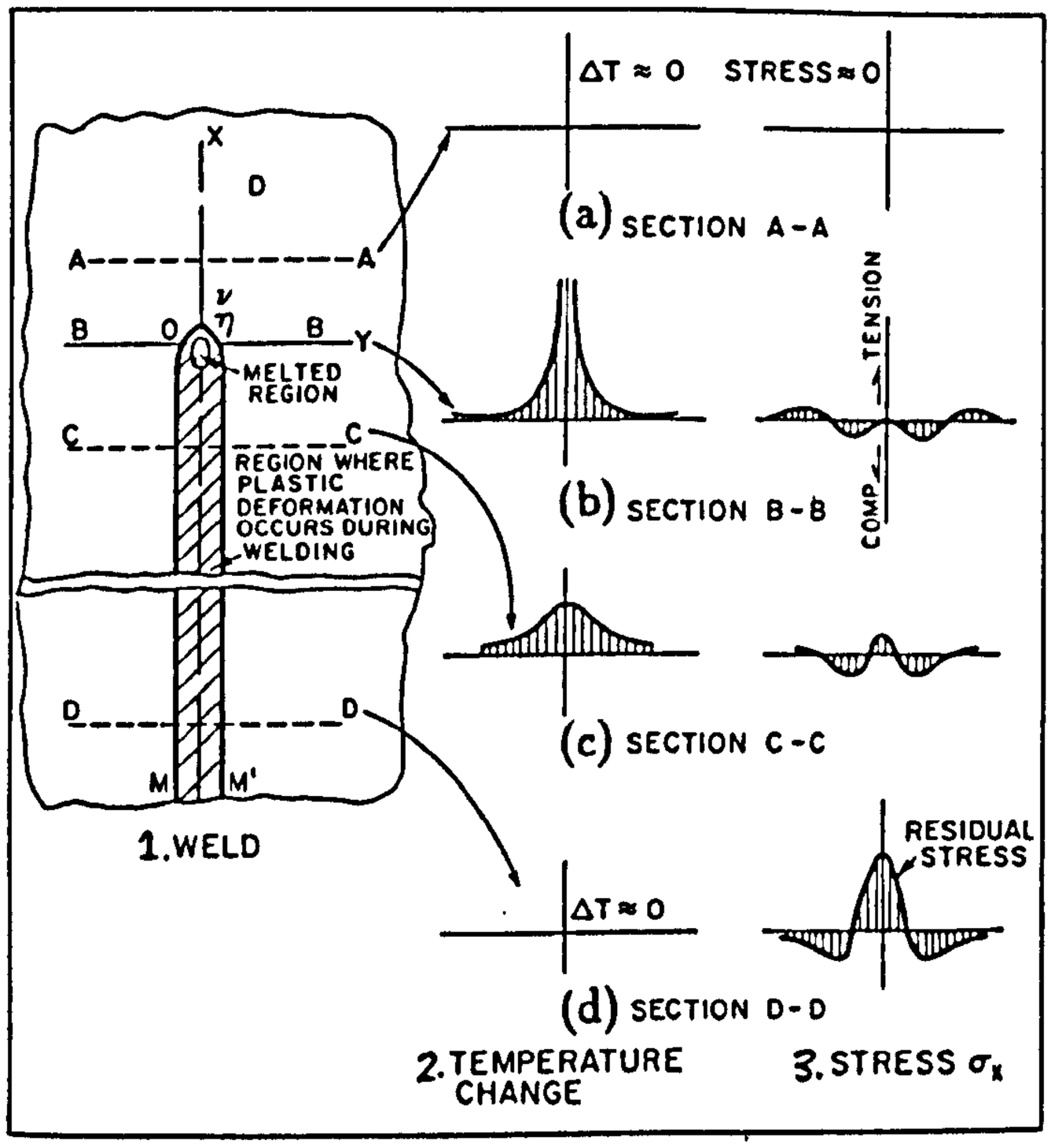

Figure 7.27: Schematic representation of the changes in temperature and stress during welding due to Masubuchi [146]. (a) (b) (c)

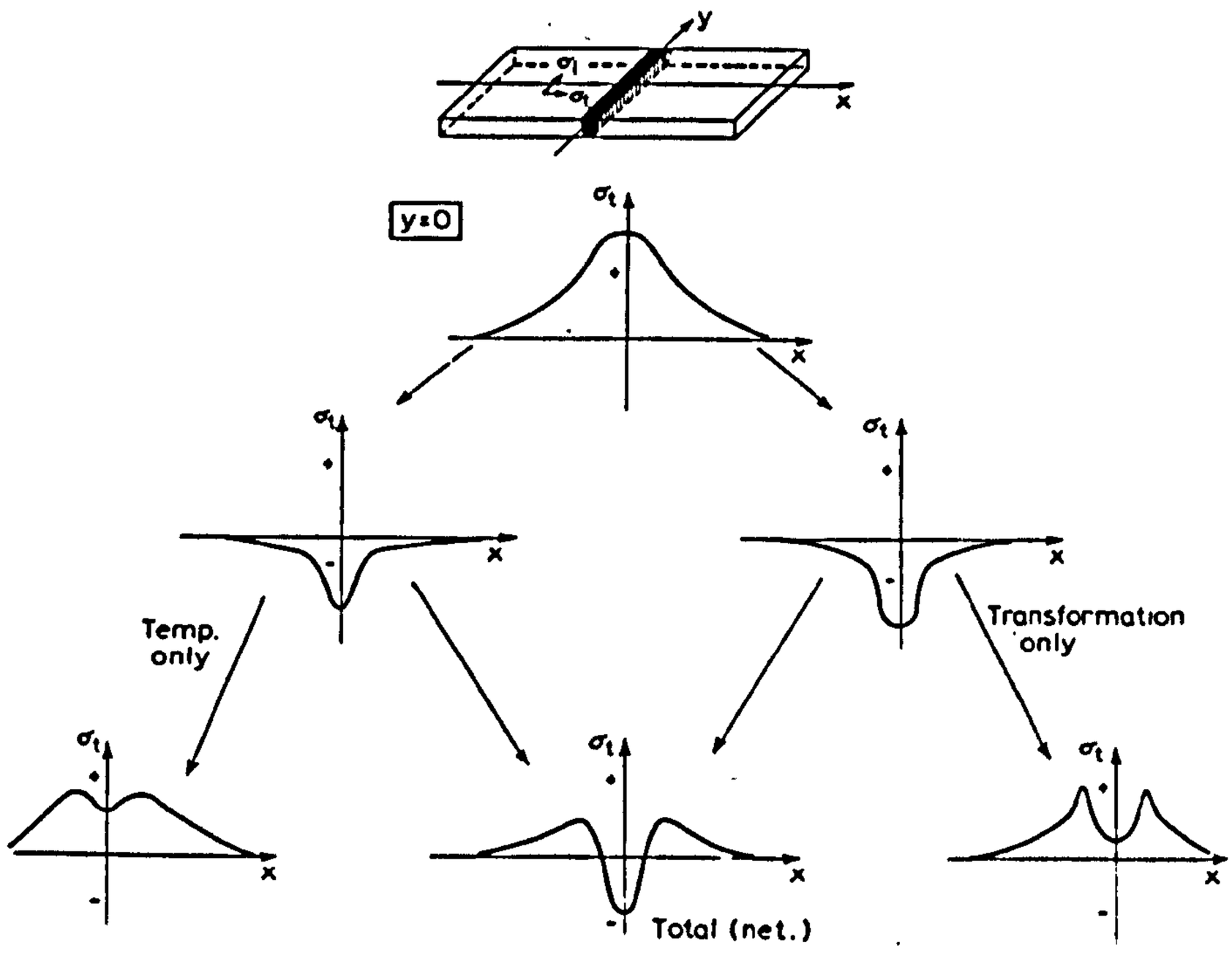

Figure 7.28: Transverse residual stresses at the weld metal center line caused by the seperate effects of temperature and phase transformation which are additive producing the net residual stress distribution. After Macherauch and Wohlfahrt [147].

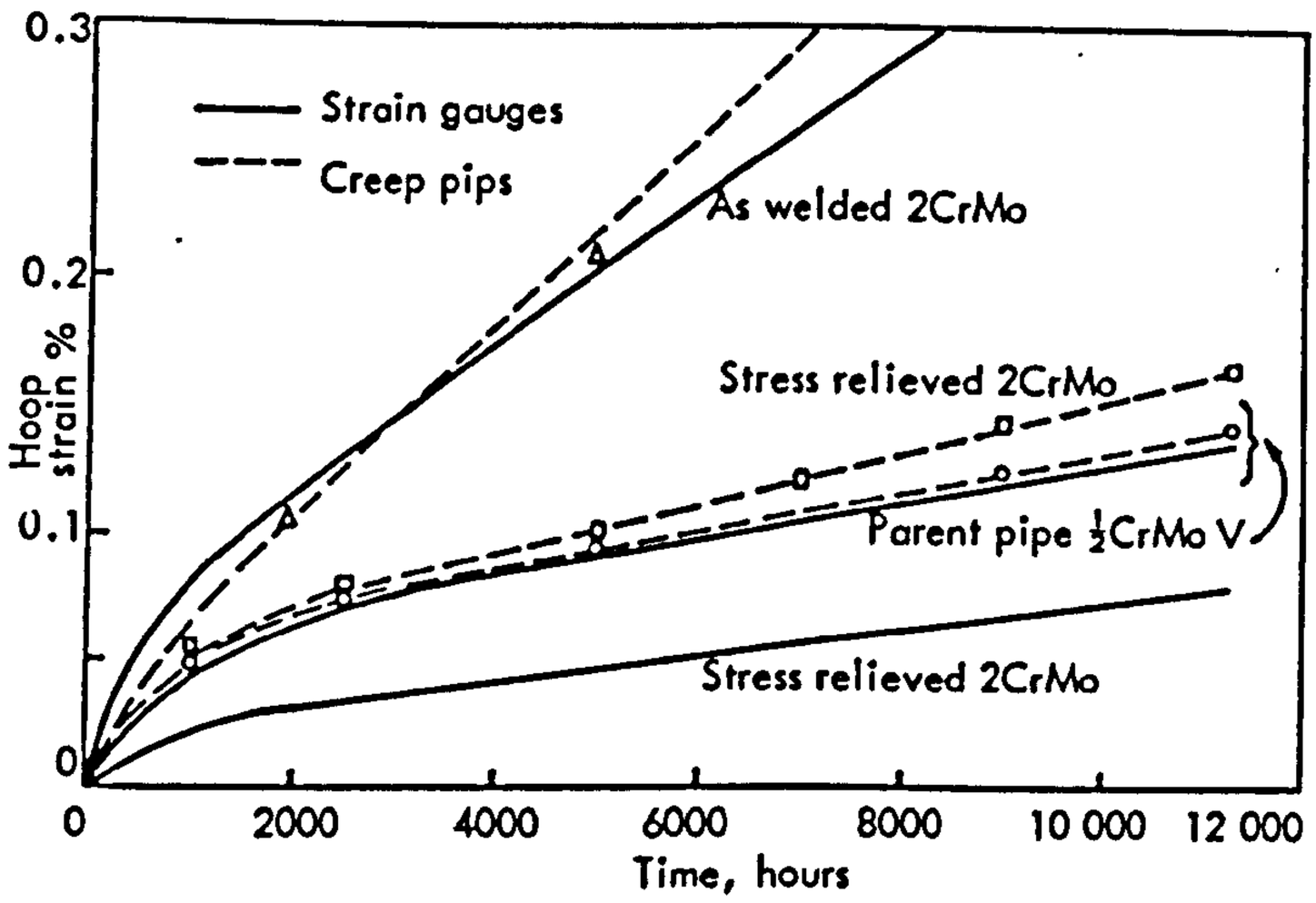

Figure 7.29: The variation of hoop strain with time for stress relieved and as welded 2.25Cr 1Mo welds, tested at 455bar and 565°*C*. After Coleman and Parker [136].

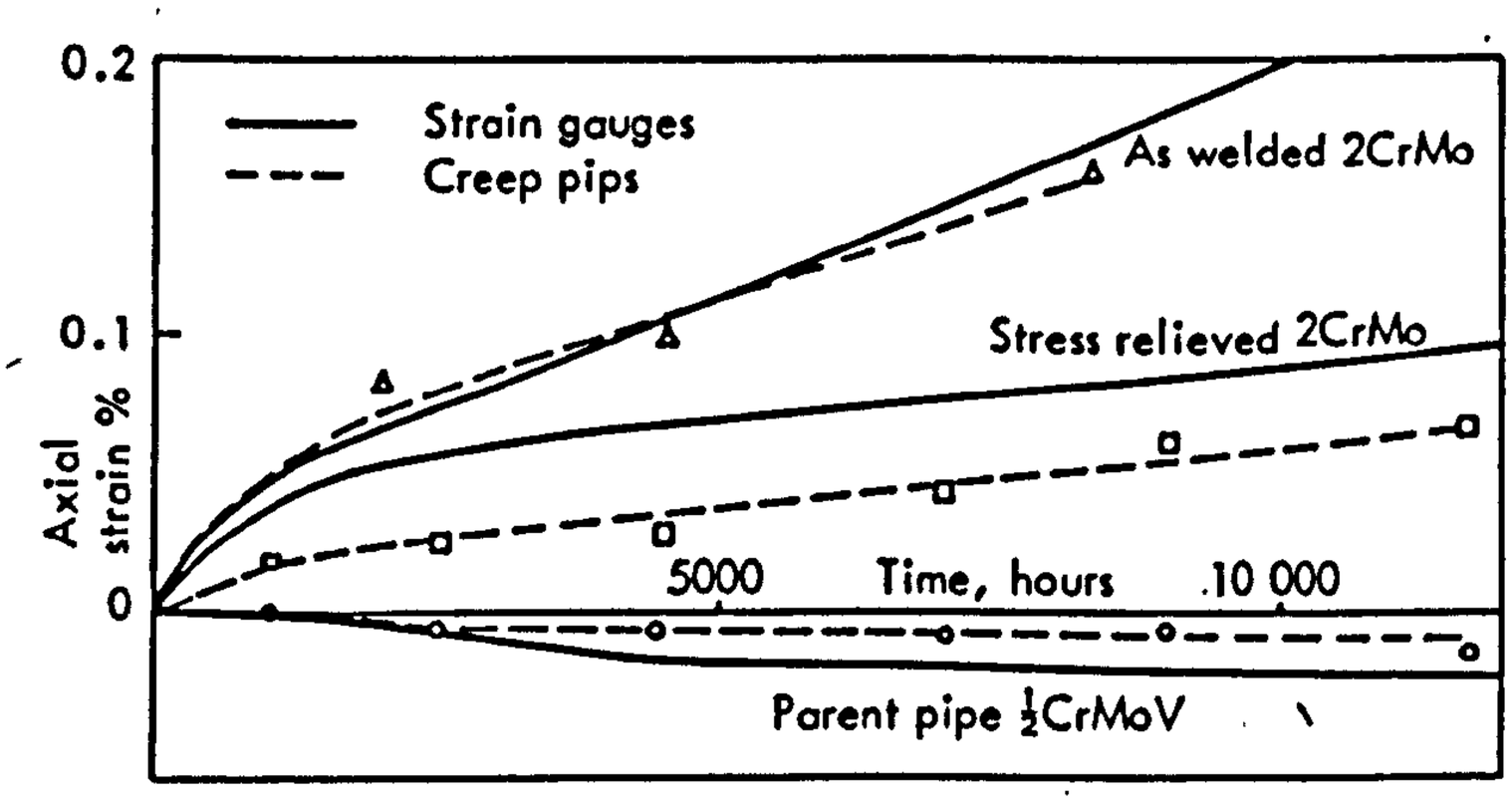

Figure 7.30: The variation of axial strain with time for stress relieved and as welded 2.25Cr 1Mo welds, tested at 455bar and 565°*C*. After Coleman and Parker [136].

Chapter 8.

Finite Element Creep Continuum Damage Modelling Of The High Temperature Deformation And Failure Of A 2.25Cr 1Mo:0.5Cr 0.5Mo 0.25V Steam Pipe Weldment.

8.1 Introduction.

Coleman [148] has compiled creep strain data and the complete failure history of a 2.25Cr 1Mo:0.5Cr 0.5Mo 0.25V thick steam pipe weldment from a C.E.G.B. constant pressure (455 bar) vessel test, at a constant temperature of $565°C$. In this test, transverse cracks are initially observed in the coarse columnar regions of the outer buttered layers of the weld metal [133]. Subsequent failure includes bending, and the weld bulges outwards with the formation of circumferential cracks in the outer weld beads, close to the fusion boundary.

This deformation and failure through macroscopic cracking is to be modelled using axisymmetric finite element creep continuum damage models, with a full creep curve representation for each constituent material microstructural zone of the weld. Initially a simple three material weld model is used, where discrete regions of the finite element mesh are assigned the creep properties of the parent metal, the heat affected zone and the weld metal. This model is then refined and a new solution performed. Finally, a four material model is developed where both coarse and fine grained bainitic regions inside the multipass weld metal are represented, to try to predict the exact effects of the material inhomogeneity on the damage field within the joint. Comparisons are made between the damage distributions predicted by the models and the cracked weldment of the full-size pressure vessel test. Computer predictions of strain and failure times are also correlated with the experimental results.

8.2 Experimental Description.

Pressure vessels have been constructed to test circumferential welds in thick steam pipes at high temperature [131]. One such pressure vessel was constructed from 0.5Cr 0.5Mo 0.25V parent metal in the normalised and tempered condition, using two 1Cr 0.5Mo and two 2.25Cr 1Mo multipass welds, Fig.8.1(a). The steam pipe section was of 60 mm wall thickness, having an external diameter of 350 mm and an external to internal diameter ratio of approximately 1.52. The end caps of the vessel were forged and the seamless pipe sections of parent metal were hot drawn. The welds were made with the Manual Metal Arc fusion process, using a standard 'J' type weld preparation, Fig. 8.1(b). Welding was performed at a preheat of $200°C$ and the welds were subsequently stress relieved for 3 hours at $700°C \pm 10°C$. A cross-section through a similar 2.25Cr 1Mo weld is shown in Fig.8.2, where the parent metal, heat affected zone and the weld metal coarse and fine zones, (section 7.5), may be identified. The choice of the materials used for the pressure vessel, the welding parameters and construction were arranged to reproduce both a microstructurally and a macrostructurally realistic component typical of those used in power generating plant. Auxiliary weldments were produced using exactly the same materials and procedure from which specimens were cut, to give uni-axial creep data from constant load tests of microstructural regions within the weld [109].

The pressure vessel was tested at a temperature of $565°C$ and a pressure of 455 bar giving an accelerated test factor of about 10, in comparison with the component design life (calculated using I.S.O. stress rupture-data for the parent metal). An air circulation bell furnace is used to heat the pressure vessel, which is pressurised incrementally with steam up to the test pressure. During the test elastic and creep strain measurements were obtained by two strain measurement methods. The first is a manual method where the relative displacements between stellite domes (creep pips), (Fig.8.1), welded to the surface of the pressure vessel are measured at test intervals when the test temperature is reduced to the ambient temperature. The creep pips are positioned on either side of the welds (Fig.8.1(a)), and are used to measure the displacements across each weld and the parent metal pipe sections, in both diametral and axial directions. The hoop strains are calculated from the displacement of diametrically opposite creep pips and have a gauge length of approximately 400 mm.

The axial strains are calculated from the axial displacements of the creep pips, using gauge lengths of 100 mm to obtain the axial weld strains and a gauge length of 150 mm to obtain the axial parent metal strains.

The second method of strain measurement gives a continuous reading of strain with test time. This method uses planar high capacitance gauges developed by the C.E.G.B. to function up to a temperature of $700°C$ with a low drift rate. The capacitance gauges were situated locally on the weld metal centre lines of the two inner most welds of the pressure vessel; positioned to measure both hoop and axial weld surface strains. Capacitance gauges were also placed in the centre of the middle parent metal pipe section of the vessel, (Fig.8.1(a)). The capacitance gauges used have a gauge length of 20 mm.

8.3 Deformation And Failure History Of The 2.25Cr 1Mo:0.5Cr 0.5Mo 0.25V Steam Pipe Weldment.

The strains measured using the capacitance gauges, during the pressurisation of the vessel at the test temperature, showed a linear relationship with pressure in both the welds and the parent metal. This indicated that the initial deformation was elastic with measurements giving a hoop to axial strain ratio in both the welds and parent metal of 4 to 1; which gives a hoop to axial stress ratio of 2:1 as expected from elastic theory.

Creep strains were then observed to accumulate with time. A primary creep region was observed in the hoop direction for both the parent metal and the weld metal, lasting for about 4,000 hours followed by a secondary creep region. The secondary creep hoop strain rate in both the weld and the parent metal were observed to be similar. Hoop strain measurements obtained from both the creep pips and capacitance gauges gave a secondary creep rate of approximately $7x10^{-8}$ /hour.

Axial creep strain measurements from the creep pips for the parent metal were observed to be zero over the test period until severe cracking and bulging was observed. Capacitance gauges in the parent metal indicated a small amount of primary creep followed by a secondary creep strain rate of zero. Axial creep strain measurements for the weld metal, from both the creep pips and capacitance gauges, indicated primary creep strain stages lasting for about 4,000 hours followed by a secondary

creep strain rate of approximately $5x10^{-8}$/hour. From calculations performed by Coleman et al [131] using the measured surface secondary creep strain rates and the Bailey equations (8.15), (8.16) and (8.17) [132], the hoop to axial steady state stress ratio at the centre of the 2.25Cr 1Mo weld is approximately bi-axial.

The creep deformation history of the welded pressure vessel is summarised by the creep curves of Fig.8.3, measured from both the creep pips and capacitance strain gauges. With reference to Fig.8.3 the secondary creep region gives way to increased strain rates of the tertiary creep region after approximately 20,000 hours. This figure highlights the difference between the magnitudes of the hoop strains measured from the creep pips with those from the capacitance gauges. These differences are explained as a result of the creep pip measurements being taken across the periphery of the vessel, giving a global measurement of the deformed and cracked regions of the weldment, whereas the capacitance gauges give measurements locally on the surface of the weldment. It must also be remembered that the creep pips for the weld actually lie in the parent metal, a few millimetres away from the fusion boundary, whereas the capacitance gauges lie on the centre line of the weldmetal. The creep curves of Fig.8.3 will be used in comparison with the finite element results obtained from the developed weld models later in this chapter.

The observed failure history of the pressure vessel is briefly summarised in Table8.1 with reference to Figs.8.4 to 8.8.

8.4 Weld Model Specifications.

As the failure of the pipe weldment occurs at the weld, the geometry and behaviour of the materials and microstructures within the welded joint and its viscinity are important. A micrograph of a radial section taken from the 2.25Cr 1Mo:0.5Cr 0.5Mo 0.25V pipe weldment is given in Fig.8.2. A detailed investigation of a single 2.25Cr 1Mo:0.5Cr 0.5Mo 0.25V weld was presented by Middleton and Cane [102], where 13 separate material structures were identified in the heat affected zone. Many of these microstructures have not been isolated in sufficient volume, so that creep test can be performed to determine the individual material properties of these microstructures. Coleman [96] detailed a simplified representation of the main microstructures and the spatial distribution in a multipass ferrite weld (Fig.7.6 and section 7.5).

With the added restriction of the limited creep test data made available Cane [109], simplifications in the analysis must be made to model such welds.

All the weld models developed will use an axisymmetric representation of the thick steam pipe, with plain strain triangular finite elements. Only half of the weld will be modelled due to symmetry. The first weld model, which will be termed WM1, will model the three main microstructural regions of the weldment, namely; the parent metal, the heat affected zone and the weld metal. The geometry, boundary conditions and loading specifications for WM1 are shown in Fig.8.9. The second model will have the same microstructural regions and the same specifications as WM1, but it will have a refined finite element mesh to examine the convergence of the solution. This second model will be termed WM2. The third weld model will be an improvement of weld model two (WM2), in that it will include a representation of the coarse and fine bainitic regions of the weld metal (Fig.7.6). The modelling of these regions is thought important, since initial cracking occurs in the weld metal coarse columnar bainite regions of the outer weld beads, with creep crack growth extending radially inwards through alternate coarse and fine grained regions in a circumferential mode until failure.

The welding specifications for this welded joint (i.e. heat input and bead overlap) have been controlled so that each weld bead, between the capping beads, contain approximately 20% coarse grained bainite by area, on metallurgical examination [149]. A simplified representation of the 2.25Cr 1Mo weld metal microstructures may be made (Fig.8.10), where successive coarse grained bainite regions are represented as crescent shapes. These coarse grained crescent shapes will be later represented topologically as groups of triangular finite elements with the material properties of the coarse grained weld metal. The size and position of these groups of elements is in accordance with careful examination of the distribution of coarse and fine grained regions in the weld metal using the micrograph of Fig.8.2. The weld capping layer is mainly coarse grained columnar bainite and is represented as a fully coarse grained region in the weld model. This weld model will be termed WM3.

In all the weld models it is assumed that the residual welding stresses in the pressure vessel weldment are small after the stress relief heat treatment, and no allowance for the effects of residual stress distributions is made in the finite element

analysis. The thermal expansivity differences across the different material zones of the weldment are also assumed to be small, and no allowance for thermal strains is made in the weld models.

8.5. Materials Data.

The elastic behaviour of each material zone of the weldment is assumed the same, which is in accordance with the experimental results of Coleman [131]. Therefore each material zone has the same value of the elastic modulus (E), which is taken as that of the parent metal (E=170 GPa), with reference to Jones [150].

The creep deformation and failure characteristics of each material zone in the weld model are obtained from the uni-axial and multi-axial creep data of Cane [109]. Some additional long term creep data, from tests which continued to failure after this report [109] was written, were obtained through Jones [150] (due to Cane) and have been used to supplement the data of the report.

As Coleman et al [131] have previously determined that Norton's power-law adequately describes the creep deformations observed in the pressure vessel weldment, from their secondary creep finite element analysis, no reference is made to the Ashby mechanism maps; as the materials in the weldment operate in the power-law creep region at low stress levels. Hence the standard creep constitutive and damage rate laws (2.19) and (2.20) will be used. At high stress levels the bi-linear modifications to these equations (section 2.6) will be used to model the high stress excursion from the mechanism map power-law creep region, partially into the dislocation glide region.

8.5.1 Obtaining The Uni-Axial Creep Constitutive And Damage Law Material Constants For The Weld Materials For Low Stress Conditions.

The uni-axial creep test specimens for the weld metal were machined from blanks cut chordally from the middle and outer regions of the pipe section, Fig.8.11. The creep test specimens for the parent metal were obtained from blanks only cut from the middle of the steam pipe section, to give average properties at the mid wall section of the pipe in accordance with Coleman and Williams [129,130]; who suggested

that through thickness effects are of secondary importance in pipe models and that average mid wall creep properties are adequate. The uni-axial creep specimens had a diameter of 9 mm and a guage length of 60 mm. The uni-axial creep test data for the coarse grained heat affected zone was obtained by testing furnace heat treated parent metal to simulate this weld microstructure. The simulated heat affected zone material is termed grain coarsened parent metal (G.C.P.) for short. All the creep tests were constant load tests, performed for a wide range of stress levels. The selected results from the uni-axial creep tests for the parent metal, the heat affected zone microstructure and the weld metal are summarised in Table 8.2. From results of Table 8.2, the uni-axial stress-rupture and stress vs. minimum creep rate diagrams are given in Figs.8.12 and 8.13, respectively, for each material zone. All of the materials show bi-linear strain rate and stress-rupture characteristics, due to different high and low stress behaviour. Uni-axial strain/time creep curves were only available for low stress tests (i.e. for tests conducted below the knee of the stress-rupture lines; the knee is known as the break stress). The strain time curves for the creep tests marked with (o) in Table 8.2 have been digitized by the author, following an algorithm [54] to obtain a distribution of data points which has been observed to improve the accuracy of constitutive model fits to experimentally obtained creep strain vs. time data. The uni-axial creep constitutive equation (3.2) and damage law (3.3) material constants are obtained by optimum fitting of the uni-axial primary, secondary and tertiary creep strain/time relationship (equation 3.4) to the digitised creep curves for a range of test stress levels, as detailed in section 3.6. Plots of the experimental (digital) and fitted creep curves are presented in Fig.8.14(a) (b) and (c) for the parent metal, heat affected zone and the weld metal respectively. The corresponding material constants are given in Table 8.3 (a), (b) and (c). Some of the creep curves given by Cane [109] have not been selected for inclusion within the fitting procedure as only well shaped creep curves, which consistently increase in height for higher applied test stress levels, are used; so as not to downgrade the curve fits. The fits obtained are seen to be good and are representative of the low stress creep test data. The curve fits obtained for the heat affected zone material could be better for the 100 MPa and 85 MPa curves (Fig. 14(b)).

8.5.2 Obtaining The High Stress Material Constants.

Uni-axial creep curves were not available for the high stress rupture tests (i.e. for tests above the break stress). Hence the material parameters could not be obtained using the fitting procedure, as was used to obtain the low stress material constants. Therefore the high stress material constants are obtained by hand fitting calculations, using the gradients of the stress-rupture and stress-minimum creep rate diagrams of Figs.8.12 and 8.13, and the data of Table 8.2. The bi-linear representation detailed fully in section 2.6 is used, where the assumption is made that the high stress creep curves have the same primary creep curve shape, and therefore the same value of the material constant (m), as the low stress creep curves. The break stresses ($\hat{\sigma}$) used for each material are shown in Figs.8.12 and 8.13. Their values for each weld material are given in Table 8.3 and are the same for both the stress-rupture and stress-minimum creep rate diagrams for simplicity. High and low stress constants are subscripted I and II respectively. The values of the high stress constant (χ_I) may be obtained from the gradient of the high stress stress-rupture line for each material. The gradient of the high stress-rupture line may be shown to be $(-(m+1)/\chi)$. Alternatively the value of (χ) may be calculated by taking the values of failure time and stress at a point on the high stress-rupture line and substituting these values into equation (2.56) with the low stress values of the constants M_{II}, χ_{II}, m and the value of the break-stress ($\hat{\sigma}$). Equation (2.56) may be re-arranged and by taking logs of each side of the equation the value of (χ_I) determined. (M_I) is obtained from equation (2.47).

The high stress value of the creep exponent (n_I) is obtained from the gradient of the high stress vs. minimum creep diagram which is identified as $(1/n)$. The value of (K_I) is then obtained using equation (2.37), the value of (n_I) and the low stress values of (K_{II}) and (n_{II}). The compatibility of failure strain is maintained at the break stress by defining (ϕ_I) such that equation (2.57) is satified. A full description of the method for obtaining the high and low stress material constants for the bi-linear continuum damage mechanics analysis is given in section 2.6.

The high stress material constants for each material zone of the weldment are summarised in Table 8.3. Checks are made using both the high and low stress material parameters by determining the theoretical failure strains and failure times at certain test stress levels using the uni-axial equations (3.4) and (3.5) respectively,

where $M = A(\phi + 1)$.

8.5.3 Determination Of The Multi-Axial Rupture Criterion Parameters For The Weld Materials.

Cane [109] gives multi-axial rupture data for the parent material and the simulated heat affected zone material, from double shear, torsion and uni-axial tension tests. He uses a multi-axial stress rupture criterion of the form:

$$t_f = \frac{1}{B\sigma_1^q \sigma_{ef}^{(r-q)}} \tag{8.1}$$

where (t_f) is the rupture time, (σ_1) is the maximum principal tension stress, (σ_{ef}) is the von Mises effective stress, (r) is related to the gradient $(-1/r)$ of the uni-axial stress-rupture diagram, $(q)$is the principal stress exponent of rupture, determined from torsion/tension creep rupture tests and (B) is a constant. Values (σ_{ef}), (σ_1), (r) and (q) are given in Table 8.4.

The finite element program Damage-(XX) to be used for the weld modelling has a multi-axial rupture criterion formulated by Hayhurst [22] of the form:

$$t_f = \frac{1}{M\left\{(\alpha\sigma_1 + (1-\alpha)\sigma_{ef}\right\}^{\chi_T}} \tag{8.2}$$

where (χ_T) is related to the gradient $(-1/\chi_T)$ of the uni-axial stress-rupture plot, (α) is a material constant where $(0 \leq \alpha \leq 1)$ which determines the bias of the multi-axial rupture behaviour of the material between a maximum principal stress and an effective stress rupture criterion (section 2.4.6); M is a constant. Here for simplicity the expression for the rupture criterion of Hayhurst is written without the inclusion of the material constant (m), which appears in equation (2.29) as (m) does not affect the form of the isochronous rupture surface (equations (2.32) and (2.33)). (β_H) in equation (2.29) is assumed to be zero for lack of tri-axial rupture data to suggest otherwise. Both equations (8.1) and (8.2) represent multi-axial rupture criterion based on the maximum principal stress and the effective stress. It is to be shown that these two expressions are in fact equivalent and may be expressed in terms of one another, so that values of (α) may be obtained from the values of (r) and (q) given by Cane [4], enabling Hayhurst's form of the rupture criterion to be used.

For uni-axial plane stress conditions: $\sigma_1 = \sigma_o$, $\sigma_2 = \sigma_3 = 0$; and $\sigma_1 = \sigma_{ef} = \sigma_o$.
Substituting for σ_1 and σ_{ef} into (8.1) gives:

$$t_{f_1} = \frac{1}{B\sigma_0^q \sigma_0^{(r-q)}} = \frac{1}{B\sigma_0^r} \tag{8.3}$$

Substituting σ_1 and σ_{ef} into (8.1) gives:

$$t_{f_2} = \frac{1}{M\left\{\alpha\sigma_0 + (1-\alpha)\sigma_0\right\}^{\chi_T}} = \frac{1}{M\sigma_0^{\chi_T}} \tag{8.4}$$

Since $t_{f_1} = t_{f_2}$, (r) and (χ_T) are identified to be the same and equal to (ν), which is related to the gradient $(-1/\nu)$ of the uni-axial stress-rupture plot; this implies that $(B = M)$. Since both (B) and (M) are constants, $(B = M)$, must hold true for multi-axial states of stress as well as uni-axial. Equations (8.1) and (8.2) may therefore be combined:

$$\sigma_{Rup}^{\nu} = \sigma_1^q \sigma_{ef}^{(\nu-q)} = \left\{\alpha\sigma_1 + (1-\alpha)\sigma_{ef}\right\}^{\nu} \tag{8.5}$$

where (σ_{Rup}) is the representative rupture stress, which when applied to the uni-axial stress rupture data gives the life of a structure under a multi-axial state of stress.

Substituting values of (σ_{ef}), (σ_1), $(\nu = r)$ and (q) from Table 8.4 into equation (8.5) values of (α) for the parent metal and the heat affected zone are obtained and are also given in Table 8.4. The shapes of the isochronomous rupture surfaces in plane stress, principal stress space, due to the equations of Cane and Hayhurst, using the newly determined (α)-parameters, may be obtained to show that the two representations are equivalent for a range of bi-axiality ratios. First the equations representing the multi-axial rupture surfaces for equations (8.1) and (8.2) must be determined:-

Equation (8.1) may be written in terms of the plane stress principal bi-axial stresses $\sigma_1 > \sigma_2 > \sigma_3 = 0$:-

$$t_f = \frac{1}{B\sigma_1^q \left\{\left(\sigma_1^2 + \sigma_2^2 - \sigma_1\sigma_2\right)^{\frac{1}{2}}\right\}^{(r-q)}} \tag{8.6}$$

which is normalised by writing $\Sigma_i = \sigma_i/\sigma_0$ and $T = t/t_0$, where (t_0) is the time to rupture of a uni-axial test at a stress (σ_0), equation (8.6) is re-written as:

$$T = \frac{t_f}{t_0} = \left\{\Sigma_1^q \left(\Sigma_1^2 + \Sigma_2^2 - \Sigma_1\Sigma_2\right)^{\frac{(r-q)}{2}}\right\}^{-1} \tag{8.7}$$

By writing (Σ_2) as the ratio (ζ) of the (Σ_1), equation (8.7) may be re-written as:

$$T = \left(1 + \zeta^2 - \zeta\right)^{\frac{-(r-q)}{2}} \Sigma_1^{-r} \tag{8.8}$$

T in (8.8) may be set to unity, to give the bi-axial stresses required to give a rupture time equal to the uni-axial and rupture time:

$$\Sigma_1 = \left(\zeta^2 - \zeta + 1\right)^{\left(\frac{q-r}{2r}\right)} \tag{8.9}$$

This equation may be used to give the shape of the rupture locus in the (Σ_1, Σ_2)-plane, for points having the same rupture time.

Equation (8.2) may be re-written in a similar manner giving an analogous equation to that of (8.9):

$$\Sigma_1 = \left\{\alpha + (1-\alpha)\left(\zeta^2 - \zeta + 1\right)^{\frac{1}{2}}\right\}^{-1} \tag{8.10}$$

Equations (8.9) and (8.10) obtained from the rupture criteria of Cane and Hayhurst respectively have been used with the material parameters of Table 8.4 to give values of (Σ_1) and (Σ_2) for a range of bi-axiality ratio in Tables 8.5(a) and (b), for the heat affected zone and the parent metal respectively. The values of (Σ_1) and (Σ_2) obtained using equations (8.9) and (8.10) may be compared and are seen to be closely equivalent. The shapes of the isochronous rupture surfaces in normalised principal stress space are shown in Figs.8.15 for the parent metal and the heat affected zone.

It is seen from equation (8.10) that the shape of the isochronous rupture surface is independent of (ν) and hence (χ) and therefore the values of (α) derived may be used directly in the creep continuum damage equations (equations (2.19) and (2.20) using the normalised time scale (2.18), where ($\chi = \nu(m+1)$), without further modification.

No data is available for the multi-axial rupture criteria of the weld metal, but Goodall [148] suggests a pure σ_{ef} criterion (i.e. $\alpha = 1.0$)

8.6 Development and Evaluation Of The Finite Element Program To Model A Homogeneous Pressurised Tube.

8.6.1 Development Of The Finite Element Program To Include The Internal Pressure Loading Of The Tube.

The effects of internal pressure loading, due to the constant pressure (p_0) is included within the axisymmetric finite element program by applying horizontal (radial) nodal forces to the nodes on the vertical boundary of the finite element mesh representing the inside surface of the pressure vessel. With reference to Fig.8.16 the contribution of nodal force in the horizontal direction caused by the pressure (p_0) acting on the revolute area (A_r) is given by:

$$F_i = F_j = 2\pi \bar{r}_{ij} l_{ij} \left(\frac{p_0}{2}\right) \tag{8.11}$$

where (i) and (j) indicate node numbers (they are not tensors) and (l_{ij}) is the finite element leg length and ($\bar{r}_{ij}$) is the average radial distance (which in the case of a small strain analysis of a pressure vessel is a constant and is the internal radius of the pressure vessel). (p_0) is normalised by (σ_o) in the program ($P_0 = p_0/\sigma_0$). Having calculated the nodal force contributions for each element, the nodal forces are assembled in the global force vector (F_e, in equation 4.1), where the force contributions due to the boundary elements connected to the boundary nodes are added. The subroutines developed to include the pressure loading are general and cope with different mesh sizes and varying mesh refinement. Care has to be taken when failed elements ($\omega > 0.9999$) occur on the inner surface of the mesh, as the nodal loads for these elements are effectively removed from the system. If the finite element mesh size is small and the number of damaged elements is small, this reduction of load will not be detrimental to the solution, but this situation should ideally be avoided.

The axial load on the pressure vessel wall due to the action of the internal pressure on the vessel end-caps (Fig.8.17) is included within the finite element solution by applying a uniform axial pressure load to the top boundary of the finite element mesh (Fig.8.18).

The axial pressure load is calculated referring to Fig.8.17 as follows. The internal pressure (p_0) acting on an end cap of area (πa^2) produces a reaction of

$(p_o \pi a^2)$, which is equated to the equal and opposite reaction produced in the pressure vessel of $(\sigma_z \pi (b^2 - a^2))$ giving:

$$\sigma_z = \frac{p_o}{\left(\left(\frac{b}{a}\right)^2 - 1\right)} \tag{8.12}$$

where (σ_z) is the uniform axial stress in the pressure vessel wall which is applied to the top boundary of the finite element mesh.

The vertical (axial) nodal forces applied to the top boundary of the axisymmetric finite element mesh (Fig.8.18) are calculated using:

$$F_i = \pi (r_i - r_k) \left(\frac{1}{3} r_k + \frac{2}{3} r_i\right) \sigma_z \tag{8.13}$$

$$F_k = \pi (r_i - r_k) \left(\frac{2}{3} r_k + \frac{1}{3} r_i\right) \sigma_z \tag{8.14}$$

where (σ_z) in the program is normalised by (σ_0), giving $(\Sigma_z = \sigma_z / \sigma_0)$. These forces are also included in the global force vector (equation 4.1) in the finite element program.

8.6.2 Evaluation Of The Developed Axisymmetric Finite Element Pressure Vessel Model In Comparison With A Closed-Form Solution.

Odqvist [18] has presented a plane strain analysis of an internally pressurised thick walled pressure vessel due to Bailey [132]. The pressure vessel has an external to internal diameter ratio $(b/a=2.0)$. The section of the tube, the coordinate system and the directions of the stresses are given in Fig.8.19. The model assumes that there is no through thickness strain in the (z)-direction, which may be assumed true for long pressure vessels. Equations for the hoop, radial and axial stresses are derived [18] and are:

$$\sigma_\theta = \frac{p_0}{\left\{\left(\frac{a}{b}\right)^{\frac{2}{n}} - 1\right\}} \left\{1 - \left(1 - \frac{2}{n}\right) \left(\frac{r}{b}\right)^{\frac{-2}{n}}\right\} \tag{8.15}$$

$$\sigma_r = \frac{p_0}{\left\{\left(\frac{a}{b}\right)^{\frac{2}{n}} - 1\right\}} \left\{1 - \left(\frac{r}{b}\right)^{\frac{-2}{n}}\right\} \tag{8.16}$$

$$\sigma_z = \frac{1}{2} (\sigma_r + \sigma_\theta) \tag{8.17}$$

where (n) is the creep exponent of stress in Norton's law (2.2).

These equations have been used by the author to calculate the stress distributions across the wall thickness ($1.0 \leq r/a \leq 2.0$) of the pressure vessel with an internal pressure of (p_0) and a creep exponent of ($n = 1$); which corresponds to the elastic solution (the lines in Fig.8.20). Another solution has been performed for a creep exponent of ($n = 2$), which results in secondary creep stress redistribution. The solution gives the stress distributions through the wall thickness of the pressure vessel at the stationary state (the lines if Fig.8.21). All the stresses are normalised with respect to the internal pressure (p_o), and the radial distance (r) is normalised with respect to the internal radius of the pressure vessel (a).

A uniform crossed-triangular finite element mesh generated by the author to represent the thick pressure vessel of Odqvist is shown as the original green mesh of Fig.8.22. Subroutines developed in accordance with the details given in section 8.6.1, are used to load the mesh radially with a normalised internal pressure load of ($P_0 = 3$) and a normalised axial stress ($\Sigma_z = 1.0$). The axial stress is calculated from (8.21) for a ($b/a = 2.0$). The initial elastic stress distribution ($n = 1$) along the bottom boundary and the subsequent steady state stress distribution ($n = 2$) from the axisymmetric finite element analysis are compared with the analytical solution results of Odqvist in Figs.8.20 and 8.21. The correlation between the results of the analytical and the finite element solution are excellent. With reference to Fig.8.22 which shows the original finite element mesh in green and the displaced mesh in red immediately after the steady state has been reached; the deformation is noticed to be uniform away from the top edge of the mesh, but close to the top boundary an end effect is observed where the mesh has rotated clockwise. This effect is caused by radial differences in the axial Poisson contraction due to the internal pressure increasing the diameter of the vessel.

When a full primary, secondary and tertiary creep solution is performed, slight stress concentrations in the top left-hand corner of the finite element mesh caused by the end effect, results in local damage accumulation in this region, Fig.8.23. This effect would cause boundary elements at the top of the mesh to fail prior to the failure of elements in the weld at the bottom of the weld model mesh, causing the applied forces at the nodes of these elements to be set to zero. Hence damage resulting from the end-effect would affect the solution for the weld models. To overcome this

problem the mesh is increased in length, retaining the same wall thickness, taking the end-effect well away from the lower part of the mesh where the weld geometry will be modelled and uniform stress states must be obtained. The elements in the top 1/5 of the finite element mesh have damage rates set to zero for the duration of weld solution, by defining a new material data set in this region of the mesh. This region of material is still allowed to deform and has the same deformation material properties as the parent metal. Having made these modifications to the weld model, tests showed that uniform stress distributions were obtained in the middle and lower half of the finite element mesh, and failed elements ($\omega > 0.9999$) did not occur locally at the top left-hand side of the mesh (Fig.8.23).

Tests were also performed on the weld model meshes where severe mesh refinement was used in the weld. The tests involved performing homogeneous material elastic and creep solutions to check that no faults or severe stress concentrations resulted in the meshes because of poor element shape and mesh refinement.

8.7 Time Scale Transformations For The Different Weld Materials In The Weld Model.

The creep constitutive equation and the damage rate law to be used in the finite element analysis are given principally by equations (2.16) and (2.17) without allowing for the bi-linear representation (section 2.6) modifications to these equations. These two equations are normalised with the introduction of the normalised time scale equation (2.18) and the constant (V_u) giving equations (2.19) and (2.20). Equations (2.19) and (2.20) are the normalised equations used in the finite element program Damage-(XX).

Each weld material is represented by discrete regions of the finite element mesh, each having different associated material constants which dictate the respective creep behaviours of each zone. Each material zone will therefore have its own normalised time scale determined by (2.18), using its particular material constants. The finite element program uses one normalised time scale which is chosen to be that of the parent metal and the time scales of the weld metals and the heat affected zones must be transformed onto this base time scale. The time scale normalisation is achieved as follows:

If there are two different materials M1 and M2, which have different values of the material constants (K), (n), (m), (M), (χ), (ϕ) and (V_u), (subscripted 1 and 2 respectively) and the same values of (σ_0), (e_0), (E), then the creep strain rate equation (2.19) may be written for materials M1 and M2 as:

$$\frac{dV_{ij_1}}{d\tau_1} = \frac{3}{2}\frac{\Sigma_{ef}^{n_1-1}}{(1-\omega_1)^{n_1-1}}S_{ij} \tag{8.18}$$

$$\frac{dV_{ij_2}}{d\tau_2} = \frac{3}{2}\frac{\Sigma_{ef}^{n_2-1}}{(1-\omega_2)^{n_2-1}}S_{ij} \tag{8.19}$$

where

$$d\tau_1 = K_1 E\sigma_0^{n_1-1}t^{m_1}dt_1 \tag{8.20}$$

and

$$d\tau_2 = K_2 E\sigma_0^{n_2-1}t^{m_2}dt_2 \tag{8.21}$$

Only one normalised time scale, (τ_1), is used by the program to represent the behaviour of both materials M1 and M2. Equation (8.19) must be transformed onto time scale (τ_1). Using (8.20) and (8.21):

$$\frac{dV_{ij_2}}{d\tau_2}\left(\frac{d\tau_2}{d\tau_1}\right) = \frac{3}{2}\frac{\Sigma_{ef}^{n_2-1}}{(1-\omega_2)^{n_2-1}}S_{ij}\left(\frac{d\tau_2}{d\tau_1}\right) \tag{8.22}$$

where:

$$\left(\frac{d\tau_2}{d\tau_1}\right) = \frac{K_2 E\sigma_0^{n_2-1}t^{m_2}dt_2}{K_1 E\sigma_0^{n_1-1}t^{m_1}dt_1} \tag{8.23}$$

as $dt_1 = dt_2 =$ the real time scale:

$$\frac{d\tau_2}{d\tau_1} = \frac{K_2}{K_1}\sigma_0^{(n_2-n_1)}t^{(m_2-m_1)} \tag{8.24}$$

where:

$$t = \left\{\frac{\tau_1(m+1)}{K_1 E\sigma_0^{n_1-1}}\right\}^{\frac{1}{m_1+1}} \tag{8.25}$$

from the equation (2.27), and (8.24) becomes:

$$\frac{d\tau_2}{d\tau_1} = \frac{K_2}{K_1}\sigma_0^{(n_2-n_1)}\left\{\frac{\tau_1(m+1)}{K_1 E\sigma_0^{n_1-1}}\right\}^{\left(\frac{m_2-m_1}{m_1+1}\right)} \tag{8.26}$$

$$= \kappa\tau_1^{\iota} \tag{8.27}$$

where:

$$\kappa = \frac{K_2}{K_1}\sigma_0^{(n_2-n_1)}\left\{\frac{m+1}{K_1 E\sigma_0^{n_1-1}}\right\}^{\iota} \tag{8.28}$$

$$\iota = \left(\frac{m_2-m_1}{m_1+1}\right) \tag{8.29}$$

The damage rate law may be written for materials M1 and M2, and the time scale for the damage rate law corresponding to material M2 is similarly transformed onto that of material M1:

$$\frac{d\omega_2}{d\tau_2}\left(\frac{d\tau_2}{d\tau_1}\right) = \frac{\Delta^{\chi_2}(\Sigma_{ij})}{V_{u_2}(\phi+1)(1-\omega_2)^{\phi_2}}\left(\frac{d\tau_2}{d\tau_1}\right) \tag{8.30}$$

where $(d\tau_2/d\tau_1)$ is given by equation (8.27).

If other weld materials are present such as M3 and M4 etc., then multipliers must be calculated using (8.27) to scale the constitutive and damage law equations for these materials onto one time scale. The values of (κ) and (ι) for the heat affected zone and weld metal are given in Table 8.3, where the parent metal time scale defines the base scale and hence is not transformed.

Having incorporated each set of weld material parameters given in Table 8.3 (a), (b) and (c) into the code of the finite element program, the constitutive models were checked for accuracy by performing solutions for a small four element finite element mesh under uni-axial tension (Fig.4.4(a)). Solutions were performed over the stress range of the experimental uni-axial tests and the rupture times and strains at failure compared with both the experimental and analytical values.

From such tests it was observed that many of the solutions needed large numbers of computational iterative steps until rupture occurred, some solutions were not taken to rupture because of long run times. It would be computationally expensive to run the program for a larger problem, such as a refined weld mesh, for so many iterative steps. The problem seemed to be caused by the program choosing small time step increments over a long time scale. For example a uni-axial creep test for the heat affect zone material at a stress of 85 MPa lasted for approximately 10^5 hours. Reducing the integration accuracy to increase the time step increments and hence decrease the number of iterative steps until failure, had little effect on the number of iterations required and caused error in the failure time predictions. When the integration accuracy was reduced further, unstable stress solutions were produced causing the program to abort as a result of mesh inequilibrium.

These problems were overcome by the author by re-scaling both the normalised creep strain and normalised time scales for all the materials with a transformation of the material parameter V_u.

8.8 The (V_u)-Transformation.

The creep constitutive and damage law equations used by the finite element program for a single material are given in equations (2.19) and (2.20) respectively. Where the normalised time scale is defined by equation (2.18) where (τ) is the normalised time and (t) is the real time in hours. To reduce the size of the real time scale the normalised time scale is reduced by a factor of (Θ) to give:

$$d\tau' = \frac{d\tau}{\Theta} = KE\sigma_0^{n-1}\frac{t^m}{\Theta} \tag{8.31}$$

Defining (2.19) in terms of the transformed normalised time scale (τ') gives:

$$\frac{dV_{ij}}{d\tau'} = \Theta\frac{3}{2}\frac{\Sigma_{ef}^{n-1}}{(1-\omega)^n}S_{ij} \tag{8.32}$$

If (Θ) is not included in (8.32) in the finite element code then the normalised creep strain scale is also scaled by the factor (Θ):-

$$dV'_{ij} = \frac{dV_{ij}}{\Theta} \tag{8.33}$$

Substituting (8.33) into (8.32) gives:

$$\frac{dV'_{ij}}{d\tau'} = \frac{3}{2}\frac{\Sigma_{ef}^{n-1}}{(1-\omega)^n}S_{ij} \tag{8.34}$$

Similarly, normalising the damage rate equation (2.20) by the new transformed normalised time scale (8.31) gives:

$$\frac{d\omega}{d\tau'} = \frac{\Theta}{V_u}\frac{\Sigma^x}{(1+\phi)(1-\omega)^\phi} = \frac{\Sigma^x}{V_{uTRAN}(1+\phi)(1-\omega)^\phi} \tag{8.35}$$

where:

$$V_{uTRAN} = \frac{V_u}{\Theta} = \frac{KE\sigma_0^{(n-x-1)}}{M\Theta} \tag{8.36}$$

(Θ) therefore scales the normalised creep curve in both the axes of strain and time through the replacement of the material parameter (V_u) by (V_{uTRAN}). When (V_u) is replaced by (V_{uTRAN}) both the normalised creep strain and the normalised time results obtained from the computer program must be multiplied by (Θ) to give the true values of the creep strain and normalised time, as would be obtained if (V_u) was used:

$$\tau = \tau' \times \Theta \tag{8.37}$$

$$V_{ij} = V'_{ij} \times \Theta \tag{8.38}$$

$$V_u = V_{uTRAN} \times \Theta \tag{8.39}$$

The value of (Θ) of 1.96758 was used to give a parent metal (V_{uTRAN}) value of 5.0 % strain, originally having a value for (V_u) of 9.83792 % strain, which enabled a uni-axial finite element tests to run to failure requiring fewer iterative time steps and hence computer time. The values of (V_u) for the other materials are scaled consistently in the computer program using the same (Θ) value and are given in Table 8.3. The time steps used in the program were relatively longer, but solution accuracy was retained and improved accuracy and solution stability was obtained by increasing the integration accuracy in reducing the integration parameter sizes (EPSL) and (EPSR), (section 4.3.3). The possibility exists for homogeneous material finite element meshes of normalising (V_u) out of the program allowing for the effects of (V_u) by purely scaling the finite element results. This may enhance the consistency of future solutions for comparison with one another, in requiring similar numbers of iterative time steps for stress redistribution to occur, and similar numbers of steps in which elements may damage.

It is also noted that in the weld analysis (τ_1) in (8.27) must also be multiplied by (Θ) when using the (V_u)-tansformation.

8.9 The New Constitutive Equation And Damage Laws As Used For The Weld Modelling.

The new constitutive equation and damage laws used in the computer weld analysis involving the bi-linear representation, time scale transformation and the (V_u)-transformation are:

$$\frac{dV'_{ij}}{d\tau'_1} = \frac{3}{2}\hat{\Sigma}^{(n_{II}-n_I)}\frac{\Sigma_{ef}^{n_I-1}}{(1-\omega)^{n_I}}S_{ij}\kappa\,(\tau_1\Theta)^{\iota} \tag{8.40}$$

for $\Sigma ef > \hat{\Sigma_{ef}}$.

$$\frac{dV'_{ij}}{d\tau'_1} = \frac{3}{2}\frac{\Sigma_{ef}^{n_{II}-1}}{(1-\omega)^{n_{II}}}S_{ij}\kappa\,(\tau_1\Theta)^{\iota} \tag{8.41}$$

for $\Sigma ef \leq \hat{\Sigma_{ef}}$.

$$\frac{d\omega}{d\tau_1} = \frac{\hat{\Sigma}^{(x_{II}-x_I)}\Delta^{x_I}\,(\Sigma_{ij})}{V_{uTRAN}(1+\phi_I)(1-\omega)^{\phi_I}}\kappa\,(\tau_1\Theta)^{\iota} \tag{8.42}$$

for $\Delta(\Sigma ij) > \Delta(\Sigma_{ij})$.

$$\frac{d\omega}{d\tau_1} = \frac{\Delta^{x_{II}}\,(\Sigma_{ij})}{V_{uTRAN}(1+\phi_{II})(1-\omega)^{\phi_{II}}}\kappa\,(\tau_1\Theta)^{\iota} \tag{8.43}$$

for $\Delta(\Sigma ij) \leq \Delta(\Sigma_{ij})$. where I and II indicate high and low stress material constants respectively. The same assumptions made in section 5.6 are applied here to model

the growth of damage in compressive stress situations using the equations (8.42) and (8.43).

The true creep strain values are given using equation (8.38) and the real time is given by:

$$t = \left\{ \frac{\Theta \tau_1 (m_1 + 1)}{K_1 E \sigma_0^{n_1 - 1}} \right\}^{\frac{1}{m_1 + 1}} \tag{8.44}$$

where the constants are those of the parent metal (subscripted (1)), which defines the base time scale given in Table 8.3(a), and $\Theta = 1.96758$. This implies that the creep strains and real times from the use of the $\hat{\hat{\text{c}}}$ostitutive and damage laws above, are obtained using:

$$V_{ij} = V'_{ij} \times 1.96758 \tag{8.45}$$

and

$$t = \left(11.1721 \times 10^3\right)^{1.25486} \tag{8.46}$$

Having incorporated all the developed constitutive theories for the weld modelling in the above four equations, future work may involve the simplification of these equations. The present work concentrates on the equations abilities to predict weld deformation and failure behaviour using the finite element method.

8.9.1 Initial Results From The Finite Element Solution For The First Weld Model.

A part of the first weld model (WM1) finite element mesh is shown in Fig. 8.24. This finite element mesh has 156 nodes and 261 elements. The regions coloured dark blue, light blue and green represent the parent metal, the heat affected zone and the weld metal of the circumferential steam pipe weld, having the material properties given in Table 8.3(a), (b) and (c) respectively. The first weld solution has a multi-axial rupture parameter value for the weld metal of ($\alpha = 0$) in accordance with Goodall [148], because experimental data is not available to determine the true (α) value. A colour damage contour plot is given from the finite element solution in Fig.8.25 showing the damage distribution, on the background of the finite element mesh of Fig.8.24, at a life fraction of 31.2%. The maximum damage zone occurs towards the inner surface of the pressure vessel weld in the heat affected zone. The maximum damaged zone emanates radially outwards from the inner bore along the heat affected

zone close to the fusion boundary and the first elements to fail ($\omega > 0.9999$) do so in the inner 1/3 of the wall thickness in the heat affected zone. This failure behaviour is not observed in practice, as the first signs of macroscopic damage or cracking are observed in the outer 1/3 of the weld metal. The predicted failure time of the structure from the finite element solution is 39,119 hours.

As there is no material data available for the multi-axial rupture criterion of the weld metal, it was thought that the (α) value chosen for the weld metal was in error. Another solution was performed using weld model (WM1) with (α) for the weld metal set to the same value as that for the heat affected zone material (i.e. $\alpha = 0.4298$). The damage distribution on the background of a displaced mesh at a life fraction of 90.0% is shown in Fig.8.26. The damage distributions for ($\alpha = 0$) gave a similar failure prediction as that for ($\alpha = 0.4298$). Though the former solution showed elements failing only in the heat affected zone, whereas the latter solution involved several elements also failing in the middle to outer weld metal region close to the fusion boundary. The failure time predicted for this weld model using a value of ($\alpha = 0.4298$) for the weld metal, is 39,002 hours.

Consideration of the lower stress creep curve fits for the heat affected zone material Fig.8.14(b), indicates that the constitutive equation fits to the lower stress data at the uni-axial test stress levels of 100 MPa and in particular 85 MPa are not good. Whereas the curves fitted to the higher stress data are reasonably good. The creep exponent (n) obtained from the curve fits is given as ($n = 1.3654$), which when substituted into the Bailey equations (8.15), (8.16) and (8.17) is shown to promote low stress redistribution, with a maximum steady state stress at the internal bore of the pressure vessel. The maximum stress occurring at the inner bore induces elements to fail here at the inner bore. As the heat affected zone spends most of its life at the lower stresses shown in Fig.8.14(b) it is important to obtain good constitutive equation fits to this data.

The heat affected zone of weld model (WM1) is 4 mm wide and is given the properties of the coarse grained simulated heat affected zone material (G.C.P.). In the real heat affected zone of the weldment this 4 mm zone incorporates the coarse grained and fine grained bainite regions, the intercritical and the overtempered zones. The coarse grained material is brittle in character with failure strain decreasing with

increasing stress; whereas from the results of Cane [109] for thermally simulated refined and doubly refined grain microstructures of the heat affected zone, much larger failure strains are observed in uni-axial tests, which increase and decrease respectively with increasing test stress level. The rupture ductility is seen to increase from the coarse heat affected zone, across the refined grain structures to the highest rupture ductility of the parent metal. Therefore, to truly represent the average properties of the heat affected zone materials only the low stress curves are used to give material constants (Fig.8.27) and the failure strains are adjusted to increase slightly up to the break stress of 180 MPa, consistent with the increasing rupture ductility of the refined heat affected zone material of Cane [109], termed refined parent metal (RP). The high stress material parameters are obtained from the stress-rupture and stress vs. minimum creep strain rate properties of the grain coarsened parent material (following the procedure of section 8.5.2 , with reference to section 2.6), having a rupture ductility behaviour dictated by the high stress values of (χ_I) and (n_I).

The resultant high stress rupture ductility using the new high stress constants is intermediate between that of the grain coarsened parent material and the refined parent material, having a slightly decreasing failure strain as the test stress increases. The new high and low stress material constants for the heat affected zone are summarised in Table8.3 (d), where the low stress creep exponent is given as ($n = 3.3685$) which is close to that of ($n = 4.0$) obtained by Cane [109].

Weld model (WM1) is re-solved using the new heat affected zone (HAZ(2)) material parameters, which are thought to be more representative of the average properties of the heat affeced zone material. The first solution has a multi-axial rupture criterion value of ($\alpha = 0$) for the weld metal of zero. The predicted failure time is 52,781 hours. The damage distribution close to failure at a life fraction of 99.9% is given in Fig.8.28. Failed elements elements ($\omega > 0.9999$) are observed in the weld metal, the heat affected zone and in the parent metal.

The damage distribution plots are contour plots using interpolation between nodal values, which are obtained from area averaged centroidal values. This averaging lowers the actual damage value shown in the contour plots slightly, but the dark red colour contour indicates the maximum damaged region and dark blue the least damaged region at any one life fraction. The dark red colour contour having a damage

value greater than about 0.8 shows the region where the material is totally ineffective to carry load and has failed through the formation of macrocracks. The elements of the finite element mesh in these regions are removed from the finite element solution. Therefore the red regions of the damage distribution diagrams having ($\omega > 0.8 - 0.9$) shows the locus of macrocracking in the pressure vessel wall.

A corresponding solution has been performed for ($\alpha = 0.4298$) for the weld metal. The corresponding damage distribution close to failure at a life fraction of 99.9% is given in Fig.8.29. Here the first elements failed ($\omega > 0.9999$) in the outer 1/3 of the weld metal close to the fusion boundary. Further elements fail as the maximum damage zone grows inwards along the fusion boundary, which is consistent with the experimental results. The predicted failure life is 47,247 hours, which may be compared with 46,000 hours life from the pressure vessel test of Coleman [133]. The results from the final computer solution for the weld model WM1 are discussed in more detail next, and comparisons are made with the experimental results.

8.9.2 Detailed Final Results From the Finite Element Solution For the First Weld Model And Comparisons With Experimental Results.

Here, detailed results are given with the use of colour contour plots. Where a figure has been omitted for brevity a detailed explanation of the omitted figure is given or a similar figure is referred to.

Figure 8.30 shows the distribution of damage early in the lifetime of the pressure vessel at a life fraction (t/t_f) of 0.12%. The maximum elastic stress components for the pipe are initially greatest on the inner bore (Fig.8.20), so causing the initial damage rates to be highest at this location. This causes damage to grow most rapidly in that region and subsequently causes stress redistribution across the section.

The damage distribution at a life fraction of 45.2% shows that the damage distribution in the weld is now more uniform across the pipe section, with the maximum damaged region occuring along the fusion boundary between the weld metal and the heat affected zone.

The damage distribution of a life fraction of 63.5% shows the width of the most damaged zone (red) on the fusion boundary has become wider and more intense

in the outer 1/3 of the weldment.

Figure 8.31 shows the damage distribution at a life fraction of 77.2%. The maximum damaged zone on the fusion boundary close to the outer surface of the pipe bulges and becomes still more intense in the region of damage ($\omega > 0.303$).

Figure 8.32 shows the damage distribution now at a life fraction of 80.8%. The damage now localises in the same region noted in the previous figure, close to the outer surface of the pressure vessel. The centroid of the damaged zone has moved slightly off the fusion boundary into the weld metal.

Figure 8.33 shows the damage distribution at a life fraction of 87.0%. The intense damage on the fusion boundary now propagates both inwards and outwards towards the pipe surface.

The damage distribution at a life fraction of 99% shows that the region in the previous figure which had undergone the most intense damage now has a damage level in the region of 0.5 to 0.7. The damaged zones either side of this region and in a zone closer to the inner bore of the pipe, on the fusion boundary now have higher damage levels, which suggests that stress redistribution has occurred from the most damaged region of Fig.8.33; causing damage evolution at higher rates outside this region.

Figure 8.29 shows the damage distribution at a life fraction of 99.9% and shows the coalescence of the most damaged zones (described in the previous paragraph) into two main localized damaged regions.

Figure 8.34 shows the original axisymmetric finite element mesh of weld model (WM1) with a superimposed deformed mesh at a life fraction of 77.2%. It shows how the weld metal has less resistance to creep deformation under the action of the internal pressure. The predicted characteristic bending and bulging of this 2.25Cr 1Mo weldment at failure may be compared with the badly cracked and bulged radial section taken through the pressure vessel at failure shown in Fig.8.8.

Figure 8.35(a) shows the damage distribution very close to failure. Failure is through the formation of localised macrocracking in this (red) band of intense damage along the fusion boundary. The finite element solution at this point becomes numerically stiff as a result of extremely large strain rates present due to high section stress across the small remaining ligament length. The finite element program

automatically chooses infinitely small time steps at the point of breakage and the solution does not progress further. As the time of breakage is very small the failure time of the structure is taken as that corresponding to this figure ($t_f = 47,247$ hours). It is noted that the most damaged zone (in red) closest to the outer surface of the pipe spreads into the weld metal.

The prediction of macrocracking by the most damaged region of Fig.5.35(a) may be compared with the micrograph of a radial section taken from the failed pressure (Fig 5.35(b))
vessel, courtesy Coleman C.E.G.B, showing the formation of a deep circumferential weld metal crack. Comparison may also be made with another more badly cracked section from a locally bulged region of the pressure vessel Fig.8.8 where some damage is also seen in localized regions of the heat affected zone.

The following seven, colour, normalised stress contour plots of Fig.8.36 to 8.42 are for a life fraction of 77.2%, taken just prior to the first element failure ($\omega > 0.9999$) and have a corresponding damage distribution given in Fig.8.31. All stress values are normalised by ($\sigma_0 = 45.5MPa$).

Figure 8.36 shows the distribution of the normalised radial stress in the pressure vessel weldment. The maximum compressive stress occurs on the inner bore and is equal in magnitude to the internal pressure. The stress discontinuity across the heat affected zone is observed.

Figure 8.37 shows the axial components of the normalised stress, where the inner dark blue region at the inner bore of the weld metal and heat affected zone is compressive, showing the presence of localized bending in the weldment. The maximum tensile stress is at the surface of the vessel in the heat affected zone and local parent metal.

Figure 8.38 shows the axial/radial normalised shear stress distribution in the weldment, where a concentration of shear stress in the region of the weld metal close to the fusion boundary is observed. Towards the inner bore of the pipe, dark blue and blue regions show negative shear stresses and towards the outer bore the red regions show positive shear stresses of approximately the same magnitude. The diagram clearly shows the highly localised nature of the shear stress across the section.

Figure 8.39 shows the distribution of the normalised hoop stress in the weldment. It is noticed that all the stresses are positive, but that the stresses in the weld

metal are typically one half of those in the parent metal with a very abrupt change taking place across the fusion boundary. This arises due to the differences in the creep characteristics of the weld metal and the parent metal, the weld metal having a ductility of the order of 12% in comparison with that for the parent metal of about 5% at a uni-axial stress level of 100 MPa ($\sigma/\sigma_0 = 2.2$). The difference in the material properties results in this severe stress redistribution out of the weld metal into the heat affected zone and parent metal. The maximum hoop stress is observed to be in the heat affected zone and the parent metal at the outer surface of the pipe.

Figure 8.40 shows the normalised Von Mises stress distribution in the weldment. It is observed that within all regions of the weldment the Von Mises stress is highest at the inner bore and least at the outer outer. The stress is seen to peak at the boundary between the heat affected zone and the parent metal at the inner bore. Again a dramatic stress gradient occurs in the heat affected zone and across the fusion boundary.

Figure 8.41 shows the normalised maximum principal stress (P1) variation in the weldment. Note that this graph is very similar to that of the hoop stress (c.f. Fig.8.39); this is not surprising since the maximum principal stress is close to the hoop stress.

Figure 8.42 shows the normalised effective strain distribution in the weldment. This shows the differences in the creep deformation occurring in the weld metal in comparison with that in the parent metal. Note the vertical step in the contours which highlights the discontinuity in shear stress across the fusion boundary and hence relates to the localized bulging that takes place in the pipe. The maximum effective strain occurs at the at the bore of the pipe in the weldmetal.

Figure 8.43 shows the distribution of the normalised hoop stress at a life fraction of 99.9%, having a damage distribution given by Fig.8.29. This figure shows that very little stress is carried by the weld metal region extending about 2/3 across the wall thickness from the outer bore, due to complete material failure in the blue and dark blue regions through the formation of macroscopic cracks. Thus the parent metal and remaining inner weld metal still sustain the stresses.

Figure 8.44 shows the distribution of the normalised axial stress at a life fraction of 99.9%. The figure shows that there are two concentrated regions of stress on

the fusion boundary at the tips of the most damaged regions of Fig.8.29. These severe stress concentrations induce speedy creep crack growth across the ligament resulting in vessel failure.

Figure 8.45 shows the variation of the surface hoop strain with test time, close to the weld in the parent metal measured from the diametrically opposite creep pips. These strains are compared with those predicted from the finite element solution. The predicted strains are calculated from the radial displacement of a node of the finite element mesh approximately situated at the same position on the pressure vessel as the creep pips.

Figure 8.46 shows the variation of the surface hoop strain with test time, at the weld centre line, measured from the capacitance strain gauge. These strains are compared with those predicted from the finite element solution. The predicted strains are taken from a finite element in the pressure vessel mesh at the location of the capacitance gauge.

Figure 8.47 shows the variation of the surface axial strain with test time, across the weld, measured from the creep pips. The strains are again compared with those predicted from the finite element solution.

Figure 8.48 shows the variation of the surface axial strain with test time, at the weld metal centre line, measured from the capacitance gauge; which is compared with the strains predicted from the finite element solution.

The predicted creep pip strains from the finite element solution (Figs.8.45 and 8.47) compare very well with the experimental results up to a test time of 30,000 hours where the predicted tertiary creep strains deviate from the experimental curves. These deviations are due to large deformations and rotations occurring due to geometry changes in the pressure vessel caused by tertiary creep damage accumulation during the test, which cannot be modelled by the small strain finite element analysis solution used in the weld model. The predicted strains are therefore lower than the experimental.

The predicted capacitance gauge strains from the finite element solution (Figs.8.46 and 8.48) compare reasonably well with the experimental results. Though the predicted secondary creep hoop strains (Fig.8.46) are larger than those of the experiment. Again the predicted tertiary creep strains are smaller than the experimental strains

because the model uses a small strain analysis.

Figure 8.49 shows the predicted surface hoop strains measured on the parent metal pipe section of the weldment corresponding to creep pip and capacitance strain gauge measurements. Here no comparison is made with experimental data. The hoop strains are observed to be of a similar size to the predicted surface hoop strains at the weld (Figs.8.45 and 8.46), and also have similar secondary creep region gradients; consistent with the compatibility of the hoop strain rates along the outer surface of the weld metal and the parent pipe detailed by Coleman et al [131], from the pressure vessel test. Though the strain time plots look fairly linear, a primary region does exist below about 3 to 4 thousand hours test time, and the secondary region does turn upwards slightly showing a tertiary creep region.

Figure 8.50 shows the predicted surface axial strains for the parent metal pipe section of the pressure vessel corresponding to both creep pip and capacitance strain gauge measurements. Reasonable agreement is obtained between predicted creep pip and capacitance gauge strains. The graph indicates that the axial creep strain rate in the parent metal is approximately zero throughout the life of the pressure vessel until the last 10% of life, where compressive strains occur possibly due to bending as a result of severe bulging in the damaged weld. Which is consistent with the experimental findings of Coleman et al [133, 131].

Figure 8.51 shows predicted normalised hoop stress distributions along the inner bore of the welded pressure vessel at various life fractions. Initially at $(t/t_f = 0)$ a uniform stress of $(\Sigma_\theta = 2.5)$ is present in the weld metal, heat affected zone and the parent metal. As time progresses stress is redistributed from the weld into the heat affected zone. Stress is also redistributed from all the material zones at the inner bore towards the outer surface of the pressure vessel, which is seen as the gradual decrease in the stress levels with time in all the zones below the initial elastic stress level at $(t/t_f = 0)$. Close to failure $(t/t_f \approx 99.9\ \%)$ the hoop stresses at the internal bore increase because of the growth of circumferential cracks from the outer diameter increasing the net section stress. Close to failure the parent metal carries the maximum hoop stress at the pipe bore.

Figure 8.52 shows predictions of the normalised hoop stress with axial distance along the outer surface of the pressure vessel at various life fractions. The initial elastic

stress distribution is uniform across all the zones of the weldment($\Sigma_\theta = 1.5$). As time progresses creep stress redistribution occurs from the weld metal to the heat affected zone, causing the peak stress to occur in the heat affected zone. Redistribution of the elastic stresses from the internal bore of the pressure vessel towards the outer surface raises the level of the stresses in all zones with time until significant creep damage occurs in the weld metal close to the fusion boundary ($t/t_f > 87.0$ %), after which the materials at the outer surface of the pipe (in particular the weld metal) offload stress towards the inner bore.

Figure 8.53(a) and (b) shows the distributions of the normalised hoop stress along the fusion boundary of the weldment (Fig.8.9) at various life fractions. The abscissa represents distance along the fusion boundary moving, left to right, from the internal surface to the external surface of the pipe. The elastic stress distribution is shown as the dotted line in Fig.8.53(a). The elastic stress is seen to redistribute very quickly to an almost horizontal uniform distribution within 56 hours ($t/t_f = 0.12$ %). As time progesses and stresses redistribute further a maximum stress, above the initial elastic stress level, occurs approximately 10 mm under the surface of the pipe. It is noticed that the surface stress remains almost constant until elements with damage ($\omega > 0.9999$) are removed from the finite element mesh at the fusion boundary (Fig 8.29), when the distribution of stress (Fig.8.53(b)) drops to zero as further elements are removed, modelling the inward growth of a large circumferential crack from the outer surface of the pipe. It is noticed that the first element to fail at the fusion boundary is approximately 10mm inward of the outer surface in the region of maximum hoop stress (see curve at $t/t_f = 80.0$ %). As elements fail the net section stress close to the inner bore of the pipe increases.

Fig.8.54(a) and (b) show the normalised radial stress distribution along the bottom boundary of the finite element mesh (Fig.8.9) for various life fractions. The bottom boundary of the finite element mesh corresponds to the centre line of the weld metal. The abscissa represents radial distance; ($R = 0$) is the internal diameter of the pipe and ($R = 60$) the external diameter. The elastic stress distribution is shown as the dotted line Fig.8.54(a), where the stress at the inner bore of the pipe is equal and opposite to the normalised internal pressure (Po) and the stress at the outer surface is zero. The stress increases uniformly across the weld metal centre line until close to

failure (t/t_f >87.0%).

Figure 8.55 (a) and (b) show how the stresses in the axial direction redistribute with time along the weld metal centre line, (Fig.8.24). The initial elastic stress distribution is uniform across the section ($\Sigma_z = 0.75$). The stresses subsequently redistribute with time giving a maximum stress close to the outer diameter of the pressure vessel. As fully damaged ($\omega > 0.9999$) elements are removed from the solution unloading occurs under the most damaged regions of the weldment. (See curve $t/t_f = 100\%$ and the damaged zones of Fig.8.35(a)).

Figure 8.56 (a),(b) and (c) show how the normalised stresses in the hoop direction are redistributed along the the weld metal centre line for various life fractions. The initial elastic stress distribution is shown as a dotted line Fig.8.56 (a). Again the elastic stress redistributes quickly with time giving a maximum stress at the outer diameter of the pressure vessel. Fig.8.56(b) clearly shows the existence of a skeletal point approximately 20 mm from the internal diameter of the pipe, where the stress remains stationary at a value of ($\Sigma_\theta = 1.2$), whilst stress from the outer 2/3 of the pipe wall thickness redistributes to the inner 1/3 of the pipe wall, as creep damage propagates from the outer diameter inwards. Finally the stress increases at the inner section of the pipe as the circumferential cracking grows inwards across the pipe ligament.

8.10 Results From The Finite Element Solution For The Second Weld Model.

This weld model (WM2) has three material zones namely the parent metal, the heat affected zone material and the weld metal, represented as the dark blue, blue and green regions respectively in Fig.8.57. The material parameters used for each region are the same as those used in the previous weld model (WM1) and are given in Table8.3(a), (c) and (d) respectively. Figure 8.57 shows a more refined mesh in comparison with that of weld model (WM1) Fig.8.24. The mesh (Fig.8.57) has 350 nodes and 637 elements. The damage distributions for weld model (WM2) presented on the background of the finite element mesh are given at fractions of the lifetime in Figs.8.58 to 8.62(a). Distinct similarities in the damage distribution are noticed with those of weld model (WM1) given in figures 8.30 to 8.33; and Fig.8.35(a) at

failure. Figure 8.58 shows a similar damage distribution to that of weld model (WM1) Fig.8.30. The highest damage region Fig.8.58 (red) towards the inner bore of the pipe in the weld metal causes stress to re-distribute radially towards the outer surface giving a more even damage distribution in the weld metal Fig.8.59. Stresses are also re-distributed along the heat affected zone from the inner bore outwards, causing the maximum damaged region (Fig.8.59 coloured red) to move along the heat affected zone Fig.8.60. The peak stress is now at the outer bore of the pipe in the heat affected zone which initiates high damage growth in the outer 1/3 of the weld metal and the heat affected zone - along the fusion boundary. This initiates an inward growing highly damaged region along the fusion boundary Fig.8.61. These figures in comparison with those of weld model (WM1) show similar trends in damage distribution, but the damaged zones are more localized due to the increased mesh refinement. The maximum damaged zone at a life fraction of 99% is shown in Fig.8.62(a), which predicts the growth of a circumferential crack in the weld metal close to the fusion boundary, which is compared with the radial section through the failed pressure vessel weld (Fig.8.62(b)). It is noticed that instead of the two failed element regions ($\omega > 0.9999$) observed in weld model (WM1) shown in figure 8.29, this weld model predicts one circumferential failed region, (as with the fine mesh it is possible to define more accurately the damage location).

The solution again became numerically stiff as the circumferential damage crossed the mesh ligament close to failure, requiring infinitely small time steps to progress the solution. The predicted failure time is therefore slightly greater than 43,882 hours. This is compared with the actual failure time of the pressure vessel test by Coleman [133] of 46,000 hours (Table 8.1)

Distributions of the normalised stress components in the radial(R), axial(Z), shear(RZ) and hoop(θ) directions given in Figs.8.63, 64, 65 and 66, respectively, and show the same features as the corresponding distributions for weld model (WM1) shown in Figs.8.36, 37, 38 and 39, respectively, at a similar life fraction of approximately 80%. The distributions of the normalised Von Mises stress, the maximum principal stress and the effective strain for weld model (WM2) at a similar life fraction also show similar features to the distributions for weld model (WM1) given in Figs.8.40, 41 and 42, respectively, except that the stress distributions for (WM2) are

more localised and the peak stresses are slightly larger, as a result of the increased mesh refinement. The comments made for the stress distribiutions for weld model (WM1) hold true for the stress distributions obtained from weld model (WM2).

Figure 8.67 shows the distribution of the normalised hoop stress in the weldment at a life fraction of 99%, having a corresponding damage distribution given by Fig.8.62(a). The red zone of Fig.8.67 shows the severity of the stress concentration at the tip of the circumferentially cracked region of Fig.8.62(a). The heat affected zone running parallel with the highly damaged region sustains a high level of hoop stress. Figure 8.68 shows the distribution of the normalised axial stress in the weldment also at a life fraction of 99%. The red zone shows the axial stress concentration (Fig.8.67), which is of a similar magnitude to the hoop stress concentration ($\Sigma_z \approx \Sigma_\theta = 3.2$) at the tip of the most intensely damaged zone of Fig.8.62(a). The maximum stressed region (red) in the axial direction is sustained almost in equal proportions by both the heat affected zone and the weld metal. Figures 8.67 and 8.68 for weld model (WM2) may be compared with Figs.8.43 and 8.44 for weld model (WM1), where two stress concentrations are observed at the tips of the most damaged regions, caused by a small region at the centre of the mesh at the fusion boundary remaining unfailed. The axial compressive stress in the dark blue region Fig.8.68 at the inner bore of the pipe in the weld metal, shows the effects of bending as the pipe bulges outwards at failure.

Hoop creep strain predictions at the weld are compared with the measured strains from the pressure vessel test in Fig.8.69 and 8.70. The comparison between the predicted and experimental strains corresponding to the creep pip measurements is observed to be good (Fig.8.69). The predicted hoop strains at the weld centre line corresponding to the capacitance strain gauge measurements (Fig.8.70), overestimate the size of the measured secondary creep strains . The axial creep strain predictions at the weld are compared with the measured strains from the pressure vessel test in Figs.8.71 and 8.72. The predicted and experimental strains corresponding to both the creep pip and capacitance strain gauge measurements compare well. The tertiary creep strains in all the predictions are noticed to be smaller than the experimental strains because the weld model uses a small deformation analysis. The hoop and axial strains predicted from the finite element analysis corresponding to both creep pip and

capacitance strain gauge measurements are shown in Figs.8.73 and 8.74. Figure 8.74 shows that predicted the axial strain in the parent metal corresponding to the creep pip measurements is effectively zero, until damage in the weldment causes bending and compressive strains close to failure. Though the local strain values from an element at a corresponding point in the finite element to where the capacitance strain gauge is situated indicates slight tensile strains are present close to failure at this location, but the strains are small of magnitude (< 0.04 %) and are effectively zero. Figures 8.69 to 8.74 may be compared with those for weld model (WM1), Figs.8.45 to 8.50, respectively, and are observed to be similar.

Figures 8.75 and 8.76 show the predicted normalised hoop stress distributions with life fraction (t/t_f) along an axial line on the inner bore and the outer surface of the pressure vessel weldment (Fig.8.9), respectively. Stress redistributes from the weld metal into the heat affected zone and from all the weld zones from the inner bore towards the outer surface through the pipe wall. Figures 8.75 and 8.76 show similar features to those of weld model (WM1) Figs.8.51 and 8.52, except that steeper stress gradients across the heat affected zones are observed for weld model (WM2), which is evidence of an improved finite element mesh representation, giving superior results to those of weld model (WM1).

Figures 8.77(a) and (b) show the predicted redistribution of the normalised hoop stress along the fusion boundary with life fraction. The initial elastic stress distribution, shown as the dotted line, redistributes giving a stress distribution with a peak stress close to the outer surface of the pressure vessel. As elements fail ($\omega > 0.9999$) in the outer weld metal close to the fusion boundary, the stress in the outer region of the fusion boundary is reduced to zero (Fig.8.77(b)). Stress distributions close to failure show how the peak stress at the tip of the circumferentially cracked zone moves towards the inner surface of the pipe and increases in height, as the crack grows forwards along the fusion boundary. Slight variations in the stress distributions may be due to some mesh dependency.

Figures 8.78, 8.79 and 8.80 show the distributions of the computer predicted normalised radial, axial and hoop stresses along the weld metal centre line with life-fraction respectively. Figures 8.78 to 8.80 may be compared with those of weld model (WM1) of Figs.8.54 to 8.56 respectively which are seen to be similar. Note that in

(Fig.8.80) insufficient graphical plots at different life fractions have been presented to identify the skeletal stress point, shown in (fig.8.56).

8.11 Obtaining Material Parameters To Model The Behaviour Of the Weld Metal Coarse And Fine Grained Bainitic Regions.

No experimental uni-axial creep test data is available for the coarse and fine grain bainitic regions of the weld metal (Fig.8.10). The as-cast weld metal has a coarse columnar grained bainitic structure, which is tempered by subsequent weld beads giving a coarse and fine equiaxed bainitic structure (Fig.8.10(a)). For simplicity and the lack of experimental creep data, the microstructural regions of the weld metal will be considered to be fine or coarse grained bainitic regions (Fig.8.10(b)).

The material constants for the fine grained bainite regions of the weld metal are taken to be those previously determined from the creep tests of the weld metal containing both coarse and fine grained bainite regions, and are given in Table 8.3(c). This is a reasonable approximation as the welding parameters used in the construction of the weld are arranged to produce 80% fine grain bainite and 20% coarse grain bainite in the weldmetal; Coleman [133].

The material parameters for the coarse grained bainite regions of the weld metal are calculated using the uni-axial creep data of Cane [109] for coarse and fine grained heat affected zone microstructures, to scale the fine grained weld metal creep data. The uni-axial creep data for the simulated coarse grained heat affected zone material is given in Table 8.2 and by the material parameters of Table 8.3(d); and the creep data for fine heat affected zone material is given in Table 8.6.

The fine grained heat affected zone data is plotted on both stress-rupture diagrams and the stress vs. minimum creep rate diagrams in figures 8.81 and 8.82, respectively. Lines, parallel to the coarse grained heat affected zone lines, are drawn through the fine grained heat affected zone points on both diagrams. The distances between the coarse grain heat affected zone lines and the derived fine grain heat affected zone lines are used to judge how to translate the lines of the fine grained weld metal, to give lines representing coarse grain weld metal creep data. The translations of the fine grained weld metal lines in each diagram are adjusted so that the break

stress point is the same for both stress-rupture and stress vs. minimum creep rate diagrams. The choice of the lines was not easy, due to the difference in gradients between the heat affected zone and the weld metal lines. The final stress-rupture and stress vs. minimum creep rate lines chosen for the coarse grained weld metal are shown as the solid lines in Figs.8.81 and 8.82, respectively. Both pairs of lines have a break stress of ($\hat{\sigma} = 125$ MPa), ($\hat{\Sigma} = 2.747$). As the new lines for the coarse grain weld metal have the same gradients as the fine grain weld metal lines, the same values of (n), (m), (ι), (χ) and (ϕ) can be used for the coarse grain weld metal as for the fine grain weld metal. New values of (K), (M), (V_u) and (κ) are calculated using the new break stress for the coarse weld metal, which defines the translation of the fine grain weld metal lines. The stress-rupture lines of the fine grain weld metal are translated vertically from a break stress of 100 MPa to that of 125 MPa. The stress vs. minimum strain rate lines are translated both vertically and horizontally to have a break point also at 125 MPa, with a strain rate of 1.25 ($\mu\epsilon h^{-1}$) at the break point. From the positions of the new break stress points in each diagram (Figs.8.81 and 8.82) values of (M_{II}) and (K_{II}) are calculated, using failure time and strain rate relationships, respectively, for the low stress data. High stress values of (M_I) and (K_I) are obtained using equations (2.47) and (2.37) respectively. The material parameters for the coarse grained bainitic regions of the weld metal are given in Table 8.3(e). The value of (α) defining the multi-axial rupture criterion for the coarse grained weld metal is taken as that used for the fine grained weld metal ($\alpha = 0.4298$). Failure strain calculations are performed to check that the rupture ductility of the material model for the coarse grained weld metal is reasonably in line with expected rupture ductility behaviour of the coarse grained bainite material, which should be more creep brittle than the softer fine grained bainite,(Coleman [149]). At a stress of 100 MPa the coarse grained bainite has a rupture ductility a factor of approximately 5 times smaller than that of the fine grained bainite, using the material parameters of Table 8.3(e) and (c) respectively in equation (3.4) at ($t = t_f$). This is consistent with the relative rupture ductilities of the coarse grained and fine grained heat affected zone microstructures at a test stress of 100MPa (see Table 8.6 and Table 8.2); having on-average ductilities in the ratio 1:4.7 respectively.

8.12. Results From The Finite Element Solution For The Third Weld Model (WM3).

This weld model is a four material model, where the parent metal, the heat affected zone and the weld metal coarse and fine grained bainite regions are represented respectively as the dark blue, blue, brown and green regions of the finite element mesh shown in Fig.8.83. The coarse and fine grained regions of the weld metal are assumed to have the same multi-axial rupture behaviour as the average weld metal used in weld models (WM1) and (WM2),(i.e. $\alpha = 0.4298$). The material parameters used for each material zone are given in Table 8.3 (a), (c), (d) and (e). The finite element mesh used has 747 nodes and 1374 elements. The results from the finite element creep continuum damage analysis are summarised as follows:

Figure 8.84 shows the distribution of damage at a life fraction of 0.73% against the background of the finite element mesh (Fig.8.83). The damage distribution is observed to be similar to that of (WM1) and (WM2) Figs.8.30 and 8.58, except that more intense damage is seen in the locality of the coarse grained weld metal.

Figure 8.85 shows the damage distribution at a life fraction of 44%, where due to stress redistribution from the inner bore of the pipe, the damage spreads along the heat affected zone and also through the weld metal towards the outer surface of the pipe.

Figure 8.86 shows the damage distribution at a life fraction of 32.0%. Now the damage grows most rapidly in the coarse grained bainite regions of the weld metal close to the outer surface, due to the stress redistribution which has occured towards the outer surface. This correlates with observed transverse weld metal cracking in the coarse columnar regions of the outermost weld beads, which initiate at a life fraction of 43% in the pressure vessel test (Table 8.1 and Fig.8.4). Note also the high levels of damage on the inner bore of the heat affeced zone.

Figure 8.87 shows the damage distribution at a life fraction of 66.0%. The damage distribution is similar to that of Fig.8.86, but damage values are now much higher. The rate of damage growth now is noticed to be much faster in the coarse grain weld metal than in the heat affected zone at the inner bore, as a result of the stress redistribution from the bore to the outer surface of the pipe.

Figure 8.88 this figure shows the damage distribution at a life fraction of

86.2%. The damage in the coarse grain bainite region of the weld metal at the outer surface has intensifield in a region close to the fusion boundary. This region of intense damage may be identified as the place where the growth of an inwardly growing circumferential macro-crack initiates in the weld metal. Circumferential cracks are observed to initiate at a life fraction of 76% in the pressure vessel test (see Table 8.1 and Fig.8.6).

Figure 8.89 shows the distribution of damage at a life fraction of 89.5%. The regions of maximum damage in the coarse grain bainite regions of the weld metal move closer to the fusion boundary.

Figure 8.90 shows the original mesh in green and the displaced mesh geometry at a life fraction of 89.5% showing the bending in the weldment as the weldment bulges outwards.

Figure 8.91(a) shows the distribution of damage at a life fraction of 99.9%. Failure of the weldment is observed in the coarse grained bainite regions of the weld metal; namely: in the outer weld bead and close to the fusion boundary. Though some local failures do occur further in-board. It is noticed that the highly damaged regions of the coarse grained bainite close to the fusion boundary link, through the slower damage growth in the fine grained bainite between these regions, to form a large jagged circumferential crack. The damage distribution is compared with a radial section through the pressure vessel weldment at failure (Fig.8.91(b)). Localised damaged zones are also observed in the weld metal of Fig. 8.91(b) and circumferentially inward growing cracks are seen to divert along coarse grained structures, perpendicular to the circumferential growth direction of the main crack in the weldment.

The finite element solution again became stiff, at a time of 33,433 hours. The predicted lifetime of the structure is therefore taken as slightly greater than 33,433 hours, which is compared with the life of the pressure vessel test of 46,000 hours. The life prediction for (WM3) is not good in comparison with the predictions of weld model (WM1) and (WM2) which are close to the real life of the structure. Though, the damage distributions obtained seem to predict the failure history of the pressure vessel extraordinarily well. The failure prediction may be improved if actual creep data and multi-axial stress rupture data were available for the weld metal coarse and fine bainitic regions.

Figure 8.92 shows the distribution of the normalised radial stress at a life fraction of 66.0%, which is observed to be similar to that of weld model (WM2) Fig.8.63.

Figure 8.93 shows the distribution of the normalised axial stress at the same life fraction. Here, stress concentrations are observed in the outer weld metal coarse grain bainitic regions and in the outer heat affected zone and local parent metal.

Figure 8.94 shows the distribution of the normalised radial/axial shear stress also at a life fraction of 66%, where similar shear zones are observed to those in weld model (WM2) Fig.8.65, except the red positive shear zone has been dispersed in a wider more jagged zone through the outer weld beads, as a result of the inclusion of the coarse and fine weld metal zones in the weld model.

Figure 8.95 shows the normalised hoop stress distribution at a life fraction of 66.0% which is observed to be similar to that of Fig.8.66 for the weld model (WM2), except a moderate stress concentration is observed in the outer coarse weld metal regions. The Von Mises stress distribution for weld model (WM3) is given in Fig.8.96 at a life fraction of 66.0% and is also observed to be similar to that of weld model (WM2) except for stress concentrations occurring in the coarse regions of the weld metal.

The distributions of the normalised Von Mises stress, the maximum principal stress and the effective strain at a life fraction of 66% are given in Figs 8.96 to 8.98, respectively. These figures show similarities in comparison with the corresponding plots for (WM1), (Figs.8.40 to 8.42), except that the stress distributions are more localised, particularly across the heat affected zone. Stress is also observed to concentrate in the localities of the coarse grained bainitic regions of the weld metal.

Figure 8.99 shows the normalised hoop stress distribution at a life fraction of 99.9% . Here the stress concentration is shown, at the tip of the circumferential damaged zone, which has grown along the weld metal close to the fusion boundary (Fig.8.91(a)). The stress concentrates in the heat affected zone, spreading along the remaining ligament length of the pressure vessel pipe. This figure is compared with that of weld model (WM2) Fig.8.67 where the stress concentration is seen to be much more localised.

Figure 8.100 shows the distribution of the normalised axial stress also at a life

fraction of 99.9%. Here the coarse grain weld metal zones carry most of the stress off-loaded from the failed ($\omega > 0.9999$) regions in the outer half of the weld metal. This figure may be compared with that of Fig.8.68 for weld model (WM2) where the stress concentration at the tip of the circumferential damaged zone close to the fusion boundary is observed to be similar but is more localised. The red columnar zones in Fig.8.100 show that the coarse grained weld metal sustains most of the axial stress ahead of the circumferential crack-tip.

Figure 8.101 shows a local positive normalised radial stress concentration at the tip of the circumferential crack close to the fusion boundary, at a life fraction of 99.9%.

The predicted hoop strains at the weld corresponding to the creep pip and capacitance strain gauge measurements for weld model (WM3) are similar to those for weld model (WM2), (Figs.8.69 and 8.70), except the strain/time curves terminate at the predicted lifetime of 33,433 hours.

The predicted axial strains at the weld corresponding to creep pip and capacitance gauge measurements from (WM3) are similar to those for weld model (WM2), (Figs.8.71 and 8.72), except the strain/time curves terminate at the predicted lifetime of 33,433 hours. Here the axial strains are approximately 50% of the experimental values throughout the secondary creep region. This is caused as a result of the coarse grained regions of the weld metal having a ductility approximately 5 times smaller than the fine grained regions in the model, which effectively decreases the average ductility, and hence the creep deformation, of the weld metal in the joint. These weld strain comparisons indicate that, for better weld model predictions, the actual creep deformation and failure properties of the weld metal coarse and fine zones must be obtained by laboratory tests on these isolated microstructures and used within the weld model.

The predicted hoop and axial strains at the surface of the parent metal pipe sections corresponding to the creep pip and capacitance strain gauge methods measurements are similar to those of weld model (WM2), (Fig.8.73 and 8.74), except the strain/time curves terminate at the predicted lifetime of 33,433 hours. The predicted axial strains were positive and less than (0.01 %). Therefore axial strain is effectively zero, which is in agreement with experiment. As the weldment fails the predicted

axial creep strains corresponding to the creep pip measurements become negative, due to bending in the pressure vessel caused by the weld metal bulging outwards as a result of the propagation of the inwardly growing circumferential crack, but the strain still remains small (< -0.05 %), and is effectively zero.

Figures 8.102 and 8.103 show distributions of the normalised hoop stress along axial lines at the inner bore and the outer surface of the pressure vessel respectively. Similar stress redistribution is observed to that of weld models (WM1) and (WM2), (c.f. Figs.8.51, 8.52 and 8.75, 8.76, respectively) in that stress is off-loaded from the weaker weld metal into the harder heat affected zone material. Stress is also redistributed from all the zones radially from the inner bore to the outer surface of the vessel, which is observed in the decreasing height of the stress distribution ($0 < t/t_f <$66.0%) in Fig.8.102 and the increasing height of the stress distributions ($0 < t/t_f <$66.0%) in Fig.8.103. Close to failure the failed regions of the weld metal carry zero stress (Fig.8.103, $t/t_f =$ 96.8%), and some stress is redistributed towards the inner bore of the pipe (Fig.8.102, t/t_f=96.8%).

Figures 8.104 (a) and (b) show the distribution of normalised hoop stress along the fusion boundary of the weld at various life fractions. The initial elastic stress distribution ($t/t_f = 0$) redistributes with time; the maximum stress occurring at the outer surface of the pressure vessel. The stress distributions become uneven, as stress concentrates in the coarse grained regions of the weld metal. As failure of the weld metal occurs in the outer regions of the coarse grained weld metal the stresses drop to zero, off-loading stress to the local fine grained weld metal regions (Fig.8.104(b)).

Figures 8.105 (a) and (b) show the redistribution of the normalised radial stress along the centre line of the weld with life fraction. Similar stress distributions are produced to those of weld model (WM1) and (WM2), (c.f. Figs.8.54(a), (b) and Figs. 8.78(a), (b), respectively), except the distributions are uneven due to the inhomogeneity of the weld metal.

Figures 8.106 (a) and (b) show the redistribution of the normalised axial stress along the centre line of the weld with life fraction. Similarities are again observed between these stress distributions and those of weld models (WM1) and (WM2), (Figs. 8.55(a), (b) and 8.79 (a), (b), respectively). It is clearly seen that the maximum

stresses are carried by the coarse grained regions of the outer weld metal (see line $t/t_f = 66.0\%$). Close to failure compressive axial stresses are produced close to the inner bore of the pipe showing the presence of bending.

The normalised hoop stress distributions along the centre line of the weld Fig. 8.107 (a) and (b) again show similar trends to the axial stress distributions of weld model (WM1) and (WM2), (c.f. Figs. 8.56(a),(b),(c) and Figs.8.80 (a), (b), respectively).The hoop stress distributions (Figs.8.107) show similar trends to the axial stress distributions (Figs.8.106 (a) and (b)) except the stresses are generally larger in the hoop direction and compressive bending stresses are not observed at the pipe bore, although lower hoop stress values are observed here.

8.13 Discussion.

The developed axisymmetric weld models have been shown to predict both the deformation and failure history of the full size pressure vessel weldment test of Coleman et al [131] reasonably well. The results available for these finite element studies have been presented for each weld model in a systematic manner throughout the life of the weldment. It is thought by the author that this comprehensive study will provide the basis for other researchers to observe the complicated interactions of each different weld material zone within the weldment. It is only through a complete understanding of the different properties of each material zone, the stress states present and how these stress and damage fields redistribute with time, that new design methodologies for welded components may be formulated. As it is difficult to measure through thickness variations in stress, strain and damage in real welded components under high temperature service conditions, the finite element modelling of welded structures becomes an important tool to facilitate this understanding.

The weld models have shown that initially the maximum damaged region is at the inner bore of the weld metal and heat affected zone. The elastic stress from the softer weld metal off-loads into the harder heat affected zone and from every zone radially from the pipe inner diameter to the outer surface. The weld metal damage distribution becomes more even over the radial section; but damage concentrations are still present in the heat affected zone, which subsequently spreads out along the fusion boundary as the stresses redistribute. The maximum hoop and axial stresses

during secondary creep occur at the outer surface of the pressure vessel. Damage now concentrates in the outer 1/3 of the weld metal close to the fusion boundary. The damage intensifies here until elements are forced to fail ($\omega > 0.9999$). This damaged zone then grows inwards through the pipe wall raising the ligament stresses ahead of the circumferentially damaged region close to the fusion boundary, which elongates showing how a large circumferential crack propagates radially through the weld metal causing the subsequent failure of the vessel.

From the colour plot of Fig.8.65 two large (radial/axial,R/Z)-shear stress zones are observed in the weldment. The dark blue zone represents a region of negative shear in the heat affected zone at the inner half of the pressure vessel wall. The red zone represents a region of positive shear, close to the fusion boundary in the outer 1/3 of the weld metal. It is in the red region where the large circumferential crack grows. It is known that shear processes cause the nucleation of voids at grain boundaries, ledges and triple points in metals. These shear zones may provide extra impetus for cavitation formation in these regions.

It is noticed from the finite element solutions that the maximum axial and hoop stresses during secondary creep result in the heat affected zone close to the outer surface of the pressure vessel. This may not be the case for all materials as for low creep exponent materials the maximum stress may be produced at the inner bore of the pipe due to low stress redistribution of the elastic stresses. As the maximum secondary creep Von Mises stress occurs at the internal diameter of the pressure vessel and the maximum secondary creep principal stress occurs at the outer diameter, the rupture criterion, or (α), value has a strong effect on the damage distribution, the failure mode and the predicted failure time. This is observed in the difference between the damage distribution of Fig.8.28 (having a value of $\alpha = 0$ for the weld metal) and that of Fig.8.29, (having a value of $\alpha = 0.4298$ for the weld metal).

Good agreement has been obtained with the secondary creep finite element analysis solutions of Coleman et al [131] and Browne et al [128] for the same weldment. From Figs.8.79(a) and 8.80(a) an approximately equibiaxial stationary state stress is predicted at the centre line of the weld at the pipe surface. ($\Sigma_{axial} \approx \Sigma_{hoop} \approx 1.4$), which verifies the results of Coleman et al [131], although the magnitudes of the stresses, calculated by Coleman et al using the surface strain rates and the Bailey

equations (8.15) to (8.17) give ($\Sigma_{axial} \approx \Sigma_{hoop} \approx 1.1$). The stationary state hoop stress distribution at (t/t_f =53.7%) along an axial line on the outer surface of the pipe predicted from the finite element analysis (Fig.8.76), may be compared with the finite element results of Browne et al [128] Fig.7.22 (a). The stationary state axial stress distributions of Fig.8.79(a) and the hoop stress distribution along the weld metal centre line of Fig.8.80(a) at a life fraction of (t/t_f =35%) may be compared with the stress distributions of Fig.7.22 (c). Good correlations are observed.

Predicted hoop and axial strains from the weld models (WM1) and (WM2) on the whole also correlate well with the experimental results. Predicted tertiary creep strain results are observed to be lower than the experimental, which is explained as a result of the weld models only modelling small deformations and rotations. A further development of the weld models would be to transfer the weld modelling subroutines already developed to a large strain version of the creep damage program developed by Othman [77], which has been used by the author to predict the large deformations and rotations in the creep failure of a compact tension specimen in section 5.12. This would allow the geometry and rotation changes to be modelled in the finite element solution during vessel failure .

The finite element analysis predicted very small axial strains in the parent metal (less than 0.01% strain) until failure, which is also consistent with the experimental results.

Weld model (WM3) incorporated a representation of the weld metal coarse and fine grain bainitic regions. No creep data was available for the coarse grained weld metal microstructure, but material constants were derived for the coase grained weld metal from the fine grained weld metal properties, using the creep data from simulated heat affected zone coarse and fine grained materials, which was used to scale the properties of the fine grained weld metal. The axial creep strain predictions at the weld for weld model (WM3) were lower than those obtained from the experimental tests, which suggests that the ductility of the coarse grained weld metal was too low. Though damage distributions produced by the weld model (WM3) were good, predicting the growth of the large circumferential crack in the weld metal along the fusion boundary.

The life predictions for each weld model are compared with the experimental

lifetime in Table 8.7, and reference is made to the figures showing the predicted damage distributions at failure. Weld models (WM1) and (WM2) give life predictions within 5% of the real failure time of the weldment. Weld model gave a lifetime prediction 27% smaller than the real failure time of the weldment.

The Von Mises stress distributions across the weldment highlights the severity of the stress gradient present across the fusion boundary due to the mismatch in the creep properties between the weld metal the parent metal and the heat affected zone (Figs.8.40 and 8.96). The weld model must have sufficient mesh refinement to model this stress gradient. Weld model (WM1), which has the coarsest finite element mesh, gives a reasonably good life prediction. Weld model (WM2) is the same as weld model (WM1) except it has a more refined mesh in the region of the weld. Weld model (WM2) produced more localised damage and stress distributions, which gave a slightly reduced failure life prediction to that of weld model (WM1). If the mesh was refined further then this failure lifetime may be reduced further unless a localisation limiter is used. Non-local damage techniques, as described in Chapter 6 may restrict this localisation, to obtain a truly representative solution. Future work may involve the application of the non-local damage technique to model the effects of grain refinement in the weld and heat affected zones on the creep deformation and failure behaviour of the weld. This is complicated and would involve using different spatial averaging cell sizes for each weld material microstructural zone, which would overlay a very fine finite element weld model mesh. Though the predictive capability of weld model (WM3) must first be improved with the use of the exact material properties of the coarse and fine grained weld metal. This will involve futher laboratory testing.

Weld model (WM3) showed how the weld metal coarse grain regions damage at a faster rate than the fine grain regions. The damage distributions close to failure for weld model (WM3) show how the most intensely damaged zones localise close to the fusion boundary in the outer 1/3 of the weld metal coarse bainitic regions. Damage is then observed to link across the fine grain bainite regions inbetween these coarse grained regions showing how the circumferential crack close to the fusion boundary propagates inwards across the pipe wall . A restriction of the axisymmetric analysis is that the geometry of transverse weld metal cracks is not modelled; and although damage distributions in the outer coarse grained weld bead indicates where these

cracks initiate and grow they are not explicity modelled, whereas the circumferential cracks are modelled by the removal of damaged elements ($\omega > 0.9999$) from the weld model mesh.

Future improvements in the weld modelling will rely on the availability of both the uni-axial and multi-axial creep test data for each microstructural region of the weldment. Though reasonably good results have been obtained by the author using the available creep data, for truly accurate life and failure predictions several heat affected zones should also be incorporated in the weld models.

Larger materials data bases are currently being used to catalogue available and new materials data. With the assessment of the remnant life of power generating plant and the new demands of safety for nuclear power industry, the potential of these weld models must be realised. Initially these weld models provide an effective research tool, but computer solutions may be provided for a range of pipe sizes and materials, giving design data from which new design standards may be formulated; possibly utilising new procedures such as the Weld Performance Factors of Williams (section 7.9.4). The effects of weld geometry changes can be studied and material parameter surveys may help to obtain the best parent metal/weld metal material combinations to give improved weld service life.

Looking into the future, this research tool may be incorporated within a commercial Computer Aided Design facility. The design engineer would design the geometry of the component required and would determine where the welds are to be made to fabricate the component. He would then specify the weld geometry, welding parameters such as heat input and welding rod sizes and the materials to be used. A program such as that of Alberry and Jones [104] would calculate the distributions of the microstructures in the weld from heat flow equations and phase transformation diagrams and continuous cooling curves. The extent of each identified microstructural region could then be automatically represented by a finite element mesh and the relevant material properties for the microstructures would be assigned to each region of the mesh from a materials data base. A full creep continuum damage finite element solution for the prototype component under the appropriate service conditions could then be performed which would highlight any problems of cracking early in the required life of the weldment, at the design stage. The problem could then be

identified and adjustments made to geometry, welding parameters or materials, and a new solution performed, until the desired component performance is attained.

The foundations of such future research and commercial developments have been laid down and it is hoped that the abilities of the theory of continuum damage mechanics to model the complicated deformation and failure behaviour of welded components has been demonstrated. Though to truly judge the abilities of such models other more complicated geometries for a range of different materials must be modelled.

Time(hrs)	t/t_f	Observation
20,000	43%	Creep cracking initiates on the outer surface of the pressure vessel, as transverse cracks in the coarse columnar regions of the weld metal and the heat affected zones (HAZ) (see sketch of Fig.8.4).
35,000	76%	Transverse cracks are more clearly defined in the capping weld beads and are of depth less than 5 mm (see photograph of Fig.8.5).
35,000	> 76%	Circumferential cracks initiate in the weld metal coarse columnar regions close to the fusion boundaries, as a consequence of stress redistribution caused by the transverse cracking (see sketch of Fig.8.6).
42,000	91%	Significant circumferential cracking is now present. The transverse cracks have grown inwards to a depth of 20 mm and extended through the weld metal, across the heat affected zone (HAZ) into the parent metal (see the photograph of Fig.8.7).
46,000	100%	Massive transverse and circumferential cracking causes steam leakage in a bulged region of the pressure vessel. The pressure vessel is said to have reached its rupture life (see photograph of Fig.8.8).

Table 8.1: A brief summary of the failure history of the 2.25Cr 1Mo : 0.5Cr 0.5Mo 0.25V pipe weldment from a pressure vessel test by Coleman et al [133],[131].

Material	Specimen No.	Test Stress (MPa)	Min. Creep Rate (abs/hr)	Life Time (hrs)	Last Recorded Strain (%)
Weld Metal	C17 WM1	120	$9.0x10^{-6}$	2241	14.0
No.17	C17 W01	105	$2.1x10^{-6}$	6140	9.4
2.25Cr 1Mo	o C17 WM2	92	$2.0x10^{-6}$	11278	12.0
Stress Relieved	o C17 W03	66	$5.6x10^{-7}$	35840	3.5
3hrs @ 700°C	o C17 W04	56	$2.7x10^{-7}$	66376	4.7
Parent	1CM	180	$5.7x10^{-5}$	672	20.0
Metal	2CM	155	$1.2x10^{-5}$	2262	12.1
0.5Cr 0.5Mo 0.25V	3CM	140	$2.2x10^{-6}$	4459	16.0
	4CM	120	$8.5x10^{-7}$	15193	13.0
	o C17 PM1	110	$4.2x10^{-7}$	31111	6.5
	o 5CM	100	$2.5x10^{-7}$	51900	10.8
	oC17 PM2	85	$1.4x10^{-7}$	83000	2.98
Simulated	CGB9	250	$9.0x10^{-6}$	240	0.31
HAZ	CGB10	240	$6.8x10^{-6}$	-	-
(Grain	CGB8	200	$1.2x10^{-6}$	1151	0.38
Coarsened	oCGB1	160	$3.3x10^{-7}$	12960	0.64
Parent)	CGB2	140	$2.2x10^{-7}$	17856	0.90
	oCGB3	120	$1.4x10^{-7}$	34010	1.16
	o CGB4	100	$9.1x10^{-8}$	65217	2.203
	o CGB5	85	$5.5x10^{-8}$	106767	2.326

Table8.2: Summary of the uni-axial creep test data for the weld metal, parent metal and HAZ (G.C.P.) materials isolated from a 2.25Cr 1Mo:0.5Cr 0.5Mo 0.25V weld. From the laboratory tests of Cane [109].

The material constants are given for the units of stress in (MPa), strain in (%) and time in hours.

Material	Range Stress Range	m	n	K	χ	M	ϕ	$V_u\%$	$V_{uTRAN}\%$	α	$\hat{\Sigma}$ and $\hat{\sigma}$	ι	κ	Row
Parent Metal	$\sigma \leq \hat{\sigma}$	-0.2031	4.8971	2.8531×10^{-14}	3.0110	1.4522×10^{-10}	5.4141	9.8379	5.0000	0.5955	2.6374	-	-	(a)
	$\sigma > \hat{\sigma}$	-0.2031	10.3442	1.3485×10^{-25}	6.9613	8.8846×10^{-19}	12.5486	9.8379	5.0000	0.5955	(120 MPa)	-	-	
HAZ (1) (G.C.P.)	$\sigma \leq \hat{\sigma}$	-0.1700	1.3654	1.0358×10^{-7}	2.7858	2.3062×10^{-10}	1.4231	74.0930	38.0822	0.4298	3.9560	4.1536×10^{-2}	5.9872	(b)
	$\sigma > \hat{\sigma}$	-0.1700	8.9364	8.7207×10^{-25}	9.0972	1.3459×10^{-9}	14.8589	74.0930	38.0822	0.4298	(180 MPa)	4.1536×10^{-2}	5.9872	
Weld Metal (Fine)	$\sigma \leq \hat{\sigma}$	-0.2031	4.3680	2.93965×10^{-12}	2.8554	1.15878×10^{-9}	4.9667	30.5238	15.5133	0.0/0.4298	2.1978	1.0	13.6686	(c)
	$\sigma > \hat{\sigma}$	-0.2031	7.2496	5.07102×10^{-18}	5.7669	1.74182×10^{-15}	8.9029	30.5238	15.5133	0.0/0.4298	(100 MPa)	1.0	13.6686	
HAZ (2) (G.C.P.)	$\sigma \leq \hat{\sigma}$	-0.2148	3.3685	1.55065×10^{-11}	2.3009	3.25906×10^{-9}	3.6778	10.4701	5.3213	0.4298	3.9560	-1.46819×10^{-2}	1.49625	(d)
	$\sigma > \hat{\sigma}$	-0.2148	8.9364	4.29914×10^{-24}	9.2793	5.95355×10^{-25}	11.4099	10.4701	5.3213	0.4298	(180 MPa)	-1.46819×10^{-2}	1.49625	
Weld Metal (Coarse)	$\sigma \leq \hat{\sigma}$	-0.2031	4.3680	3.0076×10^{-13}	2.8554	6.1275×10^{-10}	4.9667	5.9057	3.0015	0.4298	2.7473	1.0	1.39844	(e)
	$\sigma > \hat{\sigma}$	-0.2031	7.2496	2.72746×10^{-19}	5.7669	4.80986×10^{-16}	8.9029	5.9057	3.0015	0.4298	(125 MPa)	1.0	1.39844	

Table8.3: The material constants used for the 2.25Cr 1Mo:0.5Cr 0.5Mo 0.25V weldment microstructural zones in the weld models (WM1),(WM2) and (WM3). The material constants are obtained from the tests data of Cane [109].

Material	σ_{ef}	σ_1	q	r	α
Parent Metal	155	90	3.7	7.0	0.5955
Simulated HAZ (G.C.P.)	250 200	144 115	3.1 2.8	8.5 8.5	0.4298 0.3921

Table8.4: Values of the multi-axial rupture criterion constants from the double shear, torsion and uni-axial tension tests of Cane [109], giving the values of (q) and (r) for use in equation (8.1). Corresponding values of (α) have been calculated by the author for use in equation (8.2).

(a) Heat Affected Zone Material: $\alpha = 0.4298$; $q = 3.1$; $r = 8.5$.

Bi-Axiality Ratio ζ	Cane Equation (8.9) Σ_1	Cane Equation (8.9) Σ_2	Hayhurst Equation (8.10) Σ_1	Hayhurst Equation (8.10) Σ_2
-1.5	0.6096	-0.9144	0.5979	-0.8968
-1.0	0.7054	-0.7054	0.7055	-0.7055
-0.5	0.8371	-0.4186	0.8445	-0.4222
0.0	1.0	0.0	1.0	0.0
0.1	1.0304	0.1030	1.0270	0.1027
0.5	1.0957	0.5478	1.0827	0.5414
1.0	1.0	1.0	1.0	1.0

(b) Parent Metal. $\alpha = 0.5955$; $q = 3.7$; $r = 7.0$.

Bi-Axiality Ratio ζ	Cane Equation (8.9) Σ_1	Cane Equation (8.9) Σ_2	Hayhurst Equation (8.10) Σ_1	Hayhurst Equation (8.10) Σ_2
-1.5	0.6765	-1.0147	0.6770	-1.0155
-1.0	0.7719	-0.7719	0.7715	-0.7715
-0.5	0.8764	-0.4382	0.8845	-0.4422
0.0	1.0	0.0	1.0	0.0
0.1	1.0225	0.1022	1.0190	0.1019
0.5	1.0702	0.5351	1.0573	0.5286
1.0	1.0	1.0	1.0	1.0

Table 8.5: The values of (Σ_1) and (Σ_2) are calculated from equations (8.9) and (8.10) using the equations of Cane and Hayhurst respectively, for a range of bi-axiality ratio ($\zeta = \Sigma_2/\Sigma_1$) defining the shapes of the isochronous rupture surfaces given in Fig. 8.15.

Table (a) is for the heat affected zone material and (b) is for the parent metal.

The values of (Σ_1) and (Σ_2) show that equations (8.9) and (8.10) are equivalent.

Material	Specimen No.	Test Stress (MPa)	Min. Creep Rate (abs/hr)	Life Time (hrs)	Last Recorded Strain (%)
Refined Parent(RP)	R1P1	160	$6.9x10^{-6}$	2242	10.7
	R2P2	100	$4.4x10^{-7}$	20405	7.9
Doubly Refined Parent (R_2P)	R2P1	160	$1.4x10^{-5}$	1686	10.0
	R2P2	100	$8.0x10^{-7}$	19691	12.7

Table8.6: Uni-axial creep data for refined parent metal, simulated heat affected zone material, after Cane [109].
The heat affected zone microstructure is obtained by furnace heat treatment of the 0.5Cr 0.5Mo 0.25V parent plate.

Weld Model No.	Life Time Prediction (hrs)	Damage Distribution in Figure No.
WM1	47247	8.35(a)
WM2	43882	8.62(a)
WM3	33433	8.91(a)

Table 8.7: Summary of weld model predictions. c.f. the experimental lifetime of approximately 46,000 hrs, and the cracked weldment section, Fig.8.91(b).

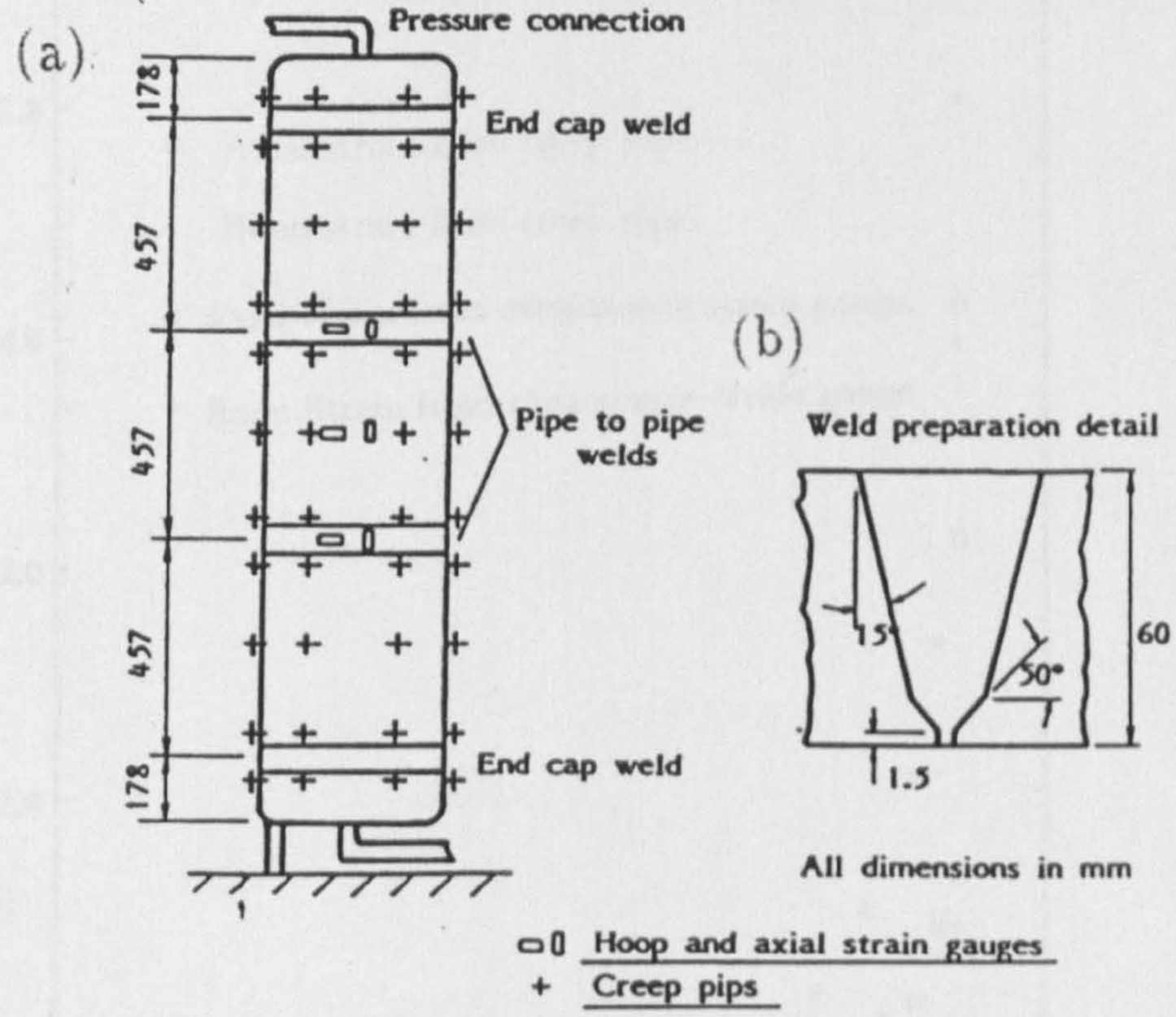

Figure 8.1: End elevation of the welded pressure vessel as tested by Coleman et al [131], (a) showing the four circumferential welds and the positions of the capacitance strain gauges and the creep pips from which surface strain measurements were taken. (b) shows the J-type weld preparation.

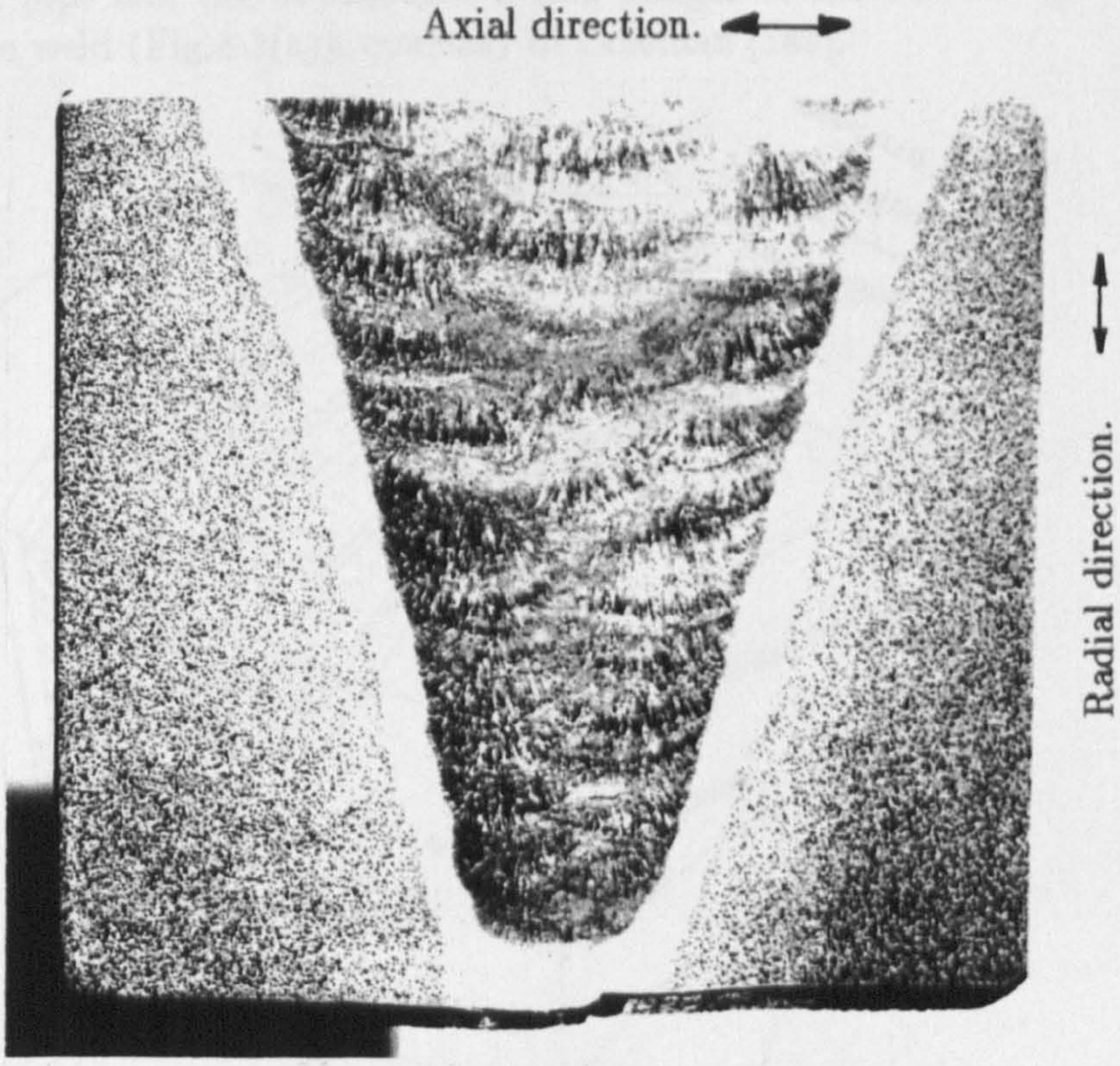

Figure 8.2: Micrograph showing a section through a 2.25Cr 1Mo:0.5Cr 0.5Mo 0.25V multipass weld, identical to the welds used in the thick steam pipe tests of Coleman et al [131].

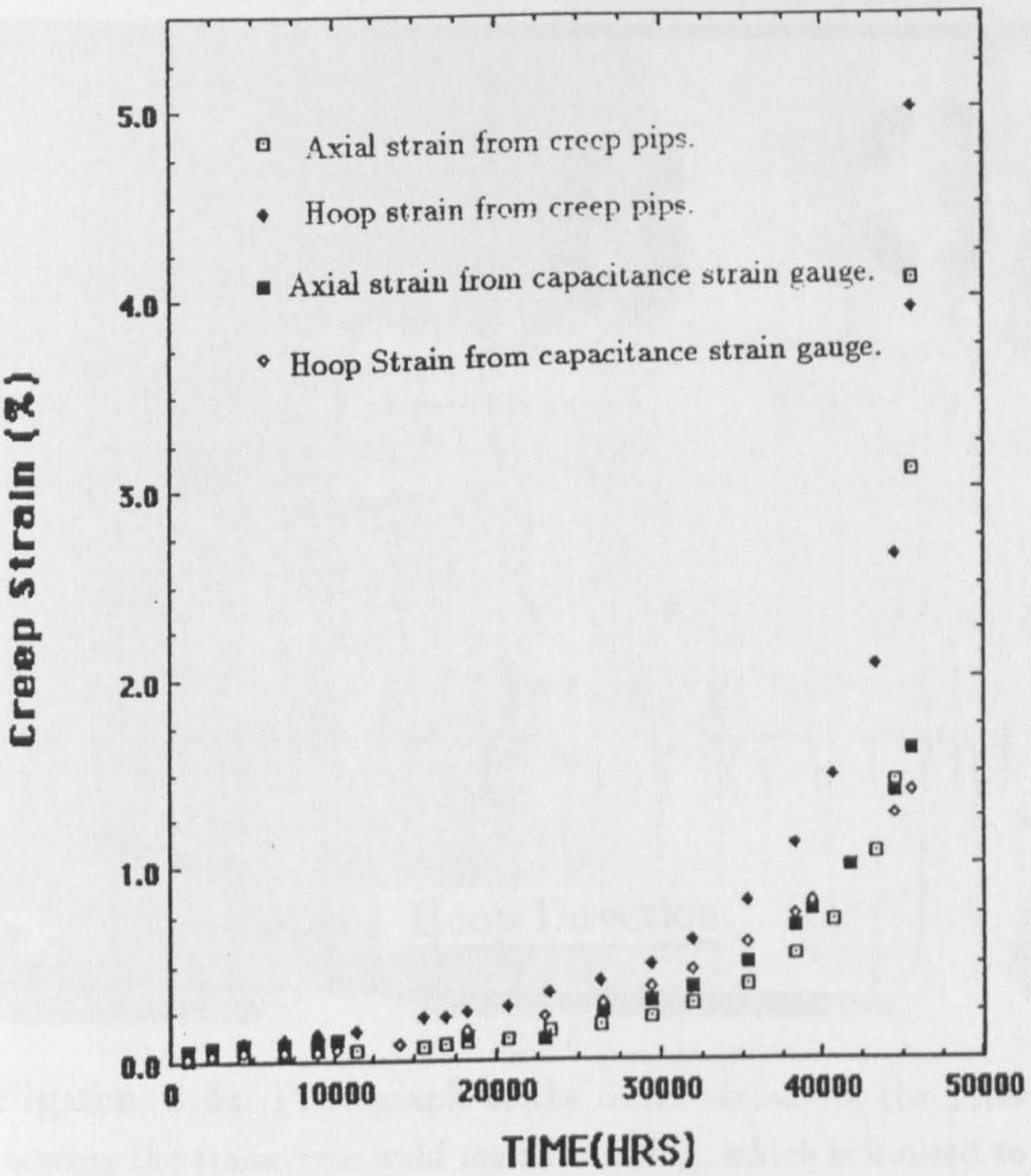

Figure 8.3: Experimental creep strain measurements with test time from the creep pips and the capacitance strain gauges at the surface of the 2.25Cr 1Mo weld (Fig.8.1(a)), courtesy of Coleman [149].

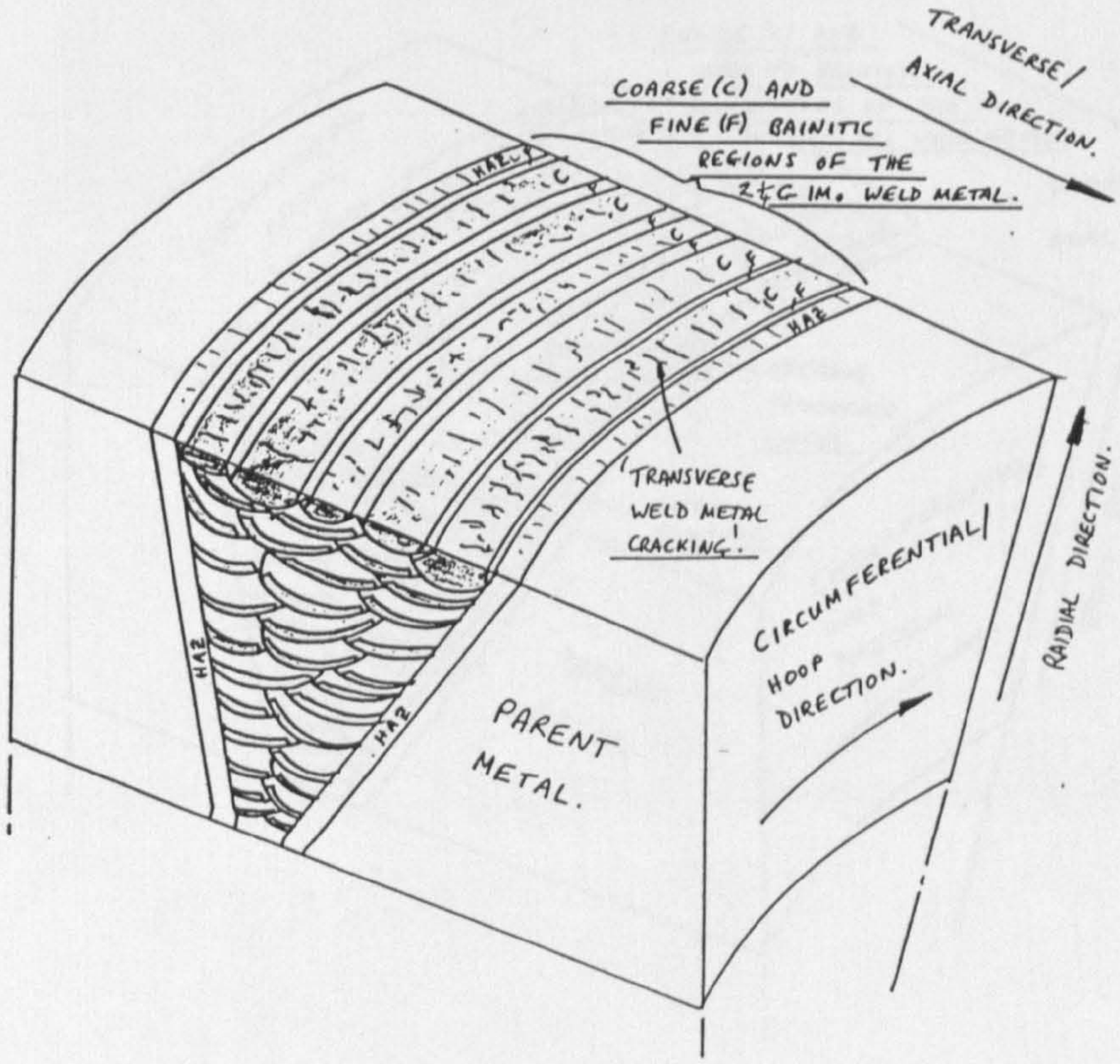

Figure 8.4: Sketch of a section taken from the 2.25Cr 1Mo:0.5Cr 0.5Mo 0.25V steam pipe weldment, showing the initial transverse cracking in the coarse columnar grained bainitic regions of the weld metal. ($t/t_f \approx 43\%$).

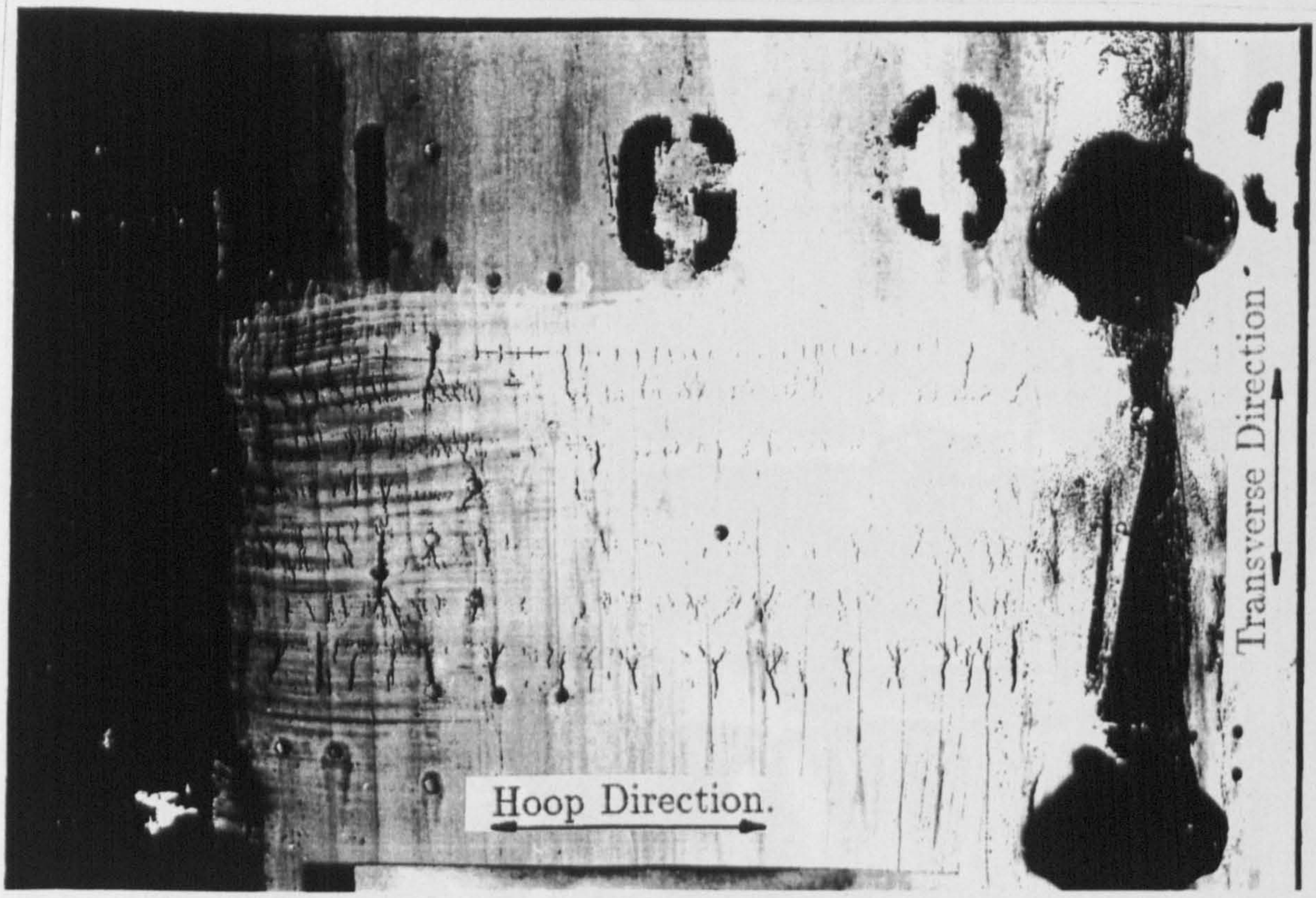

Figure 8.5: Photograph of the outer surface of the pressure vessel, showing the transverse weld metal cracking, which is limited to the coarse columnar grained bainitic regions of the weld. Courtesy Coleman, CEGB

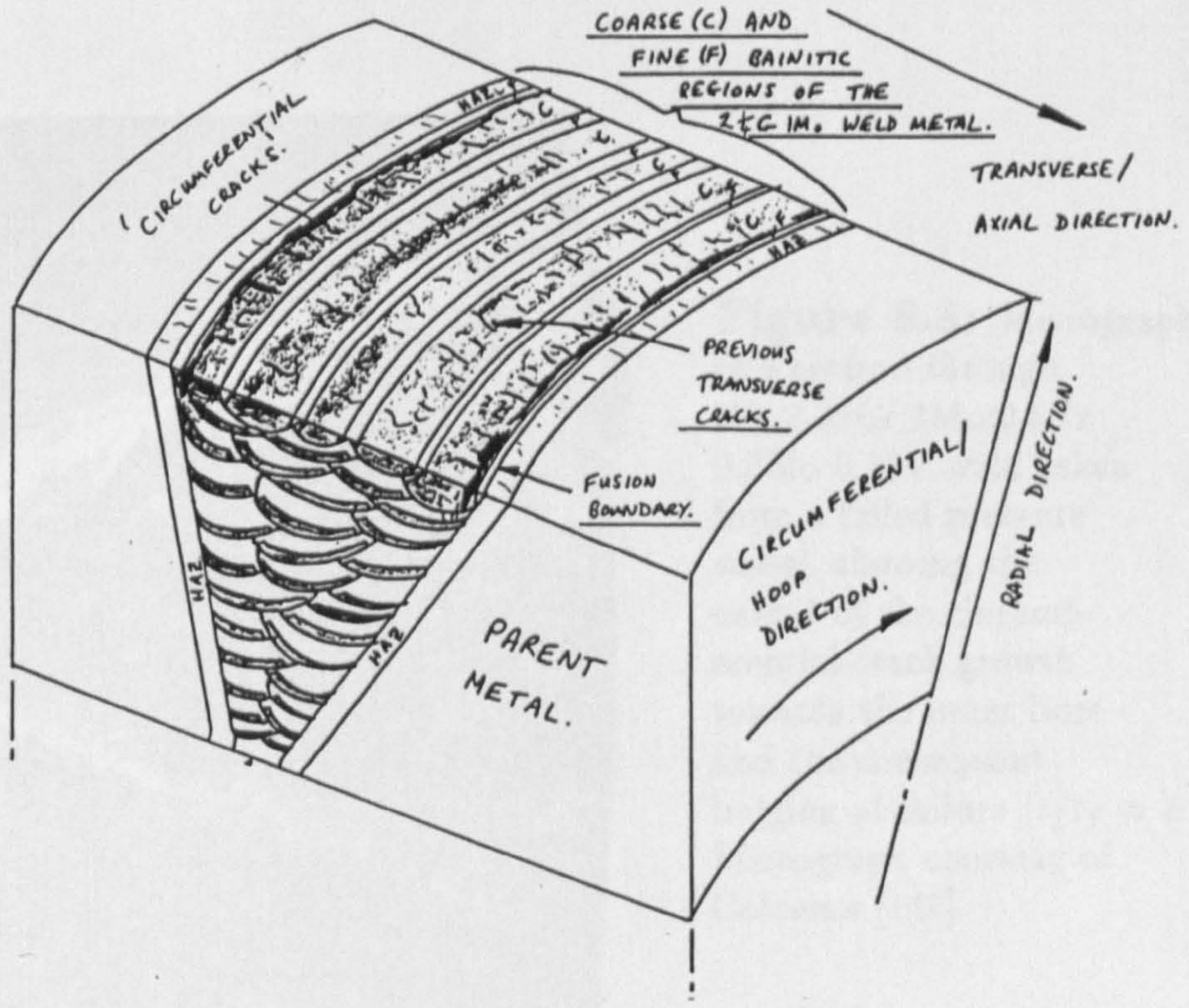

Figure 8.6: Sketch of a section taken from the 2.25Cr 1Mo:0.5Cr 0.5Mo 0.25V steam pipe weldment, showing the initial circumferential cracking in the coarse grained bainitic regions of the weld metal close to the fusion boundary. ($t/t_f \approx 76\%$).

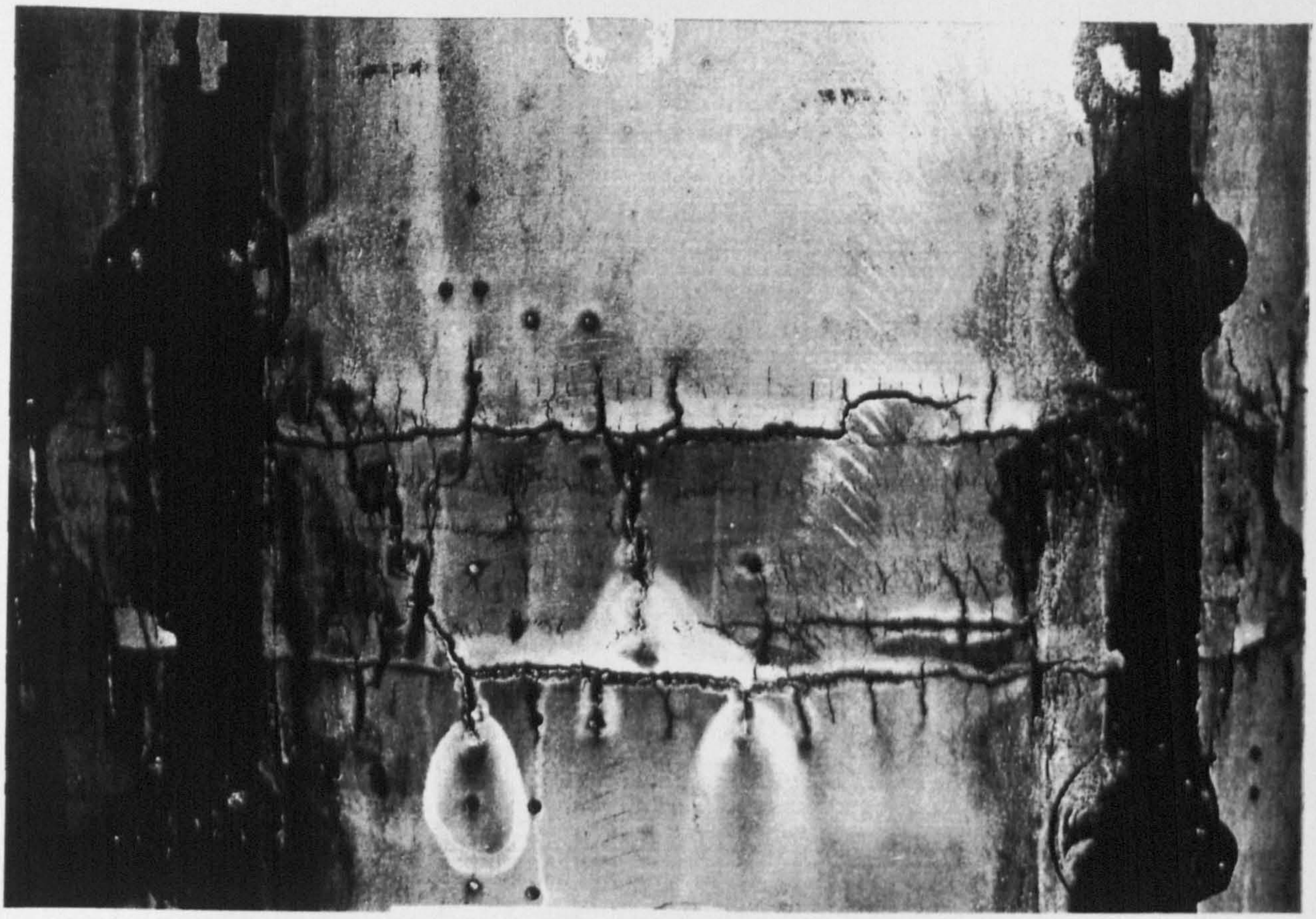

Figure 8.7: Extensive transverse and circumferential cracking in the 2.25Cr 1Mo pipe weldment, ($t/t_f \approx 91\%$). Photograph courtesy of Coleman [149].

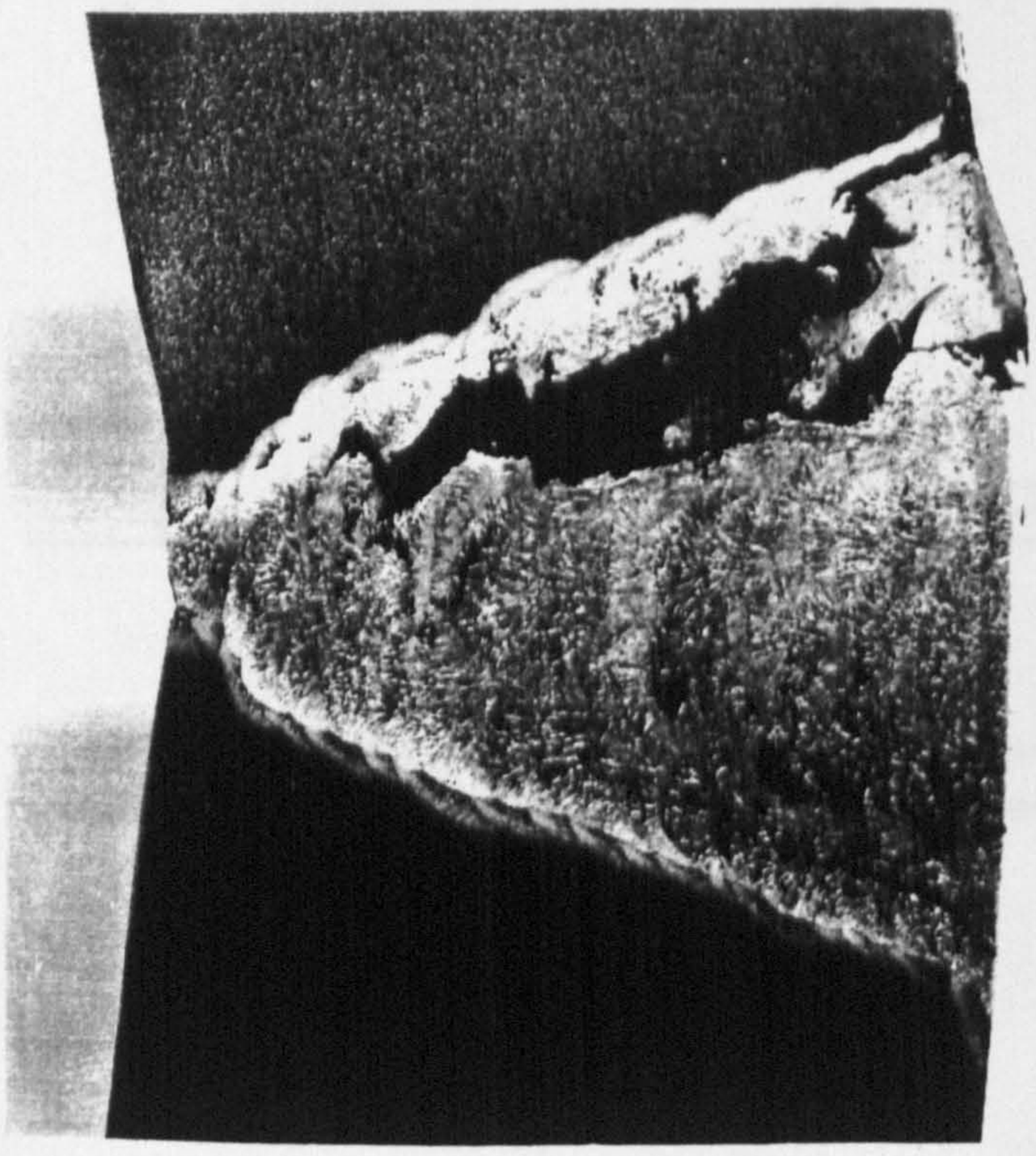

Figure 8.8: Micrograph of a section through the 2.25Cr 1Mo:0.5Cr 0.5Mo 0.25V weld taken from a failed pressure vessel, showing the extent of the circumferential crack growth towards the inner bore and the consequent bulging at failure ($t/t_f \approx 100\%$). Micrograph courtesy of Coleman [149].

Figure 8.9 : Diagram showing the axisymmetric finite element model and the boundary conditions used to represent the thick-steam pipe weld laboratorty test of Coleman et al [131].

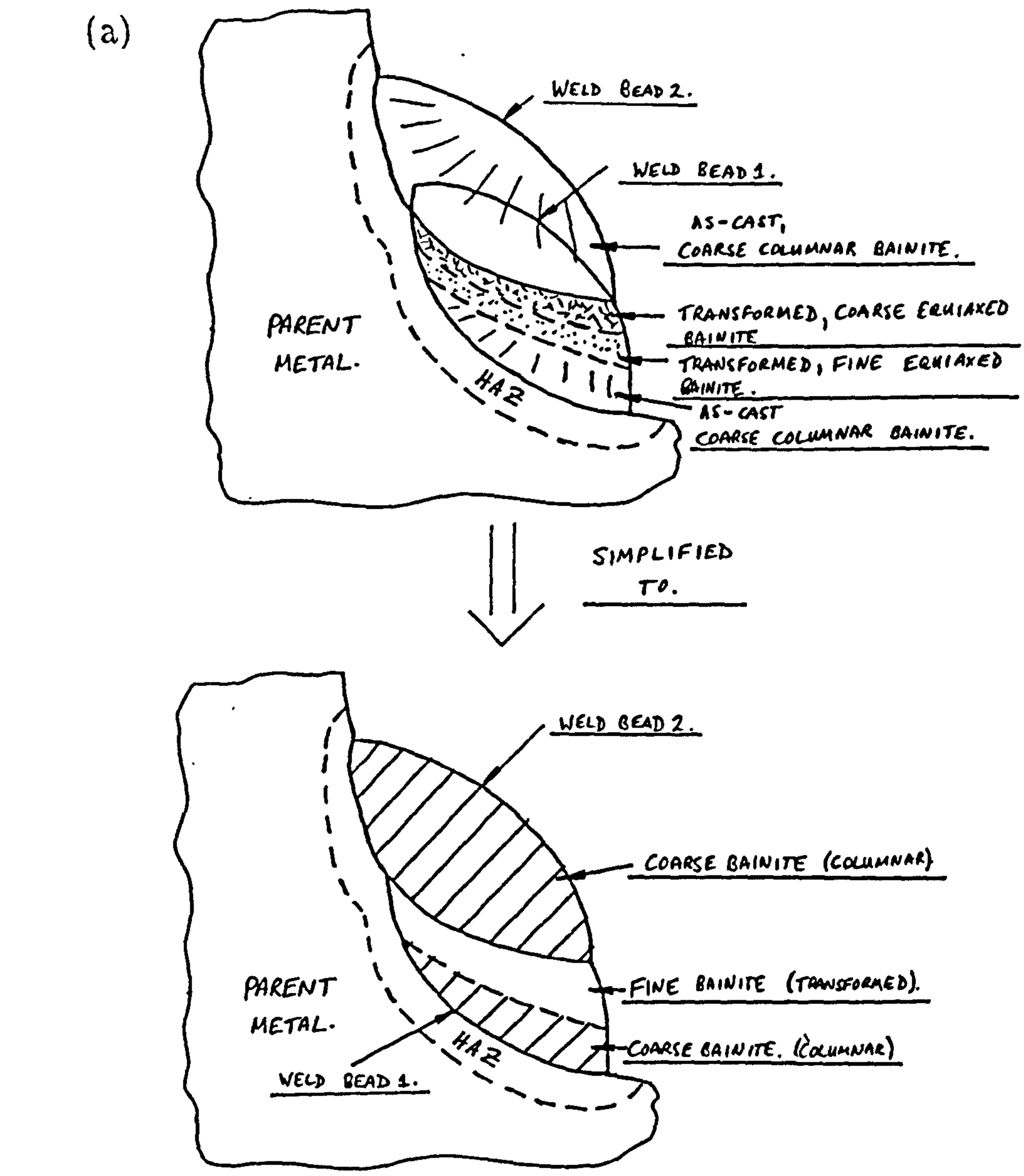

Figure 8.10: Simplified representation of the coarse and fine grain bainitic microstructual regions in a 2.25Cr 1Mo multipass weld. The three microstuctural regions identified in (a) are simplified in (b) to two microstructural regions : the coarse grain (columnar) and fine grain (transformed) bainitic regions.

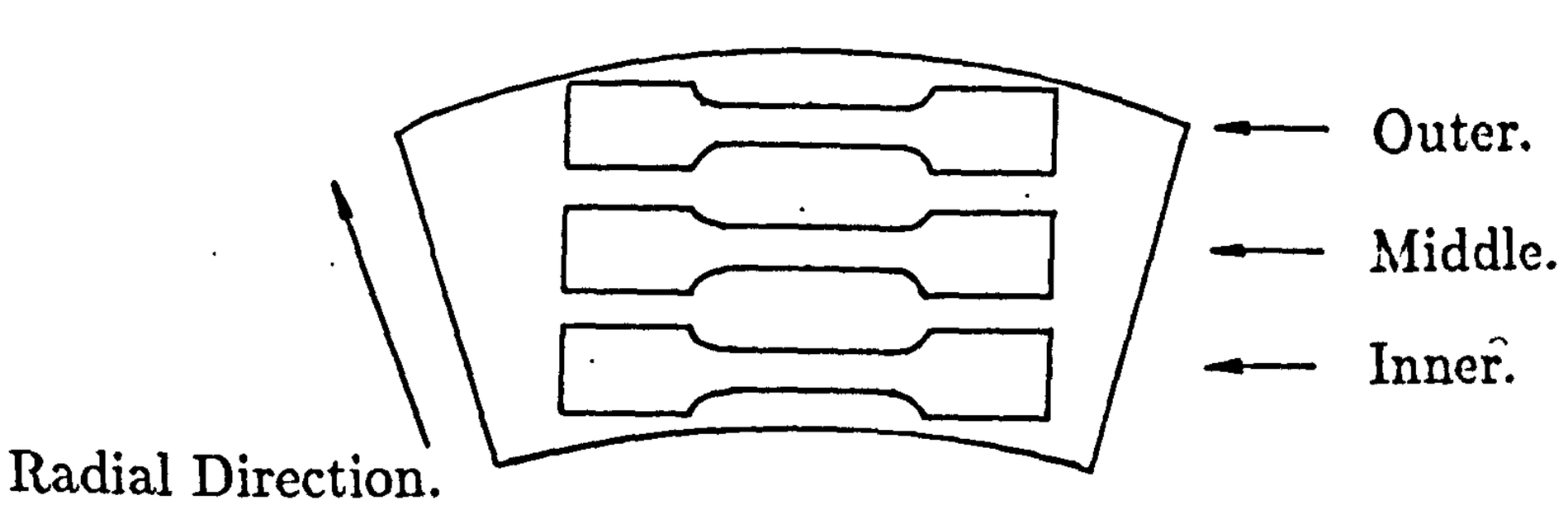

Figure 8.11: Section through the steam pipe wall showing the positions where uni-axial specimens were cut from the parent metal and weld metal pipe.

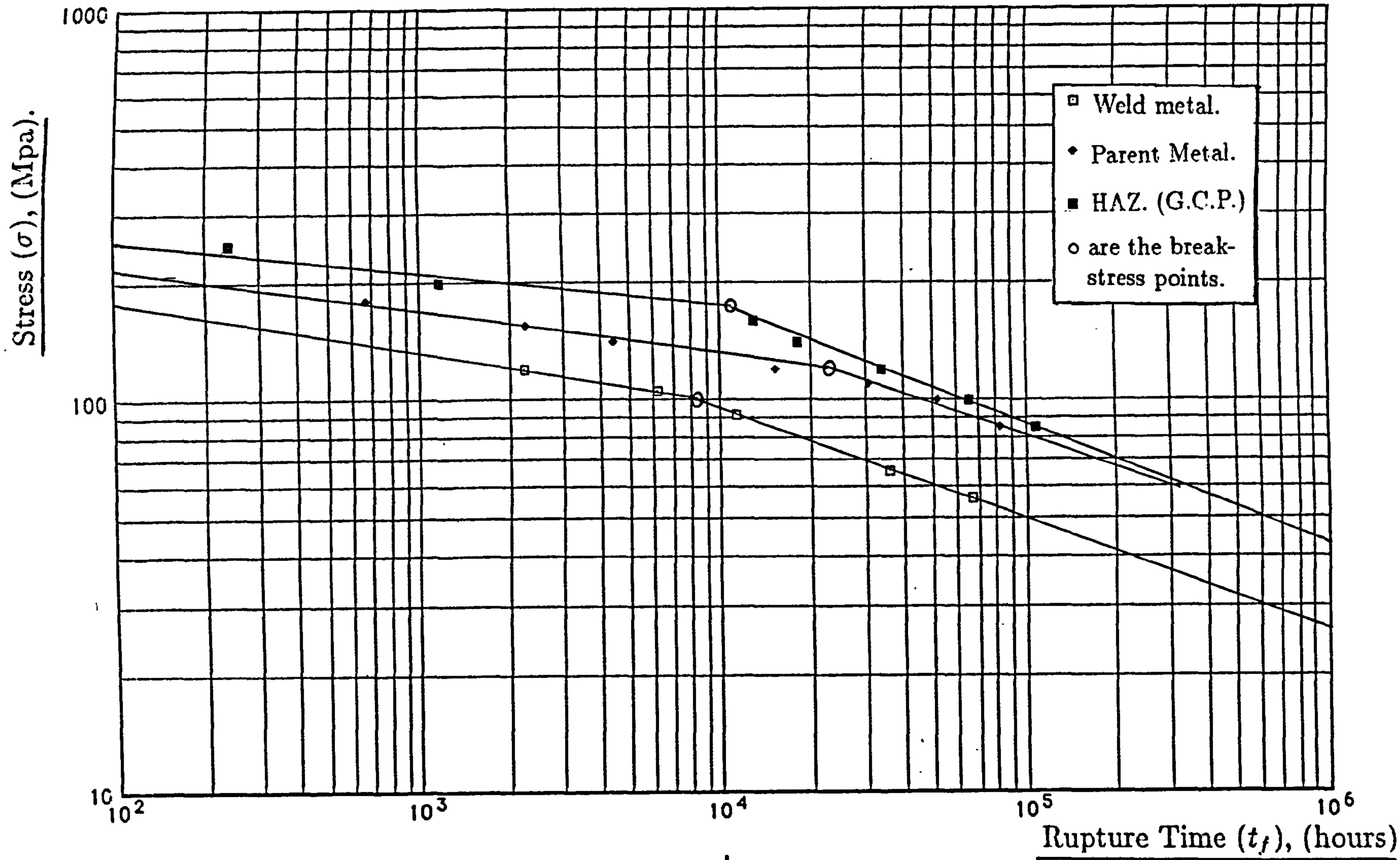

Figure 8.12: Uni-axial stress-rupture diagram for the weld metal, the parent metal and the heat affected zone (G.C.P.) materials corresponding to a 2.25Cr 1Mo:0.5Cr 0.5Mo 0.25V multipass weld.

The numerical data plotted is summarised in Table 8.2 from the creep tests of Cane [109].
The low stress lines are the best fits to the low stress data. The high stress lines are hand fitted lines used to obtain the high stress material constants in the bi-linear representation.

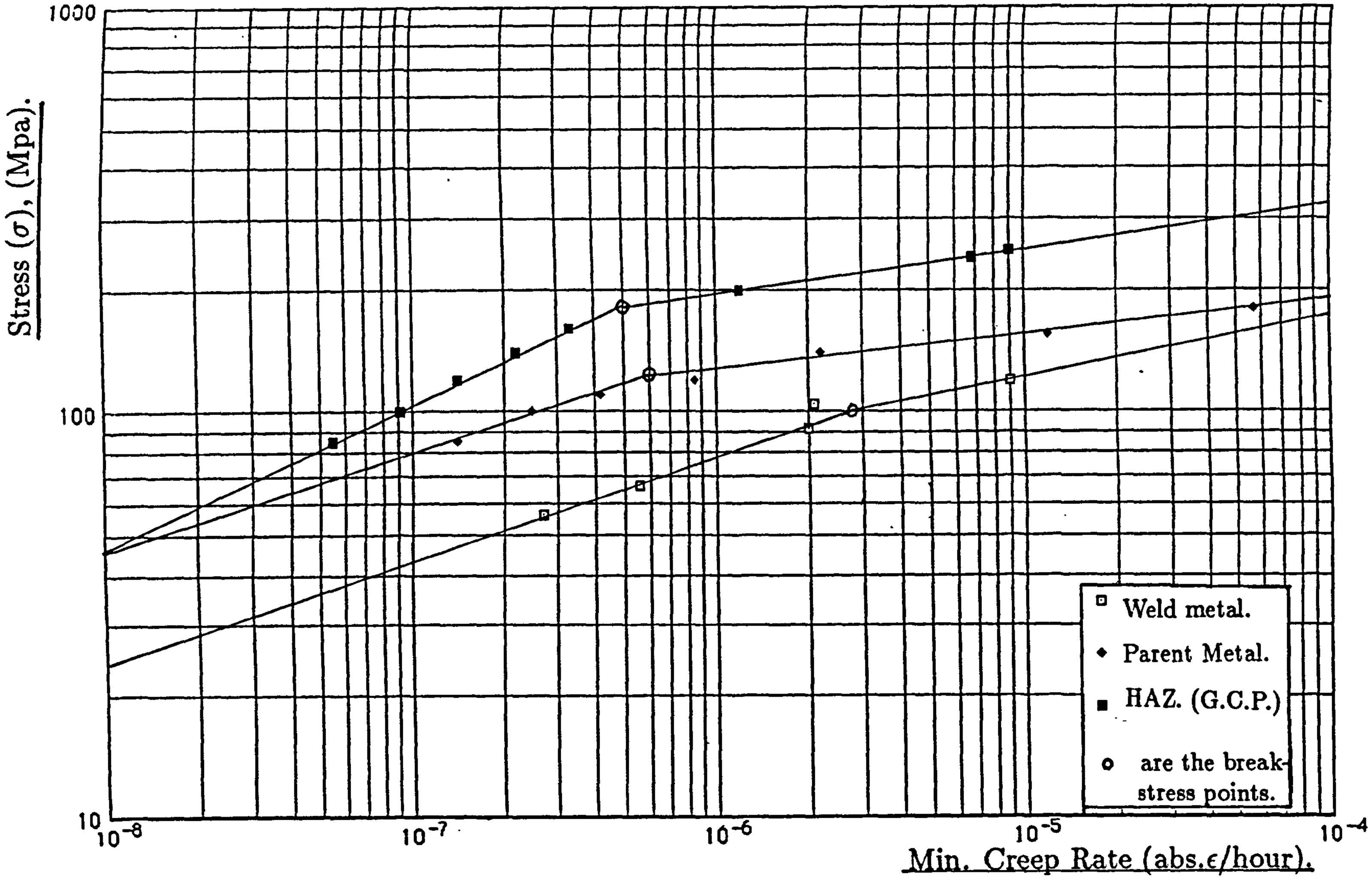

Figure 8.13: Uni-axial stress vs. min. creep rate diagram for the weld metal, the parent metal and the heat affected zone (G.C.P.) materials corresponding to a 2.25Cr 1Mo:0.5Cr 0.5Mo 0.25V multipass weld.

The numerical data plotted is summarised in Table 8.2 from the creep tests of Cane [109].
The low stress lines are the best fits to the low stress data. The high stress lines are hand fitted lines used to obtain the high stress material constants in the bi-linear representation.

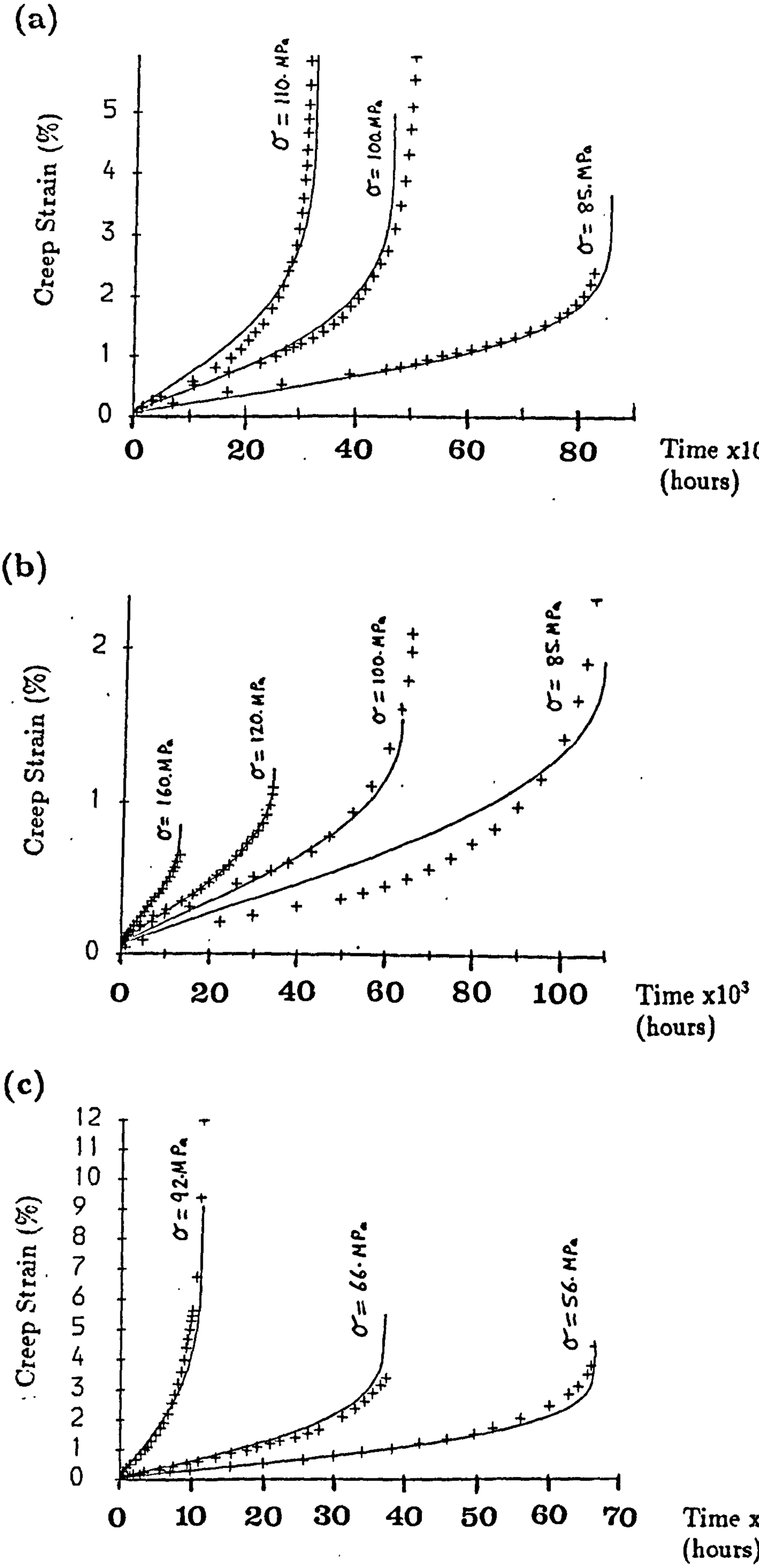

Figure 8.14: Comparisons of the experimental uni-axial creep test data and the predicted creep curves for (a) the parent metal, (b) the HAZ (G.C.P.) and (c) the weld metal, for various test stress levels in MPa.

Experimental: +

Predicted: ———

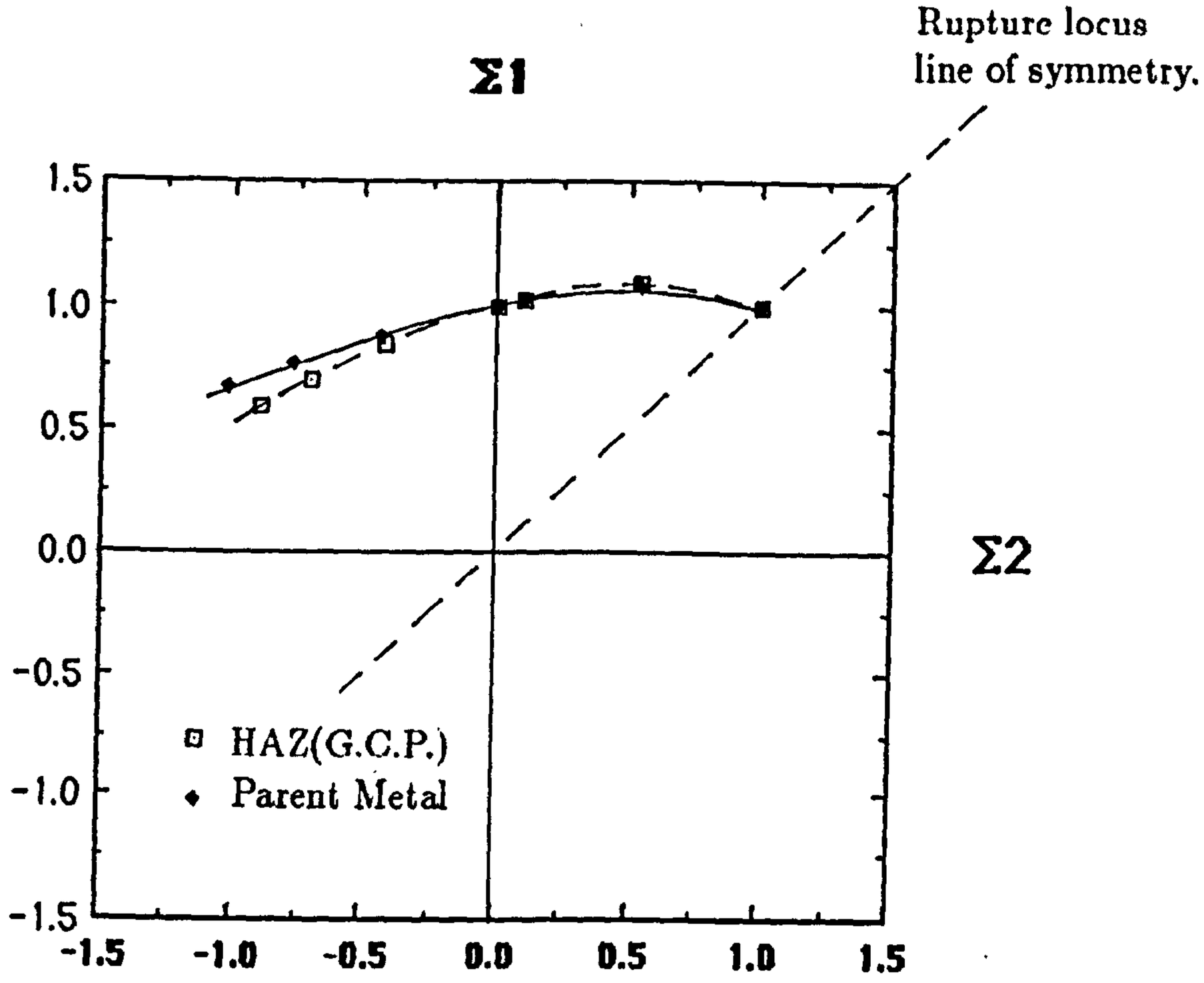

Figure 8.15: Isochronous rupture surfaces plotted in principal plane stress space ($\Sigma_1 > \Sigma_2 > \Sigma_3 = 0$), for the HAZ (G.C.P.) material ($\alpha = 0.4298$) and the parent metal ($\alpha = 0.5955$).

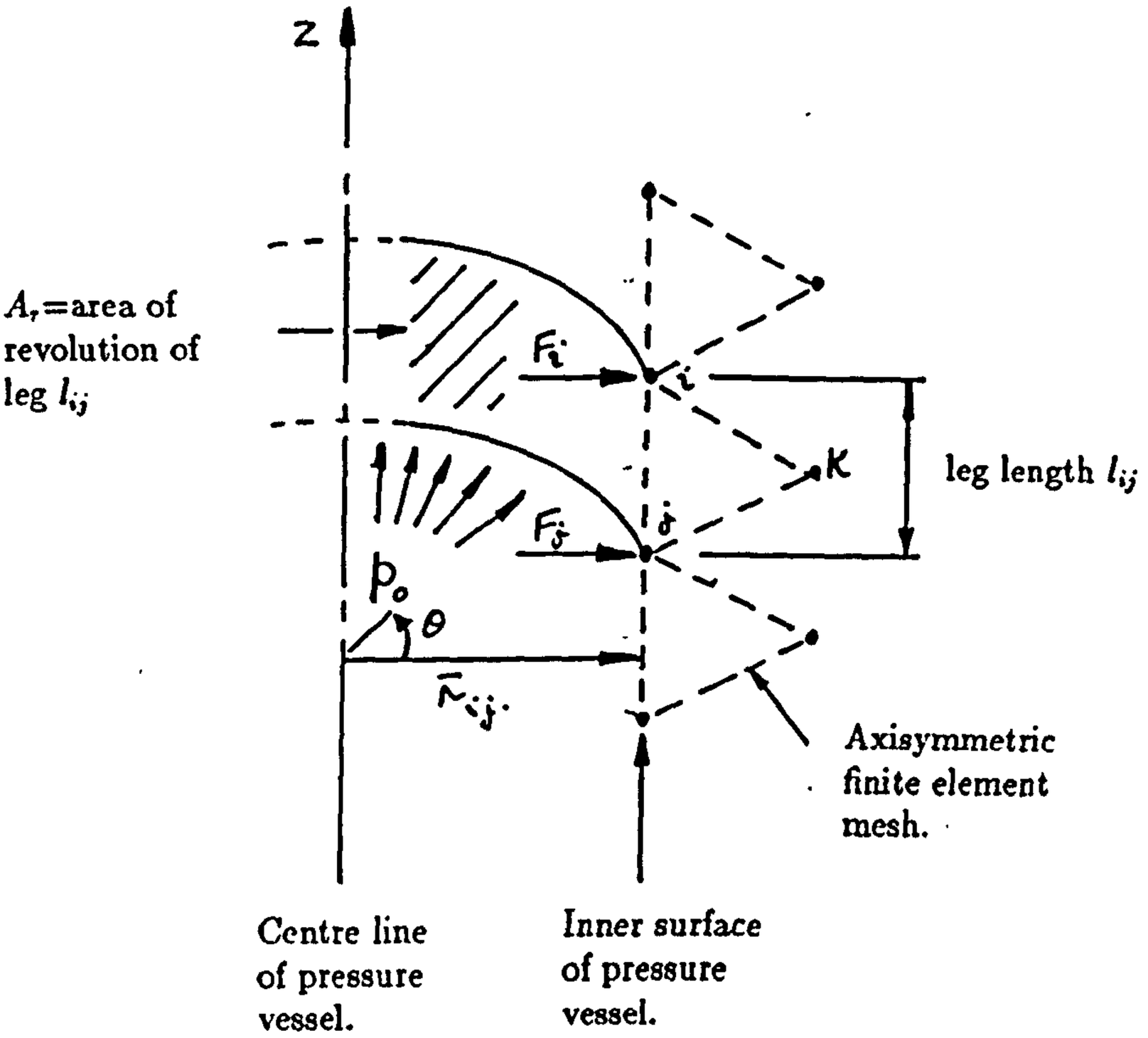

Figure 8.16: Diagram showing the radial nodal forces on the inner surface of an elemet in the axisymmetric finite element mesh of the pressure vessel, to model the internal steam pressure loading. (F_i) and (F_j) are given by equation(8.11).

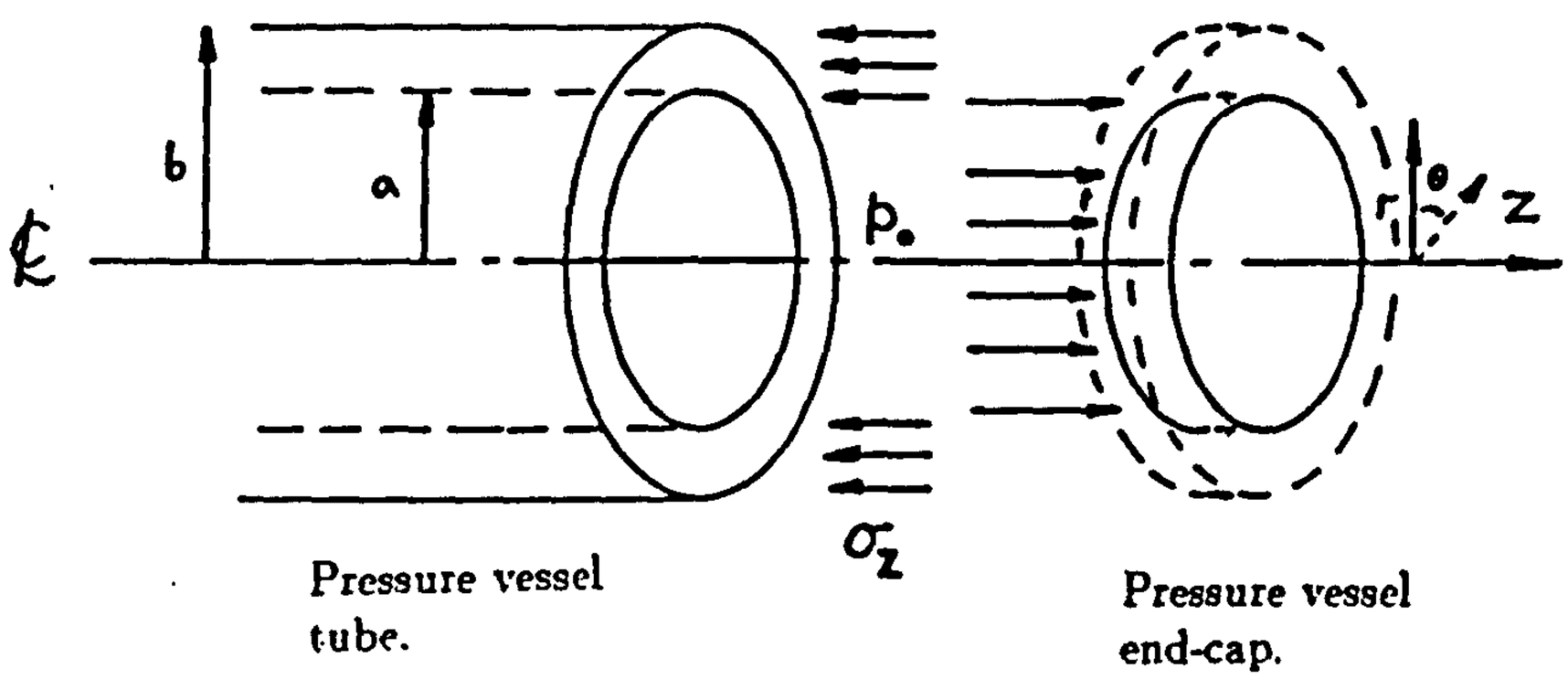

Figure 8.17: Diagram showing the constant axial stress in the pressure vessel wall, produced by the action of the internal pressure on the end caps.

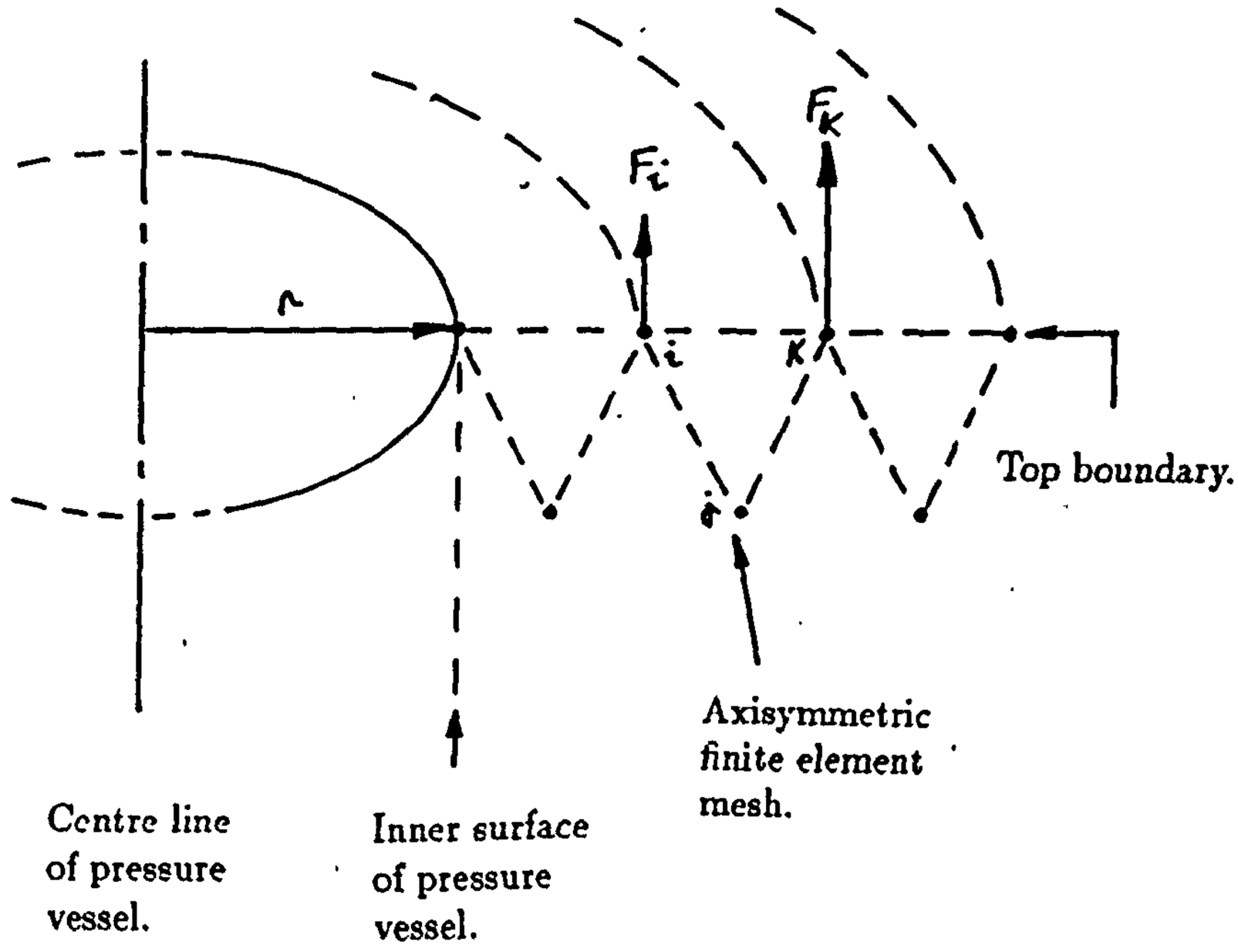

Figure 8.18: Diagram showing the axial nodal forces on an element at the top boundary of the axisymmetric finite element mesh of the pressure vessel tube, to model the constant axial stress due to the action of internal steam pressure on the end-caps. (F_i) and (F_k) are given by equations (8.13) and (8.14) respectively.

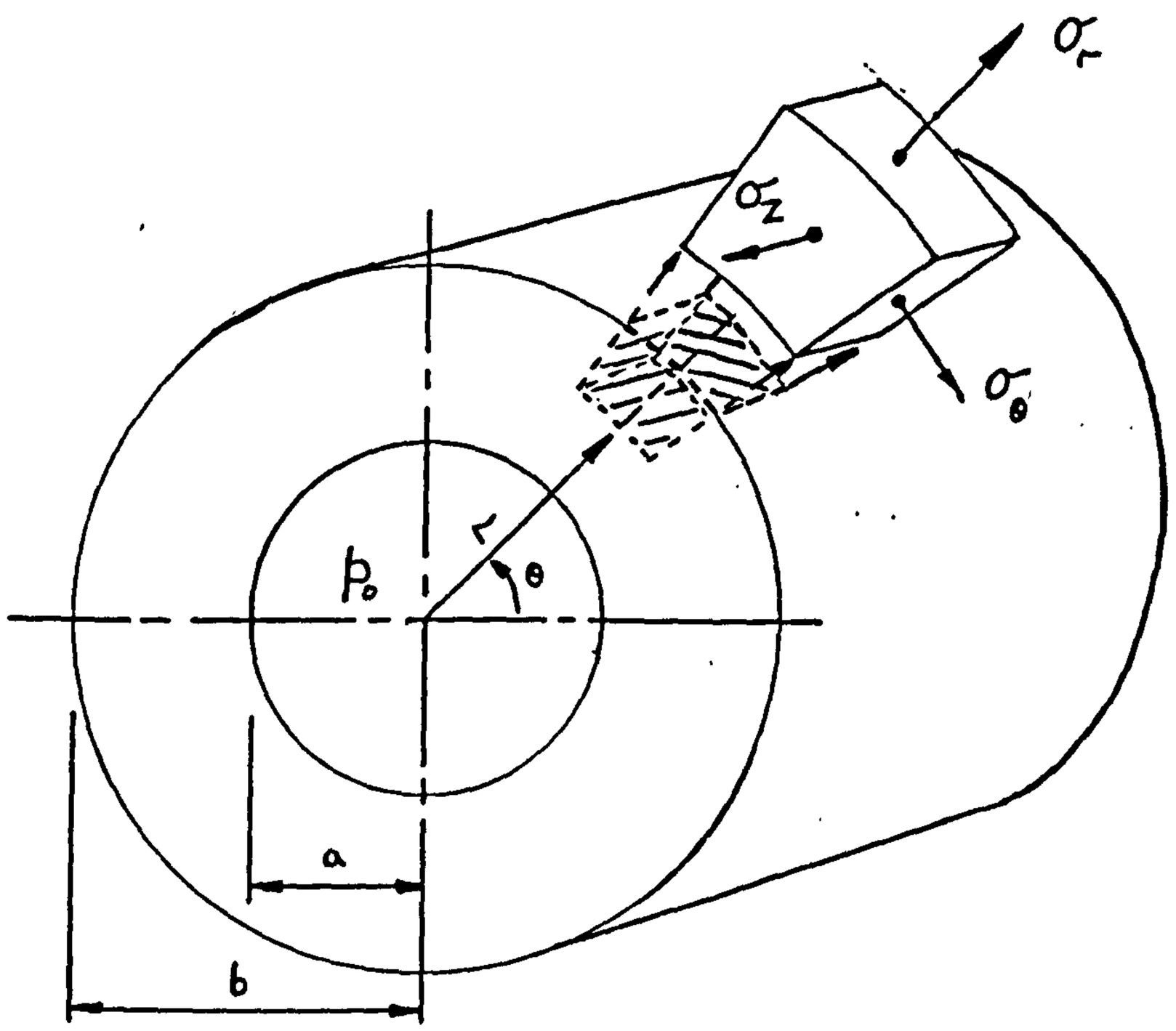

Figure 8.19: Diagram of the thick walled pressure vessel used by Odqvist[18], showing the dimensions, the coordinate system and the stress directions.

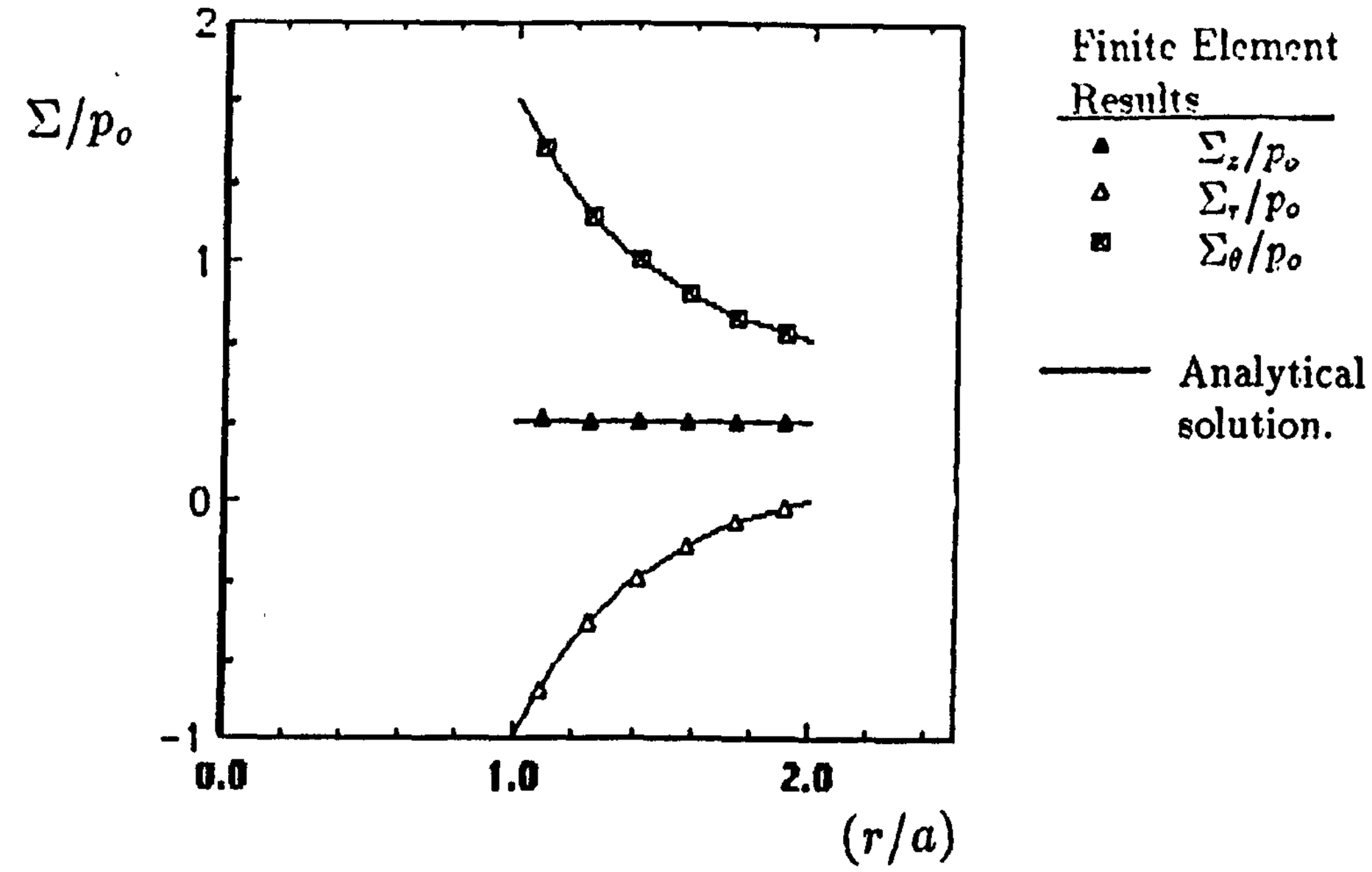

Figure 8.20: Comparison between the stress distributions across the wall thickness of the thick pressure vessel from the Bailey equations (8.15), (8.16), (8.17), and the finite element stationary state stress results, for a creep exponent ($n = 1.0$) giving the elastic stress distributions.
($r/a = 1.0$) is the inner bore and (r/a=2.0) is the outer bore.

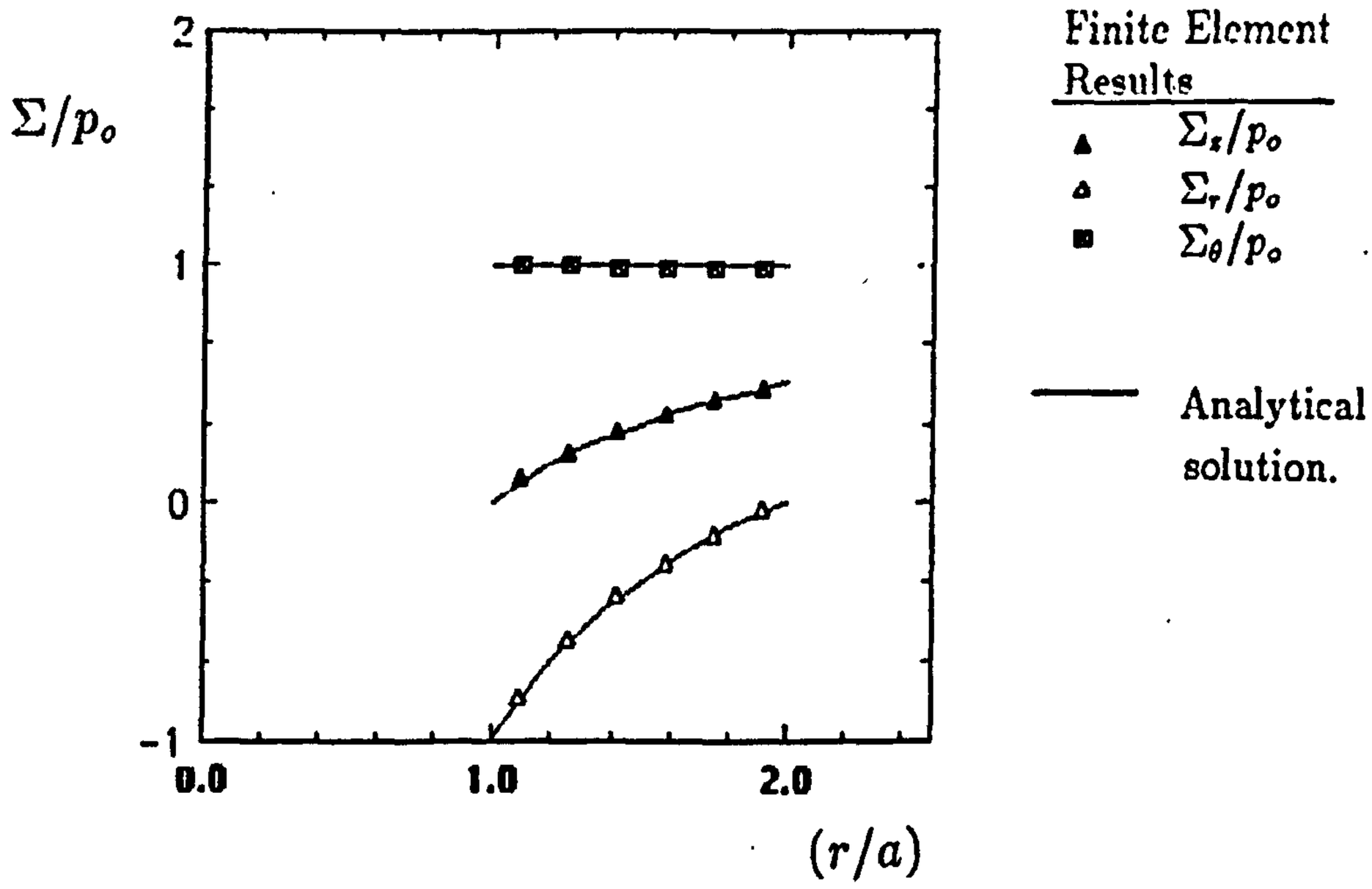

Figure 8.21: Comparison between the stress distributions across the wall thickness of the thick pressure vessel from the Bailey equations (8.15), (8.16), (8.17) and the finite element stationary state stress results, for a creep exponent ($n = 2.0$).
($r/a = 1.0$) is the inner bore and (r/a=2.0) is the outer bore.

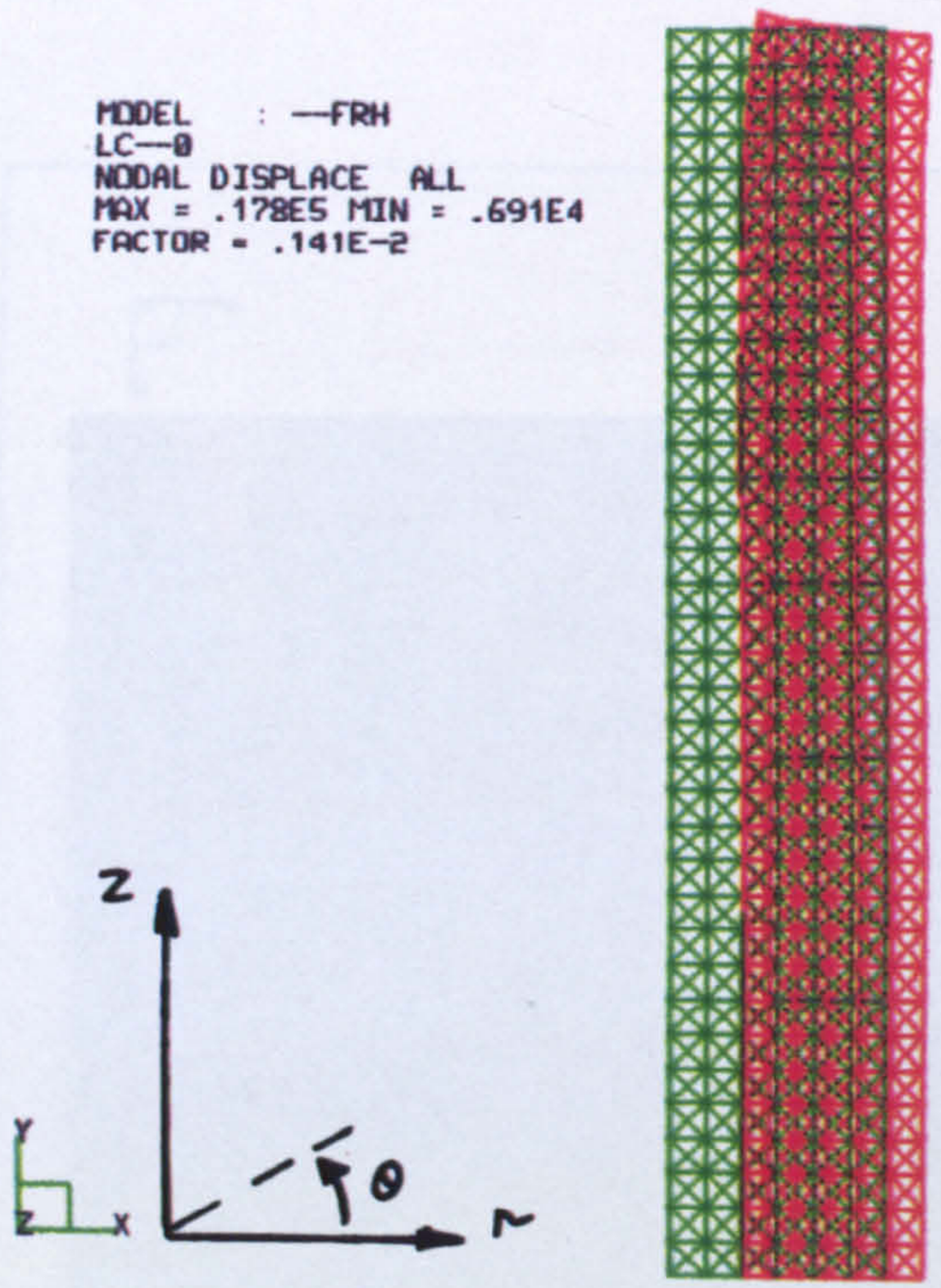

Figure 8.22: The original homogenous material pressure vessel mesh (green) and the displaced mesh (red). The mesh has a ratio ($b/a = 2.0$), (Fig.8.19) and ($n = 2.0$). Note the end-effect at the top left hand side of the displaced mesh.

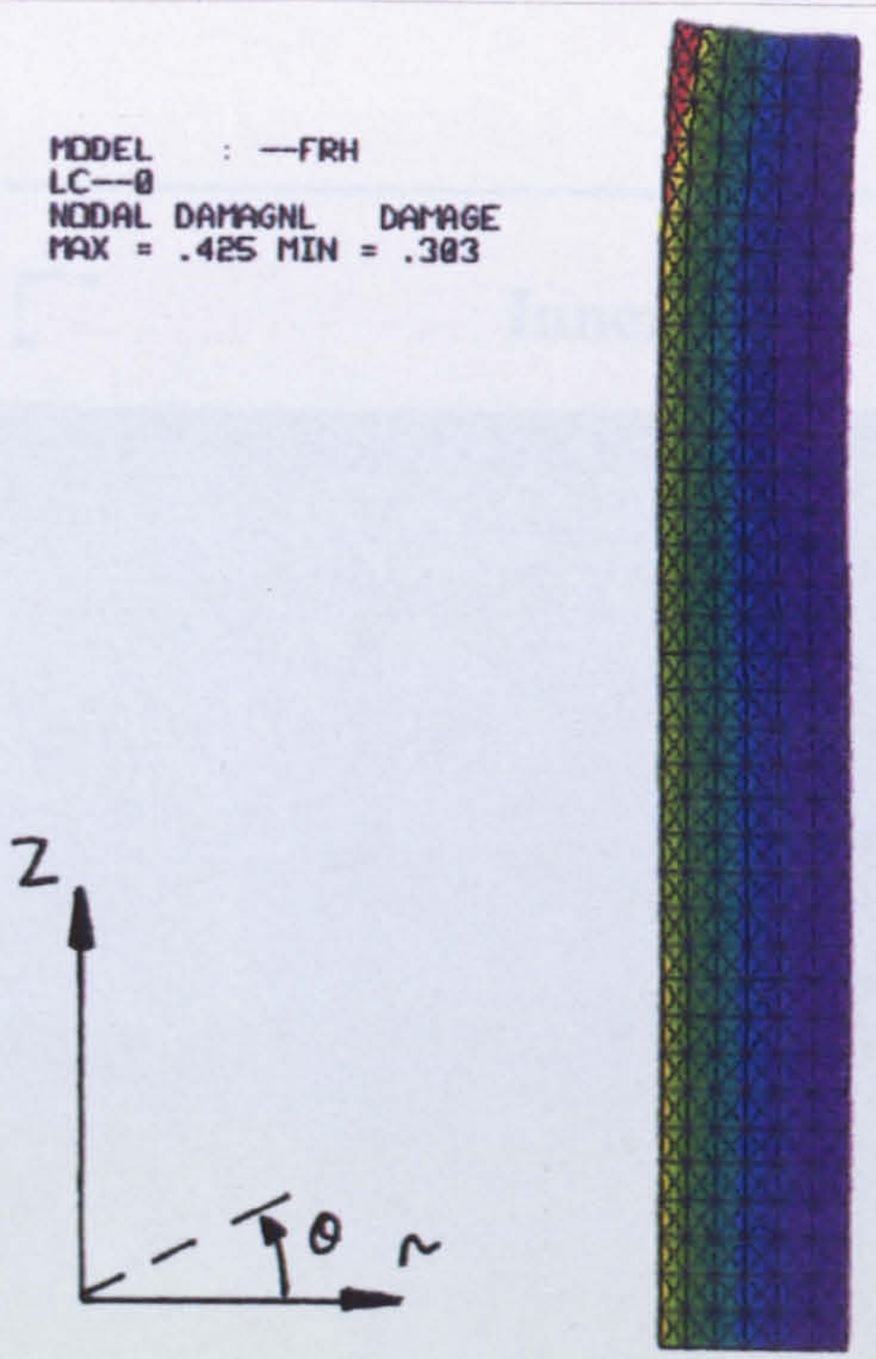

Figure 8.23: Colour damage distribution for the homogenous pressure vessel showing that the region of maximum damage (red) concentrates at the locally deformed region at the end of the pressure vessel tube.

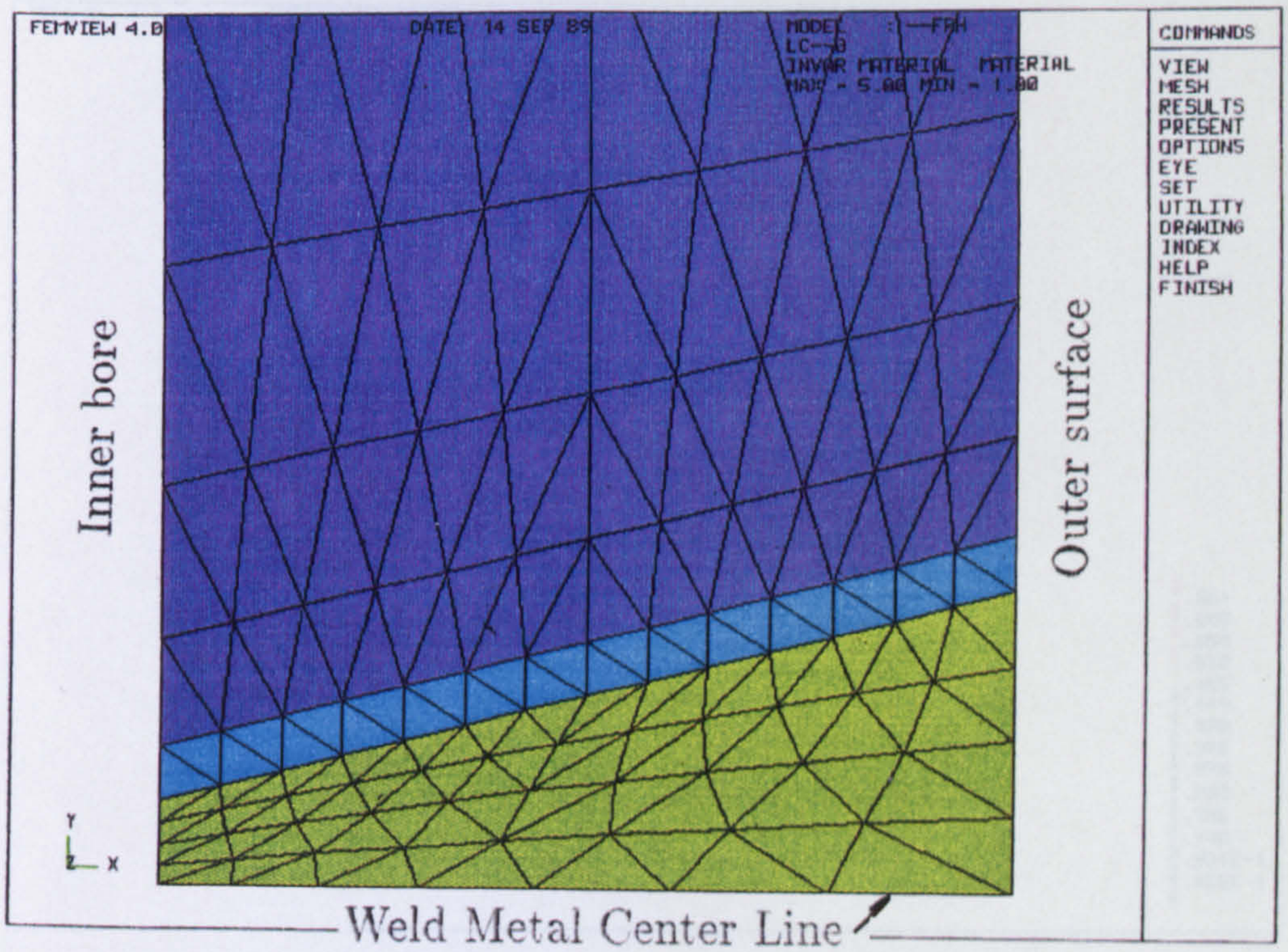

Figure 8.24: The lower section of the axisymmetric finite element mesh for the first weld model (WM1) (Fig.8.9), as used to model the 2.25Cr 1Mo:0.5Cr 0.5Mo 0.25V thick steam pipe weld. The dark blue, the blue and the green regions are assigned the material properties (Table 8.3) of the parent metal, the HAZ(G.C.P.) and the weld metal, respectively.

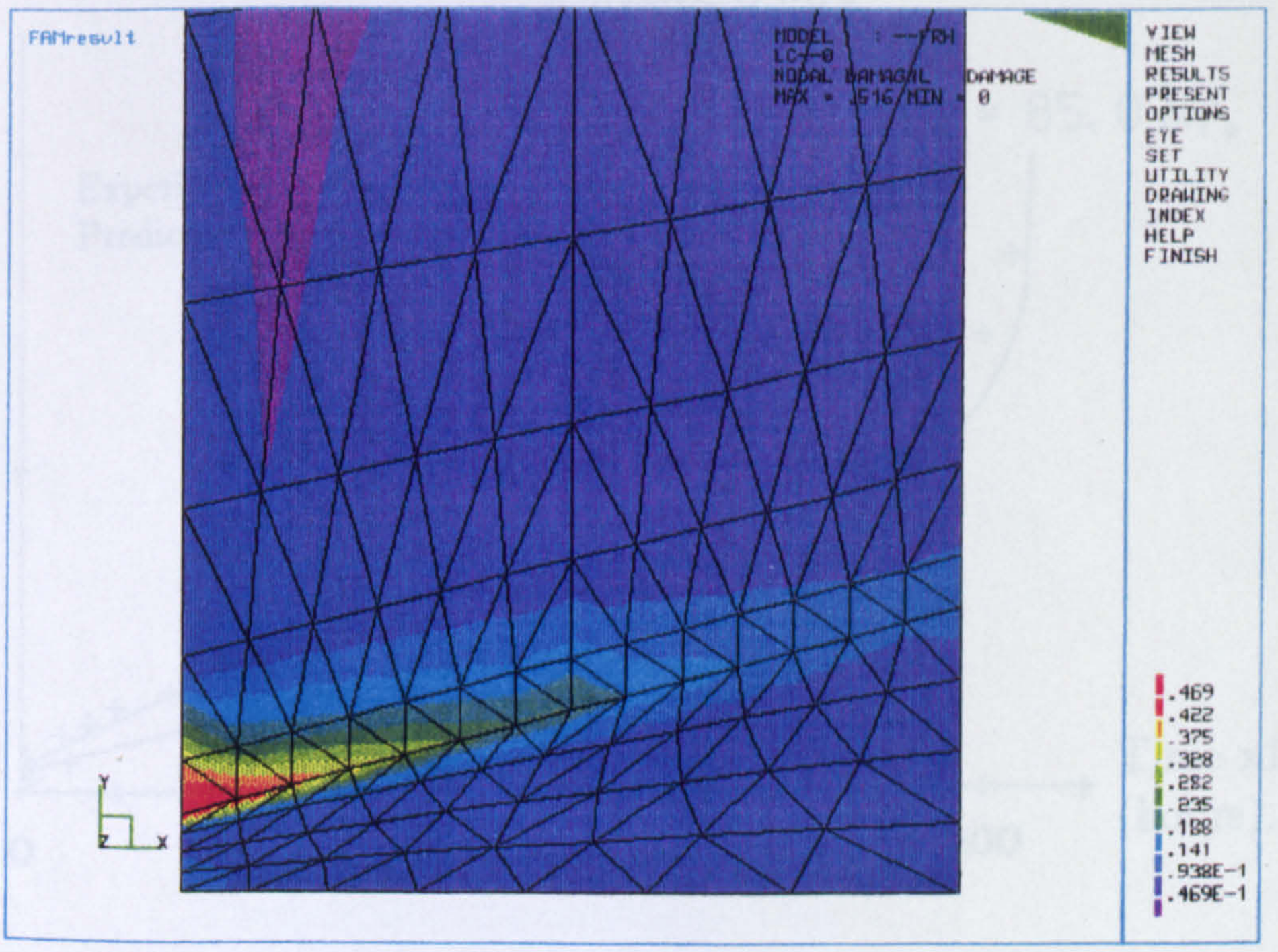

Figure 8.25: Damge distribution at a life fraction (t/t_f = 31.2%). The value of (α=0.0) for the weld metal. The maximum damaged region occurs in the HAZ at the inner bore.

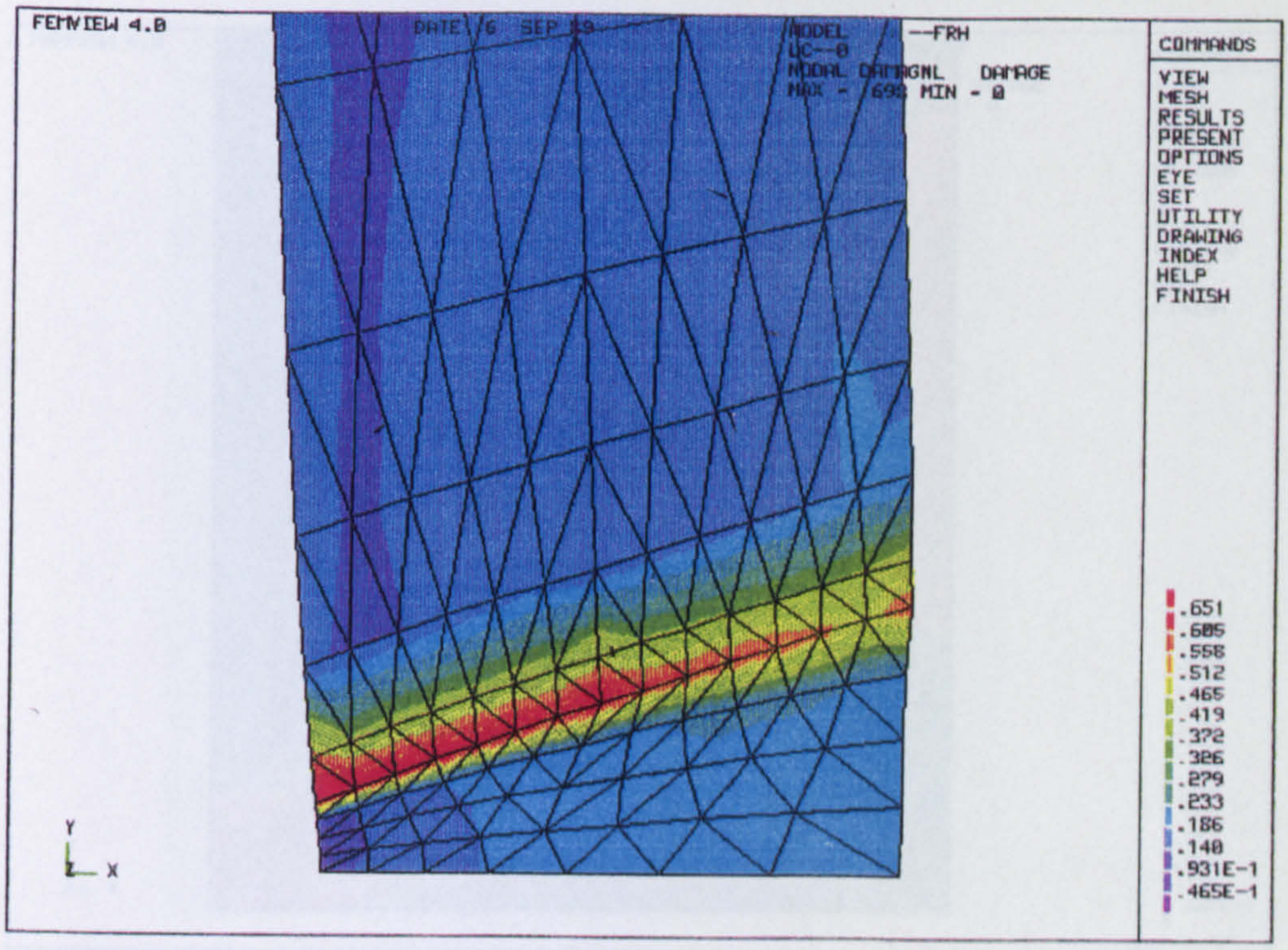

Figure 8.26: Damge distribution at a life fraction (t/t_f = 90.0%). The value of (α=0.4298) for the weld metal. The maximum damaged region occurs in the HAZ.

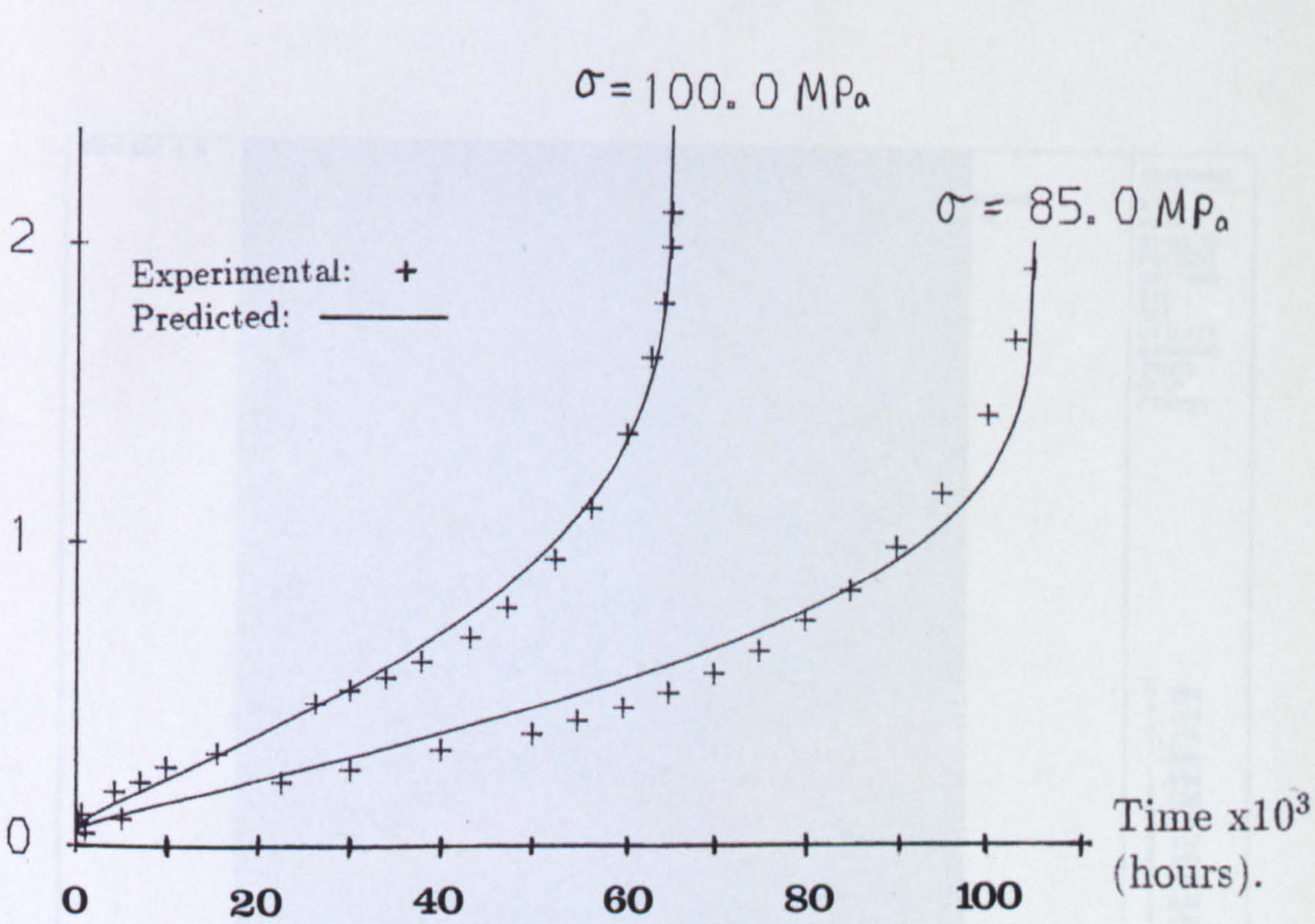

Figure 8.27: Comparison between the experimental uni-axial creep strain data and the predicted creep curves for the 100MPa and the 85.0 Mpa HAZ(G.C.P.) creep tests. These new curves creep curves give an improved low stress fit to the creep data (c.f.Fig.8.14(b)). The new material parameters are given in Table 8.3(d).

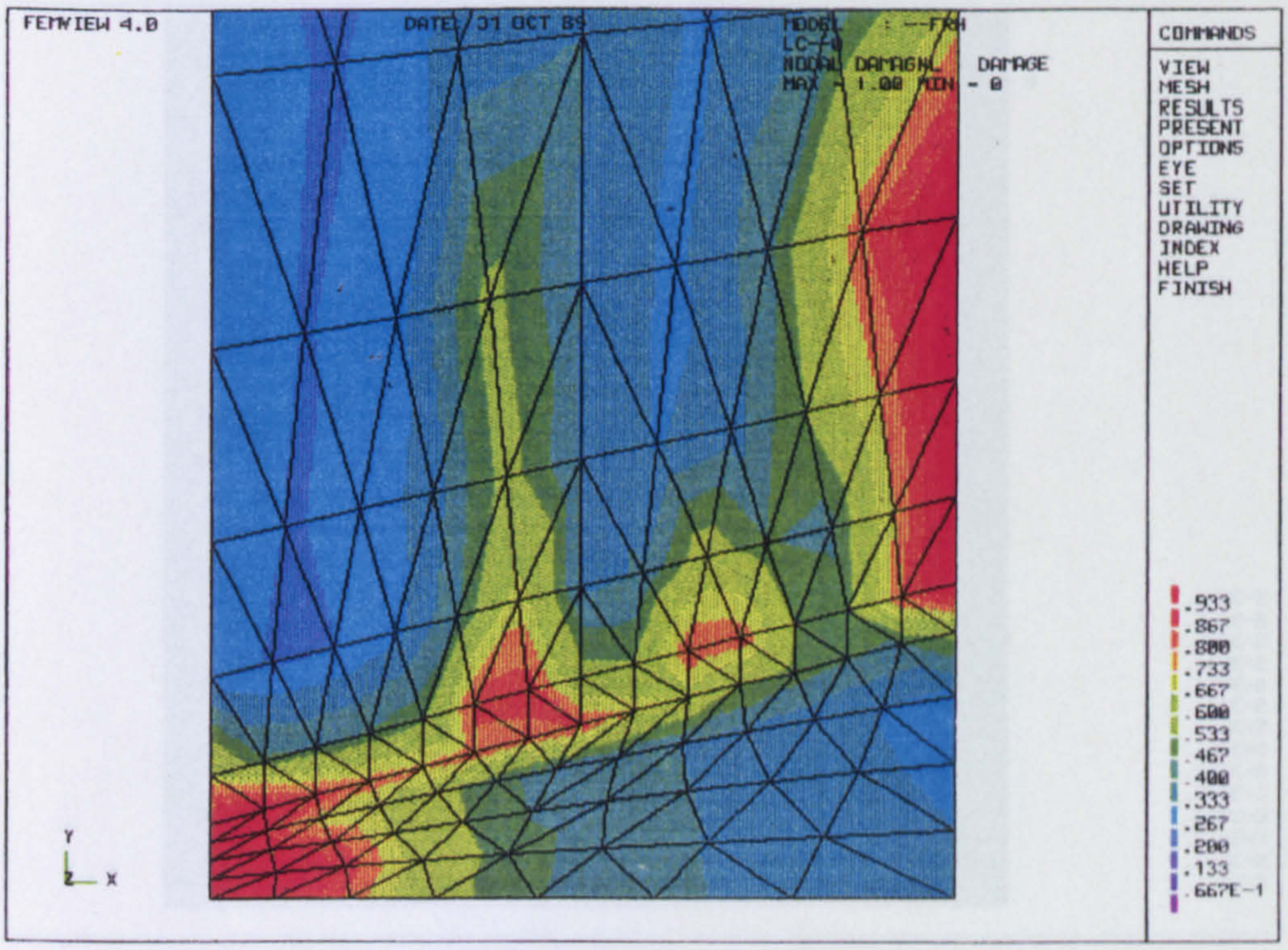

Figure 8.28: Damage distribution for weld model (WM1), at a life fraction ($t/t_f = 99.9\%$), using the new HAZ(2) material constants Table 8.3(d) and a value of (α=0.0) for the weld metal.

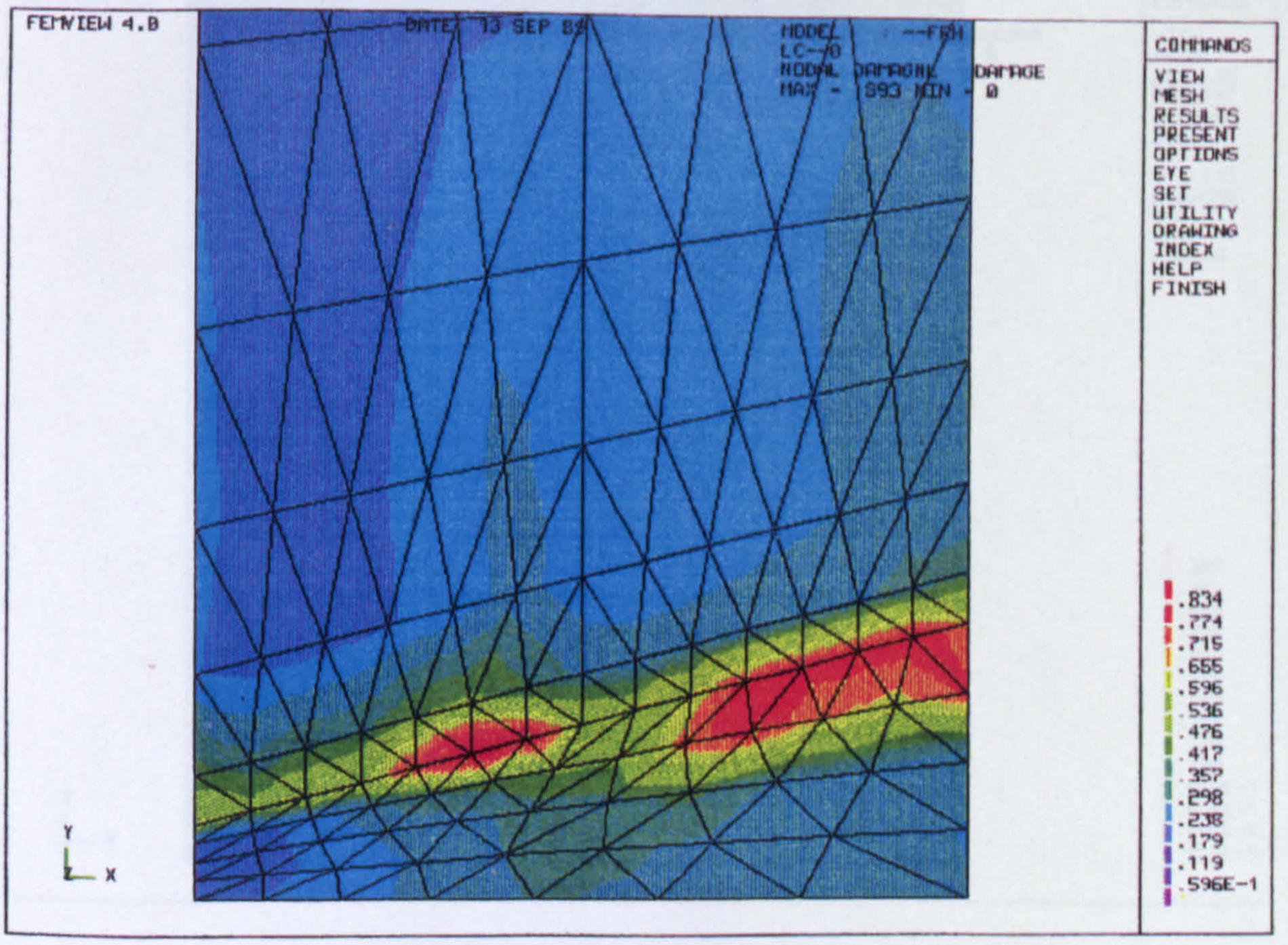

Figure 8.29: Damage distribution for weld model (WM1), at a life fraction ($t/t_f = 99.9\%$), using the new HAZ(2) material constants (Table 8.3(d)) and a value of (α=0.4298) for the weld metal. The region of maximum damage localises mainly in outer weld metal at the fusion boundary.

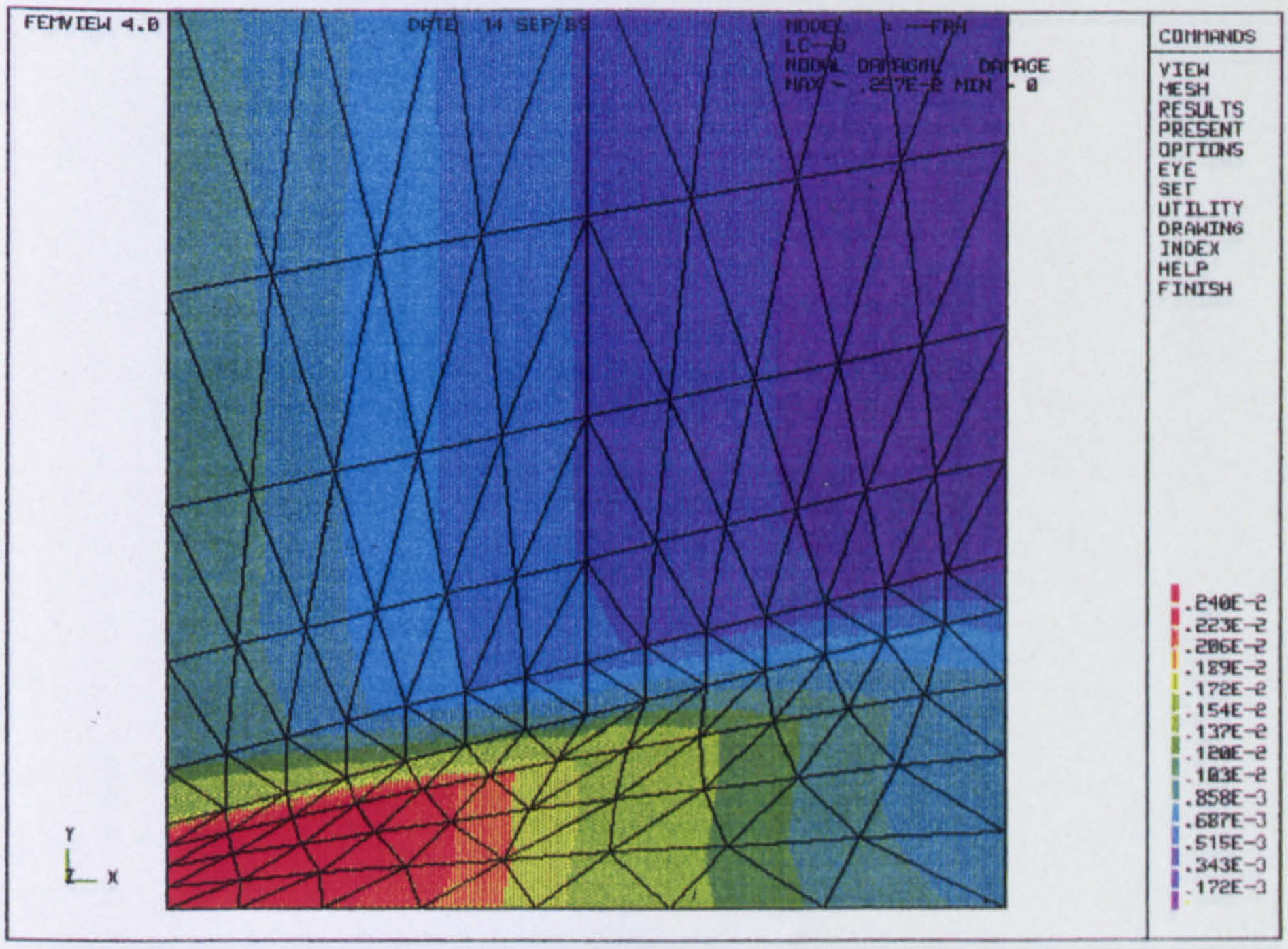

Figure 8.30: Damage distribution for weld model (WM1), at a life fraction ($t/t_f = 0.12\%$), using the new HAZ(2) material constants (Table 8.3(d)) and a value of (α=0.4298) for the weld metal. The region of maximum damage is at the inner bore of the weld metal.

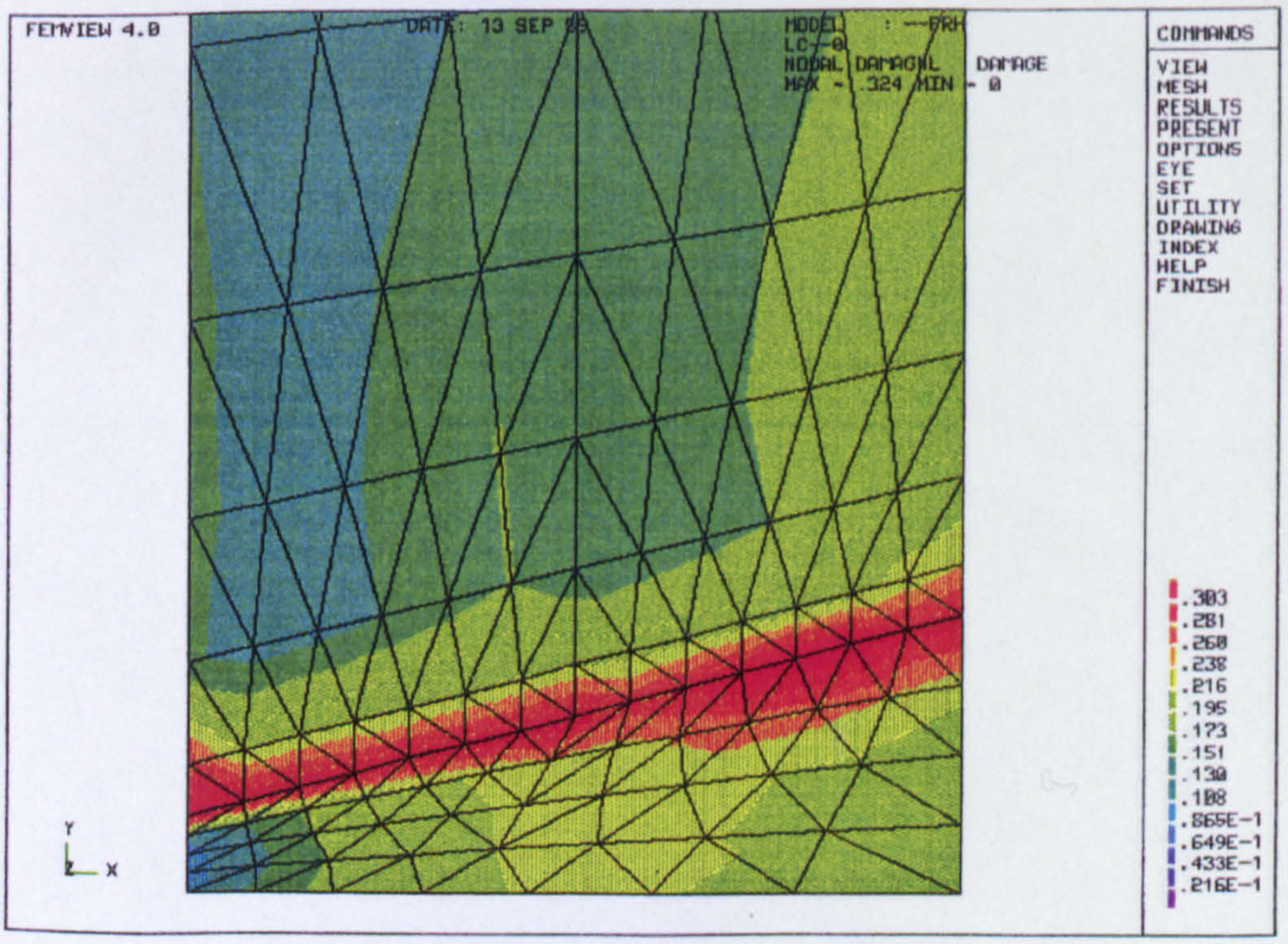

Figure 8.31: Damage distribution for weld model (WM1) at a life fraction ($t/t_f = 77.2\%$).

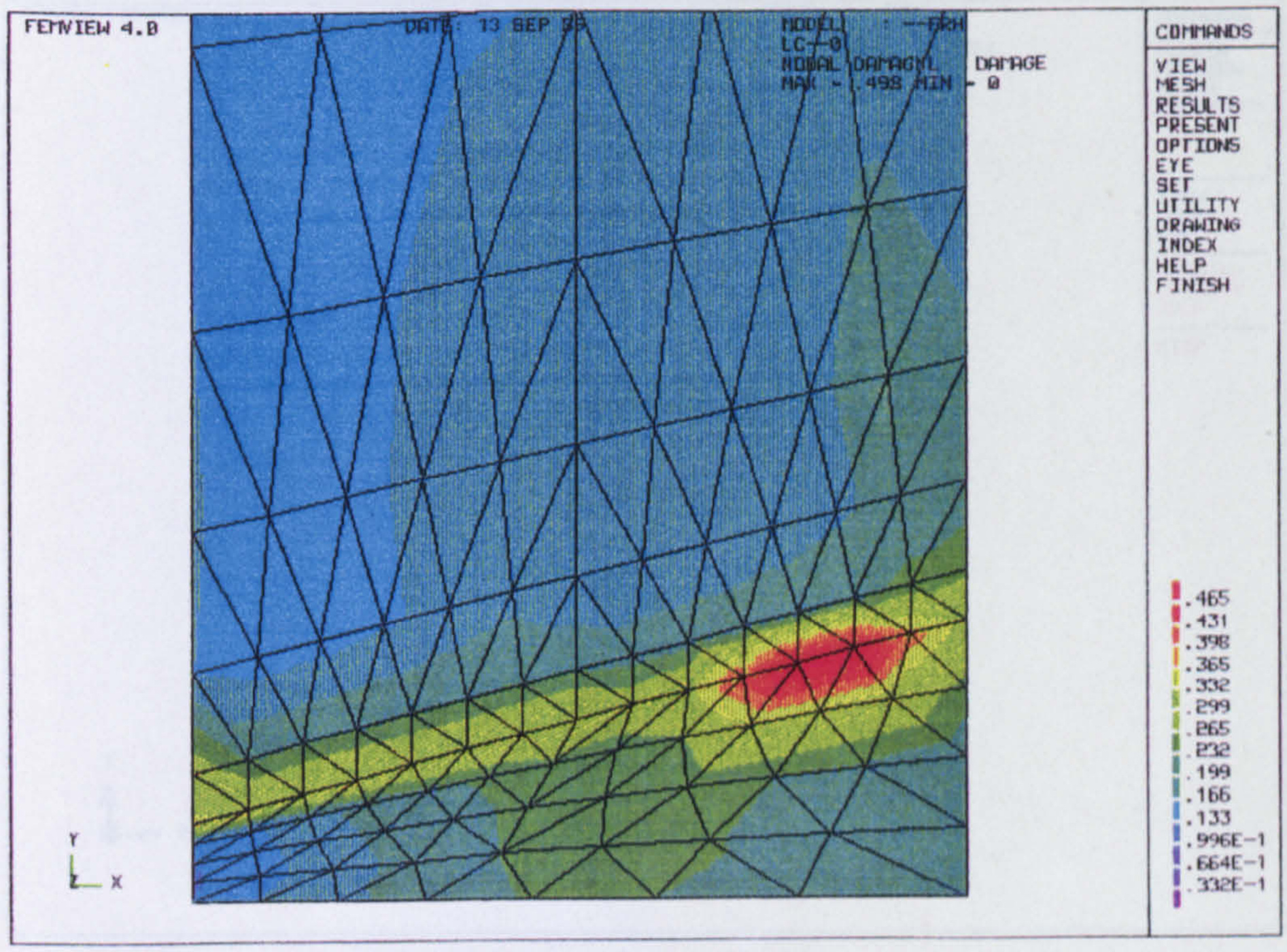

Figure 8.32: Damage distribution for weld model (WM1) at a life fraction ($t/t_f = 80.8\%$).

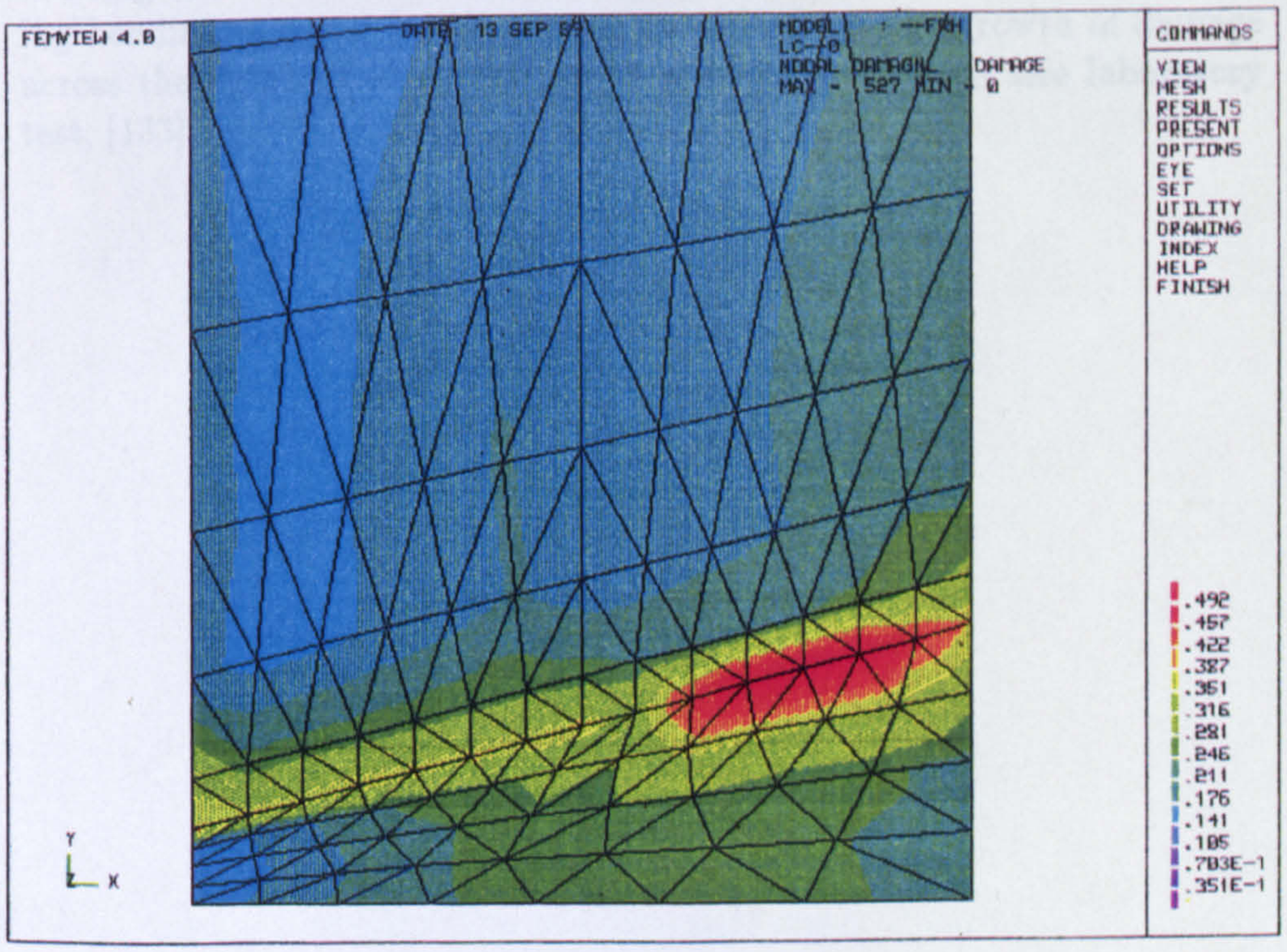

Figure 8.33: Damage distribution for weld model (WM1) at a life fraction ($t/t_f = 87.0\%$).

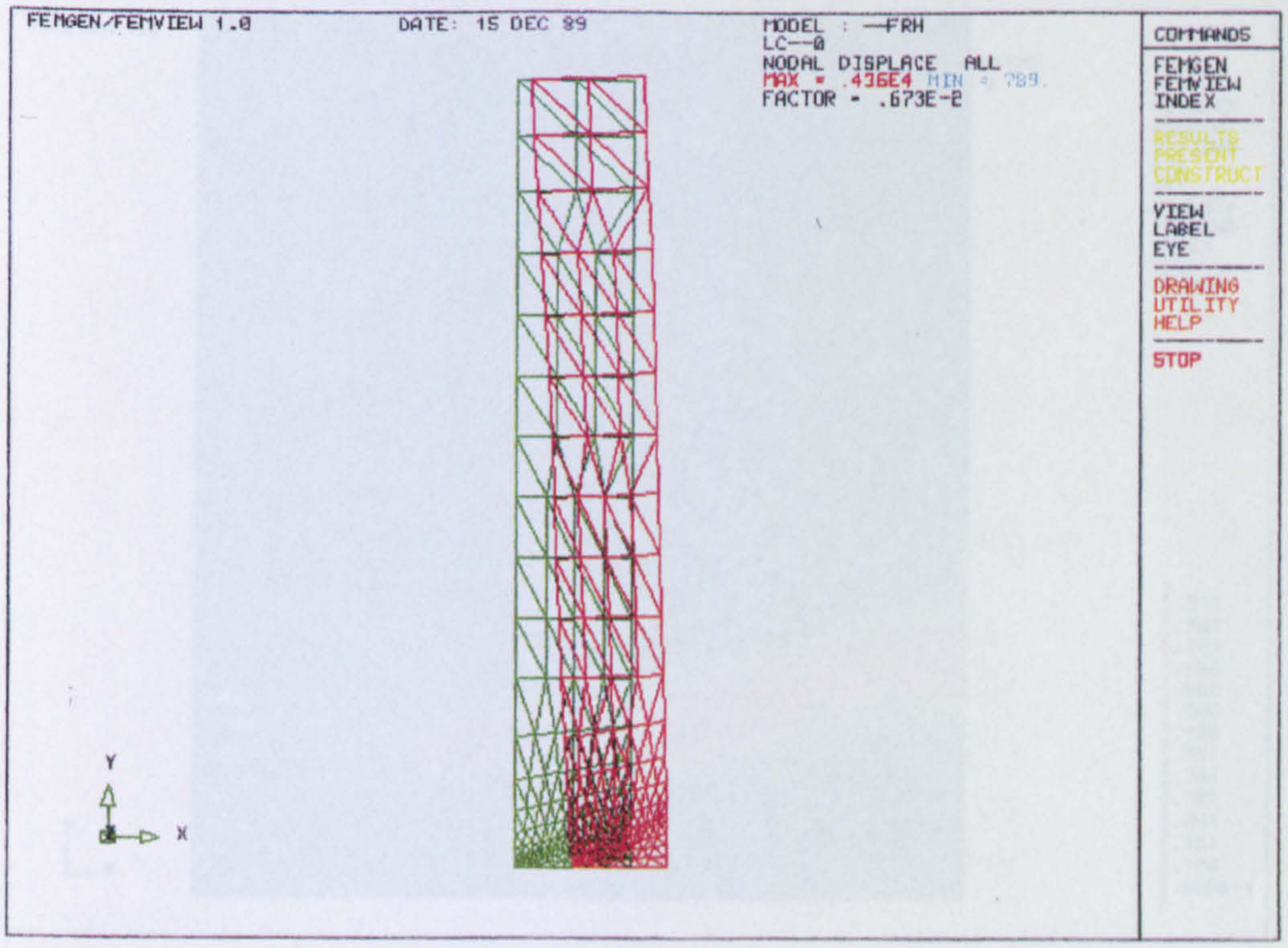

Figure 8.34: The original finite element mesh for weld model (WM1) is shown in green and the displaced mesh is shown in red at a life fraction of ($t_f \approx 77.2\%$), havig a corresponding damage distribution given in Fig.8.31. The displaced plot shows how the weld metal deforms most, it being the weakest in creep strength, and how then weld bulges causing bending to occur in the pressure vessel due to the growth of damage across the ligament (Fig.8.31); as is observed in the full size laboratory test, [133], and Fig.8.8.

(a)

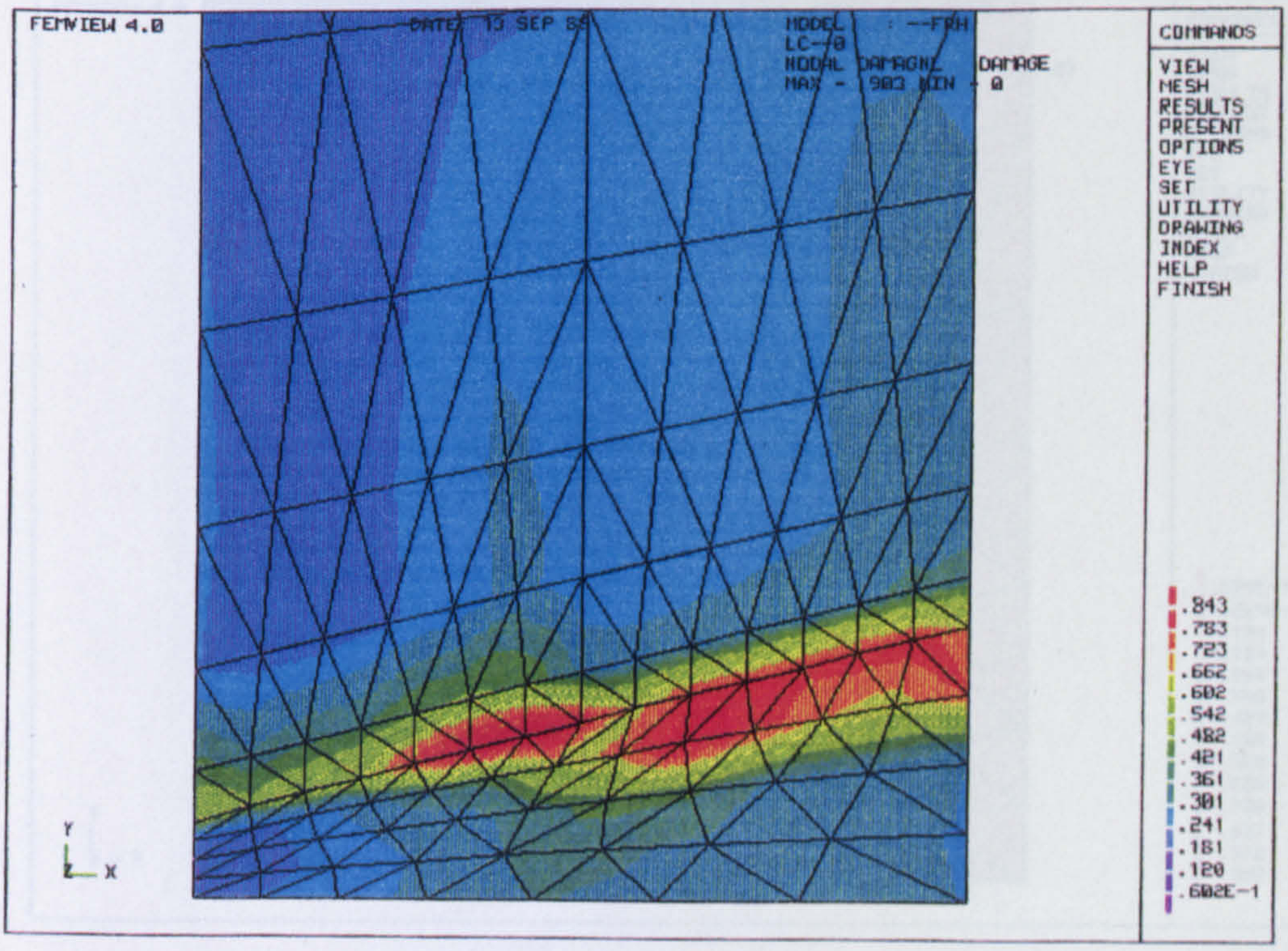

(b)

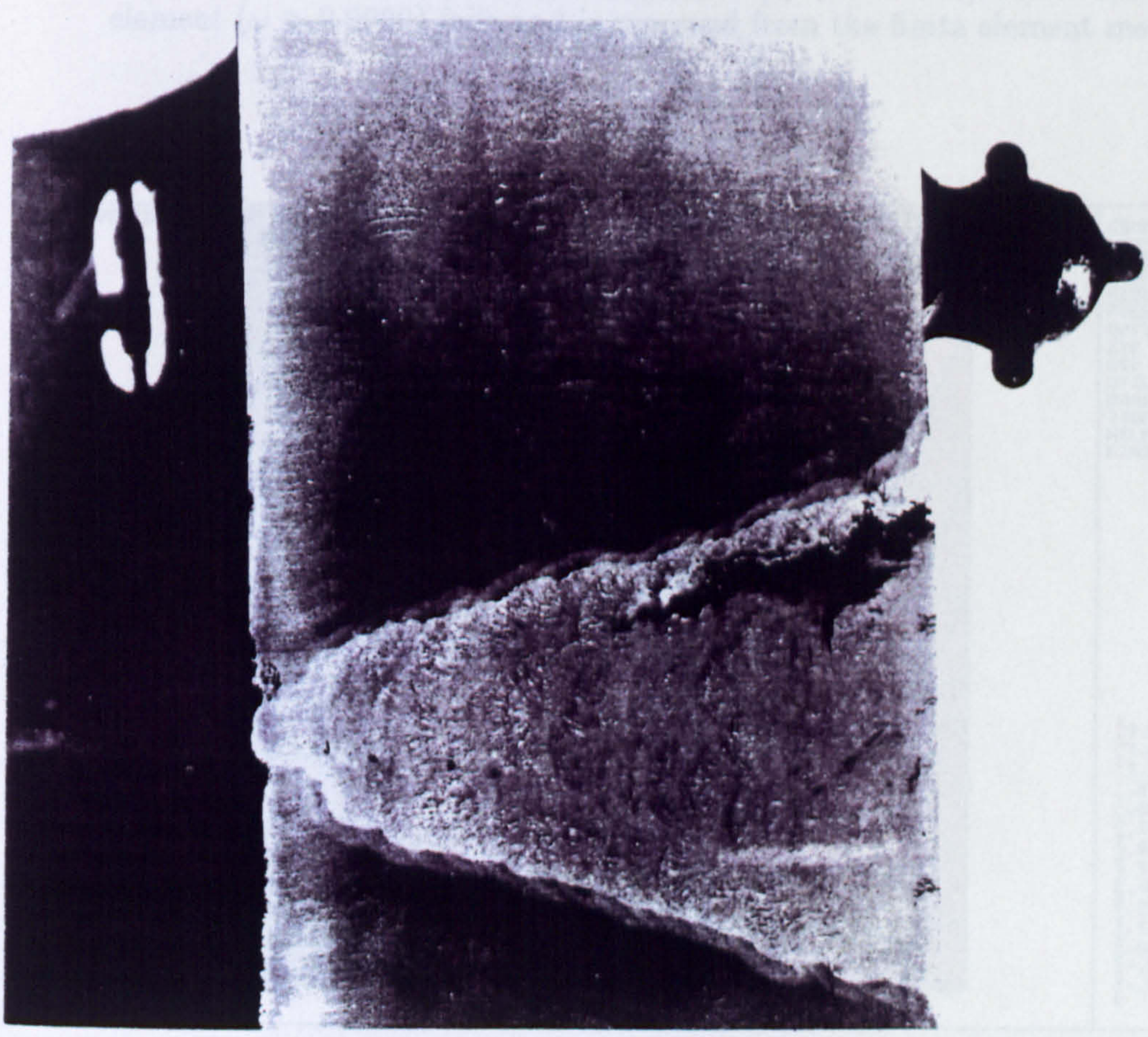

Figure 8.35: (a) Damage distribution for weld model (WM1) at a life fraction ($t/t_f \approx 100.0\%$) predicting the formation of a failed region ($\omega > 0.8$ in the colour plot key), which may be compared with (b) which shows the cracking observed in a section taken through the 2.25Cr 1Mo steam pipe weld at vessel failure. Micrograph courtesy Coleman [149].

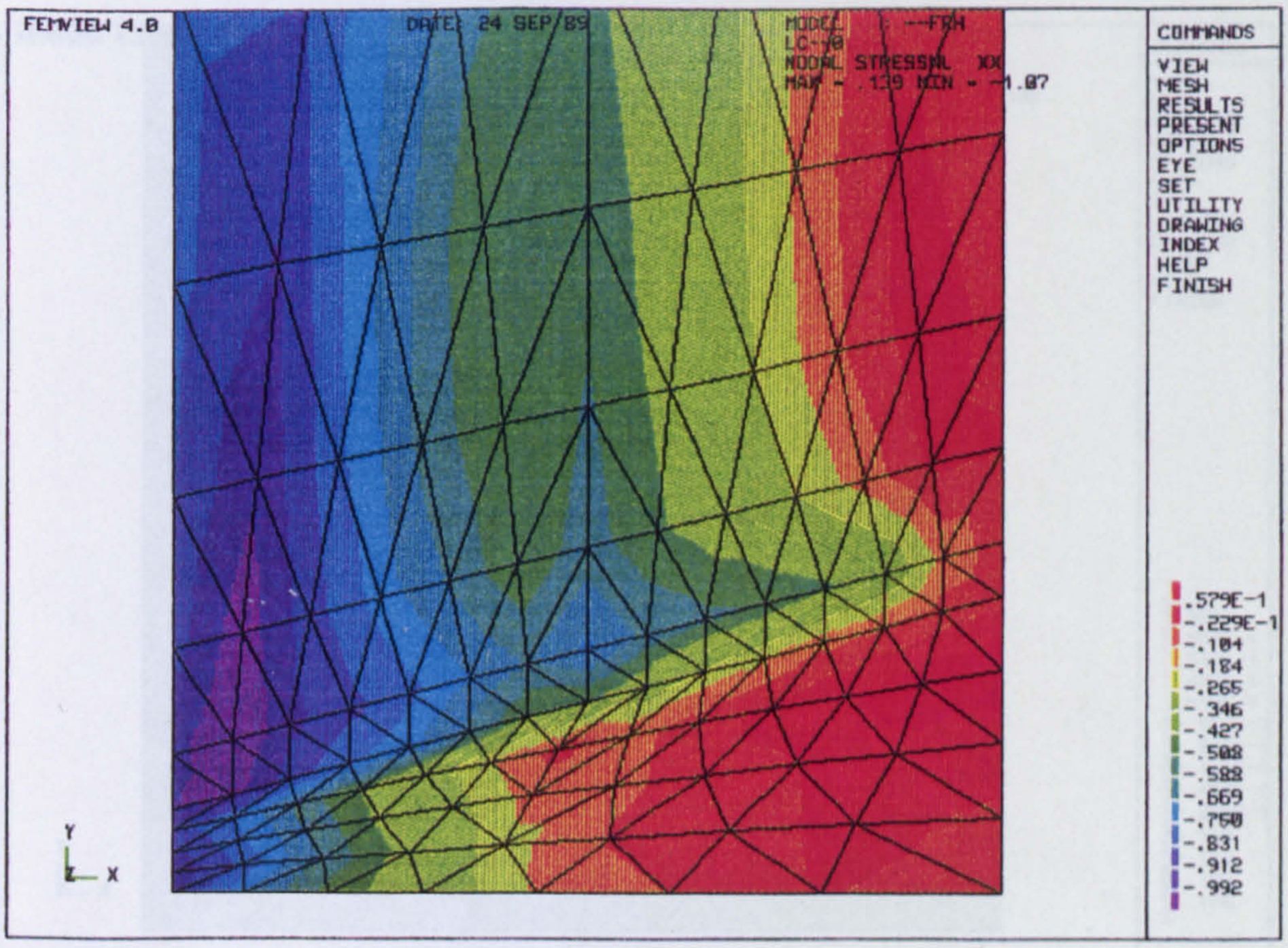

Figure 8.36: Distribution of the normalised radial stress ($\Sigma_r = \sigma_r/\sigma_o$) for weld model (WM1) at a life fraction of ($t/t_f = 77.2\%$) before the first element ($\omega > 0.9999$) fails and is removed from the finite element mesh.

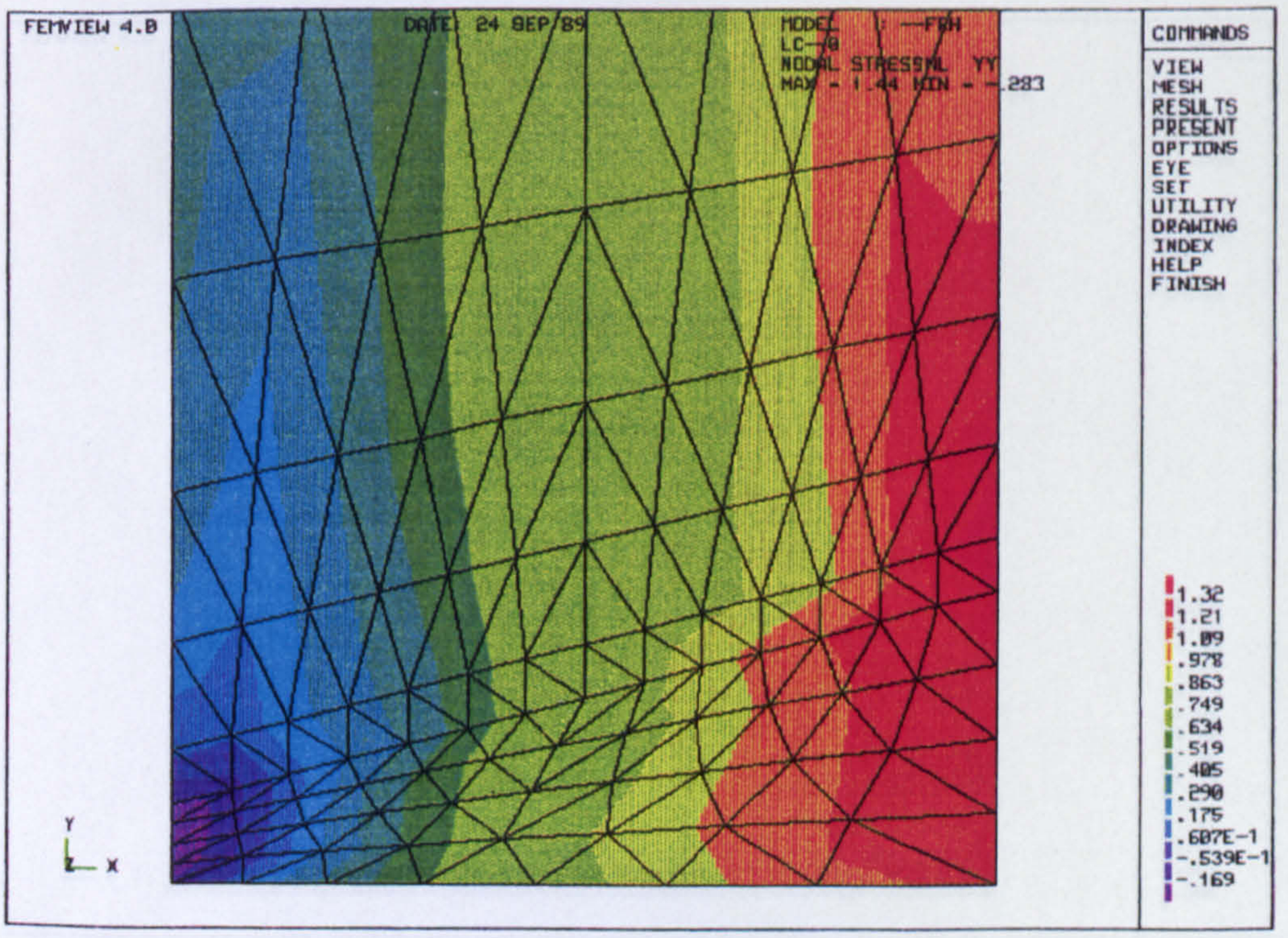

Figure 8.37: Distribution of the normalised axial stress ($\Sigma_z = \sigma_z/\sigma_o$) for weld model (WM1) at a life fraction of ($t/t_f = 77.2\%$) before the first element ($\omega > 0.9999$) fails and is removed from the finite element mesh.

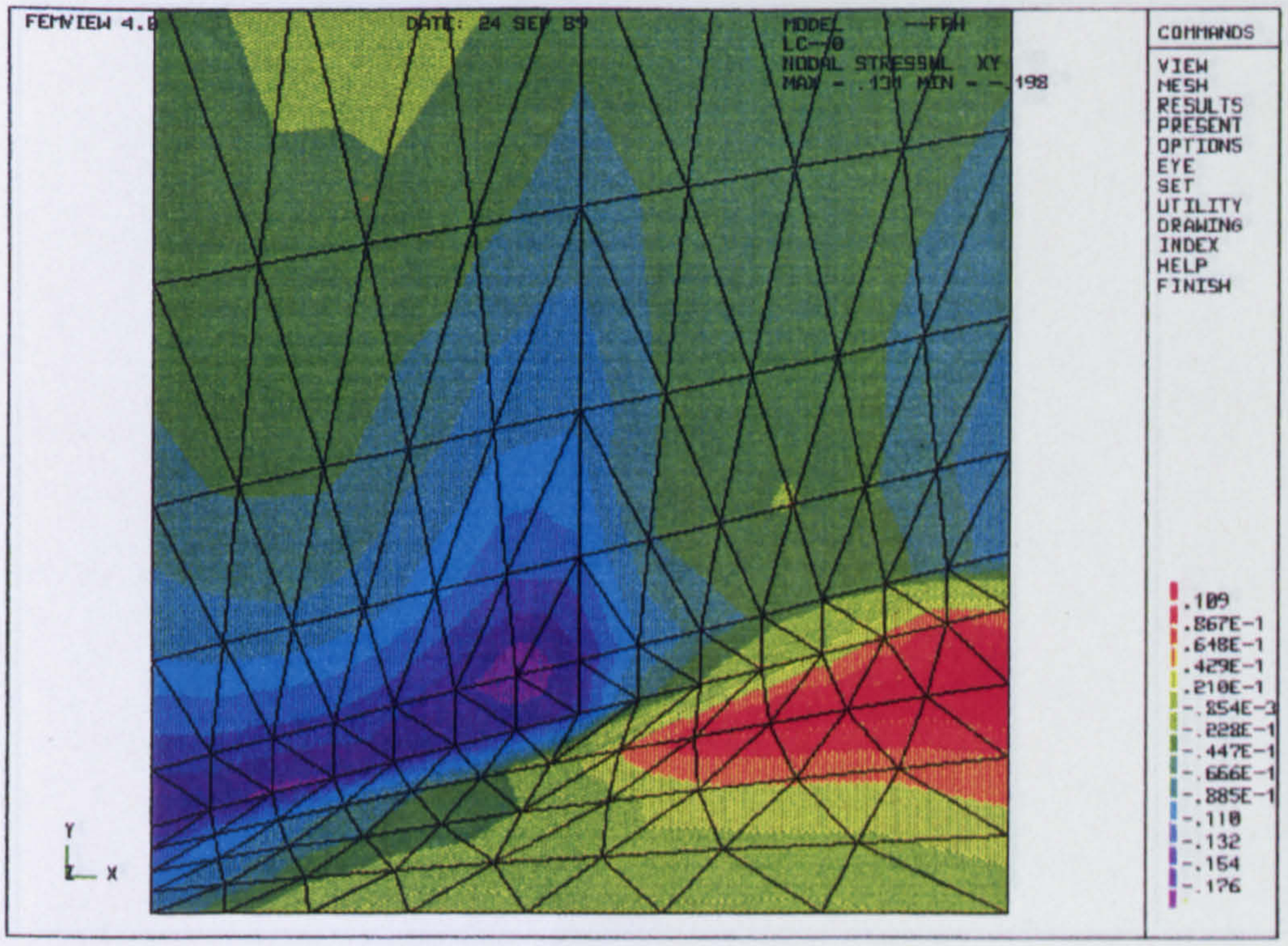

Figure 8.38: Distribution of the normalised radial/axial shear stress ($\Sigma_{rz} = \sigma_{rz}/\sigma_o$) for weld model (WM1) at a life fraction of ($t/t_f = 77.2\%$) before the first element ($\omega > 0.9999$) fails and is removed from the finite element mesh.

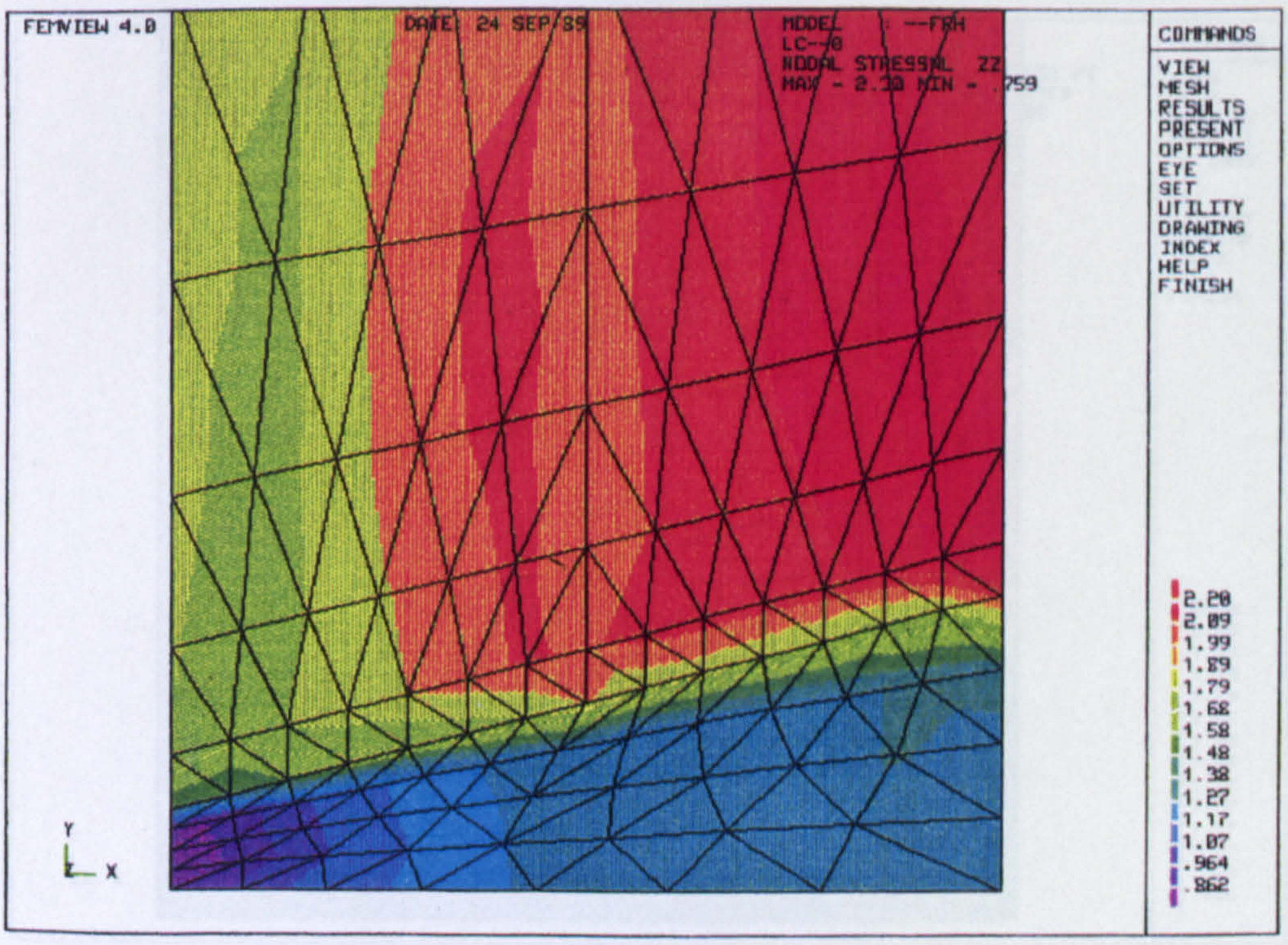

Figure 8.39: Distribution of the normalised hoop stress ($\Sigma_\theta = \sigma_\theta/\sigma_o$) for weld model (WM1) at a life fraction of ($t/t_f = 77.2\%$) before the first element ($\omega > 0.9999$) fails and is removed from the finite element mesh.

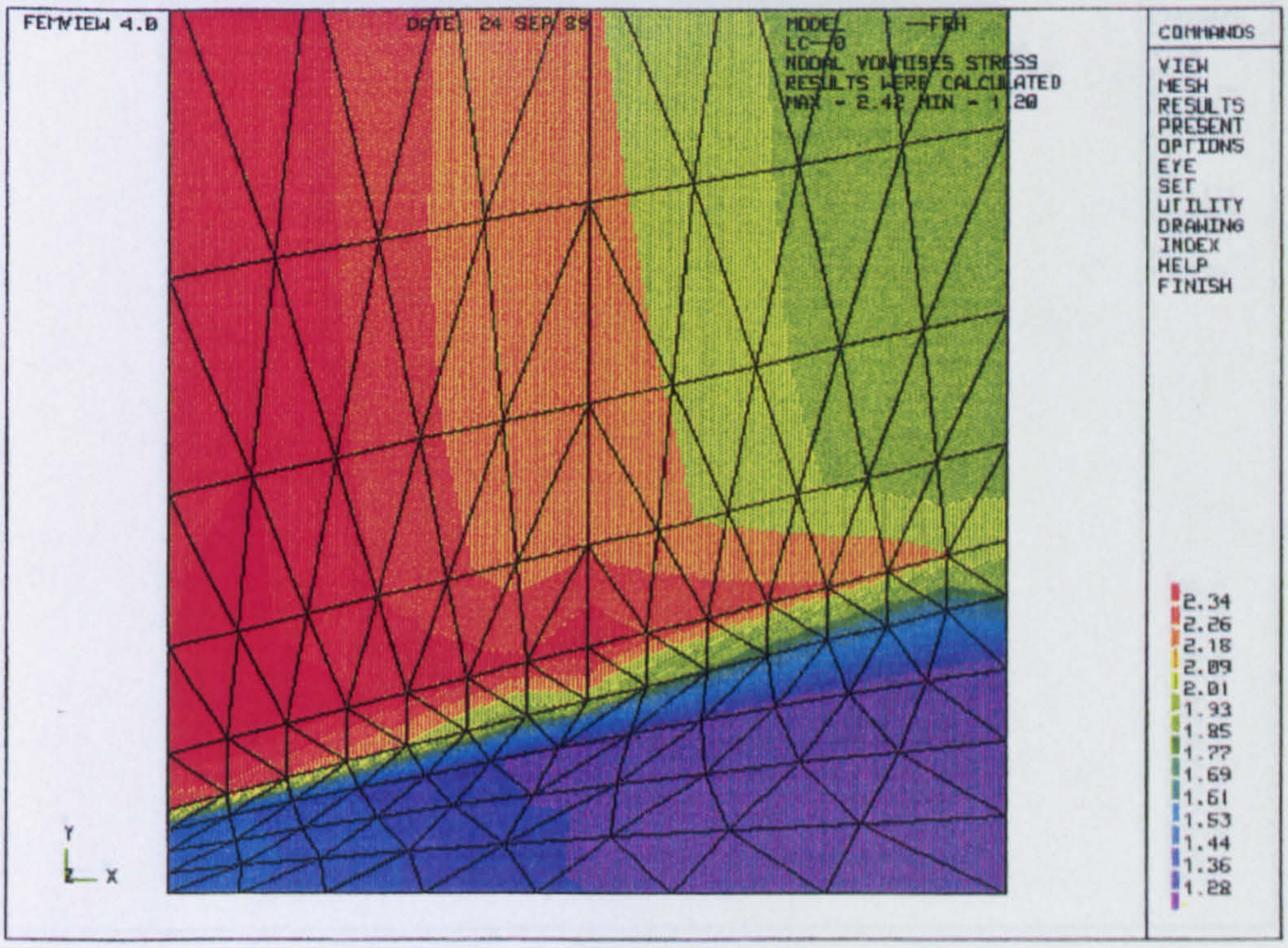

Figure 8.40: Distribution of the normalised Von Mises (effective) stress ($\Sigma_{ef} = \sigma_{ef}/\sigma_o$) for weld model (WM1) at a life fraction of ($t/t_f = 77.2\%$) before the first element ($\omega > 0.9999$) fails and is removed from the finite element mesh.

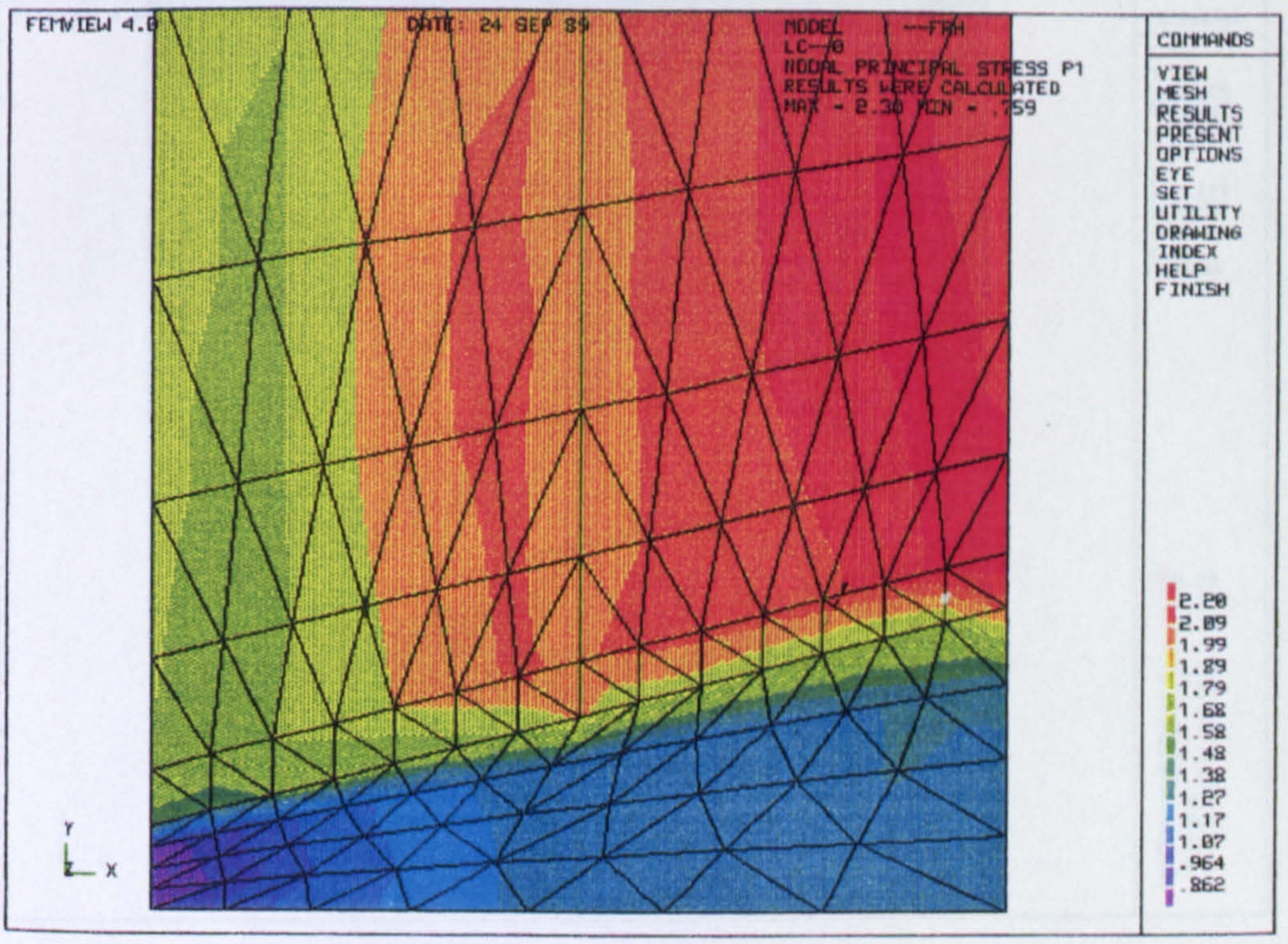

Figure 8.41: Distribution of the normalised maximum principal stress ($\Sigma_1 = \sigma_1/\sigma_o$) for weld model (WM1) at a life fraction of ($t/t_f = 77.2\%$) before the first element ($\omega > 0.9999$) fails and is removed from the finite element mesh.

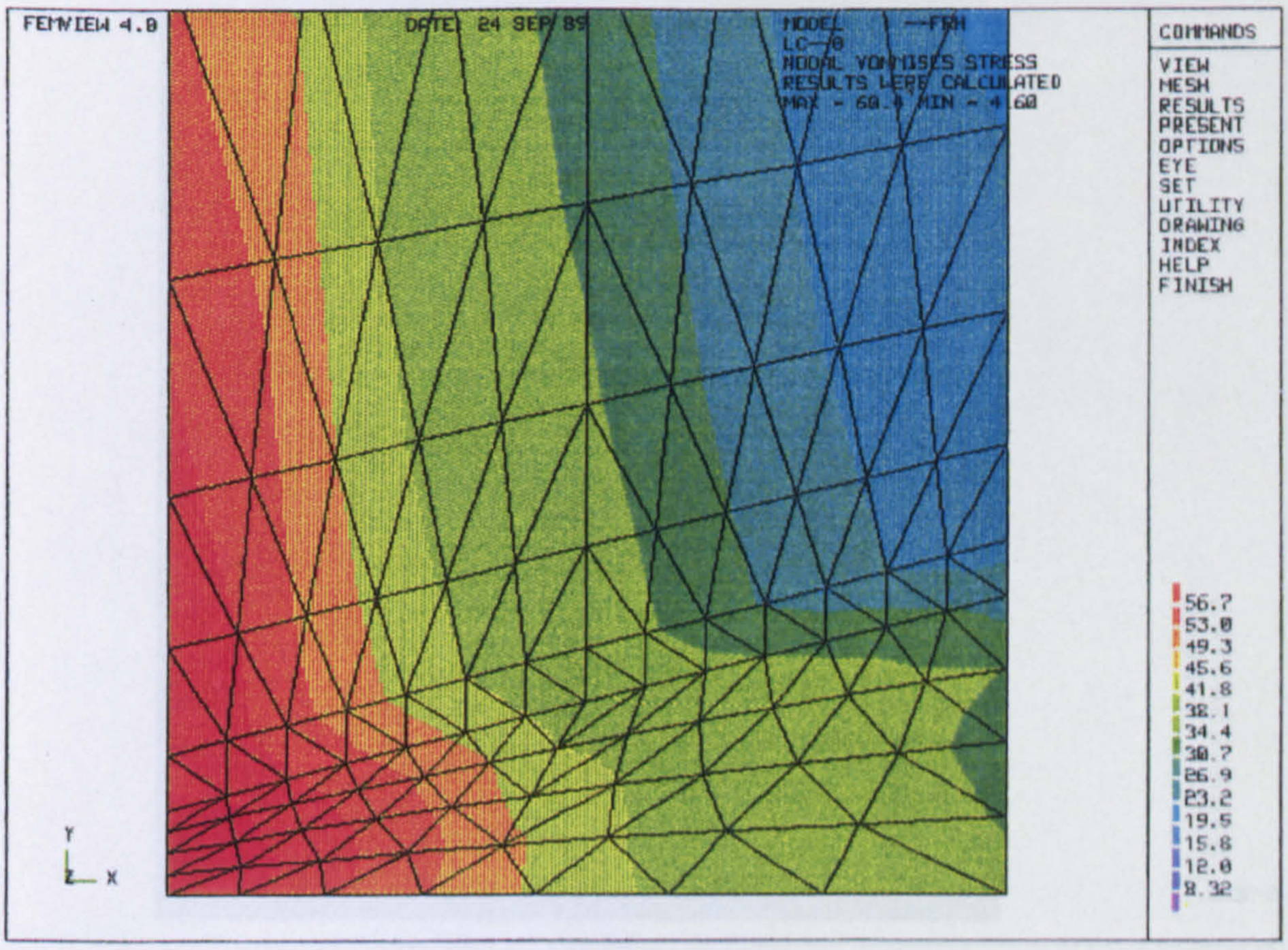

Figure 8.42: Distribution of the normalised Von Mises (effective) creep strain ($V_{ef} = \epsilon_{ef}/\sigma_o$) for weld model (WM1) at a life fraction of ($t/t_f = 77.2\%$) before the first element ($\omega > 0.9999$) fails and is removed from the finite element mesh.

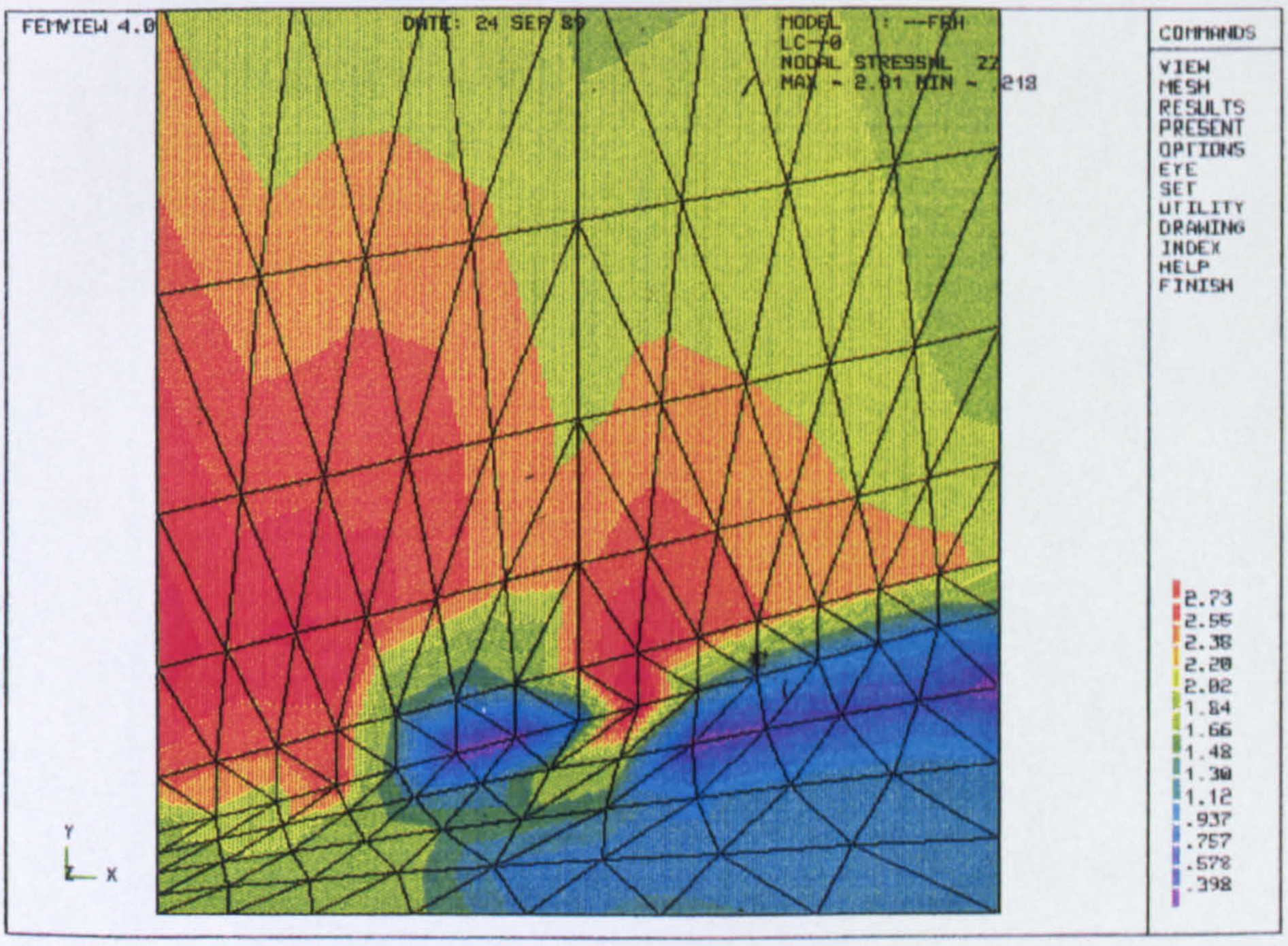

Figure 8.43: Distribution of the normalised hoop stress ($\Sigma_\theta = \sigma_\theta/\sigma_o$) for weld model (WM1) at a life fraction of ($t/t_f = 99.9\%$).

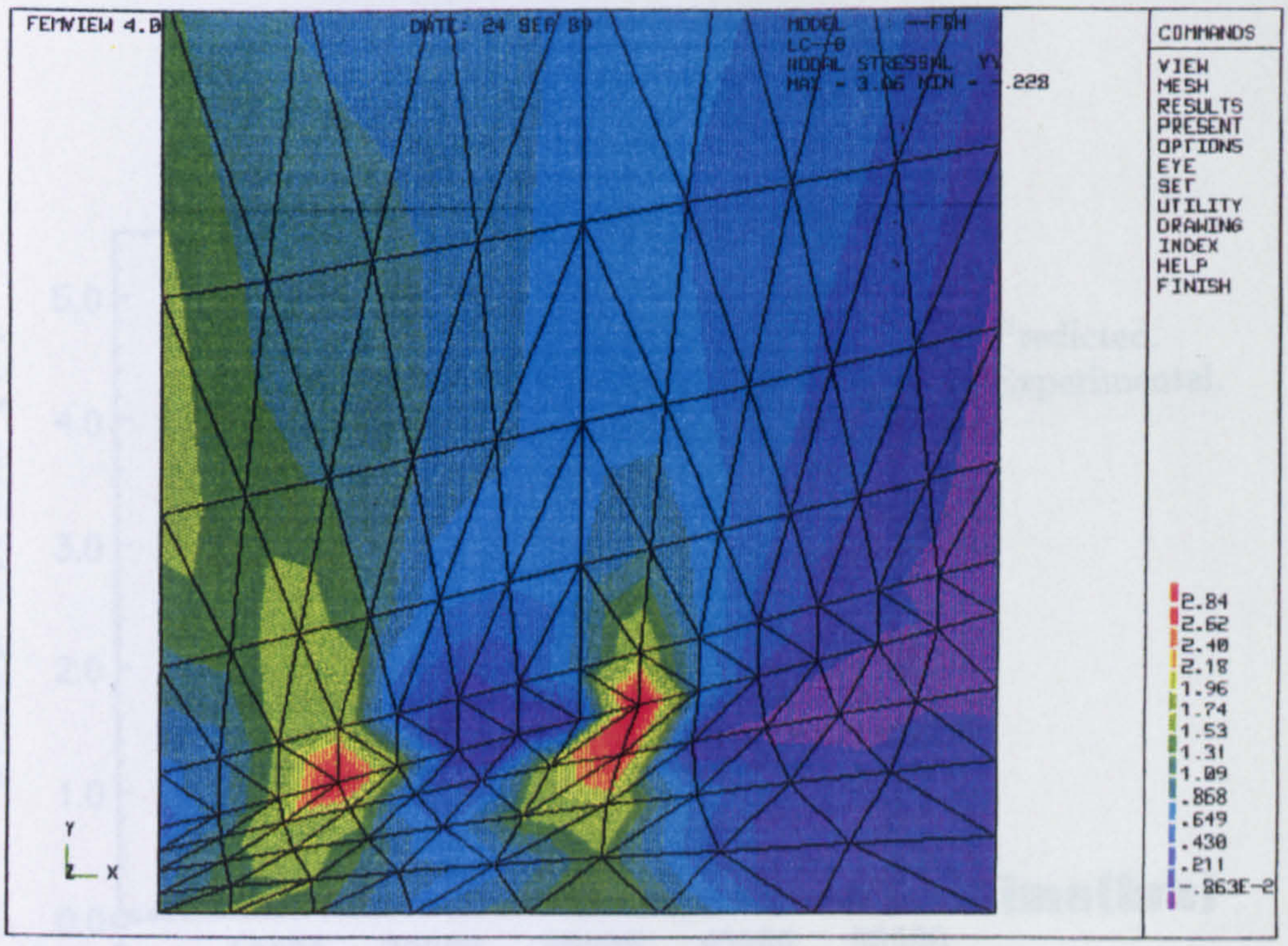

Figure 8.44: Distribution of the normalised axial stress ($\Sigma_z = \sigma_z/\sigma_o$) for weld model (WM1) at a life fraction of ($t/t_f = 99.9\%$).

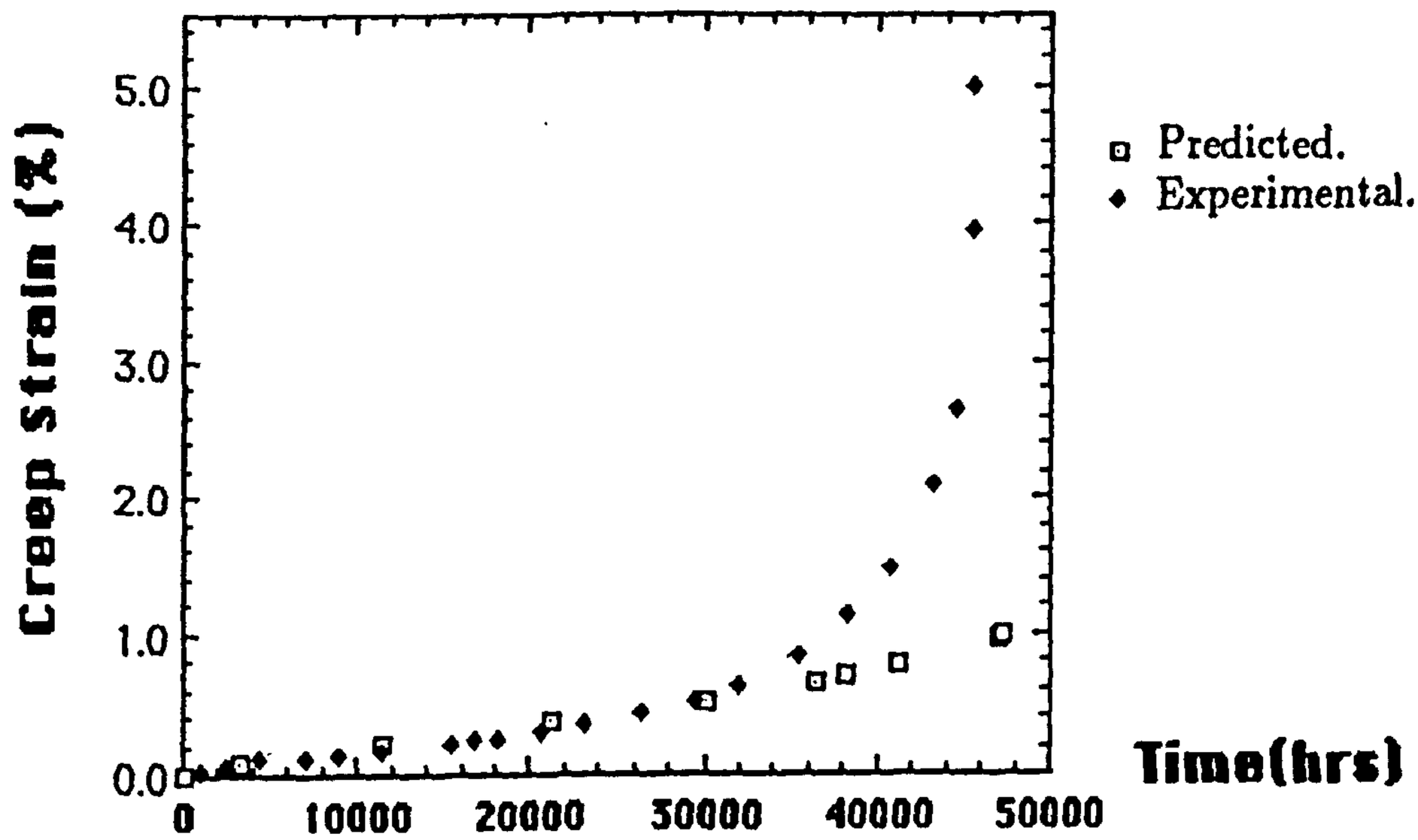

Figure 8.45: Comparison between the experimental hoop strains and those predicted from weld model (WM1) corresponding to the pip measurements at pipe weld.

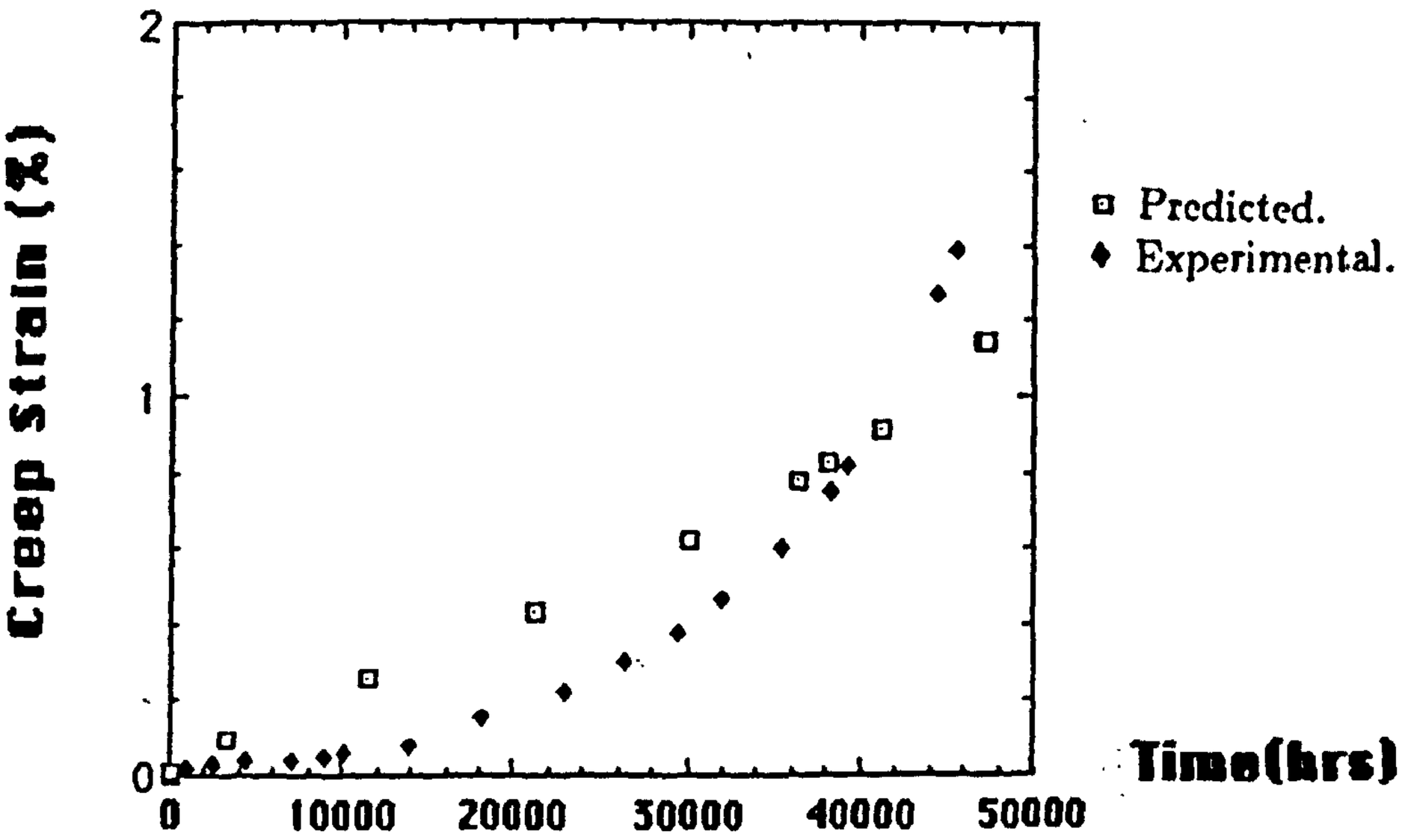

Figure 8.46: Comparison between the experimental hoop strains and those predicted from weld model (WM1) corresponding to the capacitance strain gauge measurements at the weld metal centre line.

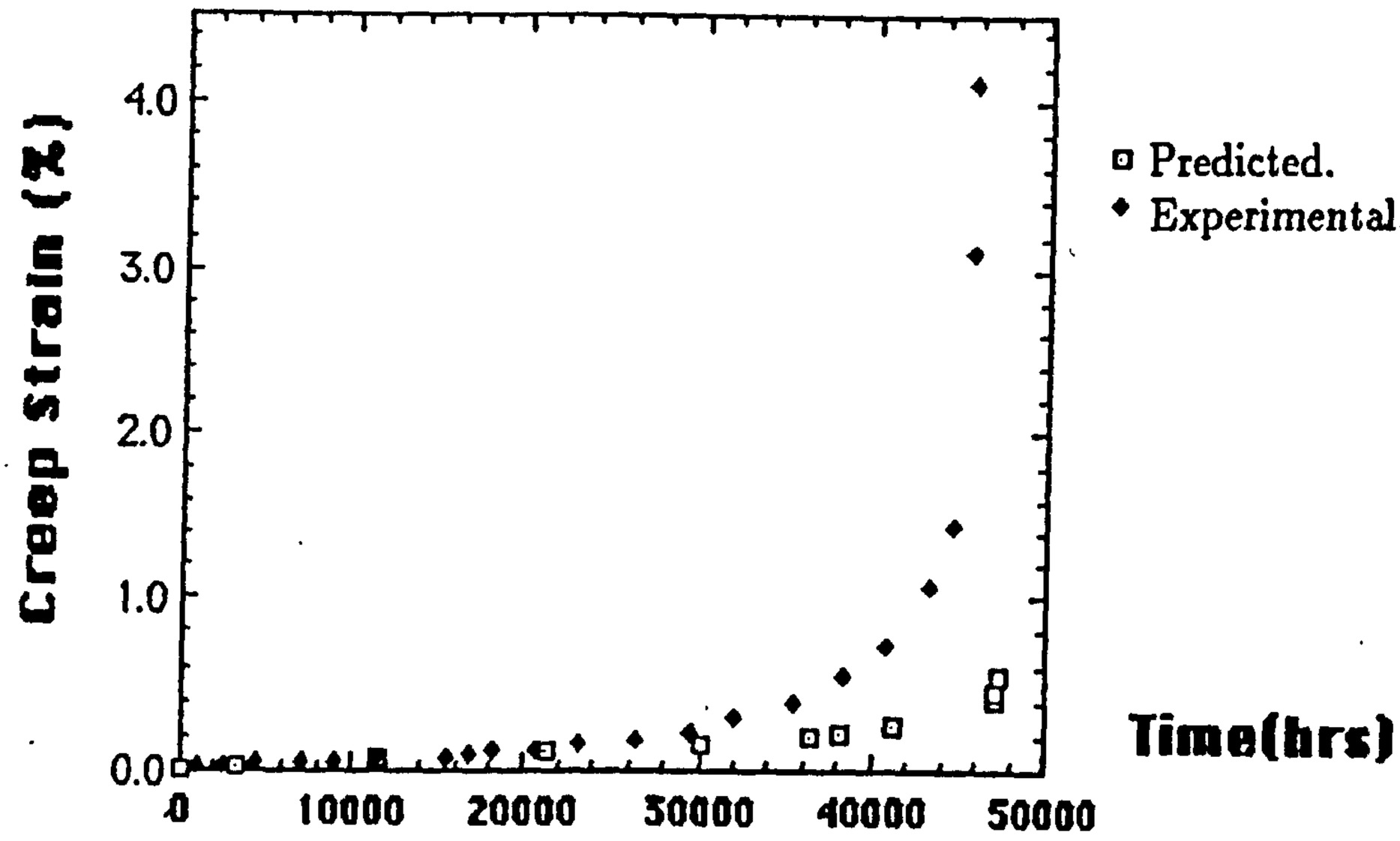

Figure 8.47: Comparison between the experimental axial strains and those predicted from weld model (WM1) corresponding to the pip measurements across the pipe weld.

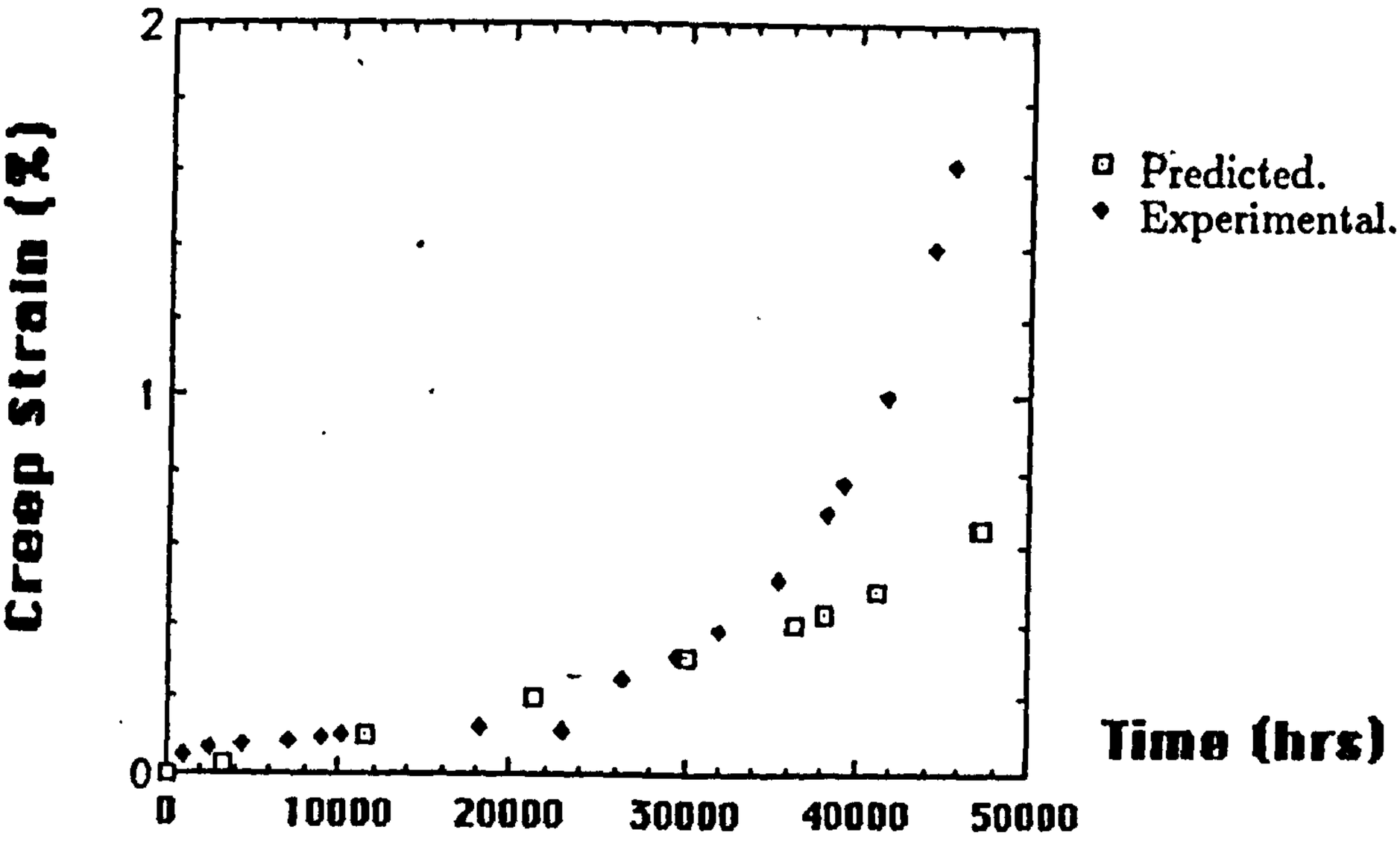

Figure 8.48: Comparison between the experimental axial strains and those predicted from weld model (WM1) corresponding to the capacitance strain gauge measurements at the weld metal centre line.

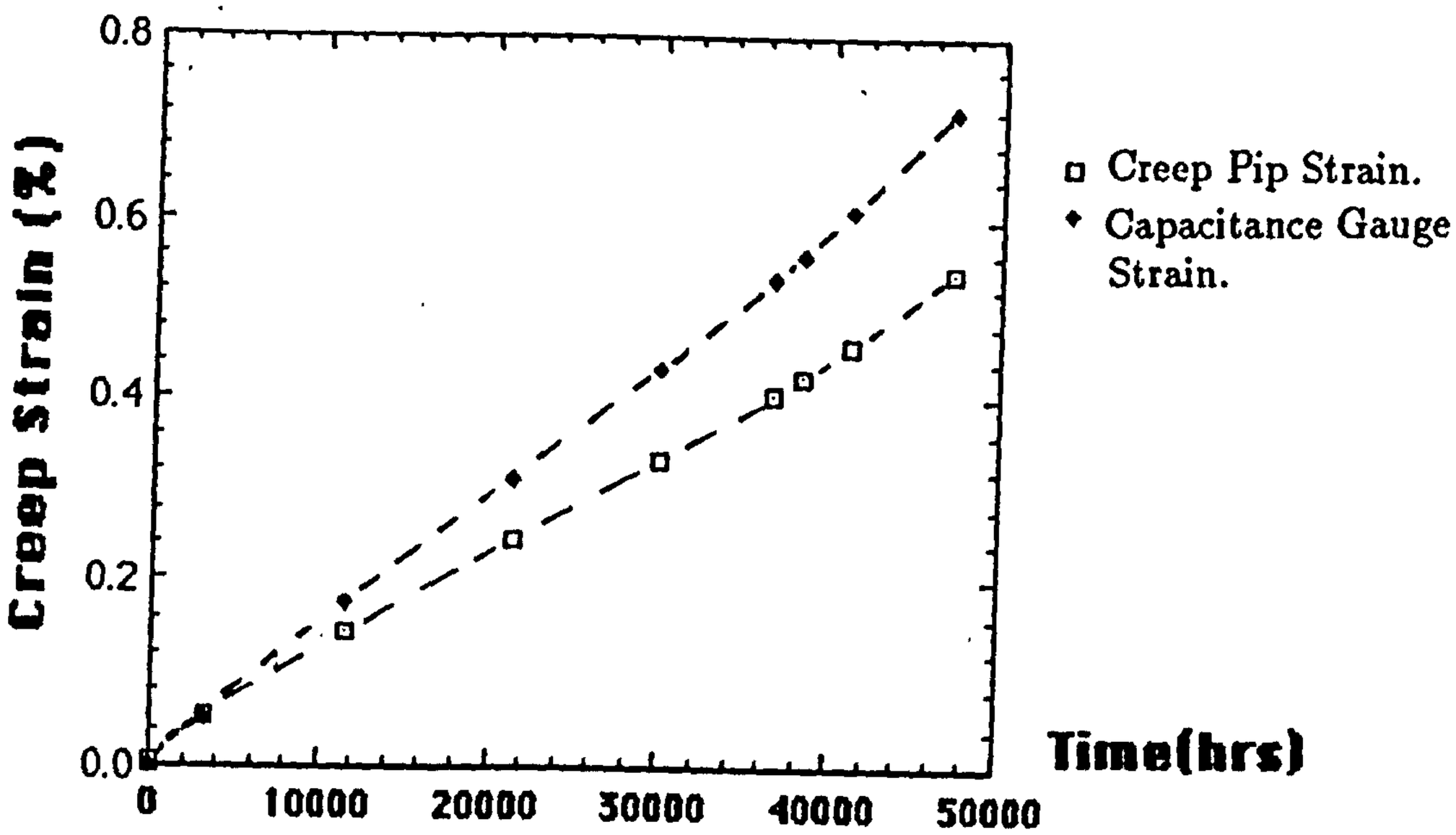

Figure 8.49: Comparison between the predicted hoop strains corresponding to the creep pip and capacitance strain gauge measurements in the parent metal pipe from weld model (WM1).

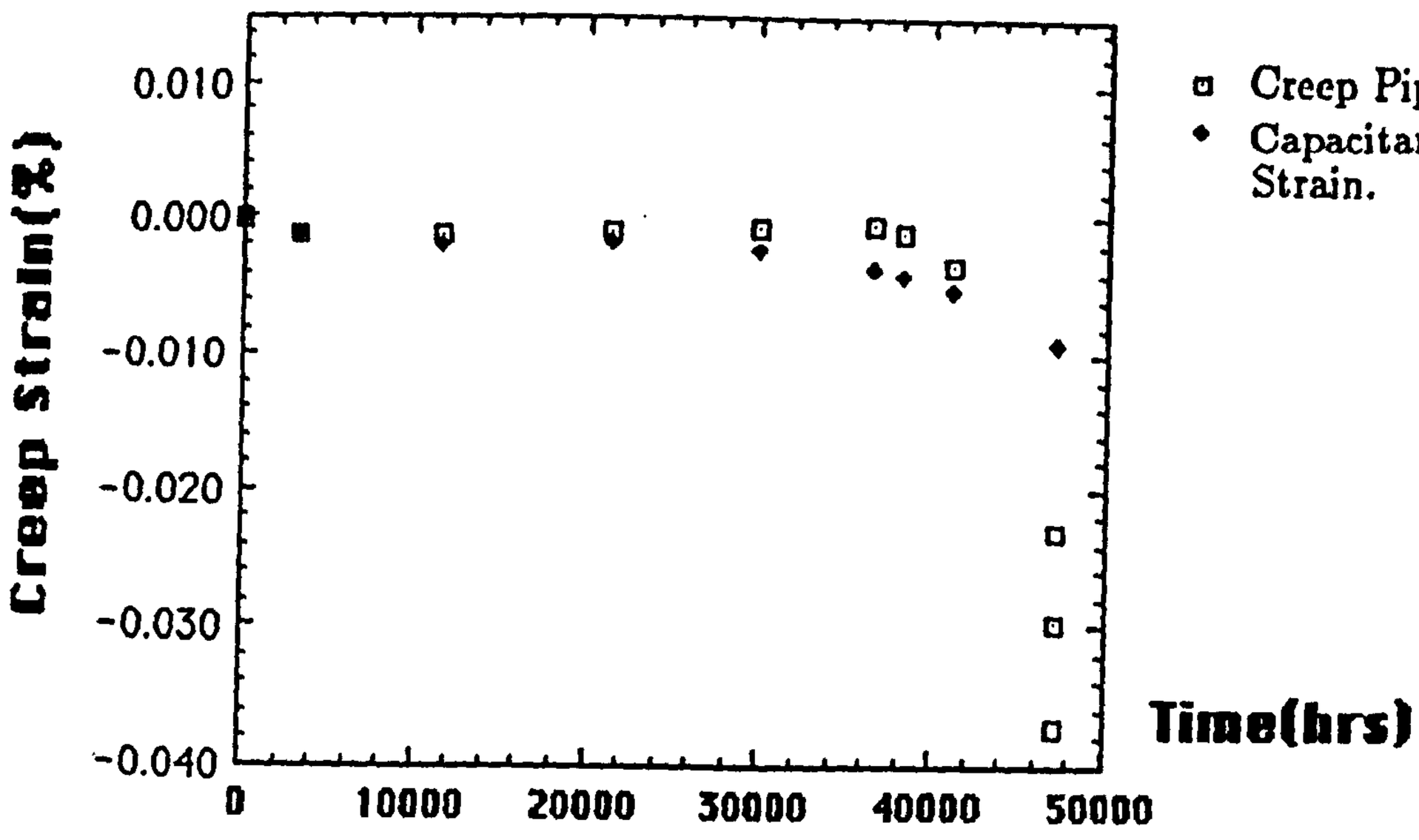

Figure 8.50: Comparison between the predicted axial strains corresponding to the creep pip and capacitance strain gauge measurements in the parent metal pipe from weld model (WM1).

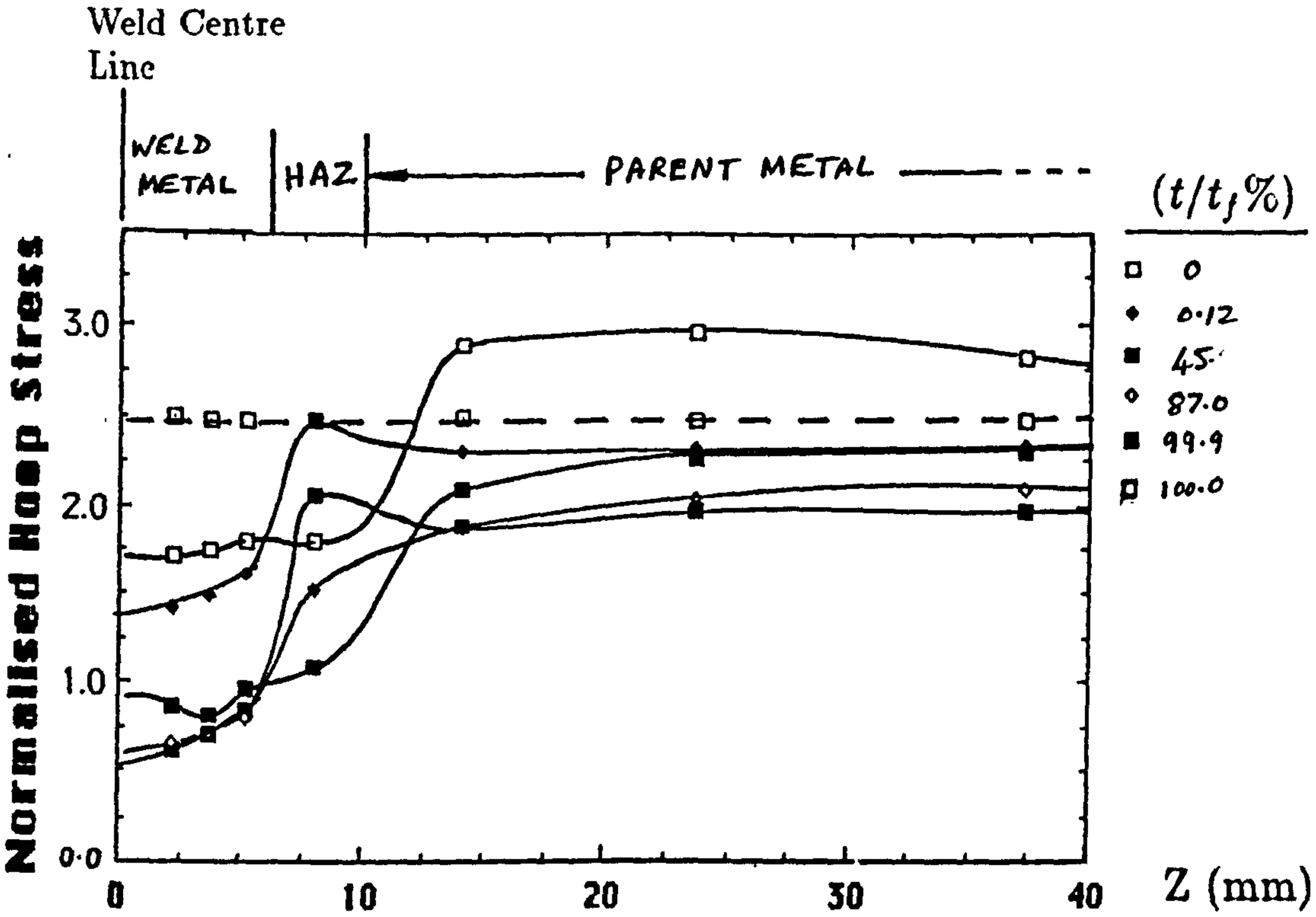

Figure 8.51: Normalised hoop stress (Σ_θ) distributions along the inner bore (Fig.8.9) of the steam pipe at various life fractions. The z-distance is measured in the z-direction from the weld metal centre line (Fig.8.9).

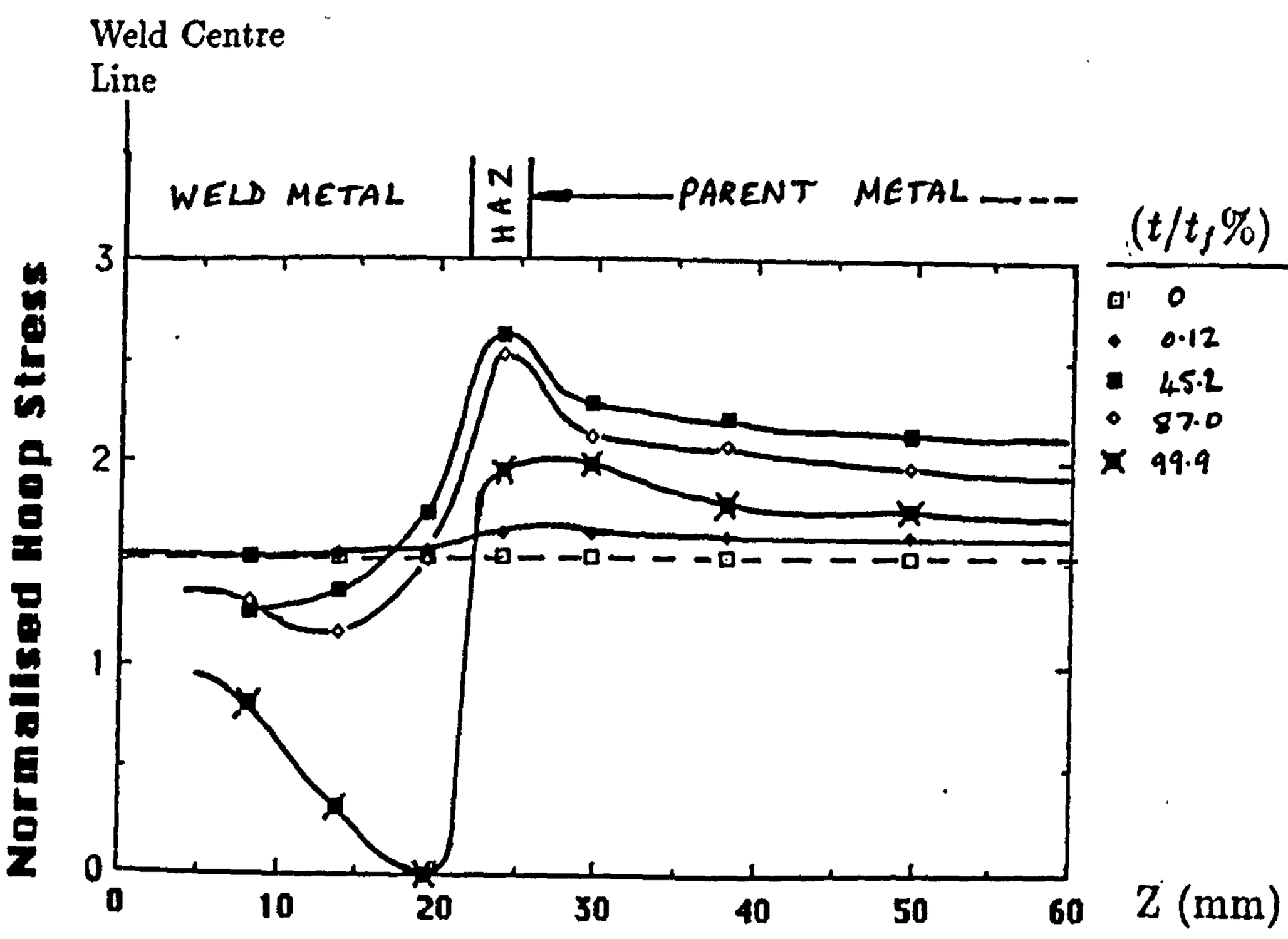

Figure 8.52: Normalised hoop stress (Σ_θ) distributions along the outer surface (Fig.8.9) of the steam pipe at various life fractions. The z-distance is measured in the z-direction from the weld metal centre line (Fig.8.9).

(a)

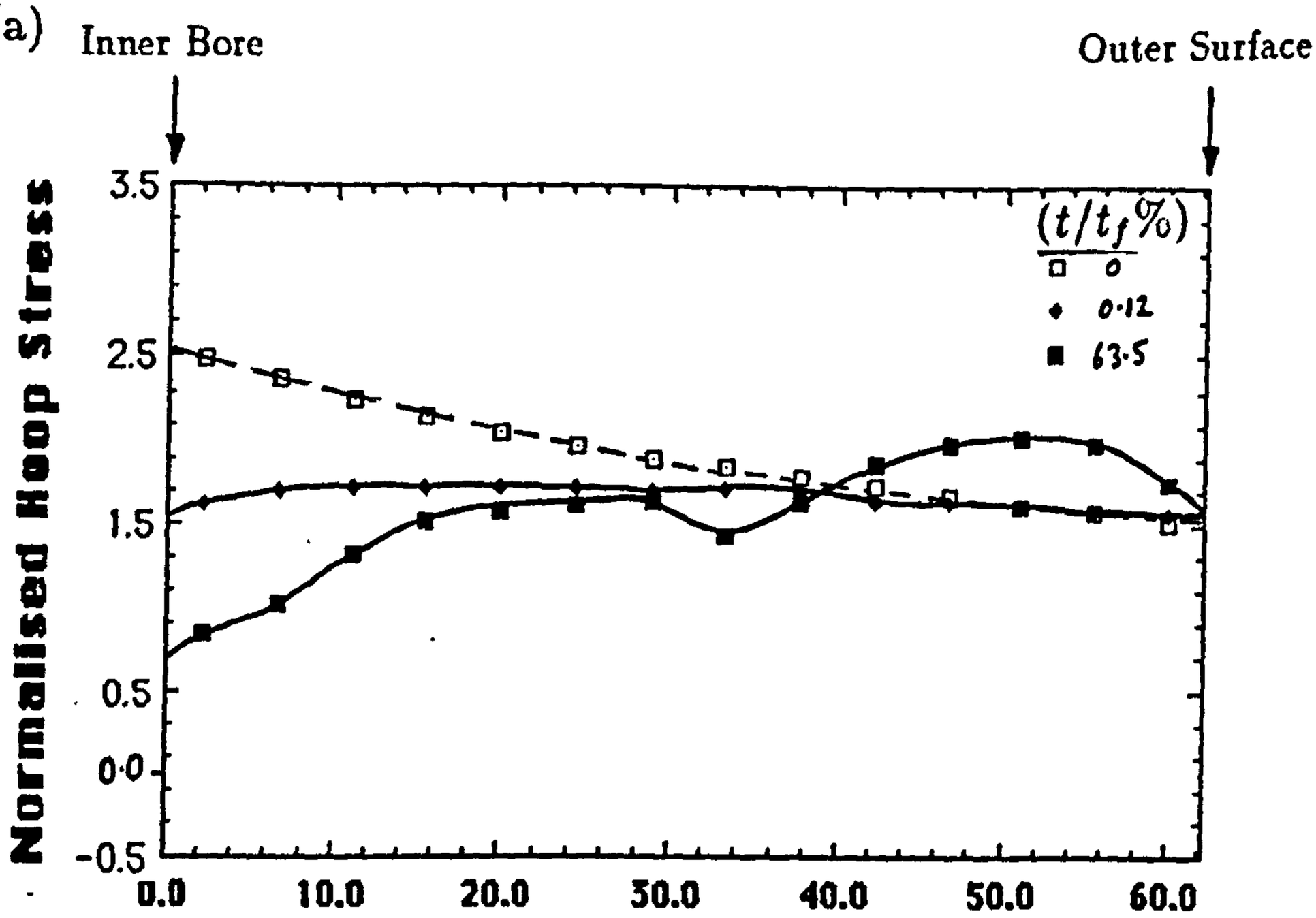

(b)

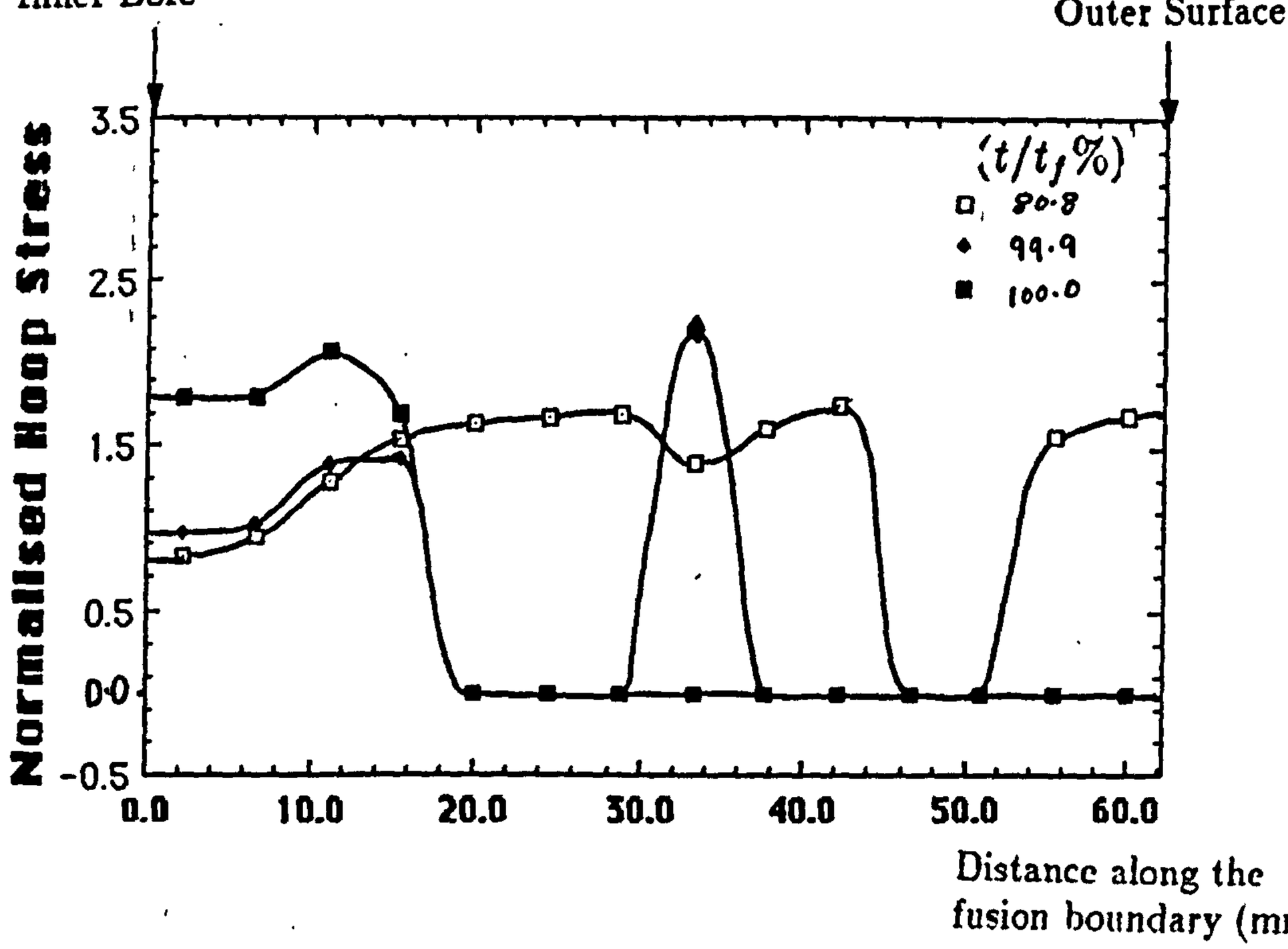

Figure 8.53(a) and (b): Normalised hoop stress (Σ_θ) distributions along the fusion boundary (Fig.8.9) of the steam pipe at various life fractions. The distance along the fusion boundary is measured from the internal diameter (Fig.8.9).

(a)

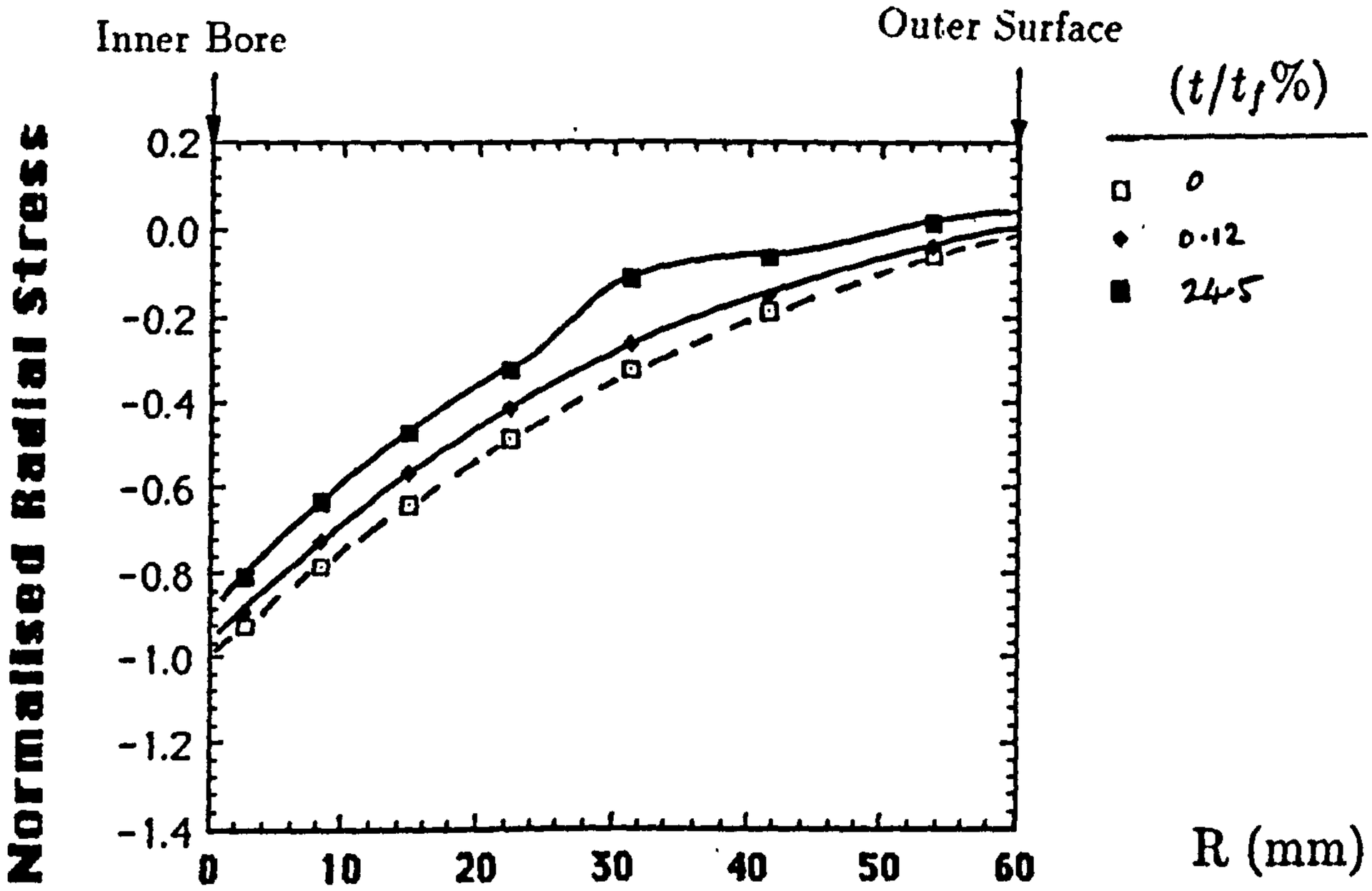

(b)

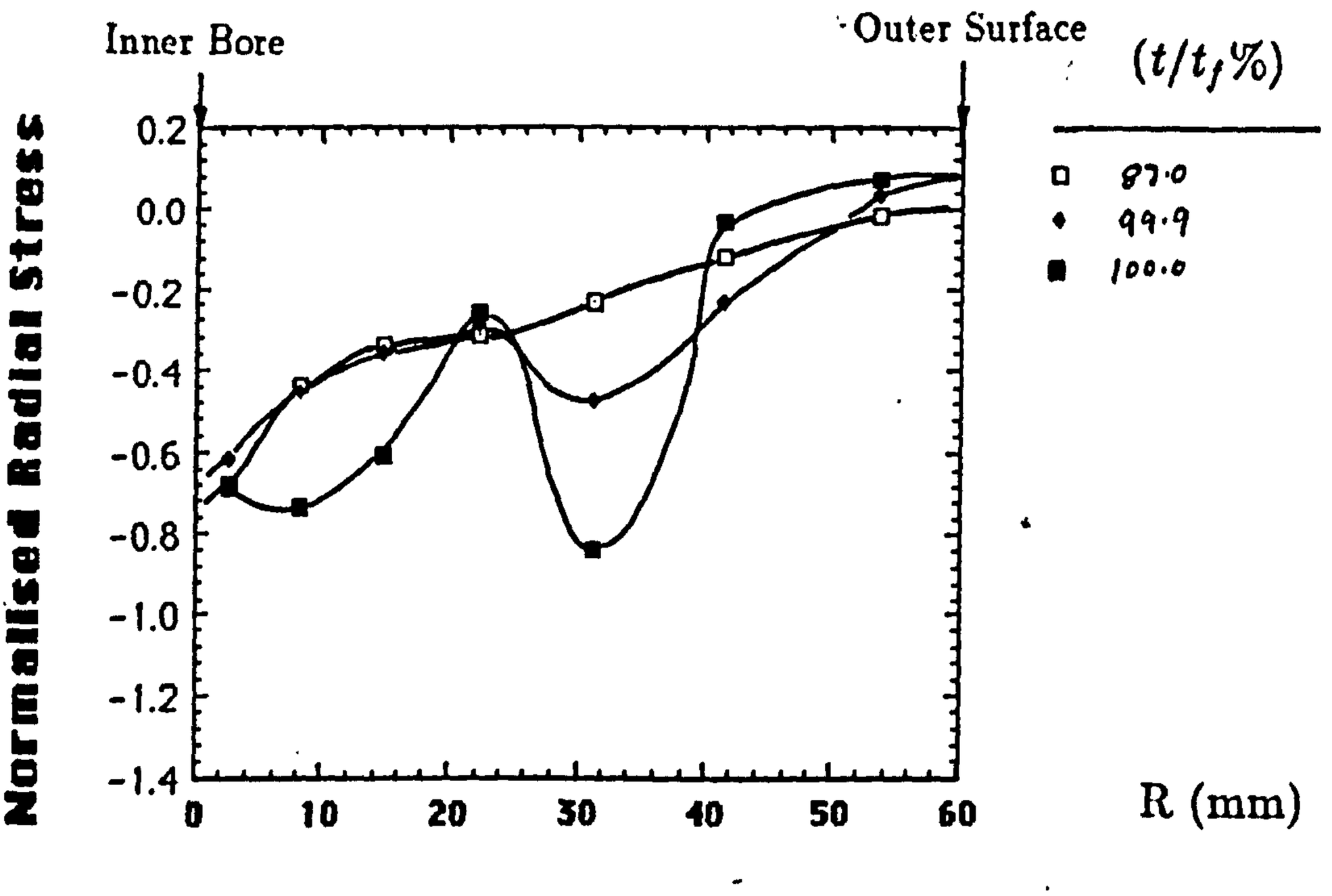

Figure 8.54(a) and (b): Normalised radial stress (Σ_r) distributions along the weld metal centre line (Fig.8.9) of the steam pipe at various life fractions. The distance along the weld metal centre line is measured from the internal diameter (Fig.8.9).

(a)

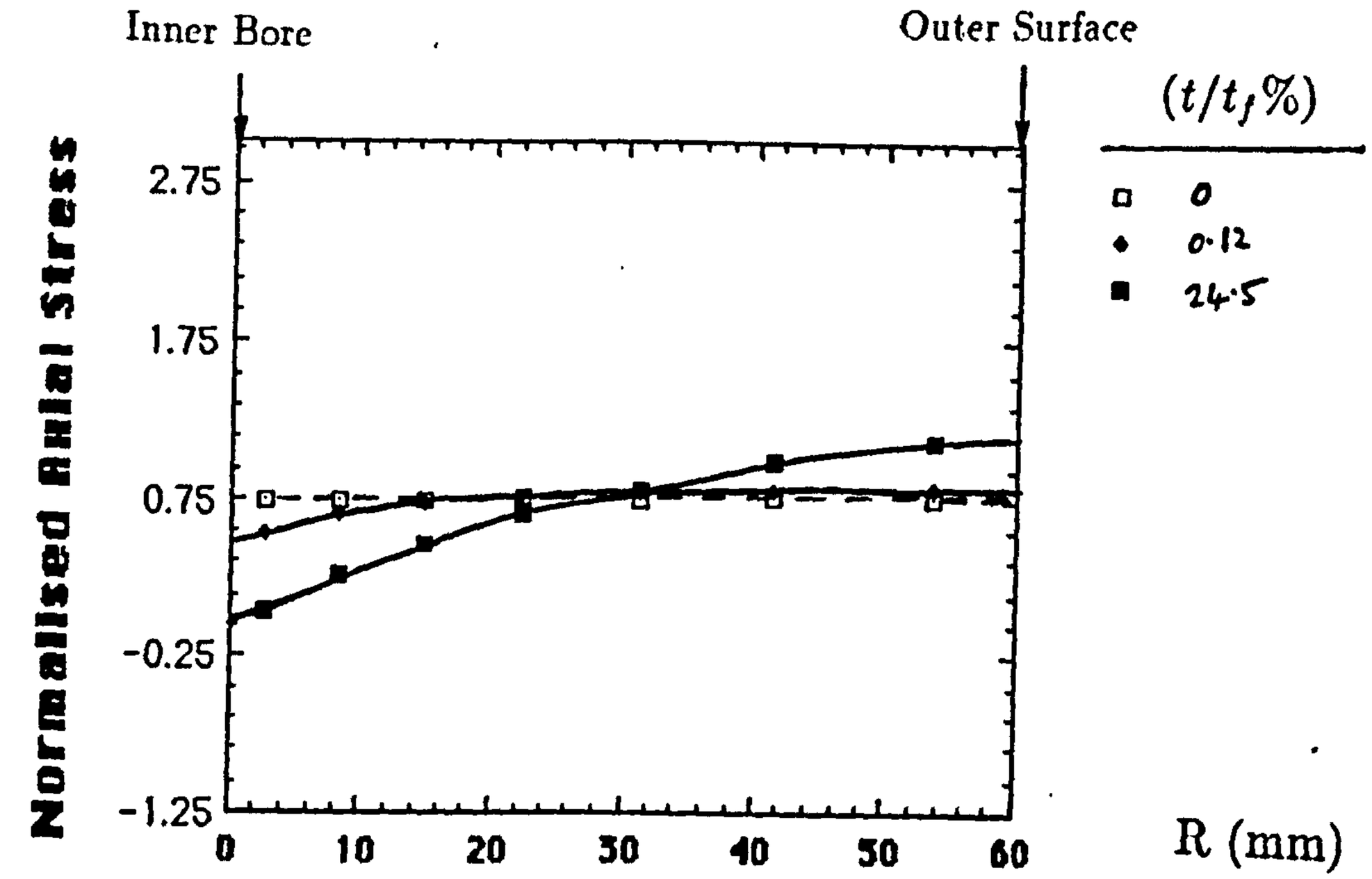

(b)

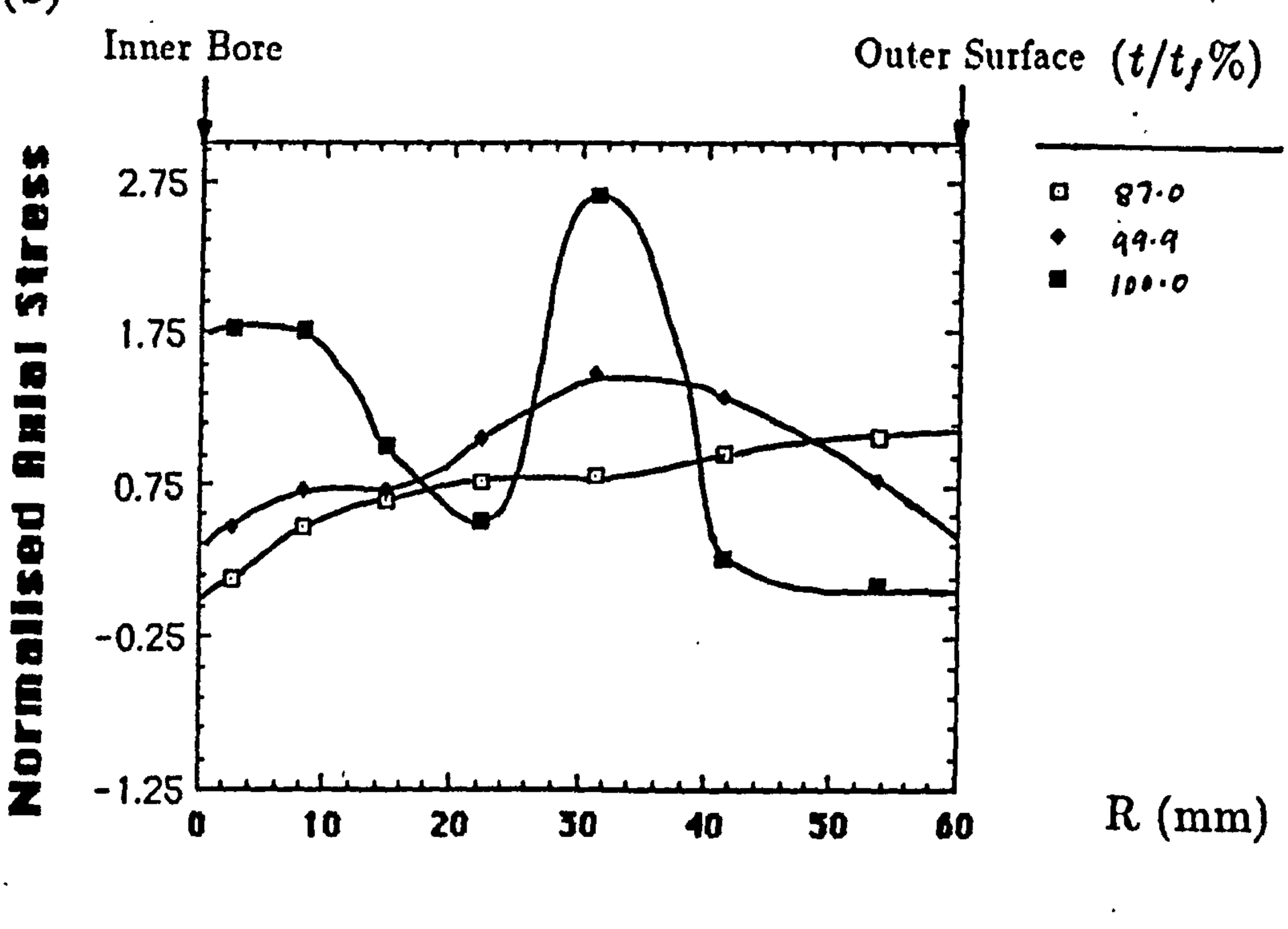

Figure 8.55(a) and (b): Normalised axial stress (Σ_z) distributions along the weld metal centre line (Fig.8.9) of the steam pipe at various life fractions. The distance along the weld metal centre line is measured from the internal diameter (Fig.8.9).

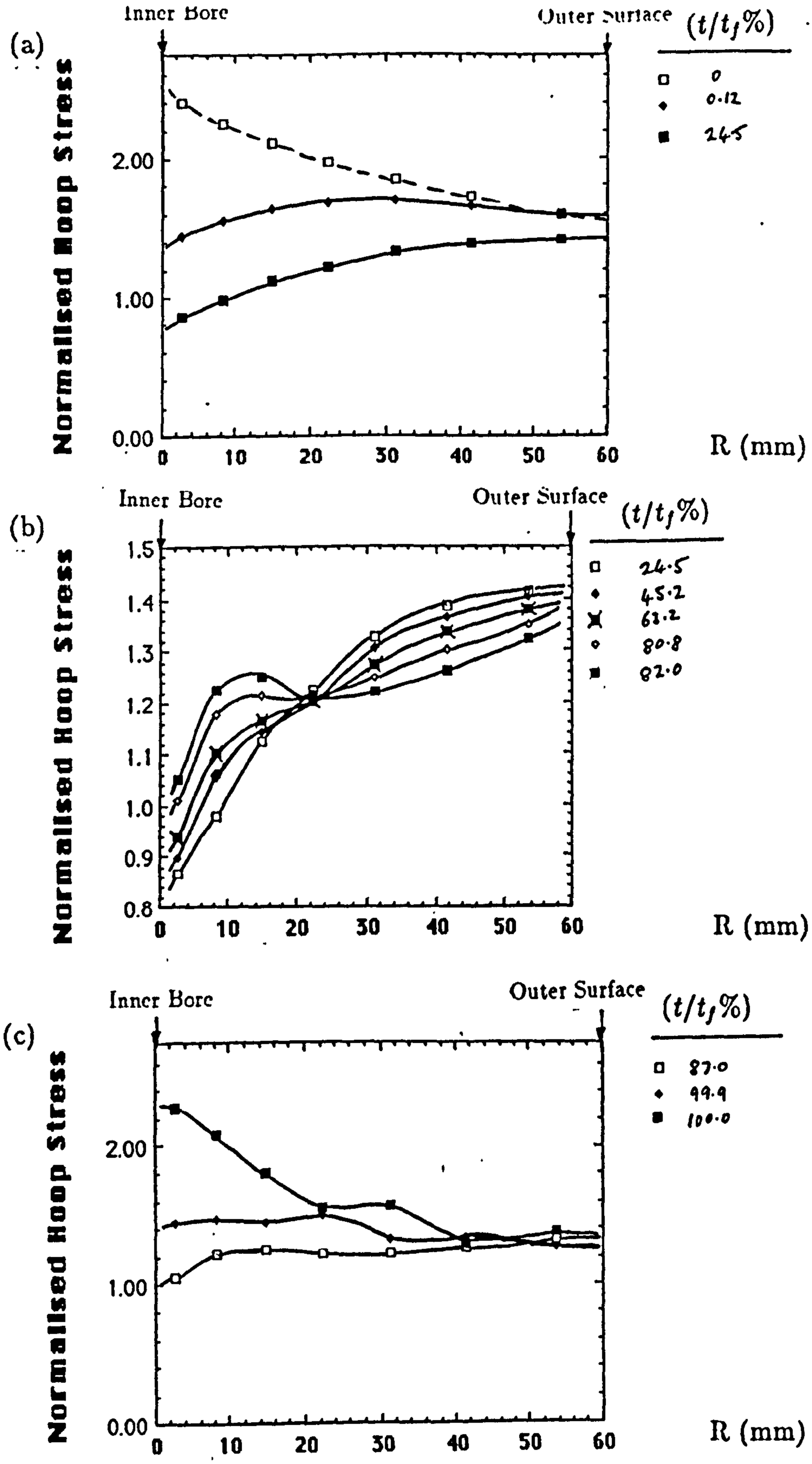

Figure 8.56(a), (b) and (c): Normalised hoop stress (Σ_θ) distributions along the weld metal centre line (Fig.8.9) of the steam pipe at various life fractions. The distance along the weld metal centre line is measured from the internal diameter (Fig.8.9). Note the skeletal stress point (P), in (b).

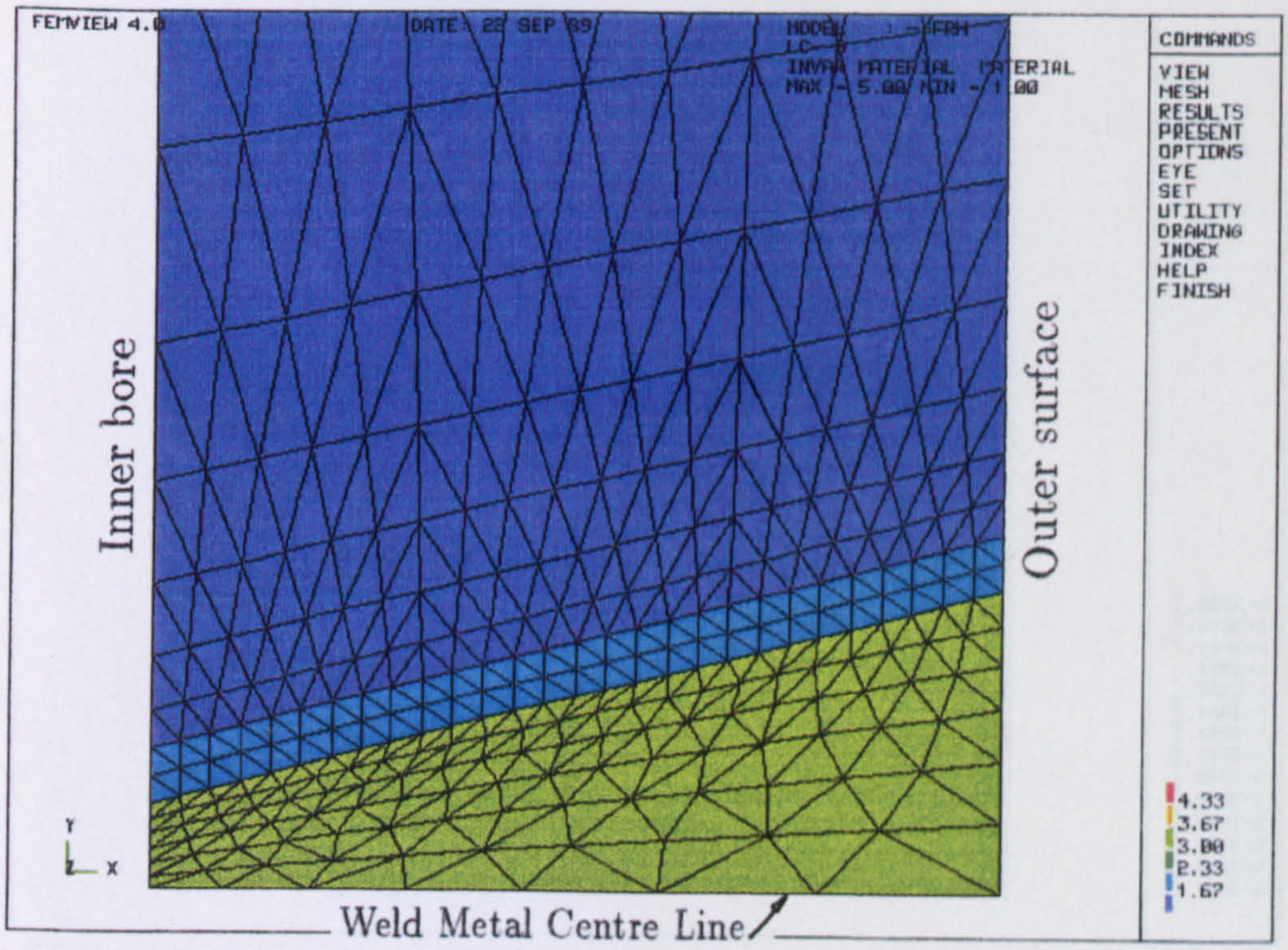

Figure 8.57: The lower section of the axisymmetric finite element mesh for the second weld model (WM2) (Fig.8.9), as used to model the 2.25Cr 1Mo:0.5Cr 0.5Mo 0.25V thick steam pipe weld. The dark blue, the blue and the green regions are assigned the material properties (Table 8.3) of the parent metal, the HAZ(G.C.P.)(2) and the weld metal(fine), respectively.

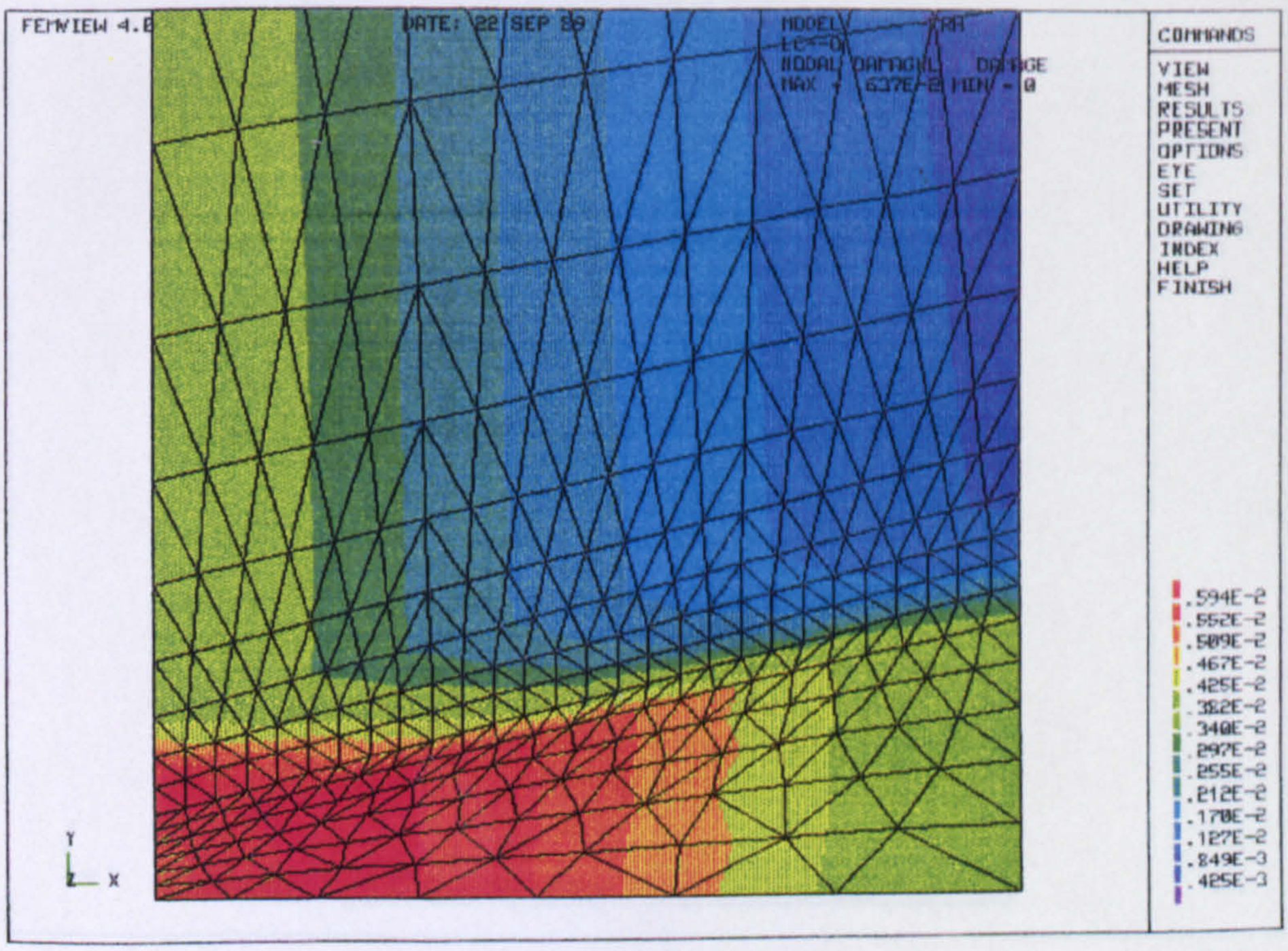

Figure 8.58: Damage distribution for weld model (WM2) at a life fraction (t/t_f = 0.72%). The maximum damaged region occurs in the weld metal and the HAZ at the inner bore.

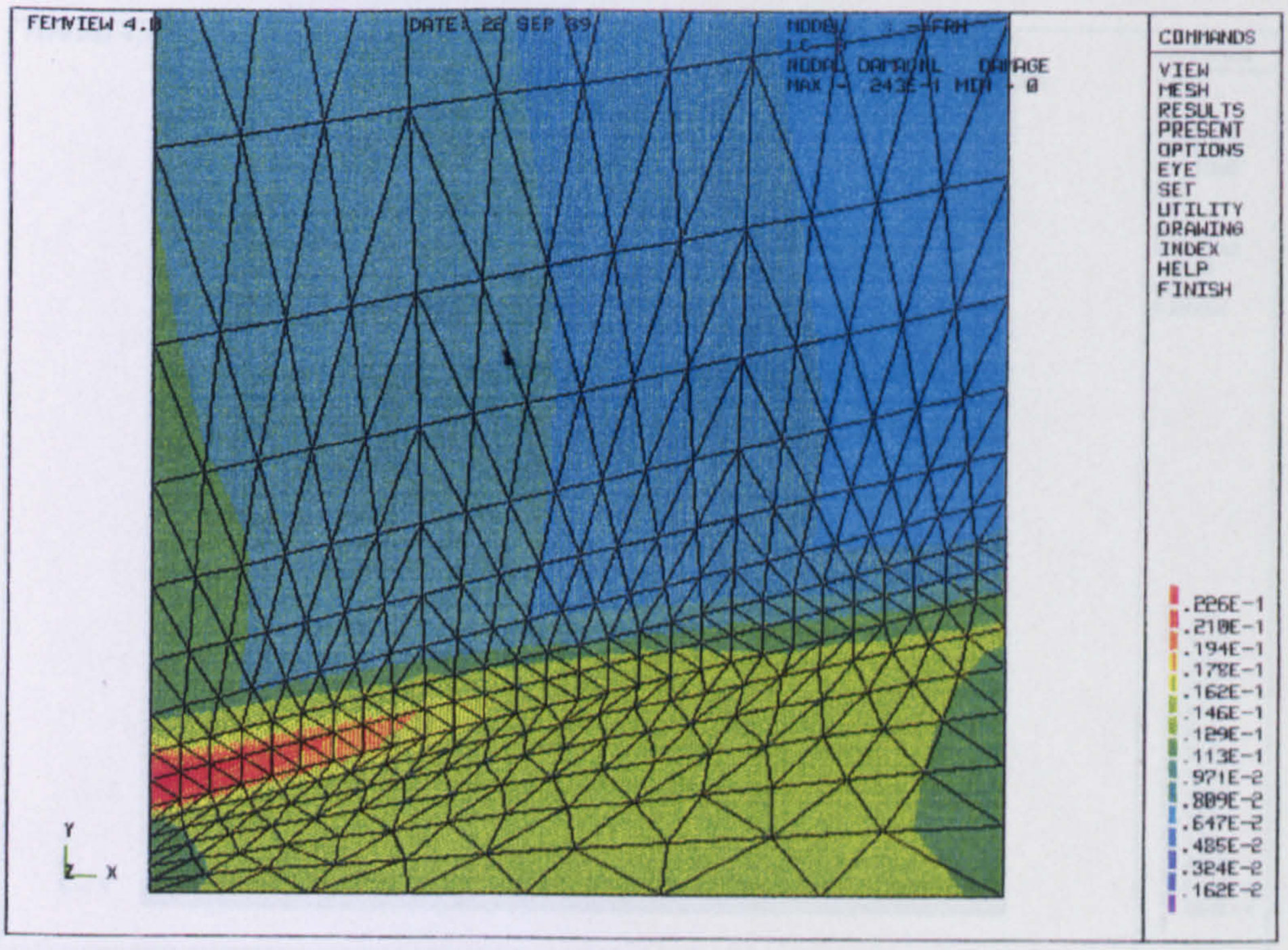

Figure 8.59: Damage distribution for weld model (WM2) at a life fraction ($t/t_f = 3.9\%$).

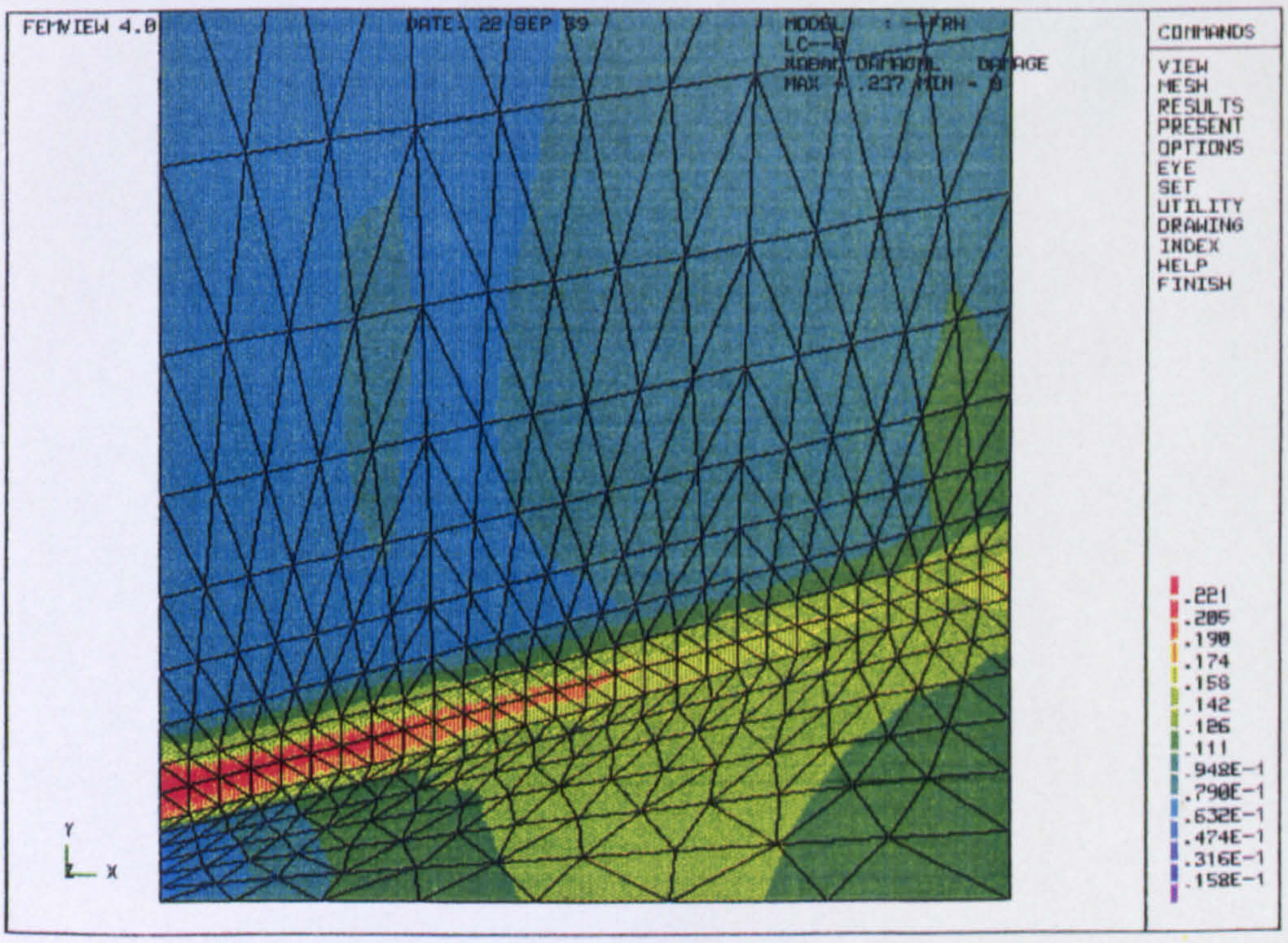

Figure 8.60: Damage distribution for weld model (WM2) at a life fraction ($t/t_f = 53.7\%$).

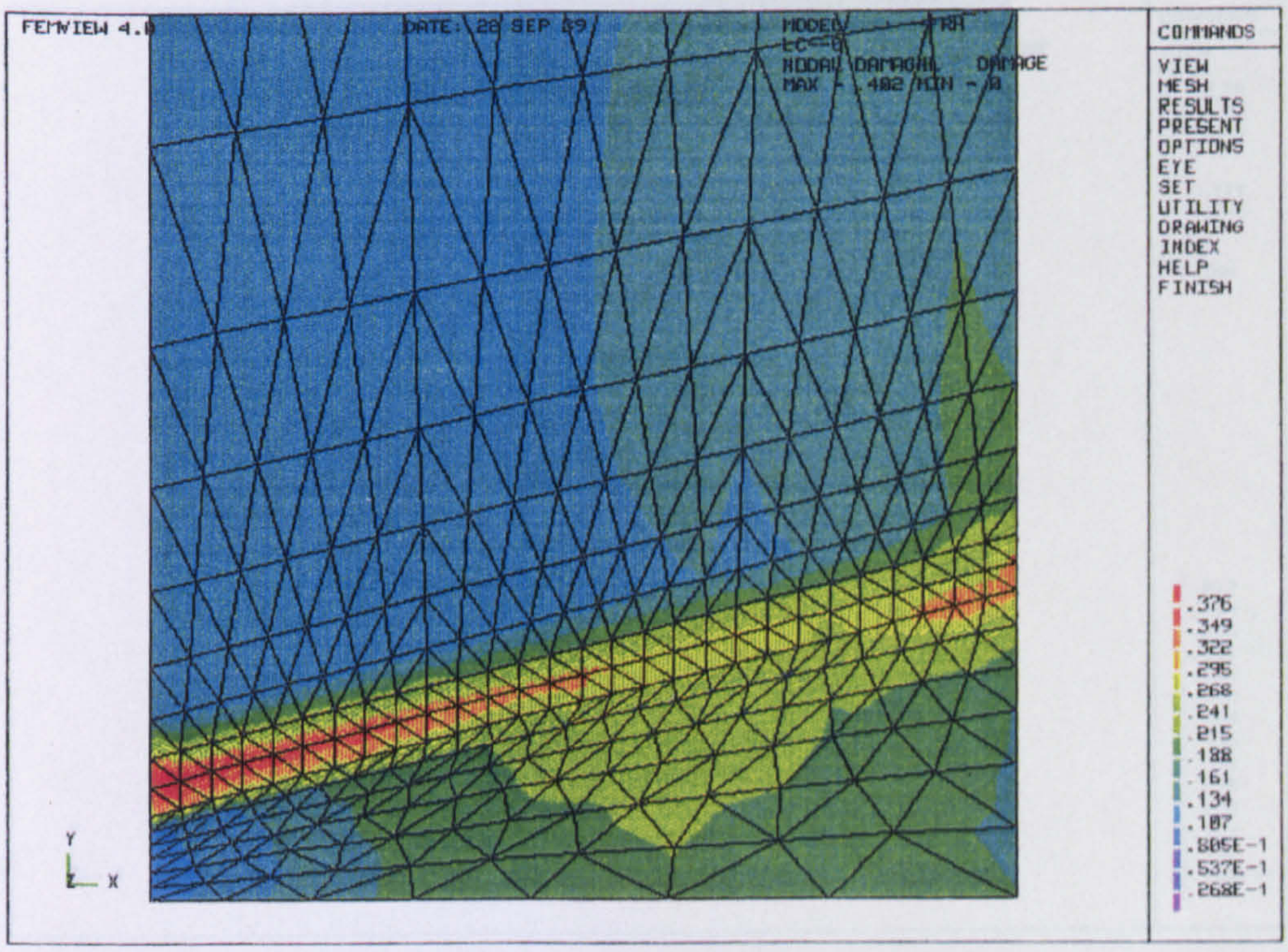

Figure 8.61: Damage distribution for weld model (WM2) at a life fraction ($t/t_f = 81.1\%$).

(a)

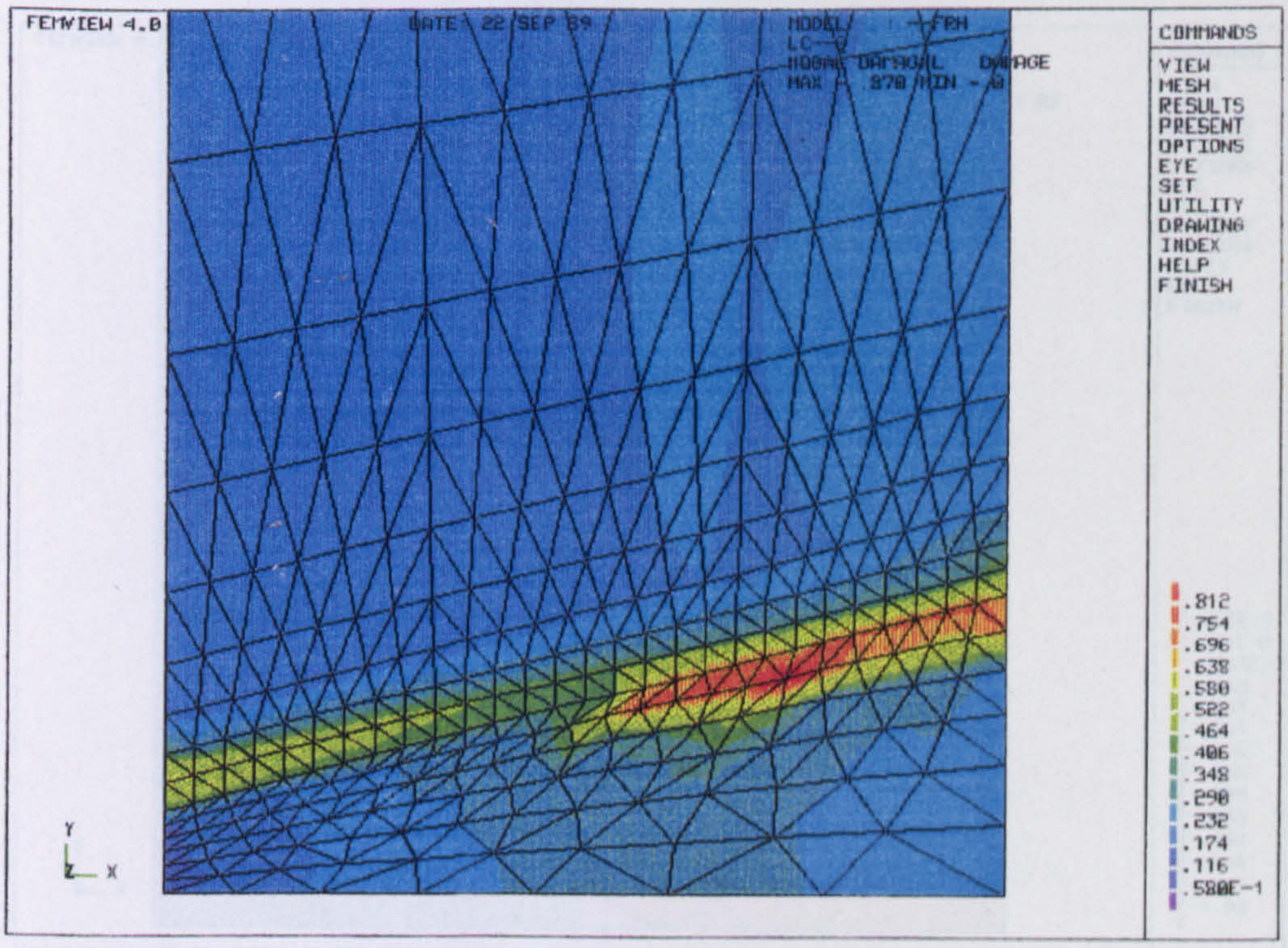

(b)

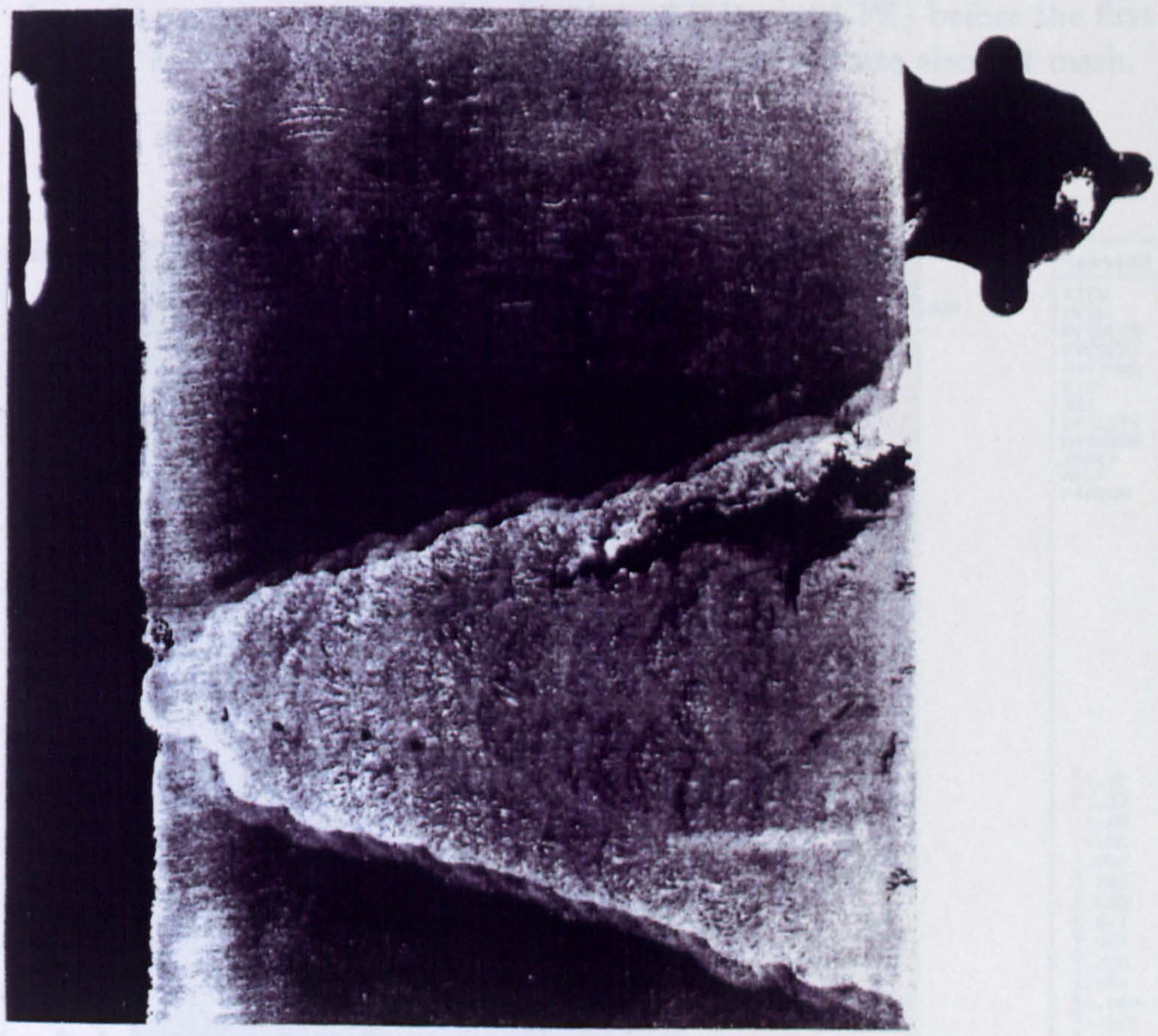

Figure 8.62: (a) Damage distribution for weld model (WM2) at a life fraction ($t/t_f \approx 100.0\%$) predicting the formation of a failed region ($\omega > 0.8$ in the colour plot key), which may be compared with (b) the observed cracking in a radial section through the 2.25Cr 1Mo steam pipe weld at vessel failure. Micrograph courtesy Coleman [149].

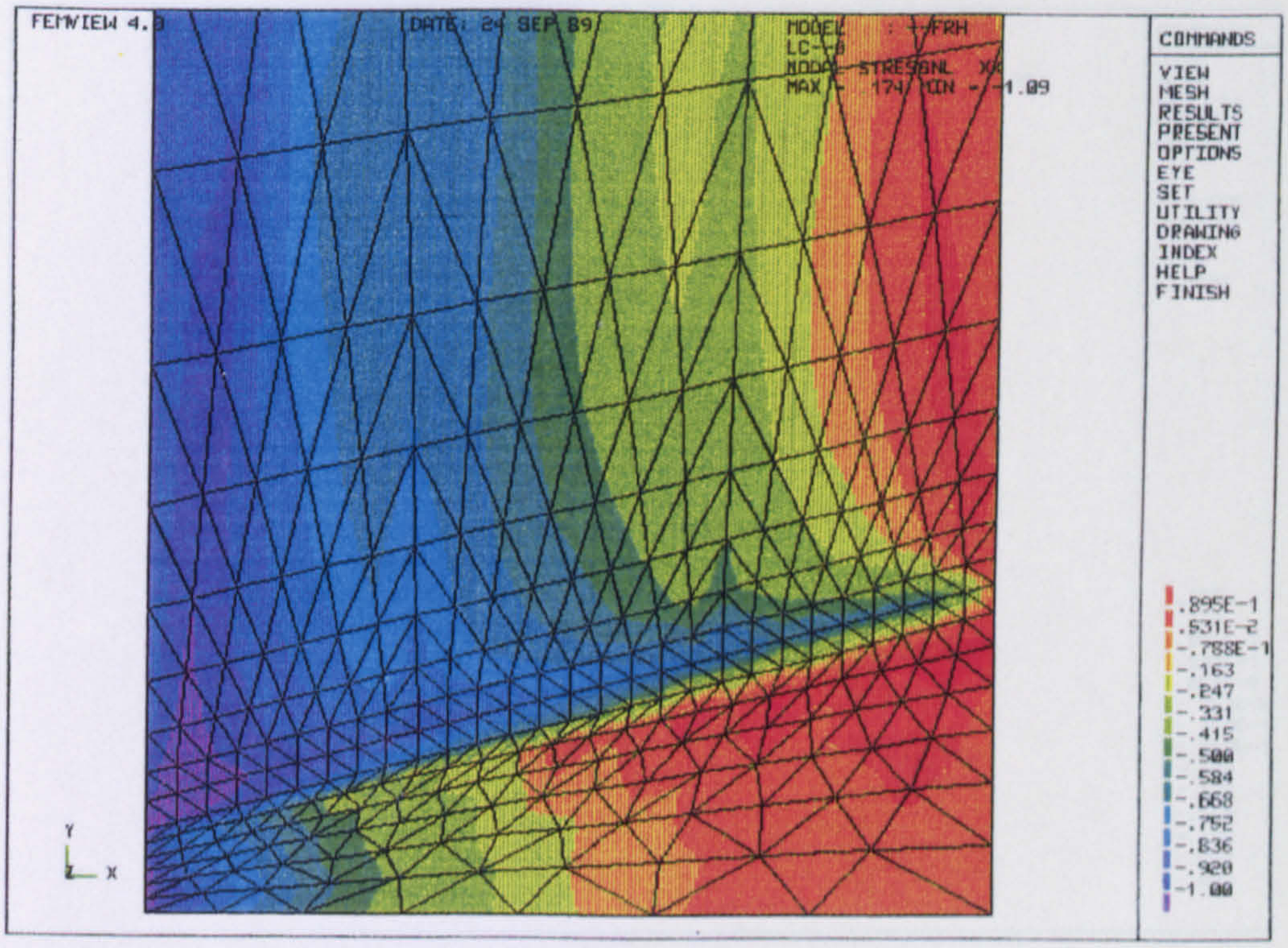

Figure 8.63: Distribution of the normalised radial stress ($\Sigma_r = \sigma_r/\sigma_o$) for weld model (WM2) at a life fraction of ($t/t_f = 81.1\%$) before the first element ($\omega > 0.9999$) fails and is removed from the finite element mesh.

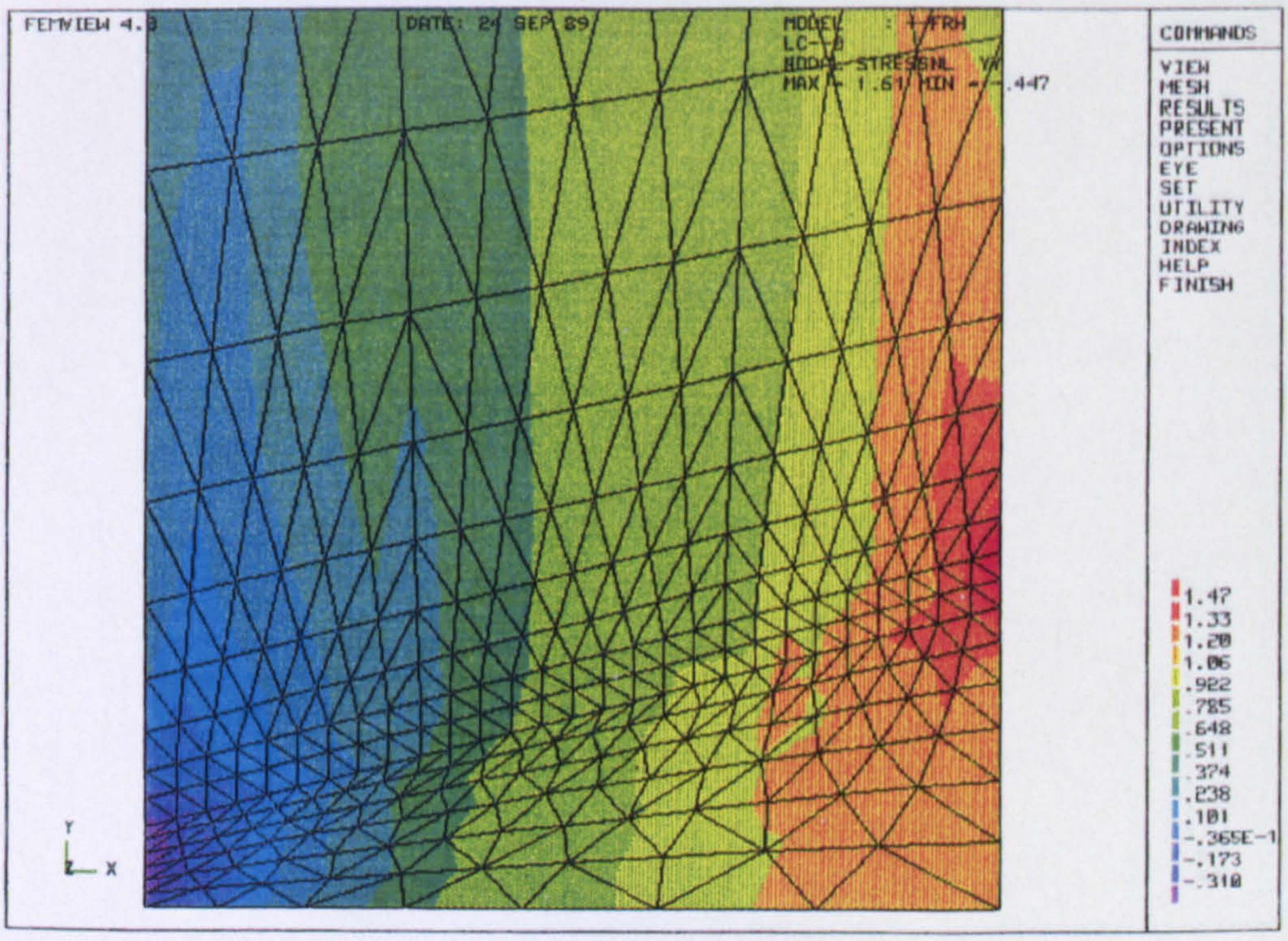

Figure 8.64: Distribution of the normalised axial stress ($\Sigma_z = \sigma_z/\sigma_o$) for weld model (WM2) at a life fraction of ($t/t_f = 81.1\%$) before the first element ($\omega > 0.9999$) fails and is removed from the finite element mesh.

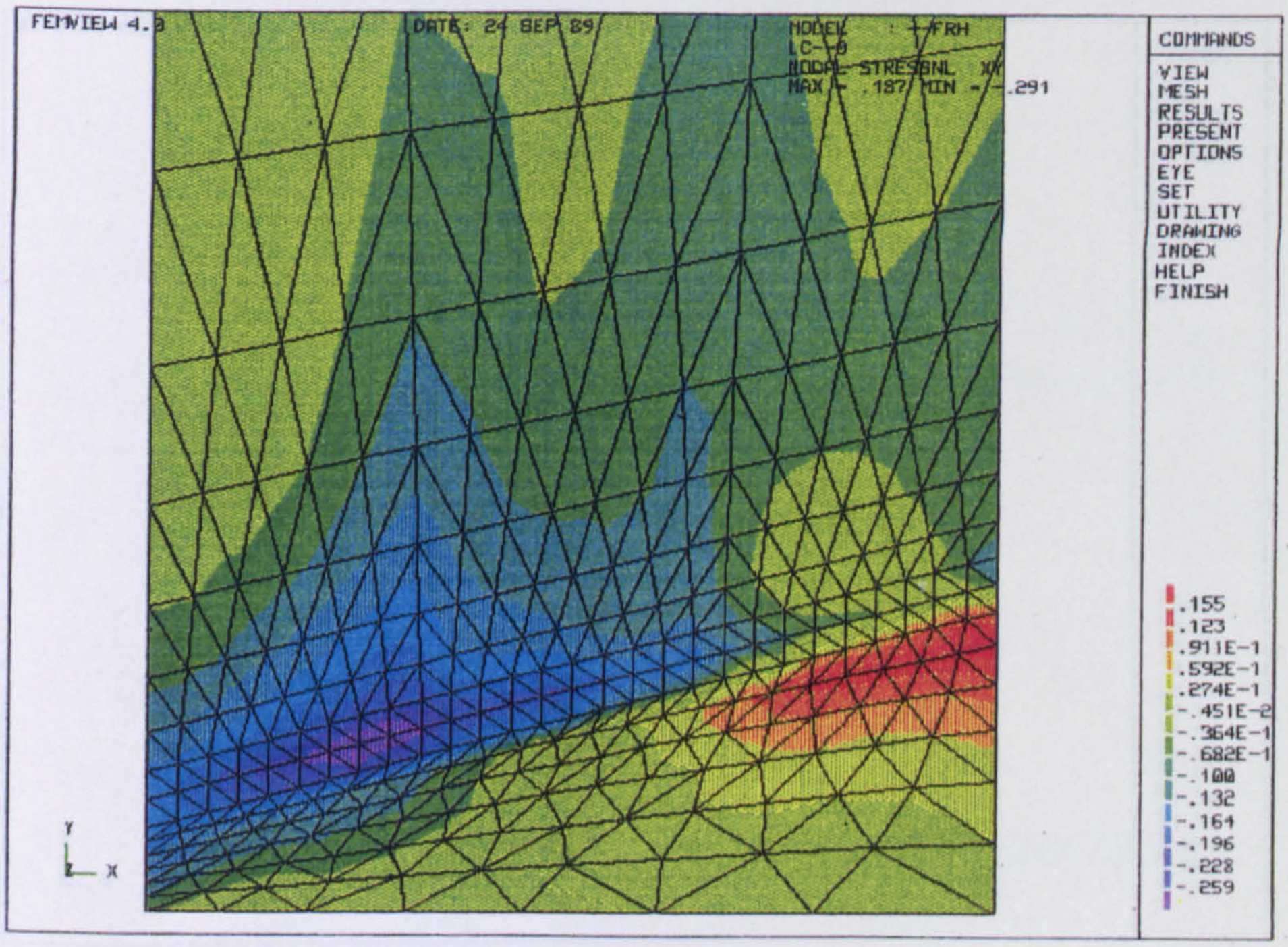

Figure 8.65: Distribution of the normalised radial/axial shear stress ($\Sigma_{rz} = \sigma_{rz}/\sigma_o$) for weld model (WM2) at a life fraction of ($t/t_f = 81.1\%$) before the first element ($\omega > 0.9999$) fails and is removed from the finite element mesh.

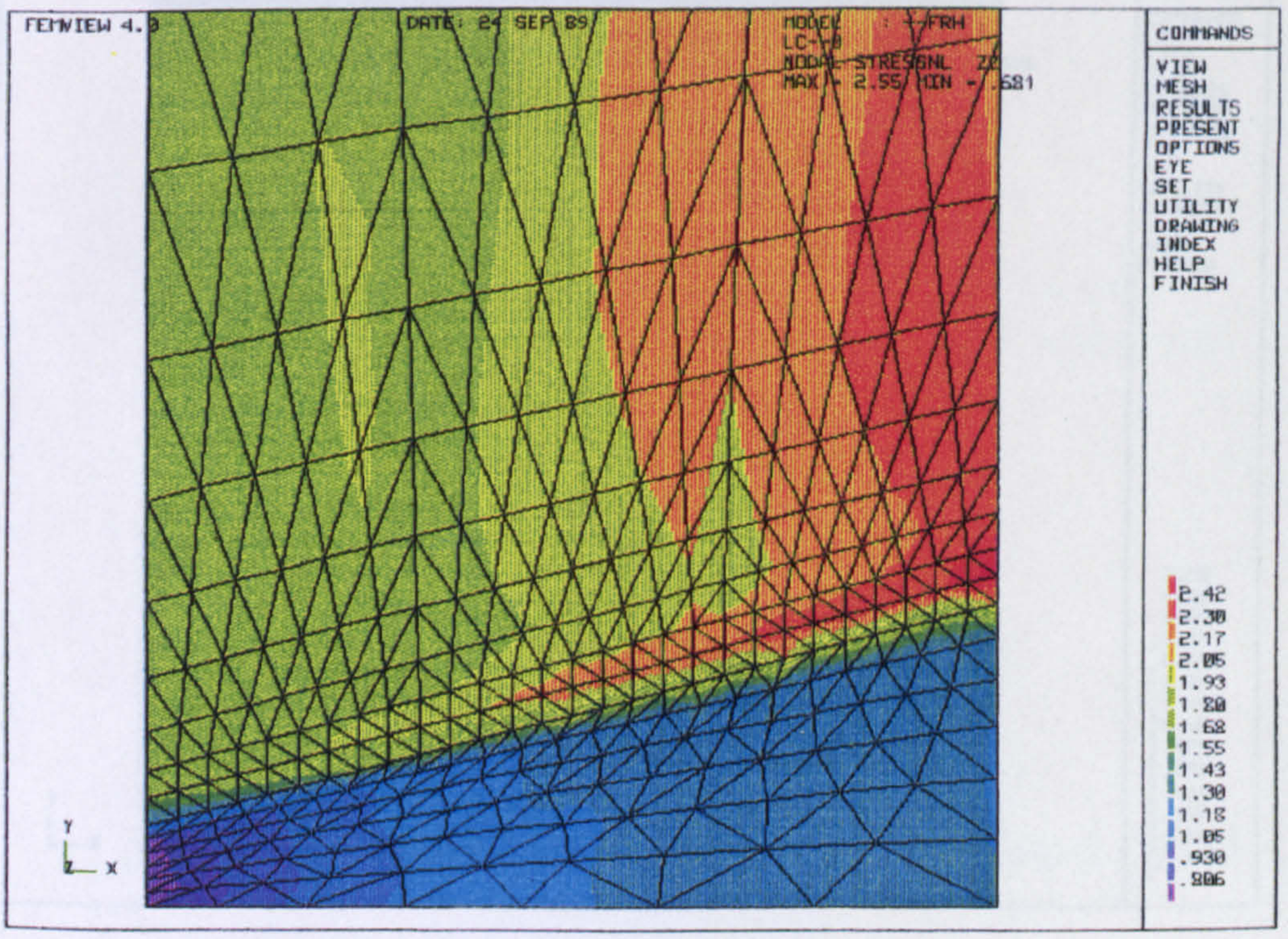

Figure 8.66: Distribution of the normalised hoop stress ($\Sigma_\theta = \sigma_\theta/\sigma_o$) for weld model (WM2) at a life fraction of ($t/t_f = 81.1\%$) before the first element ($\omega > 0.9999$) fails and is removed from the finite element mesh.

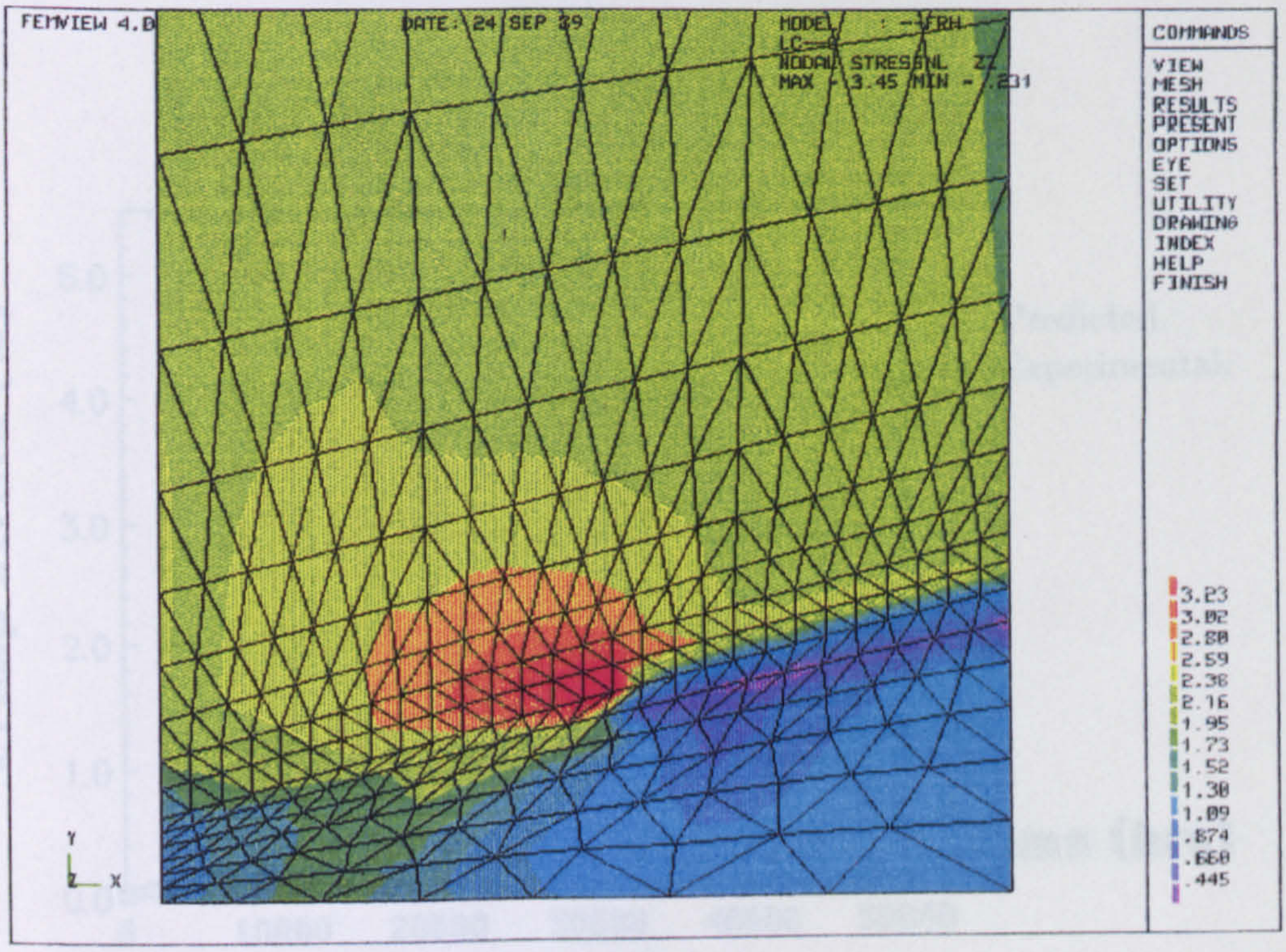

Figure 8.67: Distribution of the normalised hoop stress ($\Sigma_\theta = \sigma_\theta/\sigma_o$) for weld model (WM2) at a life fraction of ($t/t_f = 99.9\%$).

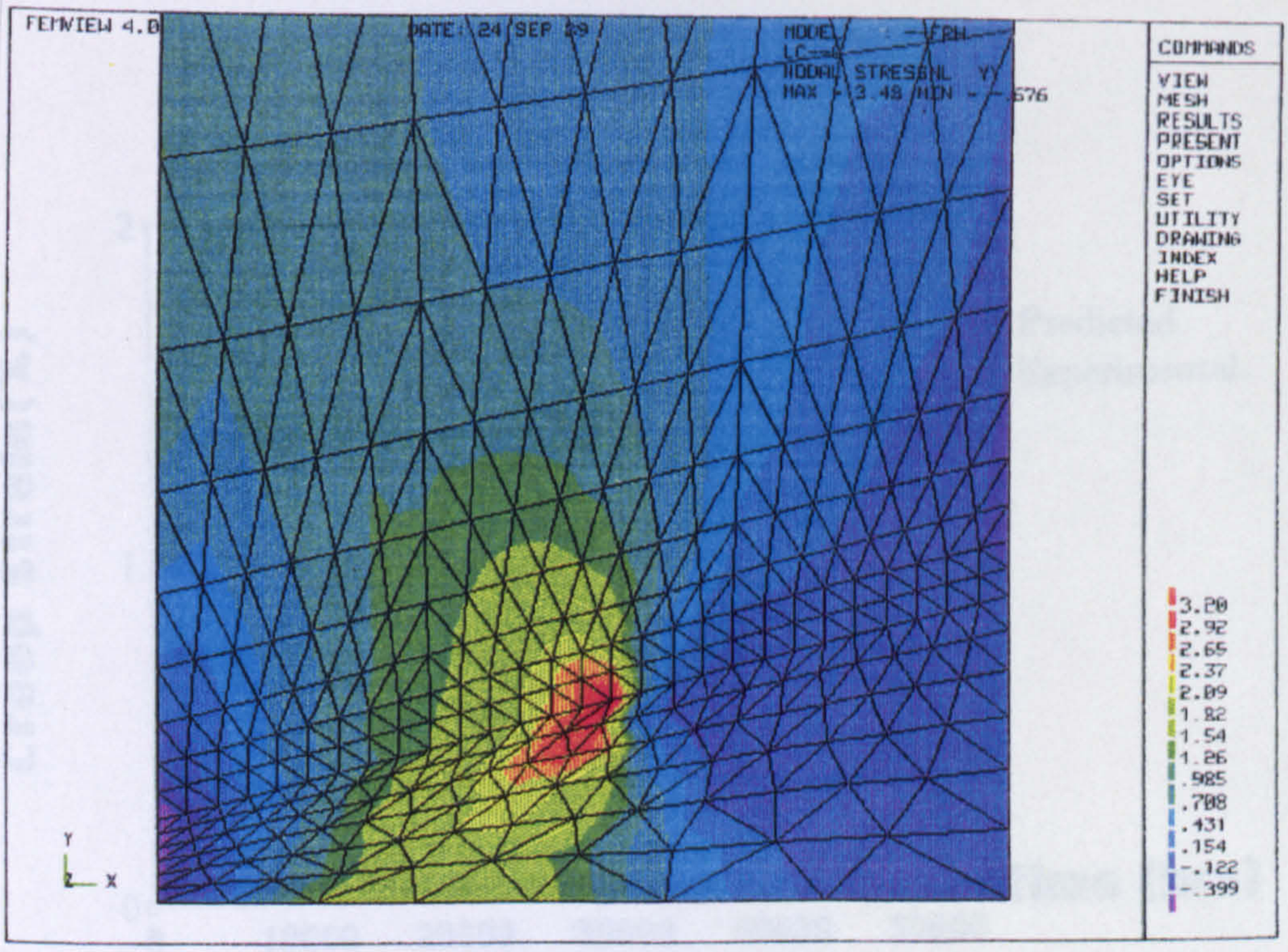

Figure 8.68: Distribution of the normalised axial stress ($\Sigma_z = \sigma_z/\sigma_o$) for weld model (WM2) at a life fraction of ($t/t_f = 99.9\%$).

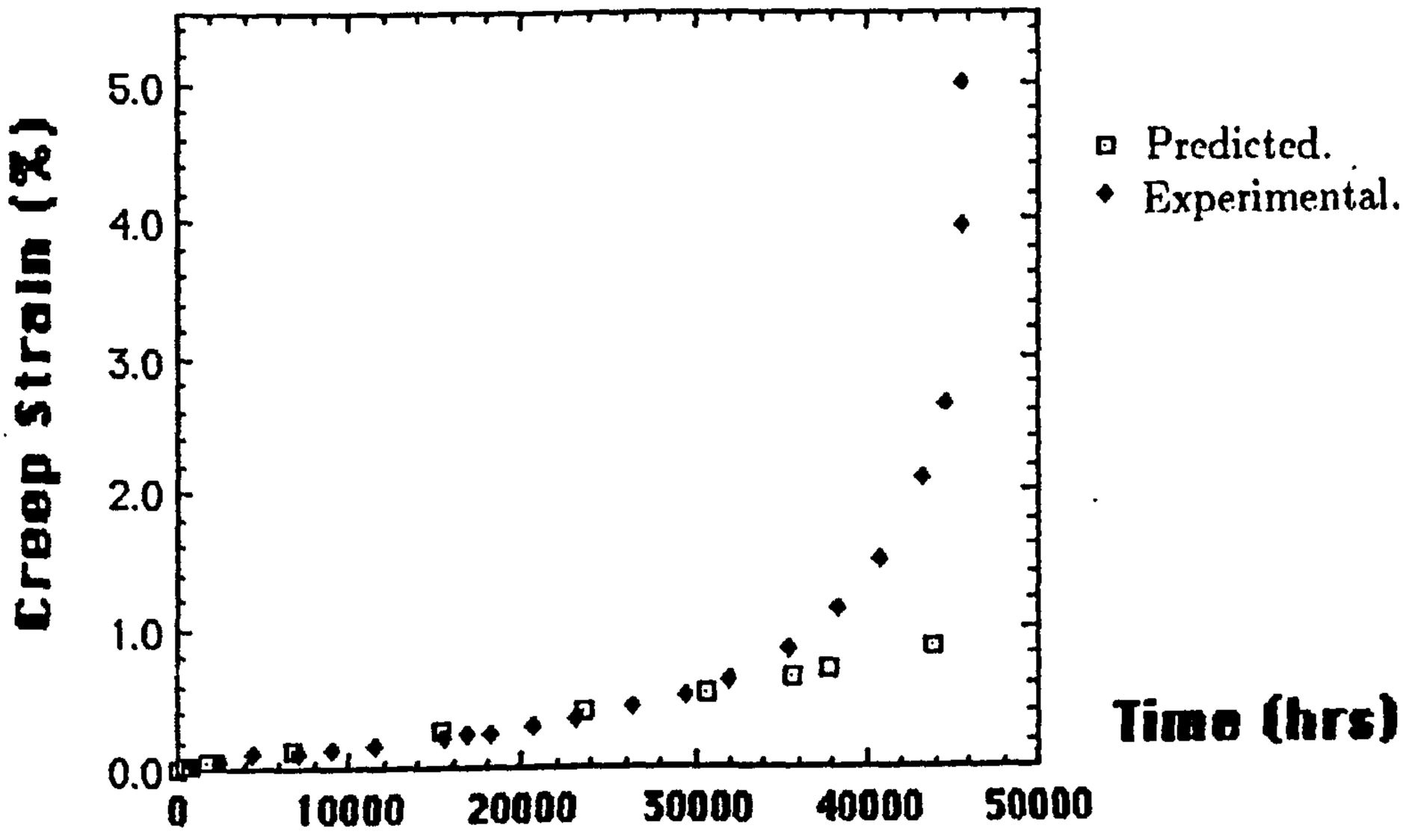

Figure 8.69: Comparison between the experimental hoop strains and those predicted from weld model (WM2) corresponding to the pip measurements at pipe weld.

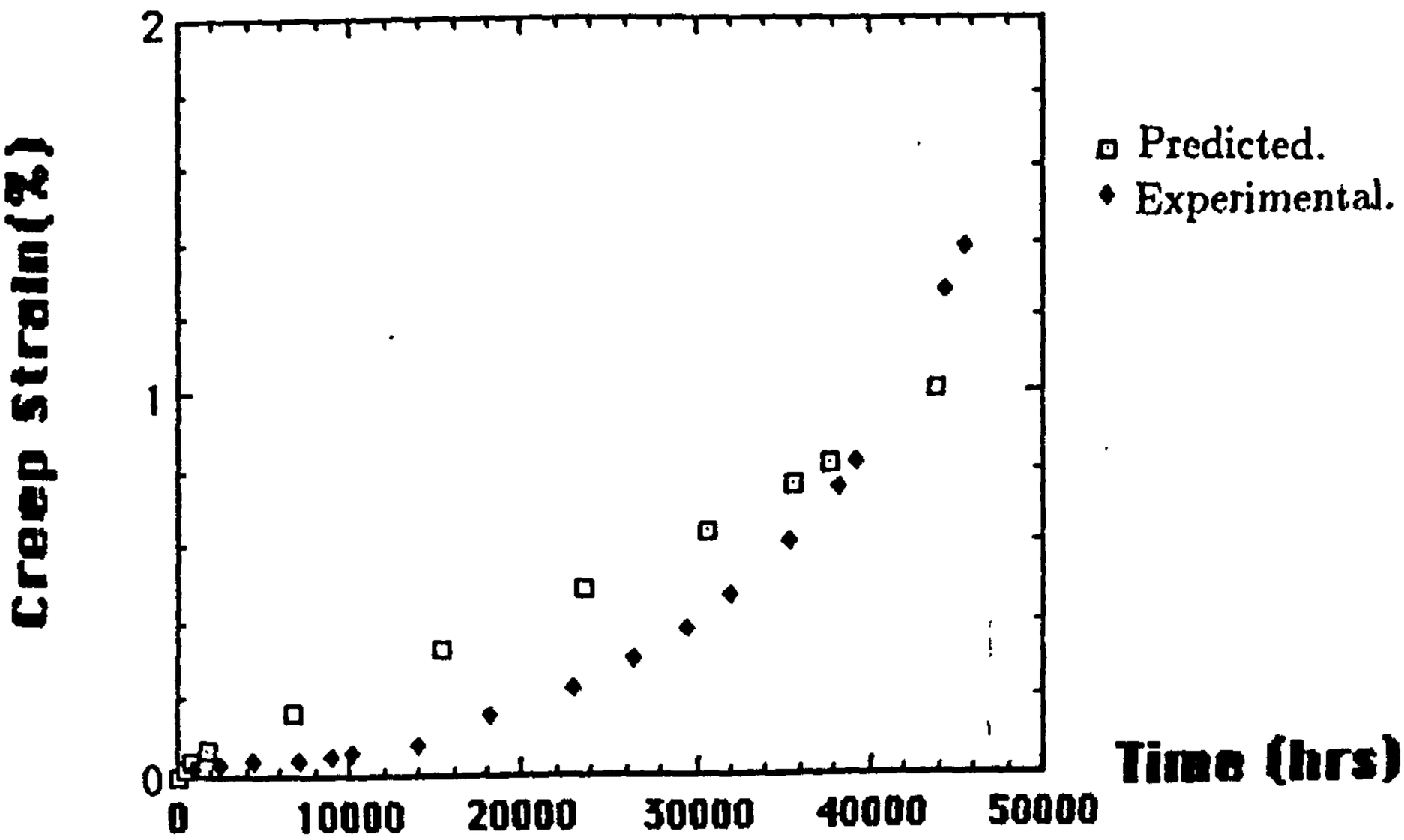

Figure 8.70: Comparison between the experimental hoop strains and those predicted from weld model (WM2) corresponding to the capacitance strain gauge measurements at the weld metal centre line.

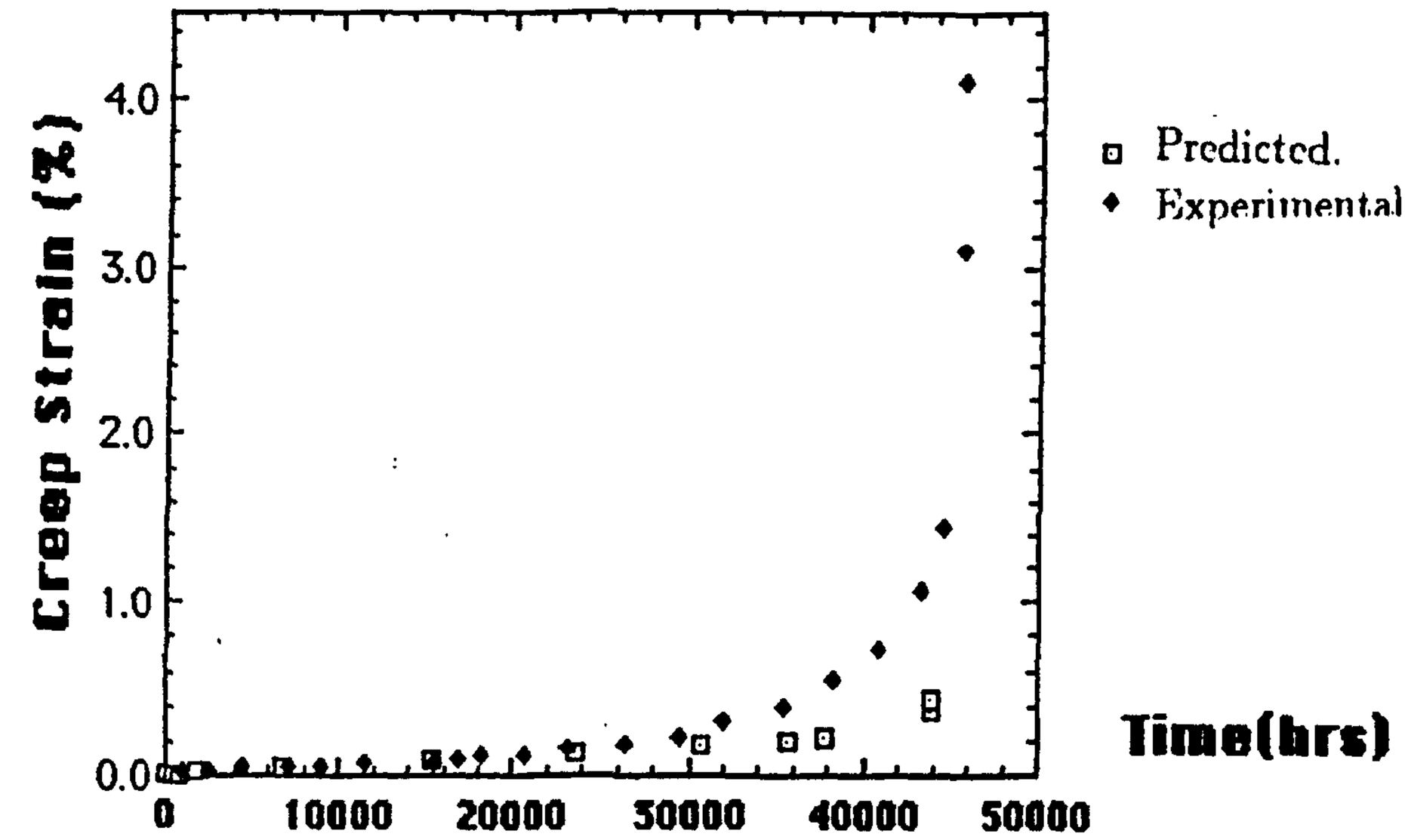

Figure 8.71: Comparison between the experimental axial strains and those predicted from weld model (WM2) corresponding to the creep pip measurements across pipe weld.

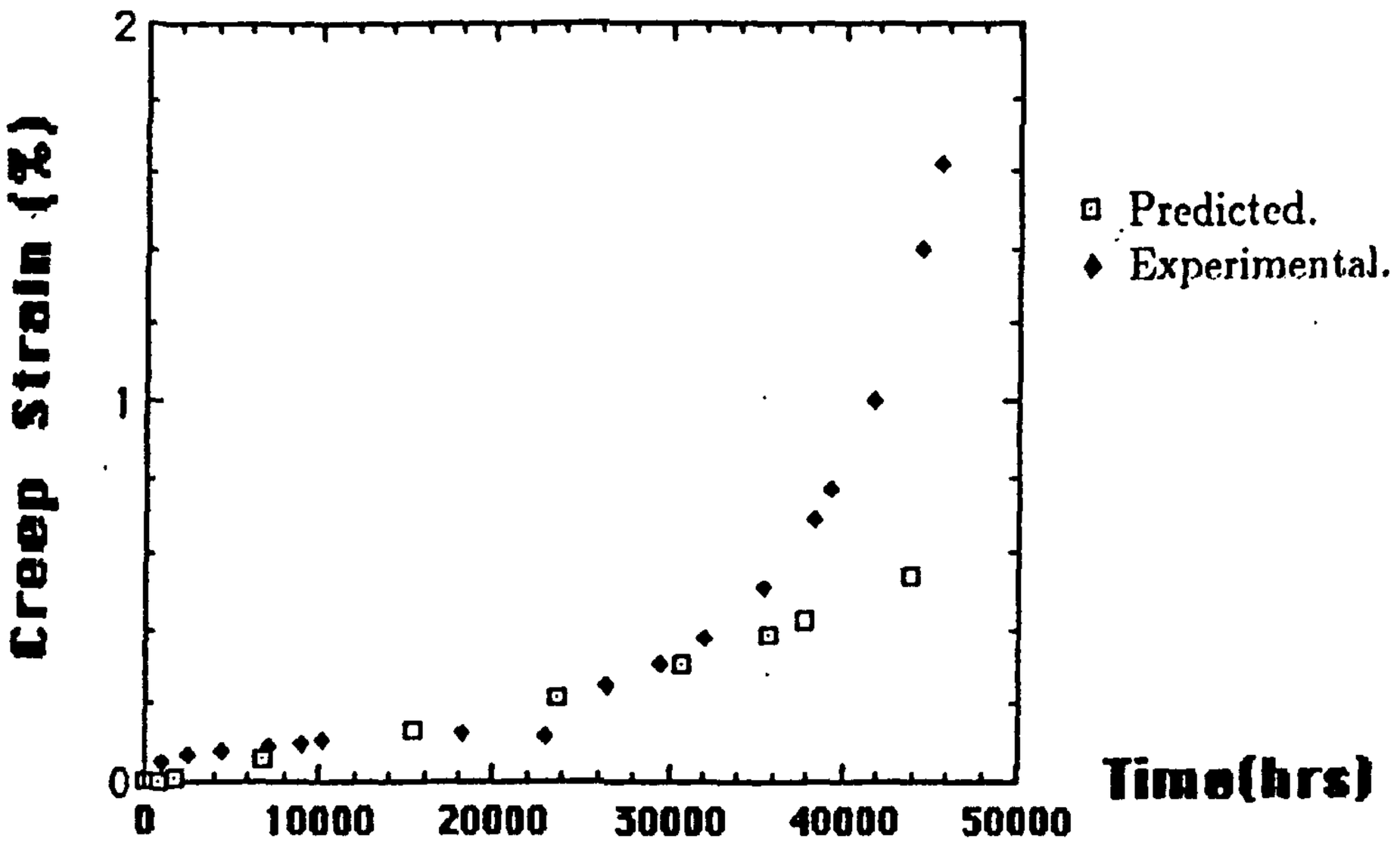

Figure 8.72: Comparison between the experimental axial strains and those predicted from weld model (WM2) corresponding to the capacitance strain gauge measurements at the weld metal centre line.

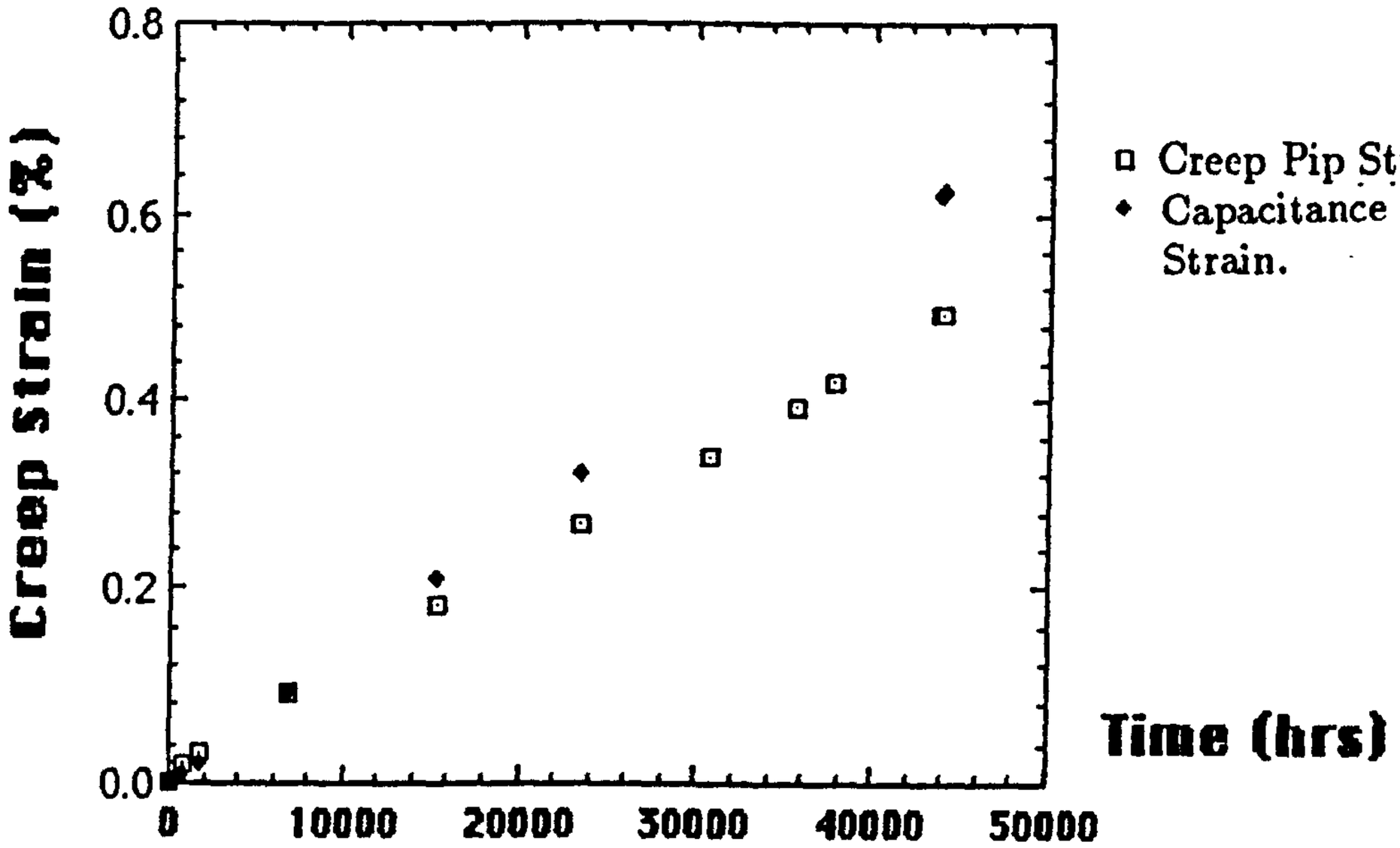

Figure 8.73: Comparison between the predicted hoop strains corresponding to the creep pip and capacitance strain gauge measurements in the parent metal pipe from weld model (WM2).

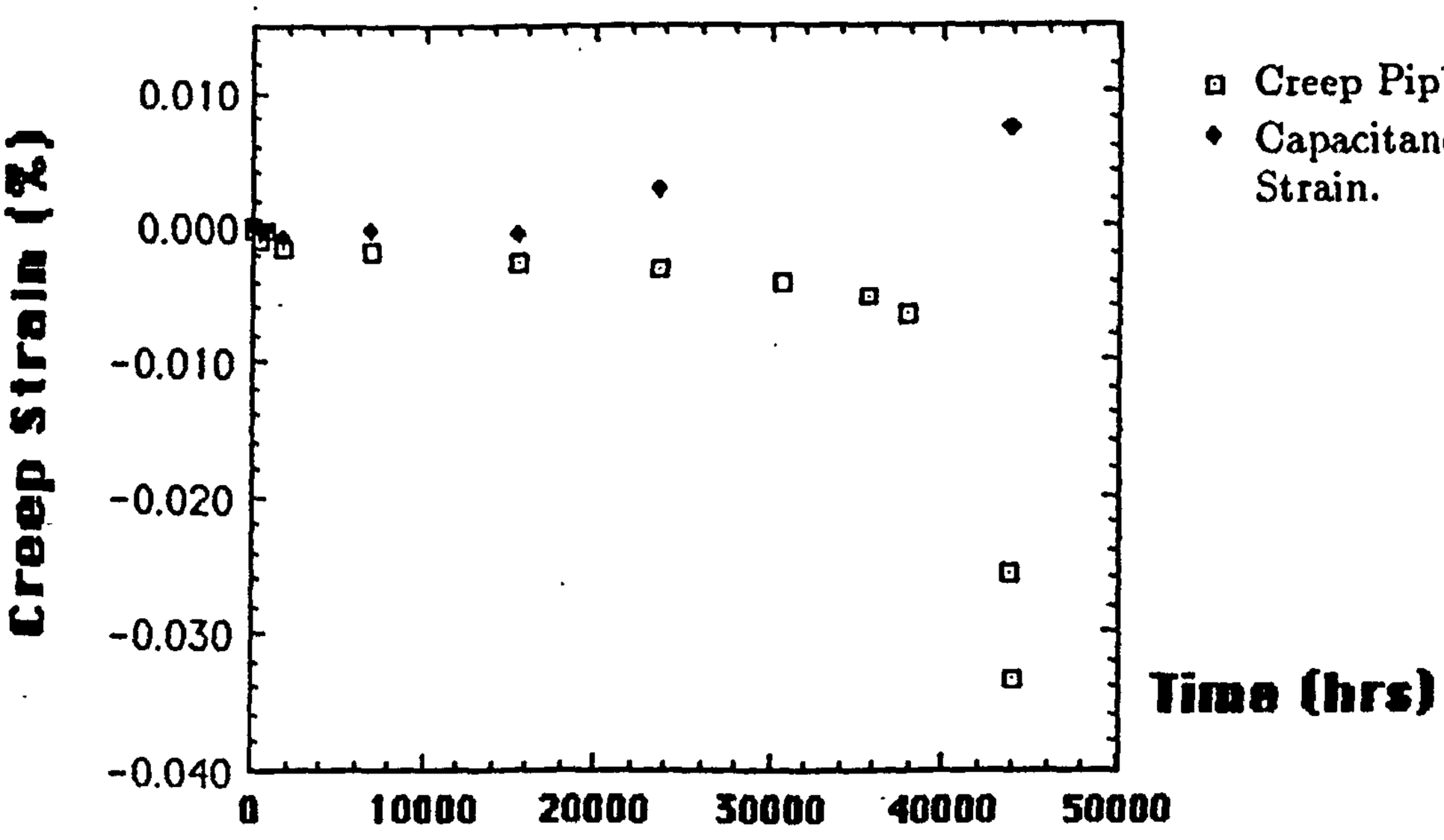

Figure 8.74: Comparison between the predicted axial strains corresponding to the creep pip and capacitance strain gauge measurements in the parent metal pipe from weld model (WM2).

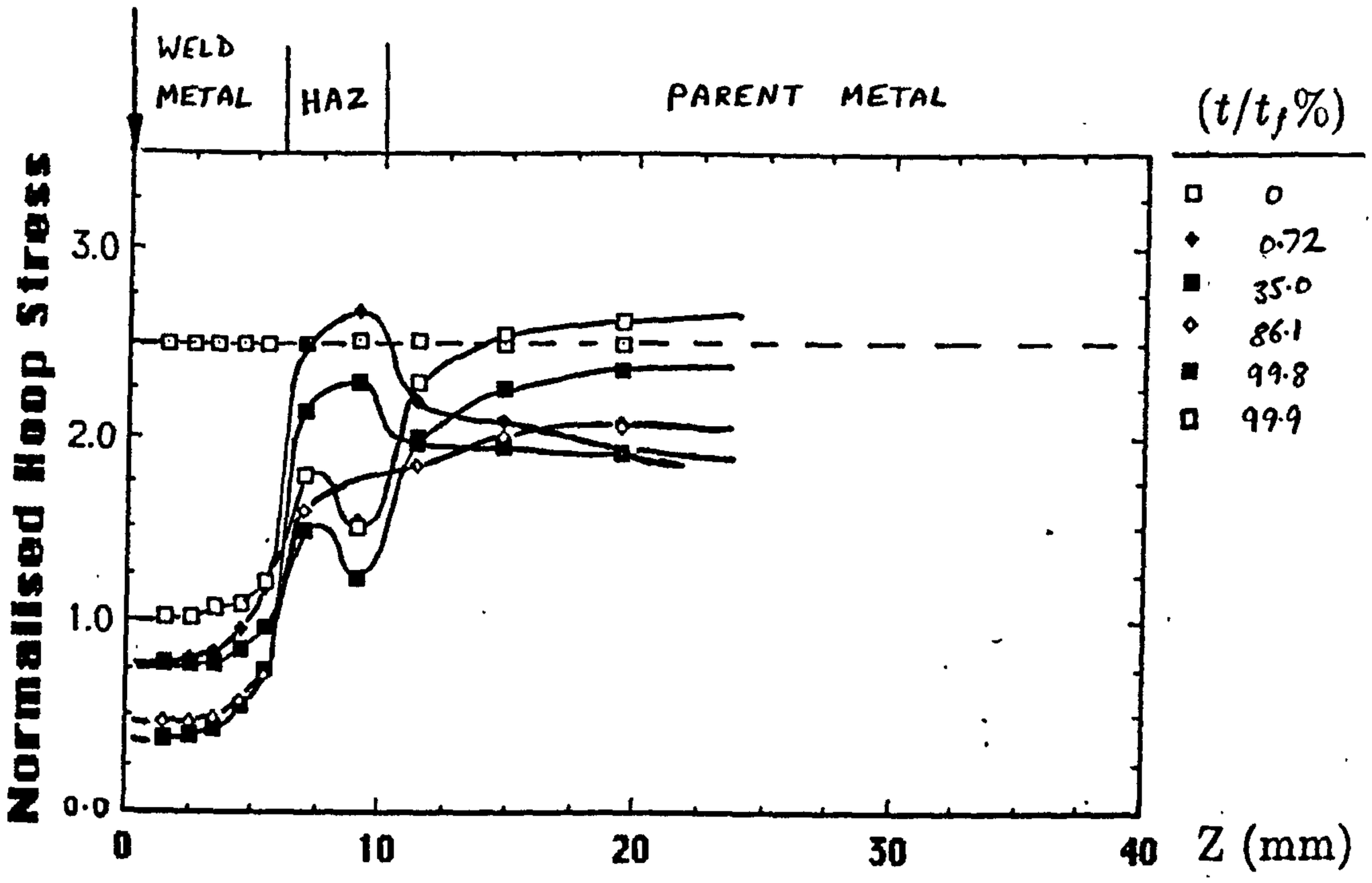

Figure 8.75: Normalised hoop stress (Σ_θ) distributions along the inner bore (Fig.8.9) of the steam pipe at various life fractions for weld model (WM2). The z-distance is measured in the z-direction from the weld metal centre line (Fig.8.9).

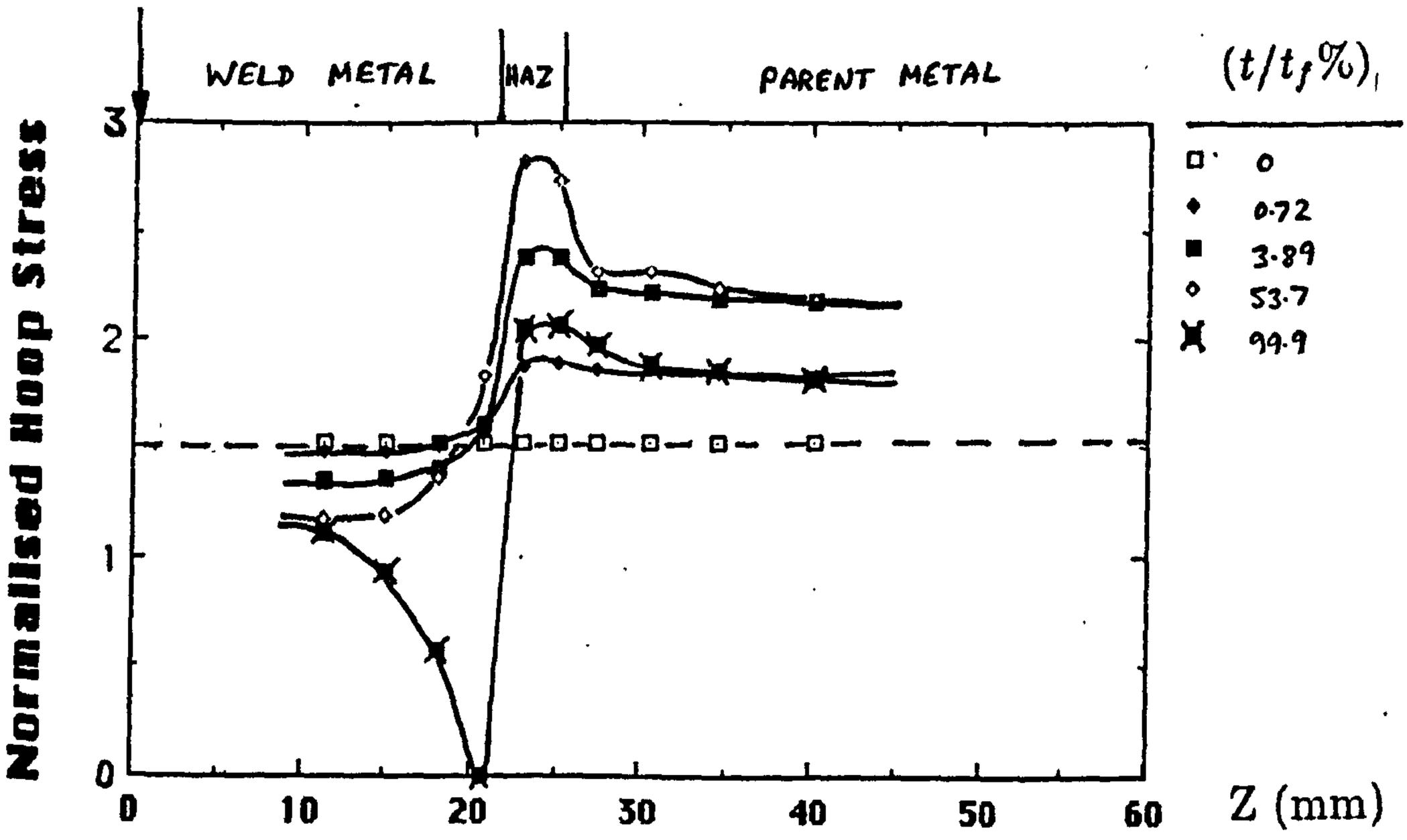

Figure.8.76: Normalised hoop stress (Σ_θ) distributions along the outer surface (Fig.8.9) of the steam pipe at various life fractions for weld model (WM2). The z-distance is measured in the z-direction from the weld metal centre line (Fig.8.9).

(a)

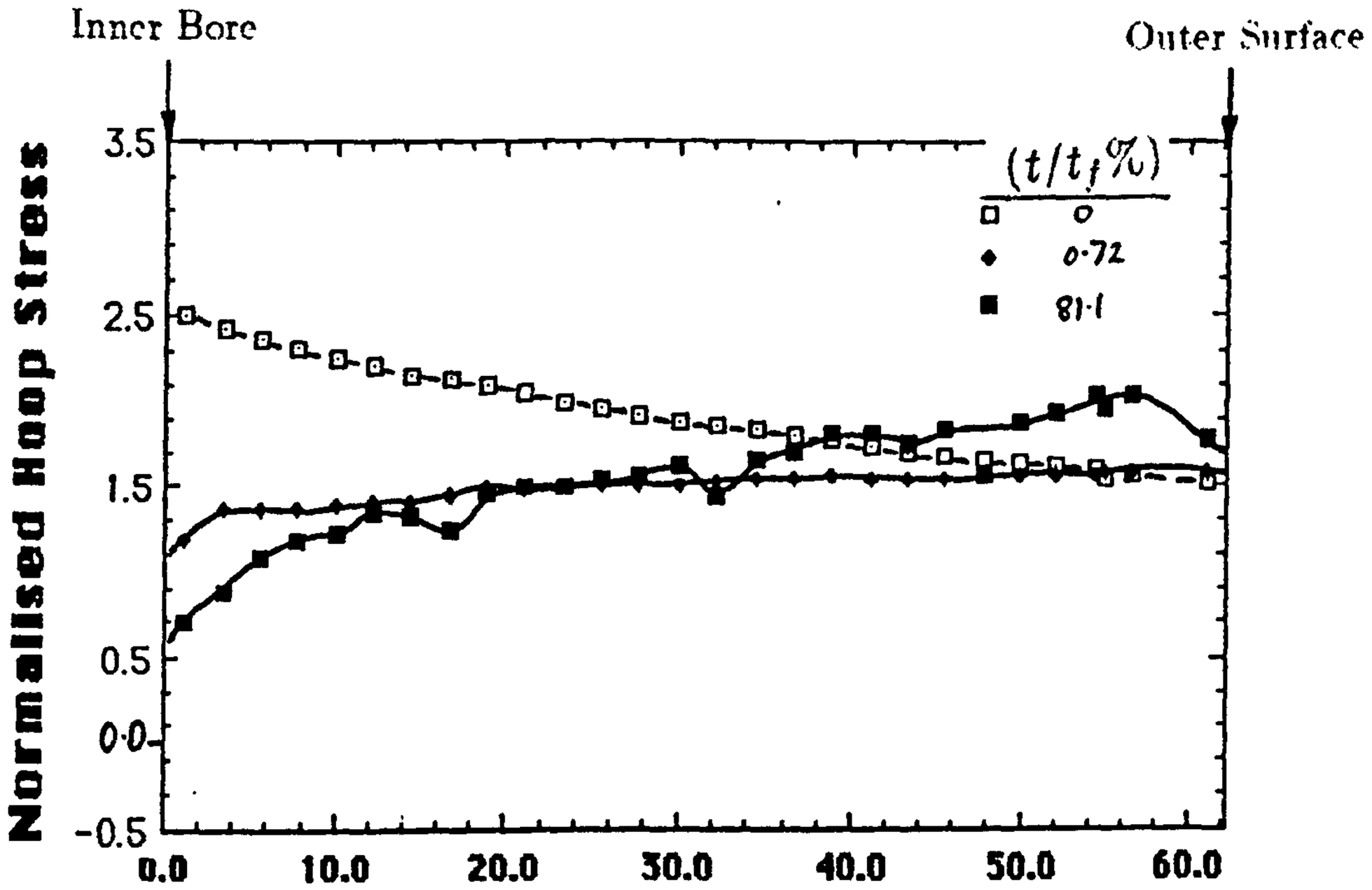

(b)

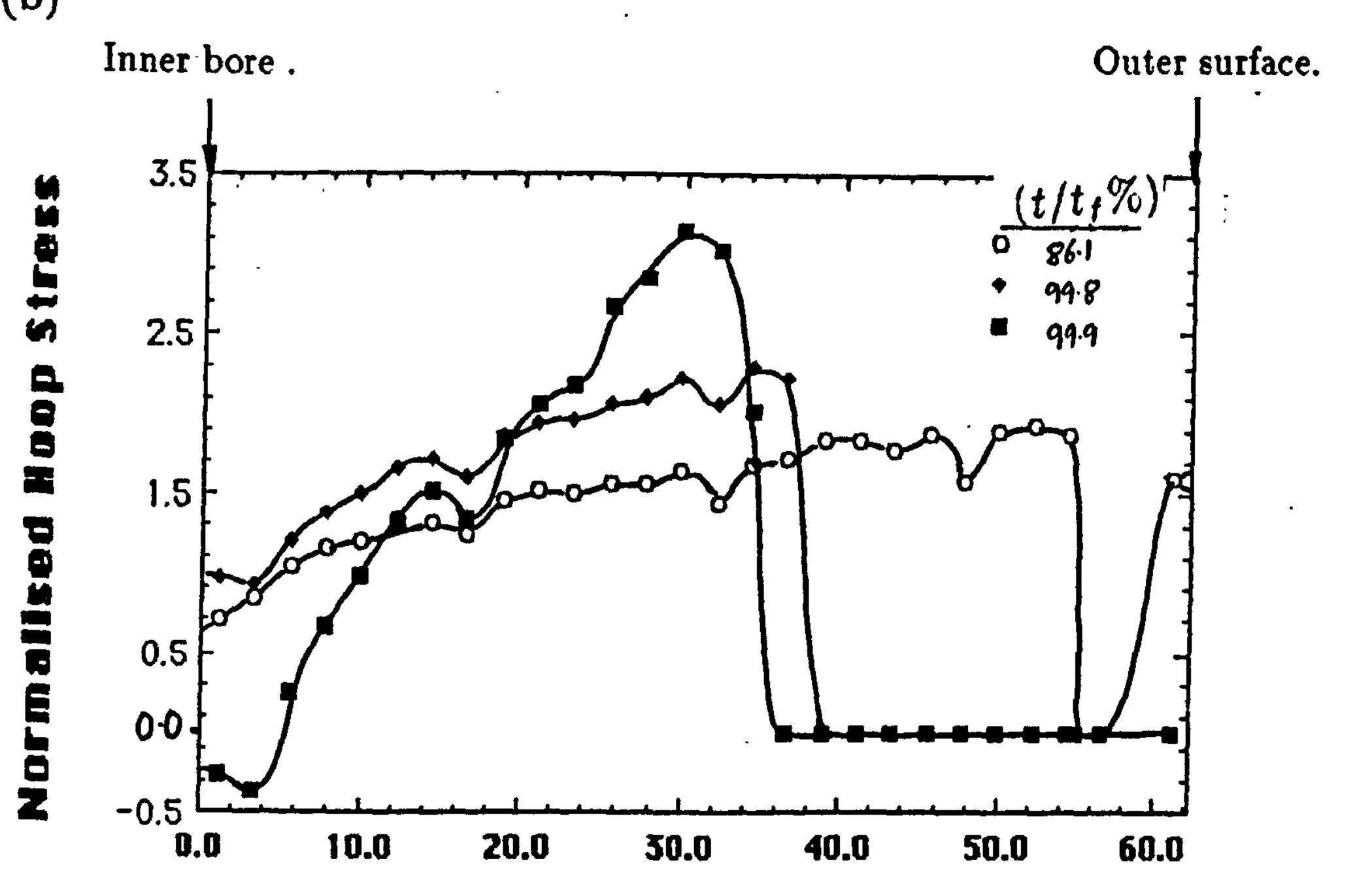

Figure 8.77(a) and (b): Normalised hoop stress (Σ_θ) distributions along the fusion boundary (Fig.8.9) of the steam pipe at various life fractions for weld model (WM2). The distance along the fusion boundary is measured from the internal diameter (Fig.8.9).

(a)

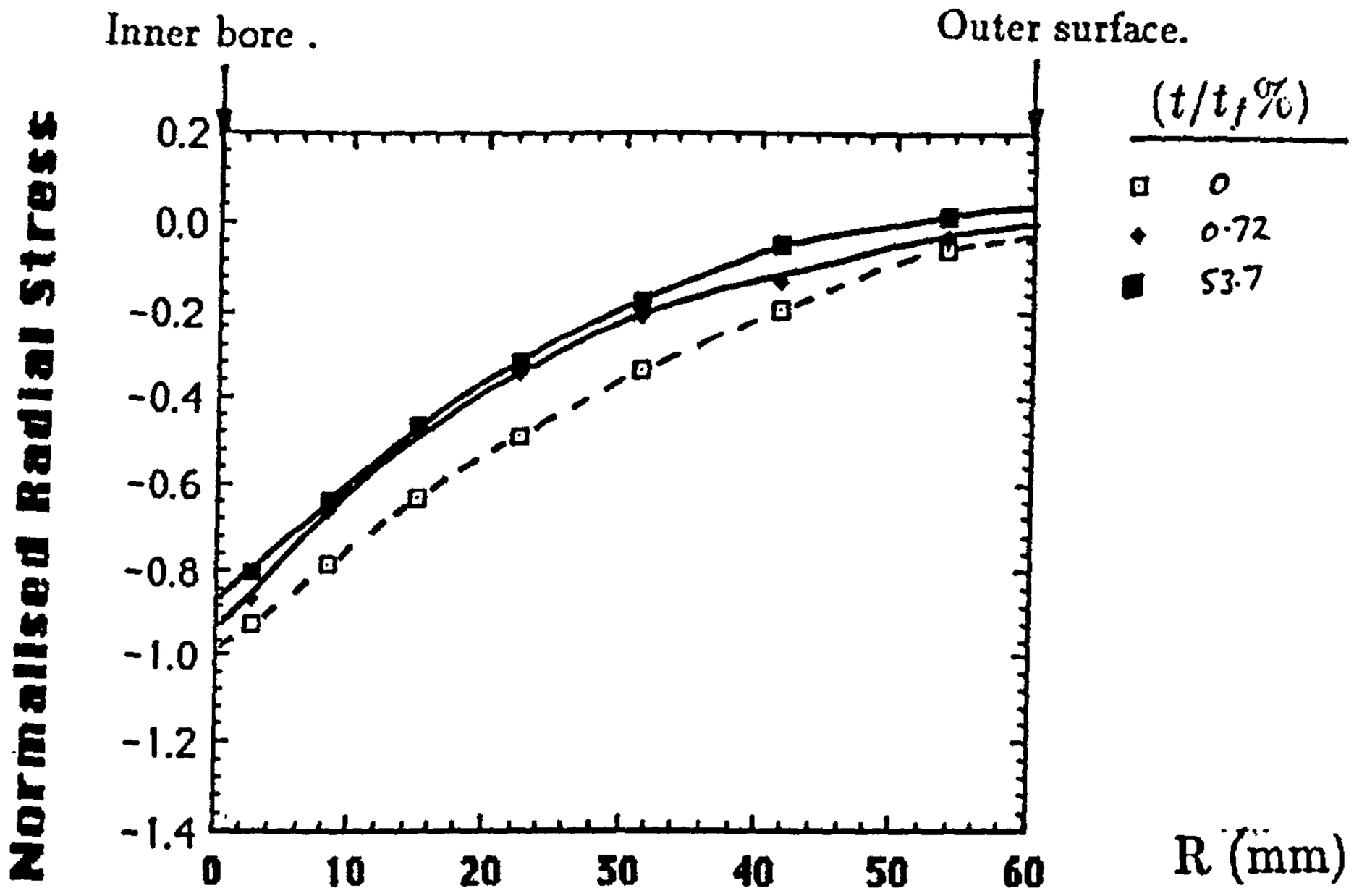

(b)

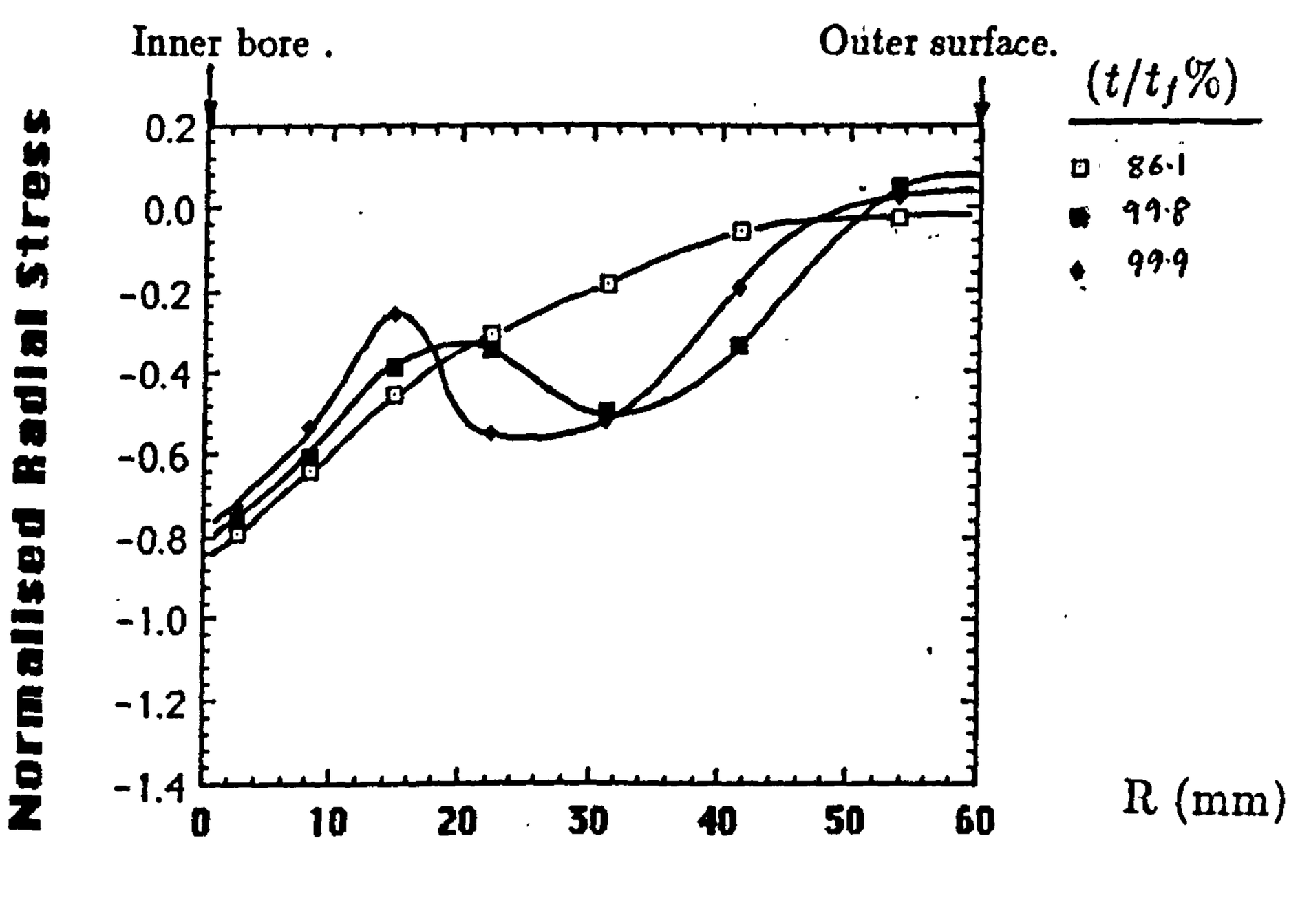

Figure 8.78(a) and (b): Normalised radial stress (Σ_r) distributions along the weld metal centre line (Fig.8.9) of the steam pipe at various life fractions for weld model (WM2). The distance along the weld metal centre line is measured from the internal diameter (Fig.8.9).

(a)

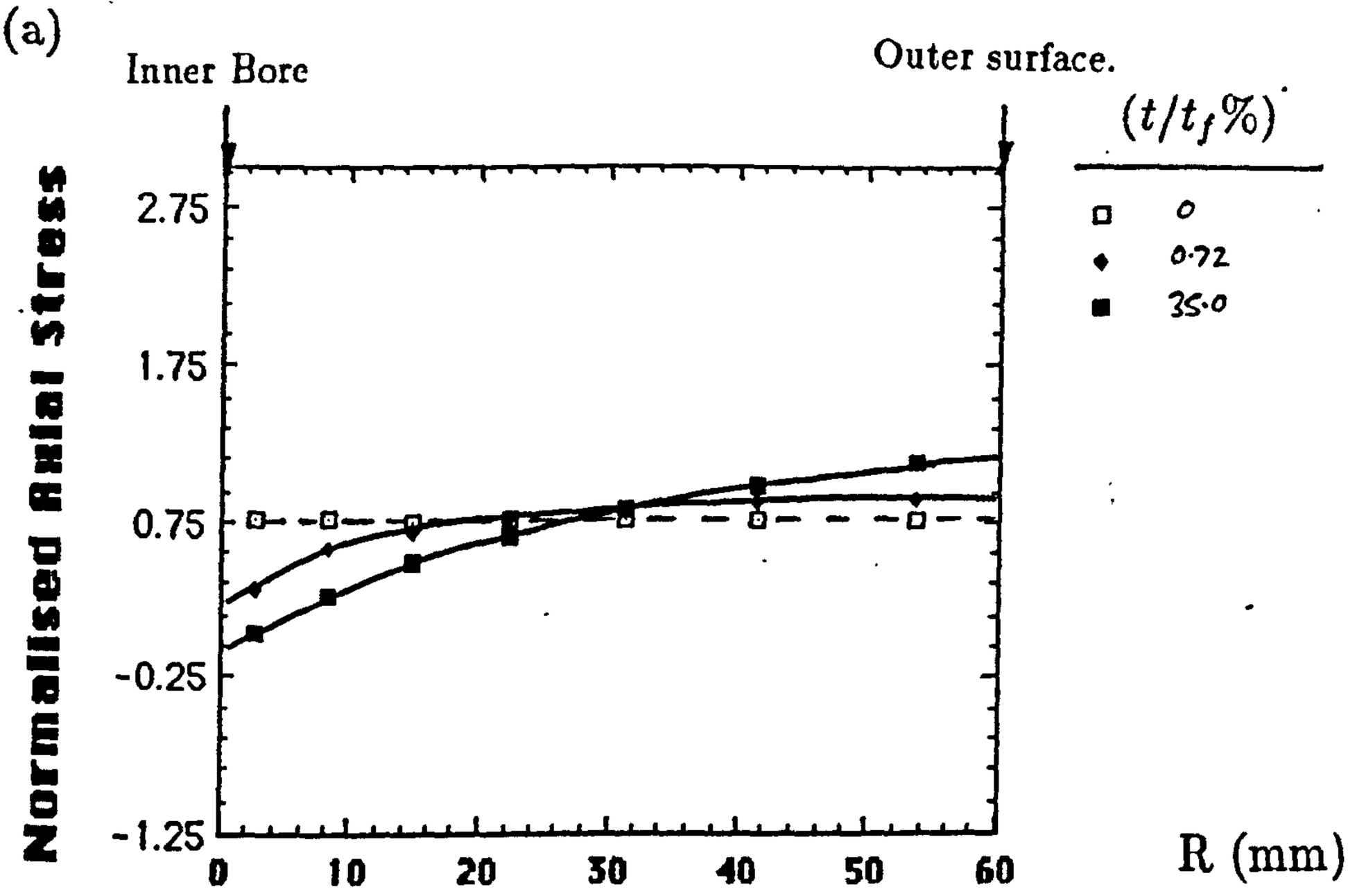

(b)

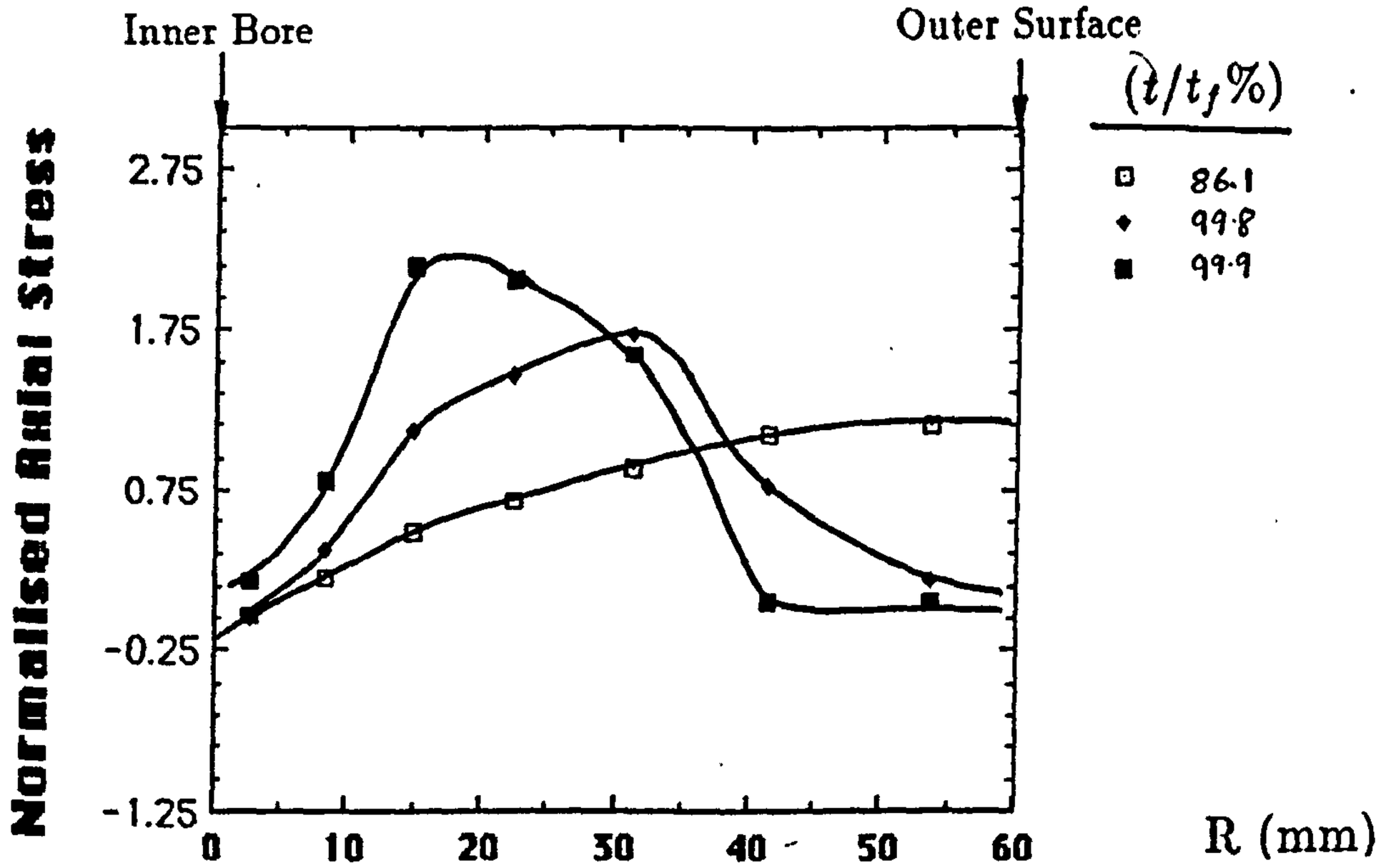

Figure 8.79(a) and (b): Normalised axial stress (Σ_z) distributions along the weld metal centre line (Fig.8.9) of the steam pipe at various life fractions for weld model (WM2). The distance along the weld metal centre line is measured from the internal diameter (Fig.8.9).

(a)

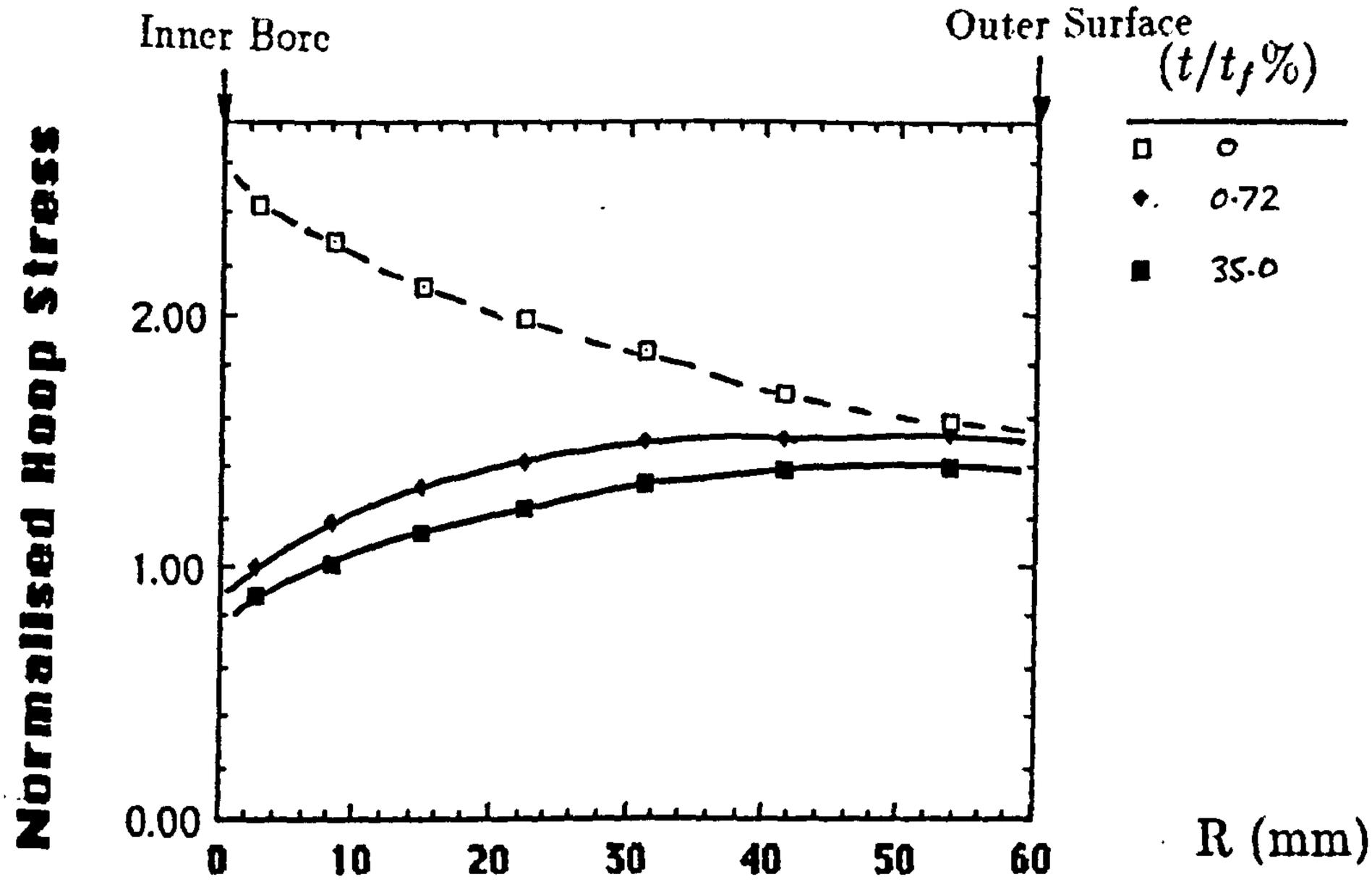

(b)

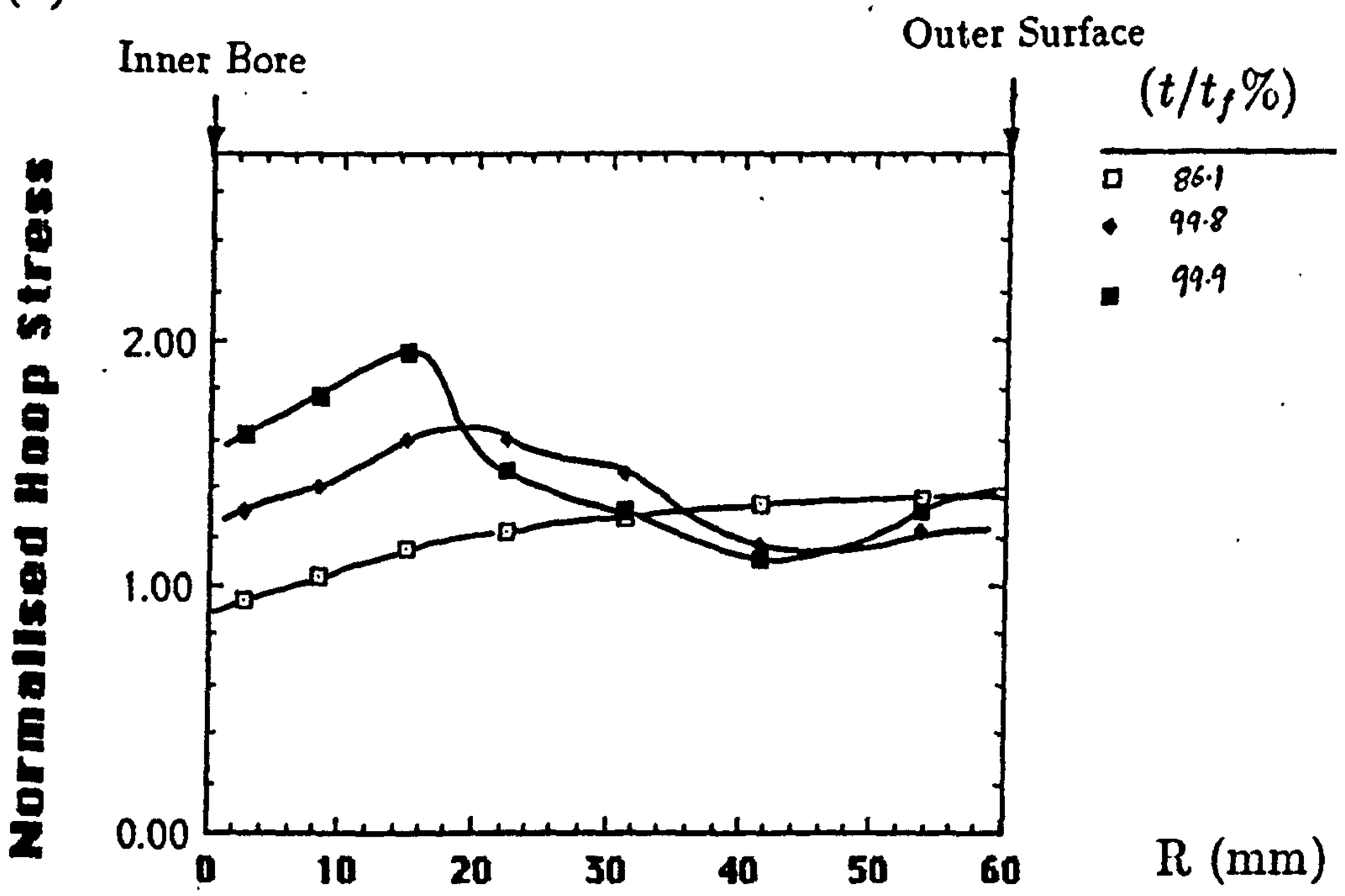

Figure 8.80(a) and (b): Normalised hoop stress (Σ_θ) distributions along the weld metal centre line (Fig.8.9) of the steam pipe at various life fractions for weld model (WM2). The distance along the weld metal centre line is measured from the internal diameter (Fig.8.9).

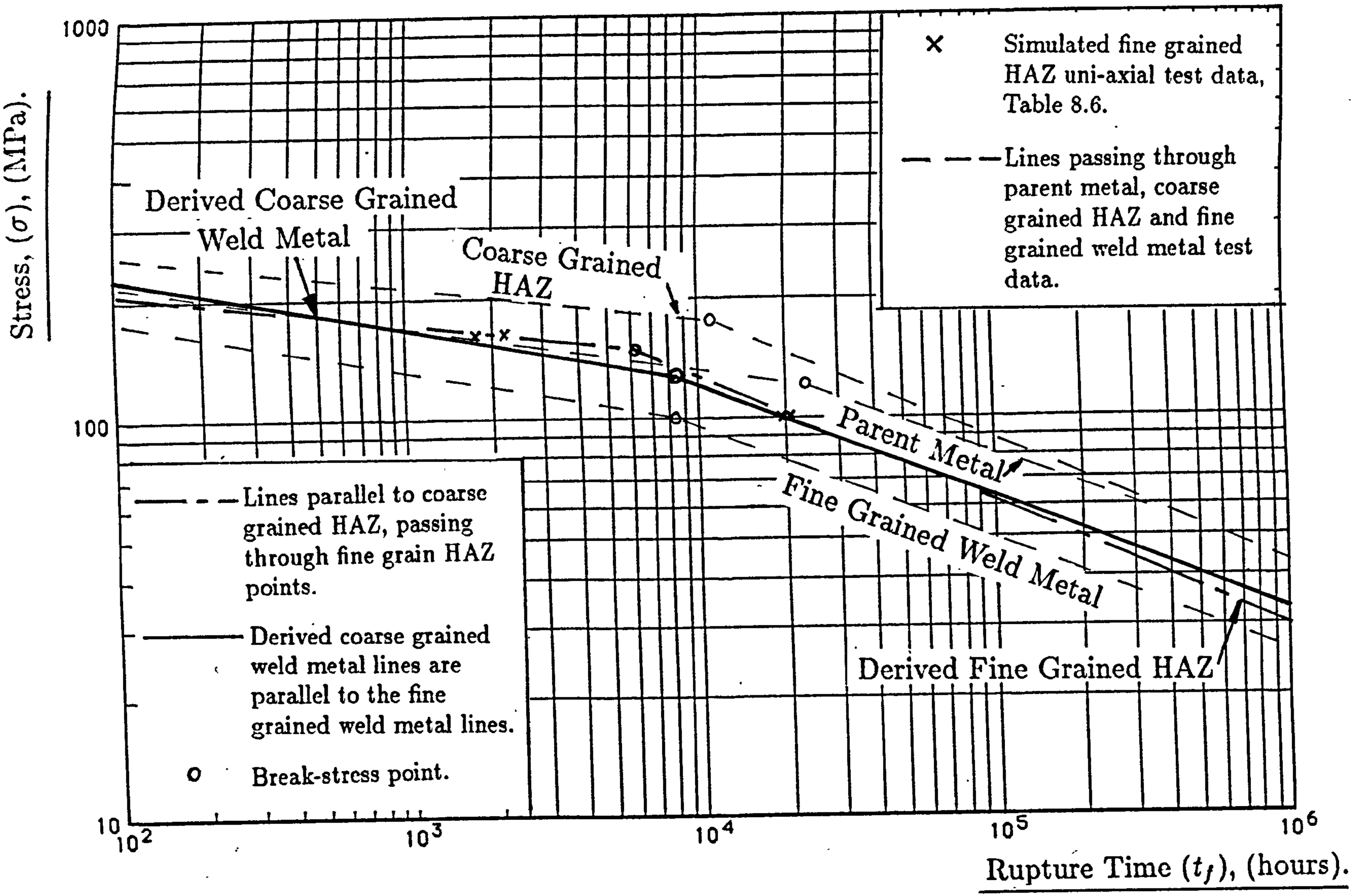

Figure 8.81: Uni-axial stress-rupture diagram showing how the rupture behavior of the coarse grained weld metal is derived.

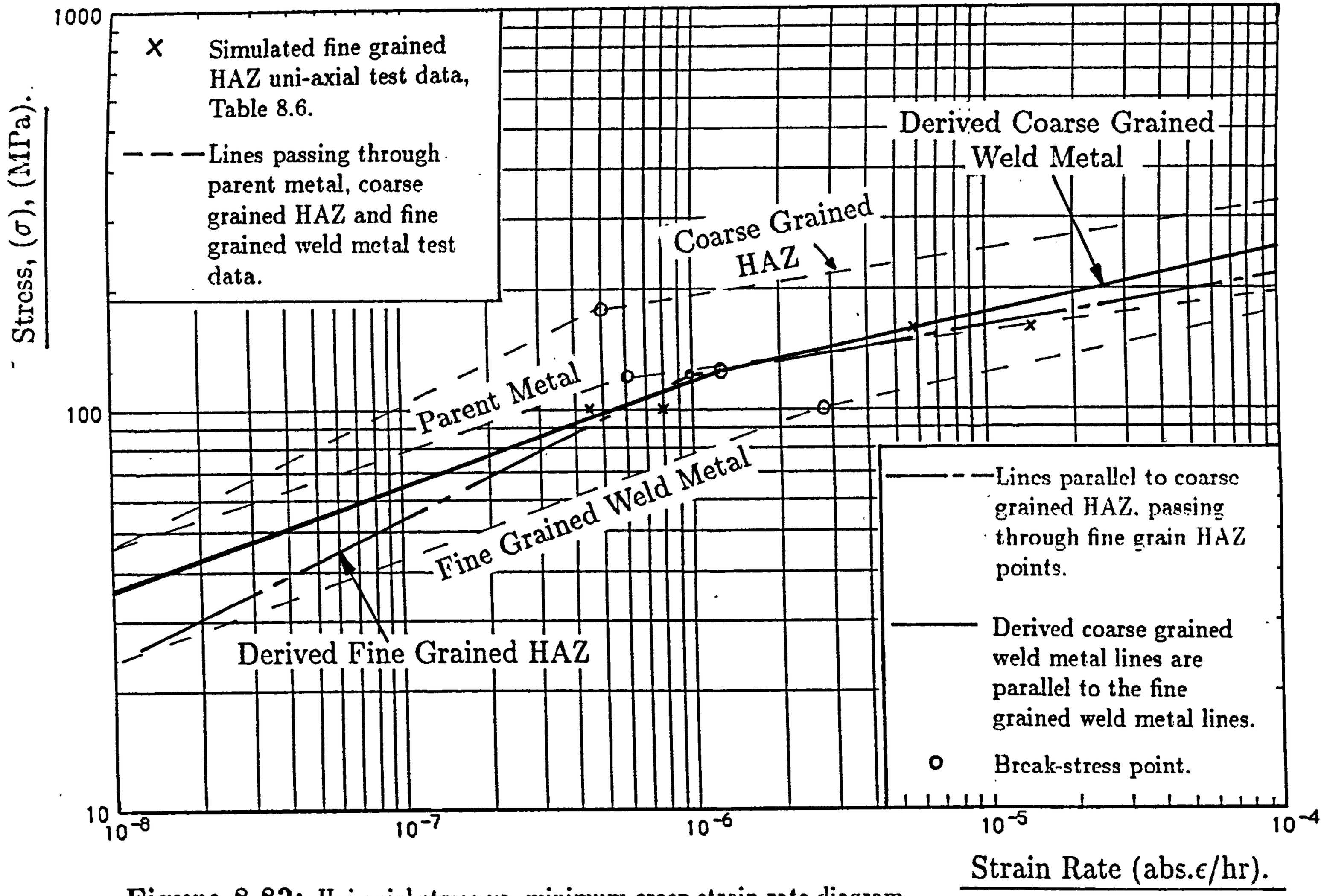

Figure 8.82: Uni-axial stress vs. minimum creep strain rate diagram showing how the deformation behaviour of the coarse grained weld metal is derived.

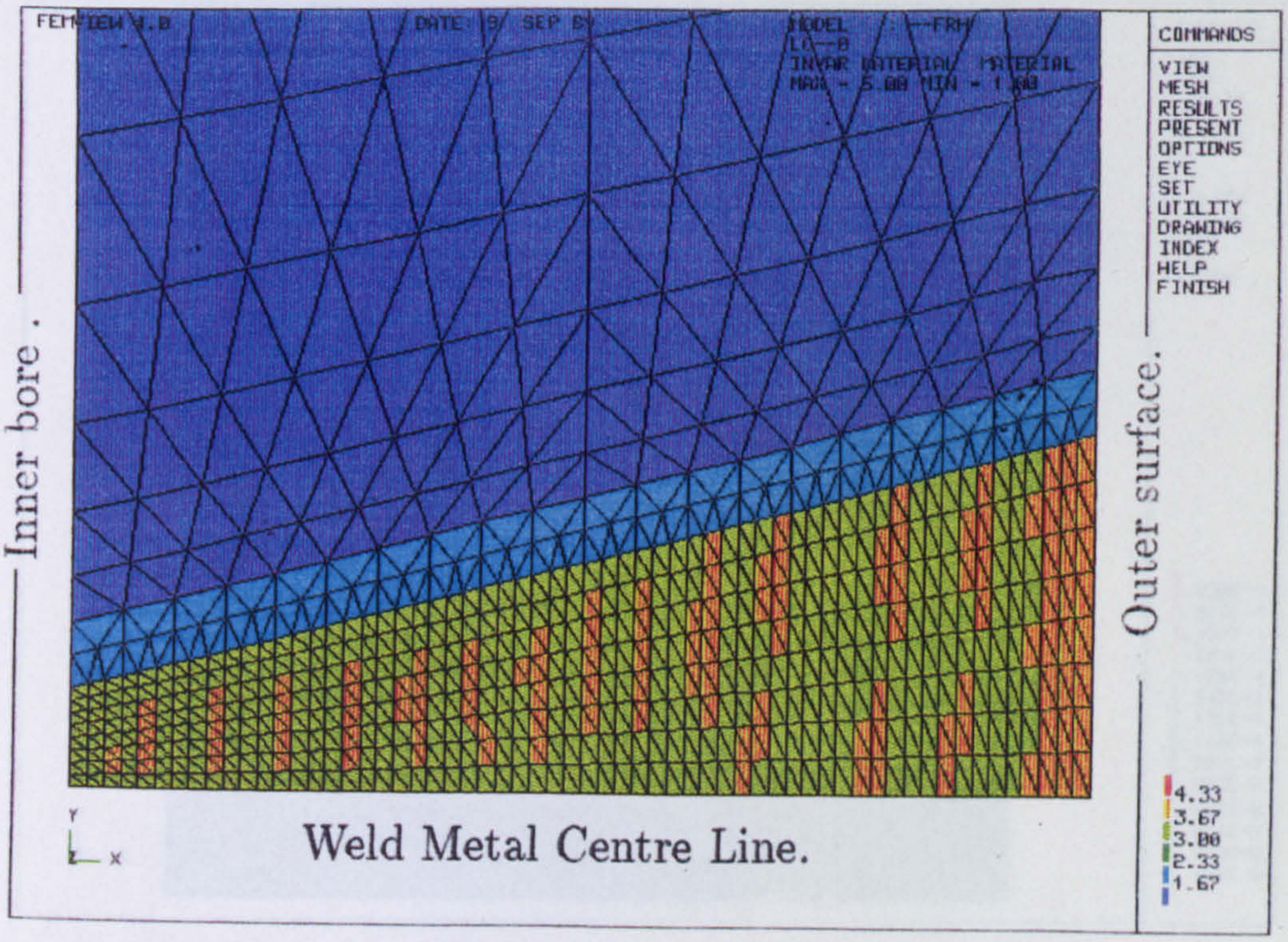

Figure 8.83: The lower section of the axisymmetric finite element mesh for the third weld model (WM3) (Fig.8.9), as used to model the 2.25Cr 1Mo:0.5Cr 0.5Mo 0.25V thick steam pipe weld. The dark blue, the blue, the green and the brown regions are assigned the material properties (Table 8.3) of the parent metal, the HAZ(G.C.P.)(2), the weld metal(fine) and the weld metal(coarse) grained banitic regions, respectively.

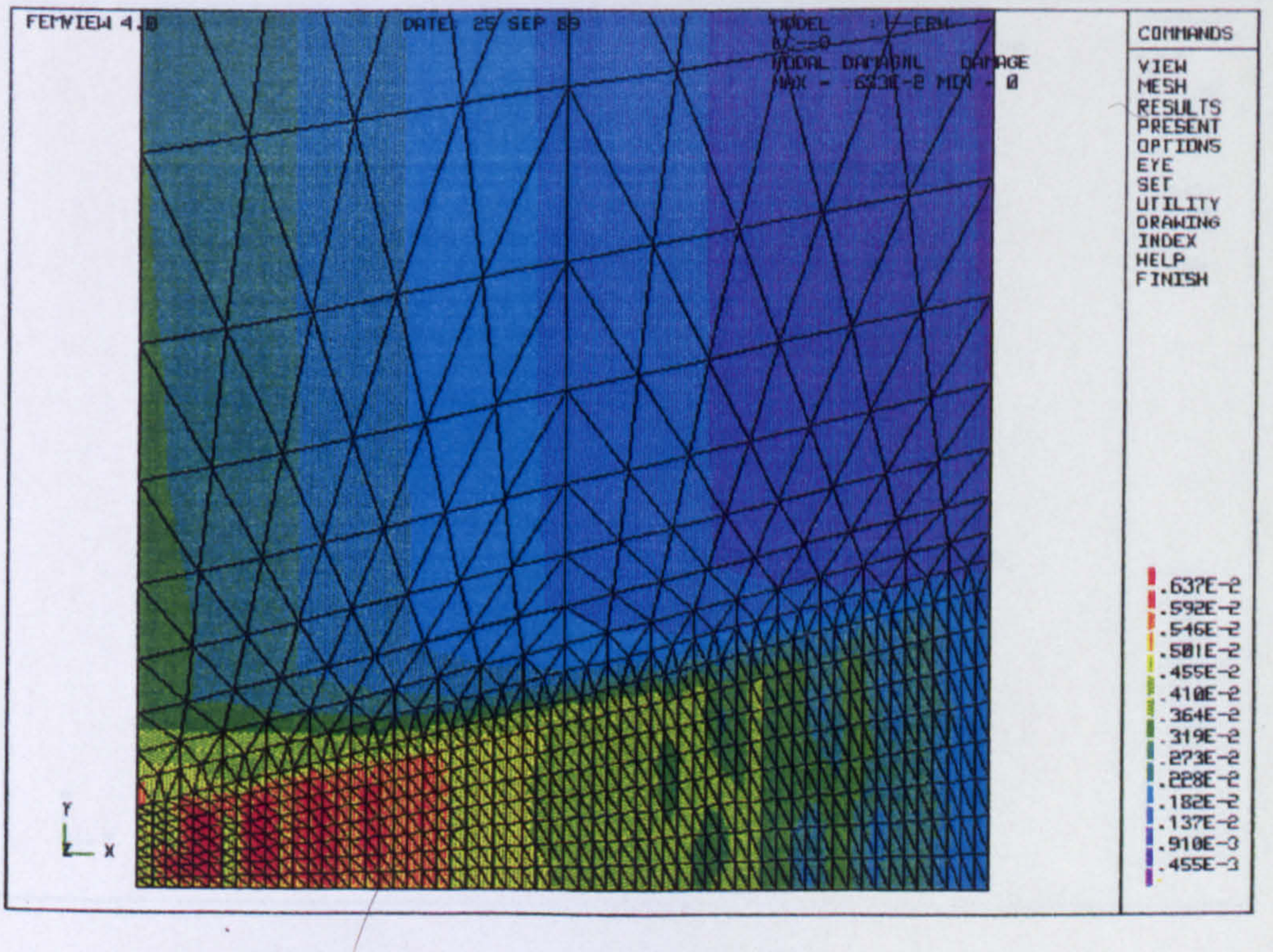

Figure 8.84: Damage distribution for weld model (WM3) at a life fraction ($t/t_f = 0.73\%$). The maximum damage occurs in the inner 1/3rd of the weld metal, concentrated in the coarse grained banitic regions.

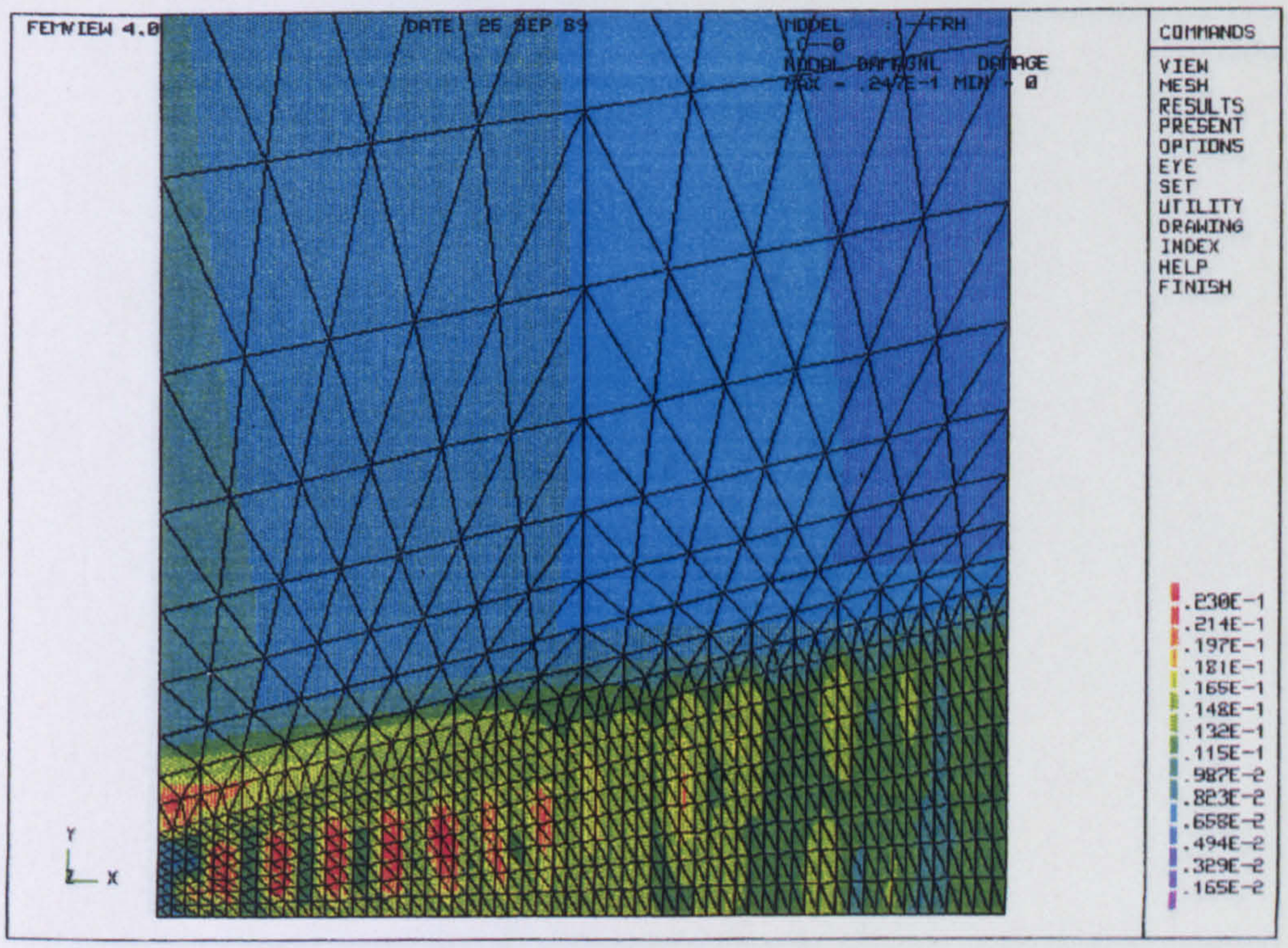

Figure 8.85: Damage distribution for weld model (WM3) at a life fraction ($t/t_f = 4.4\%$).

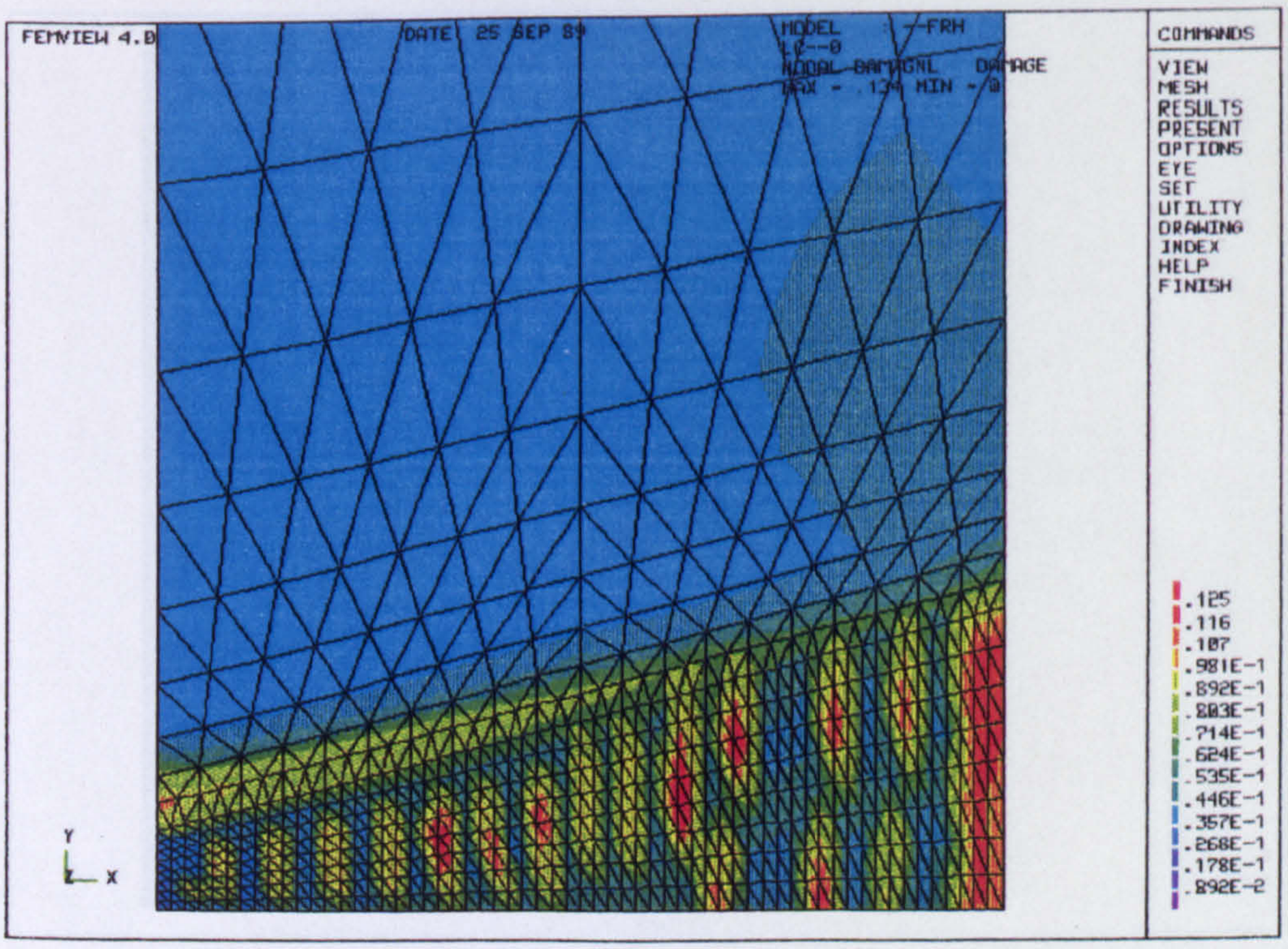

Figure 8.86: Damage distribution for weld model (WM3) at a life fraction ($t/t_f = 32.0\%$).

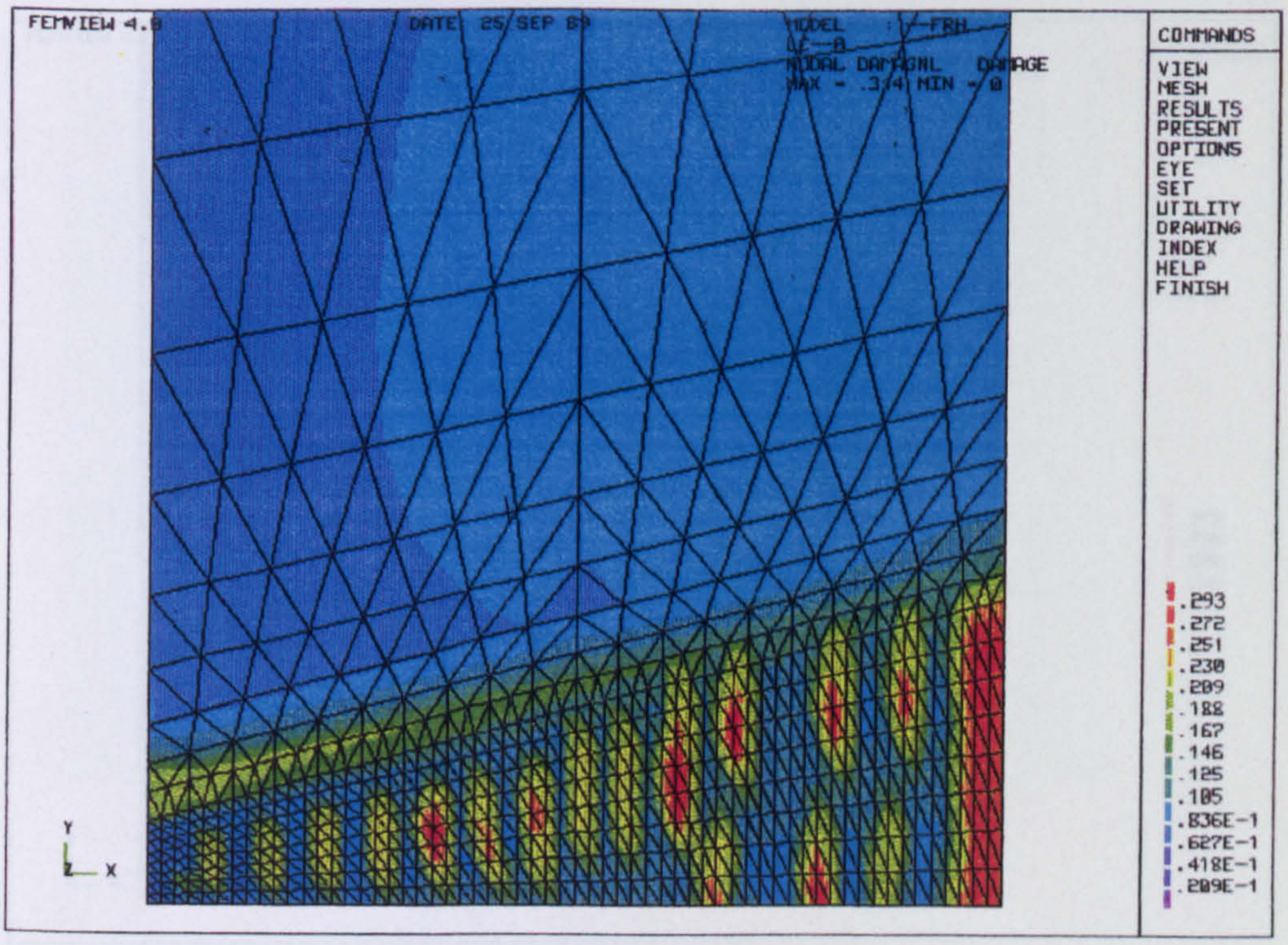

Figure 8.87: Damage distribution for weld model (WM3) at a life fraction ($t/t_f = 66.0\%$).

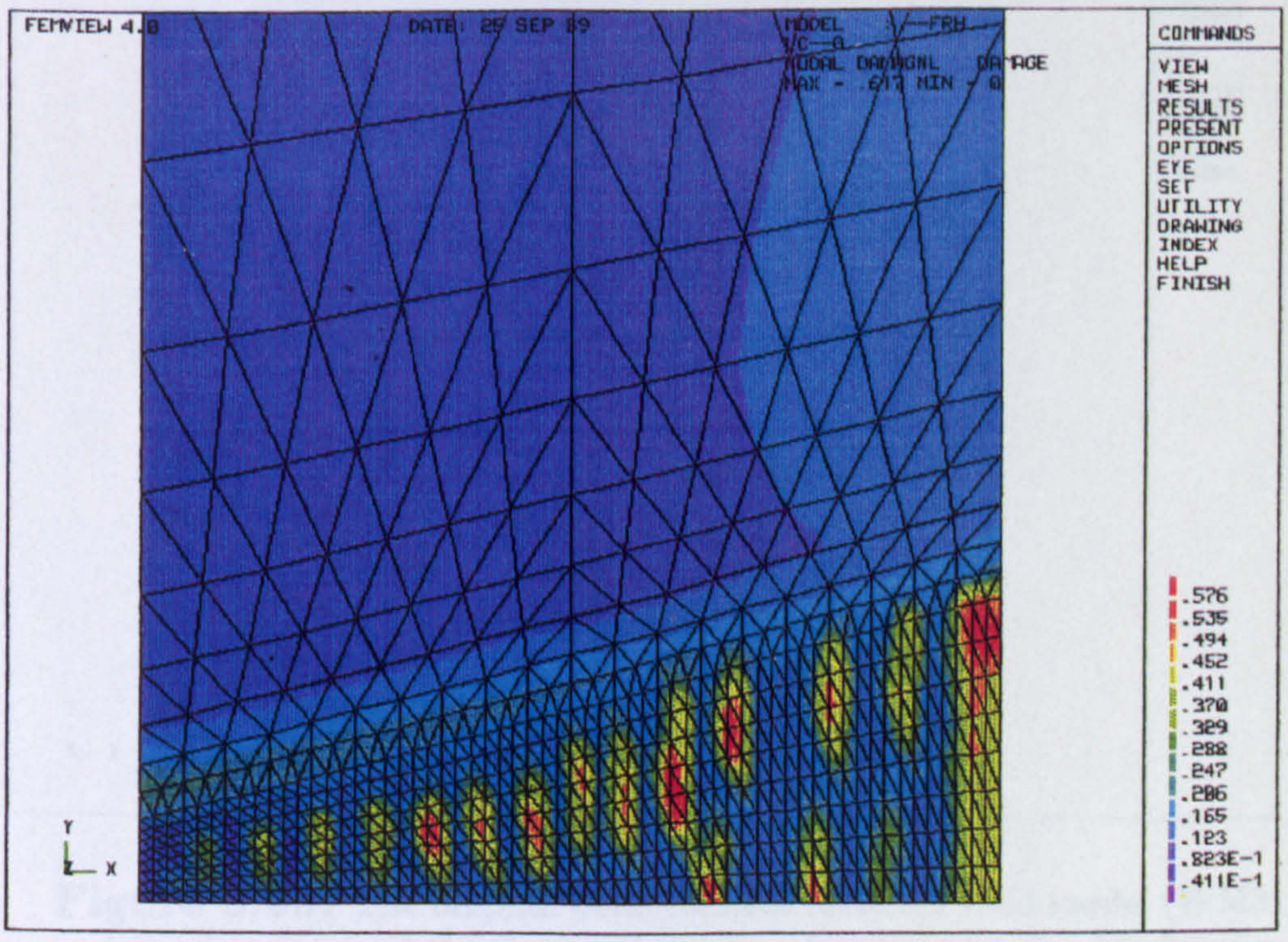

Figure 8.88: Damage distribution for weld model (WM3) at a life fraction ($t/t_f = 86.2\%$).

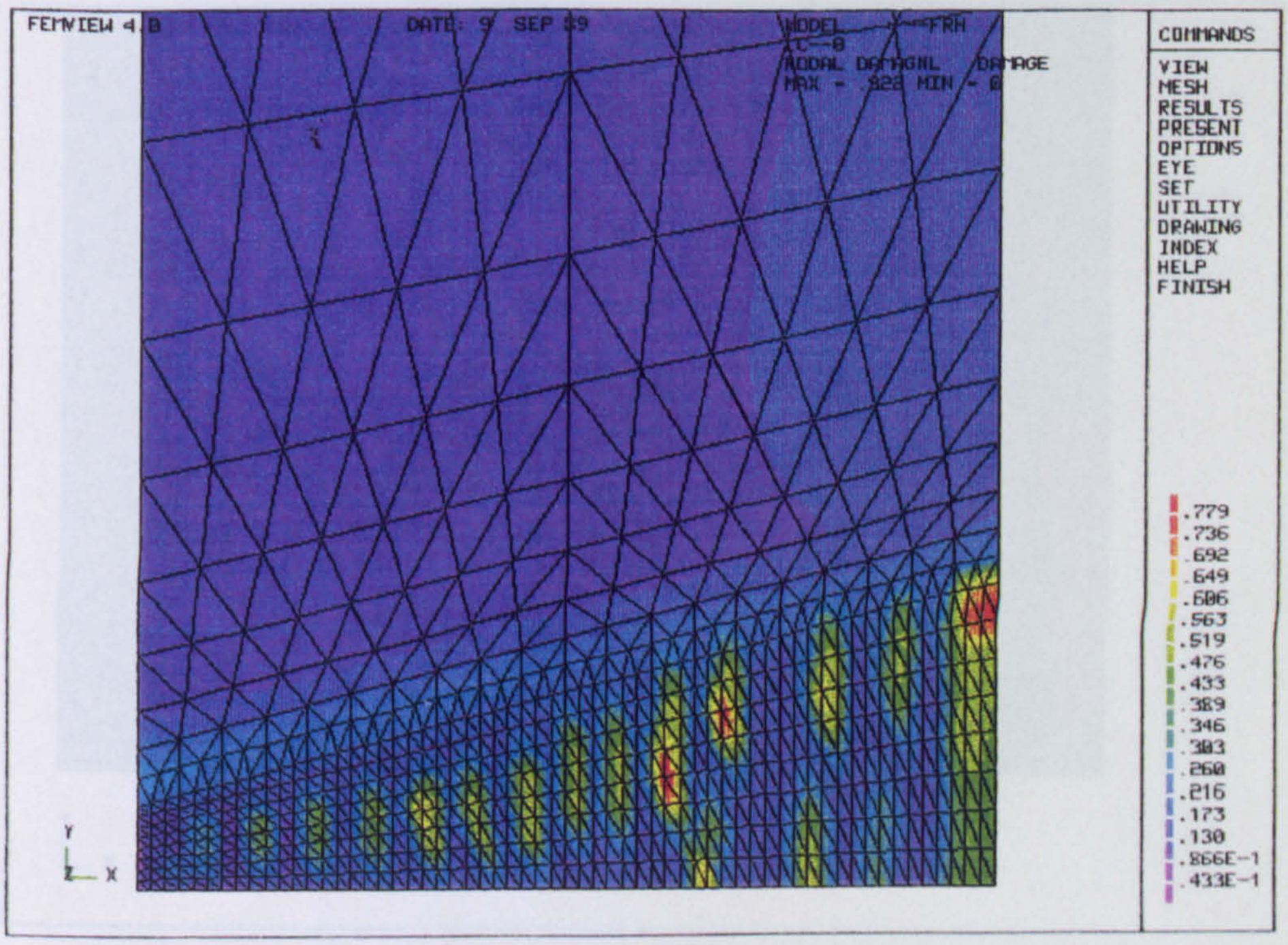

Figure 8.89: Damage distribution for weld model (WM3) at a life fraction ($t/t_f = 89.5\%$).

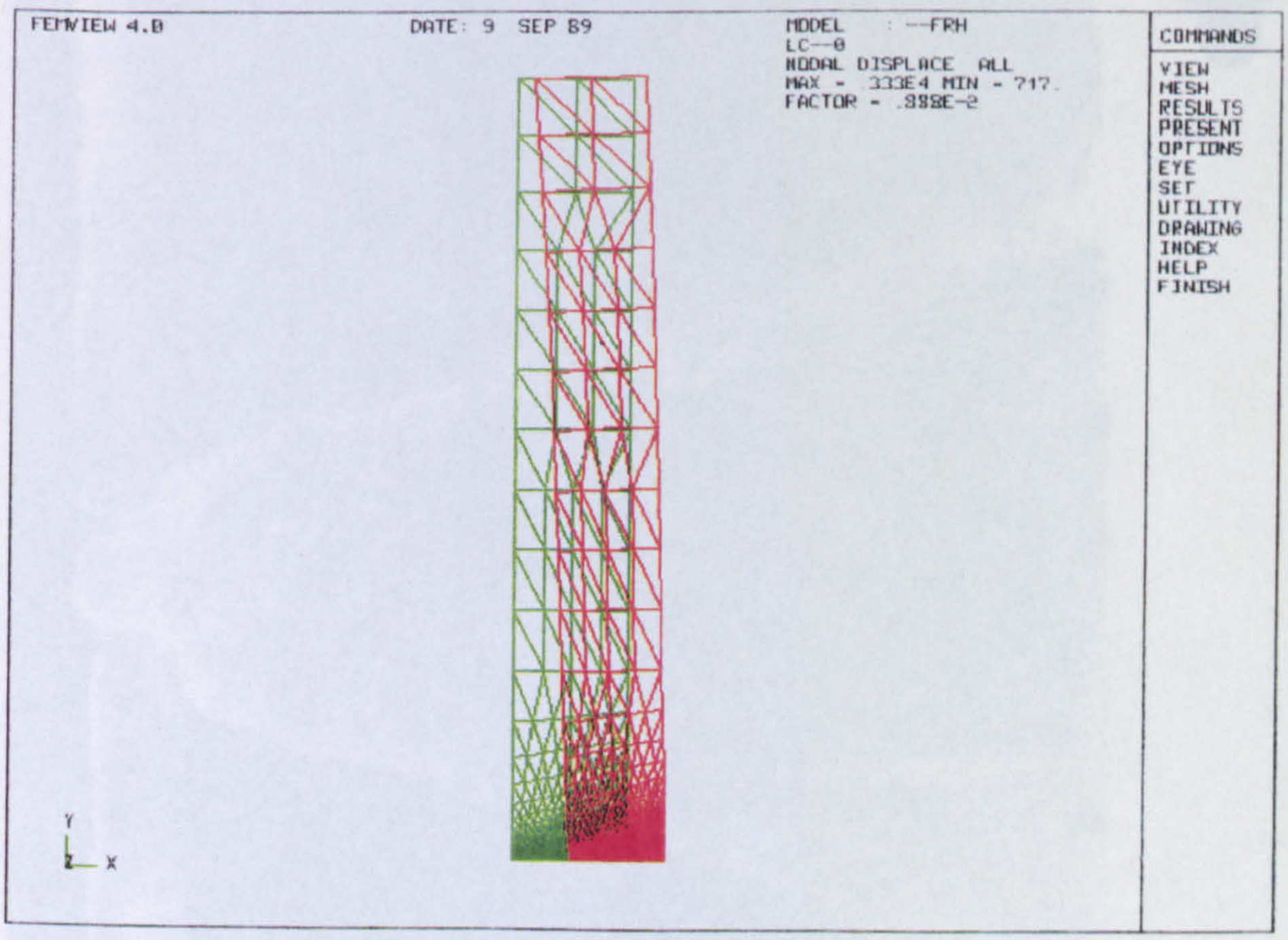

Figure 8.90: The original finite element mesh for weld model (WM3) is shown in green and the displaced mesh is shown in red at a life fraction of ($t_f \approx 89.5\%$), corresponding to the damage distribution of Fig.8.89, above. The displaced plot shows how the weld metal deforms most and how the weld bulges outwards causing bending to occur in the pressure vessel as is observed in the full size laboratory test, [133], and Fig.8.8.

(a)

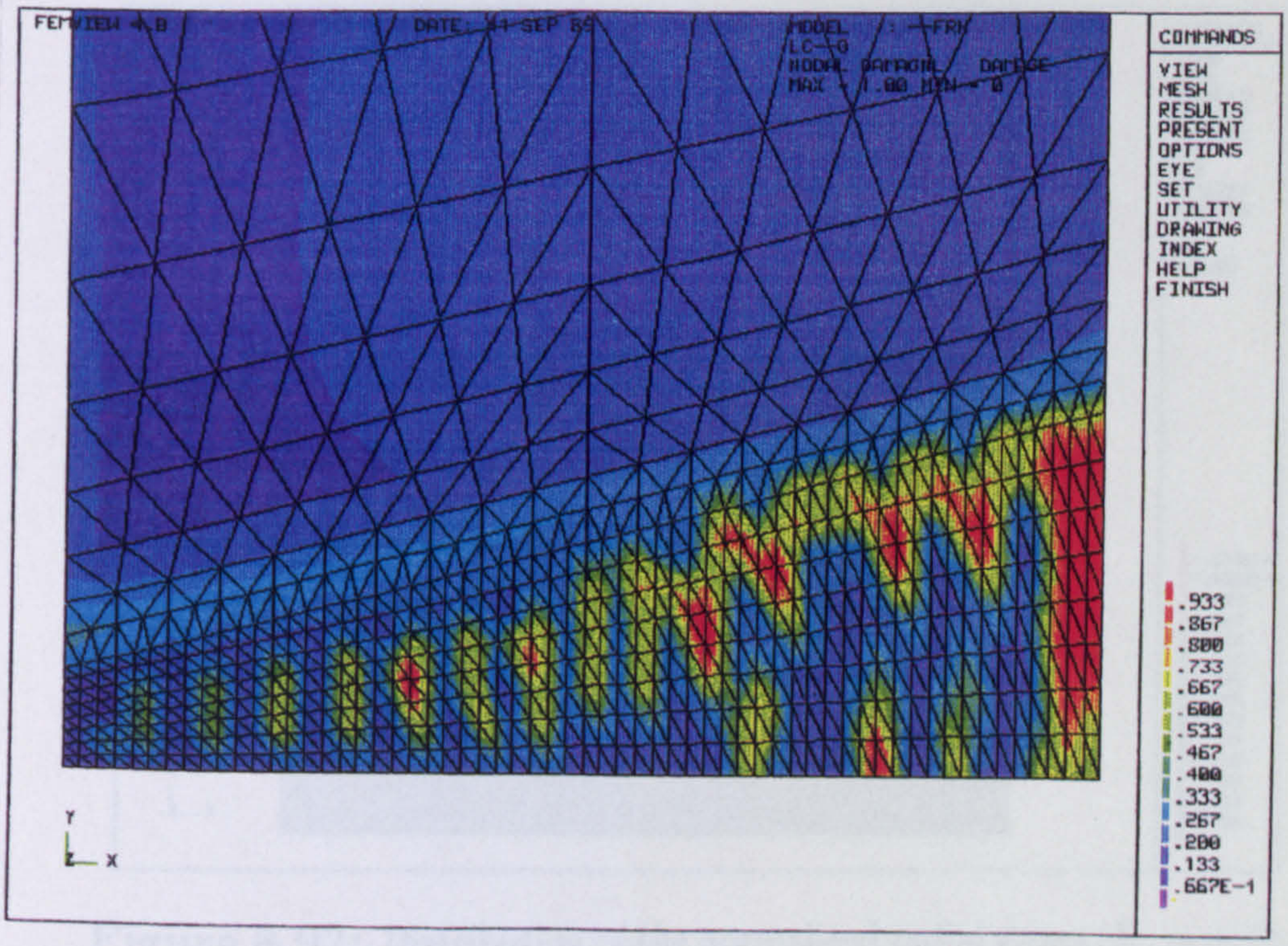

(b)

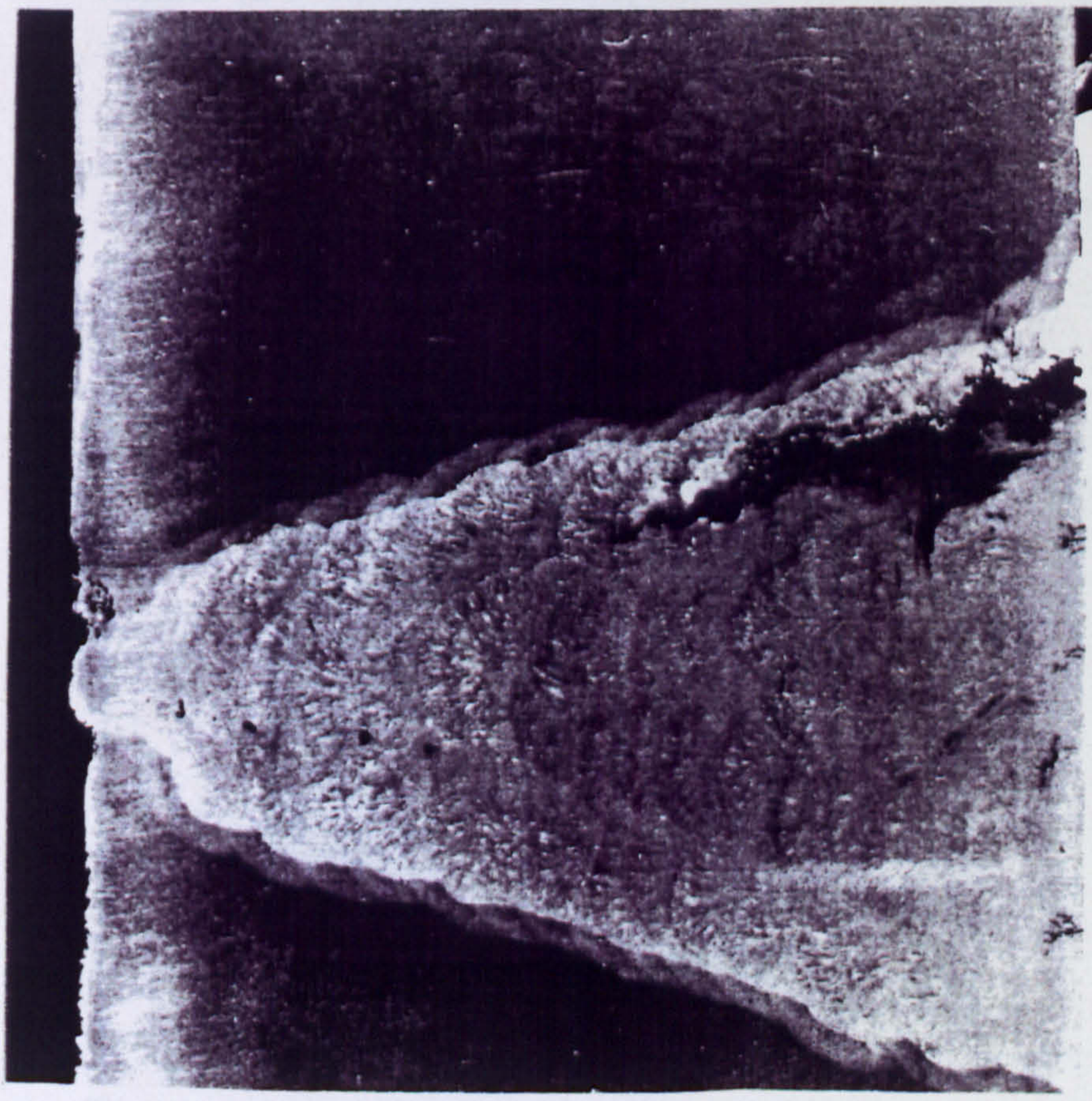

Figure 8.91: (a) Damage distribution for weld model (WM3) at a life fraction ($t/t_f \approx 100.0\%$) predicting the formation of failed regions ($\omega > 0.8$ in the colour plot key) in the weld metal, which may be compared with (b) the observed cracking in a radial section through the 2.25Cr 1Mo steam pipe weld at vessel failure. Micrograph courtesy Coleman [149].

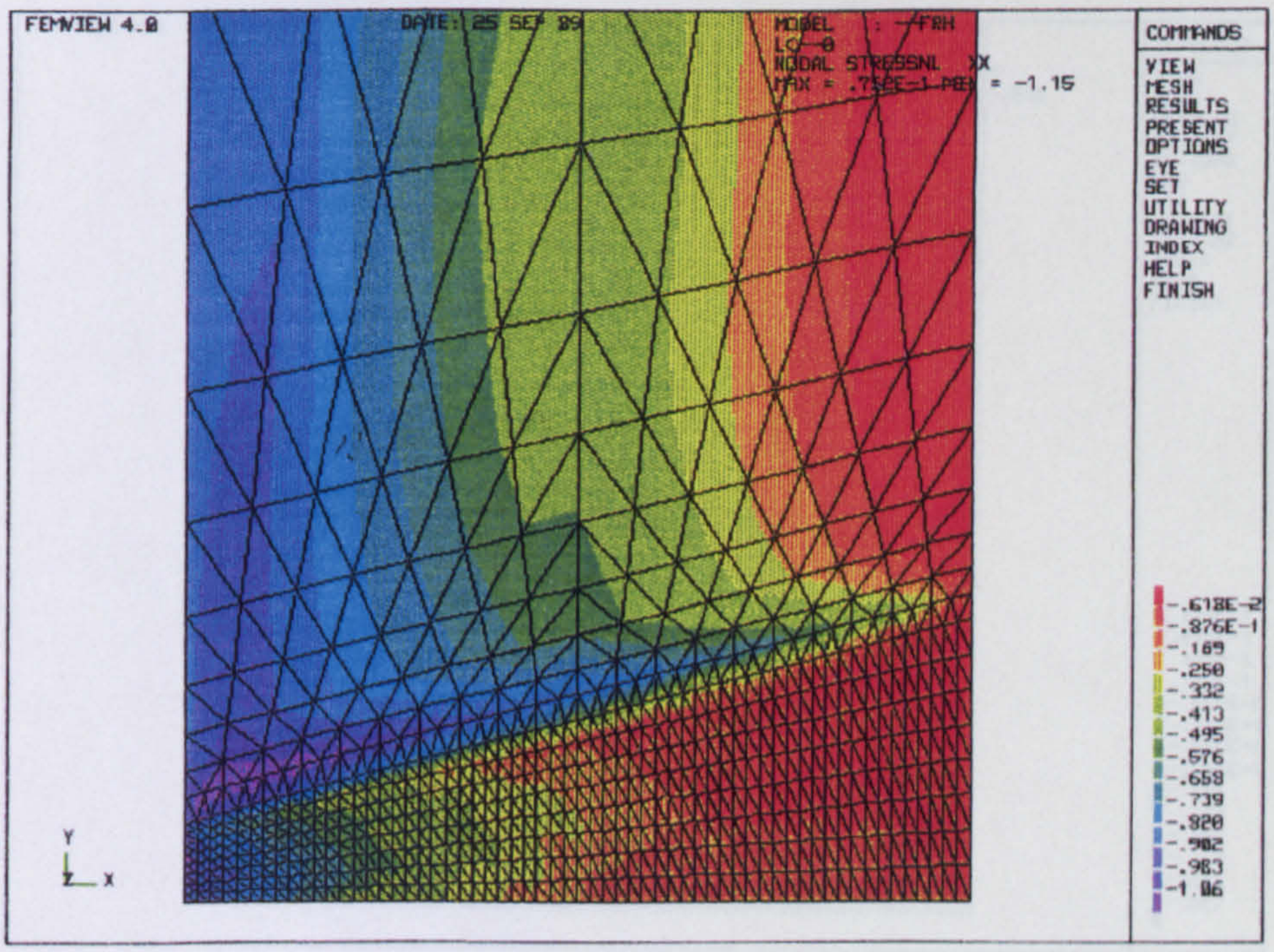

Figure 8.92: Distribution of the normalised radial stress ($\Sigma_r = \sigma_r/\sigma_o$) for weld model (WM3) at a life fraction of ($t/t_f = 66.0\%$) before the first element ($\omega > 0.9999$) fails and is removed from the finite element mesh.

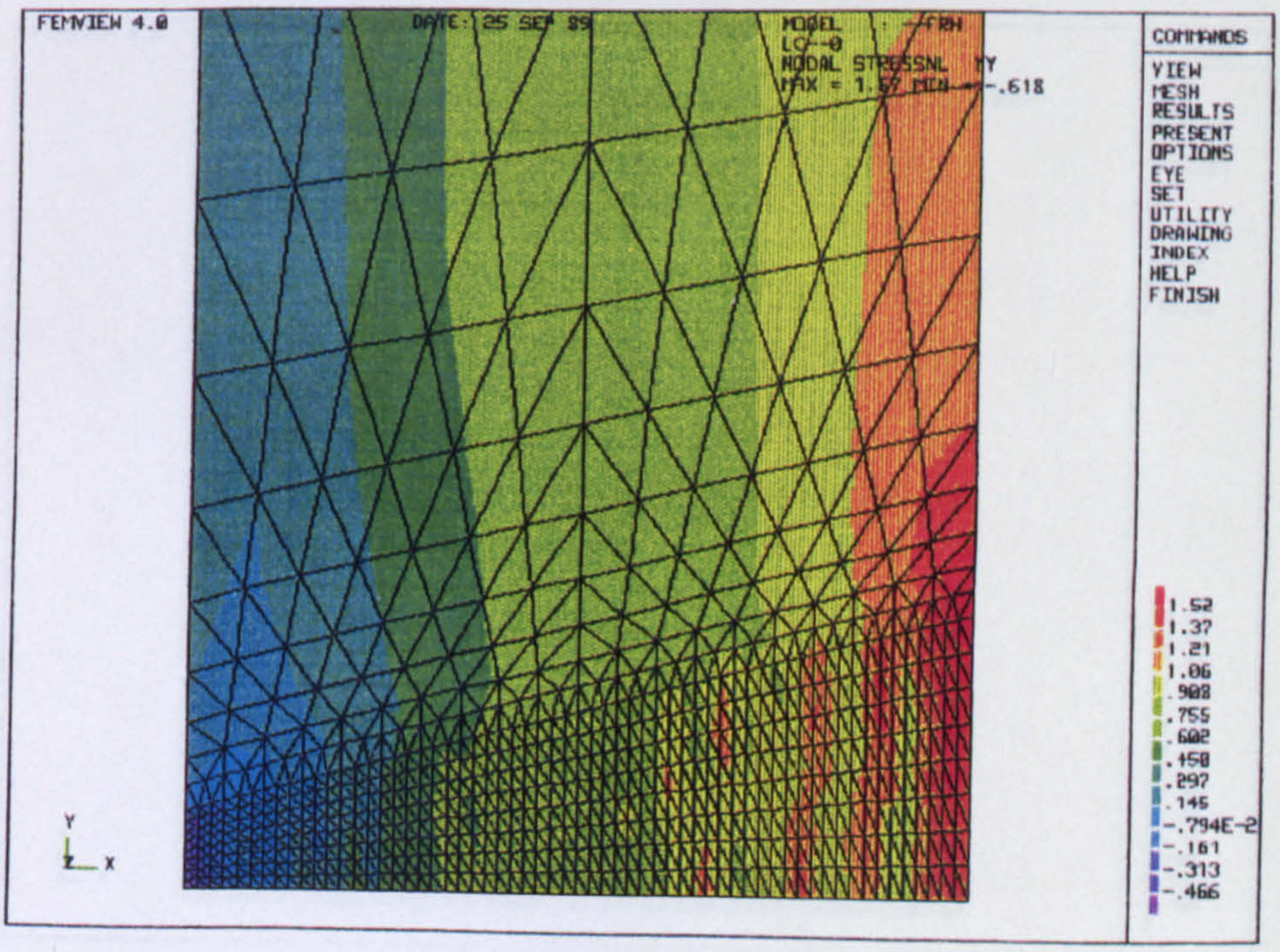

Figure 8.93: Distribution of the normalised axial stress ($\Sigma_z = \sigma_z/\sigma_o$) for weld model (WM3) at a life fraction of ($t/t_f = 66.0\%$) before the first element ($\omega > 0.9999$) fails and is removed from the finite element mesh.

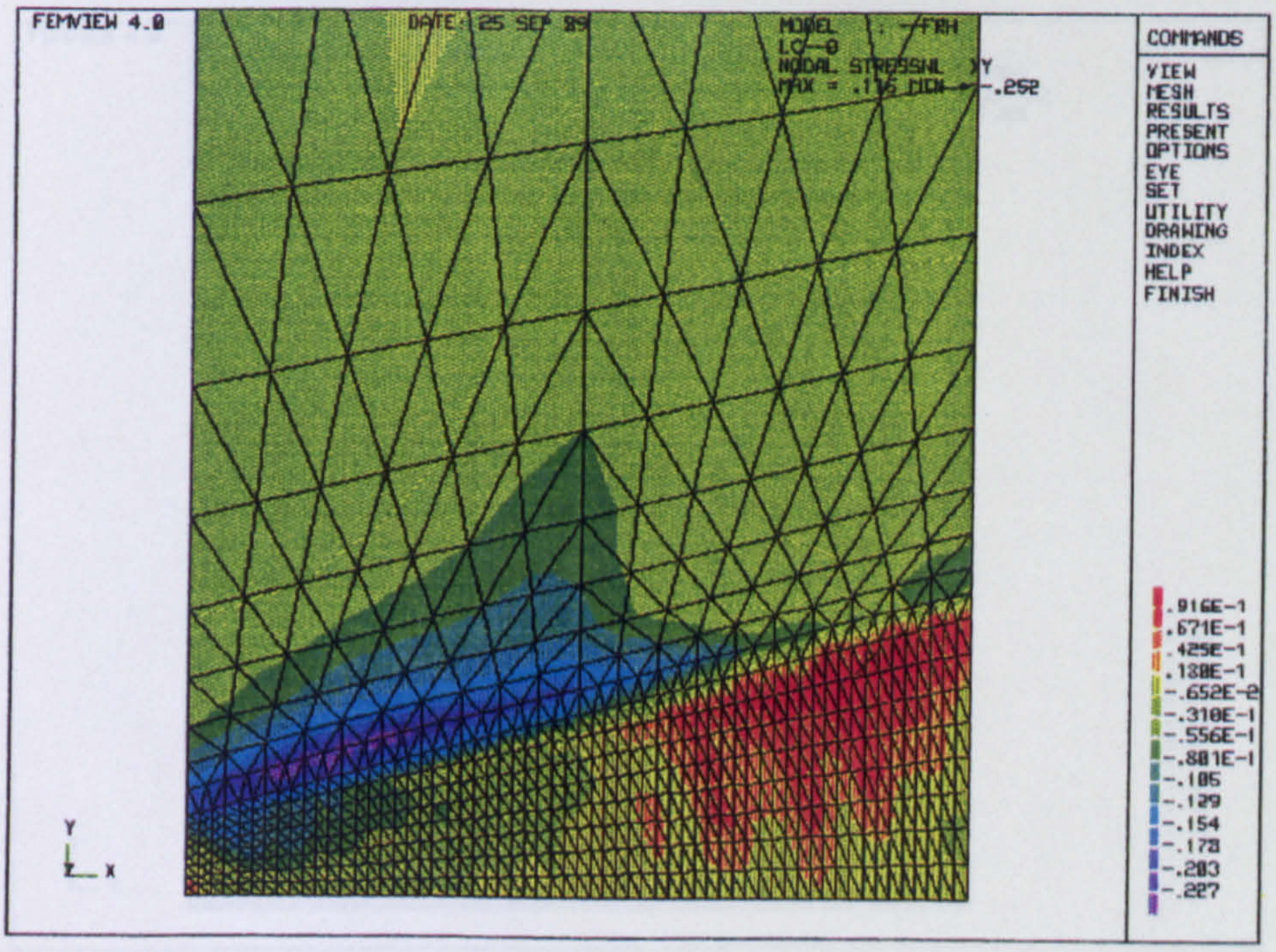

Figure 8.94: Distribution of the normalised radial/axial shear stress ($\Sigma_{rz} = \sigma_{rz}/\sigma_o$) for weld model (WM3) at a life fraction of ($t/t_f = 66.0\%$) before the first element ($\omega > 0.9999$) fails and is removed from the finite element mesh.

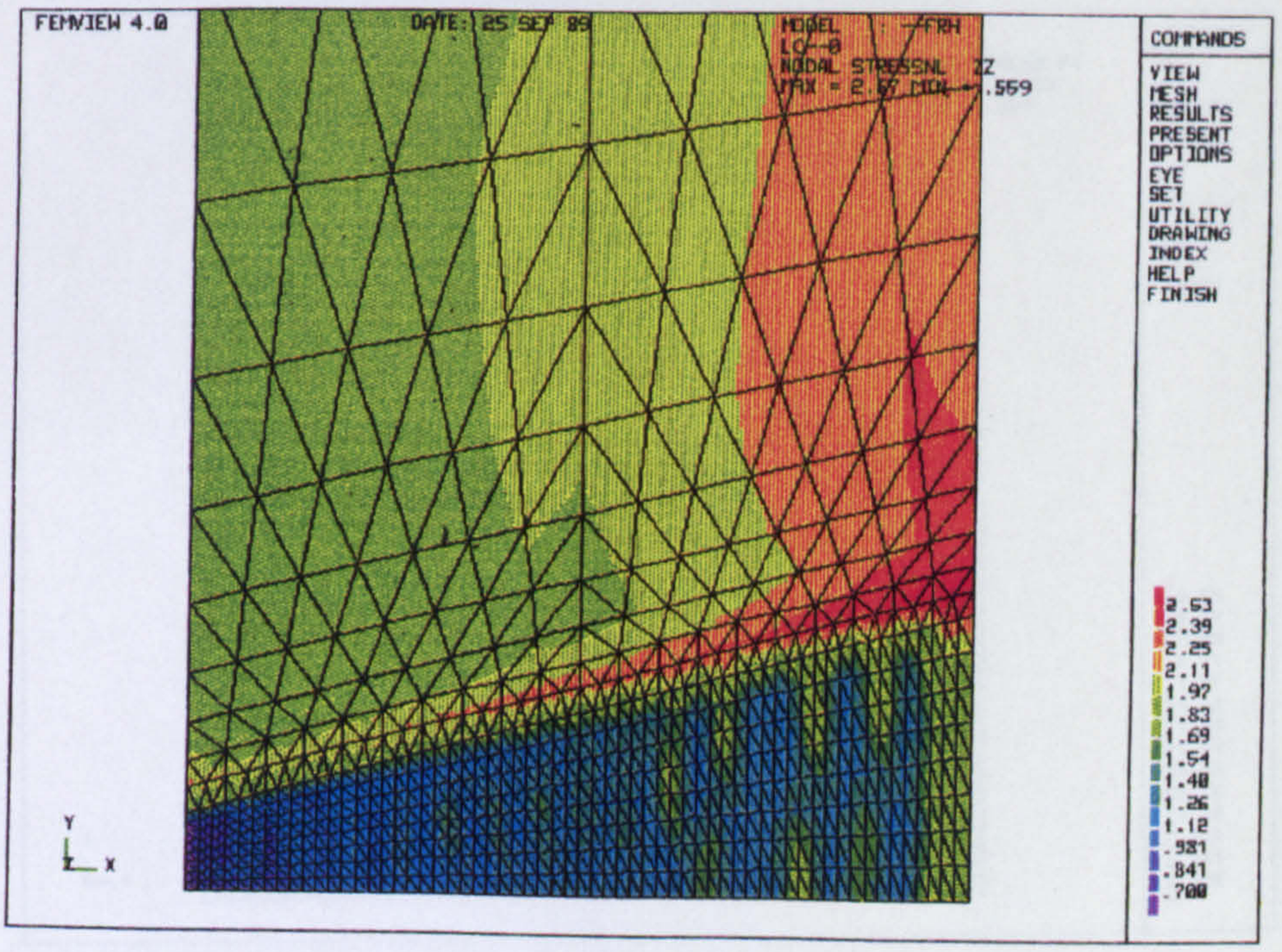

Figure 8.95: Distribution of the normalised hoop stress ($\Sigma_\theta = \sigma_\theta/\sigma_o$) for weld model (WM3) at a life fraction of ($t/t_f = 66.0\%$) before the first element ($\omega > 0.9999$) fails and is removed from the finite element mesh.

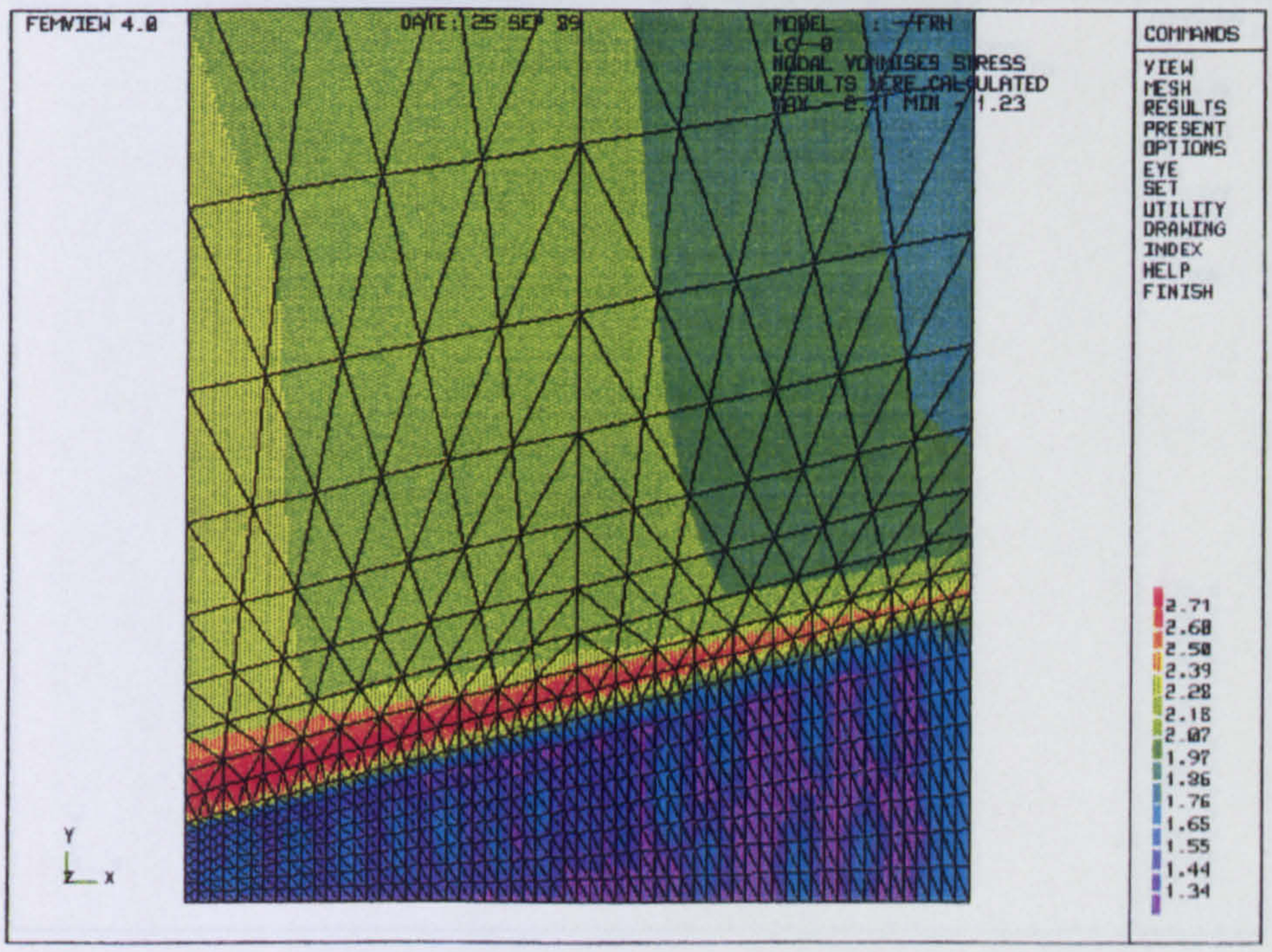

Figure 8.96: Distribution of the normalised Von Mises (effective) stress ($\Sigma_{ef} = \sigma_{ef}/\sigma_o$) for weld model (WM3) at a life fraction of (t/t_f = 66.0%), before the first element ($\omega > 0.9999$) fails and is removed from the finite element mesh.

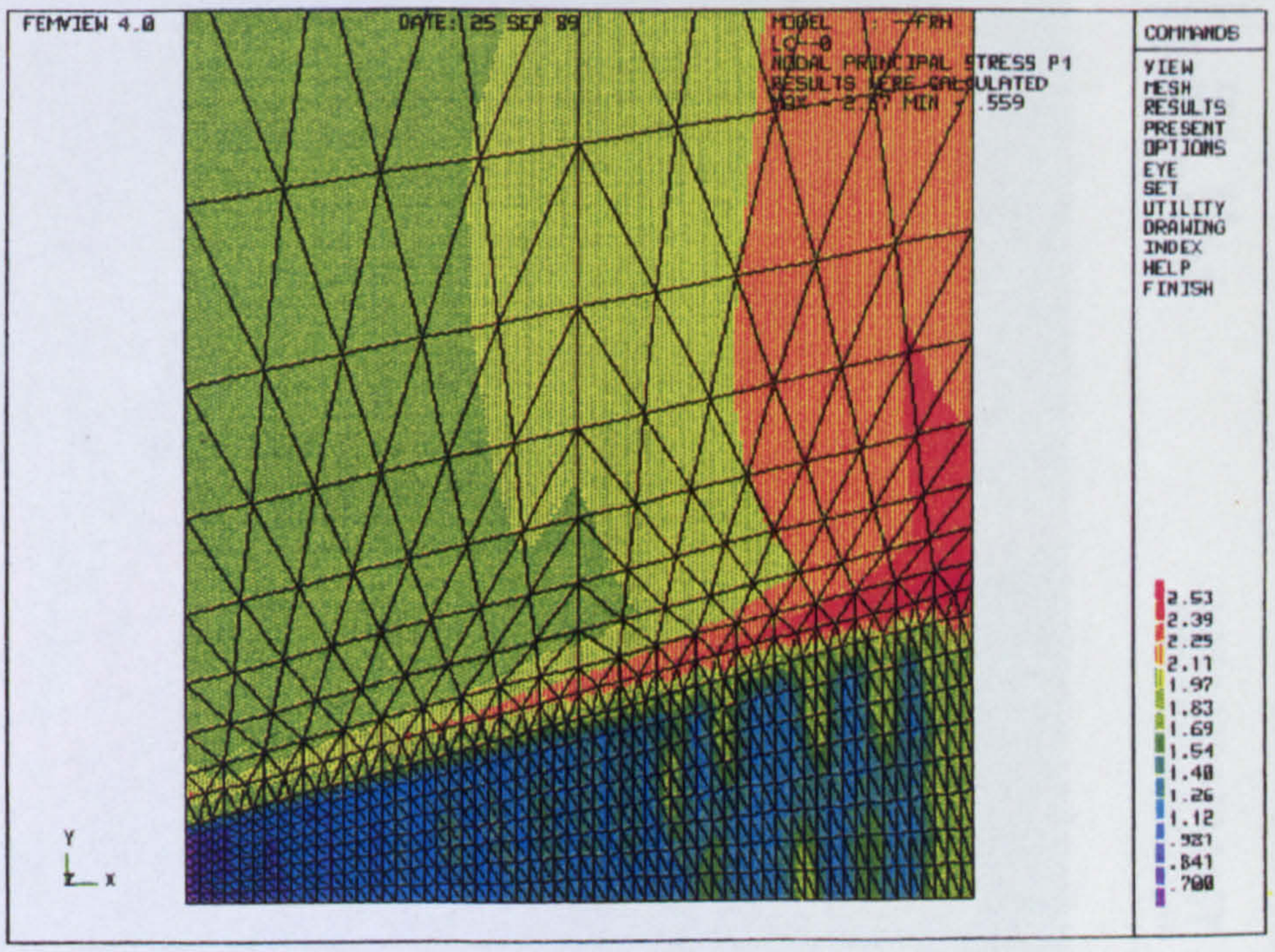

Figure 8.97: Distribution of the normalised maximum principal stress ($\Sigma_1 = \sigma_1/\sigma_o$) for weld model (WM3) at a life fraction of (t/t_f = 66.0%),before the first element ($\omega > 0.9999$) fails and is removed from the finite element mesh.

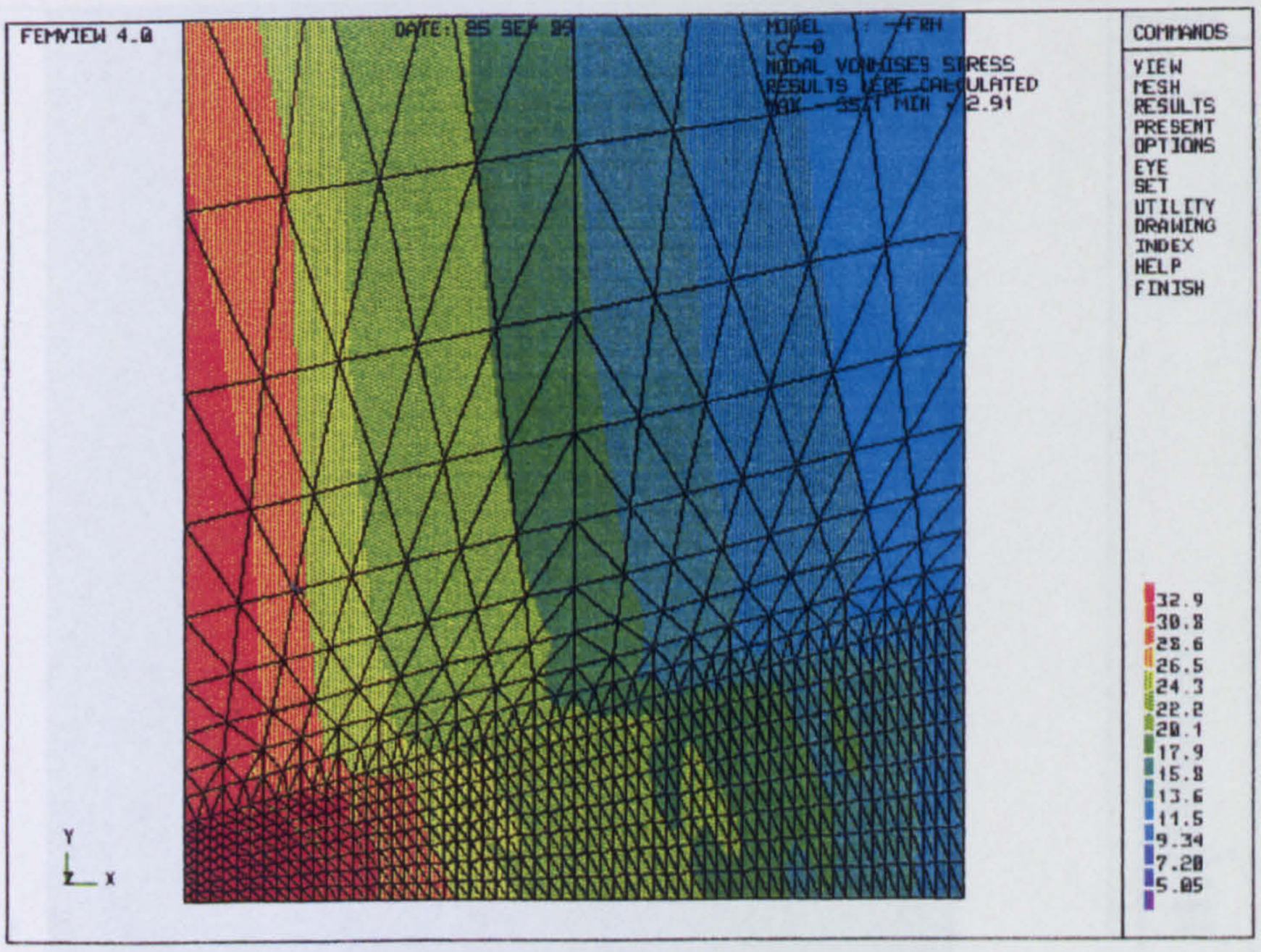

Figure 8.98: Distribution of the normalised Von Mises (effective) creep strain ($V_{ef} = V_{ef}/\sigma_o$) for weld model (WM3) at a life fraction of ($t/t_f = 99.9\%$).

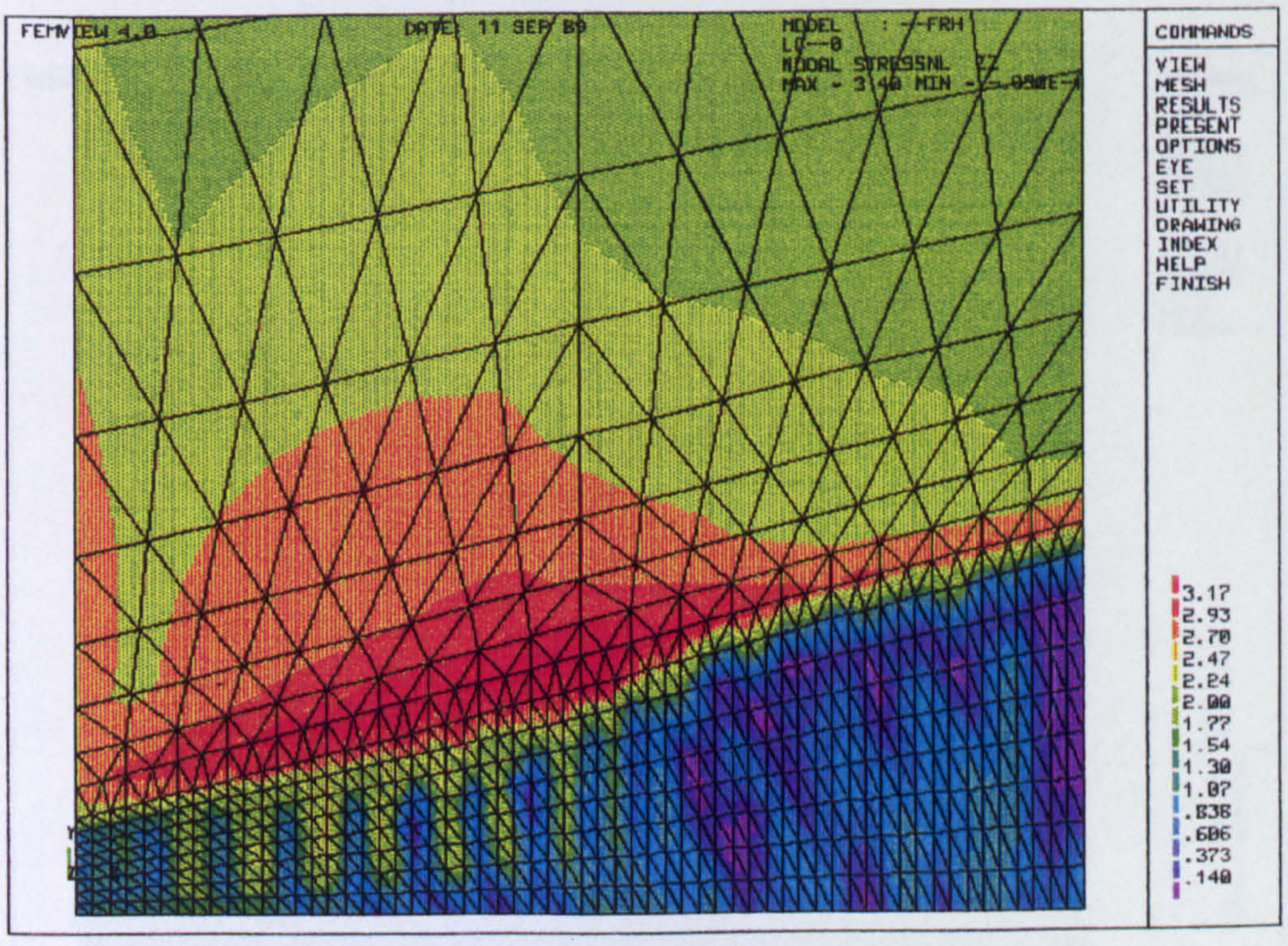

Figure 8.99: Distribution of the normalised hoop stress ($\Sigma_\theta = \sigma_\theta/\sigma_o$) for weld model (WM3) at a life fraction of ($t/t_f = 99.9\%$).

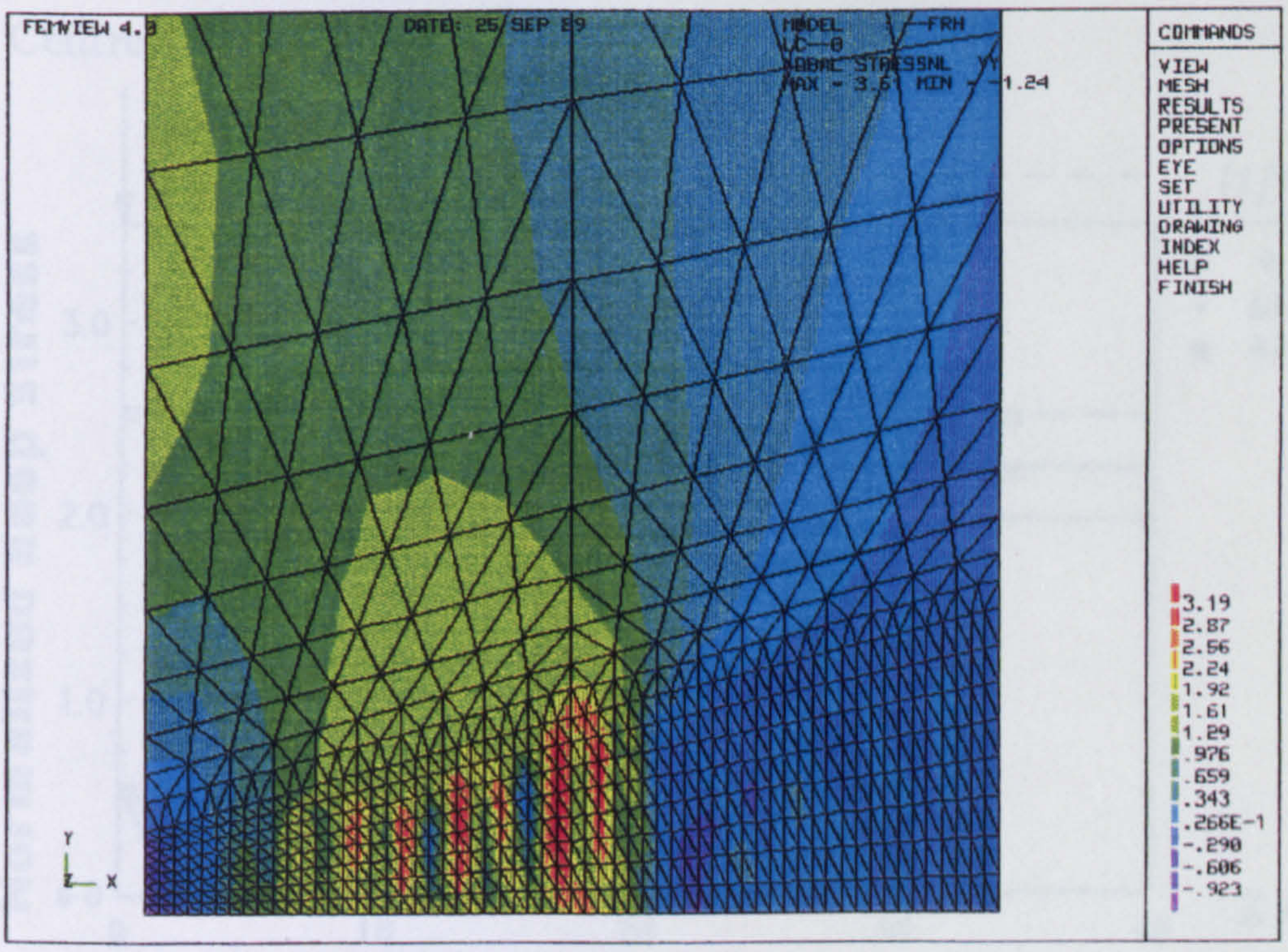

Figure 8.100: Distribution of the normalised axial stress ($\Sigma_z = \sigma_z/\sigma_o$) for weld model (WM3) at a life fraction of ($t/t_f = 99.9\%$).

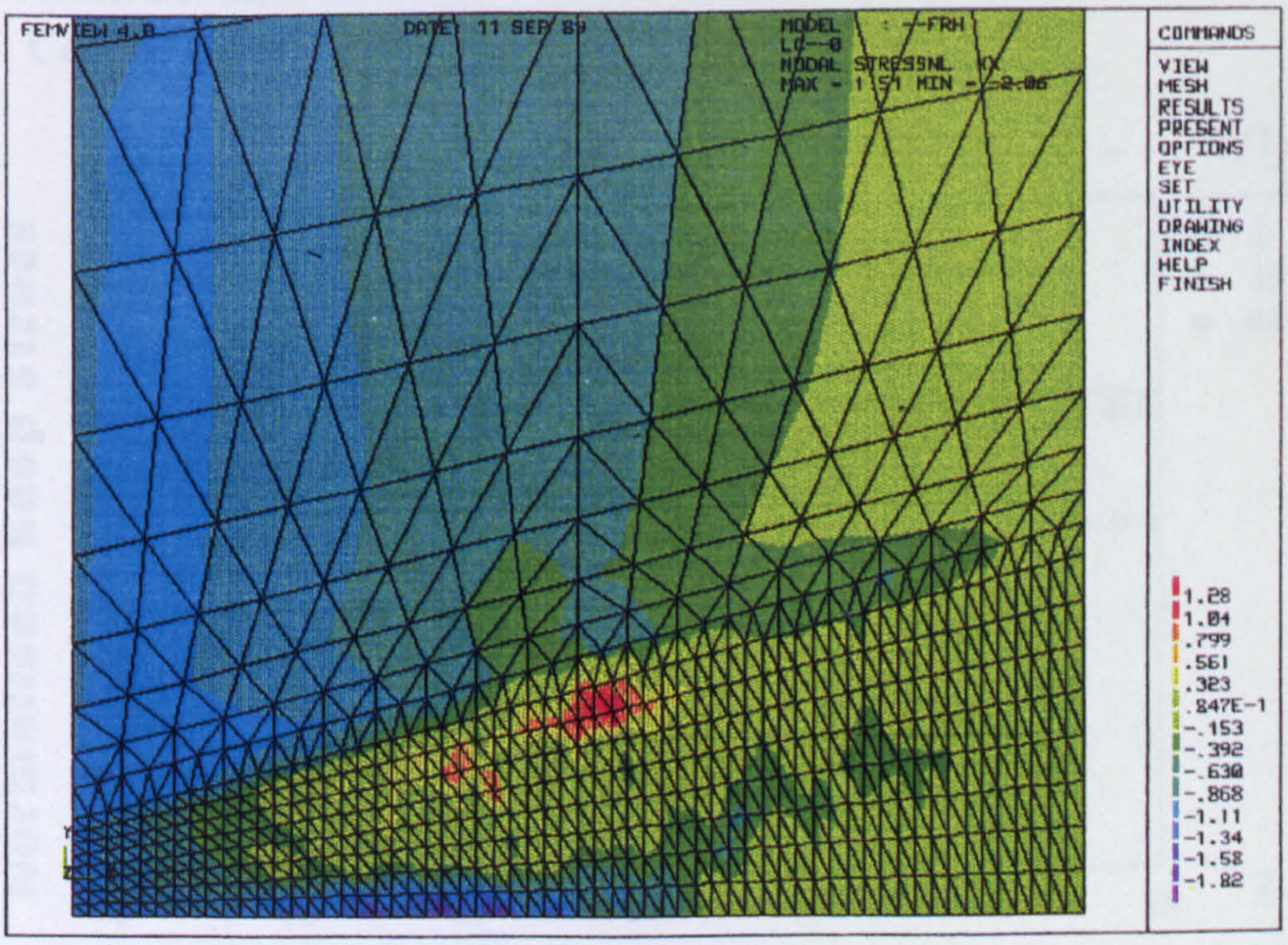

Figure 8.101: Distribution of the normalised radial stress ($\Sigma_r = \sigma_r/\sigma_o$) for weld model (WM3) at a life fraction of ($t/t_f = 99.9\%$).

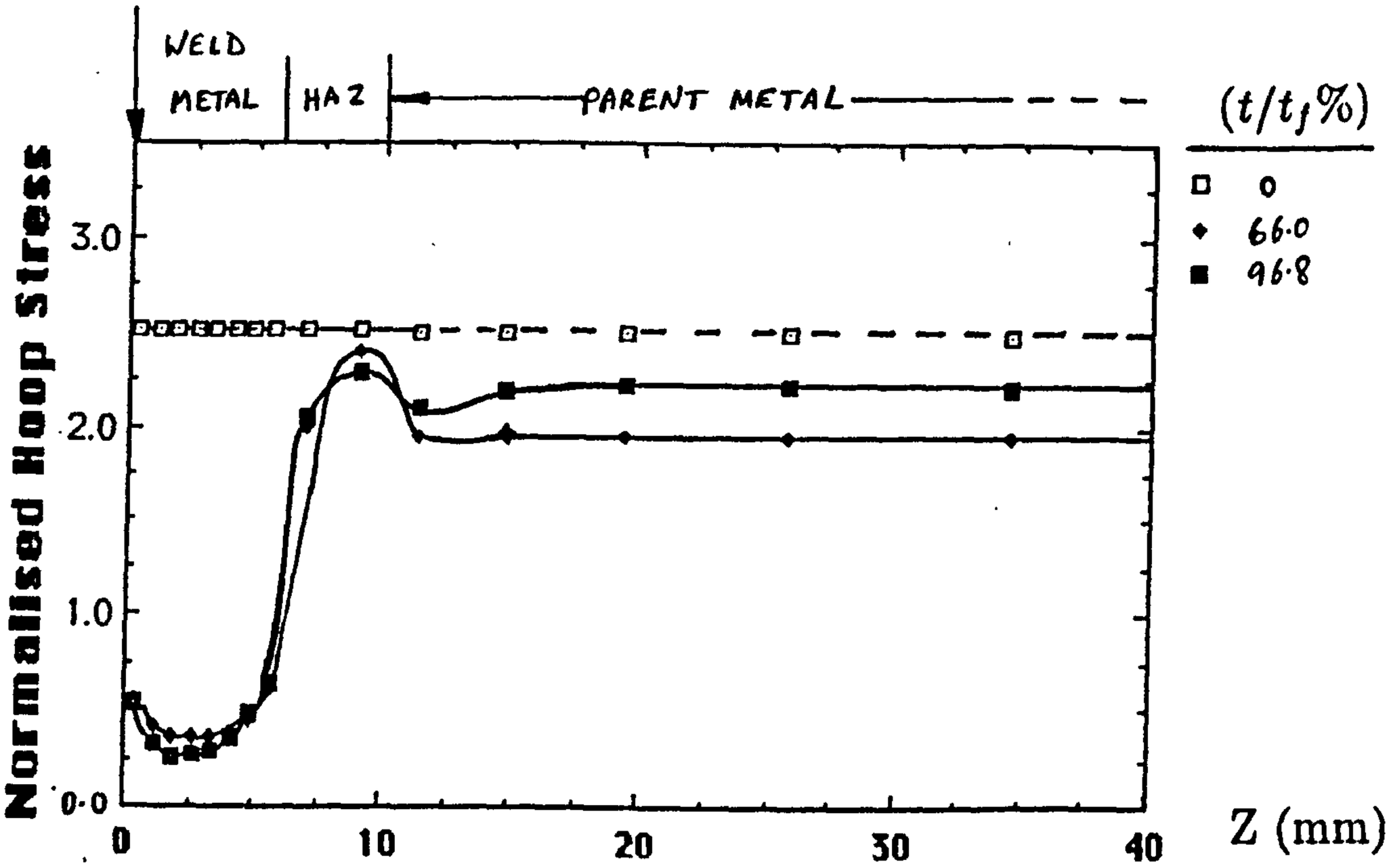

Figure 8.102: Normalised hoop stress (Σ_θ) distributions along the inner bore (Fig.8.9) of the steam pipe at various life fractions for weld model (WM3). The z-distance is measured in the z-direction from the weld metal centre line (Fig.8.9).

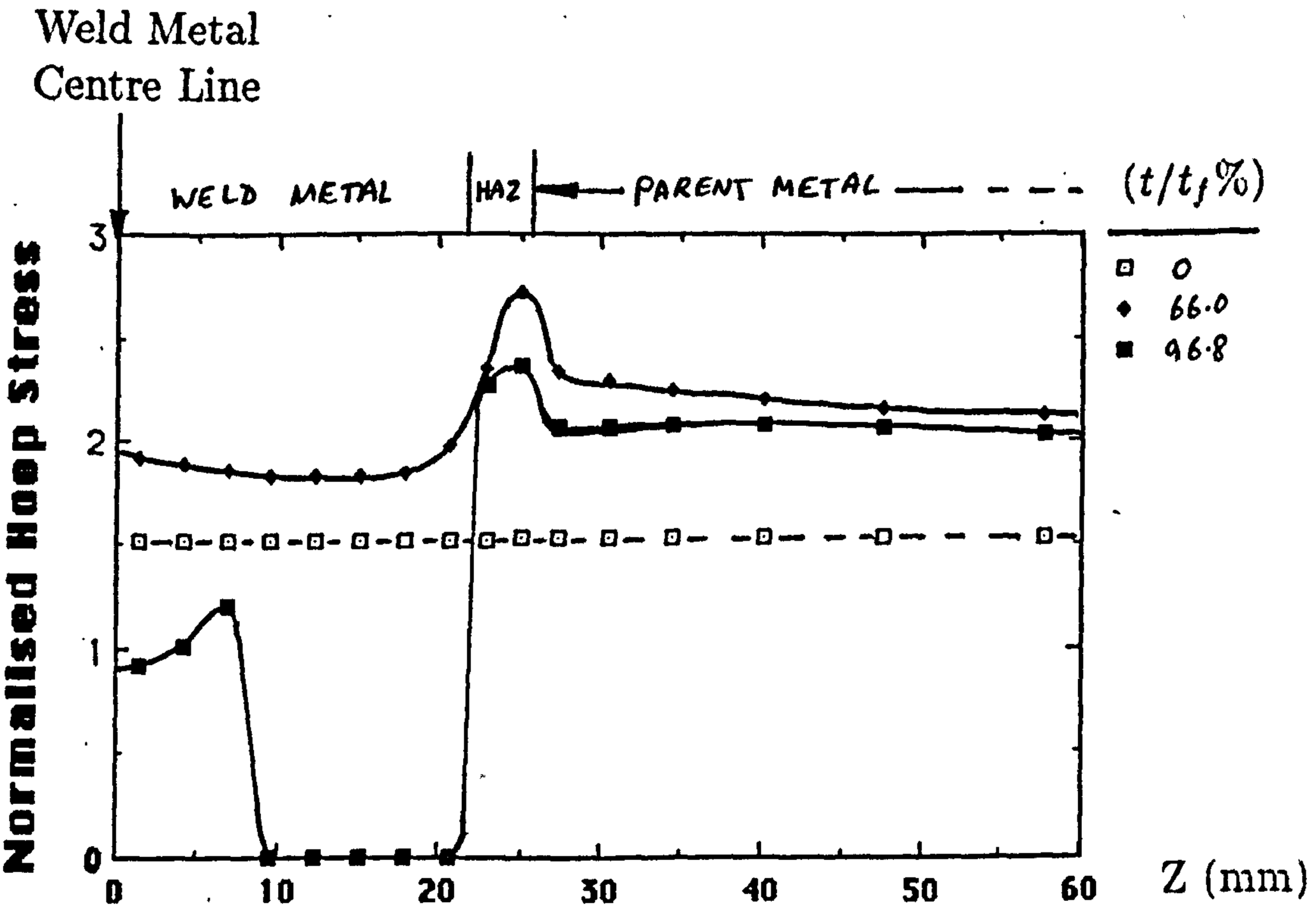

Figure 8.103: Normalised hoop stress (Σ_θ) distributions along the outer surface (Fig.8.9) of the steam pipe at various life fractions for weld model (WM3). The z-distance is measured in the z-direction from the weld metal centre line (Fig.8.9).

(a)

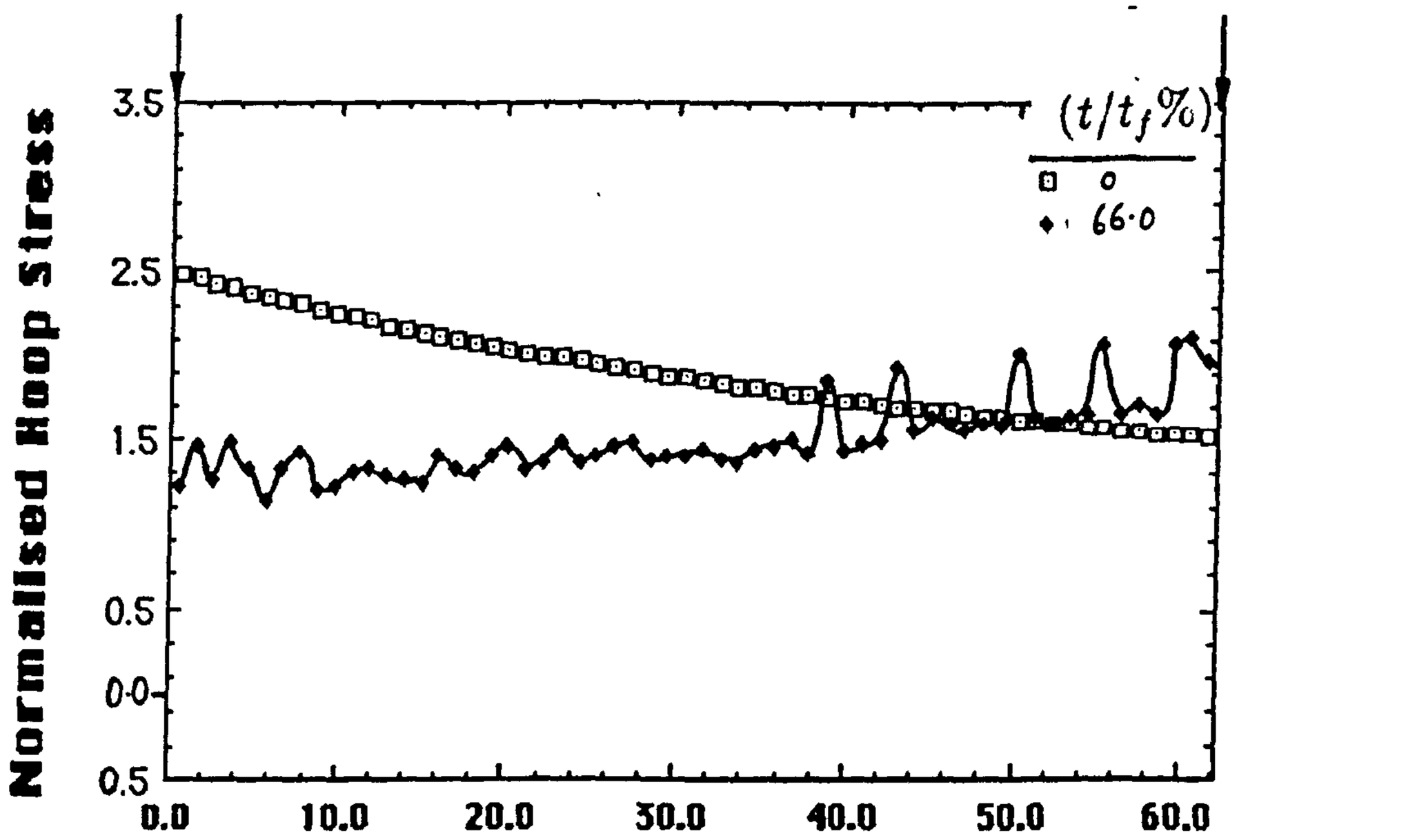

(b)

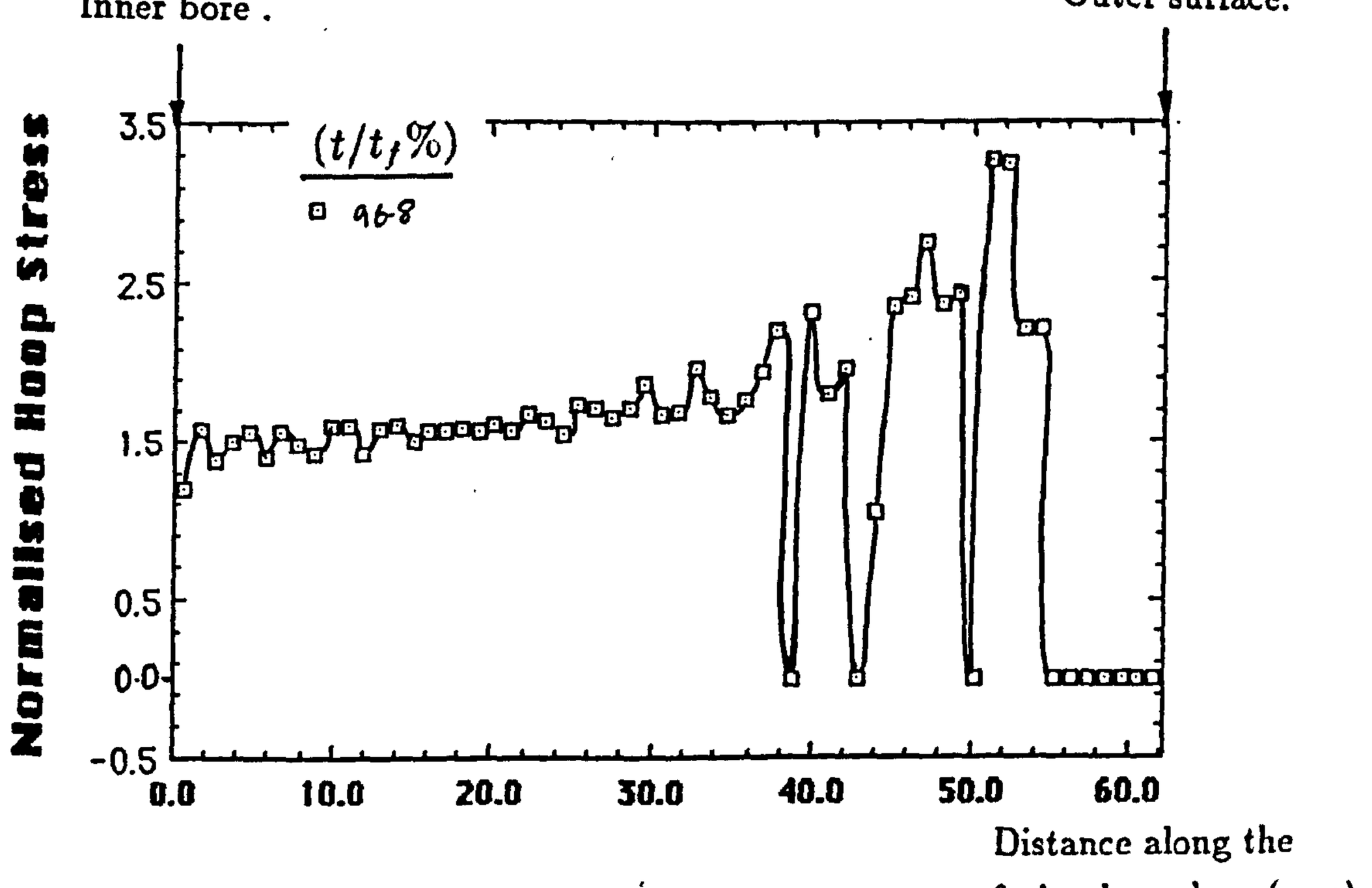

Figure 8.104(a) and (b): Normalised hoop stress (Σ_θ) distributions along the fusion boundary (Fig.8.9) of the steam pipe at various life fractions for weld model (WM3). The distance along the fusion boundary is measured from the internal diameter (Fig.8.9).

(a)

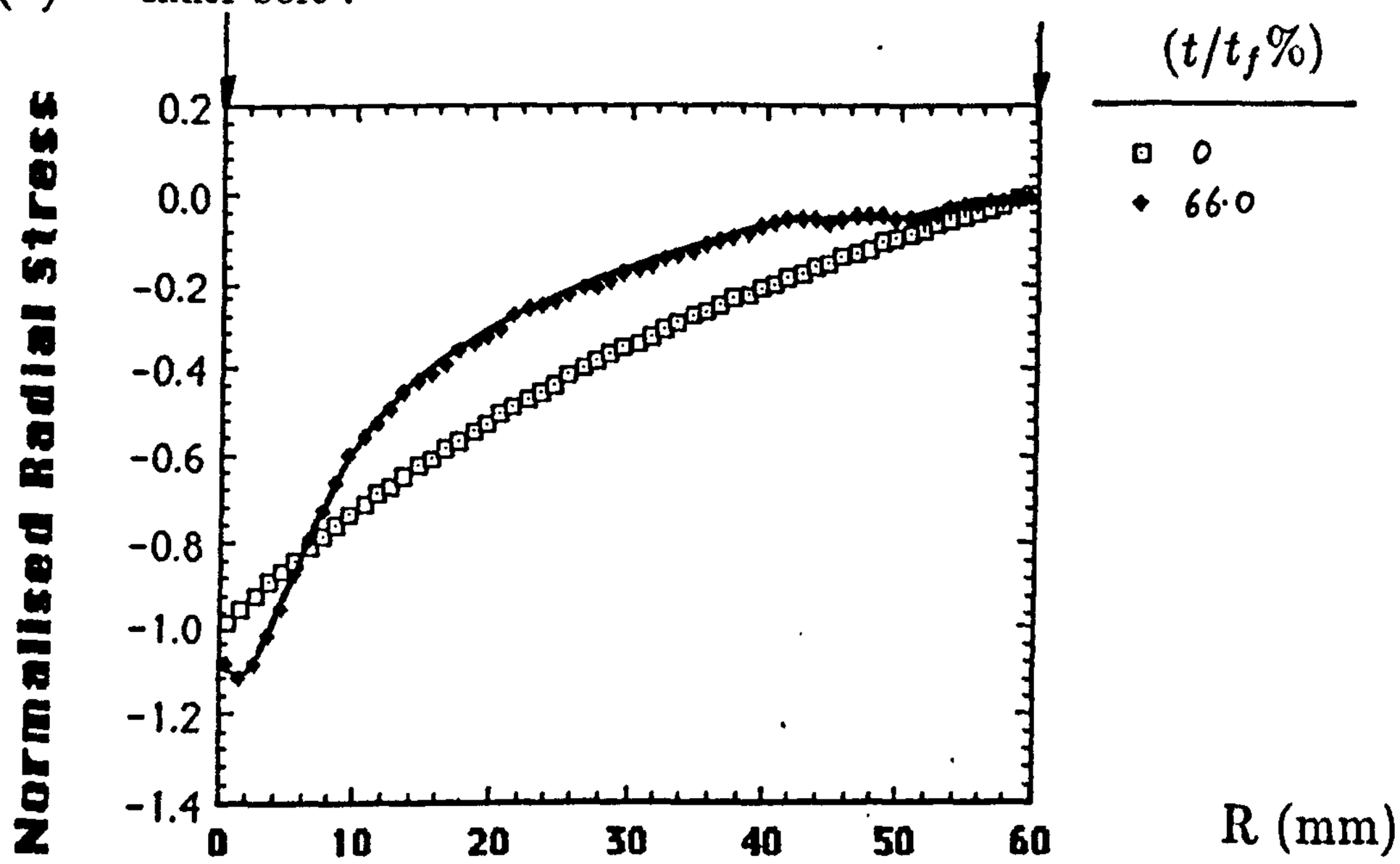

(b)

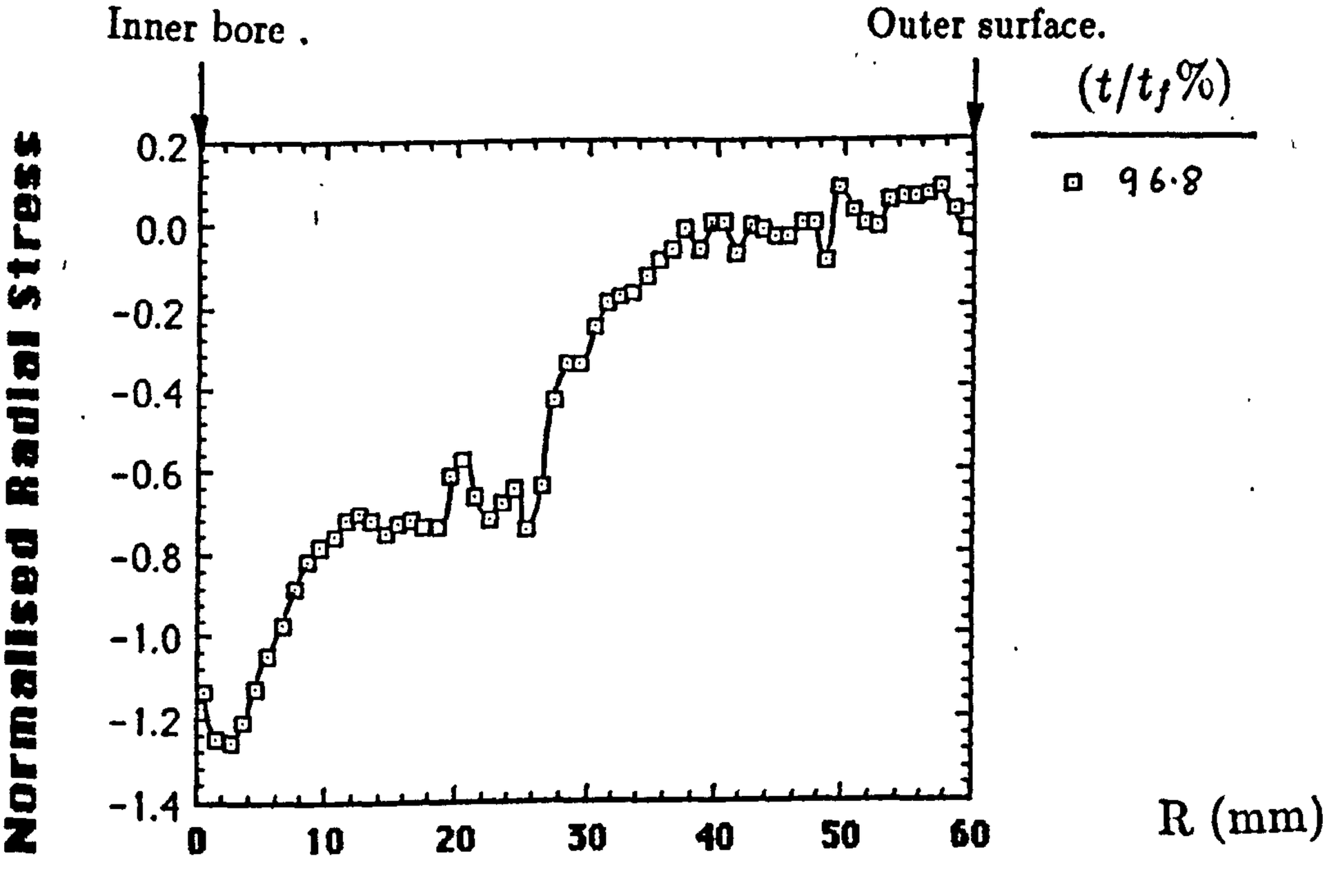

Figure 8.105(a) and (b): Normalised radial stress (Σ_r) distributions along the weld metal centre line (Fig.8.9) of the steam pipe at various life fractions for weld model (WM3). The distance along the weld metal centre line is measured from the internal diameter (Fig.8.9).

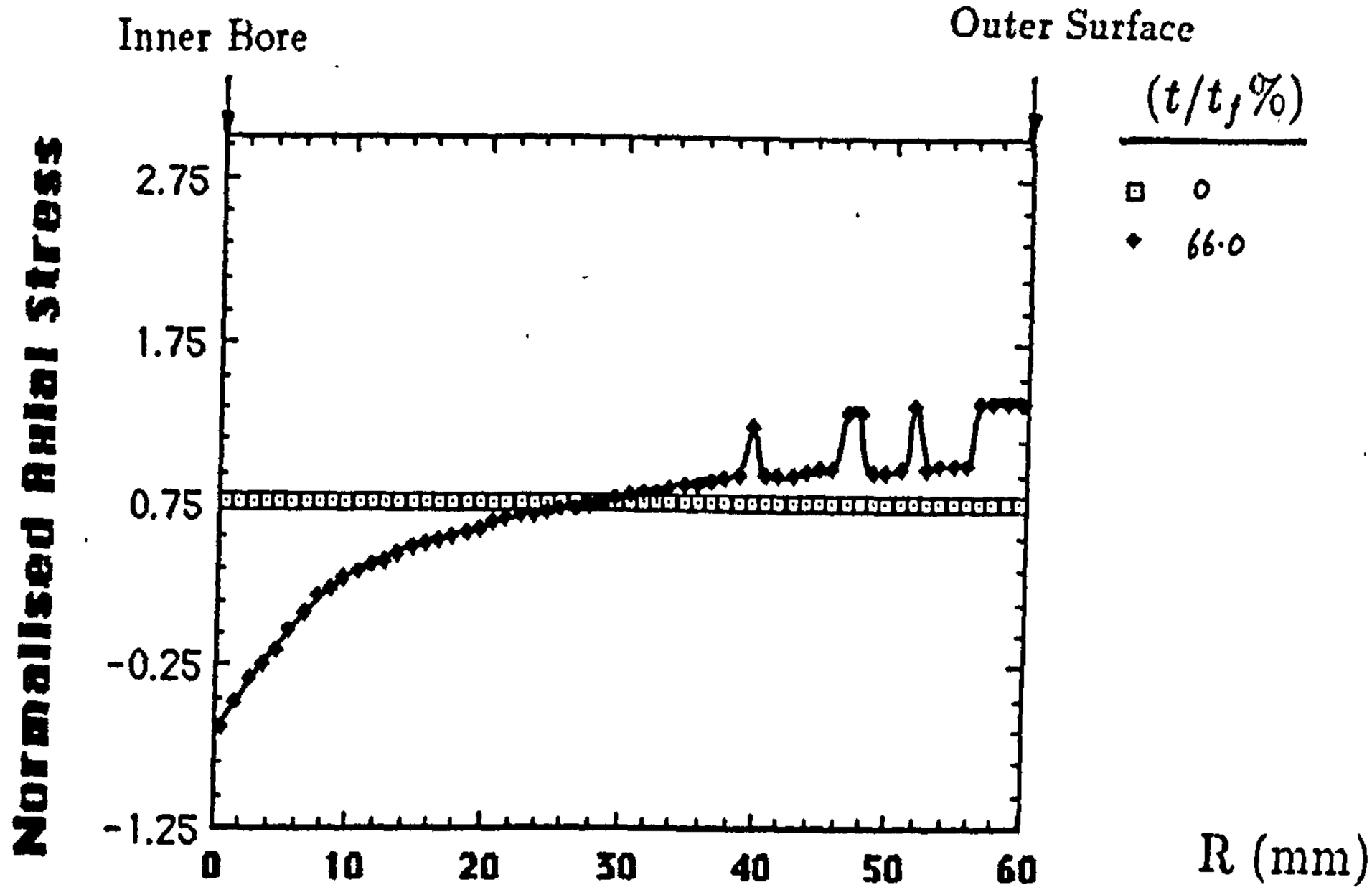

(b)

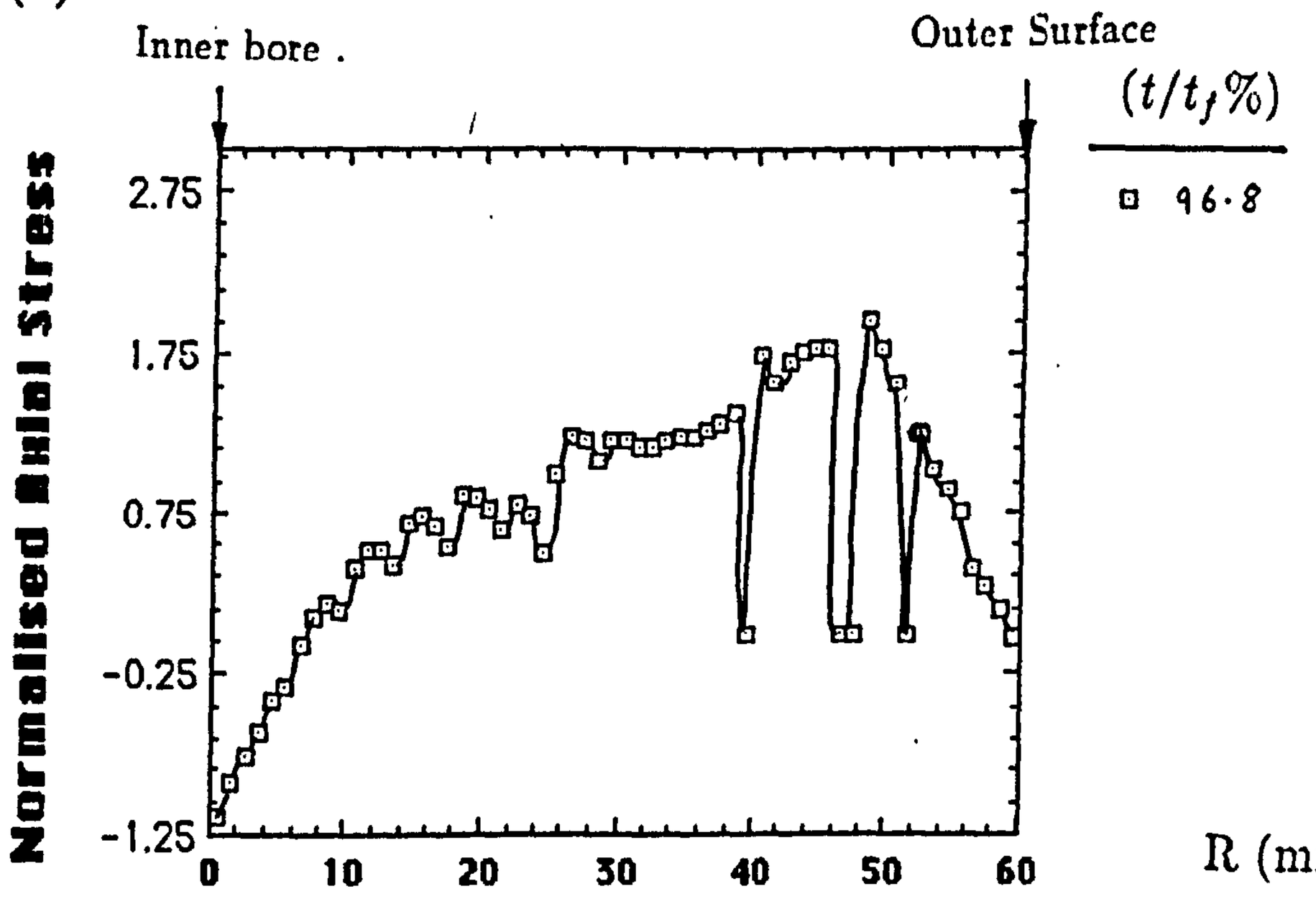

Figure 8.106(a) and (b): Normalised axial stress (Σ_z) distributions along the weld metal centre line (Fig.8.9) of the steam pipe at various life fractions for weld model (WM3). The distance along the weld metal centre line is measured from the internal diameter (Fig.8.9).

(a)

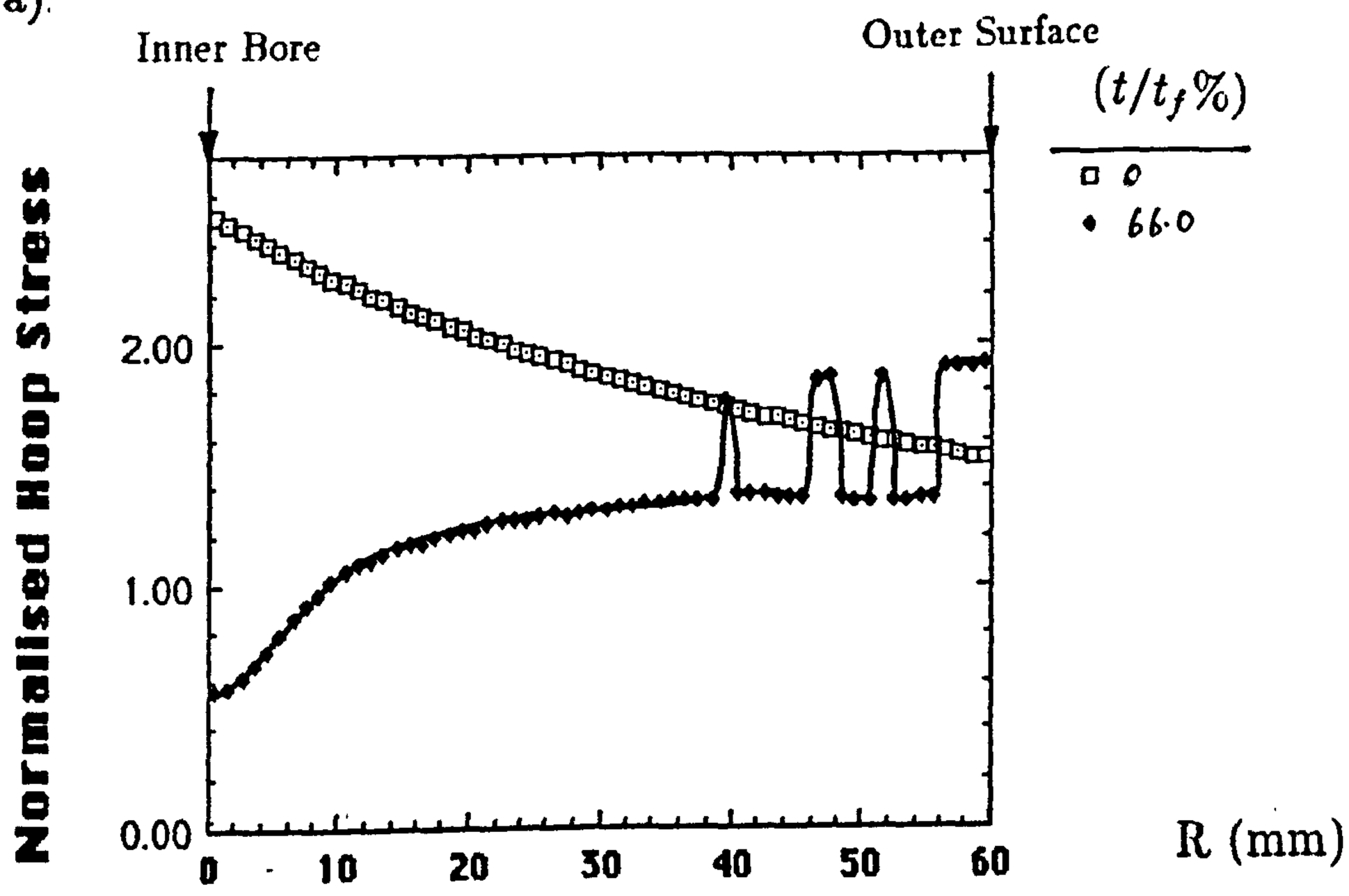

(b)

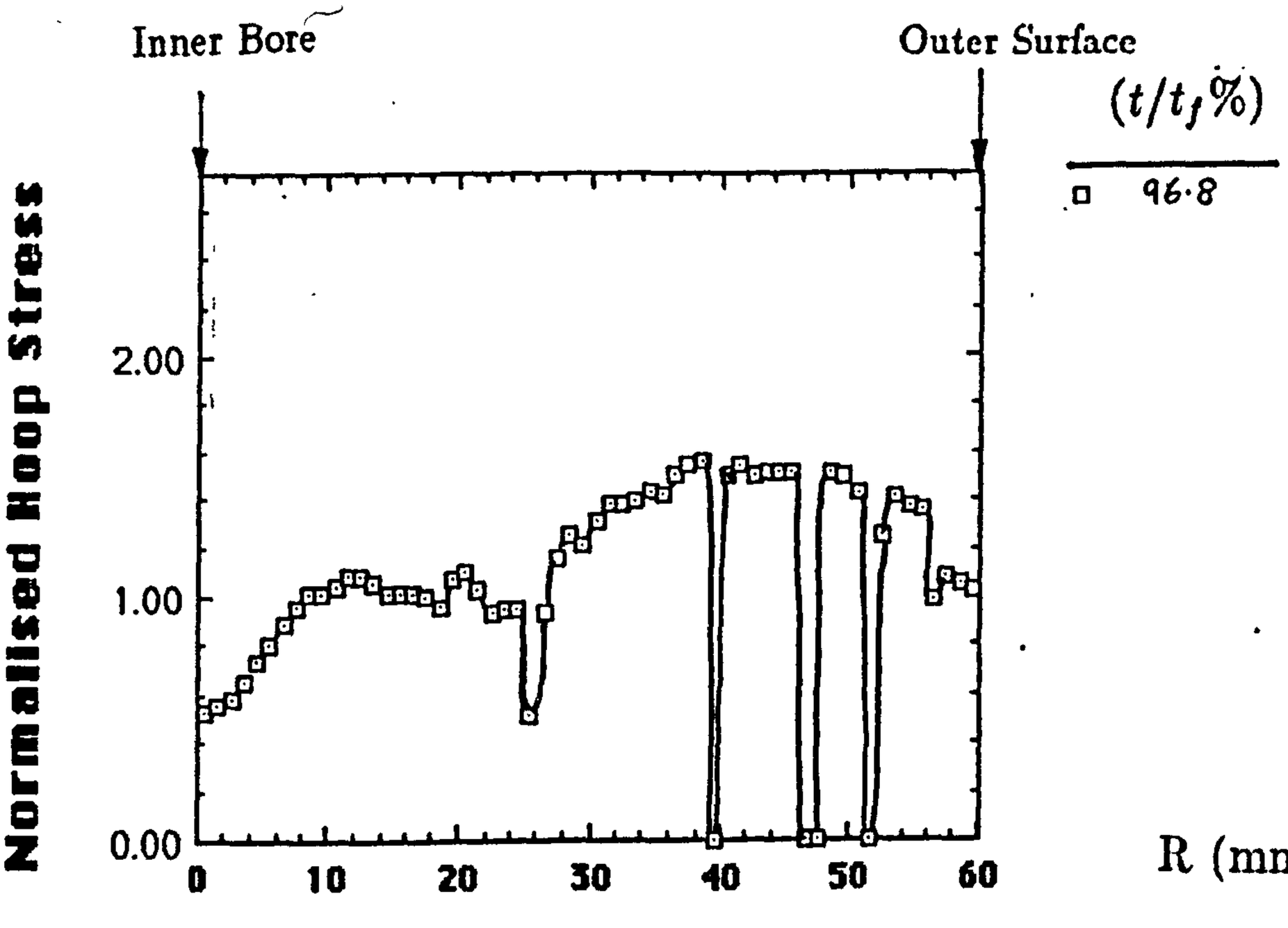

Figure 8.107(a) and (b): Normalised hoop stress (Σ_θ) distributions along the weld metal centre line (Fig.8.9) of the steam pipe at various life fractions for weld model (WM3). The distance along the weld metal centre line is measured from the internal diameter (Fig.8.9).

Chapter 9.

Conclusions.

The research work has resulted in some important findings:

1. From the mechanical creep testing of different batches of material it has been observed that grain size variation can produce a marked difference in both deformation and rupture characteristics. Grain size variation within a single batch of material may be related to the production route and causes considerable scatter in the results of uni-axial creep tests.

2. For (OFHC) Copper it has been found that the Arrhenius law may only be applied to model the variation of creep strain rate and damage rates with temperature, for a temperature range of approximately $50°C$. For larger temperature ranges exponential terms have been fitted to the isothermal creep constants at descrete temperatures within the temperature range; giving the functional change of creep constants with temperature, which when used with the creep strain rate and damage rate laws predict creep deformation and failure behaviour at intermediate temperatures, over a wide temperature range. Reasonable predictions of creep test behaviour have been obtained for the temperature range $250°C$ to $500°C$ for (OFHC) Copper.

3. The 4th order Runge-Kutta numerical integration method of Merson [59] is found to be particularly suited to the finite element creep continuum damage method. The time integration accuracy of the solution may be improved by adjusting parameters which control the allowable strain error using Merson's integration error estimate. Improved accuracy solutions implies the choice of smaller time steps and hence incurs an increased computational overhead.

The Z-transformation Runge-Kutta integration method provides a better failure time prediction over the standard Runge-Kutta method, but the standard method provides an improved failure strain prediction over the Z-transformed method, for the same integration accuracy. Therefore a choice exists, where one of these two methods may be selected, using a low integration accuracy, giving either accurate failure time or accurate failure strain predictions, requiring less computer processing time; than using either method with a high integration accuracy.

4. New techniques for removing both elemental stiffness and creep forces such as the techniques of Tvergaard and Chaboche provide no advantage over the instantaneous removal method due to Hayhurst et al, giving very similar damage distributions and life predictions for the compact tension specimen.

The use of the creep rate and damage rate laws due to Hayhurst, equations (2.19) and (2.20), using a bi-axial rupture criterion does not model the failure of the compact tension specimen under plane strain conditions.

New creep constitutive and damage rate laws have been formulated by the author, analogous to the equations by Cocks and Ashby [66], for creep fracture due to constrained cavity growth, allowing for the effects of the tri-axial stress state on rupture. The new constitutive model predicts the expected damage distribution and growth ahead of the crack tip in the CT-specimen and a failure time close to that of the expected experimental results. The effect of a constant mesh refinement across the CT-specimen ligament produces improved damage distribution definition and a reduced life prediction.

5. The concept of non-local continuum damage has been used in a finite domain method, through the grain size characteristic dimension, to spatially average local damage fields in both small and large cracked Copper plates having the same grain size. The method has correctly predicted the difference in the lifetimes and damage distributions, between the large and small sized external cracked specimens. This method should prove important to restrict damage and strain localisation into small regions of refined finite element meshes, giving some representation of grain size and/or inhomogeneity effects through the grain characteristic dimension, to give more physically related finite element solutions. The grain characteristic dimension has been defined as 6 grain sizes. It is thought important to apply this non-local damage method to model the effect of grain refinement across the heat affected zone of a weld, in the finite element modelling of the high temperature deformation and failure of a welded joint. This method may also be used to restrict localisation of strain and damage into refined finite element regions, in and close to the heat affected zone; where high mesh refinement is required to model the high stress gradient here, and the size of small heat affected zone regions.

6. Current British Standard codes make no allowance for the presence of the welded joint, which have been shown to produce over-conservative designs. From the available literature the British Standards could be modified in line with the American codes, which include strain limits and could include a simple multi-axial rupture criterion using the representative rupture stress, for improved lifetime predictions using simple hand calculations.

7. Weld models have been developed to represent the high temperature deformation and failure of a thick-walled steam pipe circumferential weld. Very good lifetime and damage distribution predictions have been obtained from simple three material zone, weld models, representing the parent metal, weld metal and heat affected zone material. It was found that extremely fine mesh refinement is not required in and close to the heat affected zone to model the stress gradients here, for this particular weld.

It is thought that the modifications to standard creep constitutive and damage laws, (2.19) and (2.20), allowing for the effects of the tri-axial stress state on rupture, which were used to model crack growth in the CT-specimen, was not necessary for the weld models; due their being a lower degree of constraint, or tri-axiality, present at the metallurgical notch (between the HAZ and the weld metal), than at the tip of the sharp line crack in the CT-specimen. If the weld models were to be used to model the growth of sharp cracks, which have been observed to grow in weldments subjected to fatigue conditions, then the tri-axial modification to the standard creep constitutive and damage laws will have to be used.

The effect of modifying the rupture criterion of the weld metal had a marked effect on the damage distribution and the lifetime predictions and highlighted the importance of accurate multi-axial testing of weld microstructures, for accurate weld failure prediction.

The final weld model inlcuded the geometries of the coarse and fine grained bainitic regions of the weld metal and shows how damage growth concentrates in the hard coarse grained regions and eventually links across the fine grained weld metal regions, to form a jagged circumferential crack along the fusion boundary, comparable with that obtained from a full size pressure vessel weld test.

Improved weld models will rely heavily upon new uni-axial and multi-axial test data, for the coarse and fine grained bainitic weld metal regions, and other heat affected zone microstructures. Much finer finite element meshes will be required if more material regions are used in the weld model to represent the heat affected zone microstructures, possibly requiring a non-local damage technique to prevent effects of localisation.

8. The creep constitutive and damage rate laws due to Hayhurst et al are only valid for the dominant mechanism of power-law creep. The application of these constitutive models is extended part way into other Ashby mechanism map areas, such as the dislocation glide creep region by the use of the bi-linear creep strain rate and damage rate law modification. Fortunately most engineering structures operate in the power-law creep region at moderate service stresses and temperatures. Further development of the creep strain rate and damage laws must be made, to truly model creep in the power-law breakdown region. As many high performance alloys used in gas turbines and nuclear power plant now operate well within the diffusional flow region of the Ashby mechanism maps at high homologous temperatures, the ability of the creep constitutive and damage rate laws due to Hayhurst to model this type of creep deformation must be studied further and possibly modified in line with the constitutive laws sugested by Cocks and Ashby [66].

9. Therefore it is important before modelling a new material component, to know the predominant creep mechanisms at the component stress and temperature levels; it is also important to understand the stress-states present, so that the correctly modified constitutive and damage rate laws, representative of the physical processes occuring during the service life of the component, are used in the finite element model. A criticism of the Ashby mechanism and fracture maps is that the effects of stress-state on the predominant creep and fracture mechanism is neglected. Three dimensional Ashby maps could be developed, with a third axis (I_1/σ_{ef}), which would include the effect of the degree of the tri-axial stress state on the predominant mechanism, enabling the correct choice of constitutive equations for the component model. Having determined the constitutive equations for each predominant creep mechanism, material constants for each mechanism, are determined from the relevant creep test data. The constitutive models are then only applied for the range of stress

and temperature were they are valid; and when a mechanism map boundary is crossed a different constitutive model and creep constants are used. Therefore enabling the finite element technique to model the changing physical behaviour of the material with component stress and temperature history.

Chapter 10.

Future Work And Developments.

Future work should include the aquisition of futher experimental multi-axial test data, to provide a better understanding of the effect of the tri-axial stress-state on creep rupture behaviour. A materials data base could be formulated to store a wide variety of both uni-axial and multi-axial materials data for use in the program Damage-(XX). The standard creep constitutive and damage laws must be modified to represent all the creep deformation and fracture mechanisms in the Ashby mechanism maps, including the allowance for the effect of the multi-axial stress-state on rupture; so that problems outside the power-law creep region may be solved with confidence.

Currently a wide range of high performance materials are available to the design engineer. For example the metal matrix composites, ceramics and sintered materials, which are used for high temperature applications, where strength yet low weight is required. The properties of these new materials are very different from those of the steels. It is important to be able to model and predict the behaviour of these new materials, which should be possible using the computer program Damage-(XX); but the success of this will require further research effort. At each stage of development the program has to model various test specimens and component structures consistently to reproduce observed experimental results.

With the availability of increasingly faster computers having larger memories and with their current parallel processing capability, larger finite element problems can be solved with a reduced overhead. Hence, the computer program Damage-(XX) may be used as a Computer Aided Design and Research Tool. The Computer Aided Design methodology of such a computer package is shown in the flow diagram in Fig.10.1. Here as an example, the component to be designed is a welded pipe bend for an aircraft engine. The design engineer initially forms the 3D-geometry of the component using the Solid Modeller. He specifies the working conditions for the pipe, in terms of operating stresses, temperatures, any special corrosion resistance and the component lifetime required. An expert system analyses the requirements and chooses the material with the optimum properties, from which the pipe will be made. The solid model is converted into a finite element mesh and boundary conditions

are applied appropriate to the working conditions. A continuum damage mechanics finite element solution is obtained for the problem providing a prediction of the deformation and failure of the pipe in service. This deformation and failure information is processed with an advanced animated graphics facility, which provides a person to computer interface, presenting all the information to the designer in a succinct way, enabling him to make speedy decisions to modify parts of the original design using the Solid Modeller. Another finite element solution may be performed without making costly prototypes, until the desired component performance is achieved. The final component specifications are automatically drafted in the form of an engineering drawing or a file which may be processed by a Computer Aided Machining centre and Welding center, which will automatically profile then weld the final product. As new materials become available, the materials database may be up-dated and the new material incorporated into the same design procedure. The developed algorithms may be linked and mounted as a package into a computer workstation for use in industry.

The potential of the creep continuum damage method, and the predictive capabilities of this method, embodied in the computer program Damage-(XX), has been demonstrated; and, that future development of this program will result in the formation of a major research and design tool.

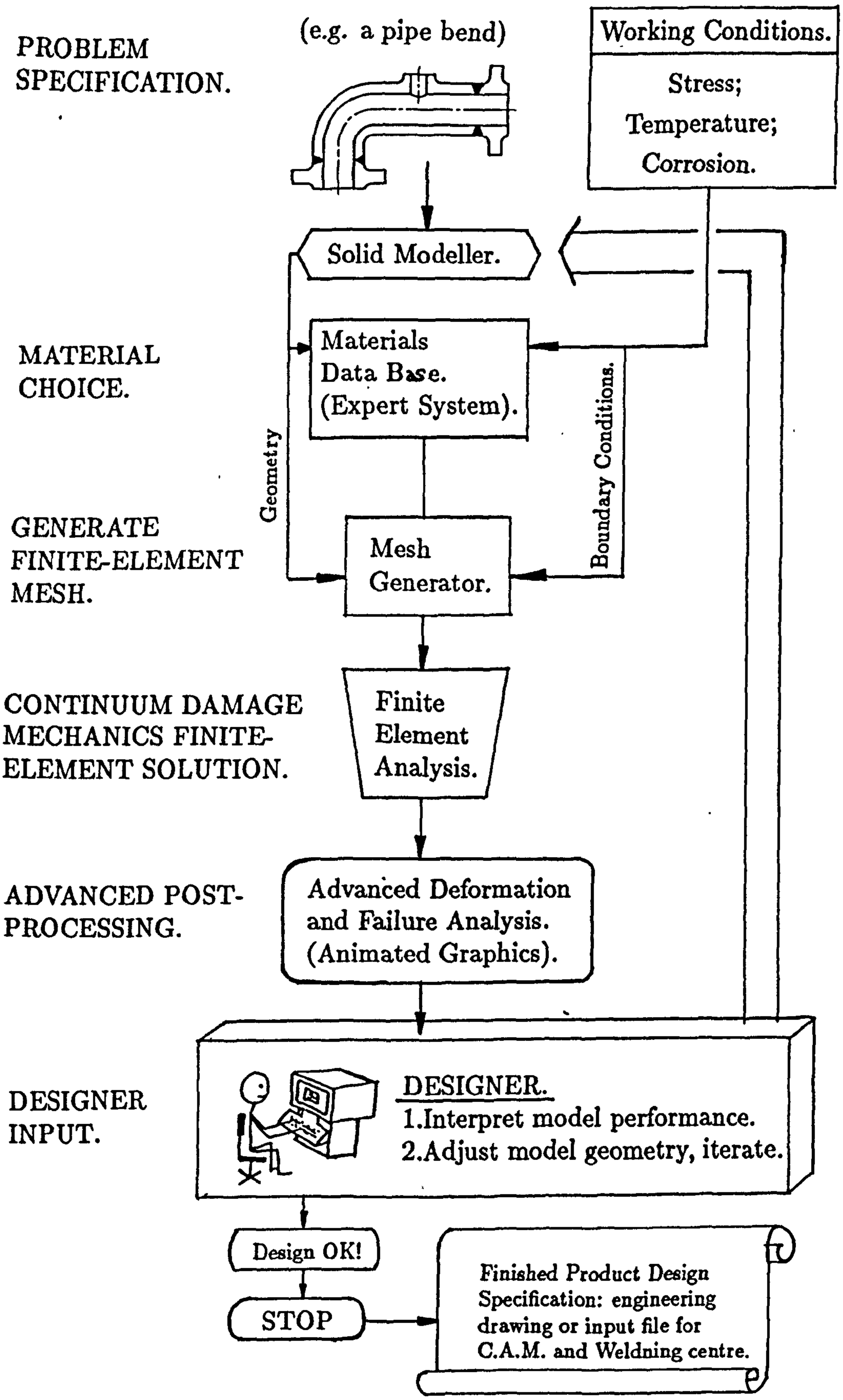

Figure.10.1: Advanced Computer Aided Design Route.

References.

[1] Da Costa Andrade E.N. Proc. Roy. Soc. A84,1 (1910) and Pro. Roy. Soc. A90,329 (1914)

[2] Rollason E.C. Metallurgy for Engineers, 4th Ed. Arnold Publishers Ltd.

[3] Ashby M.F. and Jones D.R.H. Engineering Materials, An Introduction To Their Properties and Applications. International Series on Materials Science Technology, Vol. 34. Pergamon Press Ltd., Oxford.

[4] Harper J.G. and Dorn J.E. Acta Met., Vol. 5, P 654, 1957.

[5] Nabarro F.R.N. Report of a Conference on Strength of Solids. Physical Society, London, P 75, 1948.

[6] Herring C. Journal of Applied Physics, Vol. 21, P 437, 1950.

[7] Coble R.L. Applied Physics, Vol. 34, P 1679, 1963.

[8] Frost H.J. and Ashby M.F. Deformation-Mechanism Maps. The Plasticity of Metals and Ceramics. Pergamon Press 1982.Pergamon Press.

[9] Ashby M.F. A first Report on Deformation Mechanism Maps. Acta Met. , Vol. 20, 1972.

[10] Garofalo F. Fundamentals of Creep and Creep-Rupture in Metals. Macmillan Series in Materials Science, New York, 1965.

[11] Ashby M.F. Ganda C. and Taplin D.M. Fracture Mechanism Maps and their Construction for F.C.C. Metals and Alloys, Acta Met.,Vol 27, PP 699 - 729.

[12] Ashby M.F. and Brown L.M. Perspectives in Creep Fracture. Pergamon Press Ltd., Oxford, 1983.

[13] Hall F.R. The Fundamentals of Creep in Metals and Alloys. Internal Report FRH01, 1987. The University of Sheffield, Dept. of Mechanical and Process Engineering, Mappin St., Sheffield.

[14] Da Costa Andrade E.N. Creep and Recovery. PP176-198. American Society for Metals, Metal Park, Ohio. 1957.

[15] Norton F.H. Creep of Steel at High Temperatures. McGraw-Hill, New York. 1929

[16] Garofolo F. Properties of Crystalline Solids. ASTM. Spec.Tech.Publ.283, P82, 1960.

[17] Arrehnius S. Zietschrift Fur Physikalische Chemie, Stochiometrie Und

Verwandtschaftslehre 1-136, 1887-1928. Also referred to by name in [10] and his equations appear in [34]

[18] Odqvist F.K.G. 1966. Mathematical Theory of Creep and Creep Rupture. Oxford University Press, Ely House, London, W1.

[19] George E.Mase. Continuum Mechanics. Schaum Series. McGraw-Hill.

[20] Johnson W, Mellor P.B. Engineering Plasticity. John Wiley and Sons, Chichester.

[21] Hayhurst D.R. On the Role of Creep Continuum Damage In Structural Mechanics. Chapter 3. Engineering Approach to High Temperature Design. Edited by Wiltshire.B. and Owen.J. Piner ige Press, Swansea, UK.

[22] Hayhurst D.R. Creep Rupture Under Multi-Axial States of Stress. J.Mech.Phys.Solids. 1972. Vol 20, PP 381-290.

[23] Hayhurst D.R., Dimmer P.R. and Morrison C.J. Development of Continuum Damage In The Creep Rupture of Notched Bars. Phil.Trans.R.Soc.Lond. A311, PP103-129, 1984.

[24] Kachonov L.M. Time of the Fracture Process Under Creep Conditions. Izv.Akad.Nauk SSSR Otd.Tech. Nauk 8,26. 1958.

[25] Dyson B.F. Physically-Based Models of Metal Creep for use in Engineering Design. Poc. of the Ashby Symposium. Chicago, Sept. 1988. Published by AIME/TMS.

[26] Rabotnov Yu.M. Creep Problems in Structural Members. (English Translation. ed. F.A. Leckie). Ch6. Amsterdam, North Holland.

[27] Johnson A.E., Henderson.J. and Khan.B. Complex-Stress Creep, Relaxation and Fracture of Metallic Alloys. Ch4.HMSO, London, 1962.

[28] Hayhurst D.R., Trampczynski W.A. and Leckie F.A. Creep Rupture Under Non-Proportional Loading. Acta. Metallurgica. Vol.28. PP1171-1183. 1980.

[29] Trampczynski W.A., Hayhurst D.R. and Leckie F.A. Creep Rupture of Copper and Aluminium under Non-Proportional Loading. J.Mech.Phys.Solids. Vol.29. PP516-353. 1981.

[30] Murakami S. Mechanical Modelling of Material Damage. Trans. ASME. Vol.55. June, 1988.

[31] Dyson D.F. and McLean.D. Creep of Nimonic 80A in Torsion and Tension.

Met.Sci., 2,37, 1977.

[32] Greenwood G. Int.Congress on Metals. Cambridge. 1973. Microstructure and the Design of Alloys. Vol.2. PP91-105.

[33] Ashby M.F. and Raj.M. Proc.Conf.Mechanics and Physics of Metals Society. Institute of Physics, Cambridge. 1975.

[34] Leckie F.A. and Hayhurst D.R. Constitutive Equations for Creep Rupture. Acta Metallurgica. Vol.25. PP1059-1070. 1977.

[35] Hayhurst D.R. Private communication 4th Sept., 1987.

[36] Hall F.R. Constitutive Equations for the Mathematical Modelling of Creep Deformation and Failure of Metals and Alloys. Internal Report FRH02, 1987. The University of Sheffield, Dept. of Mechanical and Process Engineering, Mappin St., Sheffield.

[37] Dunne F.P.E. and Hayhurst D.R. An Expert System For The Determination Of Creep Constitutive Equations Based On Continuum Damage Mechanics. Internal Report FPED01, Aug., 1988. The University of Sheffield, Dept. of Mechanical and Process Engineering, Mappin St., Sheffield. (To be published).

[38] Penny R.K. Ellison E.G. and Webster G.A. Specimen Alignment And Strain Measurement In Axial Creep Tests. Materials Research and Standards. 1966. PP76-84.

[39] Penny R.K. and Leckie F.A. The Mechanics Of Tensile Testing. Int.J.Mech.Sci. 1968. Vol. 10, PP265-273.

[40] Hayhurst D.R. The Effects Of Test Variables On Scatter In High-Temperature Tensile Creep-Rupture Data. Int.J.Mech.Sci. 1974. Vol. 16, PP829-841.

[41] Hall F.R. Uni-Axial Creep Testing Procedure. Internal Report FRH03, Jan., 1989. The University of Sheffield, Dept. of Mechanical and Process Engineering, Mappin St., Sheffield.

[42] BS3500 Parts 1,3,5 and 6. 1969, (1987) Methods For Creep And Rupture Testing Of Metals.

[43] BS3688 Part 1, 1963,(1981),(1988). Methods For Mechanical Testing Of Metals At Elevated Temperature.

[44] BS4A4 Part 1, Sections 2 and 3, 1967, (1969), (1970). British Standards Aerospace Series. Specification For Test Pieces And Test Methods For Metallic

Materials.

[45] Tilly G.P. Relationship For Tensile Creep Under Transient Stresses. Journal of Strain Analysis. Vol. 7. No.1, 1972, PP61-68.

[46] Penny R.K. Strain Rate Changes During The Tensile Test. Technical Note. Journal of the Royal Aeronautical Society. Vol. 71, Dec., 1967, PP853-854.

[47] Dunne F.P.E. Private communication July, 1989, giving details of temperate cyclic plasticity test results on a similar batch of (OFHC) Copper.

[48] Mabutt Q. Optical Metallography Of Copper Fatigue And Creep Specimens From Sheffield University. British Gas Report Ref: MM1025/2103/FD. (Project BG/SERC GR/D 72839. LRS/3014/038). 1st Sept., 1989. British Gas PLC., Research And Technology Division, London Research Station, Michael Rd., London.

[49] Brown P.R. Private communication at University of Leicester. 20th Nov., 1987.

[50] Othman A.M. and Hayhurst D.R. Multi-Axial Creep Rupture Of A Model Structure Using A Two Parameter Material Model. Oct., 1988. Internal Report. The University of Sheffield, Dept. of Mechanical and Process Engineering, Mappin St., Sheffield. (To be published).

[51] Morrison C.J., Brown P.R. and Hayhurst D.R. Internal Report University of Leicester.

[52] Cho U.W. Findley W.M. Creep And Creep Recovery Of 2618-T61 Aluminium Under Variable Temperature. ASME. Vol. 51, Dec., 1984, PP816-820.

[53] Ohno N., Takahashi Y. and Kuwabara K., Constitutive Modelling Of Cyclic Plasticity Of 304 Stainless Steel. ASME. Vol. 11, Jan., 1989, pp106-114.

[54] Dunne F.P.E., Othman A.M., Hall F.R., Hayhurst D.R. Representation Of Uni-Axial Creep Curves Using Continuum Damage Mechanics. Internal Report. March., 1989. The University of Sheffield, Dept. of Mechanical and Process Engineering, Mappin St., Sheffield. To be published in the Journal of Mech. Sci., 1990.

[55] Hayhurst D.R., Dimmer P.R. and Chernuka M.W. Estimates Of The Creep Rupture Lifetime Of Structures Using The Finite Element Method. J.Mech.Phys.Solids, 1975, Vol. 23, PP335-355.

[56] Hayhurst D.R. and Krzeczkowski A.J. Numerical Solution Of Creep Problems. Computer Methods In Applied Mechanics And Engineering Vol.20, 1979,

PP151-171. North-Holland Publishing Co.

[57] Hayhurst D.R. A Time Hardening Transient Creep Solution For Steady Loaded Uni-Axial Tension Panels Containing A Circular And Elliptical Holes Under Conditions Of Plane Stress. Int.J.Mech.Sci. Pergamon Press. Vol. 14, PP885-901, 1972.

[58] Stasa F.L. Applied Finite Element Analysis For Engineers. 1976. C.B.S. International. C.B.S. Publishing, Japan Ltd.

[59] Lambert J.D. Computational Methods In Ordinary Differential Equations. John Wiley & Sons, 1973.

[60] Hall F.R. A Review Of Numerical Integration Procedures For The Solution Of Initial Value Problems; With Special Reference To Their Application Within The Absolute Method, For The Advancement Of Creep Solutions In Time. Internal Report No.FRH04, July 1987. Dept. of Mechanical and Process Engineering, Mappin St., Sheffield.

[61] O.J.A Goncalves F. On The Creep Brittle Rupture Of Structures. PhD. Thesis, Dept., Of Civil Engg., University Colledge Of Swansea, May 1984.

[62] Othman A.M. and Hall F.R. Joint Research Project: The Formulation Of The Z-Transformation Runge-Kutta Method For Inclusion Within The Finite Element Creep Continuum Damage Program Damage-(XX). December 1988.

[63] Hayhurst D. R., Brown P. R. and Morrison C. J. The Role Of Continuum Damage In Creep Crack Growth. Phil. Trans. R. Soc. Lond. A311, pp 131-168 (1984).

[64] Brown P. R. Generation Of Crossed Triangle Compact Tension Specimen Mesh (Fig.5.3) And The First C.D.M. Solution CT-Specimen, University of Leicester.

[65] Myers M.R. and Pilkington R. University of Manchester. Private communication via Prof.D.R.Hayhurst, 1989. University of Sheffield.

[66] Cocks A.C.F. and Ashby M. F. On Creep Fracture By Void Growth. Cambridge University Engineering Department, Trumpington Street, Cambridge. CUED/C/MATS/TR.67 July 1980. And Published, Progress in Materials Science vol. 27, pp 189-244, 1982.

[67] Newman Jr.J.C. Stress Analysis Of The Compact Tension Specimen Including The Effect Of Pin Loading. Fracture Analysis, ASTM STP560, American Soc. for

Testing Materials pp 105-121 (1974).

[68] Hayhurst D. R. Private communication (January 1989).

[69] Frost H.J. and Ashby M.F. Deformation-Mechanism Maps For Pure Iron, Two Austenitic Stainless Steels And A Low-Alloy Ferritic Steel. University Engineering Dept., Trumpington Street, Cambridge. July (1975).

[70] Hayhurst D.R. Private communication (December, 1989).

[71] Chaboche J.L. Continuum Damage Mechanics: Present State And Future Trends, ONERA TP No. 1986-53.

[72] Tvergaard Viggo. Analysis Of Creep Rupture In A Notched Tensile Bar, The Danish Centre For Applied Mathematics And Mechanics, Report No. 300, March 1985.

[73] Rides M. Cocks A.L.F. and Hayhurst D. R. The Elastic Response Of Creep Damaged Materials, Journal of Applied Mechanics, Sept 1989. Vol. 56, pp 493-498.

[74] Webster G.A. Modelling Of Creep Crack Growth. Euro. Mech Colloquium No. 239. Mechanics of Creep Brittle Materials, Leicester University, 15-17 August 1988.

[75] Hayhurst D. R. Private communication (February 1989).

[76] Nishida K. Nikbin K.M. and Webster G.A. Influence Of Net Section Damage On Creep Crack Growth. Journal of Strain Analysis. Vol. 24, No. 2, 1989, I.Mech.E.

[77] Othaman, A. M. Development Of Large Deformation And Rotation Finite Element Program, University of Sheffield, Dept. of Mechanical and Process Engineering, Mappin St., Sheffield. 1988.

[78] Manjoine M.J. Creep Rupture Behaviour Of Weldments. Welding Research Supplement 51-s, February 1982.

[79] Riedel H. and Detampel V. Creep Crack Growth In Ductile, Creep-Resistant Steels. Int. Journal of Fracture 33, pp 239-262, (1987).

[80] Sanauri K. On The Creep Crack Growth Prediction By Local Approach. Engineering Fracture Mechanics, Vol. 25, Nos 5/6, pp 677-691, 1986.

[81] Hayhurst D.R. Morrison C.J. and Brown P.R. Creep Crack Growth. 3rd IUTAM Symposium, Leicester, U.K., September 8-12, 1980, Springer-Verlag (1981).

[82] Kroner E. Elasticity Theory of Materials with Long-Range Cohesive Forces. Int. J. of Solids and Structures, No. 3, pp.731-742, 1967.

[83] Krumhansl J.A. Some Considerations of the Relations between Solid State

Physics and Generalised Continuum Mechanics. Mechanics of Generalised Continua, Eds. Kroner E., Springer Verlag, W. Berlin, W. Germany, pp.298-331, 1968.

[84] Eringen A.C. Linear Theory of Non-local Elasticity and Dispersion in Plane Waves. International J. of Engineering Science, No.10, pp.425-435, 1972.

[85] Bazant S.P., Lin F.B. and Pijaudier-Cabot, G. Yield Limit Degradation: Non-local Continuum with Local Strains". Pre- prints, International Conference on Computational Plasticity, held in Barcelona, Eds. Orote, E., Owen, R. and Hinton, E., University of Wales, Swansea, pp.1757-1779, 1987.

[86] Bazant Z.P. and Pijaudier-Cabot G. Non-local Continuum Damage Localisation Instability and Convergence. J. Applied Mech. June 1988, Vol.55, pp.287-293.

[87] Bazant Z.P. Mechanics of Distributed Cracking. Review Paper, Applied Mech. Rev. Vol.39, No.5, May 1986, pp.665-705.

[88] Chaboche J.L. Phenomelogical Aspects of Continuum Damage Mechanics. XVII International Congress of Theoretical and Applied Mechanics, Grenoble, August 21-27, 1988. ONERA T.P.No.1988-105.

[89] Hayhurst, D.R. Private Communication, 2nd May 1988.

[90] Neville D.J. On the Critical Distance Criteria for Failure at the Tips of Cracks, Minimum Fracture Toughness, and Non-Dimensional Toughness Parameters. J. Mech. Phys. Solids, Vol.36, No.4., pp.443-457, 1988.

[91] Eringen A.C. Theory of Micropolar Elasticity. Fracture, Vol.II., Edited by H. Liebowitz, Academic Press, Ch.7, pp.621-726.

[92] Von der Giessen E. and Tvergaard V. Effect of Creep Cavitation at Sliding Grain Boundaries. Report No.376, D.C.A.M. Denmark, 1988.

[93] Tvergaard V. On Localisation in Ductile Materials Containing Spherical Voids. Int. J. of Fracture. Vol.18, No.4, April 1982.

[94] Tvergaard V. An Analysis of Ductile Rupture Modes At A Crack Tip. J. Mech. Phys. Solids, Vol.35, No.2., pp.151-183, 1987.

[95] Gurson A.L. J. of Engineering Materials and Technology, 99(1977) 2-15, 1977.

[96] Coleman M. C. The Structure Of Weldments And Its Relevance To High Temperature Failure, C.E.G.B. Report M.E.L. No. R/M/N1028, October 1978.

[97] Williams J. A. Prediction Of Residual Lifetime Of Constructions Operating At High Temperature, Proceedings of an International Symposium, Netherlands Inst.

of Welding, 1977, pp 171-200.

[98] Shibily I. A., Summers A. A. P. and Ham W. M. Property Validation Of A Graded Composition Transition Joint. Proceedings of the Third International Conference on Creep and Fracture of Engineering Materials and Structures, The Institute of Metals, pp 741-759.

[99] Rosenthal D. Etude Theorique Du Regime Thermique Pendant La Soudune A L'Arc. Congres National Des Sciences, Comptes Rendus, Bruxelles, 2, 1277, 1935.

[100] Rosenthal D., The Theory Of Moving Sources Of Heat And Its Application To Metal Treatment, Transactions ASME, 68, 849, 1946.

[101] Kohno R. and Jones S. B. An Initial Study Of Arc Energy And Thermal Cycles In The Submerged Arc Welding Of Streel. The Welding Institute, 1978.

[102] Middleton, C. J. and Cane, B. J., Characteristics Of Nature And Distribution Of Constituents Of Multipass Butt Welds, CEGB Report No. RD/L/NTR4.

[103] Alberry P. J. and Jones W.K.C. Diagram For The Prediction Of Weld Heat Affected Zone Microstructures. Metals Technology, July 1977, pp 360-364.

[104] Alberry P. J. and Jones W.I.C.C. Computer Model For Prediction Of Heat Affected Zone Microstructures in Multipass Weldments. Metal Technology, October 1982, vol. 9, pp 414-426.

[105] Alberry, P. J. et al, Weld-Met. Fab, 1977 45, pp 549-653.

[106] Krutz G. and Segerlind L. J., Finite Element Analysis Of Welded Structures, Welding Journal, Welding Research Supplement, vol. 57, 1978, pp 211-216.

[107] Savage W. Apparatus For Studying The Effects of Rapid Thermal Cycles And High Strains Rates On The Elevated Temperature Behaviour of Materials, J. of App. Polymer Science, Vol. VI, issue no. 2, pp 303-315 (1962).

[108] Alberry, P. J. and Jones, W.K.C., Structure And Hardness Of 0.5Cr-Mo-V And 2Cr-Mo Simulated Heat Affected Zone. Metals Technology, December 1977, pp 557-566.

[109] Cane B. J. Collaborative Programme On The Correlation Of Test Data For High Temperature Design Of Welded Steam Pipes. Presentation And Analysis Of Materials Data. CEGB Laboratory Note No. RD/L/210IN81 March 1981.

[110] Coleman M.C. Private Communication, June 1989, CEGB.

[111] Roode F., Etienne C.F. and Von Rossum O. Stress and Strain Analysis For

Creep and Plasticity of Welded Joints In AISI 316. I.Mech.E. 1980, C329/80, pp123-129.

[112] Coleman M. C. Creep Crack Growth In A Cr Mo V Throttle Valve Pressure Vessel, CEGB., Marchwood Engineering Laboratories (MEL), Marchwood, Southampton.

[113] Gooch D. J. and King B. L. Creep Crack Growth In Controlled Microstructure Cr Mo V Heat Affected Zones. Welding Jounral, 59, 10s-18s (1980.

[114] Schuller H. J., Hagn L. and Woitscheck A. (1974) Der Maschinenschaden, 47, pp 1-13.

[115] Coleman, M. C., Type IV Cracking In Ferritic Steel Weldments. CEGB Report No. RD/M/R309 Jan 1981.

[116] Nicholson R. D. Creep Rupture Properties Of Austenitic And Nickel-Based Transition Joints. Metal Technology August 1982, vol. 9, pp 305-311.

[117] Evans R. W. and Wilshire B. An Analysis Of The Creep Fracture Characteristics Of Austenitic Ferritic Steel Transition Welds. Mechanics of Materials 4 (1985), pp 51-65, North Holland.

[118] Nicholson R. D., Williams, J. A., Price D. A. and Lloyd D.J.R. Interface Microstructures And Cracking In Heavy Sectional Dissimilar Metal Welds After Accelerated Thermal Cycled And Creep Loading. CEGB Report No. TPRD/M/1620/R87., March 1987.

[119] Clark J. N. and Allberry P. J. An Observation Of A Creep Rate Mismatch Interaction, Scripta Metallurgica, vol. 14, pp 595-600, 1980.

[120] Clark J. N. The Effect Of A Mismatch In Creep Properties On Creep Damage Rate Distributions. Scripta Metallurgica, vol. 15, pp 1285-1290, 1981.

[121] Nicol D. A. C. Creep Behaviour Of Butt Welded Joints, CEGB Report No. TPRD/M/1257N82, Nov 1982.

[122] Nicol D. A. C. and Williams J. A. The Creep Behaviour Of Cross Weld Specimens Under Uniaxial Loading, CEGB Report No. TRD/M/1302/R83, February 1983.

[123] Bashu S. A., Singh K. and Choudary K. M. Creep Rupture Behaviour Of Low Alloy Ferritic Steel Weldments. High Temperature Technology vol. 5, No. 1, February 1987.

[124] Williams J. A. A Simplified Approach To The Effect Of Specimen Size On the Creep Rupture Of Cross Weld Samples. CEGB Report No. RD/M/N1149, May 1981.

[125] Etienne C. F., Von Rossum O. and Roode F. Creep Of Welded Joints In AISI 316. Int. Conf.,on Eng. Aspects of Creep vols. I and II, I.Mech.E C328/80 pp 113-121 (1980).

[126] Ivarson B. G. and Sandstrom R. Creep of Butt-Welded Tubes. Conf. Creep and Fracture of Engineering Materials and Structures, Swansea 1981, Pineridge Press, Swansea, U.K.

[127] Ivarson B. and Sandstrom R. Creep Deformation And Rupture Of Butt-Welded Tubes Of Cold Worked 316 Steel, Metal Technology, 1980, 7, 440.

[128] Browne R. J., Cane B. J., Parker J. D. and Watters D. J. Creep Failure Analysis Of Butt Welded Tubes. Int. Conf. Creep and Fracture of Engineering Materials and Structures, Swansea 1981, Pineridge Press, Swansea, U.K.

[129] Coleman M. C., Parker J. D., Walters D. J. and Williams J. A. The Deformation Behaviour Of Thick Walled Pipe At Elevated Temperatures. Proc. Int. Conf. on Material 3 (ICM3), Cambridge 1979, Oxford Pergamon Press, vol. 2, ICM3, Cambridge, England, August 1979.

[130] Williams J. A. The Effect Of Material Inhomogeneity On The Creep Deformation Of A Thick Welded Pipe. Int. J. Pres. Ves. & Piping, 11 (1983), pp 1-18.

[131] Coleman M. C., Parker J. D and Waters D. J. The Behaviour Of Ferritic Weldments In Thick Section 0.5Cr 0.5Mo 0.25V Pipe At Elevated Temperature. Int. J. Pres. Ves. & Piping, 18 (1985) pp 277-310.

[132] Bailey R. W. The Utilisation Of Creep Test Data In Engineering Design. Proc. Inst. Mech. Engrs., 131 (1935) p 131.

[133] Coleman M. C. High Temperature Behaviour Of Ferritic Pipe Welds: Experience Of Long-Term Testing. The First Finnish Sea Symposium On Materials Aspects In Life Extension Of Power Plants, Helsinki-Stockholm, pp 19-22, Sept. 1988.

[134] Coleman M. C. Metallurgical Examination Of A Failed Mild Steel 0.5Cr 0.5Mo 0.25V Pipe Weldment, CEGB Report No. TRPD/M/1581/R86, August 1986.

[135] Coleman M. C. and Parker J. D. The High Temperature Deformation and Fracture of Mild Steel Weldments In Thick Section 0.5Cr 0.5Mo 0.25V Pipe, CEGB Report TPRD/M/1494/R85, May 1985.

[136] Coleman M.C. and Parker J.D. Deformation In 2CrMo-0.5CrMoV Pressure Vessel At Elevated Temperature. 1st International Conf. On Creep And Fracture Of Engineering Materials And Structures. University Of Swansea,1981, pp629-643.

[137] Walters D. J. and Coleman M. C. A Comparison Of Measured And Calculated Creep Strains Occurring In A Thick Section 0.5Cr 0.5Mo 0.25V Pipe Component. Proceedings of the Third Intrernational Conference on Creep and Fracture of Engineering Materials, The Inst. of Metals.

[138] Fairbairn J. and Mackie W. W. The Creep Of Thick-Walled Tubes Subjected To Internal Pressure. In Creep in Structures, 1970, Berlin, Springer-Verlag.

[139] Johnson A. An Alternative Definition Of Reference Stress For Creep. Proc. Int. Conf. on Creep and Fatigue in Elevated Temperature Applications, Sheffield, 1974, London, Institute of Mechanical Engineers.

[140] Williams J. A., Coleman M. C. and Walters D. J. Weld Performance Factors For High Temperature Welded Components. 2nd Int. Conf. on Creep and Fracture of Engineering Materials and Structures, University of Swansea, 1984.

[141] Monkman F. C. and Grant N. J. An Empirical Relationship Between Rupture Life And Minimum Creep Rate In Creep Rupture Tests, 59th Annual Meeting, ASTM, ASTM 56, 91 (1956).

[142] Fidler, R., The Effect Of Weld Width On The Performance Of Main Steam Pipes By The Narrow Gap Process. CEGB Report No. TPRD/M/1583/R86.

[143] Fidler R. The Performance Of Narrow Gap Welds In Creep Conditions, CEGB Report No. RD/M/1696/RR88.

[144] Easterling K. Introduction To The Physical Methodology Of Welding. Butterworths Monographs in Materials - University of Lulea, Sweden.

[145] Yeldman D. E., Rowberry T. R., Winnett W. E. and Wright U. S. (1972), CEGB Report SSD/MID/R.8/72.

[146] Masubuchi K. Models Of Stresses And Deformation Due To Welding - A Review, Modelling Of Casting And Welding Processes, p 223,. eds Brody, H. D. and Apelion, D., Metall. Society of AIME, 1981.

[147] Macherauch E. and Wohlfahrt H. Different Sources Of Residual Stress As A Result Of Welding. Conference on Residual Stresses in Welded Construction Construction And Their Effects. p 267 ed Nichols, R. W., The Welding Institute, London, Nov. 1977.

[148] Meeting of 31st May 1989 at CEGB Berkeley between Dr I. Goodall, Dr M. C. Coleman, Dr D. Walters and Dr M. Jones for the CEGB and Prof. D. R. Hayhurst and Mr F. R. Hall of the University of Sheffield.

[149] Coleman M. C. Private Communication 5th June 1989.

[150] Jones, M. R., Private Communication 6th June 1989.

Bless and praise we famous men—

Men of little showing—

For their work continueth,

And their work continueth,

Broad and deep continueth,

Great beyond their knowing!

Stalky & Co., Rudyard Kipling.